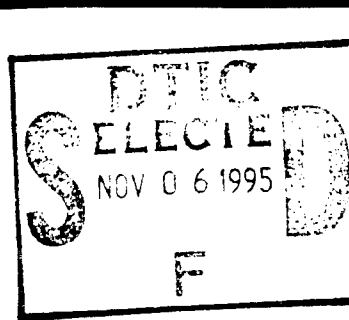


GUIDED-WAVE OPTOELECTRONICS

***Device Characterization,
Analysis, and Design***



DISTRIBUTION STATEMENT A
Approved for public release
Distribution Unlimited

19951103 038

**Edited by
Theodor Tamir,
Giora Griffel,
and
Henry L. Bertoni**

Professor Theodor TAMIR
Department of Electrical Engineering

Tel: (718) 260-3320
Fax: (718) 260-3906

Polytechnic
UNIVERSITY

*"Brooklyn Poly" **

October 24, 1995

Scientific Officer Code: 312
Dr. Yoon S. Park
Office of Naval Research
Ballston Tower One
800 North Quincy St.
Arlington, VA 22217-5660.

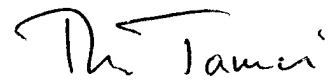
Dear Dr. Park:

Re: Grant No. N00014-95-1-0709 for partial support of the International Symposium on Guided-Wave Optoelectronics, held at the Polytechnic University on October 26-28, 1994.

Attached here please find 3 copies of the Symposium Proceedings, in compliance with the grant awarded to us as above. Additional copies (one each) are being sent to the Grant Administrator and the Defense Technical Information Center, as per the Distribution List accompanying the award letter.

On behalf of the Polytechnic, I wish to express our appreciation for your supporting the Symposium.

Sincerely,



T. Tamir,
University Professor.

cc: J. Schelso

Guided-Wave Optoelectronics

Device Characterization, Analysis, and Design

DTIC QUALITY INSPECTED 1

PREFACE

In 1945, Dr. Ernst Weber founded, and was the first Director of, the Microwave Research Institute (MRI) at Polytechnic University (at that time named the Polytechnic Institute of Brooklyn). MRI gained worldwide recognition in the 50s and 60s for its research in electromagnetic theory, antennas and radiation, network theory and microwave networks, microwave components, and devices. It was also known through its series of 24 topical symposia and the widely distributed hardbound MRI Symposium Proceedings. Rededicated as the Weber Research Institute (WRI) in 1986, the institute currently conducts research in such areas as electromagnetic propagation and antennas, ultrabroadband electromagnetics, pulse power, acoustics, gaseous electronics, plasma physics, solid-state materials, quantum electronics, electromagnetic launchers, and networks. Following MRI tradition, WRI has launched its own series of in-depth topical conferences with published proceedings. Previous conferences in this series were:

Directions in Electromagnetic Wave Modeling; October 1990
Ultra-Wideband Short-Pulse Electromagnetics; October, 1992
Ultra-Wideband Short-Pulse Electromagnetics, II; October, 1994

The proceedings of these conferences were also published by Plenum Press.

This volume constitutes the proceedings of the fourth WRI International Conference dealing with Guided-Wave Optoelectronics: Device Characterization, Analysis and Design. The conference was held October 26–28, 1994, at the Polytechnic University in Brooklyn, New York, in cooperation with the IEEE Lasers and Electro-Optics Society, and with the Optical Society of America.

Theodor Tamir
Giora Griffel
Henry L. Bertoni

CONTENTS

INTRODUCTORY

Scanning the symposium	1
T. Tamir and G. Griffel	
Photonics in telecommunications	3
H. Kogelnik	

LiNbO₃ DEVICES

Development and applications of commercial LiNbO₃ guided-wave devices	5
F. J. Leonberger and R. W. Ade	
Field induced waveguides in LiNbO₃: New developments	9
S. Ruschin and E. Arad	
Electrooptic tunable filters for WDM networks	17
O. Eknayan and H.F. Taylor	
Demonstration of 250 Gb/s all-optical routing control of a photonic crossbar switch	25
I. Glesk and P. R. Prucnal	
An electrode-less integrated Mach-Zehnder interferometer electric field sensor	35
D.H. Naghski, J.T. Boyd, H.E. Jackson, S. Sriram, S.A. Kingsley, and J. Latess	

LASER DEVICES

Monolithic semiconductor MOPAs: How the Watt was won	45
R.J. Lang, R. Parke, D. Mehuys, J. Osinski, S. O'Brian, J. Major and D. Welch	
Multi-wavelength vertical cavity laser arrays grown on a patterned backup substrate	49
C.J. Chang-Hasnain	

Polarization induced enhancement of relative intensity noise and modulation distortion of vertical cavity surface emitting lasers	59
M.S. Wu, L.A. Buckman, G.S. Li, K.Y. Lau and C.J. Chang-Hasnain	
InP based multiple quantum well lasers with an integrated tapered beam expander waveguide	67
R. Ben-Michael, U. Koren, B.I. Miller, M.G. Young, M. Chien and G. Raybon	
Optimal design of combined distributed-feedback/Fabry-Perot structures for vertical cavity surface emitting semiconductor lasers	75
J. Zhou, J. He and M. Cada	
Transmission-line modeling of multi-section DFB lasers	83
C.H. Chen and G. Griffel	
Analysis of gain coupled DFB semiconductor lasers with absorption grating	93
F. Randone and I. Montrosset	
Linewidth reduction by the formation of a fiber external cavity with the vertical emission of a distributed Bragg reflector laser . . .	105
A.L. Cook and H.D. Hendricks	
Distributed feedback lasers for diode laser gas sensing	115
P. York, R. Martinelli, R. Menna, D. Cooper, H. Riris and C. Carlise	
Modeling of optical gain due to excitonic transitions in index-guided ZnCdSe/ZnMgSSe multiple quantum well blue-green lasers	125
W. Huang and F.C. Jain	
Low threshold current density wavelength shifting between N=1 and N=2 transitions in n-type modulation doped GaAs/AlGaAs quantum well lasers	133
G.E. Kohnke and G.W. Wicks	

SWITCHES AND COUPLING DEVICES

High-speed photonic waveguide switch arrays and optical amplifier gates in InGaAsP/InP for communications applications . .	139
H. Melchior	
Analysis of N x M waveguide splitters and couplers with multimode guiding sections	143
E.R. Thoen, L.A. Molter and J.P. Donnelly	
Wavelength-flattened three core optical coupler power splitters in ion-exchanged glass	155
G. Hewa-Gamage, H. Hatami-Hanza and P.L. Chu	

Single-band and multi-band optical waveguide wavelength filters using ion-exchange process	167
G. Hewa-Gamage and P.L. Chu	
Synthesis of optical interconnects and logic gates	177
L.S. Tamil and A.K. Jordan	
Modelling of a versatile all-optical Mach-Zehnder switch	187
G.J.M. Krijnen, A. Villeneuve, G.I. Stegeman, S. Aitchison, P.V. Lambeck and H.J.W.M. Hoekstra	
A guide/antiguide structure for implementing self-imaging waveguide beamsplitters	197
T.J. Tayag and G.W. Bryant	
Strained-layer superlattices for polarization-insensitive integrated waveguide applications	205
D.A. Trivedi and N.G. Anderson	
Power coupling efficiency for electro-optic directional coupler switch	213
T. Wongcharoen, B.M.A. Rahman and K.T.V. Grattan	
Design optimization and fabrication of a widened X-branch demultiplexer by ion-exchange in glass	221
G.L. Yip and L.J.M. Babin	

MODULATORS

Recent progress in the development of traveling wave LiNbO₃ modulators	231
W.K. Burns	
Integrated magnetooptic Bragg cell modules and applications	237
C.S. Tsai	
High-speed wideband integrated magneto-optic frequency shifter and modulator	249
C.S. Tsai and Y. Pu	
GaAs VLSI-compatible OEIC technology: Design for a quantum well n-i-p-i phase modulator	257
S.D. Koehler and E.M. Garmire	
Design and analysis of surface-normal Fabry-Perot optical modulators in the near infrared (InGaAs/GaAs) and blue-green (ZnCdSe/ZnMgSSe) regions	269
S.K. Cheung, W. Huang, F. Jain, R. Sachs and T. Grudkowski	
Optical phase modulation of a quantum well-dielectric slab waveguide	279
H.L. Cui, C.D. Hechtman, E. Lenzing and B.S. Perlman	

Characterization of optical modulators for application in lightwave links at CERN	287
M. Glick, F. Vasey, G. Stefanini, P. Duthie, N. Green, A. Moseley, D. Robbins, D. Streames-Smith, N. Try, R. Cingolani and the RD23 collaboration	

PERIODIC STRUCTURES

Periodic waveguide structures: 101 varieties!	295
R. C. Alferness	
Waveguide grating router components for WDM networks	297
I.P. Kaminow	
Distributed feedback channel dropping filters	299
H.A. Haus, J.N. Damask and M.J. Khan	
Periodically segmented waveguides	313
A. Hardy, Z. Weissman, D. Nir and S. Ruschin	
Guided wave deflectors using gratings with slowly-varying groove depth for beam shaping	321
N. Ramanujam, J.J. Burke and L. Li	
Waveguide coupling gratings: Attractive features and dangerous pitfalls	333
O. Parriaux, V.A. Sychugov and A.V. Tishchenko	
Integrated-optic displacement sensor using a pair of grating couplers	355
S. Ura, T. Suhara and H. Nishihara	
Rigorous guided-wave solutions for planar grating structures	363
T. Tamir and S. Zhang	

NONLINEAR TECHNIQUES

Cascading: Modelling a new route to large optical nonlinearities and all-optical devices	371
G.Stegeman, R. Schiek, G. Krijnen, W. Torruellas, M. Sundheimer, E. VanStryland, G. Menyuk, L. Torner and G. Assanto	
Nonlinear phase-shifts by cascading in the Cerenkov regime	381
G.J.M. Krijnen, W. Storrueellas, G.I. Stegeman, H.J.W.M. Hoekstra and P.V. Lambeck	
Ultrashort pulse propagation in nonlinear planar optical waveguides	391
G.P. Agrawal and A.T. Ryan	

$\lambda/4$-shifted nonlinear periodic structure: Theory of low-intensity switching	399
S. Radic, N. George and G.P. Agrawal	
Frequency conversion in Ti:LiNbO₃ channel waveguides	407
M. Cada and J. Ctyroky	
Spatial solitons in superlattice with near resonant nonlinearity ...	415
C.S. Zhou, C. Liao and C. Lee	

NUMERICAL METHODS

Computer-aided analysis and design in guided-wave optoelectronics	423
W.-P. Huang, C. Xu and B. Little	
Parallel-processing finite-difference beam propagation methods ...	429
H.M. Masoudi and J.M. Arnold	
An explicit and stable finite difference BPM for applications to device analysis and design	435
F. Xiang and G.L. Yip	
An OEIC CAD system for passive and active planar waveguide circuits	445
R. Amantea, P.L. Demers, M. Ettenberg and D.J. Channin	
Finite element solution of nonlinear optical waveguides	455
B.M.A. Rahman, P.A. Buah and K.T.V. Grattan	

PHOTONIC BANDGAPS AND RESONANCES

Highly efficient light-emitting diodes with microcavities	463
E. F. Schubert, N.E.J. Hunt, M. Micovic, R.J. Malik, D.L. Sivco, A.Y. Cho and G.J. Zydzik	
Wide stop band optical filters from photonic band gap air bridges ...	477
J.C. Chen, H.A. Haus, J.N. Winn, S. Fan and J.D. Joannopoulos	
Applications and characterization of a new face-centered-cubic photonic crystal	485
K. Agi, E.R. Brown, C.D. Dill, K.A. McIntosh, O.B. McMahon, K.M. Molvar and K.J. Malloy	
Microparticle photonics: Fiber optic excitation of MDRs	495
S. Arnold, A. Serpengüzel and G. Griffel	
Index	499

Guided-Wave Optoelectronics

Device Characterization, Analysis, and Design

SCANNING THE SYMPOSIUM

T. Tamir and G. Griffel

Polytechnic University
Electrical Engineering Dept.
Six Metrotech Center
Brooklyn, NY 11201.

BACKGROUND AND PERSPECTIVES

The International Symposium on Guided-Wave Optoelectronics held October 26-28, 1994, was the fourth in the conference series sponsored by the Weber Research Institute of Polytechnic University. Following the successful format of preceding conferences, the Symposium strived to achieve a critical in-depth coverage of fundamental issues in a rapidly evolving area. Its aim was to examine guided-wave phenomena and related aspects of optoelectronics, and to review state-of-the-art techniques for solving electromagnetic problems that arise in that field.

The Symposium specifically addressed characterization and modeling methods that are most relevant to the analysis and design of optoelectronic devices. The focus was on composite devices employing guided-wave components that connect multiple optical and/or electronic elements in hybrid, integrated or other forms. Basic theory, analytical and numerical methods were stressed rather than fabrication and experimental techniques. Furthermore, all speakers were urged to start with a retrospective synopsis of approaches used in the past and to take a critical view of current techniques.

To provide a well coordinated coverage, distinguished experts in the area were invited to present review-type talks. The invited speakers were selected amongst prominent U.S. and foreign university and industry scientists who are active in the development and/or study of optoelectronics devices. The IEEE Lasers and Electro-Optics Society (IEEE/LEOS) and the Optical Society of America (OSA) agreed to cooperatively sponsor the Symposium. With their help, a call for papers was circulated and mailings were forwarded to members whose professional affiliation was in the area covered by the Symposium.

A substantial number of papers were accepted for presentation from industry, research center and academic institutes. Consistent with past WRI conferences, the Symposium program was structured so that no parallel sessions were

held. A poster session was also included in order to facilitate the presentation of a larger number of relevant papers. This format provided the participants with an interactive environment that fostered an integrated exposure to all facets covered by the Symposium.

Funding from several government agencies was obtained to support the Symposium. A major portion of this funding was used to support participating graduate students and post-Doctoral fellows from other Universities who could not otherwise afford to attend the meeting.

THE TECHNICAL PROGRAM

The finalized program included a total of 61 papers which were grouped into 13 sessions. The Symposium started with an Introductory Session involving invited overviews on optoelectronic devices and their commercial importance. This was followed by more specialized sessions, each of which opened with one or two invited talks followed by contributed papers. Discussions were encouraged after each paper. Additional lively and more detailed discussions continued during the intermissions, which were scheduled so as to offer ample time for that purpose.

The coverage of the various sessions is well described by the Table of Contents. To summarize, we note here that it includes papers on:

- passive components (filters, routers, periodic structures, etc.),
- active components (semiconductor lasers and amplifiers, modulators, switches, etc.),
- nonlinear techniques and their application to new devices,
- numerical and analytical methods,
- novel techniques for potential applications in the future.

Comments received at and after the Symposium were very favorable and its basic scientific character was highly commended. Participants also noted that, in contrast to other meetings in this technical area, they had enjoyed the more relaxed focus that was placed on fundamental issues rather than on the intricacies of very specific devices. Younger attendees expressed their appreciation for the opportunity to become better acquainted with fundamental aspects of the optoelectronics area and to meet many of its respected leaders.

The Symposium Proceedings include almost all the papers that were presented. The sequence of these papers is somewhat different from that at the conference, mostly because each one is placed under its own appropriate area.

ACKNOWLEDGMENTS

The Symposium Co-Chairs wish to express their thanks to Carletta Lino, Pat Parsons and Liz Walldov who helped greatly in achieving a smoothly running Symposium and a high quality product for its Proceedings. The support received from the National Science Foundation, the Army Research Office, the Air Force Office of Scientific Research and the Office of Naval Research is also gratefully acknowledged.

PHOTONICS IN TELECOMMUNICATIONS

Herwig Kogelnik

AT&T Bell Laboratories
Crawford Hill Laboratory
Holmdel, New Jersey, USA

Photonics has already had a major impact on telecommunications, but, at the same time, the technology continues to advance at a very rapid pace.

For long distances, the success of this technology is unquestioned. Since the deployment of the first transatlantic lightwave system in 1988, several other undersea systems have been installed in the Atlantic and Pacific, and more are planned. On land, photonics has played a major role in the digitization of the long-haul network, and more than 40 million km of fiber are now installed worldwide. Transmission systems have been developed that can transmit at 2.5 Gb/s speeds under the new SONET standards. Results from the research laboratories project even higher transmission speeds and further increased capacity by using wavelength-division multiplexing.

Recent innovations promise yet better capabilities for current applications and to open up new ones. These advances include erbium-doped fiber amplifiers, quantum-well lasers, photonic integrated circuits and a better understanding of nonlinear optics in fibers.

A major challenge for the future of photonics is the creation of cost-effective technology for shorter distance applications such as CATV transmission, fiber-in-the-loop, optical data links and optical interconnects. Advances in opto-electronic integration in semiconductors and the mastery of compact wavelength-control and wavelength-division-multiplexing techniques are among the approaches that may help realize the dream of a true mass-market for photonics.

In the field of optical integration, there has been considerable progress in the research laboratories of the world for more than two decades. The absence of practical applications, however, has been a severe test of the patience of the R&D community. Only very recently did we see the first commercial applications of integrated optics, but not yet on a large scale. These examples include the distributed feedback (DFB) laser, which was originally conceived as an integrated optical device. The DFB laser is now used in high-capacity links of long-haul fiber networks where high-spectral purity semiconductor lasers are required. It is also

increasingly utilized in fiber-optic cable TV (CATV) links, where it exhibits superior linear amplitude modulation characteristics.

Another example for the commercial application of integrated optics is the use of highspeed, guided-wave LiNbO_3 modulators, which are incorporated in lightwave test sets for the analysis of lightwave components and systems, and, recently these modulators are also used for analog CATV transmission.

The early goals of integrated optics were modeled after those of electronic integrated circuits. They include miniaturization and compactness, improved reliability, the provision of complex circuitry at low cost and the potential for convenient mass fabrication. One key word to focus on is the word **complex**. When we examine the trends in the photonic applications mentioned above, we notice that the first successes were achieved in very simple systems: point-to-point transmission of information in undersea lightwave systems and in long-haul terrestrial optical fiber systems. The recent trend, however, is to fiber systems of shorter and shorter distance and to systems of increasing complexity. This is already evident in CATV links, in fiber in the loop applications such as passive optical networks (PONs), in optical interconnects and optical cross-connects. As the complexity of these systems increases, the potential for integrated optics applications should increase. Ultimately we may see systems that are so complex that they will depend on optical integration for their effective implementation.

DEVELOPMENT AND APPLICATIONS OF COMMERCIAL LiNbO₃ GUIDED-WAVE DEVICES

Fred J. Leonberger and Robert W. Ade
United Technologies Photonics, Inc.

Integrated optic devices have been commercially available since the late 1980s. In the past several years there has been a significant increase in the availability and utilization of these devices, primarily those fabricated in LiNbO₃ and glass. There are now more than a dozen companies providing a large variety of standard and custom devices, which are being used in numerous field trials and in commercial systems. This review will focus on the available LiNbO₃ devices and some of their primary commercial applications, with examples drawn from CATV, antenna remoting, telecommunications and fiber optic gyroscopes.

Commercial LiNbO₃ devices are fabricated by either Ti indiffusion or by annealed proton exchange (APE). Several types of phase and intensity modulators are available with a variety of bandwidths in the 0.5-18 GHz range. Ti indiffused devices, offered by almost all merchant suppliers, are generally used for applications in the 1.3-1.5 micron range. APE devices, offered solely by United Technologies Photonics (UT Photonics), are also well suited for 1.3-1.5 micron applications, and are the preferred choice for use at 0.8 microns due to their power handling capacity, and for applications that exploit their inherent polarizing property.

One of the primary commercial applications of LiNbO₃ guided-wave devices has been in externally modulated transmitters for fiber optic CATV transmission systems¹. Several manufacturers of CATV transmission systems are utilizing integrated optic modulators in conjunction with high power solid state laser sources to enable long distance, high linearity transmission of AM VSB video signals. The modulator used is typically a Y-fed balanced bridge modulator with low acoustic and phase ripple across the 40-760 MHz passband. The modulator must be linearized by one of several techniques to achieve adequate low-distortion performance. Leading companies that provide commercially available systems are Harmonic Lightwaves and Synchronous Communications. These systems typically are used for AM supertrunking and fiber to the feeder and can handle up to 80 channels while meeting CATV-industry specifications (CTB and CSO <-65dB, CNR > 53 dBc)^{2,3}.

Antenna remoting is another area where there has been considerable utilization of LiNbO₃ guided-wave devices. This application involves locating an optical transmitter near the antenna and an optical receiver at a remote site where demodulation electronics are located.

Systems of this type, which utilize externally modulated transmitters consisting of LiNbO₃ modulators and diode-pumped solid state lasers, have been demonstrated for analog applications at UHF and microwave frequencies by Hughes and UT Photonics. The advantages of these systems include high dynamic range, low noise figure, wide bandwidth (to 18 GHz), possible rf gain, and environmental robustness. Typical performance specifications are zero dB gain, 4 dB noise figure and 106 dB/Hz^{2/3} spurious-free dynamic range over an 18 GHz bandwidth⁴.

In fiber-based telecommunications, LiNbO₃ devices are being used primarily for highspeed digital links. External modulation has been the technology of choice for field trials at the 5 and 10 Gbs range for systems generally operating at 1.55 microns and using EDFAs because these modulators can provide chirp-free performance. NTT has reported 10⁻⁹ BER for a 10 Gbs trial over 327 km of installed dispersion shifted fiber utilizing a LiNbO₃ modulator and a DFB laser source with 4 fiber amplifiers⁵. Similarly, AT&T has reported a field trial in which an externally modulated 1.5-micron source was used with conventional 1.3 micron zero dispersion fiber to transmit 2.5-Gbs data through 12 fiber amplifiers over a total distance of 770 km⁶. These demonstrations used 5-10 GHz traveling wave modulators with low drive voltage,⁷ and in the AT&T trial, a dual balanced electrode for chirp control⁸.

LiNbO₃ devices have been utilized for many years in the development of Fiber Optic Gyros (FOG). Because FOGs contain no moving parts, they offer many advantages over mechanical gyros; high reliability and performance over a broad range of environmental conditions, low maintenance requirements, and long operational life. Numerous field trials of LiNbO₃-based FOGs have been reported by the major guidance companies⁹. Moderate accuracy FOGs (1-0.1°/hr) have been demonstrated in these trials. Although initially designed to meet the needs of the defense community, these devices are now being investigated for commercial applications such as automotive navigation, active suspensions and robotics. Since 1988, Alcatel-Standard Elektrik Lorenz in Germany has produced over 500 FOG systems that utilize integrated optic components. For FOGs to find widespread commercial use the cost of the components, including the integrated optic chip, must be substantially reduced. As the volume of these devices continues to grow, the cost reductions required for the commercial applications are being realized. FOG applications have also driven the development of robust pigtailling and packaging, as illustrated by the <0.5 dB insertion loss variation measured during temperature cycling from 45° to +125°C. for 10 days¹⁰.

In conclusion, LiNbO₃ devices have already found numerous commercial applications and are increasingly being used in advanced system field trials. The integrated optics business undoubtedly will continue to grow as the applications described above expand and as new commercial applications emerge.

REFERENCES

1. G. S. Maurer et al, SPIE OE Fibers'92, Boston, MA.
2. M. Nazarathy et al, IEEE LEOS Topical Meeting on Broadband Analog and Digital Optoelectronics (1992).
3. R. J. Plastow, *ibid*.
4. S.W. Merritt and G.W. Drake, 4th Biennial DoD Fiber Optics/Photonics Conference (McLean, VA, 1994).
5. K. Nakagawa et al, IEEE LTS, February 1992, p. 19.
6. M. L. Kao et al, Electron. Lett. 28, 687 (1992)

7. See, for example, K. Noguchi et al, IEEE Photon. Tech. Lett. 5, 52 (1993), and references therein.
8. S. K. Korotky et al, IEEE/OSA Topical Meeting on Integrated Photonics Research, (Washington, DC, 1991).
9. Proceedings of SPIE 15th Anniversary FOG Conference (SPIE, Bellingham, WA, 1991)
10. P. G. Suchoski and G. R. Boivin, SPIE OE Fibers'92 (Boston, MA, 1992).

FIELD INDUCED WAVEGUIDES IN LiNbO_3 :NEW DEVELOPMENTS

S. Ruschin and E. Arad

Department of Electrical Engineering-Physical Electronics
Faculty of Engineering, Tel-Aviv University
Tel-Aviv 69978, Israel

INTRODUCTION

In field induced waveguides, the guiding effect is produced via the electro-optic effect by applying a voltage difference on coplanar electrodes separated by a gap where the waveguiding action takes place. These kind of guides combine inherently both, wave guiding and modulation. The first version of these modulators were introduced back in 1971 [1], and required operation voltages of the order of 300 Volts. Later developments [2]-[4], allowed operation at much lower voltages and shorter overall device lengths.

In this article, we report the structure, processing and characterization of field-induced waveguides (FIG), based on LiNbO_3 substrates, in which a planar waveguide was formed by a combined Ti-indiffusion Li outdiffusion process [5]. This planar waveguide provided the confinement of the radiation in one (depth) dimension. The confinement in the lateral direction was provided by coplanar electrodes, separated by a gap of about $2\mu\text{m}$. The permanent confinement effect of the planar guide, thus alleviated the voltage requirement on the electrodes required to produce a mode of sizable spot dimensions.

A typical transmission vs. voltage characterization curve for these type of devices is shown in Figure 1. It corresponds to the case of the permanent slab-type waveguide being single-moded. One observes here a clear cancellation of the transmission when the sign of the voltage applied is reversed. This is due to the *anti-guiding* effect induced when the direction of the applied electric field is reversed. Extinction ratios better than 20dB were measured. The decrease in transmission at higher voltages is due to a reduction of the overlap between the field induced mode and the mode of the fiber which coupled radiation into the device.

A very significant reduction in switching voltages was observed when buried modes were involved in the waveguiding structure. Interference effects, between two such adjacent buried modes were responsible for modulation effects at definite depths of from the surface of the substrate, a phenomenon we denominated *mode beating* effect. The formation of buried modes, and the beating effect are described in the next sections.

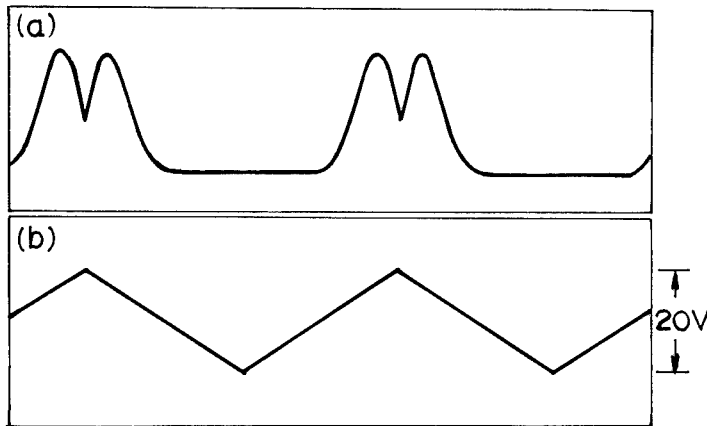


Figure 1: Transmission (upper trace) and applied voltage (lower trace) for a modulator based on single-moded permanent planar waveguide.

BURIED MODES IN Ti DIFFUSED AND Li OUTDIFFUSED LiNbO₃

Buried waveguides are of evident interest, since they are expected to possess low losses and a symmetrized mode spot. A variety of technologies have been reported that achieve buried guides, including proton exchange[6], Ti-diffusion and proton exchange combination[7] and ion implantation[8]. In this work we present a technique which yields both surface and buried modes which can be distinctly excited. The technique is based on a combination Ti diffusion and Li outdiffusion processes, which both lead to an increase in refractive indices, but at different penetration ranges.

The experiment included the fabrication of Ti:LiNbO₃ single mode x-propagating planar waveguides and the characterization of their optical waveguiding properties. 160Å of Titanium were e-beam evaporated on Y-cut LiNbO₃ substrates and indiffused at a temperature of 1050°C for 3.5 hours. The Ti in-diffusion process took place in flowing Ar gas atmosphere replaced by O₂ during cool-down, to allow reoxidation. In order to control the Li out-diffusion process the gases were passed through a water bubbler, which introduced water vapor into the diffusion furnace [9]. The water was heated to a temperature of 80°C and the gas flow rate was adjusted to 1 lit/min. For comparison purpose, samples containing channel waveguides 3 to 10µm wide were prepared under the same diffusion conditions. The planar waveguides were optically characterized by end-fire coupling of light using an optical fiber. The output facet was imaged onto a vidicon camera and monitored. Using a video analyzing system, we were able to view and plot each of the TV lines representing a vertical cross section of the mode profile. Figure 2 presents the near field profiles of the slab waveguide modes, using He-Ne (0.6328µm) light. The different graphs relate to different depth positions of the input fiber. One can see that by varying the vertical position of the fiber we could excite different field distributions which correspond to specific guided modes, as was demonstrated by means of calculations. The planar waveguide supported three TE (extraordinary polarization) and one TM (ordinary polarization) depth modes. The TE₀ and the TM₀ modes which are guided close to the surface, are attributed mainly to the indiffused Ti. The other two TE modes are buried below the surface and are attributed to Li out-diffusion. We carried out the same experiment while coupling-in light at longer wavelengths: $\lambda=0.83$ and $\lambda=1.3\mu\text{m}$.

Two TE modes were observed for $0.83\mu\text{m}$ excitation, their profiles being broader as expected, while for $1.3\mu\text{m}$ wavelength only one TE mode was observed. The samples containing channel waveguides did not show any sign of out-diffusion, since no planar extraordinary polarization modes appeared. The different results between the two kinds of specimens imply that the presence of a Ti layer at the beginning of the diffusion process affects drastically the cancellation of Li out-diffusion by water vapor. In order to examine the influence of the water vapor partial pressure inside the furnace tube on Li out-diffusion, we conducted the same experiment only raising the water bubbler temperature up to 95°C . The resulting planar waveguides supported only two TE modes, one buried below the surface. The reduced number of guided modes imply that Li out-diffusion decreases as the water vapor partial pressure increases but it cannot be completely canceled. A more extensive discussion regarding the mechanism responsible for the appearance of the buried modes, can be found in reference[5].

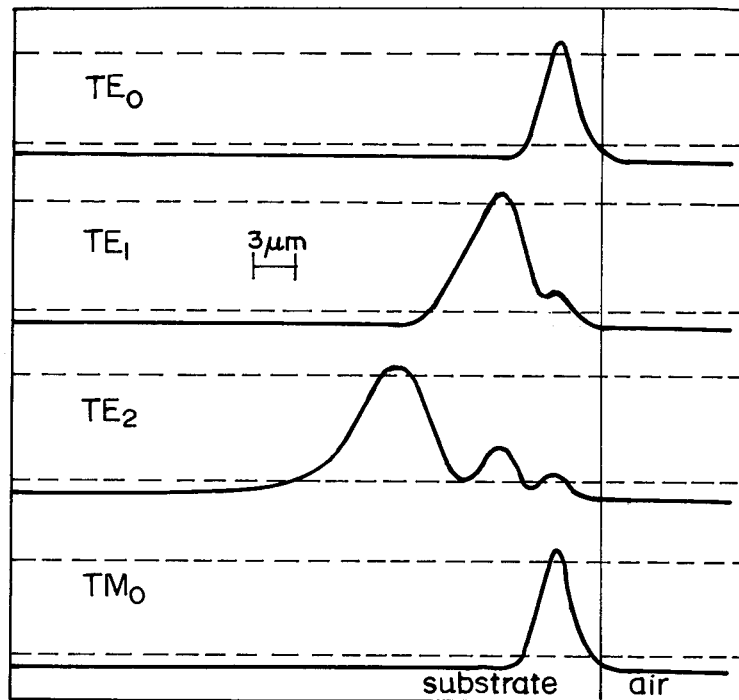


Figure 2. Measured near field profiles of the slab waveguide modes in the depth direction. The TE_0 and TM_0 modes are related to the Ti indiffusion and the two buried modes, TE_1 and TE_2 are attributed to Li outdiffusion

Substitution of the diffusion parameters used in our experiment into the theoretical Gaussian refractive index profile of a Ti diffused slab waveguide [10,11] furnishes an index profile given by:

$$n(y) = n_s + \Delta n^{\text{max}} \cdot \exp\left[-\left(\frac{y}{d}\right)^2\right] \quad (1)$$

with $\Delta n^{\max} = 2.5 \times 10^{-3}$ and $d = 3.3 \mu\text{m}$. A waveguide with these parameters, can support only one TE and one TM mode at $\lambda = 0.6328 \mu\text{m}$, with penetration depths approximately equal to $3 \mu\text{m}$, while in our experiments, two additional TE modes, much deeper penetrating, were observed (see Figure 2). On the other hand, trying to apply a pure out-diffusion model as described by Carruthers et. al.[12] results in a waveguide supporting a total of 9 TE modes, in contradiction to our experimental results. This fact emphasizes that a pure bulk out-diffusion model is also inadequate in the presence of Ti slab, and that there is another mechanism responsible for Li out-diffusion during Ti in-diffusion[5].

We deduce that there is a need to introduce a correction to the Gaussian extraordinary index profile, which accounts for the effect of Li out-diffusion in the planar waveguide. The extraordinary index profile we suggest includes a composition of a Gaussian and exponential functions as follows (see Figure 3):

$$n(y) = n_s + \Delta n_1^{\max} \cdot \exp\left[-\left(\frac{y}{d}\right)^2\right] + \Delta n_2^{\max} \cdot \exp\left[-\left(\frac{y}{b}\right)\right] \quad (2)$$

This model has two parameters to be determined, namely: Δn_2^{\max} the maximum index change due to Li out-diffusion, and b , the decay distance of the exponential profile. These parameters were found by best fitting of the calculated and measured mode profiles. A direct numerical method was used to solve the one dimensional wave equation which governs the mode spatial distribution of the waveguide. The best fit corresponded to $\Delta n_{2\max} = 0.001$ and $b = 9 \mu\text{m}$. The profiles calculated by means of these parameters fitted very well those measured and shown in Figure 2. Calculations performed at $\lambda = 0.83 \mu\text{m}$ and at $\lambda = 0.83 \mu\text{m}$ also furnished satisfactory results in terms of number of modes and mode shapes.

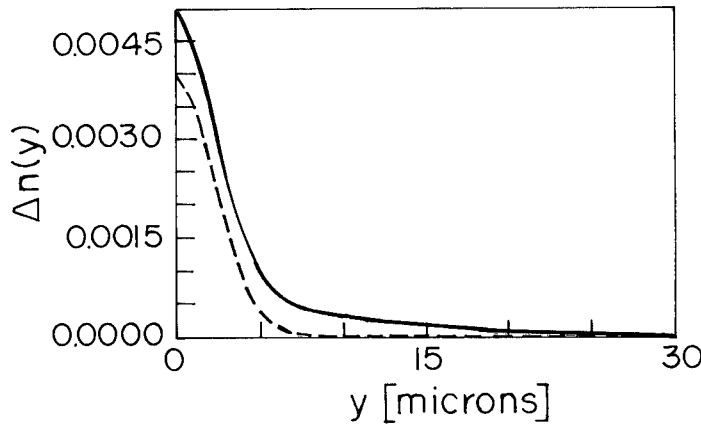


Figure 3. Theoretical refractive index profiles in the combined Ti indiffused and Li outdiffused waveguide. Dotted line indicates the profile of a pure Ti indiffused guide.

INTENSITY MODULATION BY MEANS OF BURIED MODES BEATING

The buried mode beating effect was noticed when mode profile scans were made in the depth direction in the presence of electric field induced by coplanar electrodes in a field-induced waveguide configuration. Two such scans are shown in Figure 4. Here two buried modes were excited simultaneously by suitably placing the optical fiber at the entrance plane of the device. One clearly observes the appearance of a "bump" in the upper trace profile of Figure 4 which is induced by a change in voltage of the order of 1.5 Volt.

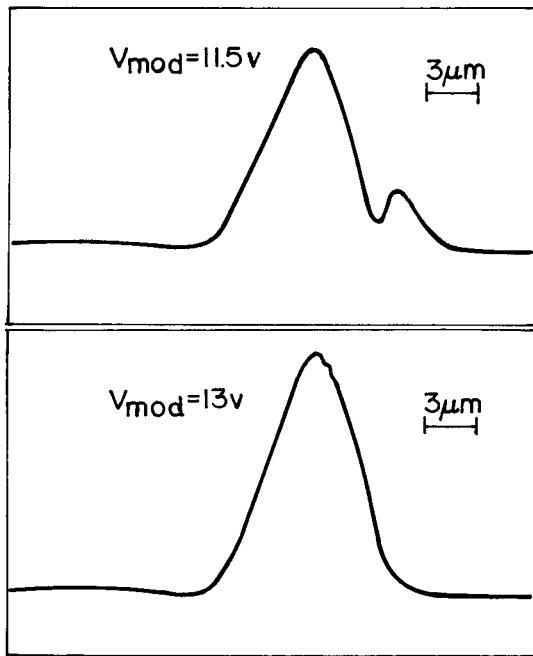


Figure 4. Intensity profile depth scans for modes affected by a transverse electric field induced by coplanar electrodes. Values of voltages applied to electrodes are indicated.

When a modulator based on FIG was fabricated by deposition of coplanar electrodes, on substrates containing buried modes, entirely distinct modulation behavior was observed as shown in Figure 5. Here the transmission of the waveguide is displayed for varying voltage when the input fiber is placed at different depth distances from the surface. In this last figure we can observe, that when the input fiber was located $6\mu m$ below the surface, a modulation effect is obtained, which is induced by very low voltage changes, of the order of 0.8 volts. This fact is particularly remarkable when considering that the entire length of the device was 15mm, and that the corresponding switching voltage-length product is lower by a factor of 1/4 as compared to conventional modulators based on $LiNbO_3$ technology. The interpretation of this modulation behavior is based on an effect we denominated *field-induced mode beating*. According to it, the application of increasing

voltage on the electrodes, not only confines better the mode in the lateral dimension, but also lifts the mode field distribution in the *depth* direction. Thus, buried modes are pushed upwards towards regions of higher refractive index, and the overall effective index change is significantly larger than the one expected from the pure electro-optic effect. If two modes are excited by the input fiber, they will experience distinctly this upwards pulling effect, their effective refractive indices will change correspondingly, and an enhanced beating effect is obtained. This mechanism was supported by numerical simulations.

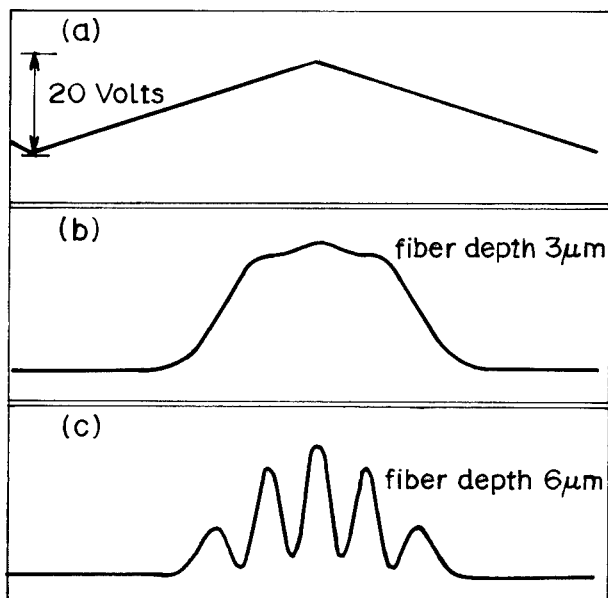


Figure 5. Transmission traces ((a) and (b)), and applied voltage trace (c) for a modulator based on buried planar modes. Different buried mode combinations were excited by varying the depth position of the input fiber.

CONCLUDING REMARKS

We expect to continue to study and improve devices based on field-induced waveguides. Among other features, we expect to reduce the insertion losses in the device by the incorporation of tapered permanent channel waveguides, and mainly to develop switching devices in different configurations, based on induced mode interference effects similar to the one discussed above.

References:

- [1] D. J. Chanin, *Appl. Phys. Lett.* **19**, 128, (1971).
- [2] I. Savatinova, S. Tonchev, K. Pushkarov, and F. Scharf, *J. Opt. Commun.* **1**, 10, (1984)
- [3] N.A.F. Jaeger and L. Young, *IEEE J. of Quant. Electron.* **25**, 720, (1989).

- [4] T.C. Huang, Y. Chung, N. Dagli and L. A. Coldren, *Appl. Phys. Lett.* **57**, 114, (1990).
- [5] E. Arad and S. Ruschin, *Appl. Phys. Lett.* **62**, 2194, (1993).
- [6] J. L. Jackel and J. J. Johnson, *Electron. Lett.* **27**, 3360, (1991).
- [7] P. Jiang, F. Zhou, P. J. R. Laybourn and R. M. De La Rue, *IEEE Photon. Tech. Lett.* **4**, 883, (1992).
- [8] P.J. Chandler, L. Zhang and P.D. Townsend, *Electron. Lett.* **26**, 332, (1990).
- [9] A. Rasch, Rottschalk and W. Karthe, *J. Opt. Commun.* **6**, 4, (1985).
- [10] C. Canali, C. De Bernardi, M. De Sario, A. Loffredo, G. Mazzi and S. Morasca, *J. Of Lightwave Tech.*, **4**, 951 (1986).
- [11] M. Fukuma and J. Noda, *Appl. Opt.*, **19**, 591 (1980).
- [12] J. R. Carruthers, I. P. Kaminow and L. W. Stulz, *Appl. Opt.* **13**, 2333 (1974).

ELECTROOPTIC TUNABLE FILTERS FOR WDM NETWORKS

O. Eknayan and H.F. Taylor

Department of Electrical Engineering
Texas A&M University
College Station, Texas 77843

BACKGROUND

An attractive component for wavelength division multiplexing (WDM) in fiber optic networks is a four-port, tunable channel-dropping filter [1]. Such components are important to increase the bit rate for high capacity optical networks by better utilization of the fiber bandwidth, and also in switching functions for efficient signal routing. Polarization independence is a key requirement, and high speed ($<1 \mu\text{s}$) tuning is needed for packet-switching. Tunable wavelength filters have been produced in a number of materials using acoustooptic and electrooptic tuning schemes as well as movable gratings [2], [3]. This paper discusses the development of electrooptically tunable filters in ferroelectric LiTaO_3 crystals. These filters make use of the static strain-optic (SSO) effect for phase matched polarization coupling in diffused channel waveguides. The use of the SSO effect in producing low-loss channel waveguides in LiNbO_3 and LiTaO_3 substrates, as well as in tungsten bronze $\text{Sr}_{0.6}\text{Ba}_{0.4}\text{Nb}_2\text{O}_6$ (SBN:60) and BSTN crystals [4] is also presented. The tungsten bronzes are attractive materials for making channel-dropping filters due to their larger r_{33} electrooptic coefficients [5], which could make it possible to increase the number of accessible wavelength channels and reduce electrooptic tuning voltages.

STRAIN-INDUCED OPTICAL WAVEGUIDES

Optical waveguides in ferroelectric crystals are generally formed by changing the composition or stoichiometry of a substrate material by processes such as outdiffusion [6], in-diffusion [7], or ion-exchange [8]. A simple technique for making waveguides in ferroelectric substrate materials has been developed recently using strain induced from a surface film deposited at an elevated temperature [9]. Waveguides are thus produced without altering the composition of the substrate. The resultant waveguides exhibit low propagation losses and support guided modes for both TE and TM polarizations.

To produce channel waveguides, a thick SiO_2 film is deposited by e-beam evaporation on a substrate while maintaining its temperature at $\sim 300^\circ\text{C}$ during evaporation, then allowing it to cool to room temperature. This induces a compressive strain in the film because the thermal expansion coefficient of the film is typically less than that in the substrates by at least an order of magnitude. Using photolithography, straight channel

patterns are next delineated in the SiO₂ film by reactive ion etching. Formation of a channel in the oxide frees the film to expand towards the center near the edges of the etched pattern. The process of strain relief in the film results in a localized compressive strain in the substrate in the vicinity of the channel. This induces an index change in the crystal via the strain-optic effect. Channel waveguides have been produced by this method in X-cut LiNbO₃ and LiTaO₃ substrates by using the longitudinal strain component S_3 that is induced in the z-direction, and also in Z-cut SBN:60 and BSTN substrates by using the longitudinal strain component S_1 that is induced in the x-direction. The refractive index changes from the strain-optic effect, Δn_i^{so} , with $i = 1, 3$ corresponding to TM and TE polarization, respectively, are given by

$$\Delta n_i^{so} = -(n_i^3/2) p_{ij} S_j \quad (1)$$

where $j=1$ for Z-cut substrates ($j=3$ for X-cut substrates) and p_{ij} is the relevant strain-optic coefficient [10]. In addition to the strain-optic effect, the net refractive index change also includes an electrooptic contribution due to the electric fields in the strained region produced by the piezoelectric effect and by surface charge redistribution [9].

Strain analysis using the relaxation method [9] in such waveguides shows that the index profile is qualitatively quite different than for waveguides produced by conventional methods [6]-[8]. The result of numerical calculations for a SiO₂ film on X-cut LiNbO₃, of thickness t to channel width w ratio $t/w = 0.25$ assuming a deposition temperature $T = 300$ °C, is shown in Fig. 1. Constant strain contours are drawn normalized relative to the strain value at the surface of the substrate in the center of the channel. The inward pointing arrows in the channel indicate the direction in which the film relaxes. The calculations show that the compressive strain at the surface of the substrate is maximum at the edges of the channel and decreases as a function of distance from the edges toward the center, and that a tensile strain develops in the regions beneath the film. This causes the index increase in the channel to be compensated by an index decrease elsewhere in the substrate.

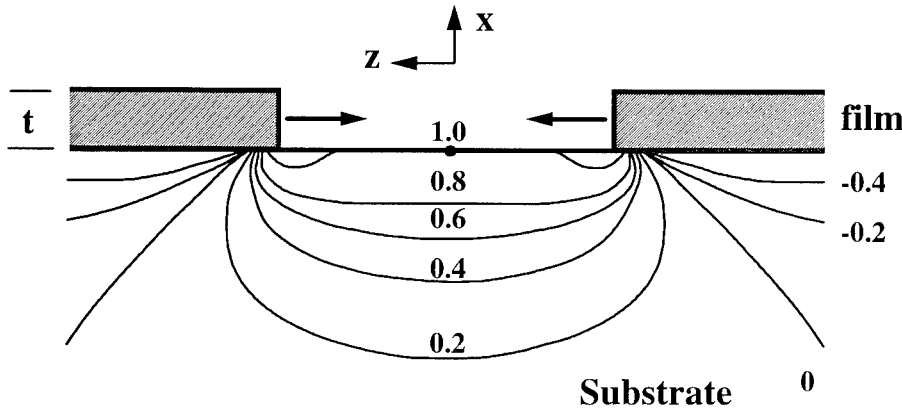


Figure 1. Normalized constant contours curves of the longitudinal S_3 strain component.

Strain-induced waveguides have been produced by depositing SiO₂ films ranging in thickness between 2.8-3.4 μm at 300°C on LiNbO₃, LiTaO₃, BaTiO₃, SBN:60, and BSTN substrates [9], [11]. All the waveguides generally supported a single depth mode, but the number of transverse modes varied with the oxide film thickness t and the gap width w of the etched channels. In X-cut LiNbO₃, single mode propagation for both polarizations at

0.633 μm wavelength was observed on 11 μm wide channels etched in a 2.8 μm thick SiO_2 film. Best propagation losses were measured in waveguides produced from a 3.4 μm thick SiO_2 film. Values of 0.8 and 0.9 dB/cm were obtained at 0.633 μm wavelength for TE and TM polarizations, respectively. Optical guiding for both polarizations was also observed in SBN:60 at 1.3 μm wavelength by depositing a 4.4 μm thick strain-inducing SiO_2 film on Z-cut substrates [11]. Measured propagation losses in the SBN:60 waveguides were 0.7 dB/cm for TM (extraordinary) polarization, and 1.6 dB/cm for TE (ordinary) polarization. The low propagation loss values are evidently a result of the low-temperature process used in making the waveguides. Electrooptic modulation was also demonstrated in these waveguides.

ELECTROOPTICALLY TUNABLE POLARIZATION CONVERTERS

The SSO effect can also be used to promote polarization conversion in birefringent crystals [12]-[14]. For a wave propagating in a diffused channel waveguide, phase-matched coupling between TE and TM modes is induced by static shear strain from a spatially periodic surface film. This eliminates the requirement of external power drives often needed to sustain coupling between the orthogonal polarizations. The phase match condition imposed by the birefringent crystal makes the coupling highly wavelength selective. Tuning of the center wavelength for maximum conversion can be realized by adjusting the birefringence Δn in the waveguide electrooptically via the Pockels effect.

A schematic illustration of an electrooptically tunable polarization converter is shown in Fig. 2. The strain-inducing SiO_2 film which is deposited at elevated temperature is patterned at room temperature with a spatial period Λ in the direction of propagation, where $\Lambda = \lambda_o / \Delta n$ is the polarization beat length for the waveguide. Polarization

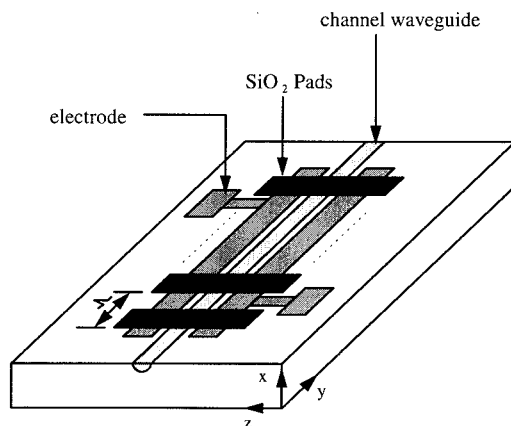


Figure 2. Schematic illustration of an electrooptically tunable polarization converter.

conversion in the waveguide is caused by the induced off-diagonal element of the refractive index tensor n_5 ($5 \rightarrow xz$) which is produced by the shear strain component S_6 ($6 \rightarrow xy$). This contrasts with the previously described strain-induced channel waveguide where changes in diagonal elements of the refractive index tensor were produced by longitudinal strain components in the substrate.

The polarization coupling can be analyzed by examining the strain induced by the patterned SiO_2 pads. By symmetry, the lattice displacement in the z -direction in the center of a pad, which also corresponds to the center of the waveguide, will vanish, and

displacements along the edges of the waveguide near the center will be small and are ignored. Considering displacements parallel to the y -axis only, it may be assumed that the strain causes the coordinates of a lattice point in the substrate to move from (x,y,z) to $(x,y+v,z)$. The displacement v varies continuously with position, and the strains in the substrate are heavily concentrated near the edges of the pads. The induced index change n_5 responsible for polarization coupling is caused by the shear-strain component $S_6 = \frac{1}{2}(\partial v / \partial x)$, and is given by

$$n_5 = -(n^3/2)p_{41}S_6 \quad (2)$$

with $n = (n_1 n_3)^{1/2}$ and p_{41} is the relevant strain-optic coefficient. The results of a numerical calculation using the relaxation method, for a $1.5 \mu\text{m}$ thick SiO_2 film deposited at 300°C and patterned with $\Lambda = 100 \mu\text{m}$ at room temperature are shown in figures 3 and 4. The graphs in both figures are normalized relative to the maximum shear strain which occurs on

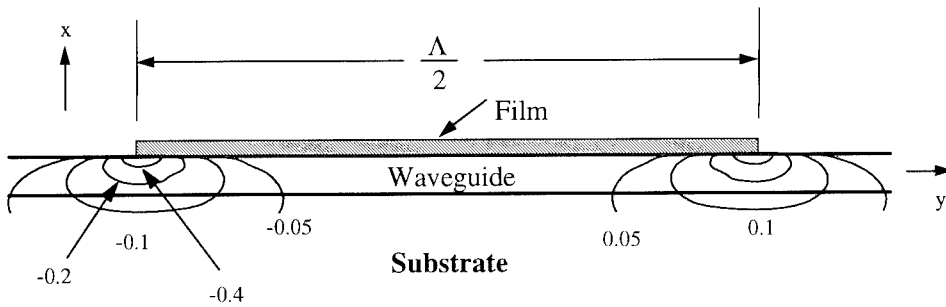


Figure 3. Normalized constant contours of the calculated shear strain component S_6 .

the surface of the substrate at the edges of the film. Figure 3 shows constant contours of the calculated shear strain (or corresponding induced index n_5). Figure 4 represents the shear strain distribution $S_6(x_0, y)$ as a function of position along the waveguide at fixed depths x_0 of $1.5 \mu\text{m}$ and $3 \mu\text{m}$ below the substrate.

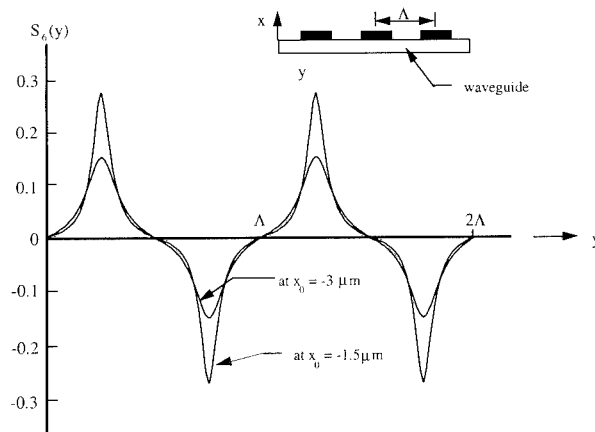


Figure 4. Calculated normalized shear strain distribution at fixed depths along the waveguide.

Spectral data for an electrooptically tunable polarization converter in LiTaO₃ are shown in Fig. 5. The channel waveguide was formed by Zn diffusion, and the strain produced from a 1.75 μm thick SiO₂ film deposited at 300°C and patterned at room temperature with $\Lambda = 100 \mu\text{m}$. Tuning of the peak wavelength from 616 nm to 654 nm was realized with an applied voltage of 70 V. The tuning is controlled by adjusting the waveguide birefringence through the z -component of the applied electric field via the r_c

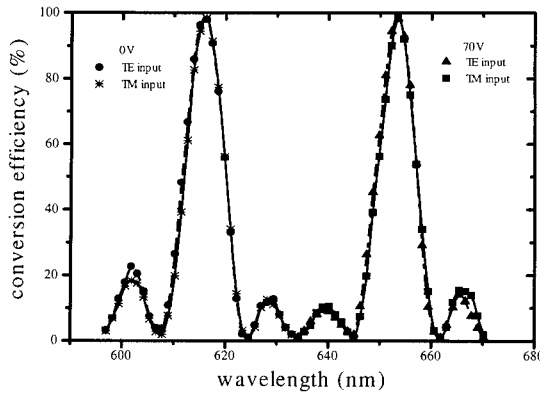


Figure 5. Measured wavelength response of TE \leftrightarrow TM conversion efficiency at $V = 0$ and 70 volts.

electrooptic coefficient [14]. The 17 nm full width of the passband between the first minima is obtained through a 5.4 mm long tuning region.

ELECTROOPTICALLY TUNABLE CHANNEL-DROPPING FILTER

The use of polarization coupling from the SSO effect can be extended to a channel-dropping electrooptic tunable filter (EOTF) using a four-port Mach-Zehnder configuration. A wavelength selective EOTF has been previously demonstrated in LiNbO₃ at AT&T Bell Laboratories [15]. The reported device represented an important step towards the realization of tunable channel-dropping filters for WDM systems. The demonstrated EOTF, however, used alternating regions in which electric fields were applied for polarization conversion and birefringence tuning, causing a large portion of the device length to be used for the required separate voltage controls. This puts a limit on the number of selectable wavelength channels and increases the required tuning voltage. The use of SSO polarization coupling makes it possible to combine the electrooptic birefringence tuning region with the polarization coupling region, leading to a more efficient utilization of the length of the tuning section.

A schematic diagram of the new four-port polarization-independent EOTF [16] is shown in Fig. 6. It consists of two polarization splitters (PS) near the input and output ends that are joined by a pair of tunable SSO converters in the center. The polarization splitters are, basically, passive directional couplers that leave an incident TM component in the straight-through arm, and route an input TE component to the cross-over arm. If the wavelength of a light entering at one of the input ports (e.g. #1) satisfies the phase matching condition of the converter section, the separated components undergo polarization rotation then recombine and emerge from port #4 at the output. The induced off-diagonal index n_j that is responsible for coupling is given by (2), as before. Wavelength tuning of the phase

match condition can be accomplished by adjusting the birefringence electrooptically in the converter sections.

Optical test results for a wavelength selective channel-dropping EOTF produced in LiTaO_3 are shown in Fig. 7. The $2.6 \mu\text{m}$ waveguides were fabricated by Zn diffusion. The strain-inducing pads ($50 \times 100 \mu\text{m}$) with a spatial period of $100 \mu\text{m}$ were produced by

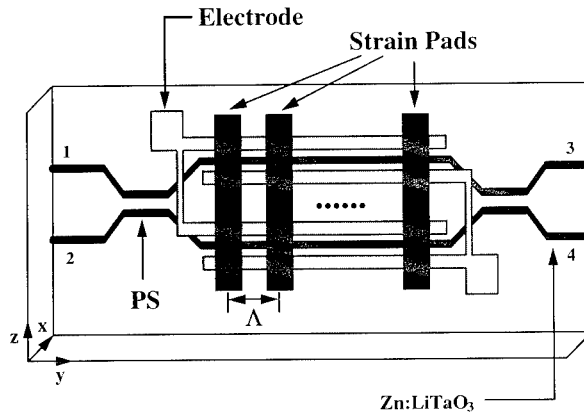


Figure 6. Schematic diagram of an electrooptically tunable channel-dropping filter.

depositing a $1.9 \mu\text{m}$ thick SiO_2 film on the substrate at 300°C and patterning it at room temperature. The spectral response of the untuned (0 V) and tuned (60 V) filter are shown for inputs at port #1 and outputs from port #4. A total shift of 37 nm for the center wavelength with an applied voltage of 90 V was achieved. The incomplete extinction is due

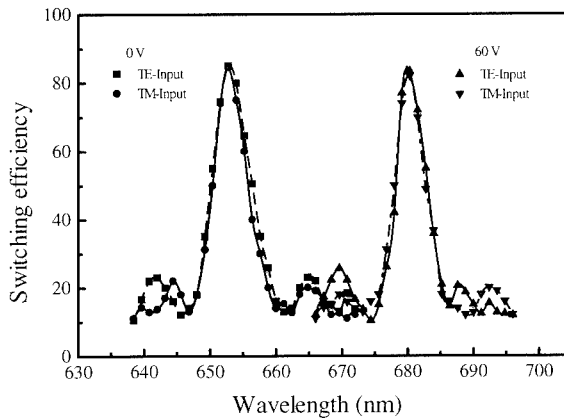


Figure 7. Measured response of EOTF for TE and TM input at port 1 and output from port 4 at 0 and 60 V.

to the splitters providing only 95% cross-over and straight through coupling for TE and TM polarizations, respectively. This and the measured maximum conversion efficiency (96%) of the polarization converter sections are major factors in limiting the filter switching efficiency to 86%, but they can be improved by optimization of the fabrication parameters. Narrower wavelength passbands could be realized in the LiTaO_3 through an increase of the number of converter pads (54 in the present device), or by the use of a substrate with larger birefringence (e.g. LiNbO_3 with $\Delta n \approx 0.07$). The sidelobe levels can be reduced by the use

of tapered polarization mode coupling [17]-[18]. Operation can be extended to the 1.3 μm and 1.55 μm regimes by proper scaling. The use of high-electrooptic-coefficient substrate materials such as SBN and BSTN provide a means of reducing the tuning voltage and increasing the number of accessible wavelength channels.

CONCLUSION

The Static strain-optic (SSO) effect has been utilized in a variety of ferroelectric substrates, to fabricate channel waveguides, and electrooptically tunable guided-wave polarization converters as well as channel-dropping filters. The static strain results from the large thermal expansion mismatch between a substrate and a thick film of SiO_2 that is deposited at elevated temperature and patterned at room temperature. Longitudinal strain was used to produce low-loss channel waveguides in LiNbO_3 , LiTaO_3 , and BaTiO_3 substrates, and tungsten bronze SBN:60 and BSTN crystals. The resulting optical waveguides support both polarizations. Propagation losses <1 dB/cm and electrooptic modulation have been demonstrated in SBN and BSTN strain waveguides at 1.3 μm wavelength. The use of SSO effect in producing waveguides does not alter the composition or stoichiometry of the crystal and allows the recovery of a substrate by etching away the SiO_2 film. Static shear strain, from a spatially periodic strain inducing surface film, has been used to promote phase-matched polarization coupling in a diffused channel waveguide. Efficient polarization conversion was obtained in Zn:LiTaO_3 waveguides without the need of an external power drive, and electrooptic tuning was accomplished using the Pockels effect to control birefringence. The SSO effect was also applied to a four-port Mach-Zehnder configuration in fabricating a polarization-independent, guided-wave electrooptically tunable channel-dropping filter. The use of SSO for polarization coupling leads to an efficient utilization of the device length for tuning and reduces the need for external voltage control. The use of SBN and BSTN in making channel-dropping EOTFs is an attractive possibility as the large electrooptic coefficient in these substrates will make it possible to access a larger number of channels through birefringence tuning.

REFERENCES

- [1] P.E. Green, Jr., *Fiber Optic Networks*, Englewood Cliffs, NJ: Prentice Hall, 1993.
- [2] C.A. Brackett, "Dense wavelength division multiplexing networks: Principles and applications," *IEEE J. Select. Areas of Commun.*, vol. 8, pp. 948-964, 1990.
- [3] K. Hirabayashi, H. Tsuda, and T. Kurokawa, "Tunable liquid crystal Fabry-Perot interferometric filter for wavelength-division multiplexing communication systems," *J. Lightwave Technol.*, vol. 11, pp. 2033-2043, 1993.
- [4] Tungsten bronze crystals supplied by Dr. R.R. Neurgaonkar, Rockwell International Science Center.
- [5] R.R. Neurgaonkar, W.F. Hall, J.R. Oliver, W.W. Ho, and W.K. Cory, "Tungsten bronze $\text{Sr}_{1-x}\text{Ba}_x\text{Nb}_2\text{O}_6$: A case history of versatility," *Ferroelectrics*, vol. 87, pp. 167-179, 1988.
- [6] I.P. Kaminow, and J.R. Carruthers, "Optical waveguiding layers in LiNbO_3 and LiTaO_3 ," *Appl. Phys. Lett.*, vol. 22, pp. 326-328, 1973.

- [7] R.W. Schmidt and I.P. Kaminow, "Metal diffused optical waveguide in LiNbO₃," *Appl. Phys. Lett.*, vol. 25, 1974.
- [8] J.L. Jackel, " High- Δn optical waveguides in LiNbO₃: Thallium-lithium ion exchange," *Appl. Phys. Lett.*, vol. 37, pp. 739-741, 1980.
- [9] O. Eknayan, H.F. Taylor, Z. Tang, V.P. Swenson, and J.M. Marx, " Strain induced optical waveguides in lithium niobate, lithium tantalate, and barium titanate," *Appl. Phys. Lett.*, vol. 60, pp. 407-409, 1992.
- [10] D.A. Pinnow, "Elastooptical materials," in *Handbook of Lasers*, edited by R.J. Presley, Cleveland, OH: CRC, 1971.
- [11] J.M. Marx, O. Eknayan, H.F. Taylor, and R.R. Neurgaonkar, "Low loss optical waveguides in strontium barium niobate (SBN:60) at 1.3 μm wavelength," submitted for publication.
- [12] K. Yamanouchi, K. Wakazono, and K. Shibayama, "Optical surface wave mode converters and modulators utilizing static strain optic effects," *IEEE J. Quantum Electron.*, vol. QE-16, pp. 628-634, 1980.
- [13] Z. Tang, O. Eknayan, H.F. Taylor and V.P. Swenson, "Tunable guided-wave optical polarization converter in lithium tantalate," *Appl. Phys. Lett.*, vol. 62, pp. 1059-1061, 1993.
- [14] Z. Tang, O. Eknayan, H.F. Taylor, and V.P. Swenson, "Electro-optically tunable wavelength selective polarisation convertor in LiTaO₃," *Electron. Lett.*, vol. 28, pp. 2248-2249, 1992.
- [15] W. Warrzanskyj, F. Heismann, and R.C. Alferness, "Polarization-independent electro-optically tunable narrow band wavelength filter," *Appl. Phys. Lett.*, vol. 53, pp. 13-15, 1988.
- [16] Z. Tang, O. Eknayan, and H.F. Taylor "Polarization-independent electrooptically tunable wavelength filter in LiTaO₃," to be published in *Electron. Lett.*
- [17] R.C. Alferness and P.S. Cross, "Filter characteristics of codirectionally coupled waveguide with weighted coupling," *IEEE. J. Quantum Electron.*, vol. QE-14, pp. 843-847, 1978.
- [18] A. Kar-Roy and C.S. Tsai, "Ultralow sidelobe-level integrated acoustooptic tunable filters using tapered-gap surface acoustic wave directional couplers," *J. Lightwave Technol.*, vol. 12, pp. 977-982, 1994.

DEMONSTRATION OF 250 GB/S ALL-OPTICAL ROUTING CONTROL OF A PHOTONIC CROSSBAR SWITCH

Ivan Glesk and Paul R. Prucnal

Department of Electrical Engineering
Princeton University
Princeton, NJ 08544, USA

In future ultra-fast packet-switched networks, individual address bits may be spaced only picoseconds apart. Address recognition will require an ultra-fast demultiplexer which examines the packet header without opto-electronic conversion and without reading the data in the packet's payload. A low-power device capable of all-optical demultiplexing is the recently-developed Terahertz Optical Asymmetric Demultiplexer (TOAD).¹⁻⁴

In this paper the operation of the TOAD will first be briefly reviewed. Then all-optical address recognition at 250 Gb/s address bit rate and self-routing of photonic packets using the TOAD, will be described. Non-polarization preserving single mode optical fiber was used to carry polarization multiplexed clock and data.

THE TERAHERTZ OPTICAL ASYMMETRIC DEMULTIPLEXER

The TOAD (see inset of figure 1) is composed of a small optical loop mirror, a nonlinear element (NLE), and intraloop 2x2 coupler which injects control pulses into the nonlinear element. When a train of closely spaced OTDM signal pulses enter the TOAD, each pulse splits into equal clockwise (CW) and counterclockwise (CCW) components which counterpropagate around the loop and arrive at the NLE at slightly different times as determined by the offset, Δx , of the near edge of the NLE from the midpoint of the loop. The control pulse arrives at the NLE just before the CCW component of the signal pulse which is to be demultiplexed, but just after its CW counterpropagating complement and

induces nonlinearities in the NLE which cause the two components to experience different losses and phase shifts, and consequently recombine and exit the loop at the output port. All other OTDM signal pulses, (for which the counterpropagating components do not straddle the control pulse arrival at the NLE) exit the loop at the input port.

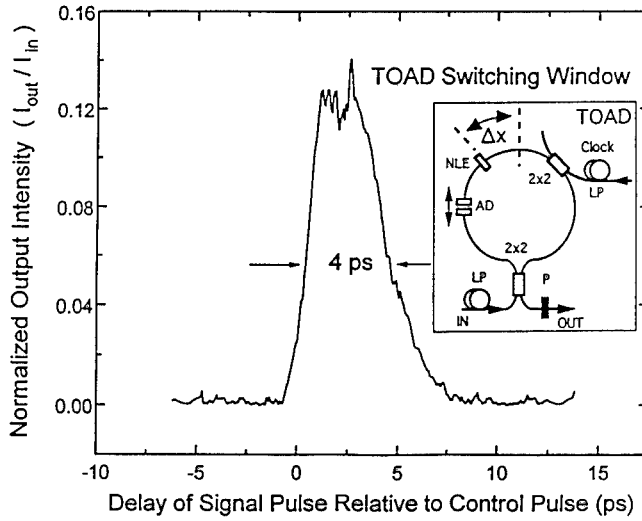


Figure 1. Four ps TOAD demultiplexing window. The inset is a schematic of the TOAD.

As seen in figure 1, the rising edge of the normalized output intensity, when measured as a function of the delay of the signal pulse relative to the control pulse, is nearly a step function (it "follows" the rising edge of the control pulse); the duration of the falling edge is limited by the transit time through the NLE, nL/c_0 , where n and L are the refractive index and length of the NLE; and the duration of the flat top is $2n_g\Delta x/c_0$, where n_g is the refractive index of the loop and c_0 is the speed of light in vacuum. The switching window is defined here as the full width at half maximum (FWHM) of the normalized output intensity as indicated in figure 1. Note that in actuality the switching window has the shape described above when the intraloop coupler is on the same side of the loop center as the NLE, but becomes a mirror image of this shape when the intraloop coupler is on the opposite side of the loop center.

The experimental measurement of the normalized output intensity function shown in figure 1 was obtained using the TOAD shown in the figure 1 inset (with the NLE and intraloop coupler on the same side of the loop center), which used a short (<1 m) length of optical fiber for the loop. The NLE was a 500 μm long, DC-biased semiconductor optical amplifier (SOA), with an injection current of 35 mA. The offset Δx was set using an adjustable delay, AD, to minimize the length of the switching window. In this case the AD was composed of a small grin rod-air gap-grin rod combination, with one grin rod on a mechanical translation stage. Loop polarization controllers, LP, and an in-line analyzer, P,

were used to discriminate the signal and control pulses at the TOAD output. The measurement setup is shown in figure 2, where B1 and B3 are temporarily absent. Modelocked pulses at $1.313\ \mu\text{m}$ are generated by a 100 ps, 100 MHz repetition rate Nd:YLF laser and shortened to 1 ps using an optimized fiber-grating compression stage, CS. One hundred fJ signal pulses were input to the TOAD, while 600 fJ control pulses were injected into the SOA to induce the nonlinearity. The control-pulse-induced nonlinearities are the gain and index changes associated with carrier depletion of the SOA.⁵

The window shown in figure 1 is the result of a measurement with the SOA set asymmetrically about the loop center with one end approximately $100\ \mu\text{m}$ from the loop midpoint, and the other end approximately $400\ \mu\text{m}$ from the midpoint. This placement of the SOA does several things: it changes the step-like rising edge of the window to a sloping edge with a duration of $n(100\ \mu\text{m})/c_0 = 1\ \text{ps}$ (thus not affecting the rising edge shape since 1 ps pulses are being used); it makes the effective length of the SOA $400\ \mu\text{m}$ which results in a slightly shorter falling edge, and a slightly smaller normalized output intensity, than if both edges of the SOA were on the same side of the midpoint. The 4 ps switching window permits the TOAD with this off-center setting to be used as a demultiplexer in a 250 Gb/s aggregate bandwidth system. Only 800 fJ switching energy is required, and cross-talk measurements of two adjacent channels exhibit a bit error of less than 10^{-9} with a strong immunity to clock jitter over the entire switching window.

ALL-OPTICAL ADDRESS RECOGNITION AND SELF-ROUTING OF PHOTONIC PACKETS USING THE TOAD

Many functions must be performed to control a switching node. One important function is routing. The routing of incoming packets at a switching node requires recognizing an address. In ultra-high speed networks individual address bits are spaced only picoseconds apart, and address recognition must be performed by using an ultra-fast demultiplexer to read each address bit. Once the address bits of each packet are read the state of the routing switch can be set to properly route the packets. A device capable of reading address bits in such an optically compressed packet header is the TOAD device described above.

Experimental demonstration

To demonstrate all-optical address recognition and packet self-routing one node of a network of 2x2 switches was used. The switching node consisted of an electro-optic switching element (e.g. 2x2 LiNbO₃ cross-bar switch) with two possible states, switched (cross) or unswitched (bar), a routing controller that decoded the destination address and set the state of the switching element, and an optical buffer that matched the delay of the input packet to the processing delay of the routing controller. The packets used were composed of 4 bit headers and empty payloads. This simplified packet generation while allowing the desired functionality, i.e. reading and routing of the packets, to be demonstrated. Two different packets were generated and sent through an optical buffer, which was simply a one meter optical fiber, and then input into one port of a 2x2 switch. Before entering the

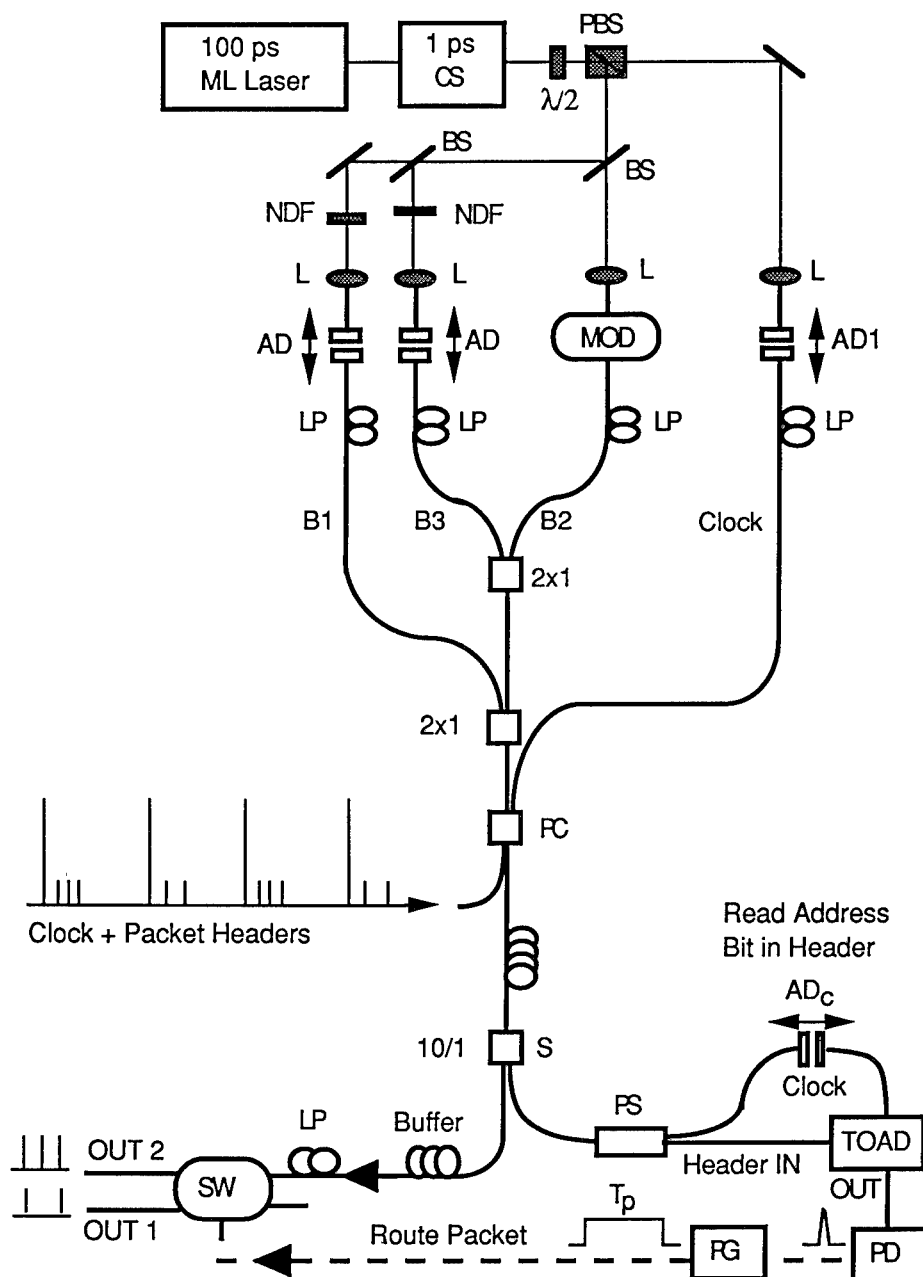


Figure 2. Experimental setup for all-optical address recognition and self-routing of photonic packet.

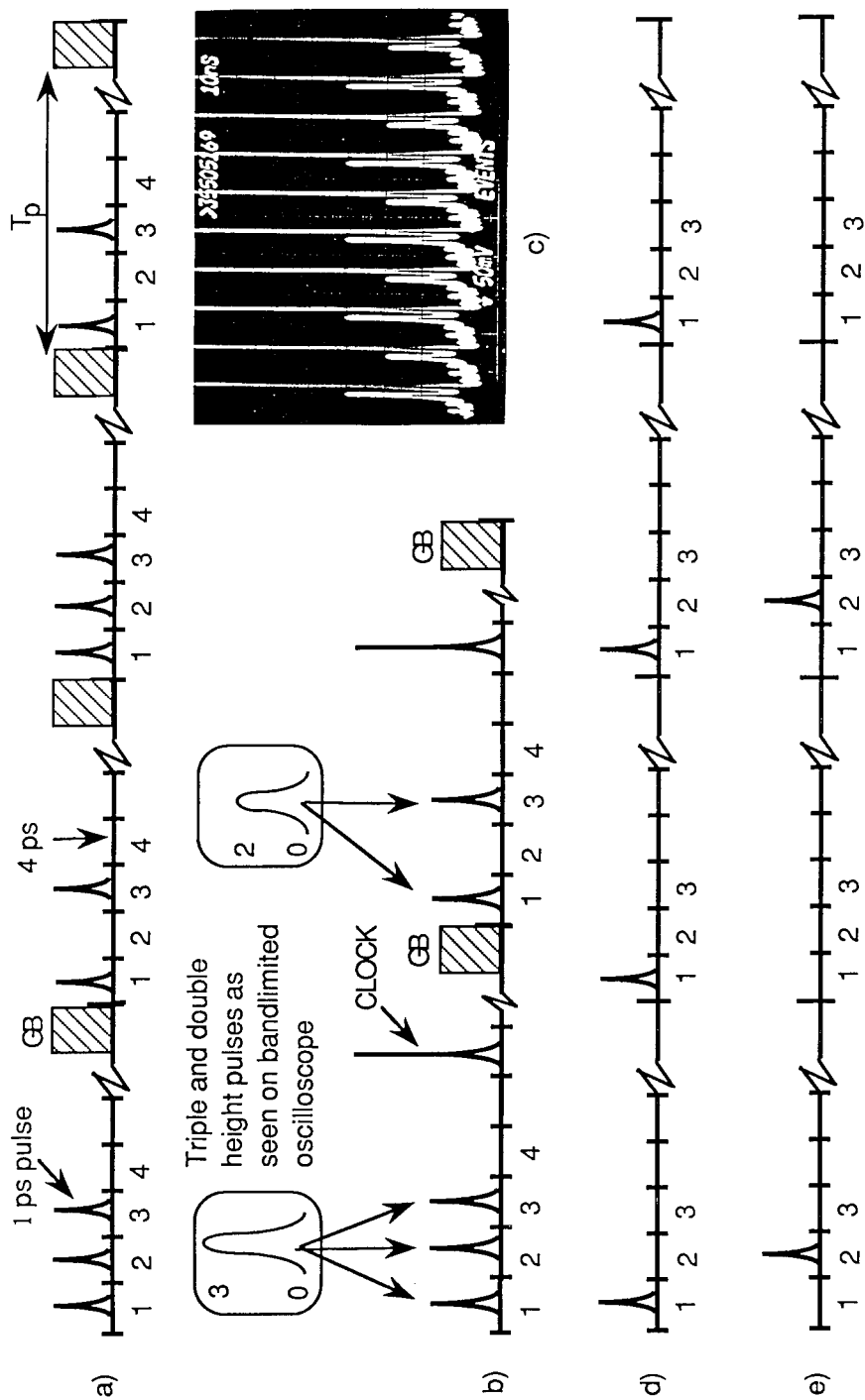


Figure 3. a) Timing diagram of the node input with two optically compressed packet headers "1110" and "1010"; b) Polarization multiplexed packets and clock; c) Oscilloscope trace of 3b; d) TOAD output after demultiplexing address bit 1; e) TOAD output after demultiplexing bit 2.

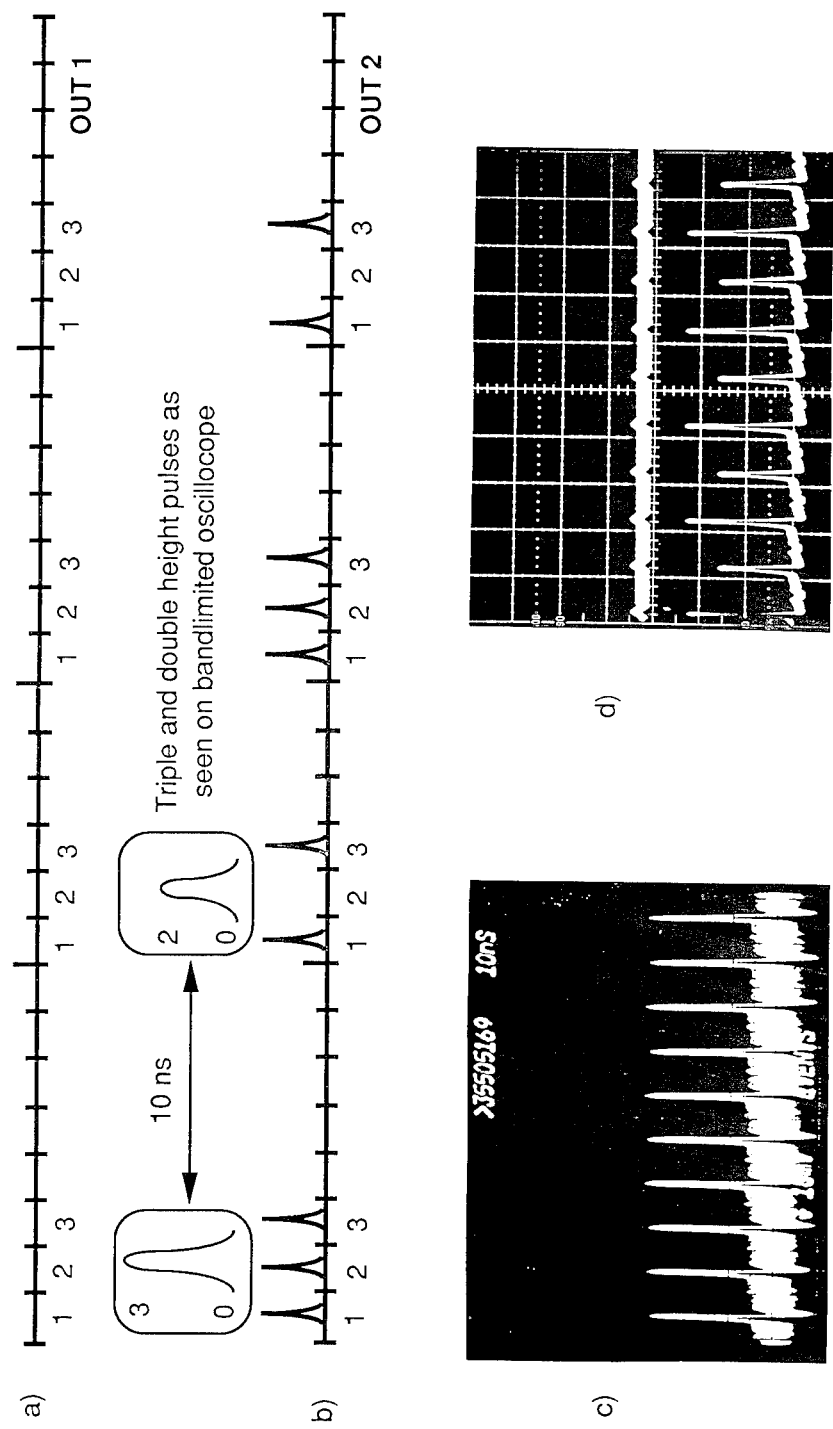


Figure 4. Output of port 1 (OUT 1) and 2 (OUT 2) of the routing switch SW when the sampled bit is number ONE (always "1"); a) and b) timing diagram; Experimental demonstration: c) oscilloscope photograph of the TOAD output - demultiplexed address bit ONE; d) oscilloscope photograph of both outputs of the routing switch SW.

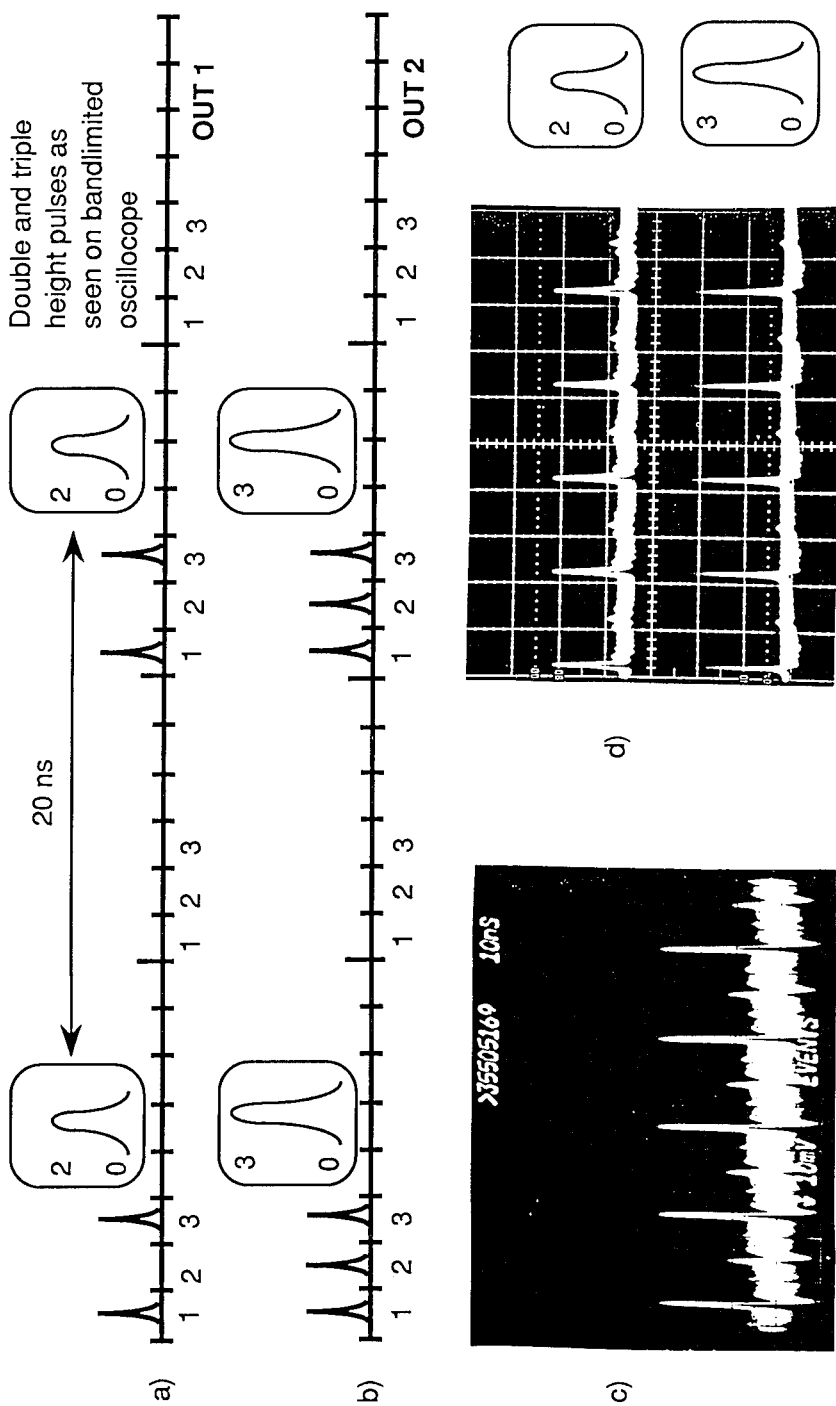


Figure 5. Output of port 1 (OUT 1) and 2 (OUT 2) of the routing switch SW when the sampled bit is number TWO ("1" or "0"); a) and b) timing diagram; Experimental demonstration: c) oscilloscope photograph of the TOAD output-demultiplexed address bit TWO; d) oscilloscope photograph of both outputs of the routing switch SW.

optical buffer a portion (10%) of the packet was split off and sent to a header reader. The packet destination address, which consisted of one bit, was read using the TOAD while the packet was in the buffer. The output of the TOAD was used to set the state of the 2x2 switch to a cross or bar state, depending on the address bit value. In this way the packet, which emerged from the buffer and input to the 2x2 switch, was properly routed.

The full experimental setup is shown in figure 2. One ps pulses at 1.313 μm are generated using a 100 ps, 100 MHz repetition rate Nd:YLF mode-locked laser followed by an optimized fiber-grating compression stage. Each of these pulse are then divided into 4 pulses: three packet header bits B1, B2 and B3; and an orthogonally polarized clock pulse which is used for synchronization at the demultiplexer as described below.

Channel B1 and channel B3 (see figure 2) use adjustable delays, AD, to position 1 ps pulses into 4 ps bit intervals situated on either side of bit 2 (channel B2). Channel B2 is modulated with a "1010..." pattern using a 3 GHz integrated Mach-Zender modulator. The three channels are set equal in intensity by variable neutral density filters, NDF. A fourth header bit with a constant value of "0" is also included in the headers. In this way packets with two different headers, "1010" and "1110", and empty payloads, "000...", are generated (see timing diagram in figure 3a). The repetition rate of the mode-locked laser $1/T = 100$ MHz determines the packet slot width. Each packet has duration $T_p = (T - T_{GB})$, where T_{GB} is a guard-band separating individual packets. The size of the T_{GB} is determined by the switching speed of the 2x2 routing switch (SW). Loop polarizers set the clock and data pulses into orthogonal polarization states, and a polarization combiner was then used to polarization multiplex the clock and the packet header data onto a common transmission line. This is the self-routing feature of the system. Any changes in the length of the transmission line are not critical, since the clock's placement within the packet is not changed. Using an adjustable delay, AD1, the clock pulse was positioned in an arbitrary time slot, i , of the packet header (see timing diagram in figure 3b).

Before entering the 2x2 LiNbO₃ routing cross-bar switch a portion of the incoming signal was split off at the 10:1 single mode splitter S. A smaller portion of the signal was sent into the address recognition unit (the TOAD). Before entering the TOAD the clock pulse was separated from the packet header by a fiber polarization beam splitter, PS. The packet was then injected into the TOAD input port while the clock pulse was directed through an adjustable delay, AD_c, into the TOAD control port. By positioning the clock pulse relative to the desired address bit within the header frame, using AD_c, different bits could be used as the address bit. This bit was then demultiplexed and appeared at the TOAD output port (see timing diagram in figure 3d-e). The output of the TOAD was monitored by the photodetector, PD, which upon receiving a pulse triggered a pulse generator, PG, which in turn gated the routing switch, SW. In this way packets with address bit of value "1" were made to exit output port 2, while packets with address bit of value "0" were made to exit output port 1. The different cases are shown schematically in figures 4a - b and 5a - b, where address bits ONE("1") and TWO("0" or "1"), respectively, are selectively demultiplexed.

The experimental demonstration of all-optical packet address recognition, including the self-routing of the packet, is shown in figures 4c-d and 5c-d. Figure 3c is an oscilloscope photograph of the signal input showing the multiplexed 100 MHz clock and

two packets "1110 . . . 0" and "1010 . . . 0". The clock is the highest intensity pulse. The two packet headers are composed of bits spaced 4 ps apart resulting in an effective aggregate bandwidth of 0.25 Tb/s. Because the temporal separation of these bits is too small for the 1 GHz oscilloscope to distinguish, the different headers appear as cumulative "double height" (101 bit sequence) and "triple height" (111 bit sequence) pulses.

Figures 4d and 5d are oscilloscope photographs of both outputs of the routing switch SW when the clock pulse has been synchronized to demultiplex address bit ONE (always "1" see timing diagram in figure 3d) and TWO ("0" or "1" see timing diagram in figure 3e), respectively. The upper trace shows the output port 1 and the lower trace output port 2. When address bit ONE, which is always "1" (see oscilloscope photograph of the TOAD output in figure 4c), is used as the address bit, both packets are routed to port 2. This results in zeroes at the output of port 1, and alternate double height and triple height pulses at the output of port 2 (see figure 4d). However, when address bit TWO, which is alternately a "0" or "1" (see oscilloscope photograph of the TOAD output in figure 5c), is used as the address bit, the packet with header "111" is always routed to port 2, while the packet with header "101" is always routed to port 1. This results in triple height pulses at port 2 with zeroes in between, and double height pulses at port 1 with zeroes in between (see figure 5d). BER measurements were made by modulating address bit TWO with a pseudorandom bit stream and monitoring the output of the routing switch. BERs of less than 10^{-9} were measured.

In conclusion, we report that the Terahertz Optical Asymmetric Demultiplexer known as TOAD is capable of all-optical address recognition in the case of 4 picoseconds spacing between address bits (0.25 Tb/s address bit rate) in the self-routing network architecture including self-routing of a packet. The bit-error at the switching element output was measured to be less than 10^{-9} .

Acknowledgment

We would like to thank the reviewers for their helpful comments and suggestions, and the Advanced Research Project Agency for supporting this research.

REFERENCES

1. J.P. Sokoloff, P.R. Prucnal, I. Glesk, and M. Kane, A terahertz optical asymmetric demultiplexer (TOAD), *IEEE Photon. Technol. Lett.* 5:787 (1993).
2. J.P. Sokoloff, I. Glesk, P.R. Prucnal, and R.K. Boncek, Performance of a 50 Gbit/s optical time domain multiplexed system using a terahertz optical asymmetric demultiplexer, *IEEE Photon. Technol. Lett.* 6:98 (1994).
3. I. Glesk, J.P. Sokoloff, and P.R. Prucnal, Demonstration of All-Optical Demultiplexing of TDM Data at 250 Gb/s, *Electron. Lett.* 30:339 (1994).
4. I. Glesk, J.P. Sokoloff, and P.R. Prucnal, All-optical address recognition and self-routing in a 250 Gb/s packet-switched network, *Electron. Lett.* 30:1322 (1994).
5. M.G. Kane, I. Glesk, J.P. Sokoloff, and P.R. Prucnal, Asymmetric optical loop mirror: analysis of an all-optical switch, *Appl. Opt.* 33:6833 (1994).

AN ELECTRODE-LESS INTEGRATED MACH-ZEHNDER INTERFEROMETER ELECTRIC FIELD SENSOR

David H. Naghski,¹ Joseph T. Boyd,¹ Howard E. Jackson,²
S. Sriram,³ Stuart A. Kingsley,³ and John Latess⁴

¹Department of Electrical and Computer Engineering

²Department of Physics

University of Cincinnati

Cincinnati, OH 45221-0030

³SRICO Inc.

664 Petworth Court

Powell, OH 43065-9398

⁴Army Research Laboratory

2800 Powder Mill Road

Adelphi, MD 20783

Abstract

Advances in the development of a newly configured Mach-Zehnder interferometric electric field sensor device utilizing the electro-optic effect are reported. The integrated optical lithium niobate device operates solely by immersion in an electric field, using no metallic electrodes. Reverse poling of one arm of the interferometer results in additive optical phase changes in the interferometer arms when the device is placed in an electric field. Recently fabricated devices have exhibited a measured minimum detectable field of 34 mV/m per $\sqrt{\text{Hz}}$ and a frequency response of greater than 10 GHz.

INTRODUCTION

We report developments in the fabrication and experimental evaluation of a novel lithium niobate (LiNbO_3) integrated optical electric field sensor. Initial results have been reported elsewhere [1]. The fabrication method allows this Mach-Zehnder device to operate using the electro-optic effect without the use of metal electrodes [2]. The passive device has measurement capabilities in the radio frequency, microwave, and millimeter wave bands.

Traditionally metal electrodes have been placed near the sensing waveguides, acting as an antenna to collect the field and apply it to the proper region of the LiNbO₃ material [3]-[6]. Although many devices having good performance have been built utilizing this technique, the removal of metal electrodes alleviates several system problems and limitations.

The absence of electrodes minimizes field disturbance and improves operational speed by eliminating electrode capacitance. The sensor has an extremely high electric field damage threshold, on the order of 10 MV/m, because there can be no electrode arcing and subsequent device damage. The device can perform remote sensing using only a fiber optic connection, obviating auxiliary electrical connections required, e.g., to bias the device. This maintains the safety of the operator and the integrity of any signal processing components in the rest of the system.

In our approach we place a Mach-Zehnder interferometric waveguide sensing device directly in the electric field without the use of metal electrodes. Asymmetry in the interferometer is obtained by placing one arm in a reverse-poled region of the z-cut lithium niobate substrate. This exploitation of the unique reverse poling property of this material [7] allows the device to turn what would be a common mode response into a differential ('push-pull') response. Devices of this type have been realized using bulk electro-optic crystals [8]-[10], but the integrated optic form have only been investigated theoretically [11].

THEORY

The basic principles of electro-optic modulation are covered extensively elsewhere (see, for example, Refs. 12, 13). In the integrated optical Mach-Zehnder interferometer phase modulation of the optical signal in the interferometer arm waveguides is converted to intensity modulation of the output. The optical power transfer function of the device can be written [12]:

$$P_{out} = P_{in} \cos^2 \left(\frac{\Delta\phi}{2} \right) = \frac{P_{in}}{2} \left\{ 1 + \cos(\Delta\phi) \right\} \quad (1)$$

where $\Delta\phi$ is the net accumulated phase difference between the arms and is composed of two terms, $\Delta\phi = \phi_0 + \Delta\phi_e(E)$. The bias term ϕ_0 is caused by physical path length and index differences. The field term $\Delta\phi_e(E)$ is linearly dependent on the electric field.

An electric field in the waveguide region induces an index change in the waveguide material, Δn_e , causing the polarized light in the guide to undergo a field dependent phase shift, $\Delta\phi_e(E)$, given by [13]:

$$\Delta\phi_e(E) = \pm \frac{\pi}{\lambda} \delta n_e^3 \left| r_{33} \right| \left| \vec{E}_z \right| L_e \quad (2)$$

Here n_e is the extraordinary index of refraction at the optical wavelength λ , L_e is the electrode length, and r_{33} is the appropriate electro-optic tensor component for a device fabricated in +z cut LiNbO₃. The sign of the phase shift depends on the relative orientations of the field and the +z axis of the crystal substrate. The sign is positive for parallel orientation and negative for opposing orientation. The coefficient δ is the value of an overlap integral ($0 \leq \delta \leq 1$) which accounts for the departure of the electric and optical fields from exact overlap.

Figure 1 shows perspective and cross-sectional views of a conventional integrated optical Mach-Zehnder interferometer with metal electrodes. In this device a voltage applied to the electrodes generates an electric field in the substrate and waveguide regions. The electrodes are oriented such that the electric field through each arm has opposite polarity and therefore the two phase changes add in determining the net phase difference when the optical signals recombine at the output. This is termed ‘push-pull’ operation. Expressing the field in terms of the applied voltage, V , and the electrode gap, g , the net phase difference at the output Y-branch is:

$$\Delta\phi_e(E) = \frac{2\pi}{\lambda} \delta n_e^3 |r_{33}| \frac{V}{g} L_e = \pi \frac{V}{V_\pi} \quad (3)$$

where the Half Wave Voltage, V_π , is defined:

$$V_\pi = \frac{\lambda g}{2 \delta n_e^3 |r_{33}| L_e} \quad (4)$$

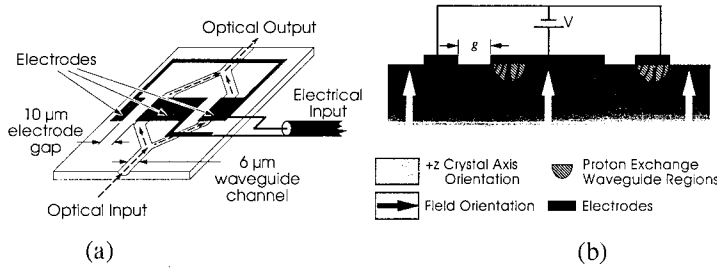


Figure 1. Schematic diagram of a conventional integrated optical Mach-Zehnder interferometer with metal electrodes fabricated in a +z-cut LiNbO₃ substrate: a) perspective view. b) Cross-sectional view transverse to the interferometer arms of the device showing the orientation of the electric field and +z crystal axis.

The novel aspect of our device is that we have achieved push-pull operation without the use of electrodes. Instead of requiring electrodes to generate fields of opposite polarity in the interferometer arms, we have used selective reverse poling (also known as domain inversion) to reverse the crystal orientation in one interferometer arm.

Reverse poling in LiNbO₃ has been widely observed and at least three inversion mechanisms have been identified [14]. We have used titanium diffusion to change the crystalline character of +z lithium niobate to -z. This inversion also reverses the orientation of the y axis. In the x direction lithium niobate possesses a mirror plane and therefore the x axis has inversion symmetry [15], i.e., no differentiation between $\pm x$.

Figure 2a shows a perspective view of our device. Note the absence of electrodes. A schematic cross section of the device in the presence of a uniform, z directed, external field is shown in Figure 2b. The crystal orientation of the domain inverted region is indicated. For this device, the net phase difference accumulated by the optical signal as it travels through the interferometer is:

$$\Delta\phi_e(E) = \frac{2\pi}{\lambda} \delta n_e^3 \left| r_{33} \right| \left| \frac{\vec{E}_z^{(ext)}}{\epsilon} \right| L_r = \pi \frac{E_z^{(ext)}}{E_\pi} \quad (5)$$

where $E_z^{(ext)}$ is $E_z^{(ext)}$ now the magnitude of the uniform external field in which the device is placed, L_r is the length of the reversed poled region of the interferometer arm, and the Half Wave Field, E_π , is defined:

$$E_\pi = \frac{\epsilon \lambda}{2 n_e^3 \left| r_{33} \right| L_r} \quad (6)$$

Using parameter values $n_e=2.2$ (for $\lambda=1 \mu\text{m}$), $\epsilon \approx 35$, and $r_{33}=30.8 \times 10^{-12}$ (m/V) [16] for our device, $E_\pi = 53(\lambda/L_r)$ kV/cm (λ in μm , L_r in cm).

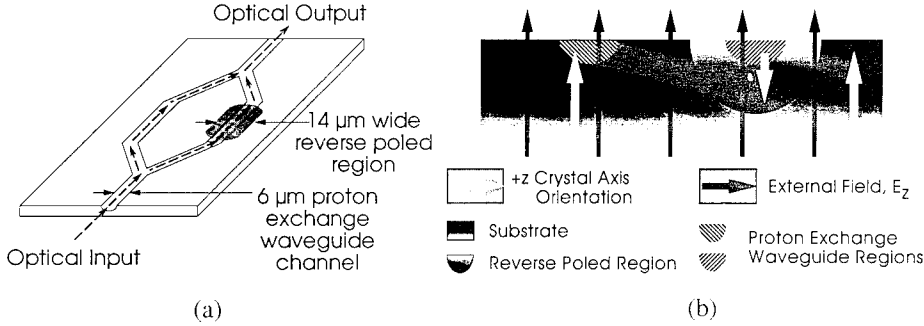


Figure 2. Schematic diagram of the Mach-Zehnder interferometer with no electrodes fabricated in a +-cut LiNbO₃ substrate: a) Perspective view, b) Cross-sectional view transverse to the interferometer arms of the device showing the orientation of the electric field and +-cut crystal axis.

A linear response to the electric field is obtained by setting the phase bias to $\phi_0 = \pi/2$ and operating with a small phase change, i.e. $\Delta\phi_e(E) \ll 1$. Substituting these values into (1) we obtain a device output linearly proportional to the incident field:

$$P_{out} = \frac{P_{in}}{2} \left\{ 1 - \pi \frac{E_z}{E_\pi} \right\} \quad (7)$$

Two performance parameters for which theoretical expressions have previously been derived for the complete fiber coupled sensor are the Minimum Detectable (electric) Field (MDF) E_{min} and the frequency response limit f_m [1]. We make the assumption of a time varying electric field, $E_z^{(ext)} = E_{z0} \cos(\omega t)$, such that the peak interferometer phase deviation in (5) satisfies the small signal limit. Then for our LiNbO₃ device at a wavelength of $\lambda=1.3 \mu\text{m}$, and using a photodetector with $\eta=0.67$, we obtain a value of:

$$E_{min} = \frac{83.5}{L_r \sqrt{P_r}} \quad \text{mV/m per } \sqrt{\text{Hz}} \quad (8)$$

where P_r is the average received optical power in milliwatts.

The frequency response is limited only by the transit time of the optical beam through the device interaction region, and the upper frequency limit is found to be:

$$f_m \leq \frac{6.8}{L_r} \text{ GHz} \quad (9)$$

Note that both E_{\min} and f_m are inversely proportional to the length of the reverse-poled region. Therefore, although lengthening the reverse-poled region improves the sensitivity of the device, this improvement is at the expense of a decrease in the operational bandwidth.

FABRICATION

Symmetric Mach-Zehnder interferometers with a full branch angle of 1° and a total device length of 30 mm were fabricated in 0.5 mm thick, +z-cut, optically polished, LiNbO_3 substrates. The arms were spaced $140 \mu\text{m}$ apart and the straight regions were 12 mm long. The channel waveguides, which were aligned along the y direction, were formed by proton exchange. The process conditions were determined by measurements of the mode structure and effective indices of channel waveguides in test samples. The reverse-poled region in each sensor was produced by titanium diffusion. The diffusion conditions and required titanium thickness were determined by fabricating planar and channel diffused regions on test samples and using the etching characteristics of the regions (5 minutes in $2 \text{ HNO}_3:1 \text{ HF}$ at 85°C) to indicate the quality and extent of reverse poling [17].

The reverse-poled regions were produced first. One hundred nanometers of titanium was deposited on the substrate by electron beam evaporation and was patterned, by photolithographic lift-off, into stripes $6 \mu\text{m}$ wide. The titanium was diffused into the substrate for eight hours at a temperature of 1025°C in a flowing (0.25 l/min.) wet oxygen atmosphere. Etched cross sections of diffused regions indicated that the completely reverse-poled regions were approximately $14 \mu\text{m}$ wide and $7 \mu\text{m}$ deep assuring that the proton exchange waveguide was entirely in reverse-poled material.

Following diffusion, the proton exchange process [18],[19] was used to fabricate the channel waveguides. Windows in the shape of the Mach-Zehnder patterns were opened by wet chemical etching through a mask of 100 nm thick aluminum. One arm of each Mach-Zehnder pattern was aligned with a titanium diffused region. The substrate was immersed in benzoic acid for 30 minutes at a temperature of 220°C . The sample was cleaned, the aluminum mask was stripped, and then the device was annealed [20] for 2 hours at 350°C in a flowing (1.0 l/min.) dry oxygen atmosphere.

The effect of placing proton exchange waveguides in reverse-poled material was evaluated. An excess loss of only 0.25 dB/cm was caused by the reverse-poled regions. After waveguide fabrication, the input and output end-faces were polished and polarization maintaining, single-mode optical fibers (Corning PRSM-PM) were attached to the input and output guides.

EVALUATION

Tests evaluating the minimum detectable field and frequency response of fiber coupled devices were performed using a low-noise Nd:YAG laser operating at a wavelength of $\lambda=1.3 \mu\text{m}$ as the optical source. Optical powers were of the order of one milliwatt. Two

methods were used to obtain a uniform electric field for testing. In the laboratory the device was placed in one of several TEM cells manufactured by Instruments For Industry (IFI) Inc. [21]. Alternatively, free space tests have been performed in an anechoic chamber facility at IFI. No measurements of E_π or of the modulation depth could be performed using these techniques due to limits on field strength generation. Due to phase bias drift, all measured results were recorded when the device was near a $\pi/2$ phase bias. The typical test set-up used is shown in Figure 3.

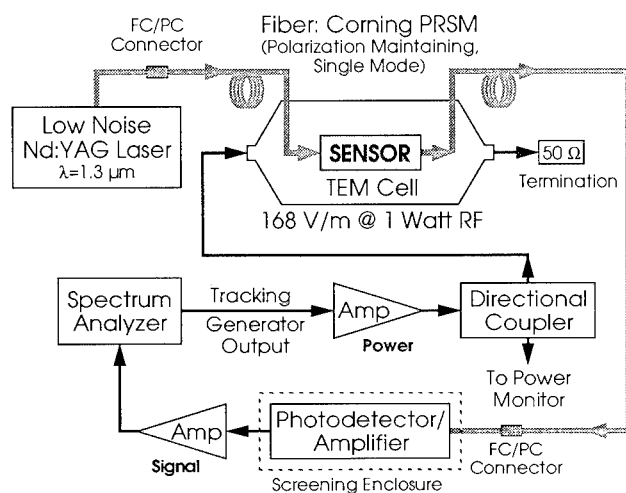


Figure 3. Block diagram of the test setup used for frequency response evaluation.

Figure 4 shows the response of a device for frequencies up to 1 GHz. The response was measured in two sweeps due to the two band operation of the power amplifier driving

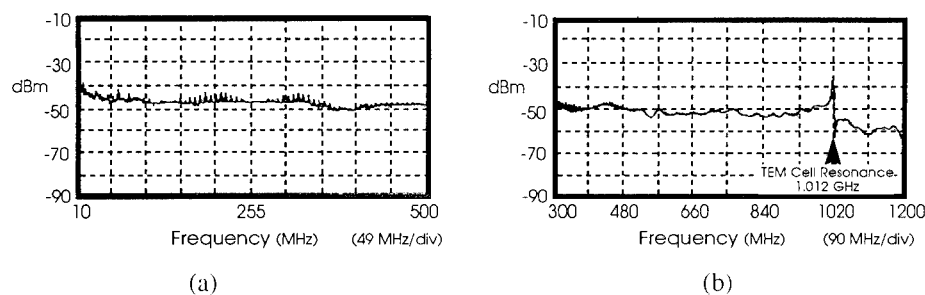


Figure 4. Sensor frequency response: a) Low frequency sweep, 10-500 MHz. b) High frequency sweep, 0.3-1.2 GHz.

the TEM cell. Figure 4a shows the response from 10 to 500 MHz. The response is flat over the band of the power amplifier except for some low frequency piezoelectric resonances. The amplitude of these resonances has been greatly reduced from those exhibited by previous devices by tapering the substrate edges and thereby disrupting the physical symmetry of the substrate. Figure 4b shows a frequency sweep from 0.3 to

1.2 GHz. The extent of this measurement was limited to the 1.2 GHz cutoff of the photodetector and the resonance of the TEM cell. The resonance of the TEM cell itself is clearly seen at 1.012 GHz.

Figure 5 shows the results of tests performed using a TEM cell designed to operate over a frequency range of 3-5 GHz. The length of the reverse-poled region of this device was 0.7 cm. The response of the device follows the field strength in the cell.

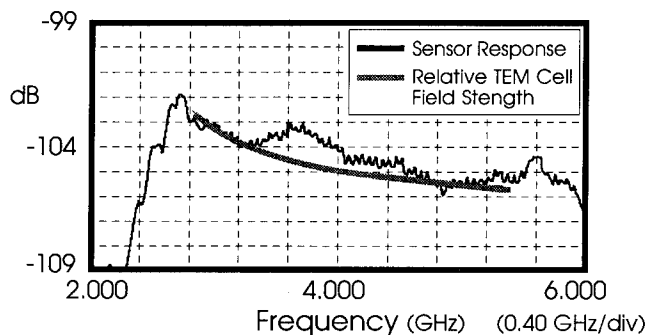


Figure 5. Sensor frequency response at 4 GHz. The shaded curve represents the theoretical field strength in the TEM cell.

The same device was tested in the anechoic chamber facility with the test field produced by a log-periodic antenna. Measurements on a 100 V/m field indicated a detection sensitivity of 34 mV/m per $\sqrt{\text{Hz}}$ while the spectral measurements exhibited a flat response to 10 GHz. Test equipment limitations precluded measurements at higher frequencies.

The devices tested to date have been sensitive to temperature induced bias drift. As Harvey has found that photorefractive induced bias drift is not a factor at $\lambda=1.3 \mu\text{m}$ for the optical powers used in our tests [22], the observed bias drift is attributed to the pyroelectric

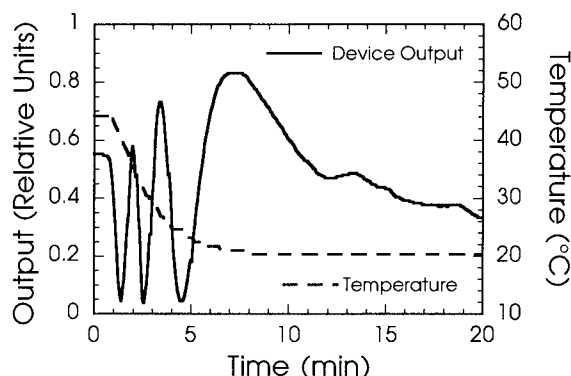


Figure 6. Measurement of temporal output stability as a function of temperature.

effect. Temperature drift of the bias point, using an optical input of 2 mW and zero field, was measured to be 2.9 rad/°C. Figure 6 shows typical results of these temperature stability measurements.

Several passive compensation schemes to improve the temperature stability are under development. These include the possibilities of reverse poling large areas of the substrate to improve charge neutralization or reverse poling through the substrate by electric pulse methods.

CONCLUSION

We are continuing to study and improve the performance of a totally passive electro-optic electric field sensor. By combining in a unique way the well established processes of selective substrate domain inversion and proton exchange waveguide formation, we have fabricated a lithium niobate Mach-Zehnder device which operates without any metal electrodes. The device can perform remote sensing using only a fiber optic connection. Detection sensitivities of 34 mV/m per $\sqrt{\text{Hz}}$ have been measured with a frequency response extending to 10 GHz. These values compare well with theoretical calculations.

ACKNOWLEDGMENTS

We gratefully acknowledge the assistance of IFI, Inc., Ronkonkoma, NY. This work was supported in part by the Ohio Thomas Edison Program, Edison Seed Development Fund under Project 200, and the SBIR under Contract DAAL-02-90-C-0078.

REFERENCES

- [1] D. H. Naghski, J. T. Boyd, H. E. Jackson, S. Sriram, S. A. Kingsley, and J. Latess, "An Integrated Photonic Mach-Zehnder Interferometer with No Electrodes for Sensing Electric Fields," *IEEE J. Lightwave Technol.*, vol. 12, pp. 1092-1098, 1994.
- [2] S. Sriram, S. A. Kingsley, and J. T. Boyd, "Electro-optical Sensor For Detecting Electric Fields," United States Patent Number: 5,267,336, Nov. 30, 1993.
- [3] C. H. Bulmer, W. K. Burns, and R. P. Moeller, "Linear interferometric waveguide modulator for electromagnetic-field detection," *Opt. Lett.*, vol. 5, pp. 176-178, 1980.
- [4] M. J. Ahmed and L. Young, "Mach-Zehnder interferometer tuning with Ta_2O_5 film loading," *Appl. Opt.*, vol. 22, pp. 4082-4087, 1983.
- [5] C. H. Bulmer, "Sensitive, highly linear lithium niobate interferometers for electromagnetic field sensing," *Appl. Phys. Lett.*, vol. 53, pp. 2368-2370, 1988.
- [6] N. A. F. Jaeger and L. Young, "High-voltage sensor employing an integrated optics Mach-Zehnder interferometer in conjunction with a capacitive divider," *IEEE J. Lightwave Technol.*, vol. 7, pp. 229-234, 1989.
- [7] S. Miyazawa, "Ferroelectric domain inversion in Ti diffused lithium niobate optical waveguides," *J. Appl. Phys.*, vol. 50, pp. 4599-4603, 1979.
- [8] G. A. Massey, D. C. Erickson, and R. A. Kadlec, "Electromagnetic field components: Their measurement using linear electrooptic and magneto-optic effects," *Appl. Opt.*, vol. 14, pp. 2712-2719, 1975.
- [9] J. Chang, C. N. Vittitoe, B. T. Neyer, and W. P. Ballard, "An electro-optical technique for intense microwave measurements," *J. Appl. Phys.*, vol. 57, pp. 4843-4848, 1985.
- [10] W. F. Filter, J. Chang, C. O. Landron, and D. J. Muron, "Photonic measurements of microwave pulses," in *Fiber Optic and Laser Sensors III*, SPIE vol. 566, pp. 227-232, 1985.

- [11] N. A. F. Jaeger and L. Young, "Asymmetric slab and strip-loaded integrated optic devices for the measurement of large electric fields," *IEEE J. Lightwave Technol.*, vol. LT-5, pp. 745-750, 1987.
- [12] B. E. A. Saleh and M. C. Teich, *Fundamentals of Photonics*. New York: John Wiley & Sons, Inc., 1991, pp. 703.
- [13] R. G. Hunsperger, *Integrated Optics: Theory and Technology*. 2nd edition, Berlin: Springer-Verlag, 1985, pp. 125.
- [14] M. Tasson, H. Legal, J. C. Gay, J. C. Peuzin, and F. C. Lissalde, "Piezoelectric study of poling mechanism in lithium niobate crystals at temperature close to the Curie point," *Ferroelectrics*, vol. 13, pp. 479-481, 1976.
- [15] R. S. Weis and T. K. Gaylord, "Lithium Niobate: Summary of Physical Properties and Crystal Structure," *Applied Physics A*, vol. 37, pp. 191-203, 1985.
- [16] A. Yariv, *Optical Electronics*. 4th edition, Philadelphia: Saunders College Publishing, 1991, pp. 317-320.
- [17] S. Thaniyavarn, T. Findakly, D. Booher, and J. Moen, "Domain inversion effects in Ti-Lithium Niobate integrated optical devices," *Appl. Phys. Lett.*, vol. 46, pp. 933-935, 1985.
- [18] J. L. Jackel, C. E. Rice, and J. J. Veselka, "Proton exchange for high-index waveguides in LiNbO₃," *Appl. Phys. Lett.*, vol. 41, pp. 607-608, 1982.
- [19] D. F. Clark, A. C. G. Nutt, K. K. Wong, P. J. R. Laybourn, and R. M. D. L. Rue, "Characterization of proton-exchange slab optical waveguides in z-cut LiNbO₃," *J. Appl. Phys.*, vol. 54, pp. 6218-6220, 1983.
- [20] P. G. Suchoski, T. K. Findakly, and F. J. Leonberger, "Stable low-loss proton-exchanged LiNbO₃ waveguide devices with no electro-optic degradation," *Opt. Lett.*, vol. 13, pp. 1050-1052, 1988.
- [21] Instruments For Industry, 731 Union Pkwy., Ronkonkoma, NY 11779.
- [22] G. T. Harvey, "The Photorefractive Effect in Directional Coupler and Mach-Zehnder LiNbO₃ Optical Modulators at a Wavelength of 1.3 μm ," *IEEE J. Lightwave Technol.*, vol. 6, pp. 872-876, 1988.

MONOLITHIC SEMICONDUCTOR MOPAs: HOW THE WATT WAS WON

Robert J. Lang, Ross Parke, David Mehuys, Julian Osinski, Steve O'Brien,
Jo Major, and Dave Welch

SDL, Inc.
80 Rose Orchard Way
San Jose, CA 95134

SUMMARY

High power spatially coherent semiconductor lasers have been a goal of diode laser researchers for years. Single-stripe devices are generally limited to a hundred mW of output power, at which point reliability problems associated with the high optical intensity at the output facet begin to limit device performance. The simple solution to the problem of facet power density has been to increase the lateral dimension of the laser facet from 3-4 to hundreds of μm . However, this approach has simply traded one problem, facet degradation, for another: control of the spatial mode.

Broad area lasers, the simplest configuration with a wide output facet, typically operate in an unpredictable combination of lateral spatial modes. Over the years, numerous geometries have been proposed and demonstrated in an attempt to reach higher optical powers while maintaining a mode that can be focused to a diffraction-limited spot with relatively simple optics. The contenders for high power lasers have included both monolithic and multi-chip solutions. Monolithic devices include laser arrays [1-3], unstable resonators [4,5], and monolithic active grating amplifiers [6,7]. Higher diffraction-limited powers have been obtained from multi-chip devices, e.g., external injection of broad area amplifiers [8-9], but the simplicity and utility of a monolithic solution makes it by far the preferred approach for most applications.

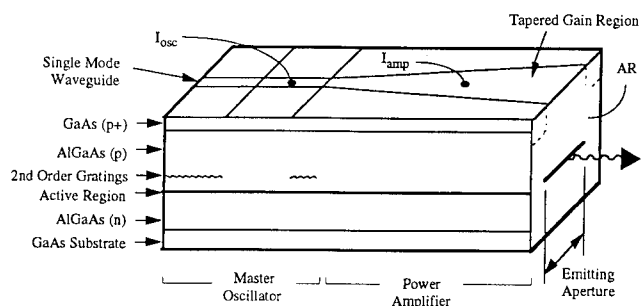


Figure 1. Schematic of a monolithic MOPA laser diode.

The configurations that have met with the most success have been master-oscillator power amplifier (MOPA) geometries. The highest single-spatial-mode powers reported to date have come from external injection of a broad area laser amplifier, which has reported 11.6 W pulsed with diode laser injection [9]. A disadvantage of broad area laser amplifiers is the relatively high injection power needed to saturate the gain of the amplifier and obtain efficient energy extraction, typically ~ 1 mW/ μm of facet width. Recently, a discrete flared optical amplifier was demonstrated by workers at MIT Lincoln Laboratory that achieved >1 W single-spatial mode output power with an externally injected signal of only 10 mW [10]. The flared amplifier combines several desirable features: a low injection power reduces the requirements on the master oscillator, while the continuous geometric demagnification of the beam lowers the power density as the beam is amplified, resulting in a power density at the facet that is actually lower than that obtained in conventional narrow-stripe lasers. Perhaps most importantly, the continuous magnification of the beam throughout the flared amplifier has the effect of demagnifying perturbations in the optical beam, thereby delaying the onset of filamentation.

Although discrete flared amplifiers offer high diffraction-limited power, their greatest utility comes with their ease of integration with a narrow-stripe master oscillator. By integrating a distributed Bragg reflector (DBR) master oscillator with a flared power amplifier, a true monolithic MOPA was demonstrated at SDL [12] that has to date produced over 3 W cw diffraction-limited output power (Figure 2).

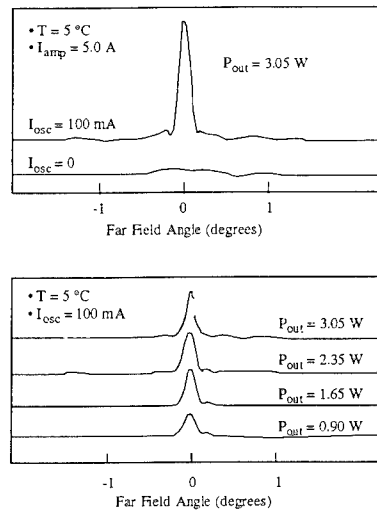


Figure 2. Far field of the monolithic MOPA at various drive currents.

Flared amplifiers are quickly being developed because of their demonstrated ability to achieve high CW single-mode powers. In fact, the highest diffraction-limited powers reported at all wavelengths from monolithic devices are based on flared MOPAs and/or flared unstable resonators (Figure 3). Furthermore, higher levels of integration are now being pursued, including tapered unstable resonators based on flared gain elements; external cavity flared lasers; mode-locked lasers; phase- and frequency-modulatable MOPAs; and MOPA arrays. The latter offers the prospect of cw diffraction-limited powers in the tens of Watts from diode lasers.

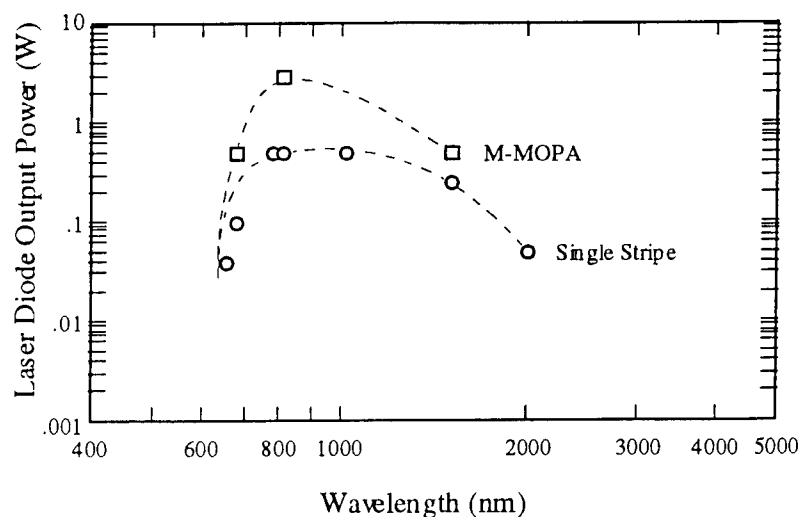


Figure 3. Maximum diffraction-limited power from monolithic devices versus wavelengths.

REFERENCES

- [1] D.F. Welch, P.S. Cross, D.R. Scifres, W. Streifer, and R.D. Burnam, "High power (cw) in-phase locked 'Y' coupled laser arrays," *Appl. Phys. Lett.*, 49, pp. 1632-1634, (1986).
- [2] L.J. Mawst et al., "CW high-power diffraction-limited beam operation from resonant optical waveguide arrays of diode lasers," *Appl. Phys. Lett.*, 58, pp. 22-24, (1991).
- [3] J.S. Major, D.F. Welch, and D.R. Scifres, "High power high efficiency antiguide laser arrays," *Appl. Phys. Lett.*, 59, pp. 2210-2212, (1991).
- [4] R.R. Craig, L.W. Casperson, G.A. Evans, and J.J. Yang, "High-loss resonators for semiconductor diode lasers," Paper ThR4, presented at Conference On Lasers and Electro-Optics, Anaheim, California, USA, June 19-22, 1984.
- [5] M.L. Tilton, G.C. Dente, A.H. Paxton, J. Cser, R.K. DeFreez, C.E. Moeller, and D. Depatie, "High power, nearly diffraction-limited output from a semiconductor laser with an unstable resonator," *IEEE J. Quantum Electron.*, 27, pp. 492-494, 1991.
- [6] D. Mehuys, D.F. Welch, R. Parke, R.G. Waarts, A. Hardy, and D.R. Scifres, "High power diffraction-limited emission from monolithically integrated active grating master oscillator cascaded power amplifier array," *Elect. Lett.*, 27, pp. 492-494, 1991.
- [7] N.W. Carlson, J.H. Abeles, D.P. Bour, S.K. Liew, W.F. Reichert, P.S.D. Lin, and A.S. Gozdz, "Demonstration of a monolithic grating-surface-emitting laser master oscillator cascaded power amplifier array," *IEEE Photonics Tech. Lett.*, 2, p. 708, (1990).
- [8] L. Goldberg and D. Mehuys, "21 W broad area near-diffraction-limited semiconductor amplifier," *Appl. Phys. Lett.*, 61, pp. 633-635, (1992).
- [9] D. Mehuys, L. Goldberg, D.F. Welch and J. Weller, "11.6 W peak power, diffraction-limited diode-to-diode optical amplifier," *Appl. Phys. Lett.*, 62, pp. 544-546, 1993.
- [10] N. Walpole, E.S. Kintzer, S.R. Chinn, C.A. Wang, and L.J. Missaggia, "High-power strained-layer InGaAs/AlGaAs tapered traveling wave amplifier," *Appl. Phys. Lett.*, 61, pp. 740-742, 1992.
- [11] D.F. Welch, R. Parke, D. Mehuys, A. Hardy, R.J. Lang, S. O'Brien and D.R. Scifres, "1.1 W cw diffraction-limited operation of a monolithically flared amplifier master oscillator power amplifier," *Elect. Lett.*, 28, pp. 2011-2012, 1992.

MULTI-WAVELENGTH VERTICAL CAVITY LASER ARRAYS GROWN ON A PATTERNED BACKUP SUBSTRATE

C. J. Chang-Hasnain and L. E. Eng

E. L. Ginzton Laboratory and Electrical Engineering Department
Stanford University, Stanford, CA 94305-4085

ABSTRACT

The capability to fabricate two-dimensional (2D) semiconductor diode laser array is a key and most important step towards making wafer-scale low-cost lasers. The recent emergence of vertical cavity surface emitting laser (VCSEL) facilitates the fabrication such large 2D arrays. In this paper, I will review recent progress on a novel large-aperture single-mode VCSEL and a 2D multiple-wavelength VCSEL array for ultrahigh bandwidth applications. We demonstrated a passive antiguide region (PAR) VCSEL which emits a stable single mode with very low threshold, a large aperture, and fixed polarization. We also demonstrated multi-wavelength VCSEL arrays with repeatable wavelength spans over 20 nm grown by Molecular Beam Epitaxy. The wavelength shift is achieved by varying the GaAs growth rate across the wafer using a patterned backing wafer to induce a temperature profile. Such multiple wavelength laser arrays are promising for ultra-high bandwidth optical transmission and switching systems using wavelength division multiplexing (WDM).

INTRODUCTION

The vertical cavity surface emitting lasers (VCSEL) are promising for many applications including optical interconnects, optical communications, and optical recording because its topology facilitates wafer-scale processing and cost-effective fiber coupling. The VCSEL structure is also highly promising for making large multiple wavelength arrays [1]. Recently, using a patterned substrate technique, we demonstrated multi-wavelength VCSEL arrays with repeatable wavelength spans [2]. This technique is promising for making cost-effective multi-wavelength arrays for ultra high bandwidth wavelength-division-multiplexed (WDM) communications.

VCSEL structure is uniquely suitable for making multi-wavelength laser array because its ultrashort cavity typically allows only one longitudinal mode, which is thus the lasing wavelength. This wavelength is determined by the laser cavity round trip phase condition, which can be varied across the array by varying the thickness of either the cavity or the mirror layers. We proposed and demonstrated a 2D VCSEL array emitting 140 distinct wavelengths over a 43 nm wide wavelength span using a spatially chirped mirror layer in the VCSEL [1]. Serving as a proof of concept, this was accomplished using the inherent beam flux gradient in a Molecular Beam Epitaxy (MBE) system. A limitation of this method is that cavity thickness is monotonically graded across the wafer, and the chirp, and thus the wavelength range, is fixed. For manufacturing purposes, it is desirable to fabricate many identical chirped arrays in a single growth. In applications such as parallel WDM architectures [3] where each array is one pixel, it is necessary to be able to reproduce many identical arrays on the same wafer.

Recently, there are a few publications reporting various techniques to fabricate multi-wavelength VCSELs [4, 5]. In ref. 4, OMCVD growth on front-side patterned substrate was used. Using the fact that the growth rate varies with the pattern size, VCSELs emitting at different wavelengths were obtained. Ref. 5, on the other hand, uses an oxide layer, which is part of the top reflector, with different thickness to attain different VCSEL wavelengths. In this paper, we discuss a novel technique using a lateral substrate-temperature profile during growth to create a varied thickness. The thickness variation is controlled by a lithographically defined pattern on the substrate back side. By bonding the substrate to a patterned backing wafer, we induce a lateral surface temperature gradient on the substrate, thereby altering the GaAs growth rate across the wafer during the growth of the cavity. We demonstrate a multi-wavelength VCSEL array with a 20 nm shift in emission wavelength. This technique allows fabrication of a large number of multi-l arrays with repeatable wavelength on the same wafer.

APPROACH

It is well known that in Molecular Beam Epitaxy (MBE) crystal growth, the GaAs growth rate decreases with substrate temperature above 640°C [6]. For temperature changes of 20 - 30°C, the growth rate can change by as much as 20%. Previously, this effect has been used to grow laterally tapered GaAs quantum wells and AlGaAs waveguides [7,8]. In that work, 1 mm grooves were machined in the molybdenum substrate holder in an MBE system, to create a nonuniform thermal contact to the substrate during growth. Here, we extend this technique by defining patterns lithographically in GaAs backing wafers and use the selective heating to alter the cavity length in vertical cavity structures. The advantage of using a GaAs backing wafer rather than a moly block is that arbitrary patterns can easily be defined using lithography. A schematic of this technique is shown in Fig. 1. A 200 μm deep pattern is defined in a GaAs backing wafer using lithography and chemical etching. The substrate is then bonded to the backing wafer using indium, and the two are held in place in the substrate holder with molybdenum wires. Due to the increased thermal contact between the wafers where there is indium, we expect an increased substrate temperature in these regions.

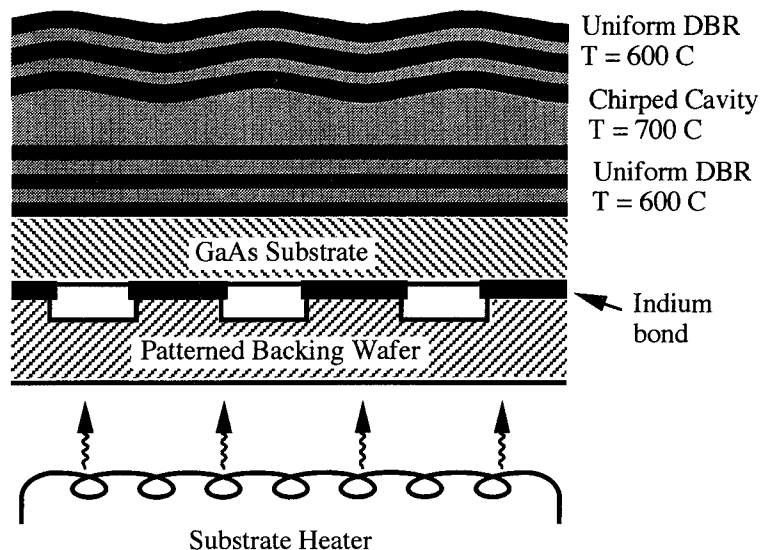


Figure 1 Schematic of techniques used to spatially vary the substrate temperature during growth. Indium is used to selectively bond the substrate to the ridges of patterned GaAs backing wafers. The increased thermal contact gives rise to higher temperatures in these regions.

PASSIVE CAVITIES

GaAs Cavities

To investigate the use of this approach for VCSEL arrays, we have designed a test structure which consists of a passive 300 nm GaAs cavity and Bragg reflectors (10.5 pairs on the substrate side and 8 pairs on the top) consisting of quarter wave layers of AlAs/GaAs designed for a 950 nm center wavelength. We calculate a cavity mode wavelength of 980 nm in this structure. Both mirrors are grown at a substrate temperature of 600°C and the cavity is grown at approximately 700°C. We expect the mirrors to be uniform since they are grown below the gallium desorption temperature. The cavity, however, will have a thickness variation across the wafer due to the induced surface temperature difference in a regime in which significant gallium desorption occurs.

We characterize the cavity structures by measuring the reflectivity spectrum across the 2" wafer. A broadband light source is coupled through a multimode fiber, reflected off the sample, and collected into an optical spectrum analyzer (OSA). The wafer is on a motorized translation stage and the entire measurement is computer controlled. For each point on the wafer, a spectrum is measured and the cavity mode is recorded. The schematic of the instrument is shown in Fig. 2. The cavity mode wavelength in this structure is very sensitive to the cavity length; thickness variations of 0.3 % translate to wavelength resolution of 1 nm, which is easily obtained. The pattern we used was an array of 1 mm stripes with a 3 mm period. In Fig. 3, we show the measured cavity mode wavelength for

this wafer along the direction perpendicular to the stripes. We observe a periodic modulation of the cavity mode, with a peak shift of 8 nm and a 3 mm period.

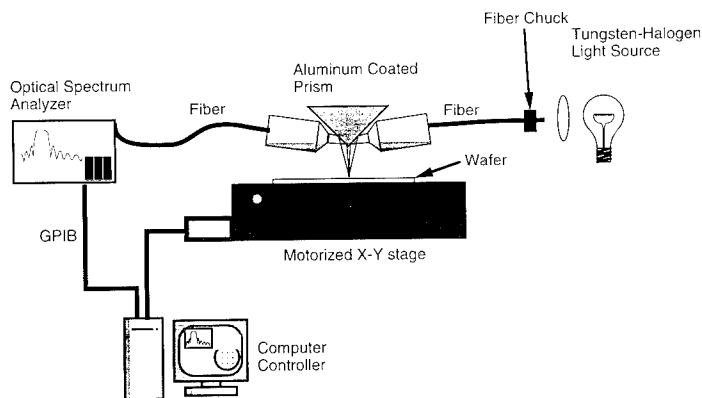


Figure 2 Schematic of wafer-scale reflectometry mapping a setup.

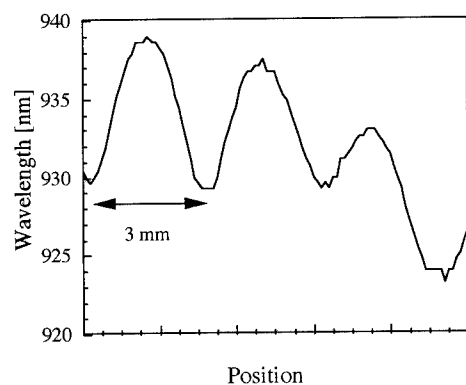


Figure 3 Cavity mode vs. position for a backside pattern with a 3mm period.

AlGaAs Cavities

For typical VCSEL designs, the cavity usually consists of AlGaAs rather than GaAs in order to increase the heterojunction barriers near the active region. This will improve carrier confinement in the well, and reduce leakage currents [9]. During growth, the aluminum sticking coefficient is unaffected by substrate temperature even in the higher temperature range we are using. Therefore, there will be an increase in aluminum content as well as a decrease in thickness in the high temperature portions of the wafer. The higher aluminum content will lower the index of the material and therefore lower the optical thickness. The fraction change in optical thickness between regions with (hot) and without (cold) Ga desorption for $\text{Al}_x\text{Ga}_{1-x}\text{As}$ growth can be written as

$$\frac{\Delta d}{d_{cold}} = \frac{d_{cold} - d_{hot}}{d_{cold}} = 1 - \frac{n_h x_h}{n_c x_c} \quad (\text{Eq. 1})$$

In Figure 4, the change in optical thickness as a function of nominal (i.e. no gallium re-evaporation) molefraction is shown for various gallium sticking coefficients. The substrate temperature dependence of the optical thickness of an AlGaAs cavity is reduced compared with GaAs molefraction typically used in VCSELs, $x = 0.2$, the effect is small.

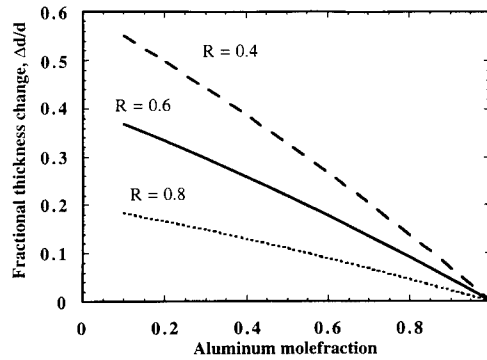


Figure 4 Calculated fractional optical thickness ($n \cdot d$) difference between regions with and without gallium desorption for an $\text{Al}_x\text{Ga}_{1-x}\text{As}$ layer, for various gallium sticking coefficients, R .

MULTIPLE WAVELENGTH VCSEL CHARACTERISTICS

A VCSEL structure was grown on a GaAs substrate bonded to another GaAs wafer with a single wide strip pattern ($w = 11 \text{ mm}$). The heterostructure growth sequence includes 22.5 pairs of n-doped AlAs/GaAs quarter-wave DBR grown at 600°C , a half-wave n-doped $\text{Al}_{0.2}\text{Ga}_{0.8}\text{As}$ spacer at 700°C , 3 undoped 5 nm $\text{In}_{0.2}\text{Ga}_{0.8}\text{As}$ quantum wells with 5 nm GaAs barriers at 500°C , another half-wave p-doped $\text{Al}_{0.2}\text{Ga}_{0.8}\text{As}$ spacer at 700°C , and 18 pairs of p-doped AlAs/GaAs quarter wave mirrors grown at 600°C . The combined thickness of the AlGaAs spacers and the InGaAs/GaAs wells and barriers add up to one full wavelength cavity at 950 nm . In order to give sufficient time to ramp down the substrate temperature, growth is interrupted for 1 minute before the quantum wells. The mirror interfaces are linearly graded over 15 nm to reduce the series resistance of the structure [9,10].

The reflectivity of the VCSEL structure was measured. A 19 nm wavelength shift was obtained between the hot and cold regions. The transition region on the two sides of the single stripe pattern is about 2 mm wide, which is the useful region for fabricating multi-wavelength VCSEL arrays. We fabricated $40 \mu\text{m}^2$ VCSELs spaced by $180 \mu\text{m}$ using Ti/Au as an etch mask, and etch through the active region using wet chemical

etching. The lasers were probe tested with 200 ns current pulses and the light was collected through the substrate.

Typical threshold currents of 70 - 80 mA was obtained for these broad area VCSELs throughout the high temperature region. Figure 5 shows typical L-I curves across the transition region. The threshold increases with lasing wavelength, which we attribute to an increasing mismatch of cavity mode and gain peak wavelength. Better threshold uniformity can be obtained with an optimized design.

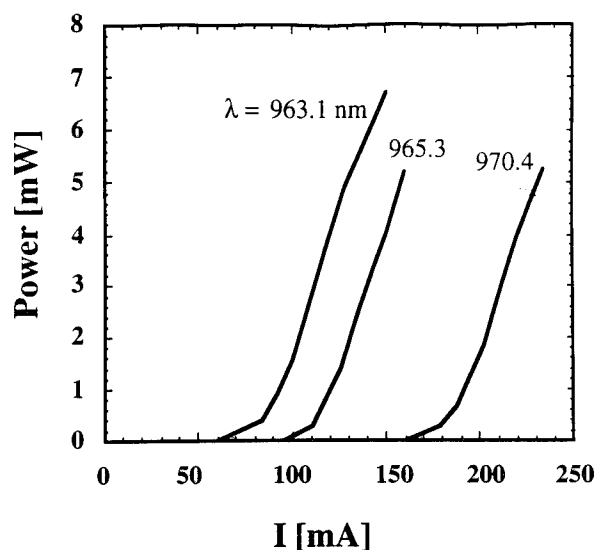


Figure 5 Light vs. current curves for neighboring VCSELs in the transition between hot and cold regions of the wafer.

The lasing spectra for two adjacent arrays fabricated across the transition region is shown in Fig. 6. The wavelengths of the two arrays are nearly the same. The wavelength separation between neighboring lasers is about 2 nm in the linear region. Near both the long and short wavelength ends, the spacing becomes smaller due to the nonlinear nature of the temperature profile. This is acceptable for certain applications. For applications requiring identical wavelength spacing, only the linear portion of the transition region can be used. However, by creating a larger temperature variation, the span of usable wavelength can still be increased and optimized.

Fig. 7 shows the wavelength distribution for 9 adjacent arrays. In the hot region, the VCSEL wavelength is nearly uniform at 963 nm. Across the transition to the colder region the lasing wavelength is blue-shifted 20 nm over 2 mm, at a rate of 14 nm/mm. The average standard deviation in laser wavelength for a given laser number is 0.9 nm, with a maximum of 1.3 nm and minimum of 0.4 nm. Although this deviation is not small enough for a number of WDM applications with narrow wavelength spacings, it is well within the range for a wavelength-coded all-optical network architecture [11].

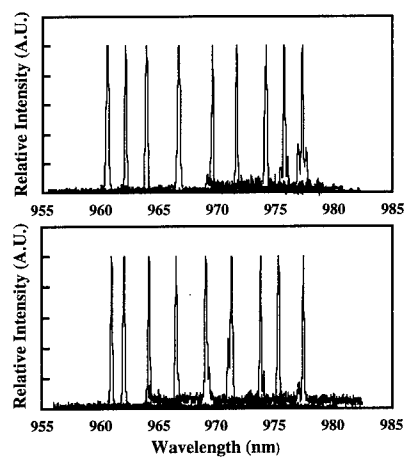


Figure 6 Spectra for two neighboring 9 element arrays.

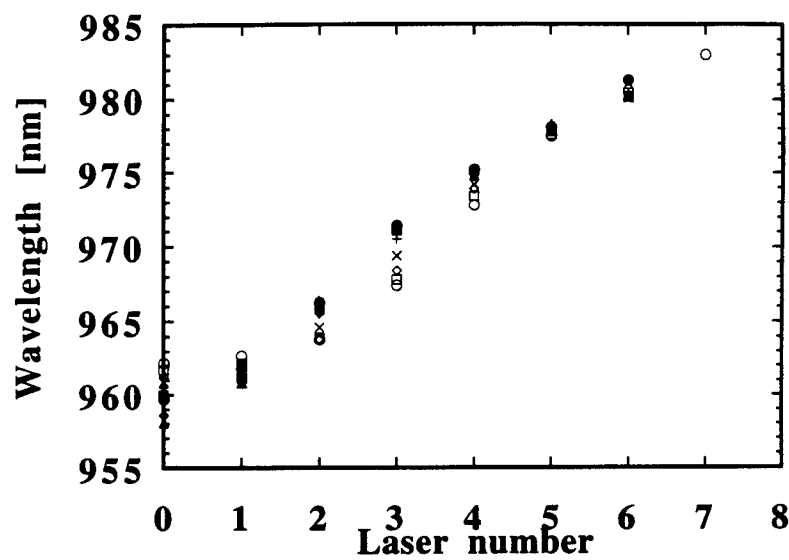


Fig. 7 Lasing wavelength for 9, 7-element, arrays fabricated in the hot-cold transition region, perpendicular to the backside heating pattern.

DISCUSSION

It is very difficult to control the absolute growth rate of GaAs during high temperature MBE growth by relying only on the substrate thermocouple temperature and separate calibrations. Since the rate is very sensitive to substrate temperature in this regime, a small variation in temperature will give rise to unacceptably large thickness differences. Also, the GaAs sticking coefficient has been shown to depend on the aluminum concentration on the surface [6]. For VCSELs, the requirement of matching the cavity mode with the quantum well gain peak makes it necessary to control the growth rate to better than 1%. In order to obtain such precision at high substrate temperature, it is therefore necessary to directly measure, or monitor, the growth rate [12-14] during growth. In this work, we have corrected for the offset in our grown cavity to match our designed thickness after the second $\text{Al}_{0.2}\text{Ga}_{0.8}\text{As}$ spacer layer as in reference [12]. In the future, it will be desirable to implement an in situ reflectivity measurement with spatial resolution to monitor both the hot and cold regions simultaneously during growth. With such a system, both the repeatability as well as the wavelength range of the array can be closely controlled.

CONCLUSIONS

We reported the first multi-wavelength VCSEL arrays with repeatable wavelength span of 20nm grown by MBE with a patterned backing substrate. The magnitude and rate of mode shift are large enough to be very useful for making multiple wavelength VCSEL arrays. We observed experimentally that the patterns transfer with a resolution on the millimeter scale. Future work using this technique will concentrate on demonstrating high reproducibility and making large 2D multi-wavelength arrays.

ACKNOWLEDGMENT

The authors thank R. Nabiev, W. P. Yuen, K. Bacher and K. Toh for their technical contributions. We also acknowledge the collaboration of Prof. J. S. Harris. This work was supported by the ARPA ULTRA program and the ARPA Optoelectronic Materials Center (contract # MDA 972-90-C-0046).

REFERENCES

1. C. J. Chang-Hasnain, J. P. Harbison, C.-E. Zah, M. W. Maeda, L. T. Florez, N. G. Stoffel and T.-P. Lee, *IEEE J. of Quantum Electron.*, vol. 27, 6 pp. 1368 - 1376, June 1991.
2. L.E. Eng, W. Yuen, R.F. Nabiev, K. Toh, K. Bacher, M. Larson, G. Ding, J.S. Harris, and C.J. Chang-Hasnain, "Multiple Wavelength Vertical Cavity Laser Arrays on Patterned Substrates", to appear in *IEEE J. Quantum Electron. Special Issue on Semiconductor Lasers*, June 1995.
3. A. Willner, C. J. Chang-Hasnain and J. Leight, "2-D WDM optical interconnections using multiple-wavelength VCSEL's for simultaneous and reconfigurable communication among many planes," *IEEE Photon. Tech. Lett.*, Vol. 5, pp. 838-841, 1993.
4. F. Koyoma, T. Mukaiyara, Y. Hayashi, N. Ohnoki, N. Hatori and K. Iga, "Wavelength Control of Vertical Cavity Surface Emitting Lasers by Using Nonplanar MOCVD," *Electronics Letters*, Nov. 1994.
5. T. Wipiejewski, M. G. Peters and L. A. Coldren, "Vertical Cavity Surface Emitting Laser Diodes with Post-Growth Wavelength Adjustment," *LEOS Annual Meeting*, Boston, Nov. 1994.
6. R. Fischer, J. Klem, T. J. Drummond, R. E. Thorne, W. Kopp, H. Morkoc and A. Y. Cho, "Incorporation rates of gallium and aluminum on GaAs during molecular beam epitaxy at high substrate temperatures," *J. Appl. Phys.*, Vol. 54, pp. 2508-2510, 1983.

7. W. D. Goodhue, J. J. Zayhowski and K. B. Nichols, "Planar quantum wells with spatially dependent thicknesses and AL content," *J. Vac. Sci. Technol. B*, Vol. 6, pp. 846-849, 1988.
8. D. E. Bossi, W. D. Goodhue, M. C. Finn, K. Rauschenbach, J. W. Bates and R. H. Rediker, "Reduced confinement antennas for GaAlAs integrated optical waveguides," *Appl. Phys. Lett.*, Vol. 56, pp. 420-422, 1990.
9. Randy Geels, Scott W. Corzine and Larry A. Coldren, "InGaAs vertical cavity surface-emitting lasers," *IEEE J. Quantum Electron.*, Vol. 27, pp. 1359-1367, 1991.
10. K. Tai, L. Yang, Y. H. Wang, J. D. Wynn and A. Y. Cho, "Drastic reduction of series resistance in doped semiconductor distributed Bragg reflectors for surface emitting lasers," *Appl. Phys. Lett.*, 56, pp. 2496-2498, 1990.
11. L. A. Buckman, M. S. Wu, G. Giaretta, G. S. Li, P. K. Pepeljugoski, J. W. Goodman, A. Varma, K. Y. Lau and C. J. Chang-Hasnain, "A Novel All-Optical Self-Routed Wavelength-Addressable Network (SWANET)", to be presented at the Optical Fiber Communications Conference, San Diego, February, 1995.
12. K. Bacher, B. Pezeshki, S. Lord and J. S. Harris, "Molecular beam epitaxy growth of vertical cavity optical devices with in situ corrections," *Appl. Phys. Lett.* 61, pp. 1387-1389, 1992.
13. Y. M. Young, M. R. T. Tan, B. W. Liang, S. Y. Wang and D. E. Mars, "In situ thickness monitoring and control for highly reproducible growth of distributed Bragg reflectors," *J. Vac. Sci. Technol. B* 12, pp. 1221-1224, 1994.
14. F. G. Bobel, H. Moller, A. Wowchak, B. Hertl, J. Van Hove, L. A. Chow and P. P. Chow, "Pyrometric interferometry for real time molecular beam epitaxy process monitoring," *J. Vac. Sci. Technol. B* 12, 1207-1210, 1994.

POLARIZATION INDUCED ENHANCEMENT OF RELATIVE INTENSITY NOISE AND MODULATION DISTORTION OF VERTICAL CAVITY SURFACE EMITTING LASERS

M.S. Wu¹, L.A. Buckman², G.S. Li¹, K.Y. Lau², C.J. Chang-Hasnain¹

¹E.L. Ginzton Laboratory, Stanford University, Stanford, CA 94305

²Department of EECS, University of California at Berkeley, Berkeley, CA 94720

INTRODUCTION

Proton implanted vertical cavity surface emitting lasers (VCSELs) are easy to fabricate and have high production yields. However, because they exhibit circular symmetry, two orthogonal polarization modes can oscillate simultaneously¹. Consequently, the polarization stability of VCSELs under modulation is of critical concern in applications such as optical recording, optical computing, and optical communications which may involve polarization sensitive components. Previous investigations of VCSEL polarization stability have considered only continuous-wave (CW) operation^{1,2,3,4}. However, practical optical transmission systems require modulation of the laser and hence consideration of the dynamic, modulated laser properties.

The quality of the transmitted laser signal is typically defined in terms of an eye diagram. A standard figure of merit, the quality factor 'Q', is given by

$$Q = \frac{m_1 - m_0}{\sigma_1 - \sigma_0} \quad (1)$$

$$BER = \text{erfc}(Q) \quad \text{for Gaussian noise} \quad (2)$$

where m_1, m_0 are the mean one and zero signal levels respectively

σ_1, σ_0 are the one-sided noise standard deviations

and BER is bit error rate

Clearly, both the transmitted pulse shape and laser noise affect the system performance. We report the pulse shape distortion and relative intensity noise of VCSELs while modulating the laser up to 2 GHz and selecting a single polarization mode. Further, we determine the impact of these characteristics on system performance by measuring the bit error rate while selecting a single polarization mode.

LASER CHARACTERISTICS

Static Performance

The CW light-current (LI) characteristics were measured with and without polarization selection. The difference between the sum of the power detected in each polarization mode and the total laser power output is due to the insertion loss of the polarizer. Three distinct regimes of operation were identified. These are illustrated in Figure 2. In the first regime ($I_{th} - 1.4 I_{th}$), lasing in a single transverse and single polarization mode is observed. In the second regime ($1.4 I_{th} - 1.7 I_{th}$), lasing in a single transverse mode but two orthogonal polarizations, or polarization modes, is observed. In the third regime, lasing in two distinct spatial transverse modes and two polarizations is detected. The existence of the second regime where two orthogonal polarizations compete within the same spatial transverse mode emphasizes the existence of unique polarization modes and consequently the need to study the behavior of these polarization modes.

Modulated response

To measure the RIN and harmonic distortion, the laser was biased with a current source and modulated with either a frequency synthesizer or pulse generator through a bias tee. The VCSEL beam was collimated and refocused onto a GaAs photodetector. The RF signal was amplified using a 45 dB gain amplifier with a 3 dB-bandwidth of approximately 3 GHz. The RF signal was then observed on a RF spectrum analyzer or sampling oscilloscope. A polarizer, mounted on a rotation stage and positioned between the collimating and focusing optics, was used to select a single polarization mode.

Pulse Distortion. A pulse generator was used to modulate the laser from 2 Mb/s to 2 Gb/s with 1 mA peak-to-peak modulation. The detected, amplified pulses with and without polarization selection, with the laser biased in each of the three regimes, were observed on a sampling oscilloscope. In the first regime, negligible distortion of the pulses occur when selecting the first polarization mode. In the second and third regimes, the pulse shape was distorted when either polarization mode was selected. This pulse shape distortion was quantified by considering the harmonic distortion introduced by polarization selection when the laser was modulated with a sinusoidal signal. With the laser biased in each regime and modulated at frequencies ranging from 100 MHz to 2 GHz, the power in the second harmonic, with and without polarization selection, was normalized to the power in the fundamental. Figure 3 shows the increase in the normalized second harmonic power when the first polarization mode is selected when compared to the case of no polarization selection. As illustrated in Figure 3, in the first regime less than 2 dB distortion is observed over the entire modulation frequency. In the second and third regimes, a distortion as high as 4 dB and 12 dB, respectively, was observed at a modulation frequency of 100 MHz. Distortion for both regimes decreases significantly with increasing modulation frequencies (> 500 MHz).

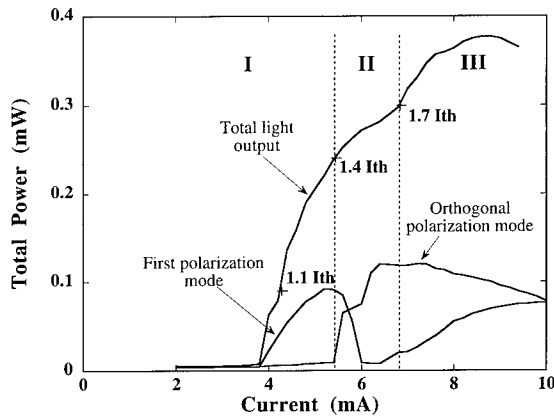


Figure 1. Laser LI characteristic with and without polarization selection

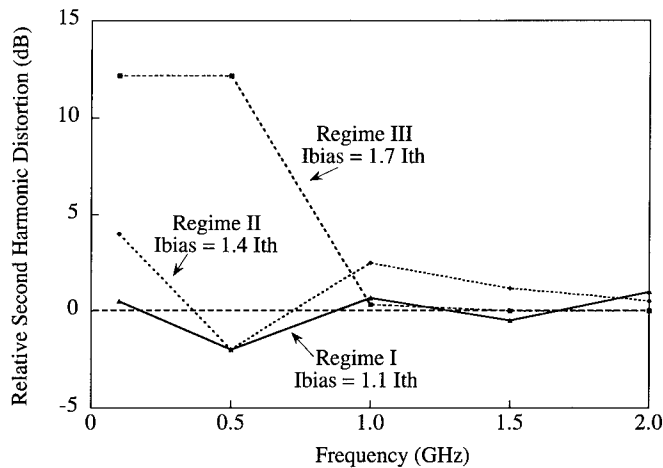


Figure 2. Increase in the normalized second harmonic power when the first polarization mode is selected.

Relative Intensity Noise. The RIN spectra, with and without polarization selection, in each of the three regimes with 1.5 GHz modulation is shown in Figure 3. The spectra was observed to be independent of the applied modulation frequency. As expected, the RIN decreases with increasing bias and the relaxation peak of the laser modulation response flattens and shifts to higher frequencies. However, substantial RIN enhancement is observed in all regimes at low frequencies when selecting a single polarization mode. As shown in Figure 4, the amount of RIN increase depends on the regime of operation. This low frequency RIN enhancement is most significant in the second and third regimes due to the onset of the additional polarization mode and transverse mode respectively. This type of low frequency RIN enhancement is characteristic of mode partition noise similar to that observed in conventional multi-longitudinal mode edge-emitting lasers⁶. The low frequency behavior may be due to either thermal effects or frequency beating of closely spaced modes. These effects are under investigation.

SYSTEM PERFORMANCE

Both the RIN and harmonic distortion are significantly enhanced when a single polarization is selected and the laser is biased in the second and third regimes. This effect was less apparent when the laser was biased in the first regime. Clearly, substantial system penalty occurs when modulating the laser and selecting a polarization while it is biased in a regime in which it is not even polarization stable for cw operation. However, in the first regime, where stable cw operation is observed, the degradation of the modulated signal due to polarization modes is not clear. To further investigate these effects, bit error rate measurements were performed.

To perform these measurements, an integrated receiver with fiber input was used. The laser was coupled into angle polished fiber to minimize any reflection induced noise. A half-wave plate and polarizer, both anti-reflection coated, were used to control the polarization selection. The laser was operated in the first regime, taking care not to modulate through the laser threshold or the threshold of the second polarization mode.

The bit error rate was measured at 155 Mb/s and 622 Mb/s using a $2^{23}-1$ pseudo-random bit sequence (PRBS). As shown in Figure 4, for 155 Mb/s modulation, when a single polarization mode was selected by tuning the half-wave plate for maximum power transmission, an error floor of 10^{-8} was measured. However, when the half-wave plate was detuned removing any polarization selection, no error floor was detected. Further, when the polarizer was removed, the bit error rate curve was steeper than either of the previous cases and showed no sign of an error floor. For 622 Mb/s modulation, no error floors were detected and the slope of the bit error rate curves was the same for the measurement with the half-wave plate tuned to maximum power transmission, with the half-wave plate detuned, and with the polarizer removed. A slight performance degradation of 0.3 dB was measured with the polarizer removed. However, this is within measurement error and is likely due to the variance in optical connector loss.

These bit error rate measurement results highlight two effects. First, polarization selection degrades the laser's system performance. As the polarization selection is removed, either by removing the polarizer or detuning the polarizer, these effects are no longer apparent. Second, the polarization partitioning noise is a low frequency effect. This is consistent with the RIN and modulation distortion measurements. These effects are analogous to longitudinal mode partitioning noise in edge-emitting lasers where the phenomenon is also a low frequency effect and the mode partition noise is not observed unless mode selective elements are used.

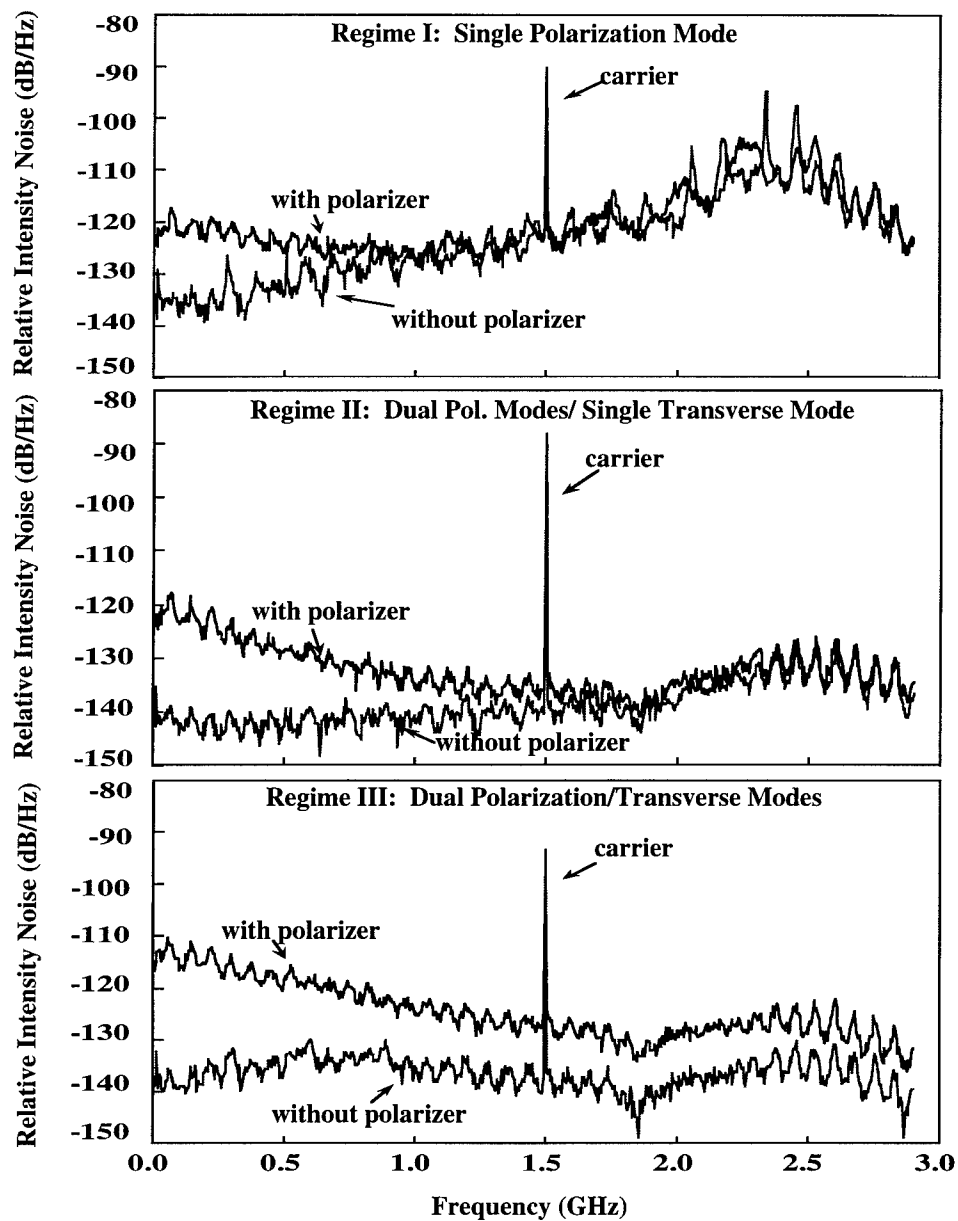


Figure 3. RIN spectra with and without polarization selection in each of the three regimes.

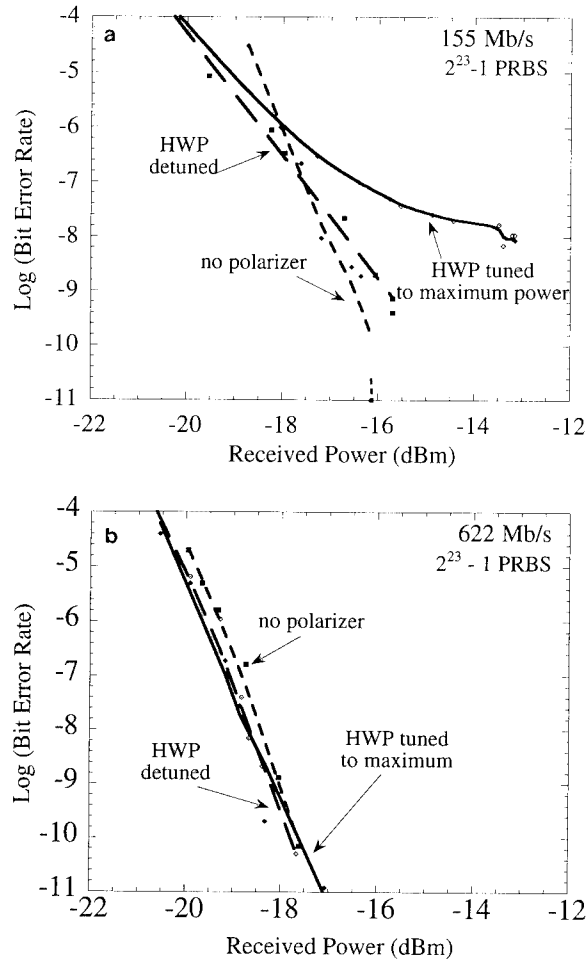


Figure 4. Bit error rate measurements with and without polarization selection.
a) 155 Mb/s b) 622 Mb/s

CONCLUSIONS

We have shown that due to the random nature of the polarization direction in proton-implanted vertical cavity surface emitting lasers, three regimes of cw laser operation exist and polarization modes are distinct modes. These three regimes are: I, single transverse mode and single polarization mode; II, single transverse mode and dual polarization modes; III, dual transverse modes and dual polarization modes. Further, polarization selection degrades system performance leading to BER floors by increasing the RIN and distorting the pulse. These polarization dependent degradations are a low frequency effect.

REFERENCES

1. C.J. Chang-Hasnain, J.P. Harbison, G. Hasnain, and A.C. Von Lehmen, "Dynamic, Polarization, and Transverse Mode Characteristics of Vertical Cavity Surface Emitting Lasers, *IEEE J. Quantum Electronics*, vol. 27, no. 6, pp. 1402-1409, 1991.
2. F. Koyama, K. Morita, and K. Iga, "Intensity Noise and Polarization Stability of GaAlAs-GaAs Surface Emitting Lasers, *IEEE J. Quantum Electronics*, vol. 27, no. 6, pp. 1410-1416, 1991.
3. K.D. Choquette, K.L. Lear, R. E. Leibenguth, and M.T. Asom, "Vertical-Cavity Laser Diode Polarization Switching and Control", *IEEE Trans. on Electron Devices*, vol.40, no.11, pp. 2117-2118, 1993.
4. A. Chavez-Pirson, H. Ando, H. Saito, and H. Kanbe, "Polarization properties of a vertical cavity surface emitting laser superlattice gain medium", *Appl. Phys. Lett.*, vol.62, no. 24, pp. 3082-3084, 1993.
5. G. Hasnain, K. Tai, L. Yang, Y.H. Wang, R.J. Fischer, J.D. Wynn, B. Weir, N.K. Dutta, A.Y. Cho, "Performance of Gain-Guided Surface Emitting Lasers with Semiconductor Distributed Bragg Reflectors", *IEEE J. Quantum Electronics*, vol. 27, no. 6, 1991.
6. C.B. Su, J. Schlafer, R.B. Lauer, "Explanation of low-frequency relative intensity noise in semiconductor lasers", *Appl. Phys. Lett.*, vol.57, no. 9, pp. 849-851, 1990.

InP Based Multiple Quantum Well Lasers with An Integrated Tapered Beam Expander Waveguide

R. Ben-Michael, U. Koren, B. I. Miller, M. G. Young, M. Chien and G. Raybon

AT&T Bell Laboratories, Holmdel, New Jersey 07733

We demonstrate the integration of a laterally tapered adiabatic mode expander waveguide inside the cavity of diode lasers operating at 1.3 and 1.55 μm wavelengths. This integration results in narrow output beam divergence with FWHM of 7° and 5° vertically and laterally respectively. The loss caused by the passive waveguide is minor and for devices operating at 1.55 (1.3) μm threshold currents as low as 12 (22) mA and quantum efficiencies as high as 52% (51%) are obtained. Coupling to a cleaved optical fiber yields broad alignment tolerance with 1dB excess loss for misalignment of $\pm 2.6 \mu\text{m}$ vertically and $\pm 3.1 \mu\text{m}$ laterally, with a minimum coupling loss of -3.5 dB.

The coupling of a diode laser to an optical fiber suffers from relatively high loss, because - a) the optical mode inside the laser is necessarily small for higher confinement to the active region and - b) the optical mode emitted from the laser is not circular. This results in low overlap between the emitted optical mode of a conventional diode laser and the optical mode of the fiber. Furthermore, the low overlap between the optical modes imposes tight alignment constraint on the laser-fiber coupling. In order to modify the optical mode emitted from a conventional semiconductor laser to more closely match that of an optical fiber, the use of an external waveguide for expanding the optical mode has been suggested by Shani et al^[1]. Also, external tapered waveguide beam expanders have been demonstrated for fiber-chip coupling^[2,3]. However, the external waveguides still need careful alignment, thus not solving the tight alignment constraint. Integration of a diode laser and a beam expander results in a simple and cost effective method of coupling to a "cleaved" (flat) optical fiber. This approach has been demonstrated by integrating vertically step-like adiabatic mode expander and a diode laser into one monolithic device^[4,5]. Recently integration of a mode expander inside the laser cavity has been demonstrated by continuously tapering the width of the active buried heterostructure waveguide before the output facet^[6]. While this approach yields some reduction in the output beam divergence, it suffers from insufficient freedom to design the output

waveguide with optimal spot dimensions at the output end. Thus, the vertical spot size is not large enough to match well to a cleaved fiber, and is more suitable for lensed fiber coupling^[6].

In this work we integrated inside the laser cavity an active gain section and a passive adiabatic mode expander which is a modification of the continuously tapered Shani-Henry design^[1]. As the mode expander is constructed from different layers, which, in general, can have a much lower refractive index step than the active region layers, a mode expander with a large symmetric spot size at the output end can be designed, and good matching to a cleaved fiber can be obtained. The structure of this new Adiabatic Mode Expander Laser Diode (AME-LD) device is shown in Fig. 1. The device consists of two sections, a gain section and a passive waveguide section, inside the Fabry Perot cavity. The gain section of the $\lambda = 1.55 \mu\text{m}$ laser includes a stack of six compressively strained 70 Å thick InGaAsP wells, and a 100 Å thick strain compensating InGaAsP barriers. The gain section of the $\lambda = 1.3 \mu\text{m}$ laser consists of six unstrained 80 Å thick InGaAsP wells with 130 Å thick barriers. As shown in Fig. 1, the QW's stack was grown on top of the waveguiding layers, which are the same in the gain and the passive sections.

In the passive section the waveguide consists of two layers. The bottom waveguiding layer of the 1.55 μm laser is a 800 Å thick InGaAsP ($\lambda_{pl} = 1.1 \mu\text{m}$), with a constant width of 5 μm . The upper guiding rib is a 1200 Å thick InGaAsP ($\lambda_{pl} = 1.3 \mu\text{m}$), tapered continuously in the lateral direction starting from 3 μm at the active/passive transition to a sharp point. The waveguide section of the $\lambda = 1.3 \mu\text{m}$ laser consists of a bottom layer of 650 Å thick InGaAsP ($\lambda_{pl} = 1.1 \mu\text{m}$), and the upper guiding rib has the same composition and is 1500 Å thick. The waveguide is buried in semi insulating InP.

The AME expands the beam size both laterally and vertically. Lateral expansion is obtained due to the width of the lower guiding layer in the passive waveguide section which is 5 μm , and is threefold wider than the gain section waveguide. Vertical expansion is obtained by the gradual change from two guiding layers in the beginning of the AME to one guiding layer in the end of the AME. The sharp point of the upper tapered waveguiding rib is formed by using two "knife edge" like masks. After each photolithographic step one side of the taper is selectively etched, to form the adiabatic lateral tapering and the sharp termination point. By using this method the radius of curvature at the termination point is smaller than 500 Å, as observed by SEM. The transition between the gain and the passive sections of the AME-LD is similar to that reported previously^[7]. The gain section consists of a 0.75 μm wide mesa, buried in semi-insulating Fe doped InP, regrown by MOVPE. The same semi insulating blocking layers are used as cladding for the passive beam expanding waveguide. The final third growth step was p-type InP and InGaAs to form the contact.

AME-LD devices consisting of a 350 μm long gain section and a 300 μm waveguide section were cleaved and mounted on copper heat sinks for measurements. The back side of the device was HR coated, while the front side was uncoated. Typical CW light versus current of a 1.55 μm and 1.3 μm uncooled device is shown in Fig 2. As shown in the figure the threshold current of the 1.55 μm device is 12 mA with quantum efficiency of 52%, and the 1.3 μm device has a 22 mA threshold current and a quantum efficiency of 51%. These results are to be compared with conventional lasers that were cleaved from the same wafers without the waveguide section. The threshold current for both wavelengths in comparison to the conventional lasers is about 5 mA higher due to the longer cavity of the AME-LD, but the quantum efficiency is the same as of the conventional lasers. The spectrum of the AME-LD laser in a drive current just below threshold shows longitudinal modes that pertain to the Fabry-Perot cavity, with small variation in the optical power of the longitudinal modes. From these variations we estimate the active/passive reflectivity to be less than 1×10^{-4} , as was observed previously in the same active/passive transition.^[8]

In order to examine the mode transformation of the lateral tapered waveguide section of the AME-LD, the near- and far-field patterns of the AME-LD devices were measured, and compared to conventional lasers cleaved out of the same wafer. The far field pattern of the conventional laser is elliptical, with Full Width at Half Maximum (FWHM) of 27° laterally, and 45° vertically for both operating wavelengths. The far field of the AME-LD devices is almost circular. For the 1.55 μm devices the far-field FWHM is 7° vertically and 5° laterally, as can be seen in Fig. 3. The main central lobe is surrounded by weak scattering from the different interfaces of the AME-LD, but most of the energy is centered in the main lobe. The 1.3 μm device has almost the same far field pattern with a FWHM of 8° vertically and 6° laterally. Near field measurements support the far-field measurements, accounting for the limited resolution of the near field apparatus. The lateral spot size of the AME-LD is measured to be 4 μm , and the vertical size is 3.1 μm . The near field of the conventional device is measured to be 2.0 μm laterally, and smaller than 1 μm vertically.

Coupling efficiency to a cleaved single mode optical fiber is measured to be 44% (-3.5 dB) in both operating wavelengths. The alignment tolerance for butt coupling of the AME-LD devices into a cleaved fiber is shown in Fig. 4. The cleaved fiber was aligned for best coupling, and then translated laterally and vertically to the junction plane. Starting at the initial minimum coupling loss of -3.5 dB, the 1 dB excess loss range of the 1.55 μm devices is as broad as $\pm 2.6 \mu\text{m}$ vertically and $\pm 3.1 \mu\text{m}$ laterally. For the 1.3 μm devices the 1 dB excess loss range is $\pm 2.5 \mu\text{m}$ vertically and $\pm 2.8 \mu\text{m}$ laterally. These results, as well as the small divergence of the far field patterns, are a significant improvement over the previously published results.^[4,5,6]

In conclusion, we have demonstrated a new device which integrates a diode laser and a passive adiabatic mode expander waveguide. The integration of the waveguide allows for sufficient design freedom for the mode expander, so that a large spot size and a very narrow far field patterns can be obtained, and does not cause significant increase in the overall loss of the device. This results in low threshold current and high quantum efficiency. The $\lambda = 1.55 \mu\text{m}$ AME-LD shows an extremely narrow far field patterns with FWHM of 5° laterally and 7° vertically ($6^\circ \times 8^\circ$ for the $\lambda = 1.3 \mu\text{m}$ device). The misalignment tolerance of butt coupling the AME-LD to a cleaved fiber is consequently broad. The 1 dB excess insertion loss range is $\pm 2.6(\pm 2.5) \mu\text{m}$ vertically and $\pm 3.1(\pm 2.8) \mu\text{m}$ laterally for the $\lambda = 1.55$ (1.3) μm device.

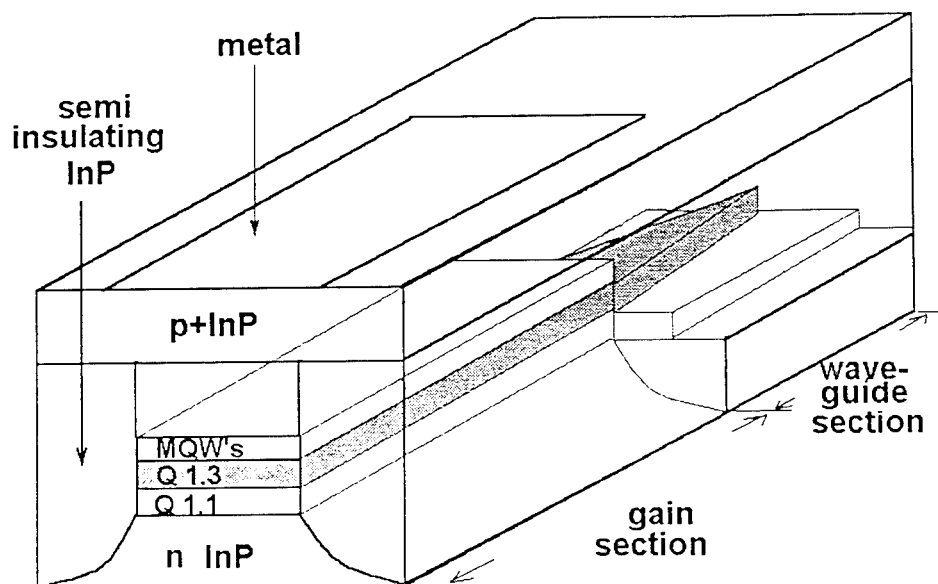


Fig. 1. Schematic description of the AME-LD laser structure for the $1.55 \mu\text{m}$ devices. The device consists of two sections, a gain section, and a passive laterally tapered adiabatic mode expander waveguide section inside the laser cavity. For the $\lambda = 1.3 \mu\text{m}$ devices the two waveguiding layers are both Q $1.1 \mu\text{m}$ layers.

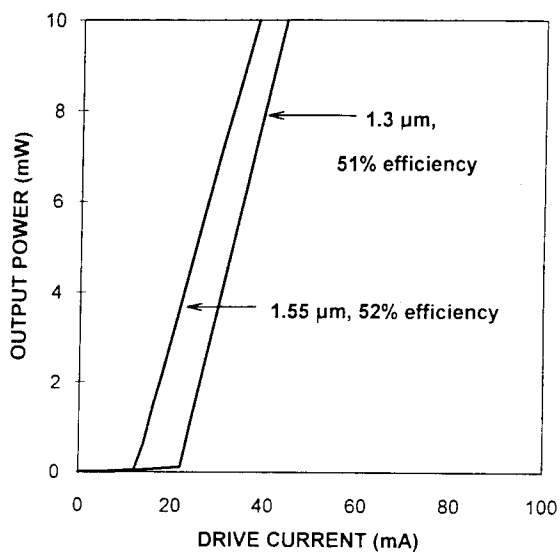


Fig. 2. Typical room temperature CW output light vs. injected current (L-I) of back HR coated AME-LD's with 350 μm gain section and 300 μm Adiabatic Mode Expander waveguide section.

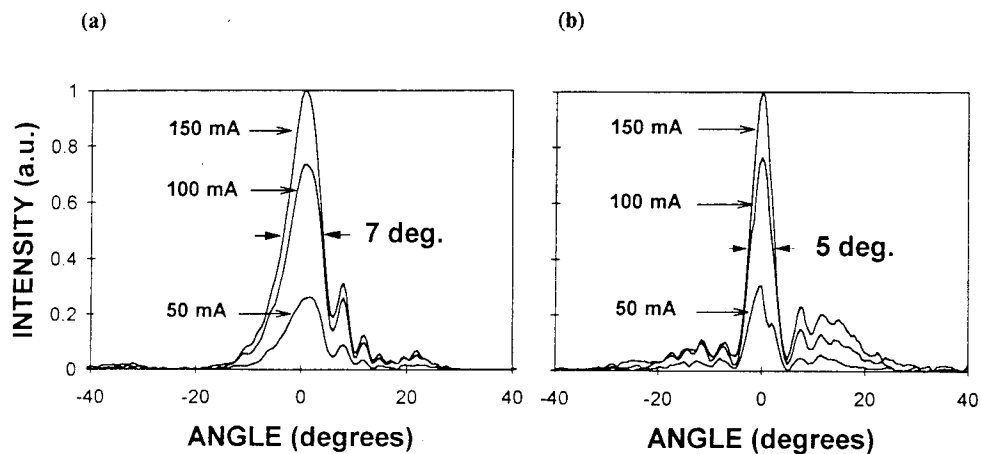


Fig. 3. Far field pattern of an AME-LD operating at 1.55 μm in drive currents of 50, 100 and 150 mA. (a) Vertical far-field pattern with FWHM of 7°. (b) Lateral far-field pattern with FWHM of 5°.

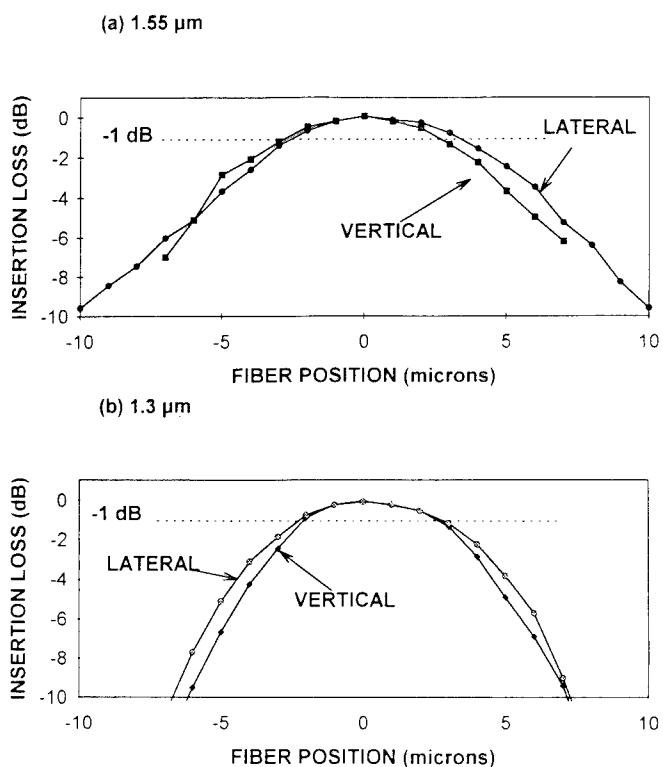


Fig. 4. Butt coupling of AME-LD to a cleaved single mode optical fiber. (a) AME-LD lasing at $\lambda = 1.55 \mu\text{m}$: the 1 dB excess loss for misalignment is $\pm 2.6 \mu\text{m}$ vertically and $\pm 3.1 \mu\text{m}$ laterally. (b) AME-LD lasing at $\lambda = 1.3 \mu\text{m}$: the 1 dB excess loss for misalignment is $\pm 2.5 \mu\text{m}$ vertically and $\pm 2.8 \mu\text{m}$ laterally.

References

- [1] Y. Shani, C. H. Henry, R. C. Kistler, K. J. Orlowsky, and D. A. Ackerman, 'Efficient coupling of a semiconductor laser to an optical fiber by means of a tapered waveguide on silicon' *Appl. Phys. Lett.*, vol. **55**, pp. 2389-2391, 1989.
- [2] G. Muller, B. Stegmüller, H. Westermeier, G. Wenger, 'Tapered InP/InGaAsP waveguide structure for efficient fiber-chip coupling', *Electron. Lett.*, vol. **27**, pp. 1836-1838, 1991.
- [3] R. Zengerle, H. Bruckner, H. Olzhausen, 'Low-loss fiber-chip coupling by a buried laterally tapered InP/InGaAsP waveguide structure', *Electron. Lett.* vol. **28**, pp. 631-632, 1992.
- [4] T. L. Koch, U. Koren, G. Eisenstein, M. G. Young, M. Oron, C. R. Giles, and B. I. Miller, 'Tapered waveguide InGaAs/InGaAsP Multiple Quantum well laser' *IEEE Photon. Tech. Lett.* vol. **2**, pp. 88-90, 1990.
- [5] M. Chien, U. Koren, T. L. Koch, B. I. Miller, M. Oron, M. G. Young, J. L. Demiguel, 'Short cavity distributed Bragg reflector laser with an integrated tapered output waveguide' *IEEE Photon. Tech. Lett.* vol. **3**, pp. 418-420, 1991.

- [6] P. Doussiere, P. Garabedian, C. Graver, E. Derouin, E. Gaumont-Goarin, G. Michuad, and R. Meilleur, 'Tapered active stripe for 1.5 μm InGaAsP/InP strained multiple quantum well lasers with reduced beam divergence' Appl. Phys. Lett. vol. **64**, pp. 539-541, 1994.
- [7] U. Koren, T. L. Koch, B. I. Miller, A. Shahar, paper MDD2, Tech. Dig. of the Topical Meeting on Integrated and Guided Wave Optics, Houston, 1989.
- [8] M.A. Newkirk, B.I. Miller, U. Koren, M.G. Young, M. Chien, R.M. Jopson, G. Raybon, C.A. Burrus, and H.M. Presby, '1.55 micron MQW semiconductor optical amplifier with low gain ripple and high coupling efficiency for photonic integration', Electron. Lett. vol. **29**, pp. 443-444, 1993.

OPTIMAL DESIGN OF COMBINED DISTRIBUTED-FEEDBACK/FABRY-PEROT STRUCTURES FOR VERTICAL CAVITY SURFACE EMITTING SEMICONDUCTOR LASERS

J. Zhou, J. He* and M. Cada

Department of Electrical Engineering
Technical University of Nova Scotia
P.O.Box 1000, Halifax, Nova Scotia, B3J 2X4, Canada,
*Institute for Microstructural Sciences
National Research Council, Ottawa, ON, K1A0R6, Canada

ABSTRACT

In this paper, we investigate the optimal design of combined distributed-feedback/Fabry-Perot (DFB/FP) structures for vertical cavity surface-emitting semiconductor lasers (VCSELs) using a self-consistent model based on coupled-wave equations and on the dependence of gain coupling on the threshold gain. Numerical results, carried out for the GaInAsP/InP material system, confirmed that a much lower threshold current density can be achieved in VCSELs with optimally designed DFB/FP structures. The results thus imply that a potential exists for realizing lower threshold VCSELs with technologically feasible mirror reflectivities and cavity lengths.

INTRODUCTION

Vertical cavity surface-emitting semiconductor lasers (VCSELs) are promising devices as two-dimensional light sources for optical parallel processing and high capacity optical fiber communications due to inherent advantages resulting from their device geometry, such as dynamic single longitudinal mode operation, a potential for high speed modulation, small divergence angles compatible with optical fibers, integrability into high-density two-dimensional arrays, compatibility with monolithic processing, etc. [1-7].

Generally, a Fabry-Perot cavity is used as a resonant cavity in VCSELs; the end mirrors are implemented by semiconductor distributed Bragg reflectors (DBRs) [1-4]. To obtain CW operation at room temperature, a high reflectivity at the end mirrors is essential due to the short cavity configuration. A low threshold current of 1 mA at room temperature in GaAs VCSELs has been achieved in a microlaser structure, i.e. the one with a single quantum well (QW) or multiple quantum wells (MQWs) placed in a high Q FP resonator

with reflectivities of DBRs over 99% [4]. However, there is a fabrication difficulty for DBRs with high reflectivities in 1.55 μm VCSELs because the lower refractive index difference of the material system (GaInAsP/InP) requires about twice as many pairs as in the case of the GaAs-based VCSELs. In addition, each layer must be about twice as thick due to the long wavelength operation [2-4]. Until now, the best reported reflectivity of DBRs in the GaInAsP/InP material system is 98%, and thus only pulsed operation at room temperature has been reported in the long wavelength VCSELs [2,3]. On the other hand, considerable improvements have been predicted for a number of years for VCSELs with periodic gain structures and most recently for VCSELs with a combined DFB/FP structure [5-9]. The electrical pumping of these VCSELs was also demonstrated by using the transverse-junction scheme [9]. These structures were shown to have a much lower threshold compared with FP configurations. Design methods of period gain structures or combined DFB/FP structures for VCSELs have also been studied [5,6]; however, gain and index coupling were not directly introduced into the analytic models, which led to some limitations in understanding the effects of structure parameters and their optimization.

In this paper, we developed a self-consistent model, based on the coupled-wave theory and on the dependence of gain coupling on the threshold gain, to study the VCSELs with combined DFB/FP structures. The results indicate that gain coupling calls for an optimal design of the combined DFB/FP structure, that leads to significant improvements in lasing characteristics of VCSELs. Simulations, carried out for the long wavelength material system, clearly indicate that the combined DFB/FP structures have a potential for realizing lower threshold operation of VCSELs with technologically feasible mirror reflectivities.

MODEL

The studied combined DFB/FP structure is shown in Fig. 1. It consists of an active DFB region, two semiconductor multilayer reflectors (DBRs) as end mirrors, two phase-matching layers (each of which is located between the DBR and the DFB region). The DFB is formed by periodically alternating active layers (GaInAsP) and passive layers (InP) with the period slightly smaller than half-wavelength. This results in coupling described by the complex coupling coefficient $k=k_i+jk_g$, where gain coupling is dependent on the threshold

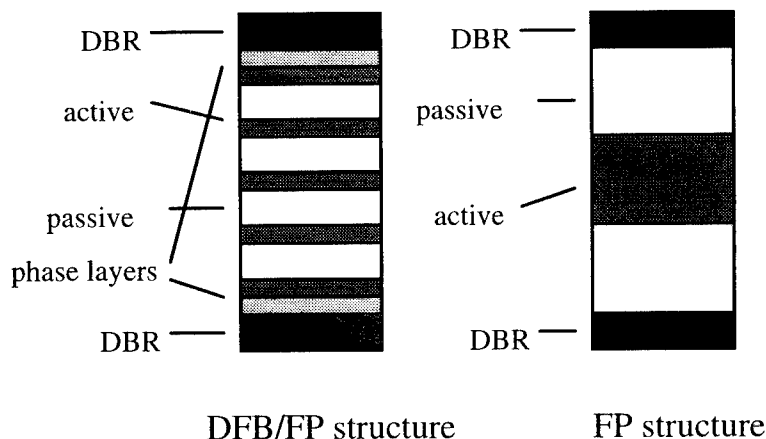


Fig. 1 Comparison between combined DFB/FP and FP structures.

gain (g_{th}) and on the absorption loss in active and passive layers, α_a and α_p , respectively [13]. Reflections of DBRs are described by $R_i^{1/2} \exp(j\phi_i)$, where R_i are effective reflectivities, and ϕ_i represent phase delays due to both the DBR mirrors and the phase-matching layers. For comparison, a FP structure is also shown in Fig. 1.

The complex coupling coefficient, the threshold current density, the operating wavelength etc. are numerically solved using a self-consistent model based on coupled-wave equations and on the dependence of the gain coupling coefficient on the threshold gain. In the calculations, the diffraction loss was neglected due to assuming that the semiconductor multilayer reflectors are grown directly on the active DFB region; the lateral confinement factor was assumed equal unity due to the VCSEL's large lateral dimension. A linear dependence of gain on carrier density $g=an-\alpha_{in}$ was assumed, where a , n , α_{in} are the gain coefficient, the carrier density and the residual absorption loss, respectively, and the threshold current density was found via $eB_{eff}n^2d/\eta_i$, where e , B_{eff} , d and η_i are the electron charge, the effective recombination constant, the total active region thickness and the internal quantum efficiency, respectively. The numerical values used in calculations (room temperature, GaInAsP/InP material system) were as follows: $a=3 \times 10^{-16} \text{ cm}^2$, $B_{eff}=10 \times 10 \text{ cm}^3/\text{s}$, $\eta_i=80\%$, $\alpha_{in}=400 \text{ cm}^{-1}$, $\alpha_a=60 \text{ cm}^{-1}$ and $\alpha_p=10 \text{ cm}^{-1}$. The refractive indices are 3.45 for GaInAsP and 3.17 for InP.

NUMERICAL RESULTS AND DISCUSSION

The effect of gain coupling on the threshold gain was investigated. It was confirmed that there exists an optimum phase relationship between the resonant modes of the FP cavity and the DFB multilayer, when enhanced resonance is obtained, which leads to the lowest achievable threshold gain. The optimum phase was found to be insensitive to variations of the reflectivity of DBR mirrors, while somewhat dependent on the fill factor (i.e. the ratio of the total active layer thickness to the cavity length). Fig. 2 shows the threshold gain versus the phase for two different fill factors (0.08 and 0.18) at a reflectivity

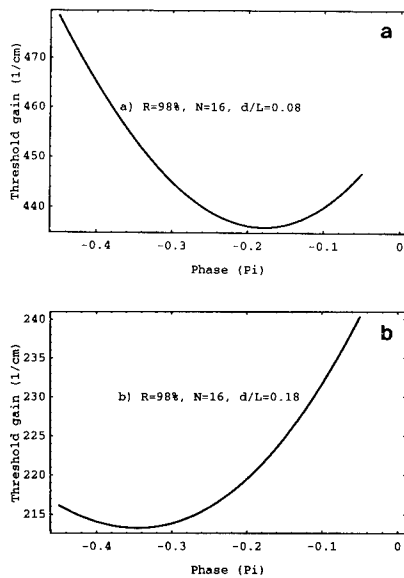


Fig. 2 Threshold gain versus phase between resonant modes of the DFB structure and the FP cavity with fill factor of 0.08 (a) and 0.18 (b).

of 98% and 16-periods gain layers, which illustrates the dependence of the optimum phase on the fill factor. In a practical device, the optimized phase can be achieved by adjusting the thickness of the phase-matching layers.

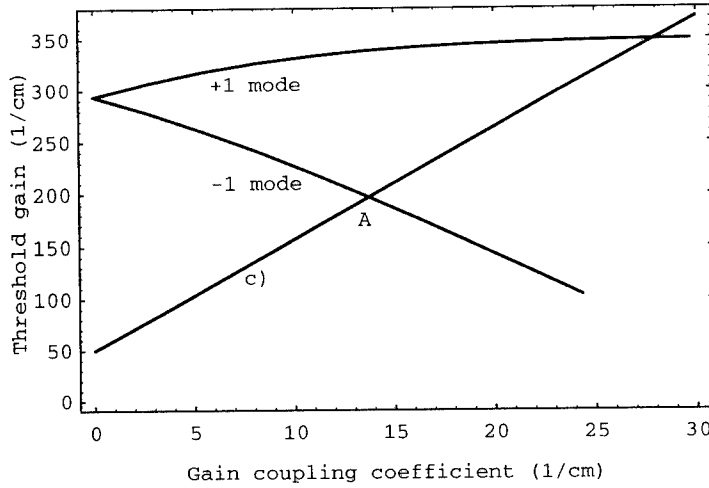


Fig. 3 Threshold gain versus gain coupling coefficient for (a) -1 mode and for (b) +1 mode. c) gain coupling coefficient versus threshold gain. A point represents the operating point at and above threshold.

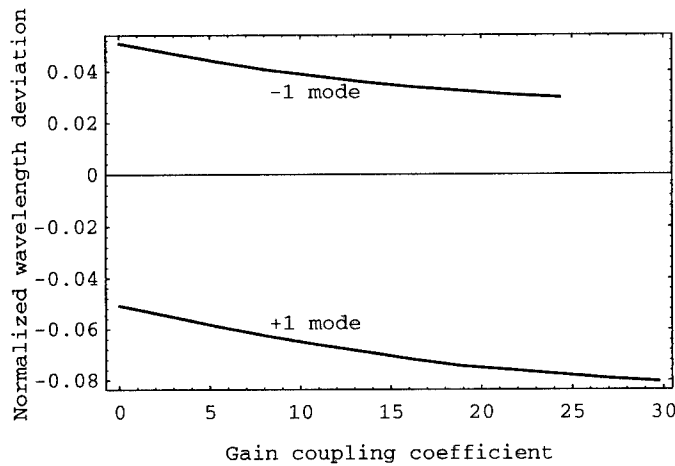


Fig. 4 Normalized wavelength deviation from the Bragg wavelength versus gain coupling coefficient for -1 mode (a) and for +1 mode (b).

The calculations also revealed a threshold gain difference between the +1 mode and the -1 mode due to gain coupling. The +1 mode is the resonant mode of the combined DFB/FP structure that lies on the shorter wavelength side of the Bragg wavelength, while the -1 mode is on the longer wavelength side. Fig. 3 (a, b) shows the threshold gain and Fig.

4 (a, b) shows the normalized wavelength deviation from the Bragg wavelength with a reflectivity of 98%, a fill factor of 0.2 and 16-periods gain layers, for both the +1 mode and the -1 mode as a function of the gain coupling coefficient. It reveals that the -1 mode with the lasing wavelength near to the Bragg wavelength has a lower threshold gain than the +1 mode. This is because the field intensity distribution of the -1 mode matches the gain distribution better than that of the +1 mode, thus producing a larger effective gain. This threshold gain difference indicates that a VCSEL with a combined DFB/FP structure has a better wavelength selectivity than that with a FP configuration.

Since the gain coupling coefficient is dependent on the threshold gain, the intersection point A in Fig. 3 is the operating point at and above threshold [13]. Using the self-consistent model developed here, one can determine the threshold gain, the lasing wavelength, the threshold current density, etc. for a given structure.

In the design of DFB/FP structures, parameters such as fill factor, can thus be optimized in order to ultimately obtain a much lower threshold current density at room temperature. Fig. 5 shows the threshold current density versus the fill factor with a cavity length of $3.7 \mu\text{m}$ (16-periods gain layers) for reflectivities of 96% and 98%. For comparison, we have also plotted the threshold current density versus the fill factor for a FP structure which has an uniform gain layer placed in the FP resonant cavity formed by two DBRs. It can be seen from Fig. 5 that the threshold current density for an optimally designed combine DFB/FP structure with a reflectivity of 98% and a cavity length of $3.7 \mu\text{m}$ is only 4.7 kA/cm^2 , while it is 9.6 kA/cm^2 for an optimally designed FP structure with the same reflectivity and the cavity length. This clearly demonstrates that a much lower threshold

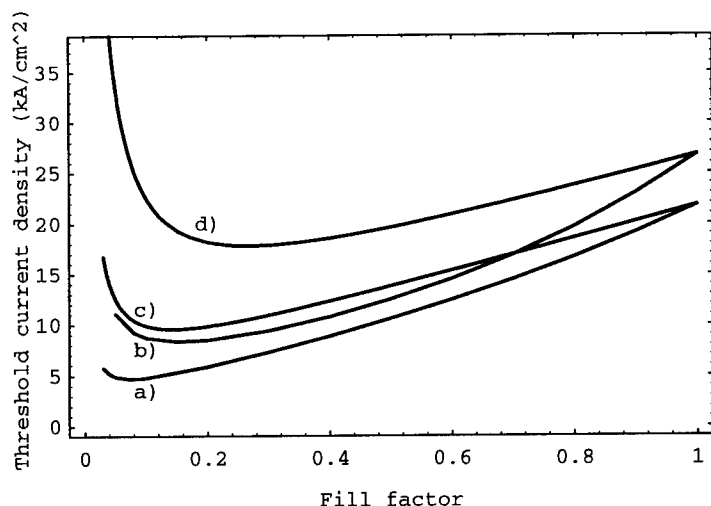


Fig. 5 Threshold current density versus fill factor at a cavity length of $3.7 \mu\text{m}$.

- a) for combined DFB/FP structure and 98% reflectivity;
- b) for combined DFB/FP structure and 96% reflectivity;
- c) for FP structure and 98% reflectivity;
- d) for FP structure and 96% reflectivity.

current density can be achieved with a combined DFB/FP structure with feasible mirror reflectivities and acceptable lengths. Simulations thus showed that the gain and index coupling coefficients play an important role in the obtained reduction of the threshold current density. It should also be noted that the active layer thickness in the optimally designed DFB/FP structure and in the optimally designed FP structure are different.

It is interesting to point out that the optimum structure parameters were found to be dependent on the reflectivity of DBR mirrors in the combined DFB/FP structure. For example, Fig. 5 illustrates that a higher reflectivity allows for a smaller fill factor and vice versa. This results from both the dependence of the threshold current density on the threshold gain and the active layer thickness, and from the dependence of the threshold gain on the reflectivities, the fill factor and the cavity length.

CONCLUSION

We studied theoretically VCSELs with combined DFB/FP structures, using a self-consistent model based on the coupled-wave theory. A strong dependence of the threshold gain on gain coupling was investigated. Simulations showed that the following conditions must be met if an optimally designed DFB/FP structure is to yield a reduced threshold current density or, alternatively, a lower required mirror reflectivity for the same threshold:

- 1) An optimum phase is required between the resonant modes of the DFB and the FP structures, which is, in turn, insensitive to the mirror reflectivity but dependent on the fill factor. The optimum phase can be achieved by adjusting the thickness of the phase-matching layers incorporated in the combined DFB/FP structure.
- 2) The optimum lasing wavelength at which the lowest threshold gain is obtained is at the -1 mode of the combined DFB/FP structure. This means that the spacing between adjacent gain layers in the DFB region should be slightly smaller than its half-wavelength, while the operating wavelength is exactly at the Bragg wavelength of DBR mirrors.
- 3) The structure parameters, such as the fill factor in the DFB region are dependent on the reflectivity of DBR mirrors and are thus required to be optimized in order to obtain the lowest threshold current density possible.

REFERENCES

1. K. Iga, M. Koyama and S. Kinoshita, "Surface emitting semiconductor lasers", *IEEE J. Quantum Electron.*, vol.QE-24, pp.1845-1855, Sep. 1988.
2. T. Uchida, T. Miyamoto, N. Yokouchi, Y. Inaba, F. Koyama and K. Iga, "CBE grown 1.5 μm GaInAsP-InP surface emitting lasers", *IEEE J. Quantum Electron.*, vol.QE-23, pp.1975-1979, June 1993.
3. T. Tadokoro, H. Okamoto, Y. Kohama, T. Kawakami and T. Kurokawa, "Room temperature pulsed operation of 1.5 μm GaInAsP/InP vertical-cavity surface-emitting laser", *IEEE Photon. Tech. Lett.*, vol. 4, pp.409-411, 1992.
4. J. L. Jewell, J. P. Harbison, A. Scherer, Y. H. Lee and L. T. Florez, "Vertical-cavity surface-emitting lasers: design, growth, fabrication, characterization", *IEEE J. Quantum Electron.*, vol.QE-27, pp.1332-1346, June 1991.
5. S. W. Corzine, R. S. Geels, J. W. Scott, R. H. Ran and L. A. Coldren, "Design of Fabry-Perot surface-emitting lasers with a periodic gain structure", *IEEE J. Quantum Electron.*, vol.QE-25, pp.1513-1524, June 1989, and the references quoted therein.
6. M. Y. A. Raja, S. R. J. Brueck, M. Osinski, C. F. Schaus, J. G. McInerney, T. M. Brennan, and B.E.Hammons, "Resonant periodic gain surface-emitting

- semiconductor lasers", *IEEE J. Quantum Electron.*, Vol.QE-25, no.6, June 1989, pp.1500-1511, June 1989, and the references quoted therein.
7. M. Mahbobzadeh, E. Gandjbakhch, E. A. Armour, K. Zheng, S. Z. Sun, C. F. Schaus, and M. Osinski, "Distributed-feedback vertical-cavity surface-emitting laser with resonant-periodic-gain active region", *SPIE Vol.1634 Laser Diode Technology and Application IV* (1992), pp.564-574, and the references quoted therein.
 8. J. He and M. Cada, "Phase-matched combined distributed-feedback/Fabry-Perot structure for semiconductor lasers", *Optics commun.*, vol.110, pp.115-119, August 1994.
 9. C. F. Schaus, A. J. Torres, J. Cheng, S. Sun, C. Hains, K. J. Malloy, H. E. Schaus, E. A. Armour, and K. Zheng, "Transverse junction, vertical-cavity surface-emitting laser", *Appl. Phys. Lett.*, vol.58, pp.1736-1738, April 1991.
 10. J. Zhou, M. Cada and J. He, in preparation for publication.
 11. H. Kogelnik and C. V. Shank, "Coupled-wave theory of distributed feedback lasers", *J. Appl. Phys.*, vol.43, no.5, pp.2327-2335, May 1972.
 12. W. Streifer, R. D. Burnham and D. R. Scifres, and S. R. Chinn, "Effects of mirror reflectivity in a distributed-feedback laser", *IEEE J. Quantum Electron.*, vol.QE-9, pp.574-580, June 1973
 13. K. David, J. Buus, G. Morthier and R. Baets, "Coupling Coefficients in gain-coupled DFB lasers: Inherent compromise between coupling strength and loss", *IEEE Photon. Tech. Lett.*, vol.3, pp.439-441., May 1991.
 14. K. Kudo, J. I. Shim, K. Komori, and S. Arai, "Reduction of effective linewidth enhancement factor α_{eff} of DFB lasers with complex coupling coefficients", *IEEE Photon. Tech. Lett.*, Vol.4, no.6, June 1992, pp.531-534.

TRANSMISSION-LINE MODELING OF MULTI-SECTION DFB LASERS

Chih-Hsiao Chen and Giora Griffel
Polytechnic University of New York
6 Metrotech Center, Brooklyn, NY 11201

I Introduction

Multi-section semiconductor lasers have been the subject of extensive study in recent years. This is due to the need for a spectrally pure, widely tunable, and high-speed lightwave source, that is a key-element for optical communication systems consisting of wavelength dependent multiplexing techniques, such as wavelength division multiplexing (WDM), as well as for frequency modulation schemes, such as frequency shift keying (FSK). In such systems high-speed, wavelength-tunable single-mode laser diodes are used as either directly modulated light sources at the transmission end, or as local oscillators for channel selection and demodulation at the detection section.

To provide the required operation performance, a variety of laser structures has been proposed and studied in detail. All share the property of having a composite, monolithic cavity structure, that consists of several sections, each having its distinctive geometry, composition, and driving current. Among these devices we find the distributed Bragg reflector (DBR) laser^[1], the two-section distributed feedback (DFB) laser^[2], the two section gain-levered Fabry-Perot (FP) laser^[3], and the two-section DFB/FP laser, which consists of one grating-section and one uncorrugated gain-section^[4, 5]. Another example of a multi-section laser is the master-oscillator power-amplifier (MOPA) structure, where the master-oscillator section has a DFB or DBR structure that is used to generate light with high spectral purity, while a non-corrugated flared amplifying section provides the gain required to obtain high output-power levels ($> 1\text{W}$)^[6].

The all-active two-section DFB and FP lasers were found to be most promising due to their high-speed operation under stimulated emission. In addition, these lasers demonstrated enhanced frequency modulation response at asymmetrical biasing conditions of the two sections^[2, 3]. However, the analysis of these lasers is fairly complicated due to the strong interaction between the different sections. Most of the analysis techniques used so far are approximated and do not include crucial parameters that

influence the static and dynamic behavior, such as the dependency of the material-gain on the operating frequency, the dependency of the gain and group-velocity on structural (grating) parameters, the reflection between the boundaries of the different sections, and accurate expressions for the facet reflectivities as a function of the frequency.

In this paper we present a transmission-line model and use it to reformulate the round-trip and rate-equations for regular and composite, multi-section DFB lasers. The model is based on the coupled-mode formulation for active, grating assisted waveguides, which is combined with Floquet's Theorem to describe the field within the laser cavity. Using this approach we construct a transmission line model, representing the multi-section laser longitudinal-structure. The model is generic and can be easily implemented to describe a wide variety of multi-section devices.

The organization of this paper is as follows: In Section II, we use the coupled-mode equations to derive the field and the characteristic impedance of a general periodic structure. In Section III we formulate the round-trip and the rate-equations using the characteristic impedance of the different sections. An application example of a two-section DFB laser is analyzed. Discussion and concluding remarks are given in Section IV. Throughout the paper we adopt the time convention $\exp(j\omega t)$, where ω is the angular frequency.

II The Transmission-Line Model

Consider a layered, waveguiding gain-medium with periodic variations in one of the layers of the form $\cos(\frac{2\pi}{\Lambda}z + \Omega)$, where Λ is the period, and Ω the phase of the sinusoidal variations at $z = 0$. A comprehensive and exact analysis of the electromagnetic field propagating in such a structure can be performed using Floquet's Theorem and Floquet's Corollary[7]. However, this method is fairly complicated and requires an exhausting computational effort. A different approach is based on the coupled-mode theory, which is an approximated technique that is easier to perform, provides good physical insight, and yields highly accurate results in most practical cases. To derive the coupled-mode equations we assume that at any given point along the longitudinal (z) axis the field can be represented by a superposition of two modes of the non-corrugated structure, propagating in opposite directions. Namely, $E(z) = p(z) + q(z)$ (By doing so, we assume that the periodic corrugations are merely a small perturbation of the waveguiding structure. Such a presumption has to be taken with great care. A detailed discussion of this issue is given elsewhere[5, 8]). The z -dependency of the two modes can be described by

$$\begin{aligned} p(z) &= P(z)e^{-j(\frac{\pi}{\Lambda})z} \\ q(z) &= Q(z)e^{j(\frac{\pi}{\Lambda})z} \end{aligned} \quad (1)$$

Using Maxwell's equations with the periodic gain-medium, it can be shown the slow-varying amplitudes of the two modes are related to each other by the following set of coupled-equations[9]

$$\begin{aligned} \frac{dP(z)}{dz} &= -j(\beta - \frac{\pi}{\Lambda})P(z) - \kappa_{pq}e^{j\Omega}Q(z) \\ \frac{dQ(z)}{dz} &= j(\beta - \frac{\pi}{\Lambda})Q(z) - \kappa_{qp}e^{-j\Omega}P(z) \end{aligned} \quad (2)$$

where β is the wave number of the mode propagating in the uncorrugated structure, and $\kappa_{pq,qp}$ are the coupling between the counter propagating modes due to the grating.

The eigen-modes of the complete structure are found using

$$\begin{aligned} P(z) &= A \times e^{-j\bar{\kappa}z} \\ Q(z) &= B \times e^{-j\bar{\kappa}z} \end{aligned} \quad (3)$$

to described the modes' longitudinal dependency, which by substituting into Eqs. (2) results in

$$\bar{\kappa} \equiv \bar{\kappa}_1 = -\bar{\kappa}_2 = \pm \sqrt{\delta^2 - \kappa_{pq}\kappa_{qp}} \quad (4)$$

and

$$(\bar{\kappa} - \delta)A + j\kappa_{pq}e^{j\Omega}B = 0 \quad (5)$$

where $\delta \equiv (\beta - \frac{\pi}{\Lambda})$. The choice of the sign in Eq. (4) is discussed in Ref. [8]. Using Eqs. (5), (4), and (3) in Eq. (1) we obtain for the total field

$$E(z) = A_1 e^{-j(\bar{\kappa} + \frac{\pi}{\Lambda})z} - \frac{j}{\kappa_{pq}e^{j\Omega}}(\bar{\kappa} + \delta)A_2 e^{j(\bar{\kappa} + \frac{\pi}{\Lambda})z} + \frac{j}{\kappa_{pq}e^{j\Omega}}(\bar{\kappa} - \delta)A_1 e^{-j(\bar{\kappa} - \frac{\pi}{\Lambda})z} + A_2 e^{j(\bar{\kappa} - \frac{\pi}{\Lambda})z} \quad (6)$$

where the first two terms correspond to $p(z)$, the field propagating to the right-hand-side, and the last two terms to $q(z)$, the field propagating to the left-hand-side. The relation between A_1 and A_2 can be determined by boundary conditions.

To derive a transmission-line model we need to find the characteristic impedance of a general corrugated-section. This can be done if the field propagating in such a section is expressed as a superposition of two exponential terms, each propagating in a different direction, and using appropriate boundary conditions to find the reflection coefficients at the boundaries. However, Eq. (6) contains four exponential terms. This problem can be alleviated by noting that for z equals an integer number of Λ , the grating period, namely $z = z_m = m \times \Lambda$, $m \in I$, then $e^{j\frac{\pi}{\Lambda}z_m} = e^{-j\frac{\pi}{\Lambda}z_m}$ and the total field (6) becomes

$$E(z_m) = (1 + \frac{j}{\kappa e^{j\Omega}}(\bar{\kappa} - \delta))A_1 e^{-j(\bar{\kappa} + \frac{\pi}{\Lambda})z_m} + (1 - \frac{j}{\kappa e^{j\Omega}}(\bar{\kappa} + \delta))A_2 e^{j(\bar{\kappa} + \frac{\pi}{\Lambda})z_m} \quad (7)$$

where it can be shown that $\kappa \equiv \kappa_{pq} = -\kappa_{qp}$ [8]. We can treat the total field as two modes propagating inside the grating waveguide in opposite directions, each of which described by one of the terms in Eq. (7), keeping in mind that this picture is correct only for $z = z_m$. Consider now the structure shown in Fig. 1. Here a semi infinite plane is comprised of two structures identical in all but a grating corrugation on half of the plane to the left of $z = 0$, and uncorrugated structure to the right of $z = 0$. By constructing this structure we enable the same modes to express the total field of each half-plane (with the distinction that in the non-corrugated region the mode amplitudes are constants, whereas in the grating region the amplitudes are varying due to mode coupling along the z -axis). Assuming that the field is propagating from the left to the right, there is no reflected wave at $z = 0$, i.e. $Q(0) = 0$. Therefore

$$A_2 = \frac{(\bar{\kappa} - \delta)}{(\bar{\kappa} + \delta)} A_1 \quad (8)$$

Using Eqs. (7) and (8), the reflection coefficient at $z = 0$ is

$$\overrightarrow{\Gamma} \equiv -\frac{\kappa e^{-j\Omega} + j(\bar{\kappa} - \delta)}{\kappa e^{-j\Omega} - j(\bar{\kappa} + \delta)} \quad (9)$$

where the right-arrow indicates the direction of incident. Reversing the position of the corrugated and uncorrugated regions in Fig. 1 and following similar derivation we obtain for a field propagating from right to left

$$\overleftarrow{\Gamma} \equiv -\frac{\kappa e^{j\Omega} + j(\bar{\kappa} - \delta)}{\kappa e^{j\Omega} - j(\bar{\kappa} + \delta)} \quad (10)$$

Expressing the reflections at the boundary between the corrugated and the uncorrugated regions as $\vec{\Gamma} = \frac{\vec{Y} - Y_L}{\vec{Y} + Y_L}$ and $\overleftarrow{\Gamma} = \frac{\vec{Y} - Y_L}{\vec{Y} + Y_L}$ along with Eqs. (9) and (10) we find

$$\vec{Z} = \frac{\kappa e^{j\Omega} + j(\bar{\kappa} - \delta)}{\kappa e^{j\Omega} - j(\bar{\kappa} - \delta)} Z_{un} \quad (11)$$

and

$$\overleftarrow{Z} = -\frac{\kappa e^{j\Omega} - j(\bar{\kappa} + \delta)}{\kappa e^{j\Omega} + j(\bar{\kappa} + \delta)} Z_{un} \quad (12)$$

Where Z_{un} is the characteristic impedance of an identical uncorrugated structure. It should be noted that $\vec{Z} \neq \overleftarrow{Z}$ because of the nonsymmetry of the unit-cell of the grating. This is the case of an arbitrary phase term Ω . For a symmetric unit cell $\Omega = 0, \pi$ and the characteristic impedance $\vec{Z} \equiv \frac{\vec{V}}{I}$ and $\overleftarrow{Z} \equiv \frac{\vec{V}}{I}$ are identical. From Eq.(9), we find that the characteristic impedance for the case of a symmetric unit-cell is

$$\vec{Z} = \frac{\delta \pm j\kappa}{\bar{\kappa}} Z_{un} \quad (13)$$

Where the $+$ and $-$ signs correspond to $\Omega = 0$ and π respectively.

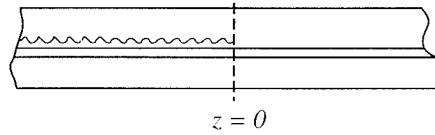


Fig. 1 A semi infinite plane with periodic corrugation in $z < 0$.

III Static and Dynamic Analysis

A generic multi-section structure is depicted in Fig. 2(a). The corresponding transmission line model is shown in Fig 2(b). We treat the case of TE modes, for which $Z_l = \frac{\omega\mu}{k_0 \times n_0}$, $Z_1 = \frac{\omega\mu}{k_0 \times n_{1eff}}$, $Z_{2un} = \frac{\omega\mu}{k_0 \times n_{2eff}}$, and $Z_r = \frac{\omega\mu}{k_0 \times n_{reff}}$. Assuming $L_2 =$

$m \times \Lambda; (m \in I)$, and $\Omega = 0$, then $Z_2 = \frac{\delta + j\kappa}{\kappa} Z_{2un}$, and $Z_R = Z_2 \frac{Z_r + jZ_2 \tan(\kappa L)}{Z_2 + jZ_r \tan(\kappa L)}$ and $Z_L = Z_1 \frac{Z_l + jZ_1 \tan(k_0 \times n_{l1} \times L)}{Z_1 + jZ_l \tan(k_0 \times n_{l1} \times L)}$ are the impedances looking toward $+z$ or $-z$ at $z = L_1$ respectively.

The round-trip condition for this device is given by transmission line resonance

$$Z_L + Z_R = 0 \quad (14)$$

The solution of this equation is the cut-off or lasing threshold-condition. Since there are two sections, there are infinite numbers of carrier-density combinations (N_1, N_2) that provide the gain required for lasing. The solution is comprised of a set of three variables - N_1 and N_2 , the carrier concentration in each of the two sections, and ω , the lasing frequency, each having a real value. As shown in Ref. [4], there is an infinite number of solutions that fulfill the round-trip condition. They can be described graphically as a set of cut-off lines in the N_1/N_2 plane, where each curve corresponds to a different longitudinal mode, as shown in Fig. 3. Due to gain-clamping, the carrier-densities of the laser segments are clamped just to the left of the cut-off line which is comprised of the lowest segments of the different longitudinal-modes cut-off lines, indicated by the dashed line in Fig. 3. Only values of (N_1, N_2) that lay on one of these segments are allowed steady-state operating points. Changing the operating conditions of the laser is performed by varying the driving currents that, in turn, vary the carrier-concentrations. In this case the laser operating point is travelling along the cut-off line. Walking along the curved segments between the cusps corresponds to a continuous frequency tuning, while passing from one segment to the neighboring one through a cusp corresponds to mode hopping.

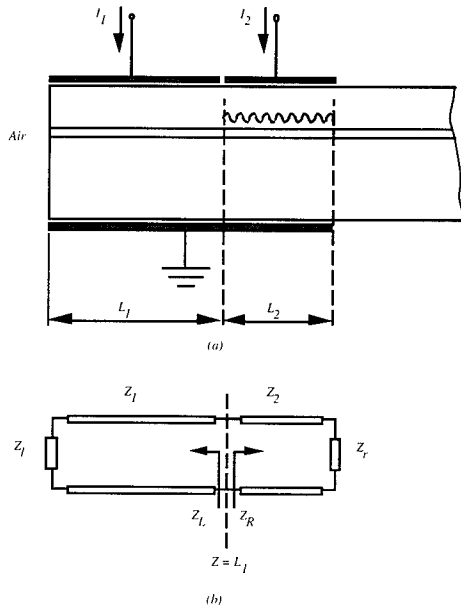


Fig. 2 (a) A schematic structure of two active-section semiconductor laser. (b) The equivalent transmission-line model.

To obtain the light-current relations, the tuning-curve, and to carry out small-signal, dynamic analysis we need the rate-equations for the carrier density and the photon-density in such a structure. The temporal variations of the carrier densities N_i and the

photon density P_i in the i -th section are governed by the following set of rate equations:

$$\frac{dN_i}{dt} = \frac{J_i}{ed} - \frac{N_i}{\tau_e} - 2v_g \text{Im}(\bar{\kappa}) P_i \quad i = 1, 2 \quad (15)$$

$$\frac{dP_i}{dt} = 2v_g \text{Im}(\bar{\kappa}) P_i - \frac{v_g}{L} \ln(\Gamma_L \Gamma_R) P \quad (16)$$

Where J_i are the current densities in the two sections, e is the electron charge, d is the active layer thickness, τ_e is the carriers' lifetime, Γ_L and Γ_R are the effective reflectivities at the left and the right boundaries of the relevant segment. For the corrugated section of the device depicted in Fig. 2 $\Gamma_L = \frac{Z_1 - Z_2}{Z_1 + Z_2}$ and $\Gamma_R = \frac{Z_R - Z_L}{Z_R + Z_L}$. $\text{Im}(\bar{\kappa})$ is the field gain coefficient of the relevant section.

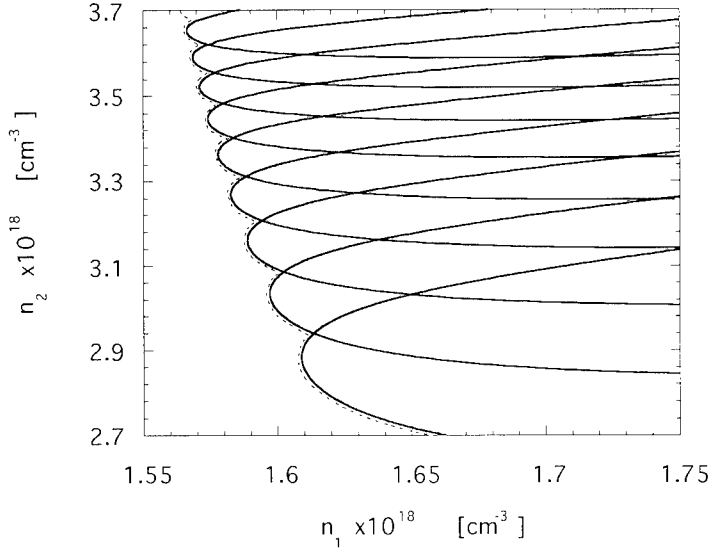


Fig. 3 Cut-off line in N_1, N_2 plane. Each continuous segment along the line corresponds to a longitudinal mode, while the cusps indicate mode hopping.

We applied the described formalism to the laser structure shown in Fig. 2 with a total length of $470\mu m$ and uncorrugated section occupying $h = 0.7$ of the total length. Other parameters taken for the calculation are given in Table I. We begin with the large-signal analysis to determine the steady-state operating conditions. To do so, we solve Eq. (14) numerically using an iterated root-searching technique.

To perform static analysis, the cut-off lines in N_1/N_2 plane are transferred to J_1/J_2 plane using Eq. (15) at steady-state ($\frac{d}{dt} = 0$) and with $P_{out} = 0$ as threshold condition. A set of equi-power lines in J_1/J_2 plane are then obtained by keeping N_1, N_2 and ω fixed and using different values of P_{out} to obtain the increase of J_1 and J_2 from their threshold values to the values required to obtain the particular output-power level. The result is shown in Fig. 4; it is described by a set of lines, similar to the cut-off line, separated from the cut-off line by a distance that is proportional to the output-power level. As we see from this procedure, each point on the J_1/J_2 plane corresponds to a particular cut-off point in N_1/N_2 plane and is therefore characterized by its output power P_{out} , operating currents J_1 and J_2 , carrier-density N_1 and N_2 , and lasing frequency ω .

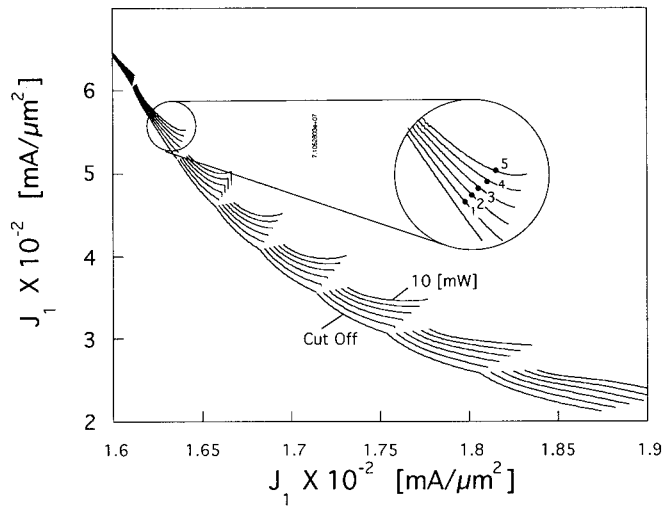


Fig. 4 Equi-power lines, corresponding to the cut-off line of Fig. 3. The lines shown represent the currents combinations that are required to obtain output power levels of 0, 2, 4, 6, 8, and 10 mW.

A complete static analysis, including the L/I curves, the tuning behavior, and low-frequency modulation response is presented in Ref. [8]. Using the described steady-state analysis, various operating points were selected and used as quiescent points for the small-signal analysis. In Fig. 5 we plot the FM modulation response $\frac{\Delta\nu}{\Delta I_1}$ as a function of the modulation frequency ω_m for operating points that have the same carrier-density combination N_1, N_2 at different output power levels. These points are shown in Fig. 4.

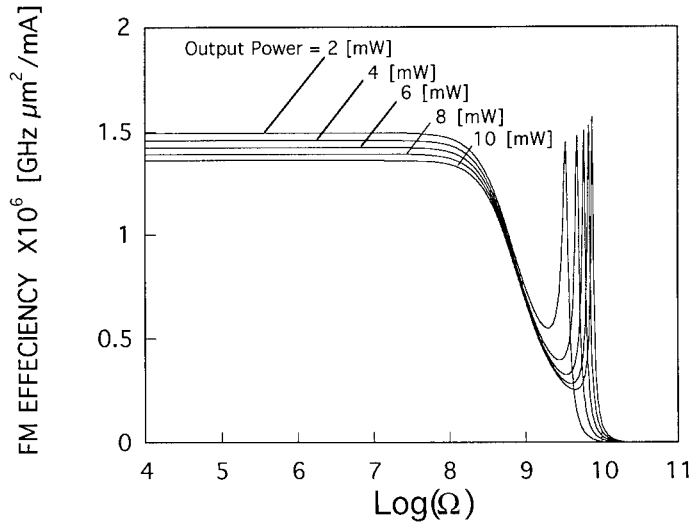


Fig. 5 The FM response at different output power levels (points 1-6 in Fig. 4). Note that the typical dip associated with the enhanced carrier-lifetime is shifted to higher frequencies at higher output-power levels.

The response is similar to that of previously analyzed two-segment lasers; it is flat at low frequencies and has a typical dip associated with the enhanced carrier-lifetime^[2] before reaching its peak at the relaxation oscillation frequency. It is clearly observed here that the response is critically dependent on the output power level, which is directly related to the photon-density inside the cavity. Increased output-power level, which is related to higher photon density, results in a stronger stimulated-emission term in the rate-equations. This stimulated emission term suppresses the carrier-lifetime and, as a result, the dip in the response curved is shifted to higher frequency along with the relaxation-oscillation peak. Increasing the output power level to 10 *mW* results in a shift of the relaxation oscillation frequency to nearly 10 *GHz*. This of course is accompanied, due to conservation of the gain-bandwidth product, by a lower level of the modulation response. Both effects have to be taken into consideration when designing a DFB transmitter that should operate at a particular output-power level.

Table I

Parameter	Value	Description
A [Sec ⁻¹]	1 x 10 ⁻⁵	Spontaneous Emission Coefficient
N ₀ [cm ⁻³]	1 x 10 ¹⁸	Carrier Density at Transparency
κ [cm ⁻¹]	50	Coupling Coefficient
n _{r 0}	3.5	Refractive Index at Transparency
α ₀	3	Linewidth Enhancement Factor at Transparency
Λ [μm]	0.245	Grating Period
d [μm]	0.2	Active Layer Thickness
L [μm]	470	Laser Length
h	0.3	Segment Length Ratio
r _I	0.1	Field Reflectivity of the Noncorrugated Section
τ _c [sec]	2 x 10 ⁻⁹	Carrier Lifetime
γ _{max}	0.325 g ₀	Gain Parameter
N _s [cm ⁻³]	3.25x10 ¹⁷	Carrier Density Parameter

IV Conclusion

We have presented a transmission-line model for rigorous analysis of composite DFB lasers. The technique is capable of handling any number of sections, each having a specific structural and material characteristics, within the laser cavity. The main advantage of the technique over previous analysis is that it provides an accurate formulation of the reflection between different section boundaries and at the facets. The model assigns a characteristic impedance to every segment, which, when connected to the adjacent

segments, form a transmission-line resonance structure. The characteristic impedance is dependent on both structural parameters and operating conditions e.g. different current levels. This approach is extremely important in the case of DFB/DBR structures, for which the dispersion-relation is critical in determining the static and dynamic operation of the devices. The technique was applied to two-section DFB/FP structure and used to find the cut-off conditions, perform static analysis and small-signal modulation response.

V Acknowledgment

This research was supported by a Research Initiation Grant from the National Science Foundation.

References

- [1] K. Kobayashi and I. Mito, "Single Frequency and Tunable Laser Diodes", IEEE J. Lightwave Technol., Vol. LT-6, pp.1623-1633, 1988.
- [2] M. Kuznetsov, "High-Speed Frequency Modulation and Switching of Tunable Distributed Feedback Lasers with Two Active Segments", J. Quantum Electron., Vol. 27, pp. 668-677, 1991.
- [3] K. Y. Lau, Appl. Phys. Lett., Vol. 57, 2068 (1990).
- [4] G. Griffel, R. J. Lang and A. Yariv, "Two-Section Gain-Levered Tunable Distributed Feedback Laser with Active Tuning Section", IEEE J. Quantum Electron., Vol. 30, pp.15-18, 1994.
- [5] G. Griffel and C. H. Chen, "Static and Dynamic Analysis of Tunable Two-Section High-Speed Distributed Feedback Laser Utilizing the Gain Lever Effect", submitted for publication in IEEE J. Quantum Electron., 1995.
- [6] K.M. Dzurko, R. Parke, J. S. Osinski, S. O'Brien, J.-M. Verdiell, R. J. Lang and D. F. Welch, "Operating Characteristics of High-Power, Diffraction-Limited MOPAs", Proceedings of LEOS94, Vol. 2, p. 397, November 1994.
- [7] H. L. Bertoni, L. H. Cheo and T. Tamir, IEEE Trans. Antennas Propagat., vol.37, pp.78-83, 1989.
- [8] C. H. Chen and G. Griffel, "Transmission-Line Model of Multi-Section DFB Lasers: Static and Dynamic Analysis", submitted for publication in IEEE J. Quantum Electron., 1995.
- [9] H. A. Haus, *Waves and Fields in Optoelectronics*, Prentice-Hall, Ch.8, 1984.

ANALYSIS OF GAIN COUPLED DFB SEMICONDUCTOR LASERS WITH ABSORPTION GRATING

F. Randone and I. Montrosset

Dipartimento di Elettronica Politecnico di Torino
Corso Duca degli Abruzzi 24, 10129 Torino, Italy

ABSTRACT - In this paper is presented an accurate model for gain coupled (GC) DFB laser with absorption grating (AG). Numerical results about the coupling coefficients dependence on AG thickness and on grating carrier density, are discussed in order to justify the new model, which solves selfconsistently the rate equations for the carriers in active and AG layers with the cavity resonance conditions. Bistability in the lighth-current characteristics, linewidth, FM response and other laser characteristics are evaluated and discussed for different structures, obtained varying some AG parameters.

I - INTRODUCTION

Gain coupled DFB semiconductor lasers have a built-in periodic longitudinal modulation of their net optical gain, which allows a coupling between the forward and backward traveling optical waves, as was demonstrated by Kogelnik and Shank [1]. In the last years many research groups have realized different GC structures, obtaining the gain modulation with a gain grating (GG) [2] or a second-order index grating [3] or an absorption grating (AG) [4]. It has been shown [2]-[8] that these lasers have a very good characteristics as high side-mode suppression ratio (SMSR) and single mode yield, narrow linewidth, 3 dB modulation bandwidth better than 11 GHz, insensitivity to external feedback, *etc.* Because of the complexity of such devices, any quantitative consideration on their actual behavior is prevented without an accurate theoretical model and a numerical analysis. This fact has led to some gain coupled laser models [4]-[6], [9], accounting for the various phenomena somehow affecting the above-mentioned lasing performances.

In this paper we analyze some characteristics and parameters of the AG-GC DFB laser described in [4], [5] and shown in Figure 1. As demonstrated in Section II, the coupling coefficients depend on the absorption grating geometric parameters and on the grating carrier density N_g ; moreover, it is possible, varying the absorption grating thickness, to cancel the index coupling coefficient or to obtain a structure with the real and the imaginary part of the coupling coefficient in phase or anti-phase.

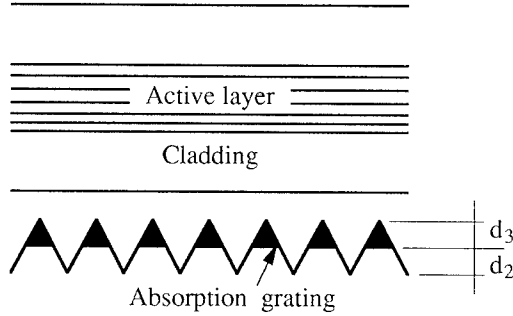


Figure 1. The gain coupled DFB laser with absorption grating investigated.

Because of the coupling coefficient and the grating loss dependence on the grating carrier density N_g , we present in Section III the features of a new laser simulator, which solve the rate equation for the carriers in the grating selfconsistently with the rate equation for the carriers in the active layer and with the cavity resonance condition. The simulator is an extension for AG gain coupled structures of the computer code presented in [10], [11]. Laser features like SMSR, linewidth and dynamic modulation responses are calculated taking into account the physical effects present in the index-coupled DFB-lasers (as spatial hole burning, shot noise, etc.) and the coupling coefficient and the grating losses dependence on N_g , typical of AG-GC lasers.

In Section IV we analyze the laser behavior and its dependence on the absorption grating material characteristics and the geometric grating parameters. The numerical results show the typical effects found experimentally [4], [5], in AG-GC DFB laser such as the SMSR improvement due to the standing wave effect, the bistable characteristics, the red frequency shift near the threshold, etc.

II - DEVICE STRUCTURE DESCRIPTION

The AG laser structure reported in Figure 1 [4] implements the gain coupling mechanism with an absorption grating. Furthermore the structure has an index grating in anti-phase with respect to the refractive index perturbation generated by the absorption grating; this allows to decrease or cancel the real part of the coupling coefficient.

With a Fourier series expansion of the refractive index and of the gain periodic perturbations, it is possible to determine [1], [12], a simple expression for the index K_I and the gain K_G coupling coefficients as a function of the index and loss grating shape and the material parameters. Been the refractive index and the loss dependent on the carrier density N_g in the absorption grating, the dependence with N_g can be written using the first terms of the Taylor series expansion in the form

$$K_I = K_{I_0} + K_{I_{N_g}} (N_g - N_{0_g}) \quad (1)$$

$$K_G = K_{G_0} + K_{G_{N_g}} (N_g - N_{0_g}) \quad (2)$$

where N_{0_g} is the carrier density at transparency in the AG layer.

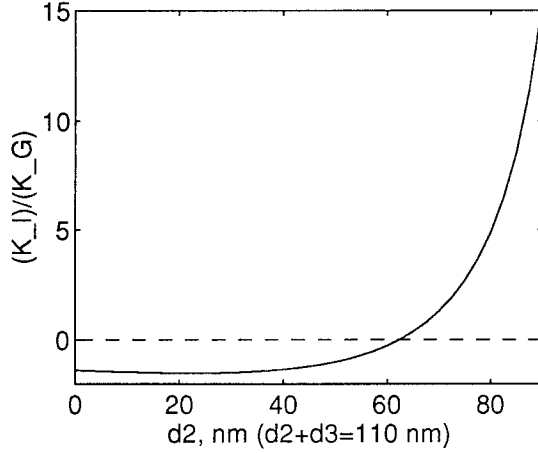


Figure 2. Coupling coefficients ratio at the transparency K_{I_0}/K_{G_0} vs index grating thickness d_2 .

With the technological data reported in [4], [5] and the modal trasversal analysis of the structure, we have determinated the coupling coefficients and their derivative respect to the AG layer thickness d_3 . Figure 2 shows that choosing different values of the index grating thickness d_2 in Figure 1 with $d_2 + d_3 = 110 \text{ nm}$, it is possible to realize a structure with anti-phase ($d_2 < 62 \text{ nm}$) or in-phase ($d_2 > 62 \text{ nm}$) coupling coefficients or a purely gain coupled device for $d_2 = 62 \text{ nm}$. The value of d_2 , instead, has not influence on the sign of the differential coupling coefficients: in fact $K_{I_{N_g}}$ and $K_{G_{N_g}}$ are respectively always positive and negative as shown in Figure 3.

The AG thickness has a strong influence on the coupling coefficient value and then on the laser performances; for example Figure 4 shows the increase of the modal gain separation at the threshold when d_2 approaches the pure gain coupling condition.

III - THE MODEL

In this section we present briefly our model for gain coupled laser with absorption grating. The computer code allows to describe almost any complex longitudinal laser structure (see [10]) with a new formulation that considers also the rate equation for the carriers in the AG layer. In particular we will report the new formulas used to calculate the laser linewidth and SMSR, following the same notation used in [10]. At last we will describe our dynamic model to determine the laser spectral characteristics.

Static Analysis

We adopt the notation used in [10] and for brevity only the modified expressions are reported. The lasing mode longitudinal field distribution is computed from the well

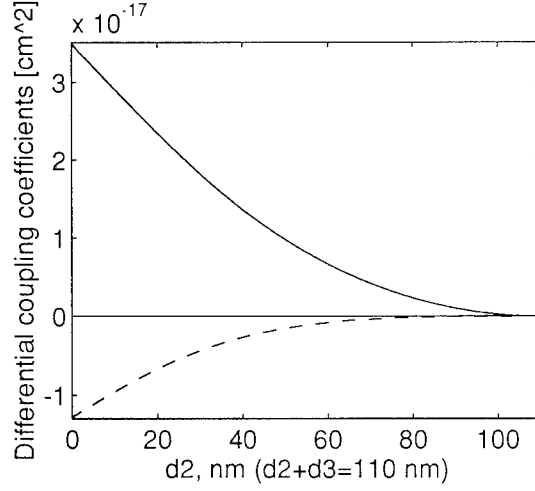


Figure 3. Differential coupling coefficients vs d_2 : $K_{I_{N_g}}$ continuous and $K_{G_{N_g}}$ dashed lines.

known [1] coupled-wave equations for the complex field envelope

$$\begin{cases} \frac{dR_k^+}{dz} = -j\tilde{\delta}_k R_k^+ + \tilde{K}_k^+ R_k^- \\ \frac{dR_k^-}{dz} = \tilde{K}_k^- R_k^+ + j\tilde{\delta}_k R_k^- \end{cases} \quad (3)$$

where $\tilde{\delta}_k = \delta_k + j\alpha_k$ is the complex detuning parameter in section k and the complex coupling coefficients are represented by $\tilde{K}_k^+ = -j(K_{I_k}e^{-j\Delta\varphi_k} + jK_{G_k})e^{-j\varphi_{i_k}}$ and $\tilde{K}_k^- = j(K_{I_k}e^{+j\Delta\varphi_k} + jK_{G_k})e^{+j\varphi_{i_k}}$. The phase $\Delta\varphi_k$ assumes only the values π or 0 ; this depends on the grating parameters and is not affected by the differential coupling coefficient sign as shown in Figures 2-3. Besides, φ_{i_k} is the grating phase at the left end side of the section for the real grating index component.

In order to consider the extra losses due to the absorption grating, we represent the modal gain α_k in the following form:

$$\alpha_k(N, \lambda, S_0, N_g) = \frac{\Gamma_k}{2} g_k(N(z), \lambda, S_0(z)) - \frac{\alpha_{F_k}}{2} + \frac{\Gamma_{gk} \alpha_{gk}(N_g(z))}{2} \quad (4)$$

where g_k is the material gain, λ and λ_B are the lasing and the Bragg wavelengths, $S_0(z)$ is the longitudinal photon density distributions, α_{gk} , $\alpha_{F_k} = \alpha_{F_{0k}} + \alpha_{F_{Nk}} N$ and Γ_{gk} , Γ_k are the grating and the internal cavity losses and confinement factors respectively. The expression for the absorption grating loss $\alpha_{gk}(N_g(z))$ is given by

$$\alpha_{gk}(N_g(z)) = \frac{a_g (N_g - N_{0g})}{1 + \epsilon_{0,g} S_g(z)} \quad (5)$$

being a_g and $\epsilon_{0,g}$ the absorption grating differential gain and the saturation coefficient and S_g the photon density interacting with the grating. To evaluate the carrier density $N_g(z)$, we introduced the following carrier rate equation

$$0 = R_{gk}(N_g) + Q_{gk}(N_g, S_g) \quad (6)$$

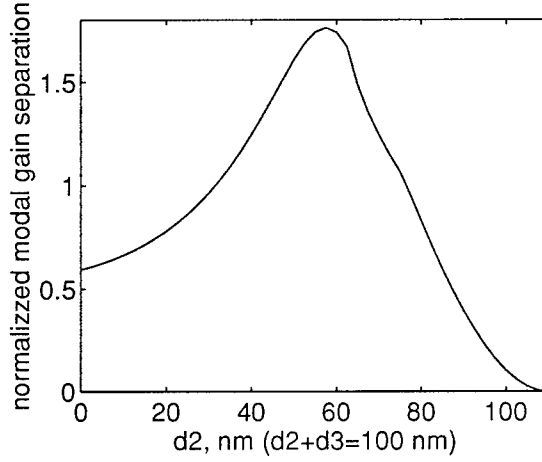


Figure 4. Normalized gain separation between the fundamental and the high order mode vs d_2 for a laser length $L = 600 \mu m$.

where $R_{gk} = A_{gk}N_g + B_{gk}N_g^2 + C_{gk}N_g^3$ is the spontaneous recombination rate with A_{gk}, B_{gk}, C_{gk} the recombination coefficients of the AG material, $Q_{gk}(N_g, S_g) = v_{gk}\alpha_g S_g$ is the single-mode approximation of the stimulated recombination rate with v_{gk} the group velocity. Equation 6 should be solved selfconsistently with (3) and the rate equation for the carrier density in the active layer (see [10], Eq. (13)).

Since the diffusion coefficient of Langevin's forces $F_m(t)$ [13] is modified by the periodic variation of the imaginary part of the dielectric constant, the spontaneous emission equation assumes the following form

$$R_{spm} = \frac{\int_L cK_z K_t n_{sp} \Gamma g |\tilde{a}_m|^2 dz}{\int_L n_g |\tilde{a}_m|^2 dz} + \frac{4 \int_L cK_z K_t n_{sp} K_G \Re\{R_m^+ R_m^{-*} e^{j\varphi_i}\} dz}{\int_L n_g |\tilde{a}_m|^2 dz} \quad (7)$$

where K_t and K_z are the transversal and longitudinal Petermann's factors [10], n_{sp} the spontaneous emission factor [13] and the integrations are carried out over the entire cavity length. This new expression takes into account the interaction between the gain modulation, due to the absorption grating, and the standing wave as clearly shown by the dependence on the gain coupling coefficient K_G and on the standing wave pattern of the second term in (7). The contribution of this term is important for an accurate SMSR and laser linewidth calculation for gain coupled structures as shown in [9].

Following the procedure used by Tromborg, Pan *et al.* in [13], [14] for index coupled or in [9] for GG-DFB lasers, we calculated the new modified laser linewidth equation, which takes into account the coupling coefficients and the extra grating loss dependence on the carrier density N_g . For brevity only final modified expressions, consistent with the notation in [10], are reported omitting for simplicity the subscript section index k .

Since the wavenumber $k(z)$ is also function of N_g , its variation Δk respect to the stationary value is given by

$$\Delta k = \frac{\partial k}{\partial \omega} (\omega - \omega_0) + \frac{\partial k}{\partial N} \Delta N + \frac{\partial k}{\partial S} \Delta S + \frac{\partial k}{\partial N_g} \Delta N_g \quad (8)$$

being ω_0 the stationary lasing angular frequency and ΔN_g the absorption grating carrier density fluctuation which is related to the photon density fluctuation interacting with the grating, ΔS_g , by

$$\Delta N_g = -\tau_g Q_{S_0_g} \Delta S_g \quad (9)$$

Table 1. AG-DFB laser parameters.

λ_B	1.58	μm	N_0	$1.5 \cdot 10^{18}$	cm^{-3}
n_{eff}	3.25		α_{F_0}	30	cm^{-1}
n_g	3.5		α_{F_N}	0	cm^2
d	0.021	μm	n_{sp}	2	
w	3	μm	K_t	1	
L	400	μm	$ \rho_l $	0.566	
Λ	0.243	μm	$ \rho_r $	0.566	
A	10^8	s^{-1}	A_g	10^8	s^{-1}
B	10^{-10}	$s^{-1} cm^3$	B_g	10^{-10}	$cm^3 s^{-1}$
C	$6 \cdot 10^{-29}$	$s^{-1} cm^6$	C_g	$9 \cdot 10^{-29}$	$cm^6 s^{-1}$
a	$7 \cdot 10^{-16}$	cm^2	b_g	$1.88 \cdot 10^{-20}$	cm^3
b	$2.64 \cdot 10^{-20}$	cm^3	$N_{0,g}$	10^{-18}	cm^{-3}
$\epsilon_{0,0}$	$2 \cdot 10^{-17}$	cm^3	$\epsilon_{0,0,g}$	0	cm^3

where τ_g is the grating carriers lifetime

$$\frac{1}{\tau_g} = \frac{\partial R_g(N_g)}{\partial N_g} + v_g \alpha_g S_g \quad (10)$$

and

$$Q_{S_0,g} = v_g \alpha_g \left(1 - \frac{\epsilon_{0,0,g} S_g}{1 + \epsilon_{0,0,g} S_g} \right) \quad (11)$$

The weight functions $C_N(z)$ and $C_{S_0}(z)$, used by Tromborg *et al.* [13] to take in account the spatial hole burning effect on the spectral linewidth and the noise properties, are written in our formalism [10] as

$$C_Y = \frac{-j c \tilde{\delta}_Y \tilde{a}^2}{\int_L \tilde{n}_g \tilde{a}^2 dz} \quad (12)$$

where Y stands for N or S_0 and $\tilde{a} = a^+ + a^-$ is the total field. Been the photon density fluctuations in the absorption grating and in the active layer proportional $\Delta S_g = (\Gamma_g d\Delta S)/(\Gamma d_g)$, the contribution of the grating to the calculation of the weight functions C_Y is analogous to that of the active layer gain saturation. The additional contributions of the grating carrier density fluctuations to the determination of $\tilde{\delta}_{S_0}$ are given by three terms dependent respectively on the AG differential gain, on the coupling coefficients variation with N_g and on the AG material saturation effects. They assume the form:

$$\tilde{\delta}_{S_0}^\alpha = -j \chi_g a_g \quad (13)$$

$$\tilde{\delta}_{S_0}^K = -2 \chi_g (K_{I_{N_g}} + j K_{G_{N_g}}) \cos(2\beta z + \varphi_i) \quad (14)$$

$$\tilde{\delta}_{S_0}^\epsilon = -j \chi_g \alpha_g \frac{\epsilon_{0,0,g}}{1 + \epsilon_{0,0,g} S_g} \quad (15)$$

with $\chi_g = (Q_{S_0,g} \Gamma_g d\tau_g)/(\Gamma d_g)$.

With these new expressions and those reported in [10], we calculate the overall lasing mode linewidth in the form [10] $\Delta\nu = \Delta\nu_E + \Delta\nu_{NN} + \Delta\nu_{NE} + \sum_m \Delta\nu_{E_m}$, where

$\Delta\nu_{NN}$ and $\Delta\nu_{NE}$ are the contributions due to the shot noise, $\Delta\nu_E$ and $\Delta\nu_m$ those due to the spontaneous emission and the side modes partition noise respectively. This new formulation is very important for a good evaluation of the AG-GC laser linewidth, especially near the laser threshold current where the absorber is not saturated and the grating carrier density fluctuation is strong.

Dynamic Analysis

In this paragraph we present the small signal dynamic analysis, showing only the rate equations to be solved for the determination of the laser dynamic characteristics.

Omitting for simplicity the section subscript index, we rewrite the coupled-wave equations (3), the rate equations for the carrier density in the active [10] and in the AG layer (6) introducing a temporal dependence in the quantities δ , α , R^\pm , \tilde{K}^\pm , N , N_g because of the current modulation. We obtain:

$$\frac{\partial R^\pm}{\partial z}(z, t) = \mp \frac{1}{v_g} \frac{\partial R^\pm}{\partial t}(z, t) \mp j\tilde{\delta}(z, t)R^\pm(z, t) + \tilde{K}^\pm(z, t)R^\mp(z, t) + \mathcal{F}_I^\pm(z, t) \quad (16)$$

$$\frac{\tilde{J}(t)}{ed} = \frac{\partial N}{\partial t} + R(N) + Q(N, S_0) + \mathcal{F}_N \quad (17)$$

$$0 = \frac{\partial N_g}{\partial t} + R_g(N_g) + Q_g(N_g, S_g) \quad (18)$$

where $\tilde{J}(t)$ is the modulated current density, $R(N)$ is the spontaneous recombination rate, $Q(N, S_0) = v_g g S_0$ is the single mode approximation for the stimulated recombination rate, \mathcal{F}_I^\pm and \mathcal{F}_N are complex Langevin's forces introduced to account for noise effects [11], [13]. Assuming the cavity left end as a reference, the instantaneous frequency shift at right end is given by

$$f_R(t) = f_L(t) + \frac{1}{2\pi} \frac{d\Phi_R}{dt} \quad (19)$$

where $\Phi_R(t) = \arg\{R^+(t)\}$ is the instantaneous phase of the electric field at right end and $f_L(t)$ is the instantaneous frequency at left end. Decomposing in real (r) and imaginary (i) parts all the quantities, we solve the equations (16), (17) and (18) introducing the following small signal phasor notation for the time dependent quantities

$$A(z, t) = \bar{A}(z) + \Re\{\Delta A(z, F)e^{j2\pi Ft}\} \quad (20)$$

where A stands for N , N_g , $R_{r,i}^\pm$, α , $\delta - \frac{2\pi}{v_g} \Re\{\Delta f_L(F)e^{j2\pi Ft}\}$, f_L , $K_{r,i}^\pm$, S_0 , J/p_F , $\mathcal{F}_{I,r,i}^\pm$ and \bar{A} is the value at bias point, F is the modulating frequency and p_F are the current weights, allowing non uniform current modulation along the cavity [10], [11]. In order to obtain a good dynamic model for AG structures, it is fundamental to take into account the effects of the spatial and time variation of the absorption grating carrier density N_g on the modal gain and the coupling coefficients; we obtained:

$$\Delta N_g = -\tau'_g(F)Q_{S_0}\Delta S_g \quad (21)$$

$$2\Delta\alpha = (\Gamma a_N - \alpha_{F_N})\Delta N - g \frac{\epsilon_{00}}{1 + \epsilon_{00}S_0}\Delta S_0 + \Gamma_g a_g \Delta N_g \quad (22)$$

$$\Delta K_{r,i}^\pm = \tilde{K}_{(r,i)N_g}^\pm \Delta N_g \quad (23)$$

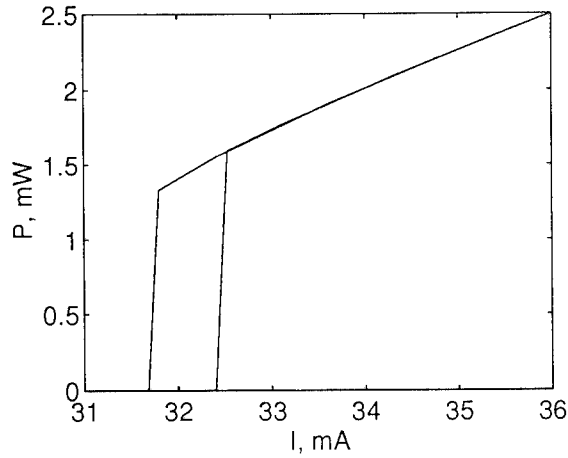


Figure 5. Output power vs injected current bistable behaviour for laser I.

with $1/\tau'_g = 1/\tau_g + 2\pi F$.

Substituting the small signal phasor notation and linearizing the model equations around the static solution formerly obtained, we obtain with complex and long mathematical procedures, omitted for brevity, a simple algebraic system of equations, whose solution provides the AM and FM modulation responses, the relative intensity (RIN) and frequency (FN) noise spectra for any modulating frequency.

IV - CALCULATED RESULTS

In this last section we report and discuss some numerical results obtained from the simulation of the AG-GC DFB laser shown in Figure 1. Few AG-GC structures, obtained changing the thickness and the differential gain of the absorption grating, are investigated with special emphasis on bistability effect in the P-I curve, red frequency shift of the operating wavelength, spectral laser properties.

Choosing two different thickness values d_3 with $d_2 + d_3 = 110 \text{ nm}$ for the structure reported in Figure 1, it is possible to obtain two devices with in-phase (laser I: $d_3 = 35 \text{ nm}$) and anti-phase (laser A: $d_3 = 60 \text{ nm}$) coupling coefficients. The index coupling coefficients and the optical confinement factors in the active and in the AG layers are $K_{I_0} = 32.56 \text{ cm}^{-1}$, $\Gamma = 0.029$, $\Gamma_g = 0.0204$ for laser I and $K_{I_0} = -38.07 \text{ cm}^{-1}$, $\Gamma = 0.027$, $\Gamma_g = 0.0389$ for laser A; we used the differential gain in the AG layer $a_g = 15 \cdot 10^{-16} \text{ cm}^2$ for both lasers. Furthermore we investigated the relevance of the AG differential gain a_g on the characteristics of laser I assuming $a_g = 7 \cdot 10^{-16} \text{ cm}^2$ (laser I1) and $a_g = 3 \cdot 10^{-16} \text{ cm}^2$ (laser I2). Using the data reported before, those of Table 1 and the characteristics shown in Figures 2-3, we obtained the static and the dynamic behaviour of the previous lasers.

Figure 5 shows the computed bistable behaviour of laser I due to the grating saturable absorber effect that has been shown experimentally also in [7]. Above threshold the absorber is saturated and the P-I curve is linear as shown in Figure 6 for the previously defined lasers. The threshold currents are typically higher in AG lasers due to the extra losses in the AG layer. The lower threshold of laser A is due to the higher coupling coefficient respect to the other considered structures.

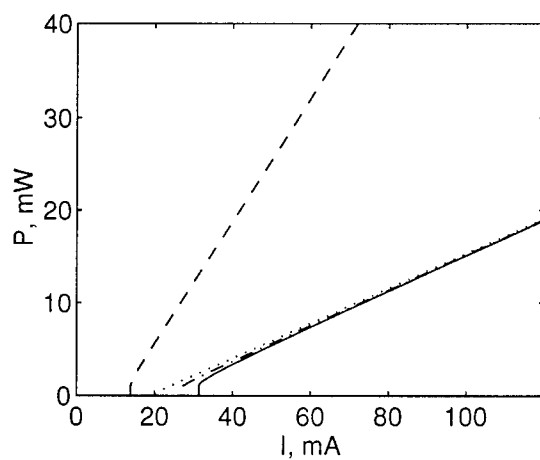


Figure 6. Power versus injected current characteristics for the lasers with in-phase coupling coefficients (I: continuous, I1: dot-dashed, I2: dotted) and anti-phase coupling coefficients (A: dashed).

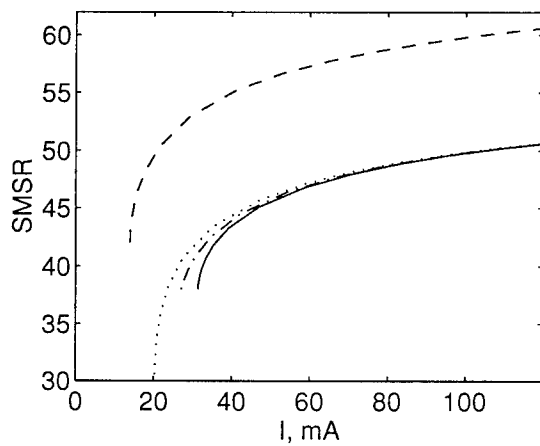


Figure 7. SMSR versus injected current for the lasers considered in Figure 6.

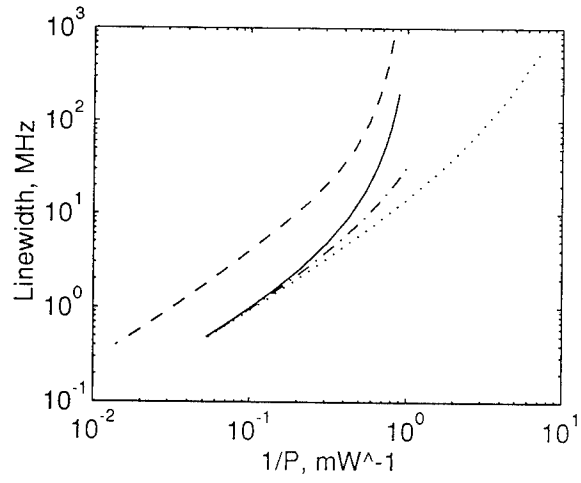


Figure 8. Linewidth versus injected current for the lasers considered in Figure 6.

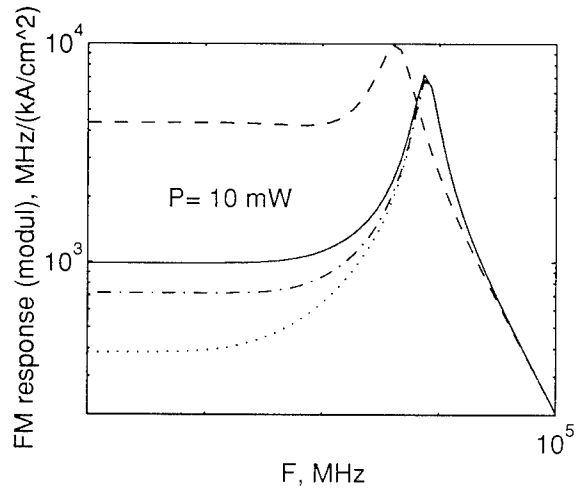


Figure 9. FM modulation response versus modulating frequency F for the lasers considered in Figure 6 at the operating point $P = 10 \text{ mW}$.

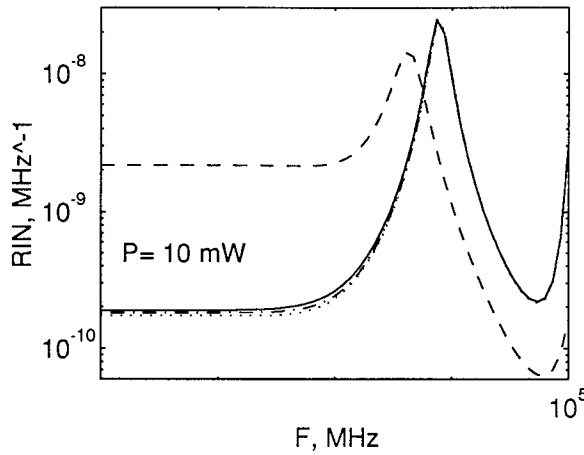


Figure 10. RIN spectra normalized respect to the output power at left-end facet vs modulating frequency F for the lasers considered in Figure 6 at the operating point $P = 10 \text{ mW}$.

The SMSR vs the injected current above threshold is shown in Figure 7; the values, larger than 45 dB, agree with experimental results [4], [5] and are higher than in ordinary DFB lasers. Furthermore near threshold the SMSR is higher for laser A, in agreement with the higher threshold gain margin deducible from Figure 4; the reduction of a_g (see laser I2 characteristics) decreases the SMSR due to the weakening of the interaction between the absorption grating and the field standing wave pattern.

The lasers linewidth characteristics, reported in Figure 8, present a strong broadening near threshold typical of AG structures; this is due to the active layer carrier density reduction produced by the AG carrier density increase [11]. This carrier density variation induces also an anomalous frequency red-shift which for medium injected current values balances the blue-shift induced by the refractive index reduction due to the increase of the carrier density in the active region consequent to gain saturation. The linewidth broadening is lower in structures with low a_g and is almost disappearing in laser I2; in the high power regime the laser linewidth characteristic becomes linear with the inverse of the output power as in ordinary DFB lasers. For the same output power anti-phase laser A has a greater spectral linewidth.

The FM responses, shown in Figure 9, report a 3dB modulation bandwidth greater than 11 GHz [4] for in-phase lasers. The anti-phase structure A, unlike the corresponding GG structure [6], has a lower modulation bandwidth but a better FM efficiency.

The relative intensive noise (RIN) is reported in Figure 10 versus the modulating frequency; the laser with in-phase coupling coefficients shows a greater suppression of the RIN respect to the anti-phase case. The decrease of a_g has very little influence on the intensity noise spectra.

The results show that the absorption grating parameters have a great influence on the AG-GC-DFB laser behaviour. The structure with anti-phase coupling coefficients (A) show different behaviour in SMSR, linewidth, dynamic and noise performances respect the in-phase structure (I) as shown also in gain grating lasers [6], [9]. Besides, decreasing the differential material gain a_g , we found that the bistable laser behaviour near threshold disappear with a worsening on the laser performances.

References

- [1] H. Kogelnik, and C. V. Shank, "Coupled-wave theory of distributed feedback lasers", *J. Appl. Phys.*, vol. 43, pp. 2327-2335, 1972.
- [2] T. Inoue, S. Nakajima, Y. Luo, T. Oki, H. Iwaoka, Y. Nakano, and K. Tada, "CW operation of an InGaAsP/InP gain-coupled distributed feedback laser with a corrugated active layer" *IEEE Phot. Technol. Letters*, Vol. 3, No. 11, pp. 958-960, 1991.
- [3] R. G. Baets, K. David, and G. Morthier, "On the distinctive features of gain coupled DFB lasers and DFB lasers with second-order grating", *J. Quantum Electron.*, Vol. 29, pp. 1792-1797, 1993.
- [4] B. Borchert, B. Stegmüller, and R. Gessner "Fabrication and characteristics of improved strained quantum well GaInAlAs gain-coupled DFB lasers" *Electronics Letters*, Vol. 29, No. 2, pp. 210-211, 1993.
- [5] J. Zoz, and B. Borchet, "Dynamic behaviour of complex-coupled DFB lasers with in-phase absorptive grating", *Electron. Letters*, vol. 30, No. 1, pp. 39-40, 1994.
- [6] L. M. Zhang, and J. E. Carrol, "Enhanced AM and FM modulation response of complex coupled DFB lasers", *IEEE Photon. Technol. Letters*, Vol. 5, No. 5, pp. 506-508, 1993.
- [7] Y. Luo, H.-L. Cao, M. Dobashi, H. Hosomatsu, Y. Nakano, and K. Tada, "Gain-Coupled distributed feedback semiconductor lasers with an absorptive conduction-type inverted grating" *IEEE Phot. Technol. Letters*, Vol. 4, No. 7, pp. 692-695, 1992.
- [8] K. David, G. Morthier, P. Vankwikelberge, R.G. Baets, T. Wolf, and B. Borchet "Gain-Coupled DFB Lasers versus Index-Coupled and Phase-Shifted DFB Lasers: a Comparison based on Spatial Hole Burning Corrected Yield" *J. Quantum Electron.*, Vol. 27, No. 6, pp. 1714-1723, 1991.
- [9] X. Pan, B. Tromborg, H. Olesen, and H. E. Lassen, "Effective linewidth enhancement factor and spontaneous emission rate of DFB lasers with gain coupling", *IEEE Photon. Technol. Letters*, vol. 4, pp. 1213-1215, 1992.
- [10] R. Bonello, and I. Montrosset, "Analysis Of Multisection and Multielectrode Semiconductor Lasers", *IEEE J. Lighthwave Technol.*, vol. 10, No. 12, pp. 1890-1900, 1992.
- [11] R. Bonello, and I. Montrosset, "Statical and dynamical analysis of multisection and multielectrode semiconductor lasers", *SPIE Multigabit Fiber Communications*, Vol. 1787, pp. 151-163, 1992.
- [12] H. L. Cao, Y. Luo, Y. Nakano, K. Tada, M. Dobashi, and H. Hosomatsu, "Optimization of grating duty factor in gain-coupled DFB lasers with absorptive gating-Analysis and Fabrication.", *IEEE Phot. Technol. Letters*, Vol. 4, No. 10, pp. 1099-1102, 1992.
- [13] B. Tromborg, H. Olesen, and X. Pan, "Theory of linewidth for multielectrode laser diodes with spatially distributed noise sources", *IEEE J. Quantum Electron.*, vol. QE-27, pp. 178-192, 1991.
- [14] X. Pan, B. Tromborg, and H. Olesen, "Linewidth rebroadening in DFB lasers due to weak side modes", *IEEE Photon. Technol. Lett.*, vol. 3, pp. 112-114, 1991.

LINEWIDTH REDUCTION BY THE FORMATION OF A FIBER EXTERNAL CAVITY WITH THE VERTICAL EMISSION OF A DISTRIBUTED BRAGG REFLECTOR LASER

Anthony L. Cook and Herbert D. Hendricks

Research and Technology Group
NASA Langley Research Center
MS-473
Hampton, VA 23681

INTRODUCTION

Narrow-linewidth sources are essential for optical systems such as coherent optical communications and optical sensors. One way of obtaining narrow linewidths is to insert the semiconductor laser into a passive external cavity containing a mirror [1, 2], a diffraction grating [1, 3-5], a GRIN rod [6], an optical fiber [7-10], or an optical fiber containing a fiber Bragg grating [11]. Linewidths of hundreds of kHz [2, 3, 6], tens of kHz [1, 3, 4, 7, 8], or even less [5, 11] have been reported for these external-cavity lasers. Almost all the reports have involved either a Fabry-Perot semiconductor laser or a DFB semiconductor laser as the active element. Furthermore, the front or rear facet emission has been used in these reports to couple the reflected light back into the laser cavity. In this paper, the use of vertical emission from a DBR laser to obtain a narrow linewidth is reported. To the authors' knowledge, this is the first report of using vertical emission to decrease the laser linewidth in an external cavity configuration.

EXPERIMENTAL

The experimental setup, which will be explained in the following four paragraphs, is shown in figure 1. A diagram of the DBR laser diode is shown in figure 2. The laser actually consists of a DBR master-oscillator with a preamplifier section in front. This device was fabricated as part of a master-oscillator power-amplifier (MOPA) laser contract between Spectra Diode Labs and NASA Langley [12]. The total length of the device is 1650 μm , which consists of 500 μm for the back grating, 500 μm for the DBR gain section, 150 μm for the front grating, and 500 μm for the preamplifier gain section. The laser was mounted p-side down, and access to the vertical emission was obtained through a window in the n-side metallization. The device has a threshold current of 30 mA at 25 degrees C. The emission wavelength of the laser is 980

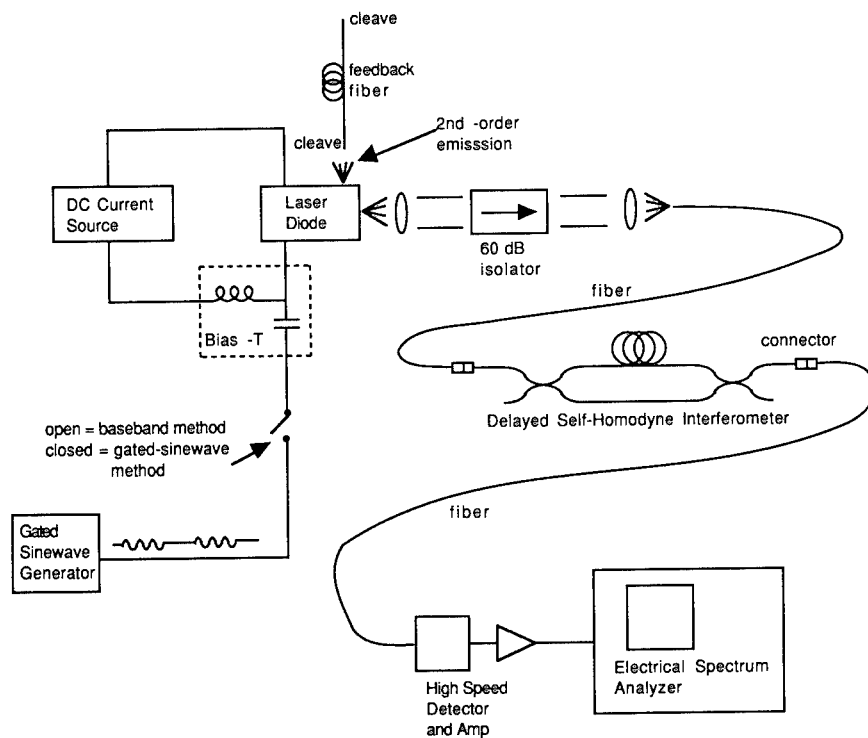


Figure 1. Experimental setup.

nm. It had a maximum recommended operating power of 100 mW. The laser stays single-longitudinal mode without mode hops from currents of 40 mA to 104 mA. The side-mode suppression ratio over that current range is greater than 25 dB. Each grating emits approximately the same vertical power, as measured by blocking the beam from one grating with a knife-edge. The vertical power emitted from each of the gratings is approximately one-sixteenth of the power emitted from the front facet. For example, at a current of 60 mA, the power emitted from the front facet was 25.7 mW and the vertical power emitted from each grating was 1.5 mW. The laser without the external cavity (i.e., the solitary laser) exhibited a linewidth of less than 4 MHz for currents above 50 mA. Although the emission wavelength of this device is 980 nm, this concept can be applied to devices with other wavelengths.

An optical fiber, cleaved on both ends, was used to form the external cavity. The use of fibers with core diameters of 6 μm , 9 μm , and 47 μm was investigated. The 6 μm fiber was Corning Flexcore 1060 fiber, and was the only fiber that was truly single-mode for the emission wavelength of 980 nm. The 9 μm fiber was standard telecommunications-grade fiber. The large-core 47 μm fiber had a graded-index core. Reduced linewidths have been obtained with all three types of fibers in this experiment, but we will focus mainly on the results obtained with the 6 μm core fiber.

The linewidth was measured with a delayed self-homodyne fiber interferometer that has a delay-leg length of 5 km, corresponding to a delay time, τ_d , of 25 μs . The linewidth resolution of this system is 40 kHz. Linewidths less than 40 kHz can be measured, but with some error. The error is such that the displayed linewidth is an overestimate of the actual linewidth.

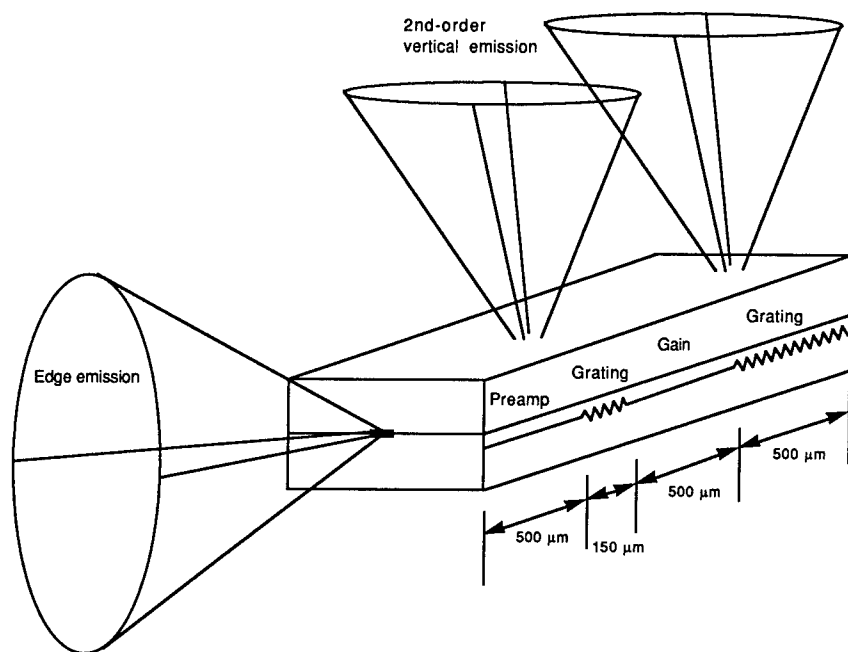


Figure 2. DBR laser diode with vertical emission.

Our delayed self-homodyne linewidth measuring system did not have an acousto-optic modulator to shift the displayed linewidth away from baseband. For convenience, measuring linewidth with this system will be referred to as the baseband method. The laser is operated CW with the baseband method. Even though narrow linewidths cannot be accurately measured with this method due to baseband instrument noise, it can still be useful to view the overall shape of the linewidth over a broad span, as will be shown later. Since it is difficult to accurately view and measure narrow linewidths at baseband, we used an alternative method to offset the linewidth from baseband. This method [13] consists of modulating the laser diode with a gated small-signal sinewave and viewing the resulting self-homodyne waveform on an electrical spectrum analyzer. This method will be referred to as the gated-sinewave method. The displayed spectrum consists of two distinct components. The first is a very narrow spike at a frequency corresponding to direct intensity modulation from the sinewave source. The second is a series of FM spectral components which are resolved to a half-width half-max (HWHM) bandwidth (BW) equal to the unmodulated linewidth of the laser. The linewidth of the external-cavity laser will be measured with this method. The gated-sinewave method was first tested on the solitary laser to prove its usefulness and accuracy for measuring laser linewidth. A linewidth of 2.5 MHz was measured for the solitary laser using both the baseband method and the gated-sinewave method when the laser was biased at 60 mA. For the gated-sinewave method, the laser was modulated with a 500 MHz sinewave (RF power = -8 dBm) which was gated with a 20 kHz squarewave.

RESULTS

The general shape of the external-cavity linewidth will first be discussed. The general shape of the linewidth, measured with the baseband method and viewed over a broad span,

consisted of a main (baseband) peak and several other peaks. Similar peaks in the displayed linewidth have also been previously observed when the laser emission is measured with a delayed self-heterodyne fiber interferometer [2]. Peaks were also present in the intensity noise spectrum of the laser [14-16]. The frequency separation of the peaks is equal to $c/2nL$ [14, 15], where c is the velocity of light, n is the refractive index of the fiber core and L is the length of the fiber. It was concluded that the peaks are beat notes between longitudinal modes of the external cavity [2, 3, 14-16].

The linewidth peaks are shown in figure 3, and the intensity noise peaks are shown in figure 4. The results shown in figures 3 and 4 are obtained by using a 6 μm fiber as the external cavity, but similar results are obtained with the other fibers. The width of each peak in figure 3 increases as the order of the peak increases. For example, the HWHM BW of the first order peak at 10 MHz was 78 kHz, the BW of the second peak at 20 MHz was 110 kHz, the BW of the third peak at 30 MHz was 155 kHz, and so on. The BW of the main peak could not be measured with this method due to baseband noise. Its BW (linewidth) was determined from the gated-sinewave method, and will be discussed later.

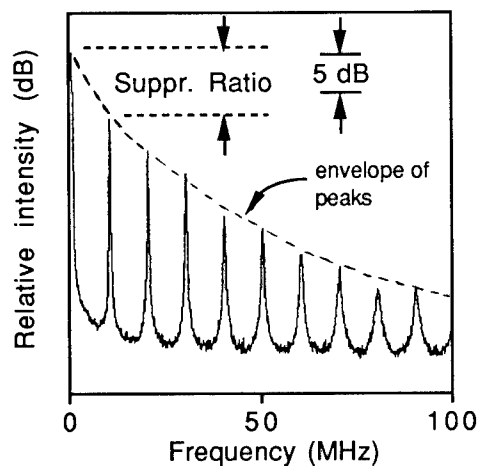


Figure 3. Presence of peaks in the linewidth of the external cavity laser. 6 μm core fiber, 10 m long. Laser operated at 60 mA, 25 degrees C. This curve shows the general shape of external-cavity linewidth measured with the baseband method. Note periodic peaks in the structure of the linewidth.

The suppression ratio (SR) will be defined as the power ratio of the height of the main peak to the height of a successive peak, as shown for convenience in figure 3. However, since the height of the main peak is distorted when viewed with the baseband method, the SR was actually measured with the gated-sinewave method with the electrical spectrum analyzer set for a span of several tens of MHz, so that the main peak and successive peaks were displayed on one screen. This SR is most likely equal to the side-mode suppression ratio (SMSR) of the external cavity longitudinal modes. However, this fact was not proven with a Fabry-Perot interferometer due to a lack of interferometer mirrors coated for 980 nm. For this experiment, the suppression ratio (SR) depends mainly on the length of the fiber and, to a lesser extent, the power coupled into the fiber. The reason the suppression ratio depends on the length of the fiber is because the peaks always lie along an envelope typical of which is shown by the dotted line in figure 3. Longer lengths of fiber have more closely-spaced peaks which lie closer to the main peak, therefore having peaks with smaller suppression ratios. Figure 5 shows the general

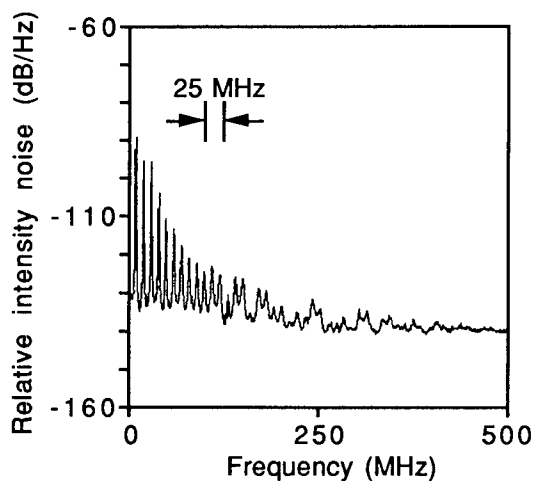


Figure 4. Presence of peaks in the intensity noise of the external cavity laser. 6 μm core fiber, 10 m long. Laser operated at 60 mA, 25 degrees C.

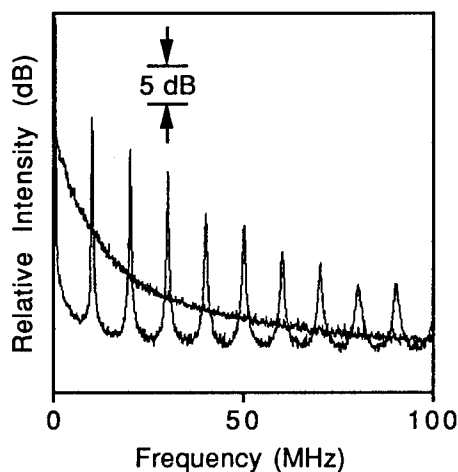


Figure 5. Comparison of solitary linewidth and external-cavity linewidth. the conditions are the same for both cases, except that the solitary laser does not have a fiber external cavity. 6 μm core fiber, 10 m long. Laser operated at 60 mA, 25 degrees C.

shape of both the linewidth of the solitary laser and of the external-cavity laser displayed on a broad frequency scale. The SR of the baseband peak to the first peak is plotted vs. fiber length for a 6 μm fiber and is shown in figure 6. Similar results are obtained for other fiber core diameters. One author [16] reported the complete suppression of these peaks with proper phase adjustment of the optical feedback by adjusting the external cavity mirror. The effects of the phase of the optical feedback in this experiment will be discussed next.

It has been previously reported [2, 3, 6, 7] that it is necessary to adjust the phase of the optical feedback to obtain the minimum linewidth. Another report [8] has specifically

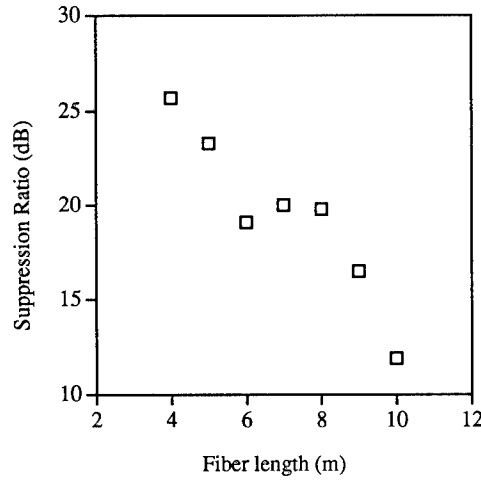


Figure 6. Suppression ratio vs. fiber length for a 6 μm core fiber external cavity. The power coupled into the fiber is 32 μW . The laser is operated at 60 mA, 25 degrees C.

mentioned not adjusting the phase and still obtaining narrow linewidths. Still other reports with weak feedback [1] and strong feedback [5] have not mentioned whether or not the phase was adjusted for minimum linewidth. The phase of the optical feedback in our experiments is determined by the random placement of the cleave on the far end of the feedback fiber. A consistent, narrow linewidth could be obtained for most cleaves, indicating that a large range of phases could be tolerated to give a narrow linewidth. It has also been reported that the phase condition can also be adjusted with slight variations in laser current or laser temperature [2, 6, 17], but adjusting those parameters had little effect on the linewidth in this experiment, supporting the fact that a wide range of phases was allowable in this experiment to obtain a narrow linewidth. It has also been reported that when operating with certain feedback levels *within* the weak (< -30 dB) feedback regime, phase does not play an important role in the linewidth reduction [10]. We believe that the laser operated in this regime. For our experiments, -30 dB of feedback means that one one-thousandth of the light vertically exiting one of the gratings is coupled back into the laser cavity.

Before we discuss how certain parameters affected the linewidth, it is necessary to first mention the feedback parameter, X [4, 7, 17]. X is equal to $\gamma\tau(\eta)^{0.5}$, where γ is the reciprocal of the roundtrip delay time inside the laser, τ is the round-trip time of the external cavity, and η is the optical feedback power ratio [7, 17]. The optical feedback power ratio is the ratio of the power coupled back into the laser cavity to the power emitted from the laser. The parameters γ and τ can be expressed as

$$\gamma = c/2n_D L_D, \text{ and}$$

$$\tau = 2nL/c,$$

where c is the velocity of light, n and n_D are the refractive indices of the fiber core and the laser cavity, respectively, and L and L_D are the one-way lengths of the fiber and the laser, respectively. The ratio of the external-cavity linewidth to the solitary linewidth is equal to $1/(1+X)^2$ when the cavity is phase-aligned for minimum linewidth [4, 7, 17]. The amount of linewidth reduction is dependent on the value of the feedback parameter, which depends on the length of the external cavity, the laser diode cavity length, and the amount of optical power

coupled back into the laser cavity. Thus for a given laser, operating with weak feedback levels (< -30 dB) [3, 4, 7, 10], the linewidth can be decreased by increasing either the length of the external cavity or the amount of power coupled back into the laser cavity. For medium feedback levels (approximately -30 dB to -10 dB) [2, 5, 9] the laser can enter a regime where linewidth broadening greater than the solitary linewidth can occur. Strong amounts of feedback (> -10 dB, or 10%) can cause the linewidth to become very narrow again [5, 6, 9, 11]. The above feedback regimes and their effects on linewidth have also been previously characterized and documented [9, 10, 18]. Feedback levels in this experiment were characterized by the weak regime, and linewidth rebroadening was never encountered. There was no measurable change in threshold current when the external fiber cavity was formed with the laser, supporting the fact that the amount of optical feedback was small [7, 19, 20].

The amount of power coupled back into the laser cavity, and thus the level of feedback, can be estimated as follows. When a length of $6\text{ }\mu\text{m}$ core fiber, cleaved on both ends, was placed $50\text{ }\mu\text{m}$ from the top of the laser which was operating at a current of 60 mA , approximately $32\text{ }\mu\text{W}$ could be coupled into the fiber. At a current of 60 mA , the laser vertically emits 1.5 mW from one of the gratings. If 4% of the fiber-coupled power is reflected from the far end of the fiber, then approximately $1.3\text{ }\mu\text{W}$ is reflected back towards the laser, not all of which actually enters back into the laser cavity. If the entire $1.3\text{ }\mu\text{W}$ was coupled back into the laser cavity, then the optical power feedback ratio would be -31 dB . However, the actual feedback ratio probably lies in the range of -40 to -50 dB , due to coupling loss from the return light exiting the fiber and entering into the laser cavity.

When the laser was operated at a current of 60 mA and the fiber was placed $50\text{ }\mu\text{m}$ from the top of the laser, the amount of power coupled into a $6\text{ }\mu\text{m}$, $9\text{ }\mu\text{m}$, and $47\text{ }\mu\text{m}$ fiber was $32\text{ }\mu\text{W}$, $60\text{ }\mu\text{W}$ and $280\text{ }\mu\text{W}$, respectively. For the $6\text{ }\mu\text{m}$ and $9\text{ }\mu\text{m}$ fibers, the lateral position resulting in the highest fiber-coupled power also resulted in the narrowest linewidth. For the

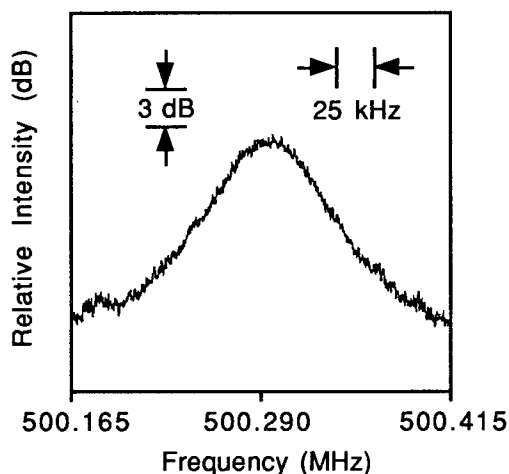


Figure 7. 26 kHz linewidth of the external cavity laser measured with the gated-sinewave method. The fiber was 10 meters of $6\text{ }\mu\text{m}$ core fiber. The laser was operated at 60 mA , 25 degrees C .

$47\text{ }\mu\text{m}$ fiber, the lateral position resulting in the highest fiber-coupled power did not always correspond to the minimum linewidth. Also, in general, the $47\text{ }\mu\text{m}$ core fibers resulted in linewidths that were more unstable and sensitive to mechanical perturbations to the fiber than the $6\text{ }\mu\text{m}$ and $9\text{ }\mu\text{m}$ core fibers. The linewidth of the external cavity laser as measured with the

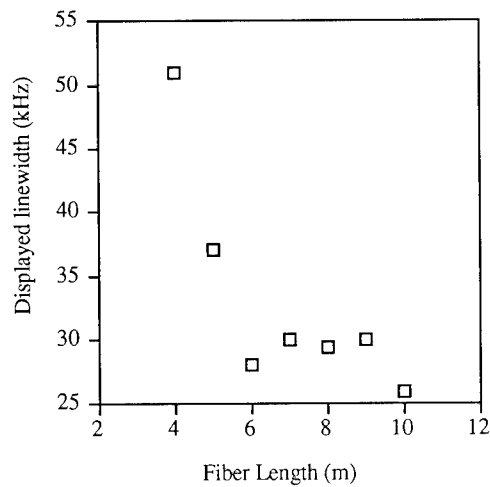


Figure 8. Linewidth vs. fiber length for a 6 μm core fiber external cavity. The power coupled into the fiber is 32 μW . The laser was operated at 60 mA, 25 degrees C.

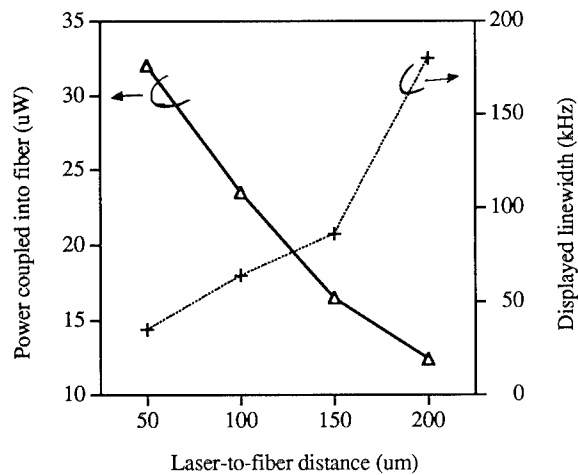


Figure 9. Linewidth and fiber-coupled power vs. laser-to-fiber distance when using a 6 μm core fiber. The fiber length is 9 m. The laser was operated at 60 mA, 25 degrees C. Δ corresponds to fiber -coupled power; + corresponds to linewidth from 10 meters to 2 meters

gated-sinewave method is shown to be 26 kHz in figure 7. For this measurement the laser was operated at 60 mA and 25 degrees C with a 10 m long 6 μm core fiber. The power coupled into the fiber was 32 μW .

To investigate how the linewidth varied with fiber length, the length of the fiber was varied in one meter increments. The linewidth vs. fiber length for a 6 μm core fiber is shown in figure 8. For fiber lengths of 6 meters or greater, a stable, narrow linewidth (< 35 kHz) could be obtained. The term "stable" here refers to a displayed linewidth that did not greatly fluctuate in amplitude, width or position as viewed on the electrical spectrum analyzer. Displayed

linewidths as low as 26 kHz have been measured for a fiber length of 10 meters. Data was not plotted for lengths less than four meters. This was because (even though the linewidth was distinguishable) it was difficult to get an accurate reading due to the fact that the displayed linewidth was constantly changing in amplitude, width or position on the screen.

It can be noted that for this experiment the cavity lengths required to obtain narrow linewidths were relatively longer than those reported in previous experiments. For example, narrow linewidths have been previously reported using a short fiber length [9] or using short external cavities with mirrors [2] or gratings [5]. However, in these reports the feedback amount was much higher, which increased the feedback parameter X . It is possible that increasing the reflectivity of the far end of the feedback fiber here could increase the feedback amount and allow for a shorter fiber external cavity.

The laser-to-fiber distance affected the linewidth more drastically for the 6 μm and 9 μm fibers than for the 47 μm fiber. The linewidth vs. laser-to-fiber distance for a 6 μm core fiber is shown in figure 9. Similar results have been obtained for 9 μm fibers.

DISCUSSION AND CONCLUSIONS

In summary, linewidth reduction has been observed when a fiber external cavity is formed with the vertical emission of a distributed Bragg reflector laser. Displayed linewidths as narrow as 26 kHz have been measured for a fiber length of 10 meters. Long lengths of fiber were needed to obtain narrow linewidths because the amount of optical feedback was small. Long lengths of fiber correspond to more closely spaced external-cavity longitudinal modes and an increased chance of mode-hopping among those external cavity modes [1, 21] due to slight changes in ambient conditions or laser conditions. Shorter external cavities should exhibit a more stable longitudinal-mode structure, but the optical feedback amount would need to be increased to maintain the same level of feedback parameter, X . Increasing the amount of power fed back to the laser by increasing the reflectivity of the far end of the fiber should allow use of a shorter fiber while still maintaining a narrow linewidth. It has also been reported that the strong feedback regime is preferred for linewidth narrowing because it is more stable and much more immune to other sources of optical feedback such as splices, connectors and receivers [9].

The results obtained here also present a possibility for linewidth reduction in high-power (> 1 W) MOPA lasers that have a master oscillator similar to the laser used in this experiment. It should be noted that access to the laser cavity of a high power MOPA would be simpler using top emission, since a special heat sink would not be necessary to allow access to the rear facet, and since the output of the front facet is highly astigmatic.

ACKNOWLEDGEMENTS

The authors would like to thank Terry Mack for his helpful discussions concerning this work. The laser used for this experiment was obtained as part of a MOPA contract with Spectra Diode Labs.

REFERENCES

- [1] S. Saito and Y. Yamamoto, "Direct observation of lorentzian lineshape of semiconductor laser and linewidth reduction with external grating feedback," *Electron. Lett.*, vol. 17, pp. 325-327, 1981.

- [2] L. Goldberg, H. F. Taylor, A. Dandridge, J. F. Weller, and R. O. Miles, "Spectral characteristics of semiconductor lasers with optical feedback," *IEEE J. Quantum Electron.*, vol. QE-18, pp. 555-564, 1982.
- [3] H. Olesen, S. Saito, T. Mukai, T. Saitoh, and O. Mikami, "Solitary Spectral Linewidth and its reduction with external grating feedback for a 1.55 μm InGaAsP BH laser," *Jap. J. Appl. Phys.*, vol. 22, pp. L664-L666, 1983.
- [4] S. Saito, O. Nilsson, and Y. Yamamoto, "Oscillation center frequency tuning, quantum FM noise, and direct frequency modulation characteristics in external grating loaded semiconductor lasers," *IEEE J. Quantum Electron.*, vol. QE-18, pp. 961-970, 1982.
- [5] R. Wyatt and W. J. Devlin, "10 kHz linewidth 1.5 μm InGaAsP external cavity laser with 55 nm tuning range," *Electron. Lett.*, vol. 19, pp. 110-112, 1983.
- [6] H. Rongqing, T. Shangping, W. Yizun, and P. Huaide, "An experimental study on stable single-frequency semiconductor lasers with external cavity," *IEEE Photon. Technol. Lett.*, vol. 1, pp. 255-257, 1989.
- [7] F. Farve, D. Le Guen, and J. C. Simon, "Optical feedback effects upon laser diode oscillation field spectrum," *IEEE J. Quantum Electron.*, vol. QE-18, pp. 1712-1717, 1982.
- [8] K. -Y. Liou, Y. K. Jhee, C. A. Burrus, K. L. Hall, and P. J. Anthony, "Narrow-linewidth fibre-external-cavity injection lasers," vol. 21, pp. 933-934, 1985.
- [9] K. -Y. Liou, Y. K. Jhee, G. Eisenstein, R. S. Tucker, R. T. Ku, T. M. Shen, U. K. Chakrabarti, and P. J. Anthony, "Linewidth characteristics of fiber-extended-cavity distributed-feedback lasers," *Appl. Phys. Lett.*, vol. 48, pp. 1039-1041, 1986.
- [10] N. Schunk and K. Petermann, "Numerical analysis of the feedback regimes for a single-mode semiconductor laser with external feedback," *IEEE J. Quantum Electron.*, vol. QE-24, pp. 1242-1247, 1988.
- [11] C. A. Park, C. J. Rowe, J. Buus, D. C. J. Reid, A. Carter, and I. Bennion, "Single-mode behaviour of a multimode 1.55 μm laser with a fibre grating external cavity," *Electron. Lett.*, vol. 22, pp. 1132-1133, 1986.
- [12] D. F. Welch, D. G. Mehuys, and R. A. Parke, "High-power CW, diffraction-limited emission from a monolithically-integrated active grating master oscillator power amplifier," NASA contractor report 4464, Contract NAS1-19287, Aug. 1992.
- [13] Hewlett Packard Application Note 371, P/N 5954-9137, Example 13, p. 40.
- [14] Y. C. Chen, "Noise characteristics of semiconductor laser diodes coupled to short optical fibers," *Appl. Phys. Lett.*, vol. 37, pp. 587-589, 1980.
- [15] H. Sato, T. Fujita, and K. Fujito, "Intensity fluctuation in semiconductor laser coupled to external cavity," *IEEE J. Quantum. Electron.*, vol. QE-21, pp. 46-51, 1985.
- [16] T. Fujita, S. Ishizuka, K. Fujito, H. Serizawa, and H. Sato, "Intensity noise suppression and modulation characteristics of a laser diode coupled to an external cavity," *IEEE J. Quantum. Electron.*, vol. QE-20, pp. 492-499, 1984.
- [17] K. Kikuchi and T. Okoshi, "Simple formula giving spectrum-narrowing ratio of semiconductor-laser output obtained by optical feedback," *Electron. Lett.*, vol. 18, pp. 10-11, 1982.
- [18] R. W. Tkach and A. R. Chraplyvy, "Regimes of feedback effects in 1.5- μm distributed feedback lasers," *IEEE J. Lightwave Tech.*, vol. LT-4, pp. 1655-1661, 1986.
- [19] D. Renner and J. E. Carroll, "Simple system for broad-band single-mode tuning of D. H. GaAlAs lasers," *Electron. Lett.*, vol. 15, pp. 73-74, 1979.
- [20] K. R. Preston, K. C. Wollard, and k. H. Cameron, "External cavity controlled single longitudinal mode laser transmitter module," *Electron. Lett.*, vol. 17, pp. 931-933, 1981.
- [21] H. Sato, T. Fujita, J. Ohya, "Theoretical analysis of longitudinal mode coupling in external cavity semiconductor laser," *IEEE J. Quantum. Electron.*, vol. QE-21, pp. 284-291, 1985.

DISTRIBUTED FEEDBACK LASERS FOR DIODE LASER GAS SENSING

Pam York¹, Ray Martinelli¹, Ray Menna¹,
Dave Cooper², Harris Riris², and Clint Carlise²

¹David Sarnoff Research Center
Princeton, NJ 08543

²SRI International
Menlo Park, CA 94025

INTRODUCTION

Cryogenic lead-salt (II-VI) diode laser spectroscopy and other infrared techniques such as fourier transform and nondispersive infrared spectroscopy have been used to sense trace gases¹. However, there are several limitations, including high cost (>\$50K) and lack of portability. Consequently, usage is limited primarily to laboratories or industries forced to comply with federal regulations. The application of room temperature diode lasers to gas sensing allows for a ~10-100x cost reduction, low power consumption, portability, part-per-billion detection sensitivity, remote sensing, real-time and interference-free sensors. Such features allow access to applications which require a small and inexpensive, yet highly sensitive gas detection system. Examples include exhaust monitors in automobiles, *in situ* industrial stack pollution monitors, semiconductor process control, natural gas leak detection in homes, and poisonous gas detection on the battle field and in manufacturing facilities. Important medical applications include glucose monitoring and the *ex situ* diagnosis of internal disorders by monitoring trace gases on human breath^{2,3}.

Fundamental molecular absorption bands typically lie in the 2-5 μm mid-infrared (mid-IR) range, where previously there were no room temperature diode lasers. While progress has been made⁴, prospects for room temperature, single mode lead-salt lasers appear slim. Furthermore, the important spectral region between 2 - 3 μm cannot be easily accessed with these materials. However, recent advances in both diode laser spectrometers and III-V materials virtually eliminate the need for II-VI lasers in trace gas sensing. In this article, an overview of this technology is given and the requirements of diode lasers is described.

SELECT MOLECULAR ABSORPTION DATA

Fundamental molecular absorption bands typically lie in the range of 2 - 5 μm . However, many molecules also have strong overtone bands in the near-IR (0.75 - 2.0 μm) where commercial lasers exist. Molecular absorption data is shown in Table I for several molecules at selected lines.

Table 1. Theoretical absorption sensitivities for selected molecules in a system that can detect absorbances of 10^{-6} at 760 Torr.

Molecule	Wavelength (μm)	Sensitivity (ppm-m)
CO ₂	1.432	17
	1.957	4.7
	2.779	0.0025
	4.235	0.00003
NO ₂	0.800	25
H ₂ O	1.365	0.006
NH ₃	1.544	5
CO	1.567	3.6
H ₂ S	1.578	15
CH ₄	1.651	0.07
HCl	1.747	0.1
NO	1.847	50
N ₂ O	1.953	10

The minimum detectable concentration in parts-per-million-meter (ppm-m) is given in the right-hand column, assuming a system which can detect absorbances of 10^{-6} at atmospheric pressure. For example, in a one meter path length at 1.432 μm , 17 ppm of CO₂ can be detected. The detection sensitivity for CO₂ at 4.235 μm increases by nearly 10^6 . Similar trends are observed for other molecules. Hence, the need for efficient room temperature lasers in the 2 - 5 μm range.

DIODE LASER SPECTROMETER

A schematic diagram of a diode laser spectrometer is shown in Figure 1. The laser dc bias and temperature are adjusted to set the emission wavelength near the molecular absorption line of interest. A saw-tooth ramp current is super-imposed on the dc bias; a linear increase in the current results in a linear increase in the output wavelength due to heating. The laser wavelength is tuned with current over the width of the molecular absorption line, which is on the order of a few GHz. A small rf signal is also applied to the laser for synchronous signal detection, greatly increasing the signal-to-noise ratio (SNR)⁵. The incident laser beam, I_0 , passes through the gas sample and is partially absorbed as its output is tuned through the molecular absorption line. The transmitted beam, I , is square-law detected at the photodetector, and the

photocurrent is amplified, filtered and synchronously detected. Signal averaging improves the SNR.

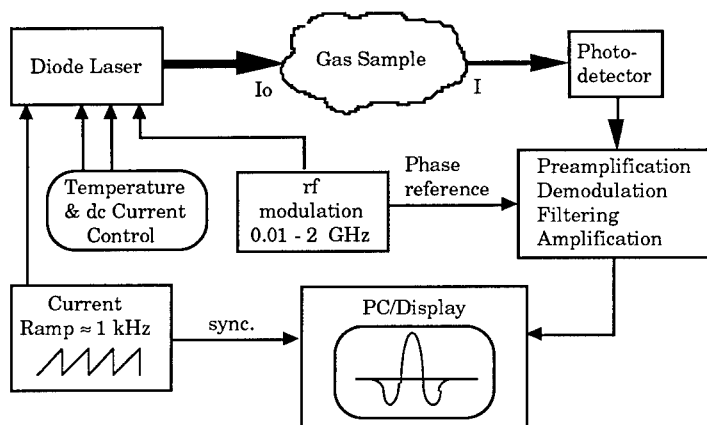


Figure 1. Schematic diagram of a diode laser spectrometer.

If detected at the first harmonic of the modulation, $2f$, the resulting signal is proportional to the second derivative of the absorption line. An example of a detected signal is shown in Figure 2⁶ for $^{12}\text{CO}_2$ and $^{13}\text{CO}_2$ on human breath measured in a multipass gas cell. The inset shows an amplified trace of $^{13}\text{CO}_2$, and the overall frequency interval scanned was ~ 8 GHz. Human breath contains $\sim 4\%$ CO_2 , of which roughly 1% is the stable isotope of $^{13}\text{CO}_2$ ⁷, and this measurement correlates with those concentrations.

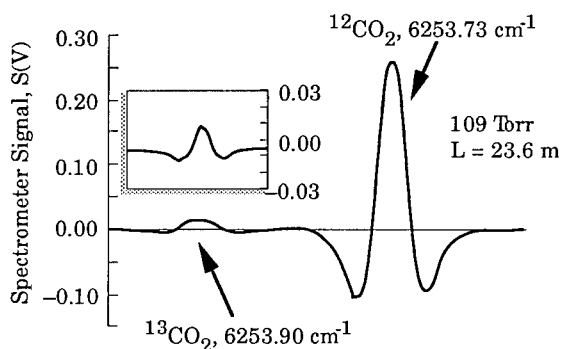


Figure 2. The diode laser spectrometer signal for $^{12}\text{CO}_2$ and $^{13}\text{CO}_2$ measured on human breath.

The concentration of the molecular species can be determined from Beer's Law

$$I = I_0 \cdot e^{-\sigma N L}, \quad (1)$$

where σ is the molecular absorption cross section, N is the molecular concentration, and L is the path length through the gas medium. The absorbance, A , is

$$A = \sigma N L = \ln \left[\frac{I_0}{I} \right], \quad (2)$$

and the concentration in ppm-m, $C \times L$, is

$$C \times L = \left[\frac{N}{N_0} \right] \cdot 10^6 = \left[\frac{\ln(I_0/I)}{\sigma N_0} \right] \cdot 10^6 \text{ ppm-m} \quad (3)$$

where $N_0 = 2.5 \times 10^{19} \text{ cm}^{-3}$ is the atmospheric concentration of molecules at 25°C . Hence, careful measurement of the incident and transmitted beam intensities, combined with knowledge of the absorption cross section at the measurement temperature and pressure yields the molecular concentration.

When detecting in the near-IR where absorption cross sections are generally weaker than in the mid-IR, concentrations in the ppm or ppb range can be detected for systems which can detect absorbances of 10^{-6} or less. The greatest detection sensitivity can be achieved when operating in quantum-limited conditions, where shot noise in the detector is the dominant noise mechanism. For diode lasers, rf modulation frequencies greater than a few MHz are required to minimize the laser noise, and quantum-limited performance requires a minimum radiation power incident on the detector of $P_{\min} \sim 2kT\hbar c / e^2 \eta \lambda_0 R_{\text{eff}}$ where η is the detector efficiency, and R_{eff} is the effective load resistance⁸.

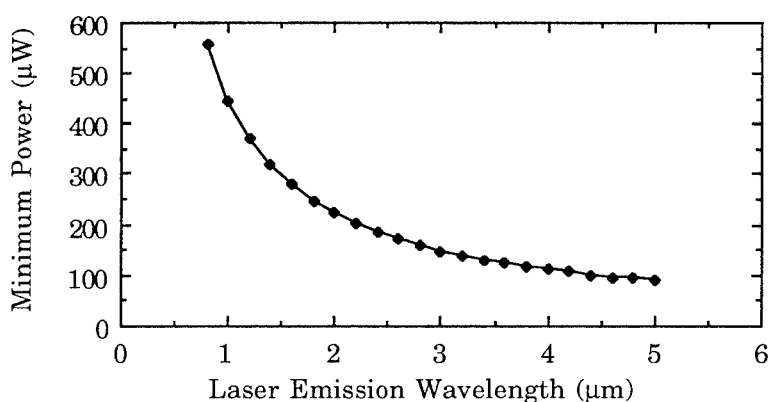


Figure 3. The minimum radiation power incident on the detector required for quantum-limited performance.

The P_{\min} is plotted as a function of laser emission wavelength in Figure 3, assuming 80% detector efficiency across the entire spectrum. The minimum power required increases if the detector efficiency decreases. Provided care has

been taken to eliminate significant sources of optical losses in the system, lasers emitting several milliwatts of power should be adequate for trace gas sensing.

CHARACTERISTICS OF DIODE LASERS FOR GAS SENSING

The primary consideration is the laser emission wavelength, which is dictated by the molecular absorption line. Additionally, lasers operating cw near room temperature, emitting a few milliwatts, and operating in a single longitudinal mode are generally the minimum requirements for lasers used in trace gas detection. Lasers must have linear wavelength-current characteristics and must be free of mode hops over the desired tuning range. Other important issues involve the wavelength tuning range, the tuning rate, and the laser efficiency.

There are several designs⁴ for single longitudinal mode laser operation including distributed feedback (DFB), distributed Bragg reflector (DBR), and multisection DFB/DBR lasers⁹. The DBR laser is less desirable for spectroscopic applications due to laser mode hops, causing discontinuous wavelength tuning. Distributed feedback lasers are used in the work presented here.

Laser Emission Wavelength

In theory, diode lasers can be fabricated from III-V semiconductor materials spanning the wavelength range of 0.2 - 5 μm . In practice, cw room temperature diode lasers have been fabricated over the range of 0.63 - 2.4 μm , and commercial lasers exist from 0.63 - 2.0 μm ¹⁰. The commercial lasers generally have threshold currents below a hundred milliamps, and output powers from a few milliwatts to a watt, although single longitudinal mode lasers typically have maximum output powers of under 200 mW. Lead-salt lasers span the range of 3 - 30 μm and require cryogenic operation. Currently, no commercial grating technology exists for these materials.

For trace gas sensing, near- (0.75 - 2 μm) and mid-IR (2 - 5 μm) spectral regions are of primary interest, and are spanned in the III-V semiconductors by GaAs- (0.75 - 1.1 μm)¹¹, InP- (1.2 - 2 μm)⁴ and GaSb- or InAs-based materials (2 - 5 μm). Although 2 - 5 μm GaSb- or InAs-based lasers are not yet commercially available, significant progress has been made. Room-temperature cw results between 2 to 2.4 μm were achieved using molecular beam epitaxy-grown InGaAsSb/AlGaAsSb multi-quantum well Fabry-Perot devices with threshold current densities of 143 A/cm² and output powers of 1.3W cw.¹² At longer wavelengths, InGaAsSb/AlGaAsSb double-heterojunction lasers operated at 3 μm and 255 K pulsed and at 170 K cw.¹³ InAsSb/AlAsSb double-heterojunction lasers operated at 4 μm pulsed to 155 K and to 80 K cw.¹⁴ Recently, pulsed room-temperature lasing at 2.78 μm in InGaAsSb/AlGaAsSb multi-quantum well lasers was achieved¹⁵, with a maximum cw operating temperature of 240 K¹⁶. Commercial cw, room temperature lasers between 2 - 3 μm are anticipated in the near future, while wavelengths beyond 3 μm require further development.

Near-IR lasers have been used to detect numerous gases. A 1.6 μm InGaAsP/InP DFB laser has been used to detect ¹²CO₂ and ¹³CO₂ in natural abundance on human breath, as described in the previous section. Similar

lasers have been used to detect CH₄ (1.654 μm), H₂O (1.393 μm), CO (1.6 μm)², and NH₃¹⁷, and recently, AlGaAs/GaAs DFB lasers were used to detect O₂ at 0.76 μm and H₂O at 0.81 μm ¹⁸.

Wavelength Tuning Rate and Range in DFB Lasers

These lasers are designed to operate in a dominant laser line over at least 15 degrees within the range of 0 - 50°C. The emission wavelength, λ_o , can be varied by changing the diode heat sink temperature or by changing the laser drive current. Increasing the heat sink temperature increases the emission wavelength, while increasing the drive current can either increase or decrease the emission wavelength. Thermal tuning is used to bring the laser emission line close to the molecular absorption line, while current tuning is used to sweep the laser across the absorption line.

Increasing the laser temperature increases the modal effective index, n_e , which shifts the Bragg resonance condition

$$\lambda_o = \left[\frac{2 \cdot n_e \cdot \Lambda}{m} \right] \quad (4)$$

to longer wavelengths, where Λ is the grating period, and m the grating order. For fixed drive current, the mode position thermally tunes according to

$$\Delta\lambda_o = \lambda_o \cdot \left[\frac{1}{n_e} \frac{dn_e}{dT} + \frac{1}{\Lambda} \frac{d\Lambda}{dT} \right] \cdot \Delta T \quad (5)$$

The second term is the linear thermal expansion of the grating, which contributes about ten percent to the increase in emission wavelength¹⁹. The refractive index coefficient is approximately²⁰

$$\frac{dn_e}{dT} \sim 4 \times 10^{-4} \quad (6)$$

The maximum range over which the wavelength can be temperature tuned is governed by the overlap of the grating gain spectrum with the laser modal gain spectrum. Distributed feedback lasers fabricated in InGaAsP/InP materials with first order gratings thermally tune at a rate of $\sim 0.1 \text{ nm}/^\circ\text{C}$, with a maximum range of roughly 10 nm. The temperature tuning curve for a 1.393 μm laser is shown in Figure 4. The laser emission spectrum was measured at each temperature, verifying a single dominant laser line with side-mode-suppression ratios of better than 30 dB for each data point. This laser temperature-tuned over a range of 7 nm.

The laser emission wavelength also varies with injected drive current. For fixed heat sink temperature, tuning with laser current, I , is given by

$$\Delta\lambda_o = \lambda_o \cdot \left[\frac{1}{n_e} \frac{dn_e}{dI} + \frac{1}{\Lambda} \frac{d\Lambda}{dI} \right] \cdot \Delta I \quad (7)$$

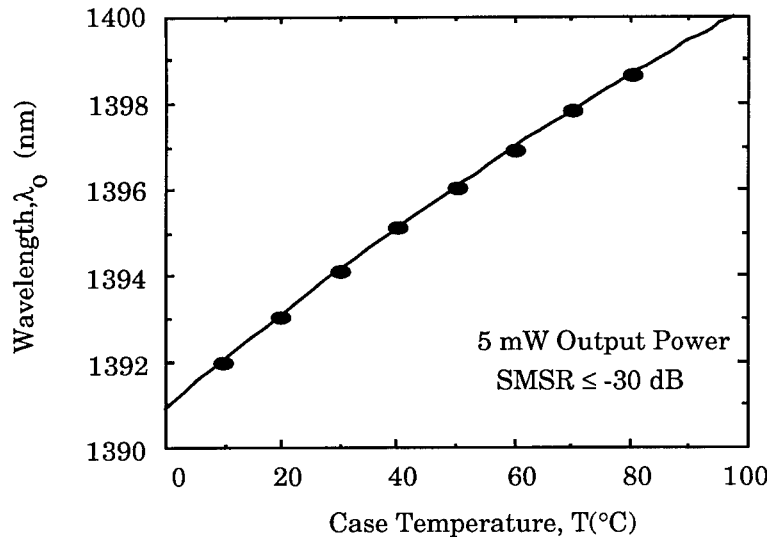


Figure 4. Temperature tuning curve for a 1.393 μm InGaAsP/InP DFB laser.

The modal index variation dominates, and has two components

$$\frac{dn_e}{dI} = \left[\frac{dn_e}{dT} \cdot \frac{dT}{dI} + \frac{dn_e}{dN} \cdot \frac{dN}{dI} \right] \quad (8)$$

where N is the injected charge density. Increasing the drive current increases the laser temperature due to increased power dissipation. The junction temperature, T_j , for a given drive current can be expressed as²¹

$$T_j = T_s + R_{th}P_d \quad (9)$$

where T_s is the heat sink temperature, R_{th} is the thermal impedance, and P_d is the net dissipated power. The increased junction temperature results in an increased modal index, and therefore an increased emission wavelength. However, increased charge injection decreases the modal index²²

$$\frac{dn_e}{dN} = n_e \cdot \left[\frac{N \cdot q^2}{2m^* \omega^2 \epsilon} \right] \quad (10)$$

Here, q is the carrier charge, m^* is the carrier effective mass, ω is the radian frequency ($2\pi/\lambda_0$), and ϵ is the dielectric constant. The hole effective mass is ten times larger than the electron effective mass; thus, the index variation is dominated by electron injection. An index increase ($\sim 10^{-3}$) caused by a few degrees temperature rise is roughly equivalent in magnitude to the index decrease caused by 10^{18} cm^{-3} electron injection.

Whether charge injection or thermal tuning dominates depends on several factors such as the laser external quantum efficiency, the drive current dc level, and the laser modulation frequency. Lasers with lower efficiencies are

better suited for thermal tuning due to the increased power dissipation. This does not pose a problem since only a few milliwatts of power are required for most spectroscopic measurements. A decrease in the emission wavelength can be observed below and near laser threshold currents due to charge injection effects, with an increase in the emission wavelength as the current is increased above threshold.²³ Typically, thermal effects dominate at sweep frequencies below 10 MHz, whereas charge injection effects dominate over the range of 10 MHz to 5 GHz²⁴. Sweep frequencies on the order of a kHz were used in this work.

Thermal current tuning dominates in our DFB lasers, and is on the order of 0.003 - 0.006 nm/mA (-500 MHz/mA to -3 GHz/mA). Current tuning curves for a 1.6 μm DFB laser at various temperatures are shown in Figure 5. The wavelength tunes continuously over the entire current range for each temperature. Both DBR and Fabry-Perot lasers experience mode hops due to the temperature induced shift of the gain-peak, while DFB lasers have a continuously tunable laser mode governed by the Bragg condition in (1).

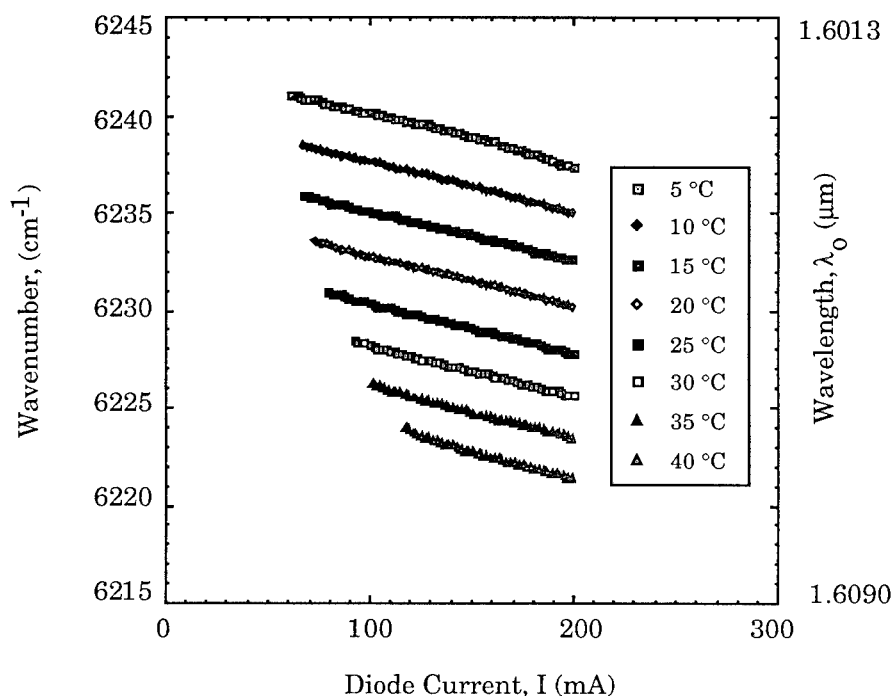


Figure 5. Current tuning curves for a 1.6 μm InGaAsP/InP DFB laser operating at various temperatures.

High laser wavelength tuning rates are desirable and allow use of a single laser to access several molecules which have closely spaced absorption lines. To increase the current tuning rate in a 1.393 μm DFB laser, alumina 125 mil-thick was inserted between the laser chip and the copper heat sink. The current tuning more than doubled, increasing from -580 MHz/mA to -1.24

GHz/mA. The alumina reduces the heat transfer from the chip to the mount, which effectively lowered the efficiency of the laser¹⁹.

SUMMARY

In summary, a diode laser spectrometer utilizing rf modulation to improve the SNR was reviewed, select molecular absorption data were given, and some of the near-IR DFB laser characteristics for trace gas sensing were described. Progress in III-V semiconductors for cw room temperature lasers emitting over 2 - 5 μm was reviewed. The development of these lasers will allow detection in the near-IR for many molecules at orders of magnitude higher sensitivity than is currently possible, and will allow detection of molecules not accessible in the near-IR.

¹Air Monitoring by Spectroscopic Techniques, Ed. Markus W. Sigrist, Vol. 127 in Chemical Analysis, Series Ed. J. D. Winefordner, John-Wiley (1994).

²David E. Cooper and Ramon U. Martinelli, Laser Focus World, November (1992).

³M. Phillips, Scien. Amer. **276**, 74 (1992).

⁴Long Wavelength Semiconductor Lasers, G. P. Aggrawal and N. K. Dutta, Van Nostrand-Reinhold (1986).

⁵D. E. Cooper and R. E. Warren, J. Opt. Soc. Am. B. **4**, 470 (1987).

⁶D. E. Cooper et al., Appl. Opt. **32**, 6727 (1993).

⁷D. A. Schoeller et al, Am. J. Clin. Nutr., **33**, 2375 (1980).

⁸Peter Werle, Franz Slemr, Manfred Gehrtz and Christof Bräuchle, Appl. Optics **28**, 1638 (1989).

⁹A. E. Willner, M. Kuznetsov, I. P. Kaminow, U. Koren, T. L. Koch, C. A. Burrus, G. Raybon, Photon. Tech. Lett. **1**, 360 (1989).

¹⁰Laser Diode Reference Manual, Industrial Laser Technology, Inc. Clinton Twp, Michigan.

¹¹Heterostructure Lasers Part A & B, H. C. Casey and M. B. Panish, Academic Press (1978); Quantum Well lasers, Ed. Peter Zory, Academic Press (1994).

¹²G. W. Turner, H. K. Choi, D. R. Calawa, J. V. Patano, and J. W. Chludzinski, J. Vac. Sci. Tech. **12** 1266 (1994)

¹³H. K. Choi, S. J. Eglash, and G. W. Turner, Appl. Phys. Lett. **64**, 2474 (1994).

¹⁴S. J. Eglash and H. K. Choi, Appl. Phys. Lett. **64**, 833 (1994)

¹⁵H. Lee, P. K. York, R. J. Menna, R. U. Martinelli, D. Z. Garbuzov, and S. Y. Narayan, submitted Appl. Phys. Lett., Sept. 1994.

¹⁶D. Garbozov, H. Lee, P. K. York, R. J. Menna, R. U. Martinelli, and S. Y. Narayan, unpublished.

¹⁷Joel A. Silver, David S. Bomse, and Alan C. Stanton, Appl. Optics **30** 1505 (1991).

¹⁸D. E. Cooper, R. U. Martinelli, unpublished data

¹⁹Ramon U. Martinelli, R. J. Menna, D. E. Cooper, C. B. Carlisle, and H. Riris, SPIE Conf. Proceed., Vol. 2148, Los Angeles CA (1994).

²⁰Soichi Kobayashi, Yoshiisa Yamamoto, Minoru Ito, and Tatsuya Kimura, J. Quantum Electron. **QE-18**, 582 (1982).

²¹Physics of Semiconductor Laser Devices, G. H. B. Thompson, Wiley (1980), p. 526.

²²N. K. Dutta, A. B. Piccirilli, T. Cella and R. L. Brown, Appl. Phys. Lett. **48**, 1501 (1986).

²³Hartmut Hillmer, S. Hansmann, Herbert Burkhard, Herbert, Walter, Alois Krost, and Dieter Bimberg, J. Quantum Electron. **30**, 2251 (1994)

²⁴Soichi Kobayahi, Yoshihisa Yamamoto, Minoru Ito, and Tatsuya Kimura, J. Quantum Electron. **QE-18**, 585 (1982).

Modeling of Optical Gain Due to Excitonic Transitions in Index-Guided ZnCdSe/ZnMgSSe Multiple Quantum Well Blue-Green Lasers

W. Huang and F. C. Jain

Department of Electrical and System Engineering
University of Connecticut, Storrs, CT 06269.

ABSTRACT

Optical gain coefficient involving excitonic transitions are calculated for index-guided ZnCdSe/ZnMgSSe multiple quantum well (MQW) layers as a function of operating wavelength. Comparison of threshold current density among unstrained, compressively strained and tensile strained cases are presented. The calculations include strain induced changes in energy band gaps and band offsets. The tensile strained $\text{Zn}_{0.8}\text{Cd}_{0.2}\text{Se}-\text{Zn}_{0.7}\text{Mg}_{0.3}\text{Se}_{0.97}$ quantum well lasers, grown on lattice matched InP substrates, are predicted to operate at threshold current density as low as 175 A/cm^2 .

INTRODUCTION

Lower threshold current densities in III-V strained quantum well lasers have been reported by several investigators^{1,2}. The reduction of current density is attributed to valence band splitting in the presence of strain, which in turn reduces the effective density of states in the valence band. This strain induced effect is desirable for laser operation since it reduces the disparity between the electron and hole density of states, which increases the quasi-Fermi level separation ($E_m - E_{fp} = \Delta\psi$) for a given injection current. Consequently, the Bernard-Duraffourg gain condition, which requires the separation of the quasi-Fermi level ($\Delta\psi$) to be greater than the photon energy ($h\nu$), is satisfied at a lower threshold current density.

For a ZnCdSe-ZnSSe (or ZnCdSe-ZnMgSSe) quantum wells (QWs), the exciton binding energies are approximately 5 times larger ($\sim 35 \text{ meV}$) than for the InGaAs-GaAs^{3,4}. Larger binding energies lead to efficient excitonic transitions, producing a higher optical gain due to excitons than for III-V QWs. Thus, the primary gain mechanism in II-VI lasers is from excitonic transitions rather than recombinations of free electrons and holes as in III-V systems. The Bernard-Duraffourg gain condition, which requires the quasi-Fermi level be larger than the photon energy, is satisfied at a lower current density in II-VI lasers, since optical gain occurs at a lower photon energy for exciton transitions than for

band-to-band transitions.

This paper presents calculations on the optical gain and the threshold current density for ZnCdSe-based quantum well lasers, taking into account the exciton as well as free carrier transitions. The effect of strain on threshold current density is analyzed. Compressive strain in ZnCdSe-ZnSSe quantum wells can be achieved by growing the wells on lattice-matched GaAs substrates. This process is demonstrated successfully for blue-green lasers operating around 500nm at room temperature^{5,6}. We found that tensile strained active layers (e.g. $\text{Zn}_{0.8}\text{Cd}_{0.2}\text{Se}-\text{Zn}_{0.2}\text{Mg}_{0.8}\text{S}_{0.03}\text{Se}_{0.97}$) yield a lower threshold current density than compressive ones (e.g. $\text{Zn}_{0.8}\text{Cd}_{0.2}\text{Se}-\text{Zn}_{0.65}\text{Mg}_{0.35}\text{S}_{0.38}\text{Se}_{0.62}$). In fact, we found $J_{th}=175\text{A/cm}^2$ for tensile strained active layers and $J_{th}=280\text{A/cm}^2$ for compressive strain. To fabricate a tensile strained ZnCdSe-ZnMgSSe active layer, we propose the use of an InP substrate. InP is lattice matched to $\text{Zn}_{0.2}\text{Mg}_{0.8}\text{S}_{0.03}\text{Se}_{0.97}$ for using both as a barrier and a confinement layer, to produce tension in the ZnCdSe quantum well.

PROPOSED STRUCTURES

Figure 1 (a) and (b) show two index guided structures realized on n-type and p-type InP substrates, respectively. The methodology used in contacting p-ZnMgSSe layers is similar to that employed for GaAs-based compressively strained systems. In a conventional ZnCdSe-ZnSSe grown on GaAs substrates laser, only compressive strained active layers can be achieved because the lattice constant of ZnSSe is always larger than that of ZnCdSe regardless of the composition. In InP-based structures, lattice-matched $\text{Zn}_{0.2}\text{Mg}_{0.8}\text{S}_{0.03}\text{Se}_{0.97}$ is chosen to be the barrier as well as the cladding layer to obtain tensile strain in the ZnCdSe quantum well. $\text{Zn}_{0.2}\text{Mg}_{0.8}\text{S}_{0.03}\text{Se}_{0.97}$ cladding/barrier layer may be replaced by other compatible materials such as $\text{ZnSe}_{0.55}\text{Te}_{0.45}$.

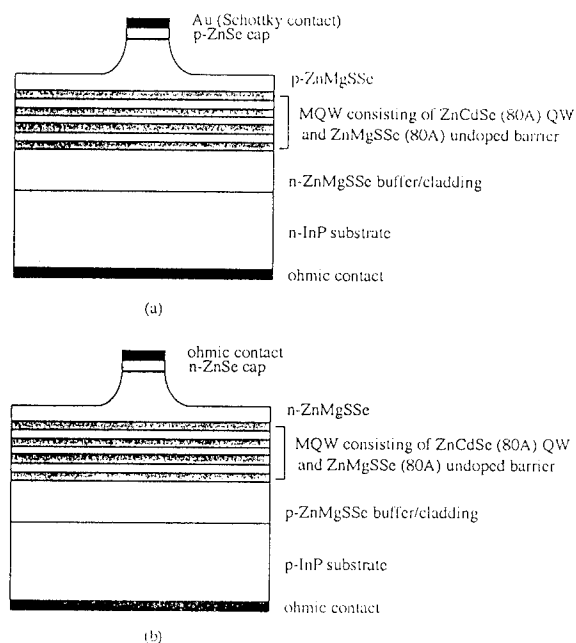


Fig. 1. Schematic of a tensile strained ZnCdSe/ZnMgSSe quantum well laser diode structure (a) n-type InP substrate (b) p-type InP substrate

STRAIN EFFECT ON BAND GAP AND BAND OFFSET

In strained ZnCdSe/ZnMgSSe QWs, a biaxial in-plane strain removes the degeneracy of the light hole and heavy hole bands which considerably influences the band gaps as well as band offsets. The variations in energy band gap and band offsets at the heterointerfaces are the important parameters in gain calculations. Previous experiments have shown that the band offsets for II-VI heterointerfaces can be estimated from Harrison's theory⁷. Under a compressive strain, the light hole is pushed away from heavy hole toward the lower energy side. While under a tensile strain, the light hole is lifted above the heavy hole, resulting in a smaller band gap. In addition to the shifting of the band edges, the strain also modifies the curvature of the valence bands. As a result, the in-plane effective mass of the heavy hole becomes lighter than that of the light hole. The effect of strain is calculated by following Pollak's procedure.⁸

The hydrostatic component (δE_{hy}) and shear component (δE_{sh}) of the strain are

$$\begin{aligned}\delta E_{hy} &= a(\epsilon_{xx} + \epsilon_{yy} + \epsilon_{zz}) , \\ \delta E_{sh} &= 2b(\epsilon_{zz} - \epsilon_{xx}) .\end{aligned}\tag{1}$$

Where ϵ_{ij} is the strain tensor, constant a and b are hydrostatic potential and shear deformation potential, respectively. For ZnCdSe, the values are $a = -5.04$ eV and $b = -1.12$ eV. The strain induced variations in the band gaps between the conduction and heavy hole bands, ΔE_{hh} , and between the conduction and light hole band, ΔE_{lh} , are calculated as follows:

$$\begin{aligned}\Delta E_{lh} &= \delta E_{hy} - \frac{\delta E_{sh}}{2} - \frac{(\delta E_{sh})^2}{2\Delta_{so}} , \\ \Delta E_{hh} &= \delta E_{hy} + \frac{\delta E_{sh}}{2} .\end{aligned}\tag{2}$$

The spin-orbit splitting, Δ_{so} , is taken as 0.42eV.

Table I summarizes various parameters used in the calculations.

Table I. Calculated band offsets and band gaps which are used in the simulations.

	Band offset (eV)			Band gap (eV)	
	ΔE_c	ΔE_{lh}	ΔE_{hh}	light hole	heavy hole
Unstrained	0.514	0.376	0.376	2.41	2.41
0.95% Compression	0.608	0.27	0.224	2.468	2.422
1% Tension	0.667	0.288	0.236	2.345	2.397

EXCITONIC GAIN

In our model, we consider the contribution of exciton as well as free carrier transitions to compute the optical gain/absorption as a function of photon energy in a quantum well system. Excitonic gain is obtained by taking the absorption coefficient term⁹ and multiplying it by the Fermi-Dirac distribution function. Either gain or absorption will appear at a given photon energy depending on the position of the quasi-Fermi levels, which are determined by the injection current.

The optical gain coefficient, including exciton transition in a quantum well, is given by

$$g(\omega) = \frac{2e^2}{\epsilon_0 n_r m_0^2 c \omega L_z} \sum_{l,h} \left[\frac{m_{eh}}{\pi \hbar^2} |M_b|^2 \left| \int \psi_e(z) \psi_h(z) dz \right|^2 \int \rho(E) \mathcal{L}(E) dE (f_c + f_v - 1) \right] \\ + \frac{4\pi e^2}{\epsilon_0 n_r m_0^2 c \omega L_z} \sum_{l,h} \left[|M_b|^2 |\phi_{ex}(0)|^2 \left| \int \psi_e(z) \psi_h(z) dz \right|^2 \rho_{ex} \mathcal{L}(E_{ex}) (f_c + f_v - 1) \right], \quad (3)$$

where $|M_b|^2$ is the average matrix element for the Bloch state. $\rho(E)$ stands for the polarization factor for an optical waveguide structure (light propagates perpendicular to the growth axis)^{10,11}. For TE modes: ρ_{ex} is 1/2 and 3/2 for light hole exciton and heavy hole exciton transitions, respectively. $\rho(E)$ is $1/4(5-3E_R)$ and $3/4(1+E_R)$ for light hole and heavy hole free carrier transitions, respectively, (where $E_R = (E_c + E_v) / (E_c + E_v + E)$; E_c and E_v are the ground state energy for the electron and hole in the quantum well). $\mathcal{L}(E)$ represents the lineshape function which is chosen to be Gaussian in the present case¹². $\psi_e(z)$ and $\psi_h(z)$ are the electron and hole wavefunctions, $\phi_{ex}(r)$ is the 2D exciton trial function which is obtained by a variational technique¹³ based on the information given in the previous section. Here, f_c and f_v are the non-equilibrium Fermi-Dirac distributions which are determined by the injection current. They are related to each other by the charge neutrality condition. L_z and m_{eh} are the quantum well width, and reduced effective hole mass, respectively. The index n_r for ZnCdSe active layer is calculated for index-guided ZnCdSe/ZnMgSSe structure using the effective index method¹⁴.

The gain coefficient g is related to the injection current density by¹⁵:

$$J = \frac{8\pi n_r^2 v^2 e L_z \Delta \nu_s}{\Gamma \eta c^2 [1 - e^{-\frac{h\nu - \Delta \zeta}{kT}}]} g. \quad (4)$$

Here $\Delta \zeta = E_{fn} - E_{fp}$, $\Delta \nu_s$, taken as 60 meV, is the spontaneous line width, η is the quantum efficiency, and Γ is the confinement factor. The threshold condition is reached when the gain overcomes the total loss in the cavity. For a cavity length of 200 μm , the calculated gain coefficient at threshold is about 50 cm^{-1} .

RESULTS

Recently, we have simulated¹⁶ the optical gain for a ZnCdSe/ZnSSe QW laser which was used by Ding et al¹⁷ in their experiment. The theoretical curve matched the experimental data for compressively strained lasers on GaAs substrates very well. Based

on this model, we further investigated the strain effect on threshold current density for index-guided ZnCdSe/ZnMgSSe lasers.

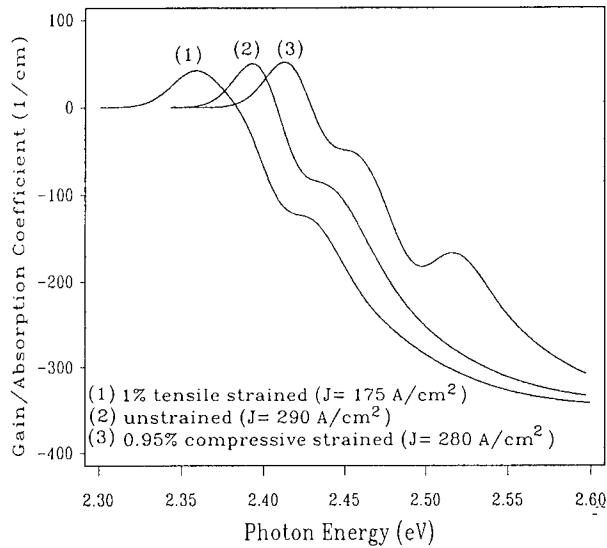


Fig. 2. A comparison of gain/absorption for a unstrained, a 0.95% compressively strained and a 1% tensile strained $\text{Zn}_{0.8}\text{Cd}_{0.2}\text{Se/ZnMgSSe}$ quantum well laser operating at threshold condition.

Figure 2 compares the gain/absorption curves for the unstrained, the 0.95% compressively strained, and 1% tensile strained quantum wells lasers operating at threshold condition. Among these three cases, the compressive and tensile strained devices yield lower threshold current density than the unstrained case. Furthermore, the tensile strain lasers exhibit much lower threshold current density than their compressive counterpart. This is because the polarization factor for the exciton transitions involving light holes for the TE mode is 3 times smaller than heavy holes. Therefore, at a given injection current, the tensile strained quantum wells manifest a larger quasi-Fermi level separation ($\Delta\epsilon$) than the compressive layers, according to equation 3. A larger $\Delta\epsilon$ in turn results in a higher gain at a given current density J (as can be seen from Eqn. 4). Hence, we predict that tensile strained lasers will have the lowest threshold current density. It is also evident in Figure 2 that the photon energy at which peak gain occurs moves to a higher value when the tensile strain is removed and we get to either the unstrained or the compressive strain case. In addition, in the tensile strain case the lasing is due to excitons formed by electrons and light holes, while lasing in unstrained or compressively strained system is due to the excitons formed by electrons and heavy holes. All these are the consequences of strain effect on band structure which is discussed in the earlier section.

The peak gain coefficient as a function of injection current for these three cases are presented in Figure 3. Figure 4 shows a comparison of the peak gain coefficient for the unstrained, the 1% tensile strained and the 2% tensile strained cases. The 2% tensile strained quantum wells have lower threshold current densities than the 1% tensile strained lasers. Thus, the threshold current density can be further decreased by increasing the tensile strain.

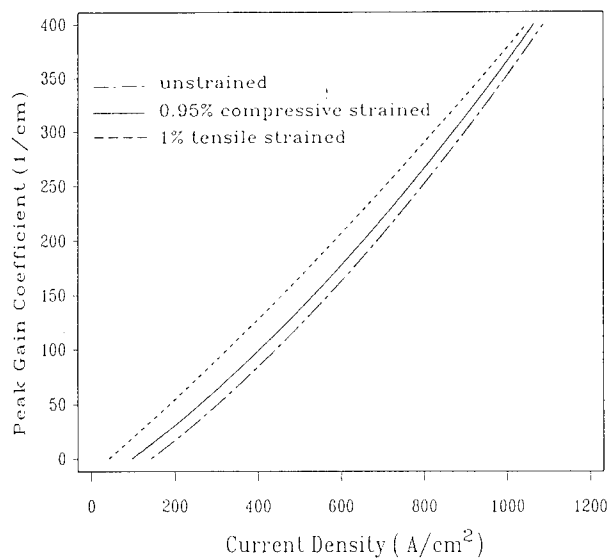


Fig. 3 Comparison of peak gain coefficient as a function of inject current density for a unstrained, 0.95% compressive strained and 1% tensile strained $\text{Zn}_8\text{Cd}_2\text{Se}/\text{ZnMgSSe}$ quantum well lasers.

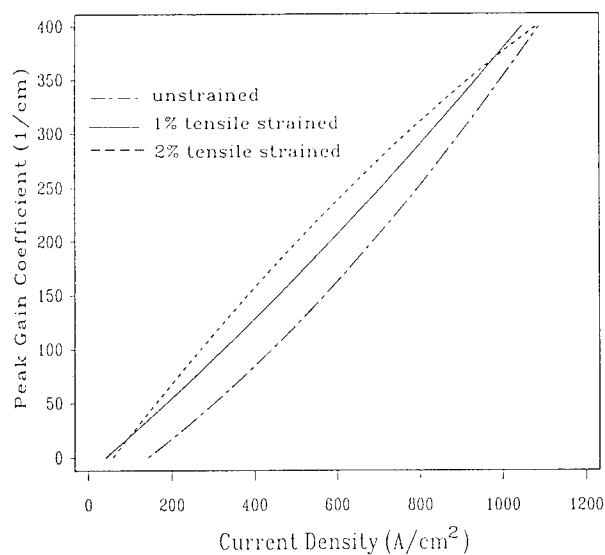


Fig. 4 Calculated peak gain coefficient as a function of inject current density for a unstrained, 1% tensile strained and 2% tensile strained $\text{Zn}_8\text{Cd}_2\text{Se}/\text{ZnMgSSe}$ quantum well lasers.

CONCLUSIONS

Similar to III-V lasers, strain reduces the threshold current density in index-guided ZnCdSe-ZnMgSSe quantum well lasers. The computed threshold current densities are lower in both compressive and tensile strained active layers than in unstrained quantum well lasers. The tensile strained quantum well lasers are predicted to exhibit the lowest threshold current density. Quantum well active layers $[\text{Zn}_{0.8}\text{Cd}_{0.2}\text{Se}(\text{well})/\text{Zn}_{0.2}\text{Mg}_{0.8}\text{S}_{0.03}\text{Se}_{0.97}(\text{barrier})]$ manifesting tensile strain, grown on lattice matched $\text{Zn}_{0.2}\text{Mg}_{0.8}\text{S}_{0.03}\text{Se}_{0.97}$ buffer layer on InP substrates, are proposed. Alternative materials such as $\text{ZnSe}_{0.55}\text{Te}_{0.45}$, lattice matched with InP, can also be used to fabricate tensile strained QW layers. The selection of a particular material may depend on the growth technique employed. This is in contrast to compressively strained QW lasers which are realized on GaAs substrates.

ACKNOWLEDGEMENT

This work is supported by the Department of Economic Development and the University of Connecticut Research Foundation grants.

REFERENCES

1. Julian S. Osinski, Piotr Grodzinski, Yao Zou, and P. Daniel Dapkus, "Threshold Current Analysis of compressive strain (0-1.8%) in low-threshold, long wavelength quantum well lasers" IEEE J. of Quantum Electronics. Vol. 29, 1993. pp 1576 -1585.
2. E. Yablonovitch and E. O. Kane, "Reduction of lasing threshold current density by the lowering of valence band effective mass," J. of Lightwave Tech. Vol. LT-4, May 1986, pp. 504-506.
3. W. Huang, F. Jain, C. Chung, and G. Drake, "Optical modulations using quantum confined Stark effect in ZnCdSe-ZnSSe structure," in Proc. Connecticut Microelectronic and Optoelectronic Symp., SNET, New Haven, CT, March 18-19, 1993.
4. S.Y. Wang, Y. Kawakami, J. Simpon, H. Stewart, K.A. Prior, and B.C. Cavenett, "ZnSe-ZnCdSe quantum confined Stark effect modulators," Appl. Phys. Lett. Vol. 62, 12 April 1993, pp. 1715-1717.
5. J. Ding, H. Jeon, T. Ishihara, M. Hagerott and A. V. Nurmikko, "Excitonic gain and laser emission in ZnSe-based quantum wells," Phys. Rev. Lett. Vol. 69, Sep. 1992, pp 1707-1710.
6. C.T. Walker, J.M. Depuydt and M.A. Haase, "Blue-green II-VI laser diodes," Physica B. Condensed matter, Vol. 185, Apr. 1993, p.27.
7. Walter A. Harrison, "Electronic Structure and the Properties of Solids," W.H. Freeman and company, San Francisco. (1980)
8. Fred H. Pollak, "Modulation spectroscopy under uniaxial stress", Surface Science, Vol. 37 (1973), pp. 863-895.
9. Y. Kan, H. Nagai, M. Yamanishi, and I. Suemune, "Field effect on the refractive index and absorption coefficient in AlGaAs quantum well structures and their feasibility for electrooptic device applications," IEEE J. Quantum Electronics, Vol. QE-23, Dec. 1987 pp. 2167-2180.
10. S.K. Cheung, "High contrast Fabry-Perot multiple quantum well modulators systems," Ph.D thesis, University of Connecticut, 1994.
11. M. Asada, A. Kameyama and Y. Suematsu, "Gain and Intervalence band absorption

- in quantum-well lasers," IEEE J. Quantum Electronics, Vol. QE-20, July 1984, pp. 745-753.
12. M. Yamanishi and Y. Lee, "Phase damping of optical dipole moments and gain spectra in semiconductor lasers," IEEE J. Quantum Electronics, Vol. 23, Apr. 1987, pp. 367-370.
 13. D. A. B. Miller, D.S. Chemla, T.C. Damen, A.C. Gossard, W. Wiegmann, T.H. Wood and C.A. Burrus, "Electric field dependence of optical absorption near the band gap of quantum-well structure," Phys. Rev. B. Vol. 32. July 1985, pp. 1043-1060.
 14. Peter K. Cheo, "Fiber Optics and Optoelectronics," Prentice Hall, New Jersey. (1990)
 15. H. C. Casey and M.B. Panish, "Heterostructure lasers," Academic Press, INC, New York.(1978)
 16. W. Huang and F. C. Jain, "Prediction of lower current threshold in tensile strained ZnCdSe/ZnMgSSe multiple quantum well blue-green lasers," in Proc. of LEOS '94 7th annual meeting, Oct 31-Nov. 3, Boston, Massachusetts.
 17. J. Ding, M. Hagerott, P. Kelkar, and A.V. Nurmikko, D. C. Grillo, Li He, J. Han, R.L. Gunshor, "Gain and dynamics in ZnSe-based quantum wells," J. of Crystal Growth 138 (1994), pp. 719-726.

LOW THRESHOLD CURRENT DENSITY WAVELENGTH SHIFTING BETWEEN $n=1$ AND $n=2$ TRANSITIONS IN n -TYPE MODULATION DOPED GaAs/AlGaAs QUANTUM WELL LASERS

G E. Kohnke and G W. Wicks

The Institute of Optics
University of Rochester
Rochester, NY 14627

INTRODUCTION

Quantum well lasers provide a number of options for altering the emission wavelength. The effective bandgap energy of these devices is a function of well width, well composition, and, to a lesser extent, barrier composition. In addition, there are multiple confined energy levels in quantum wells typically used in semiconductor laser applications. Usually, the gain provided by the first quantized state ($n=1$) is sufficient to overcome the cavity losses and the lasing emission occurs at an energy corresponding to the separation of the first confined energy level in the conduction band and the first confined energy level in the valence band. By altering the cavity losses, the laser may be forced to lase on the next highest confined energy level transition. This level has a higher density of states and therefore a higher potential gain if populated with electrons. This second quantized state or $n=2$ lasing is significantly shifted in wavelength from the $n=1$ lasing due to the large separation of confined energy levels.

Second quantized state lasing has been reported by several research groups using a variety of methods.¹⁻⁷ The simplest approach is to shorten the cavity length to approximately 100 μm .^{1-3,5,7} This dramatically increases the cavity losses such that the higher gain provided by the $n=2$ transition is required to achieve lasing. This method naturally suffers from needing high threshold current densities to implement. For longer cavity lengths, $n=2$ lasing may also be obtained by increasing the current to the point where the $n=2$ level is heavily populated with electrons.^{2,4} Finally, a judicious choice of reflection coatings on the laser facets will suppress the feedback of the $n=1$ transition in the cavity and allow $n=2$ lasing independent of cavity length.⁶ The applications of $n=2$ lasing include short wavelength operation,³ wavelength switching,^{2,4,5} dual wavelength operation,^{4,5} and high relaxation oscillation frequency.⁶ Previous $n=2$ laser work is summarized in Table 1 along with the results presented in this paper. Note that some of the devices were fabricated with very narrow stripes and therefore have exceptionally large threshold current densities. As seen in the table, all these $n=2$ lasing schemes result in large ($>2000 \text{ A/cm}^2$) threshold current densities.

In this work, we report a new approach to achieve $n=2$ lasing: modulation doping. Modulation doping provides a means of populating the quantum well with carriers without introducing impurities in the well which lead to nonradiative and/or low energy radiative centers. Regions in the barrier of the quantum well are doped with impurities and the free carriers are able to locate the lower energy states in the quantum well. The concentration of carriers populating the well is a function of the dopant concentration and the separation

Table 1. Summary of n=2 laser work.

Reference	Purpose	Quantum Well	Method	J_{th} (A/cm ²)
1	Demonstration of n=2 lasing	GaAs	Short cavity length	5200
2	Wavelength switching	GaAs	Short cavity length and High current	16500
3	Short-wavelength lasing	GaAs	Short cavity length	2700
4	Wavelength switching and Dual wavelength operation	GaInAs	High current	2500
5	Wavelength switching and Dual wavelength operation	GaInAs	Short cavity length	14000
6	High relaxation oscillation frequency	GaInAs	AR/HR coatings	2000
7	Strained QW laser study	GaInAs	Short cavity length	4500
-	Low threshold current density n=2 lasing	GaAs	Modulation doping	440

between the quantum well and the doped region. In semiconductor lasers, both p-type⁸⁻¹¹ and n-type^{12,13} modulation doping have been investigated. P-type doping reduces the linewidth enhancement factor⁸⁻¹¹ and improves modulation characteristics^{8,9} compared to undoped lasers. N-type doping has been studied in our laboratory and found to result in lower threshold current density devices than undoped lasers and to produce short wavelength lasing for heavily doped structures.^{12,13} The short wavelength lasing has been attributed to n=2 lasing caused by the increase of the electron population in the quantum well.

LASER STRUCTURES AND FABRICATION

To further characterize the shift of lasing wavelength obtained by n-type modulation doping, two series of separate confinement heterostructure laser structures were grown by molecular beam epitaxy. The epitaxial structures grown on GaAs:Si (100) substrates misoriented 4° towards the [111]A direction were: n-GaAs buffer (0.5 μm, Si=3x10¹⁸ cm⁻³), n-Al_{0.55}Ga_{0.45}As clad (1.5 μm, Si=3x10¹⁸ cm⁻³), n-Al_{0.26}Ga_{0.74}As core (0.098 μm, varied doping), undoped-Al_{0.26}Ga_{0.74}As spacer layer (20 Å), undoped GaAs quantum well (100 Å), undoped-Al_{0.26}Ga_{0.74}As spacer layer (20 Å), n-Al_{0.26}Ga_{0.74}As core (0.098 μm, varied doping), p-Al_{0.55}Ga_{0.45}As clad (1.5 μm, Be=3x10¹⁸ cm⁻³), p⁺-GaAs cap (0.15 μm, Be=5x10¹⁹ cm⁻³). The undoped spacer layers surrounding the quantum well physically separate the Si dopant atoms from the well. In the first series of lasers, the cores were doped at constant levels of 1x10¹⁸ cm⁻³, 2.5x10¹⁸ cm⁻³, and 5x10¹⁸ cm⁻³. Also, one laser structure was grown without any intentional doping in the core. The second series of lasers employs a more complicated core doping profile as shown in Figure 1. The core doping was increased in a series of three steps as the quantum well is approached. In the final 200 Å of barrier material before the spacer layer, the doping was Zx10¹⁸. Structures were grown having Z=2, 3, 4 and 5.

Lasers were fabricated into broad area devices with 50 μm stripe widths and 500 μm cavity lengths. The lasers were operated as gain guided devices with the heavily doped p-type GaAs cap selectively removed to reduce the current spreading. All measurements under lasing conditions were performed in pulsed mode with 500 ns pulses at a 1 kHz repetition rate.

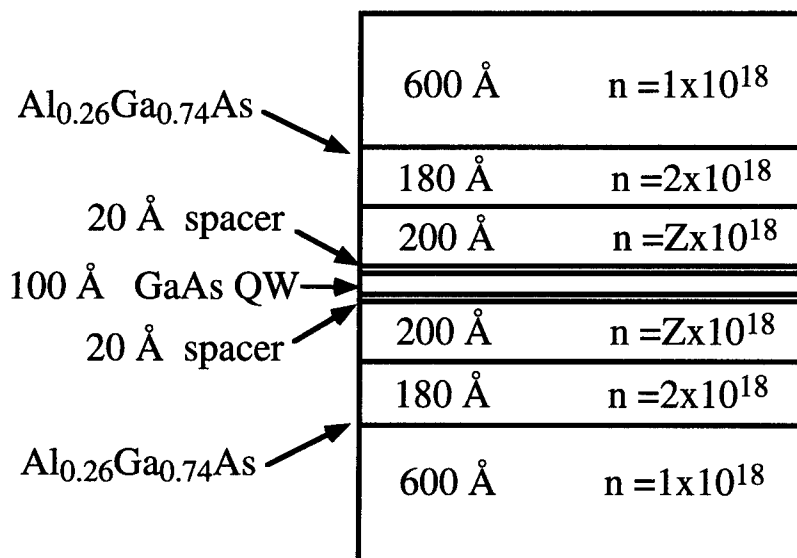


Figure 1. Schematic of stepped core doping density laser core.

EXPERIMENTAL RESULTS

Threshold current density and lasing wavelength were measured for the constant core doping sequence and the undoped core laser and the results are given in Table 2, where n is the core doping density, J_{th} is the threshold current density, and λ_L is the lasing wavelength. These devices showed the expected shift to shorter wavelength with increased doping but, in contrast to previous results,^{12,13} a very sharp increase of threshold current density is associated with the wavelength shift. The highest doped device did not lase at the upper limit of the voltage pulse generator. To further investigate the cause of this threshold current increase, the below lasing threshold spontaneous emission spectra were measured out of the laser facet for the four devices. These measurements were performed using a DC current source with 20 mA of current to provide a detectable electroluminescence signal. The normalized spectra are shown in Figure 2. The lowest doping density, $1 \times 10^{18} \text{ cm}^{-3}$, is slightly red-shifted from the undoped core which is due to bandgap renormalization. The

Table 2. Characteristics of constant core doping density laser sequence.

$n \text{ (cm}^{-3}\text{)}$	$J_{th} \text{ (A/cm}^2\text{)}$	$\lambda_L \text{ (nm)}$
Undoped	351	863
1×10^{18}	338	868
2.5×10^{18}	1112	802
5×10^{18}	>5000	---

medium doping density, $2.5 \times 10^{18} \text{ cm}^{-3}$, clearly shows a shift to shorter wavelength. Finally, the heavily doped sample, $5 \times 10^{18} \text{ cm}^{-3}$, has a spectrum with three features evident. The noise at 880-900 nm is an artifact of the measurement apparatus. A GaAs photomultiplier tube was used to detect the electroluminescence signal and its response drops precipitously beyond 880 nm. The signal from this device was also approximately 25x less than from the other devices which magnified the noise at long wavelengths. The dashed line indicates the expected lineshape tail. The three features are associated with the $n=1$, $n=2$, and $n=3$ transitions of the quantum well. The very low intensity is most likely due to reduced hole transport through 1000 Å of heavily doped n-type material since the p-n junction is located at the upper core/upper clad interface. The presence of all three features simultaneously implies that all three electron levels are populated. However, the valence band well is probably only populated with holes in the $n=1$ level since the device is being lightly pumped and the separation between the $n=1$ and $n=3$ hole levels is much greater than kT which prevents thermal population. The $n=2$ and $n=3$ electron levels are therefore recombining with the $n=1$ hole level. These transitions are usually forbidden by the $\Delta n=0$ selection rule which appears to be relaxed in this structure due to the heavy doping.

To overcome the limited hole transport, the stepped core doping sequence was grown and characterized. Wavelength and threshold current density are plotted as a function of doping layer density, Z , in Figure 3. The points at $Z=0$ and $Z=1$ correspond to the undoped laser and the lowest constant core doping density laser, respectively. As seen in the figure, there is a smoothly varying transition from the $n=1$ to the $n=2$ wavelength as the doping level

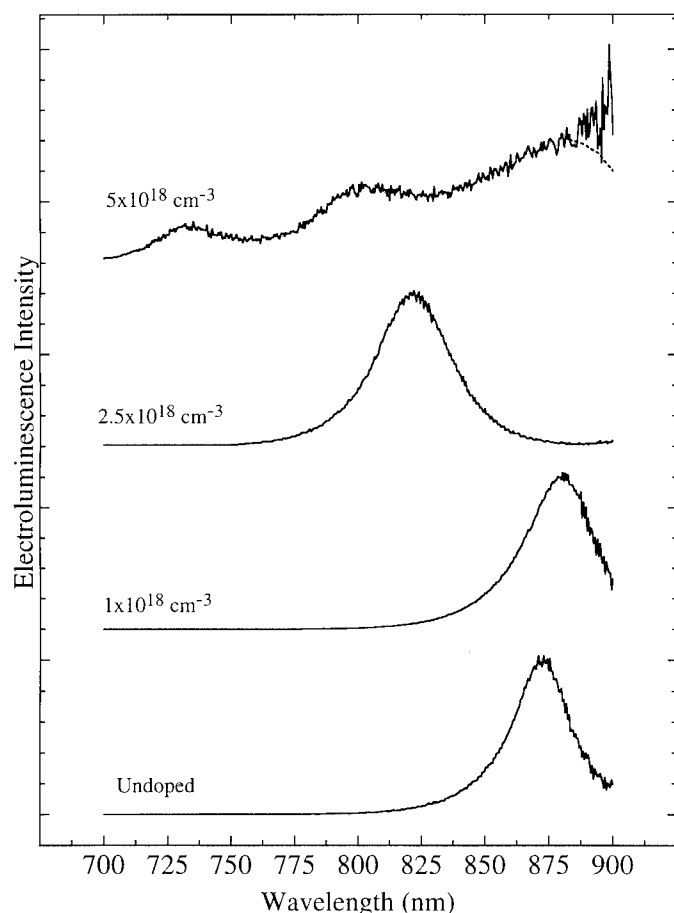


Figure 2. DC electroluminescence spectra of constant core doping density laser sequence.

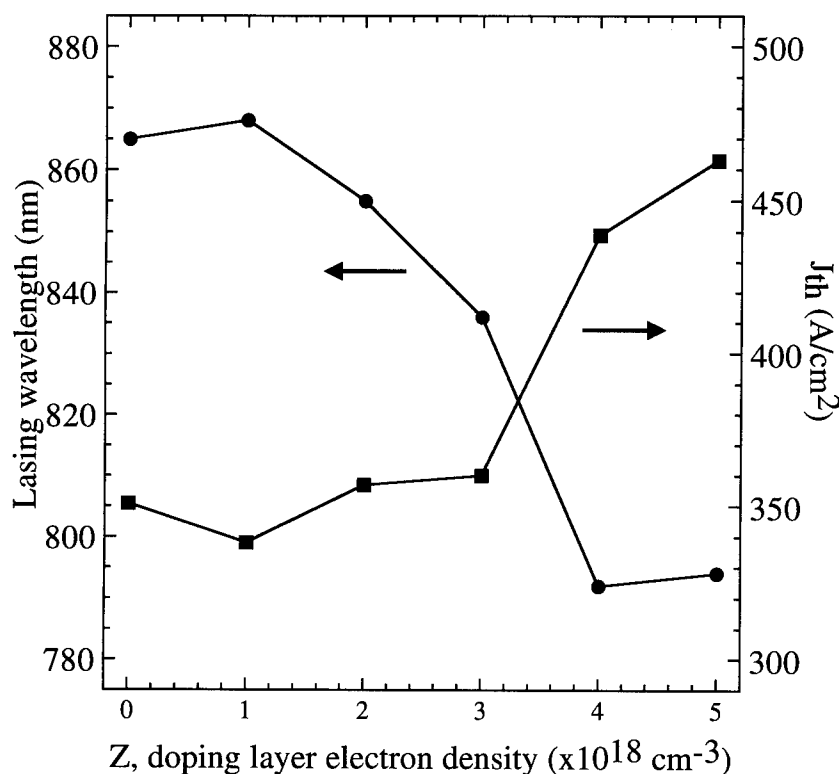


Figure 3. Lasing wavelength and threshold current density as a function of doping layer electron density for the stepped core doping density laser sequence.

increases with no further shortening occurring for the heaviest doped device. The presence of intermediate wavelengths between $n=1$ and $n=2$ is attributed to the intraband relaxation broadening of the gain spectra in the presence of a large number of carriers.¹⁴ While there is an increase in threshold current density accompanying the wavelength shift, it is relatively small and occurs primarily for the two highest doped samples. The jump in threshold current density for $n=2$ lasing may occur due to the same hole transport problem as plagued the constant core doping density devices. The $n=2$ lasing threshold current density of 440 A/cm² represents a factor of five reduction as compared to the best reported GaAs/AlGaAs $n=2$ lasers. This performance improvement has been accomplished because other techniques rely on increased current to provide the electrons which are necessary to obtain a significant population in the $n=2$ state. Modulation doping populates the well with electrons before any current is applied and therefore $n=2$ lasing becomes a hole limited, rather than electron limited, process.

CONCLUSION

Modulation doped lasers have been shown to be a viable alternative to other methods for achieving $n=2$ lasing. However, the core doping profile must be carefully designed. Constant core doping density structures exhibited a wavelength shift but also suffered from a very large increase in threshold current density. This problem was solved by growing a laser core with stepped doping density where the Si concentration increases as the quantum well is approached. The stepped doping density laser sequence showed a shift in wavelength of 80 nm with an increase of threshold current density of only twenty-five percent over undoped core devices. The $n=2$ threshold current density of 440 A/cm² is much lower than results

obtained by other methods. However, further optimization should result in lower threshold current densities as reported previously.^{12,13}

ACKNOWLEDGEMENTS

The authors acknowledge the assistance of Michael Koch for the MBE crystal growth and Steven Shank for useful discussions regarding his earlier work.

REFERENCES

1. P. S. Zory, A. R. Reisinger, R. G. Waters, L. J. Mawst, C. A. Zmudzinski, M. A. Emanuel, M. E. Givens, and J. J. Coleman, "Anomalous temperature dependence of threshold for thin quantum well AlGaAs diode lasers," *Appl. Phys. Lett.* **49**, 16-18 (1986).
2. Y. Tokuda, N. Tsukada, K. Fujiwara, K. Hamanaka, and T. Nakayama, "Widely separate wavelength switching of single quantum well laser diode by injection-current control," *Appl. Phys. Lett.* **49**, 1629-1631 (1986).
3. M. Mittelstein, Y. Arakawa, A. Larsson, and A. Yariv, "Second quantized state lasing of a current pumped single quantum well laser," *Appl. Phys. Lett.* **49**, 1689-1691 (1986).
4. K. J. Beernink, J. J. Alwan, and J. J. Coleman, "Wavelength switching in narrow oxide stripe InGaAs-GaAs-AlGaAs strained-layer quantum well heterostructure lasers," *Appl. Phys. Lett.* **58**, 2076-2078 (1991).
5. T. R. Chen, Y. Zhuang, X. J. Xu, B. Zhao, and A. Yariv, "Second quantized state oscillation and wavelength switching in strained-layer multiquantum-well lasers," *Appl. Phys. Lett.* **60**, 2954-2956 (1992).
6. T. Takeshita and M. Ikeda, "High relaxation oscillation frequency operation of a QW-LD at the second quantized level," *IEEE J. Quant. Elec.* **30**, 19-23 (1994).
7. J. J. Coleman, K. J. Beernink, "Experimental gain characteristics and barrier lasing in strained-layer InGaAs-GaAs-AlGaAs quantum well heterostructure lasers," *J. Appl. Phys.* **75**, 1879-1882 (1994).
8. K. Uomi, T. Mishima, and N. Chinone, "Modulation-doped multi-quantum well (MD-MQW) lasers. II. experiment," *Jpn. J. Appl. Phys.* **29**, 88-94 (1990).
9. T. Takahashi, M. Nishioka, and Y. Arakawa, "Differential gain of GaAs/AlGaAs quantum well and modulation-doped quantum well lasers," *Appl. Phys. Lett.* **58**, 4-6 (1991).
10. F. Kano, T. Yamanaka, N. Yamamoto, Y. Yoshikuni, H. Mawatari, Y. Tohmori, M. Yamamoto, and K. Yokoyama, "Reduction of linewidth enhancement factor in InGaAsP-InP modulation-doped strained multiple-quantum-well lasers," *IEEE J. Quant. Elec.* **29**, 1553-1559 (1993).
11. F. Kano, T. Yamanaka, N. Yamamoto, H. Mawatari, Y. Tohmori, and Y. Yoshikuni, "Linewidth enhancement factor in InGaAsP-InP modulation-doped strained multiple-quantum-well lasers," *IEEE J. Quant. Elec.* **30**, 533-537 (1994).
12. S. M. Shank, J. A. Varriano, and G. W. Wicks, "Single quantum well GaAs/AlGaAs separate confinement heterostructure lasers with n-type modulation doped cores," *Appl. Phys. Lett.* **61**, 2851-2853 (1992).
13. S. M. Shank, J. A. Varriano, M. W. Koch, and G. W. Wicks, "Characteristics of modulation-doped quantum well lasers grown by molecular-beam epitaxy," *J. Vac. Sci. Technol. B* **11**, 952-954 (1993).
14. P. S. Zory, ed., *Quantum Well Lasers* (Academic, New York, 1993).

HIGH-SPEED PHOTONIC WAVEGUIDE SWITCH ARRAYS AND OPTICAL AMPLIFIER GATES IN InGaAsP/InP FOR COMMUNICATIONS APPLICATIONS

Hans Melchior

Swiss Federal Institute of Technology
CH 8093 Zurich, Switzerland
E-mail: h.melchior@iqe.phys.ethz.ch

INTRODUCTION

Optical space switches in planar GaAs and InP waveguides are progressing rapidly in their conceptual and technological development to become serious contenders for applications in optically transparent, broadband and high-speed fiber-optical local and wide area data and telecommunication and video distribution networks. The three-five compound semiconductor materials offer a wide variety of physical effects [1,2] and device concepts that can be exploited for the realization of electronically controlled optical space switches which are transparent, polarization insensitive and of low losses over extended wavelength-ranges and needing only low control voltages and currents up to high speeds.

PLANAR COMPOUND SEMICONDUCTOR WAVEGUIDE SPACE SWITCHES

Directional coupler switches exploit the linear electro-optic effect to switch optical signals between closely spaced waveguides. These devices have progressed from early single stage units [3] with operating voltages as high as 30 to 40 Volts to integrated switch arrays with operating voltages as low as 5 to 10 Volts and complexities of up to 8x8 [4] and fully packaged optical modules [5,6,7]. While transparent over relatively wide wavelength ranges, they operate with one optical polarization only.

Polarization insensitivity is, however, of high practical importance. Fortunately three-five compound semiconductors allow other physical effects to be exploited for this purpose, even while maintaining the usual (001)-substrate and [110]-cleavage plane orientations.

Digital optical switches make use of adiabatic optical beam transitions in X or Y-InP waveguide junctions [8,9,10]. With either current injection or carrier depletion and electro-optic effects they operate in truly digital fashion with clear threshold currents or voltages. Compact 4x4 switch arrays with wide wavelength ranges and polarization insensitive operation and switching times in the low nanosecond range, have been reported [9].

Mach-Zehnder interferometer [11] type switches offer other possibilities to achieve polarization insensitivity. One version exploits quantum Stark effects in multi-quantum well waveguides [12]. The other relies on the refractive index changes induced by the voltage dependent Franz-Keldysh effect in off- [110] -axis oriented Mach-Zehnder interferometers [13].

To direct the optical signals to the different outputs, these Mach-Zehnder interferometers contain multi-mode interference couplers and splitters. Switches appropriate electrode structures and electronics operate at 5 Volts reaching switching speeds of two hundred picoseconds.

Progress is further being made in two practically most important areas, namely in the reduction of optical losses and with the introduction of cost effective and precise fiber to switch alignment and packaging techniques.

To cut optical losses, technological advances have reduced waveguide losses to the range of 0,5 to 2 dB/cm. To achieve low loss coupling between flat-ended or taper-lensed fibers and optical waveguide switches, optical mode transformers [14,15,16] are being integrated with the switches [6,7,13]. Representative for the state of the art in optical losses and packaging techniques [17] are optical switch-arrays with 4 switches, 4 input and 4 output fibers, complete with optical waveguide tapers and electronic drivers, that operate in the 1,48 to 1,6 micrometer wavelength range, are polarization insensitive to within ± 1 dB, with fiber-to-fiber insertion losses of 9 ± 1 dB. Operational voltages are 5 V and switching speeds 300 ps [13].

SEMICONDUCTOR OPTICAL AMPLIFIER GATE-SWITCHES

Another avenue towards low loss switches is opened by semiconductor optical amplifier gates [18-22]. These optical gates are especially adapted semiconductor laser structures, with low reflectivity facets and redesigned active bulk or quantum-well regions, that insure amplification for light of any polarization. Both 2x2 and 4x4 semiconductor optical amplifier gate switches operating, with gains of order 10 to 20 dB at either 1,55 or 1,3 micrometers and switching speeds of order one nanosecond have been reported [18,19], operating in single polarization. Advanced designs [21] with p-doped active regions allow polarization insensitive operation and gating speeds, up to several Gb/s. Tapered waveguides [21] and tilted facets provide efficient and essentially reflection free coupling to single mode fibers, even in fully integrated 4x1 optical amplifier gate modules [22].

CONCLUSIONS

Three-five compound semiconductors with their rich variety of physical effects and the relatively advanced state of their technology, have lead to the realization of a number of high performance planar waveguide type optical and space switches in terms of optical losses and speed their performance rivals the best LiNbO₃ switches. In terms of polarization independence at convenient control currents and voltages and in optical gain, they clearly surpass LiNbO₃. The realization of moderate switch array sizes and advances in their cost effective packaging, make them ripe for exploitation in systems. Furthermore, the capability for the integration of these switches with photonic and electronic functions and the flexibilities in heterostructure growth promise more enhancements in optical and electrooptic properties.

ACKNOWLEDGMENTS

This work was done in collaboration with M. Bachmann, P.A. Besse, W. Vogt, W. Hunziker, T. Brenner, R. Kyburz, R. Kraehenbuel and Ch. Holtmann, within the framework of the European Research Project RACE-ATMOS. Partial financial support was by the Swiss Federal Office of Education and Science.

REFERENCES

- [1] J. G. Mendoza-Alvarez et.al., J. Appl. Phys. 62, 4548-4553, 1987.
- [2] J. F. Vinchant et.al., J. Lightwave Techn. 10, 63-70, 1992.
- [3] F. J. Leonberger et.al., Appl. Phys. Lett. 31, 223-226, 1977.
- [4] K. Hamamoto et.al., El. Lett. 28, 441-443, 1992.
- [5] G. Mueller et.al., European Conf. Optical Comm. 1993.
- [6] N. Yosimoto et.al., Integrated Photonic Res. Conf. 1994.
- [7] B. Acklin et.al., European Conf. Optical Comm. 1994.
- [8] Y. Silberberg et.al., Appl. Phys. Lett. 51, 1230-1232, 1987.
- [9] J. F. Vinchant et.al., European Conf. Optical Comm. 1993. M. Erman et.al., Optical Fiber Comm. Conf. 1994.
- [10] W. H. Nelson et.al., Optical Fiber Comm. Conf., 1994.
- [11] P. Buchmann et.al., Appl. Phys. Lett. 46, 462-464, 1985.
- [12] J. Zucker et.al., Journ. Lightwave Techn. 10, 1926-1930, 1992. J. Zucker, Europ. Conf. Optical Comm. 1993.
- [13] Bachmann et.al., Optical Fiber Comm. Conf. 1992. R. Krahenbuehl et.al., European Conf. Optical Comm. 1994.
- [14] T. Koch et.al., IEEE Photonics Techn. Lett. 2, 88-90, 1990.
- [15] R. Zengerle et.al., Electron. Lett. 28, 631-632, 1992.
- [16] T. Brenner et.al., IEEE Phot. Technol. Lett. 5, 1053-1056, 1993.
- [17] W. Hunziker et.al., European Conf. Optical Comm. 1993.
- [18] M. Gustavsson et.al., Electron. Lett. 28, 2223-2225, 1992.
- [19] C. Holtmann et.al., AGEN-Communications 45-48, 1993.
- [20] G. Sherlock et. al., Electron. Lett. 30, 137-139, 1994.
- [21] P. Doussiere et.al., IEEE Photonics Techn. Lett. 6, 170-172, 1994.
- [22] W. Hunziker et.al., Optical Amplifiers and their Applications, European Conf. Optical Comm. 1994. D. Leclerc et.al., European Conf. Optical Comm. 1994.

ANALYSIS OF N X M WAVEGUIDE SPLITTERS AND COUPLERS WITH MULTIMODE GUIDING SECTIONS†

E. R. Thoen,¹ L. A. Molter,¹ and J. P. Donnelly²

¹ Swarthmore College
Department of Engineering
Swarthmore, PA 19081-1397

² M.I.T. Lincoln Laboratory
Lexington, MA 02173-0073

ABSTRACT

Highly multimode waveguides in which multiple images of the input excitation are formed at different distances along the guide can be used for splitting and switching applications. These devices are often analyzed with a paraxial approximation. In the analysis presented here the actual shapes and propagation constants of the modes were considered. The analysis was performed on splitters with one input guide, centered on a multimode region, and N output guides; uniformity and sensitivity of the outputs to changes in the length and width of the multimode section for 1x2 and 1x8 splitters at a variety of positions along the multimode region were predicted. 2x2 couplers with off-centered inputs were also analyzed. A modification to the input/output guide positions of the couplers was made to reduce the length of the guide while achieving the same absolute sensitivity to variations in the length of the multimode region.

INTRODUCTION

Highly multimode waveguides may be used for switching and splitting applications¹⁻⁵ by making use of their self-imaging properties.⁶ The intensity distribution at the input is reproduced periodically (at distances that are integral multiples of Ω , the beat length) along the guide; an inverted image of the original distribution appears at $(2m+1)/2$ multiples of Ω , where m is a positive integer. Further, multiple images are formed at fractions of the beat length. For example, a single-mode input, centered on the multimode region, produces a symmetric pattern of two intensity peaks one-half the distance between the original distribution and its image; four, eight, etc. intensity peaks appear at one-fourth, one-eighth, etc. the distance, respectively. The maximum number of images depends upon the number of modes in the wide section.

Multimode devices have been analyzed previously with a paraxial approximation, in this approximation it is assumed that the modes in the wide section are zero at the boundaries of the guide and that the phases of the various modes differ by factors of 2π at $z = \Omega$, where $\Omega = 2p\pi/(\beta_0 - \beta_1)$, where p is an integer, z is the direction of propagation, and β_i is the propagation constant of the ith mode. In this paper, a more exact analysis is completed by considering the precise shapes and propagation constants of the modes within in the guiding regions.

THEORY

The effective index method was used to simplify the modeling of the device as a dielectric slab waveguide. The two dimensional slab waveguide was infinite in the y direction and z was the propagation direction. The refractive indices of the guiding and adjacent non-guiding regions were n_1 and n_2 , respectively; the half widths of the input, multimode, and output guides were d_A , d_B , and d_C respectively; and $w = 2d_B$ was the full width of the wide section. The placement of input and output guides relative to the wide guide was measured from center to center and was d_{Ac} for the input guide and d_{Cc} for the output guide. The general guide geometry is given in Fig. 1. A, B, and C distinguish the input, multimode, and output regions of the device.

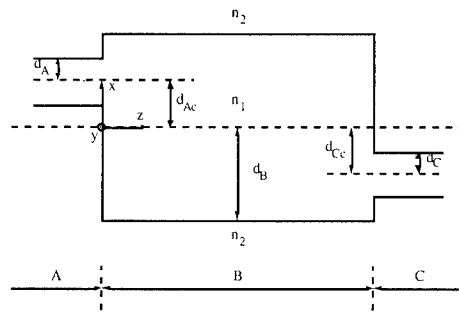


Figure 1. Dielectric slab waveguide geometry.

Symmetric solutions to the wave equation for the electric field for the geometry shown can be written in the form

$$\mathcal{E}_{Qi} = M_{Qi} e^{-j\beta_{Qi}z} \quad (1a)$$

$$M_{Qi} = \begin{cases} Q_1 e^{-\alpha_{Qi}(x - (d_{Qc} + d_Q))} & x \geq d_{Qc} + d_Q \\ Q_0 \cos(k_{Qi}x) & d_{Qc} - d_Q \leq x \leq d_{Qc} + d_Q \\ Q_1 e^{\alpha_{Qi}(x - (d_{Qc} - d_Q))} & x \leq d_{Qc} - d_Q \end{cases} \quad i = 0, 2, 4, \dots, \quad (1b)$$

where \mathcal{E}_{Qi} is the electric field; M_{Qi} gives the transverse distribution of the electric field for mode i of the guiding region Q ; i , for the symmetric case, is an even integer numbering the modes; $Q = A, B$, or C to indicate the z -position of interest; Q_0 is the magnitude of the electric field in the guiding region; Q_1 is the magnitude of the decaying electric field outside the guiding region; α_{Qi} is the decay constant; d_{Qc} is the distance from the center of the wide guiding region to the center of the input or output guide; d_Q is the half width of each guide; β_{Qi} is the propagation constant; and k_{Qi} is the transverse propagation constant. For the antisymmetric solutions, cosine is replaced by sine in the guiding region, the sign of one of the decaying tails is negative, and i ranges over odd integers. (Modes of the wide guide have $d_{Qc} = d_{Cc} = 0$.) Matching boundary conditions at the discontinuities in index and making use of the dispersion relations in each region produces the determinantal equation

$$\tan k_{Qi}d_Q = \frac{\sqrt{(k_1^2 - k_2^2)d_Q^2 - k_{Qi}^2d_Q^2}}{k_{Qi}d_Q} \quad i = 0, 2, 4, \dots, \quad (2)$$

where $k_{1,2}$ is the propagation constant in the region with refractive index $n_{1,2}$. A Newton-Raphson routine was used to numerically solve the determinantal equation for k_{Xi} , which allowed calculation of α_{Qi} and β_{Qi} .

The magnitude of the electric fields, Q_0 and Q_1 , was determined by normalizing the overlap integral of the fields in regions A, B, and C with the equation

$$O_{X_i, X_i} = \int_{-\infty}^{\infty} M_{X_i} M_{X_i} dx = 1. \quad (3)$$

The electric fields were normalized to the single-mode input guide intensity by setting

$$E_{A0} = \mathcal{E}_{A0}. \quad (4)$$

The amplitude of each mode excited in the wide region was determined by the overlap integral between the input mode and all modes supported in the multimode region using

$$O_{A0, B_i} = \int_{-\infty}^{\infty} M_{A0} M_{B_i} dx. \quad (5)$$

The electric field for each of the modes in the wide region was given by the equation

$$E_{B_i} = O_{A0, B_i} \mathcal{E}_{B_i}. \quad (6)$$

When the contribution of each mode of the wide guide to the output guide was calculated with the overlap, the phases at the positions of the output guides were taken into account:

$$O_C = \sum_{i=0}^{i_{\text{cutoff}}} e^{-j\beta_{X_i} z_0} \int_{-\infty}^{\infty} O_{A0, B_i} M_{B_i} M_{C0} dx = |O_C| e^{j\theta_C}, \quad (7)$$

where i_{cutoff} is the number of the highest guided mode, and z_0 is the position of the output guide along the direction of propagation. In general, each mode has a different phase at the output plane, and O_C will contain real and imaginary parts; it can therefore be rewritten in terms of a magnitude, $|O_C|$, and a corresponding phase, θ_C . With the magnitude of the overlap calculated, the output electric field was given by

$$|E_C| = |O_C| \mathcal{E}_{C0}. \quad (8)$$

Self-imaging in the waveguide occurs at the beat length, Ω , the distance to re-form the original intensity distribution. At this position, relative phases of the modes in the first order paraxial approximation, given by

$$\beta_0 - \beta_i = \frac{\lambda \pi}{4n_1 \omega^2} i(i+2), \quad (9)$$

are identical to those at the input and all modes have rotated by integer multiples of 2π . In general (when both antisymmetric and symmetric modes are present) Ω is given by

$$\Omega_{AS} = \frac{6\pi}{\beta_0 - \beta_1}, \quad (10)$$

where $\beta_{0,1}$ is the propagation constant of the first symmetric and antisymmetric modes, respectively. The numerator is 6π rather than 2π because the 2nd, 5th, 8th, ... modes have propagation constants that require three times the distance of the others to reestablish the original phase distribution. In the case of the 2 x 2 coupler with a single input, both symmetric and antisymmetric modes are excited; in the paraxial approximation the inverted image (a reflection in x about the y - z plane) appears at positions $z = (2m+1)\Omega_{AS}/2$. At $z = (2m+1)\Omega_{AS}/4$, two symmetric images are formed. The number of images increases as a

power of 2 until it exceeds the number of modes in the wide region. As shown below, when the actual shapes and propagation constants of the modes are considered, the images degrade with propagation distance. The degradation is mainly due to discrepancies of the phases of the modes from those predicted by the paraxial approximation.

If excitation of modes 2, 5, 8, ... could be prevented by positioning the input guide, the beat length could be reduced by a factor of three to give a modified beat length of Ω_{MAS} :

$$\Omega_{MAS} = \frac{2\pi}{\beta_0 - \beta_1}. \quad (10)$$

As described above, an inverted image of the original input appears at $\Omega/2$. When the input guide is centered on the wide guiding region ($d_{Ac} = 0$), only symmetric modes are excited and i is even; in this case the inverted image is the same as the original distribution. When only symmetric modes are present, the beat length is instead given by

$$\Omega_S = \frac{2\pi}{\beta_0 - \beta_2}, \quad (11)$$

where $\beta_{0,2}$ are the propagation constants of the two lowest order symmetric modes. In the paraxial approximation two images that are symmetrically positioned in the x direction are formed at $z = \Omega_S/2$, four at $z = \Omega_S/4$, etc.

RESULTS

Initially a symmetric 1x2 splitter was modeled with one, single-mode input guide, centered on the multimode region, and output guides placed symmetrically. For these calculations the structures were assumed to be deeply etched semiconductor ridge guides with an effective index of $n_1 = 3.13$ in the guiding region at $\lambda = 1.3 \mu\text{m}$; n_2 was assumed to be 1.0 and the substrate index was 3.08. Most calculations were performed using only modes with propagation constants greater than the propagation constant of the substrate. (The remaining modes were neglected. This assumption is reasonable because those modes radiate into the substrate. Further, they are excited with small amplitudes only.) The input and output guide widths were therefore chosen to support a single mode with a propagation constant higher than that of the substrate. Initially the output guides were placed at least a guide width apart.

The narrowest possible 1x2 splitter was modeled with the following dimensions: $d_A = 1 \mu\text{m}$, $d_B = 4 \mu\text{m}$, and $d_C = 1 \mu\text{m}$. The total width of the multimode section, w , was $8 \mu\text{m}$. The beat length of the device was determined to be $159.2605 \mu\text{m}$ from (11). Output guides were located at one-half the beat length and were centered at $d_{Cc} = \pm 2 \mu\text{m}$. With a single symmetric input the intensity distribution across the width of the guide at half the beat length is shown in Fig. 2. The positions of the output guides were superimposed on the intensity distribution to show the electric field in the wide-guide at the positions of the output guides. The magnitude of the output intensity was also calculated in each guide as a function of z near positions where images were predicted to characterize sensitivity to variations in length (see Fig. 2).

Because two intensity peaks always appear at half the beat length in sufficiently wide multimode guides, wider guides were tested for sensitivity to z variation. The width of the multimode region was expanded to $16 \mu\text{m}$, the output guides were located at $\pm 4.0 \mu\text{m}$, and the beat length was calculated to be $626.9090 \mu\text{m}$. The intensity distribution and sensitivity for this case are shown in Fig. 3. The guide width was further expanded to $32 \mu\text{m}$, the output guides were located at $\pm 8.0 \mu\text{m}$, and the beat length was calculated to be $2486.7644 \mu\text{m}$. These results are shown in Fig. 4.

As the width of the guide increased, supporting more modes, oscillations in the tails of the intensity peaks in the x -direction became more prominent. The magnitude of the intensity peaks decreased as the length of the multimode region was increased. This decrease in magnitude was reflected in the sensitivity plots indirectly, which demonstrated that maximum output intensity decreased as the guide width and propagation distance increased. The two plots cannot be compared directly, however, because the magnitude of the output intensity

depends on the overlap between individual modes in the multimode region and the mode of the output guide, as given in (7). The peaks of all sensitivity plots consistently occurred before the calculated position, $z = \Omega/2$.

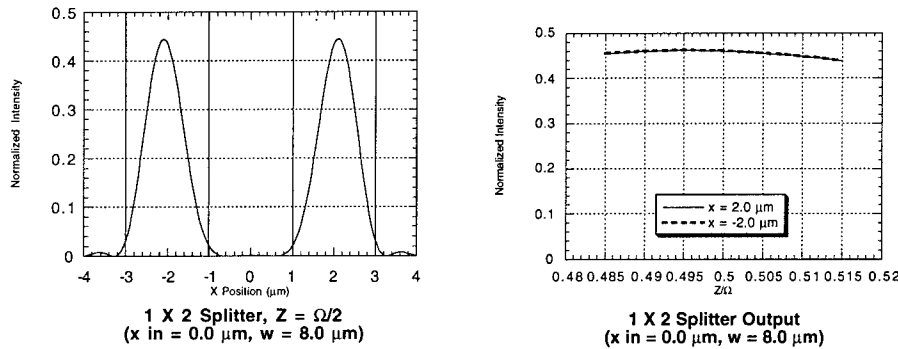


Figure 2. Intensity and sensitivity for a 1x2 splitter 8 μm in width.

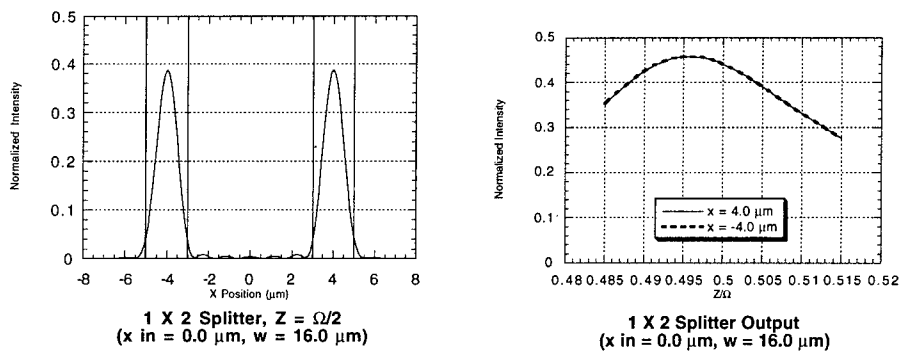


Figure 3. Intensity and sensitivity for a 1x2 splitter 16 μm in length.

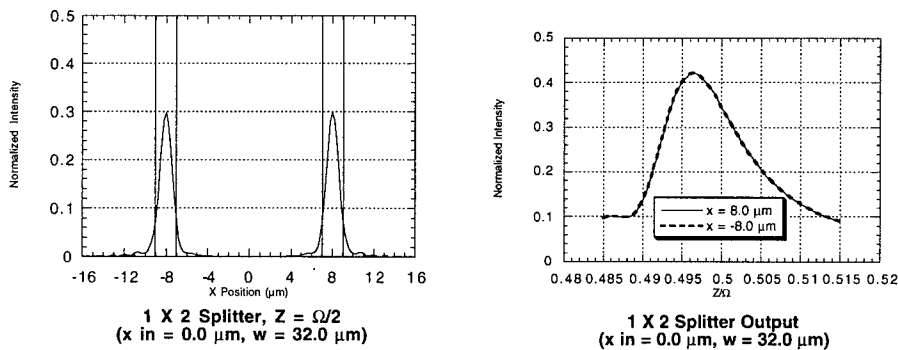


Figure 4. Intensity and sensitivity for a 1x2 splitter 32 μm in length.

Similar calculations were made for a 1x8 splitter. The minimum guide width for eight output guides separated by at least a guide width is 32 μm . Both the 32 μm and the 64 μm

case were modeled. Intensity distributions with eight peaks occurring at $\Omega_S/8$, $3\Omega_S/8$, $5\Omega_S/8$, and $7\Omega_S/8$ were examined.

For the 1x8 splitter with $w = 32 \mu\text{m}$ the output guides were located at $d_{C_c} = \pm 2 \mu\text{m}$, $\pm 6 \mu\text{m}$, $\pm 10 \mu\text{m}$, and $\pm 14 \mu\text{m}$. The beat length was calculated to be $2486.7644 \mu\text{m}$. The intensity distributions and the corresponding sensitivity plots for all positions are shown in Figs. 5 and 6, respectively. Because the results are symmetric across the guide, only half of the intensity peaks were shown in the sensitivity plots.

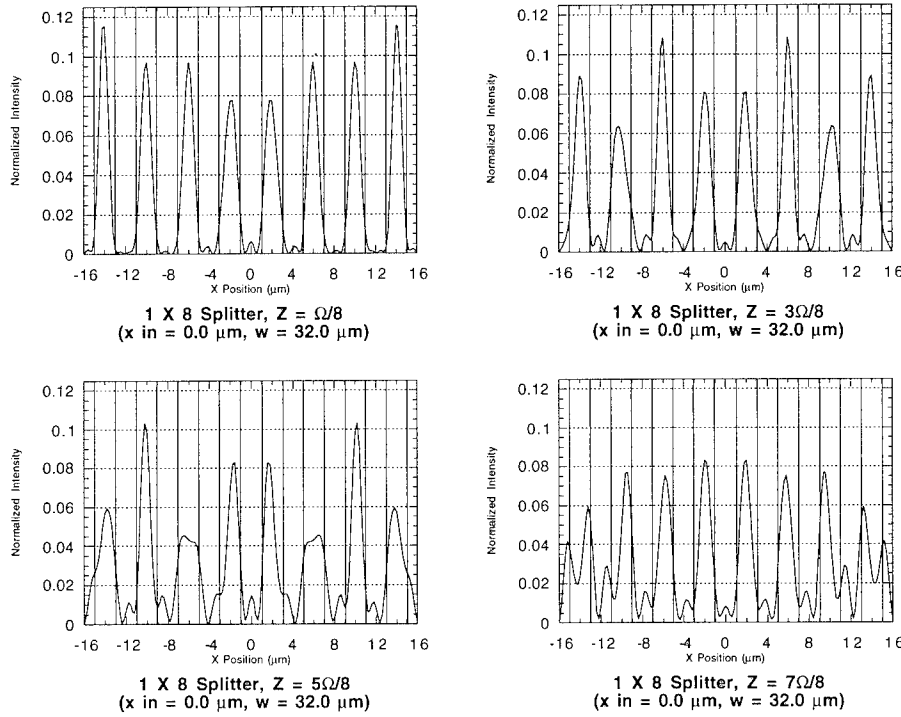


Figure 5. Intensity at several positions for a 1x8 splitter $32 \mu\text{m}$ in width.

A comparison of the intensity distributions showed that the peaks degraded significantly with propagation distance, even when the width of the multimode region was constant. As seen in the sensitivity plot near the $\Omega_S/8$ position, peaking occurred almost simultaneously in all four output guides with approximately the same intensity. As propagation distance increased, the peak intensity varied differently in each guide and the z position of the peak shifted differently in each guide, making it more difficult to achieve equal splitting between output guides.

In the $64 \mu\text{m}$ wide guide $\Omega = 9904.6930$. Output guides were placed at $d_{C_c} = \pm 4 \mu\text{m}$, $\pm 12 \mu\text{m}$, $\pm 20 \mu\text{m}$, and $\pm 28 \mu\text{m}$. Intensity and sensitivity plots are shown in Figs. 7 and 8 for $\Omega_S/8$ and $7\Omega_S/8$. A comparison of the results for the $64 \mu\text{m}$ and $32 \mu\text{m}$ case showed that the performance further degraded as a result of both increased beat length and guide width. For example, at $\Omega_S/8$ (the shortest propagation distance for a $64 \mu\text{m}$ 1x8 splitter) the maximum output intensity was lower than that of the $32 \mu\text{m}$ case.

A 2x2 coupler with a single excited input in which all modes in the wide guide were excited was examined next. The dimensions were set to $d_A = 1 \mu\text{m}$, $d_B = 4 \mu\text{m}$, $d_C = 1 \mu\text{m}$, $d_{A_c} = \pm 2 \mu\text{m}$, and $d_{C_c} = \pm 2 \mu\text{m}$, giving a guide width, $w = 8 \mu\text{m}$, and a beat length of $1275.0981 \mu\text{m}$. The device is shown in Fig. 9. Intensity distributions and the corresponding sensitivities are shown at $\Omega_{AS}/4$, $\Omega_{AS}/2$, $3\Omega_{AS}/4$, and Ω_{AS} in Figs. 10 and 11.

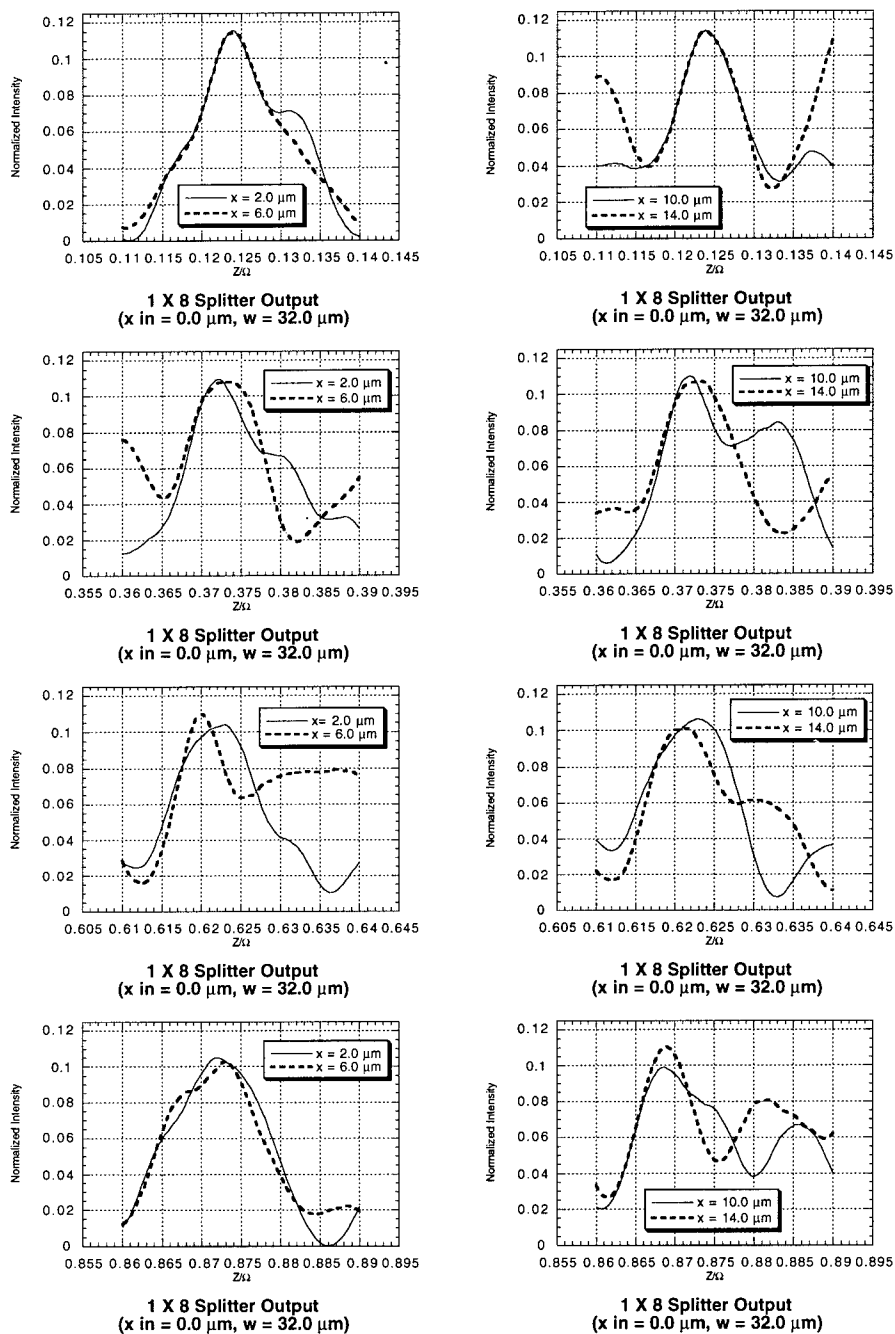


Figure 6. Sensitivity at several positions for a 1x8 splitter 32 μm in width.

The intensity distribution of the image degraded with increasing length of the multimode section. In all cases, the maximum output intensity occurred at a z position slightly less than the calculated value. The sensitivity degraded in a manner similar to the symmetric input 1xN splitter cases.

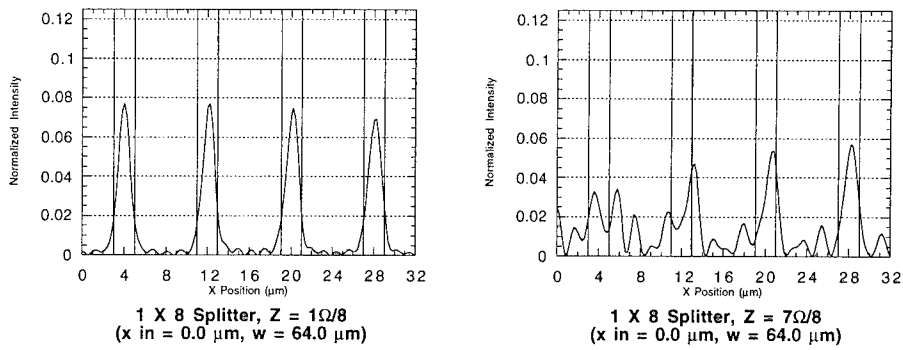


Figure 7. Intensity at several positions for 1x8 splitter $64 \mu\text{m}$ in width.

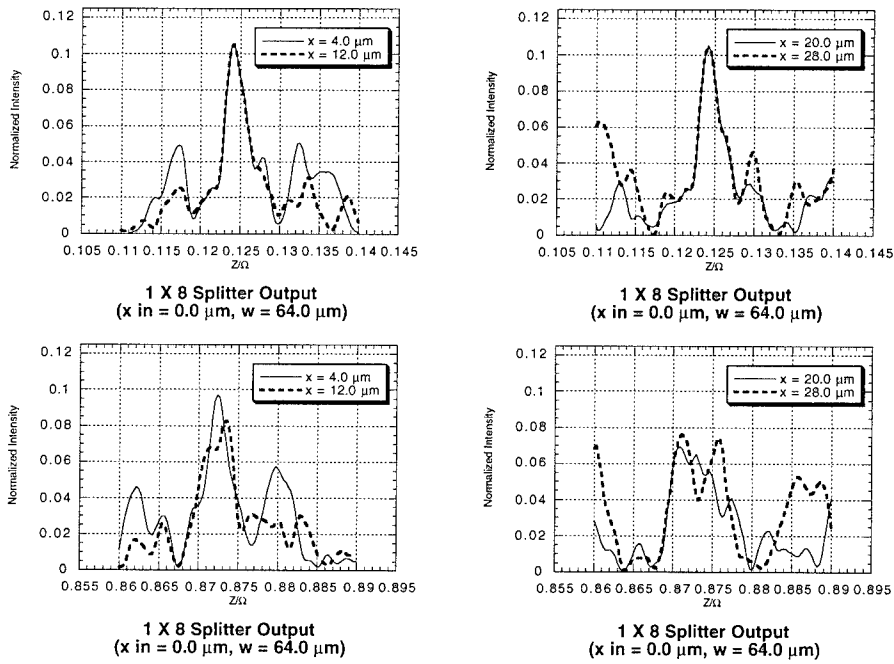


Figure 8. Sensitivities at several positions for 1x8 splitter $64 \mu\text{m}$ in width

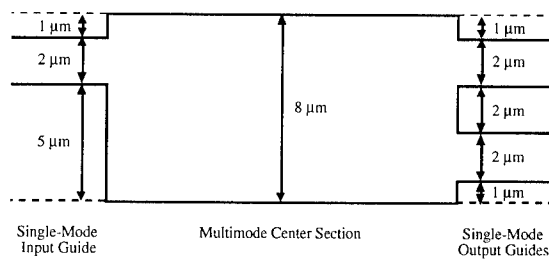


Figure 9. 2x2 splitter with a single input.

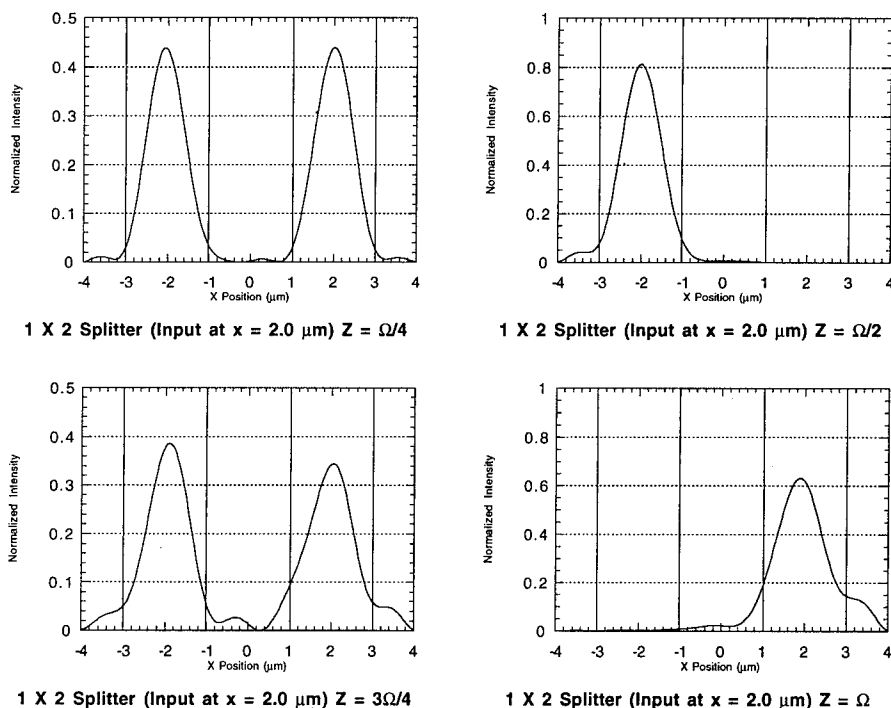


Figure 10. 1x2 splitter electric field intensity cross section.

A modified 2x2 coupler was then analyzed. In this modified case the input guides were positioned to eliminate excitation of the 2nd, 5th, 8th... modes. The centers of the input guides were initially placed at positions predicted by the paraxial approximation

$$d_{Ac} = \pm \frac{1}{3}d_B.$$

An adjustment of 1.75% was required to completely eliminate the excitation of the 2,5,8... modes.

In the new design $d_{Ac} = \pm 1.3567 \mu\text{m}$ and $d_{Cc} = \pm 1.3567 \mu\text{m}$. The modified beat length, Ω_{MAS} , was calculated to be $425.0327 \mu\text{m}$. Intensity distributions and corresponding sensitivities were plotted at $\Omega_{MAS}/4$, $\Omega_{MAS}/2$, $3\Omega_{MAS}/4$, and Ω_{MAS} in Figs. 12 and 13.

Because the beat length for the modified 2x2 splitter was three times shorter than the previous beat length, the degradation of the intensity distribution was much less than that for the standard 2x2 splitter. A comparison of the sensitivity plots was more difficult because the two were normalized to different beat lengths. However, on both normalized scales the output intensity peaks occur before the calculated positions. When the sensitivities were generated on an absolute distance scale, the output intensity amplitudes varied similarly (not shown). Although the wide guide length had been reduced by a factor of three, the output intensity sensitivity was very similar to the longer case. Much of the signal degradation that occurred in the longer case, however, was eliminated.

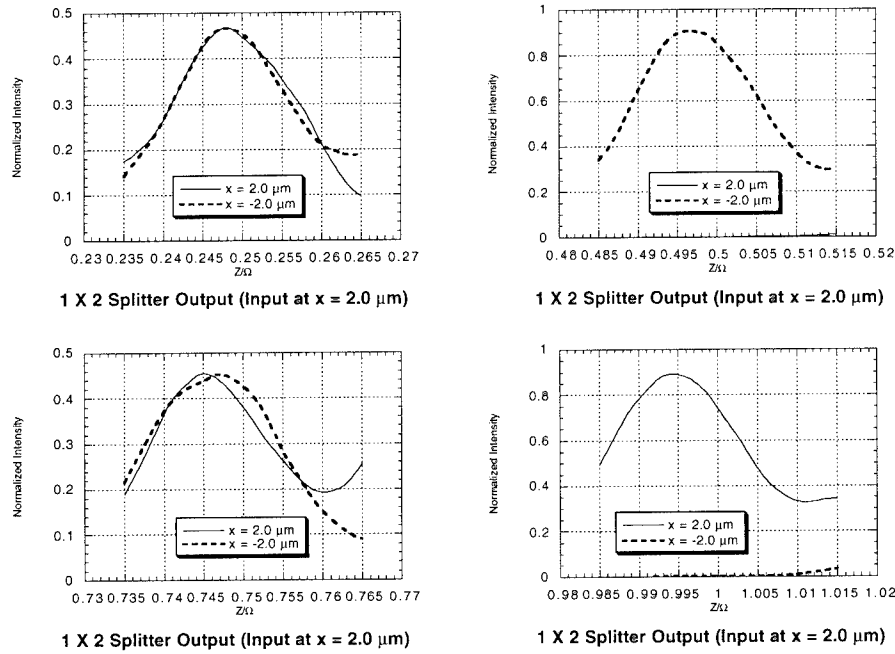


Figure 11. 1x2 Splitter output guide sensitivity.

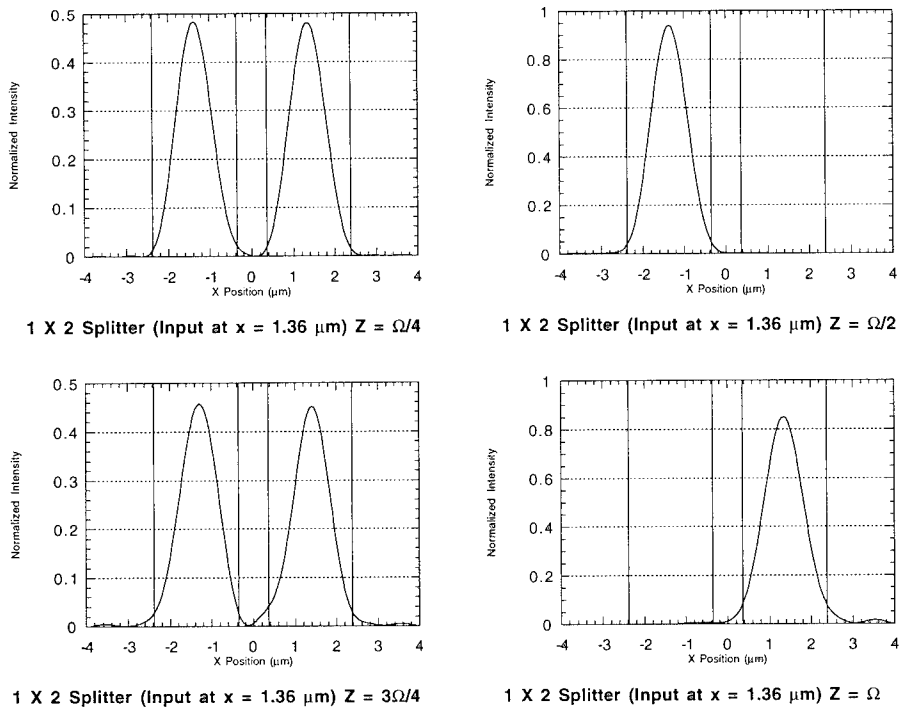


Figure 12. Modified 1x2 splitter electric field intensity cross section.

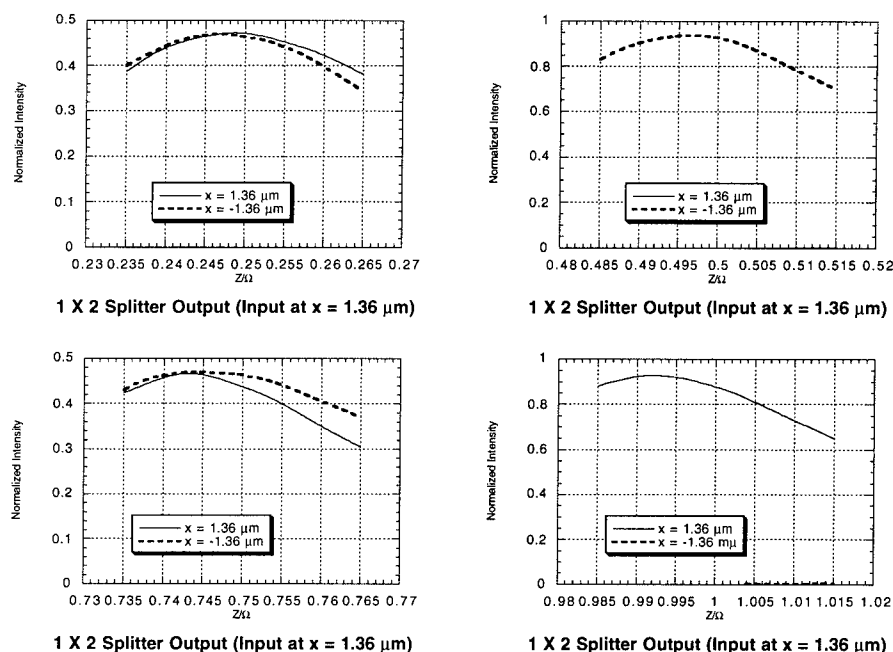


Figure 13. Modified 1x2 Splitter output guide sensitivity.

SUMMARY

Results obtained using a computer model of waveguide splitters and couplers with a highly multimode guiding section are presented. The 1x2 and 1x8 splitter with symmetric input excitations were first examined. Next two configurations of the 2x2 coupler with a single input were examined: a standard coupler with the input/output guides separated by at least one guide width, and a modified coupler with guide positions changed to reduce device length. In all cases, the actual switching or splitting lengths were shorter than those predicted by the beat length calculation. Additionally, the quality of the images degraded with propagation distance in all cases. However, the sensitivity in absolute distances did not change when the propagation distance was changed.

REFERENCES

1. E. C. M. Pennings, R. J. Deri, R. Bhat, T. R. Hayes, and N. C. Andreadakis, Ultracompact, All-Passive Optical 90°-Hybrid on InP Using Self-Imaging, *IEEE Photon. Technol. Lett.* 5(6):701-703 (Jun 1993).
2. J. M. Heaton, R. M. Jenkins, D. R. Wight, J. T. Parker, J. C. H. Birbeck, and K. P. Hilton, Novel 1 to-N Way Integrated Optical Beam Splitters Using Symmetric Mode Mixing in GaAs/AlGaAs Multimode Waveguides, *Appl. Phys. Lett.* 61(15): 1754-1756 (12 Oct 1992).
3. R. M. Jenkins, R. W. J. Devereux, and J. M. Heaton, Waveguide Beam Splitters and Recombiners Based on Multimode Propagation Phenomena, *Opt. Lett.* 17(14): 991-993 (15 Jul 1992).
4. Th. Niemeier and R. Ulrich, Quadrature Outputs from Fiber Interferometer with 4×4 Coupler, *Opt. Lett.* 11(10):677-679 (Oct 1986).
5. E. C. M. Pennings, R. J. Deri, A. Scherer, R. Bhat, T. R. Hayes, N. C. Andreadakis, M. K. Smit, L. B. Soldano, and R. J. Hawkins, Ultracompact, Low-Loss Directional Couplers on InP Based on Self-Imaging by Multimode Interference, *Appl. Phys. Lett.* 59(16): 1926-1928 (14 Oct 1991).
6. R. Ulrich and G. Ankele, Self-Imaging in Homogeneous Planar Optical Waveguides, *Appl. Phys. Lett.* 27(6): 337-339 (15 Sep 1975).

[†] This work was supported in part by the Department of the Air Force, and grants from the National Science Foundation (ECS 8958667), the Keck Foundation, du Pont Company, and General Electric Co.

WAVELENGTH-FLATTENED THREE CORE OPTICAL COUPLER POWER SPLITTERS IN ION-EXCHANGED GLASS

G. Hewa-Gamage, H. Hatami-Hanza, and P. L. Chu

Optical Communications Group
University of New South Wales
Sydney 2052
Australia

INTRODUCTION

Optical power splitters are vital devices in integrated optics and broadband signal distribution systems. Y-junctions, optical 3dB couplers and fused tapered optical fibre couplers are currently serving as power dividers in integrated optic circuits and networks. Although conventional Y-junctions are advantageous because of their less sensitivity to wavelength, they have a disadvantage of large device length because a small branching angle is necessary to keep the loss reasonably small^{1,2}. On the other hand, the performance of the conventional directional coupler strongly depends on wavelength. This wavelength dependence is not favourable for power splitter or combiner to optical signal processing systems. Therefore, wavelength-flattened couplers are essential components for dividing optical signals while maintaining given splitting ratio without wavelength dependence. Using silica-based three core planar optical coupler, this characteristics could be obtainable³. Many researchers studied the fundamental properties of three core planar optical waveguide coupler both theoretically and experimentally³⁻⁹. Among those, Donnelly et.al.⁵⁻⁷ have done significant work related to the optical power dividers and combiners with three core couplers. Also, Hardy and Streifer⁸ have done thorough mathematical investigation of three waveguide system using new coupled mode formulation. Depending on various factors, this scheme is promising for optical power dividing applications.

In this paper, we analyse the wavelength-flattened characteristics of three core optical coupler in ion-exchanged glass by means of the beam propagation method¹⁰ combined with the effective index method¹¹. The experimental results will be presented in comparison with the theoretical results.

THEORETICAL ANALYSIS

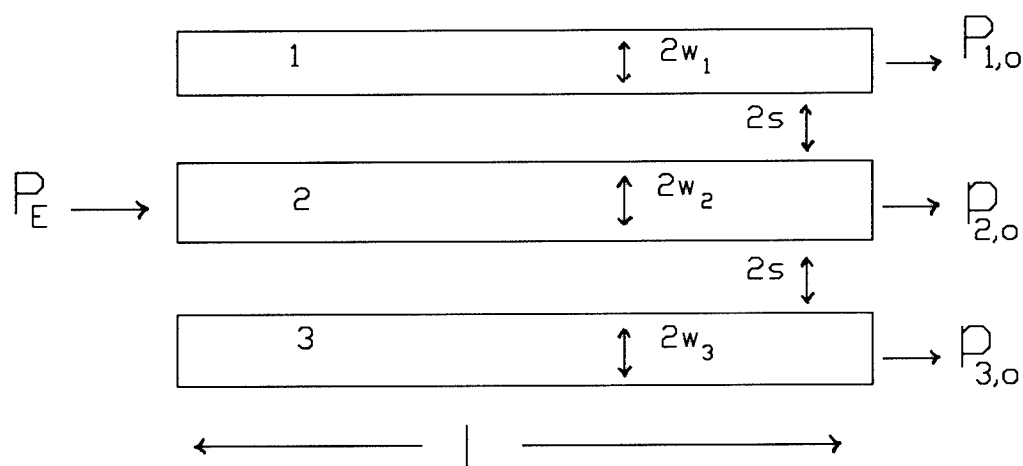


Figure 1. Schematic representation of three core optical power splitter.

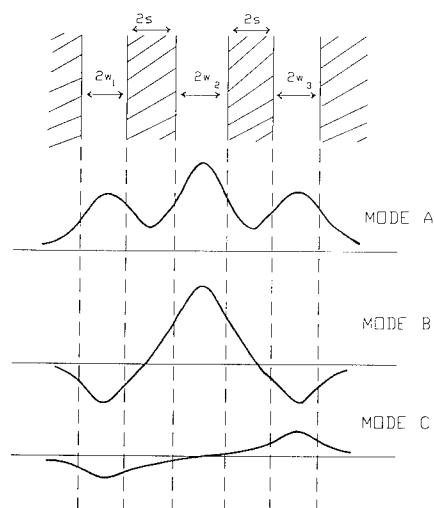


Figure 2. Three normal modes in three symmetrically coupled waveguides.

The structure of three waveguide coupler as a power splitter is shown in Figure 1. The waveguides are assumed to be single moded in the operating wavelength region. The input waveguide is symmetrically positioned in the vicinity of two output waveguides. The structure can support three normal modes in which two modes are symmetric and the other antisymmetric. According to the notation of Donnelly⁶, these modes are called mode A, mode B and mode C as shown in Figure 2.

Coupled mode solutions

Following the coupled mode analysis done by Hardy and Streifer⁸, for slab model case, the optical field amplitudes $u_j(z)$, ($j = 0, 1, 2$), in waveguides can be described by the equations (1) and (2).

$$u_1(z) = u_3(z) = i(2m_{12}/\psi) \sin(\psi z/2) e^{i\phi z/2} \quad (1)$$

$$u_2(z) = \{ \cos(\psi z/2) + i[(2m_{22} - \phi)/\psi] \sin(\psi z/2) \} e^{i\phi z/2} \quad (2)$$

where all the parameters in equations (1) and (2) are as defined in Reference 8.

As seen, even with the slab model approximation, the coupled mode solutions for the system with more than two waveguides are quite complicated. Furthermore, if we use bent sections in the coupler devices, the coupled mode analysis will be more complicated, and the coupler that have inhomogeneous refractive index profile (eg. diffused waveguides) create additional complexity. To overcome these difficulties, the beam propagation method¹⁰ combined with the effective index method¹¹ is employed to analyse the three waveguide coupler which consists of diffused channel waveguides. However, before applying the beam propagation analysis, it is necessary to construct the one dimensional effective index profile of the coupler.

Construction of the effective index profile

Following the diffusion theory¹², one can construct two dimensional refractive index profile of the ion-diffused three channel coupler.

$$n(x, y, \lambda) = n_b(\lambda) + \frac{1}{2} \Delta n_s(\lambda) \left\{ \operatorname{erf} \left(\frac{w_1 - x_1}{d} \right) + \operatorname{erf} \left(\frac{w_1 + x_1}{d} \right) + \operatorname{erf} \left(\frac{w_2 - x}{d} \right) \right. \\ \left. + \operatorname{erf} \left(\frac{w_2 + x}{d} \right) + \operatorname{erf} \left(\frac{w_3 - x_2}{d} \right) + \operatorname{erf} \left(\frac{w_3 + x_2}{d} \right) \right\} \exp \left(-\frac{y^2}{d^2} \right), \quad y \leq 0 \quad (3)$$

where,

$$x_1 = x + w_1 + 2s + w_2 ,$$

$$x_2 = x - w_3 - 2s - w_2 ,$$

and $2w_1$, $2w_2$ and $2w_3$ are the window openings for ion-diffusion, $2s$ is the separation between two adjacent windows, and d is the effective diffusion depth. $\Delta n_s(\lambda)$ is the maximum refractive index change of planar diffusion and $n_b(\lambda)$ is the substrate refractive index. Here, we assumed that Δn_s is not wavelength dependent for the operating wavelength range¹³.

Although we presented a general formulation, in our calculation we chose the identical window openings for ion-diffusion, i.e. $w_1 = w_2 = w_3 = w$ (compatible with our practical device). Figure 3 shows the two dimensional refractive index profile, $n(x, y, \lambda)$, of diffused waveguide coupler for $\lambda = 0.6328 \mu\text{m}$ with the diffusion time 3 hours and diffusion temperature 380°C . For this wavelength, n_b is found to be 1.52 and Δn_s is 0.009 for TE mode.

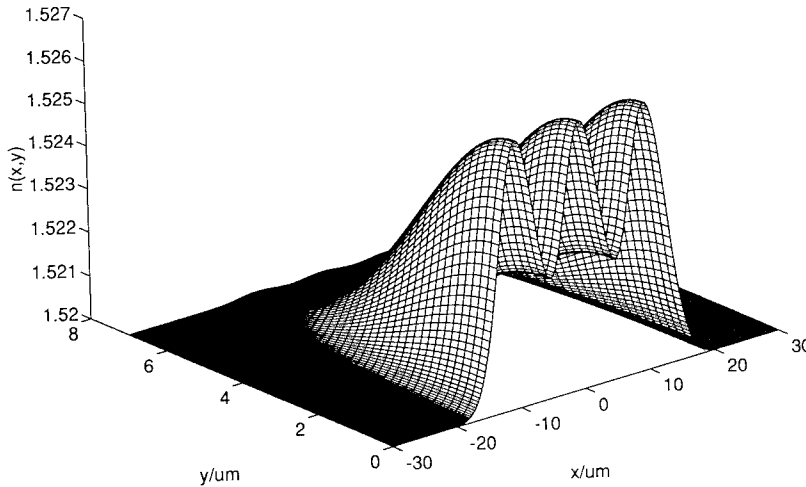


Figure 3. Two dimensional refractive index profile of ion-diffused three core coupler ($2w = 5.0 \mu\text{m}$, $2s = 5.0 \mu\text{m}$, $d = 3.5 \mu\text{m}$).

As seen in Figure 3, the minimum surface refractive index of the middle waveguide is not equal to the substrate refractive index. This makes significant influence to the propagation constant of the middle waveguide, and this is taken into account when we calculate the coupling characteristics.

Using the effective index method, the one dimensional effective index profile, $N_{eff}(x, \lambda)$, is constructed and it is given by,

$$N_{eff}(x, \lambda) = N(\infty, \lambda) + \frac{1}{2} \Delta N(\lambda) \left\{ \operatorname{erf}\left(\frac{w_1 - x_1}{d}\right) + \operatorname{erf}\left(\frac{w_1 + x_1}{d}\right) + \operatorname{erf}\left(\frac{w_2 - x}{d}\right) \right. \\ \left. + \operatorname{erf}\left(\frac{w_2 + x}{d}\right) + \operatorname{erf}\left(\frac{w_3 - x_2}{d}\right) + \operatorname{erf}\left(\frac{w_3 + x_2}{d}\right) \right\} \quad (4)$$

where

$$\Delta N(\lambda) = N(0, \lambda) - N(\infty, \lambda)$$

$N(0, \lambda)$ is effective index at $x=0$, $N(\infty, \lambda)$ is effective index at ∞ , equal to the substrate refractive index, $n_b(\lambda)$, and other parameters are as defined in the beginning of this section.

To evaluate the values of $N(0, \lambda)$ for a particular diffusion depth and wavelength, the surface refractive index profile, $n_s(x, 0)$, and dispersion characteristics of the planar diffusion have been used. Figure 4 shows the one dimensional effective index profile, $N_{eff}(x, \lambda)$, of the structure which was fabricated using identical window openings. As seen, the effective index is highly dependent on wavelength. After some wavelength, the effective index distribution is almost equal to the substrate refractive index hence no guiding in the structure. Also it is noticeable that even with the identical window openings, the centre guide of the diffused three core coupler has different propagation characteristics to the outer guides. Therefore, the coupler possesses the asymmetric coupling characteristics which is one of the important factors for the wavelength-flattened devices³.

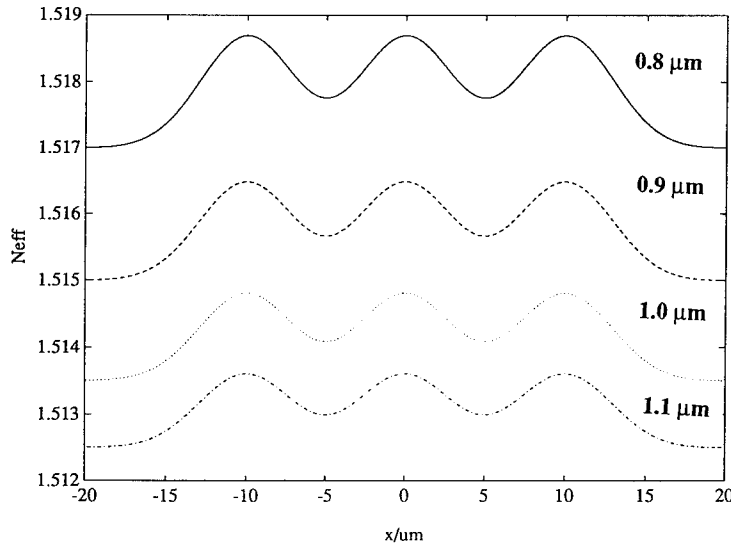


Figure 4. One dimensional effective index profile of the coupler for four different wavelengths ($2w = 5.0 \mu\text{m}$, $2s = 5.0 \mu\text{m}$, $d = 3.5 \mu\text{m}$).

Calculation of power coupling

After the construction of the effective index profile of the structure, the standard fast-Fourier transform beam propagation method (FFT-BPM)¹⁰ is employed to study the structure numerically. It was assumed that the structure consists of singlemode, weakly guiding waveguides with no sharp bends. Therefore, FFT-BPM is applicable and the propagation of optical field along the dielectric structure is simulated by the scalar wave equation¹⁰. In our calculation, we used 1024 points FFT algorithm with x resolution of $dx = 0.08\mu m$ and $dz = 0.2\mu m$ for each wavelength. When we used three waveguide coupler as a power splitter, the optical power is launched into the centre waveguide of the coupler. Figure 5 shows the power coupling behaviour of an ion-diffused three core coupler at wavelength, $\lambda = 1.0\mu m$ for the case of $w/s = 1$ and $2w/d = 1.428$ (These values corresponds to the diffusion time of 3 hrs. and diffusion temperature of $380^\circ C$). As expected, there is no 100% power coupling between the centre to the outer waveguides because the centre waveguide has larger propagation constant than the outer waveguides.

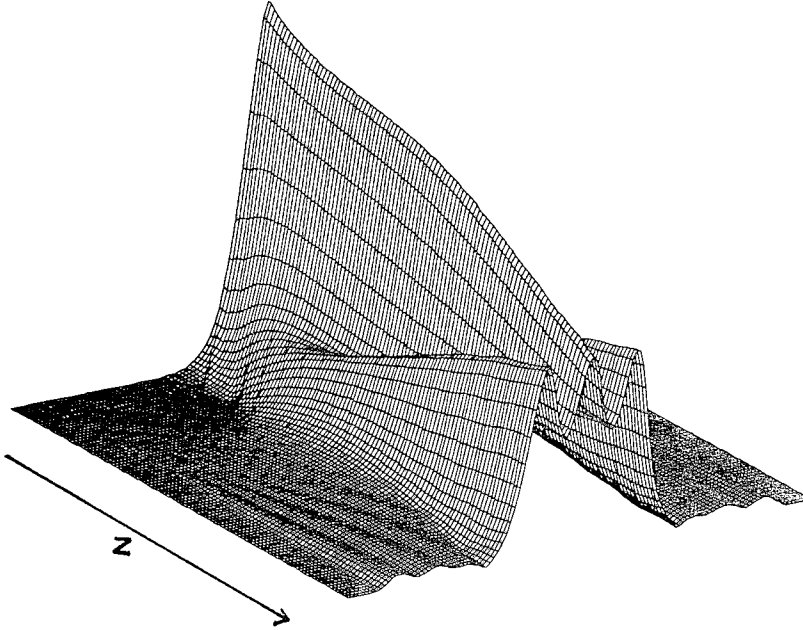


Figure 5. Optical power coupling behaviour along the structure.

The power coupling efficiency of the outer waveguides as a function of propagating distance is calculated by evaluating the normalised overlap integral between the propagating modal field and eigenmode field of the outer waveguide. The mathematical expression for power coupling efficiency, $\eta(z)$, is given by,

$$\eta(z) = \frac{\left| \int_{-\infty}^{\infty} f(x) g^*(x, z) dx \right|^2}{\left| \int_{-\infty}^{\infty} f^2(x) dx \right| \left| \int_{-\infty}^{\infty} g^2(x, z) dx \right|} \quad (5)$$

where, $f(x)$ is the eigenmode function of the equivalent slab waveguide and $g(x, z)$ is the propagating field function which is calculated numerically by FFT-BPM.

In order to understand the dependence of the power coupling characteristics on the coupler parameters such as waveguide width, depth and separation, the maximum power coupling length L_m is calculated as a function of diffusion depth as well as diffusion window separation for a number of wavelengths. Figure 6 shows the variation of maximum power coupling length with diffusion depth for several wavelengths. For small depth, i.e. small V number, the power spreading of guide mode is higher hence the coupling is stronger. Therefore, the maximum power coupling length is lower. When the diffusion depth increases, the mode spreading is decreasing, therefore, the maximum power coupling length is increasing. On the other hand, when the diffusion depth increases, because of more side diffusion, the waveguide separation (wall to wall) is decreasing. Therefore, the maximum power coupling length is decreasing. As seen, this characteristic variation can clearly be identified for shorter wavelength than longer wavelength for this particular device. However, this kind of behaviour has not been very well discussed before.

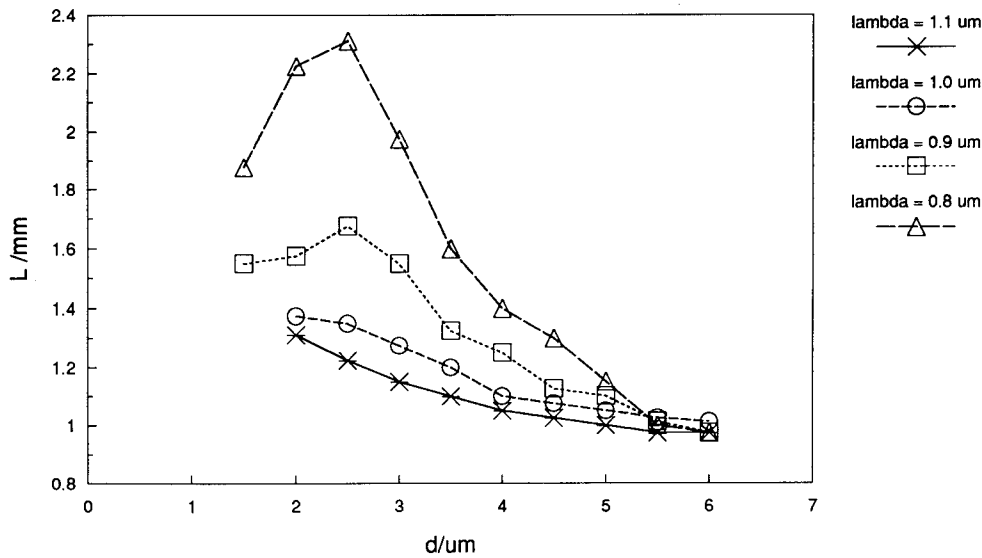


Figure 6. Maximum power coupling length of the structure as a function of diffusion depth for four different wavelengths ($2w = 5.0 \mu\text{m}$, $2s = 5.0 \mu\text{m}$).

Nevertheless, a coupler with deeper waveguide which can support more than one mode shows different characteristics. In this case, the variation of maximum power coupling with waveguide depth cannot be explained simply because each individual waveguide of the coupler becomes multimode. Furthermore, a coupler with shallow waveguides shows large differences of the maximum power coupling length with wavelength. This is not favourable for the devices construction particularly for the wavelength-flattened power splitters.

Knowing with the detail discussed here, the wavelength dependence of power coupling efficiency, $\eta(\lambda)$, of the device is calculated. In our calculations, the maximum power coupling length, L_m , for $\lambda = 1.0\mu m$, is used as the device length for each diffusion depth. Figure 7 shows the calculated wavelength characteristics of the device for three different diffusion depth.

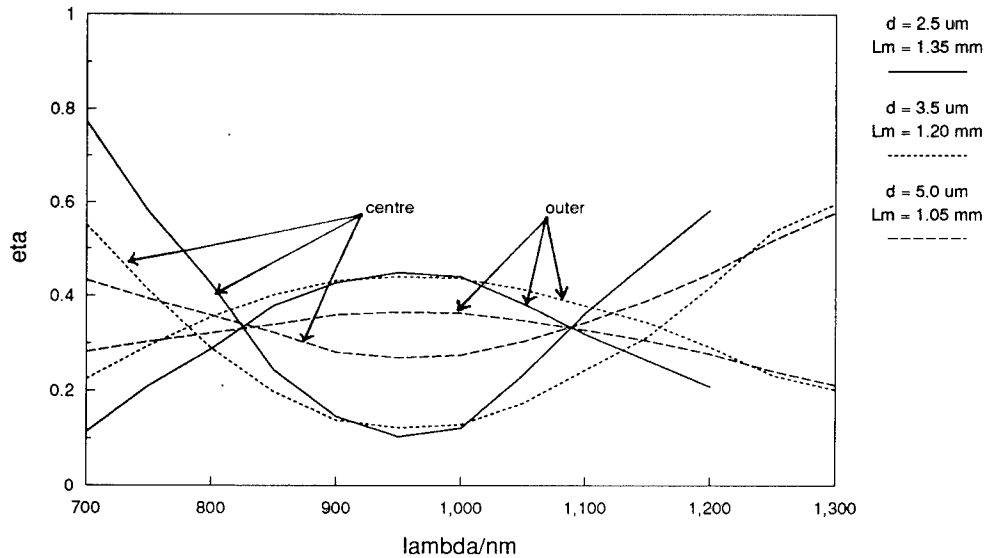


Figure 7. Power coupling efficiency of the device as a function of wavelength with diffusion depth as a parameter ($2w = 5.0 \mu m$, $2s = 5.0 \mu m$).

As seen in Figure 7, because of asymmetric condition, there is no 100% power coupling to outer waveguides. Also, the power coupling efficiency of outer waveguide is decreasing with the increasing of diffusion depth, however, wavelength-flattened characteristic is increasing.

EXPERIMENTAL INVESTIGATION

Following the above analysis, a number of power splitting devices have been fabricated using K^+/Na^+ ion-exchange process¹⁴. For easy fabrication and handling, the device length is chosen to be approximately five times that of the maximum coupling length, L_m for $\lambda = 1.0\mu m$. However, for the optimum performance, it is desirable to use shorter device length.

Using the experimental set-up is shown in Reference 15, the output optical power in each arm of the coupler is measured. $P_{i,o}$ ($i=1,2,3$) is the measured output optical power in each arm. Assuming that the propagation loss is negligible, the experimental power coupling efficiency, $\eta_i(\lambda)$, of each arm of the coupler is calculated using the following equation.

$$\eta_i(\lambda) = \frac{P_{i,o}}{P_e} = \frac{P_{i,o}}{P_{1,o} + P_{2,o} + P_{3,o}} \quad (6)$$

The experimental results of the coupler in comparison with the theoretical results are shown in Figure 8.

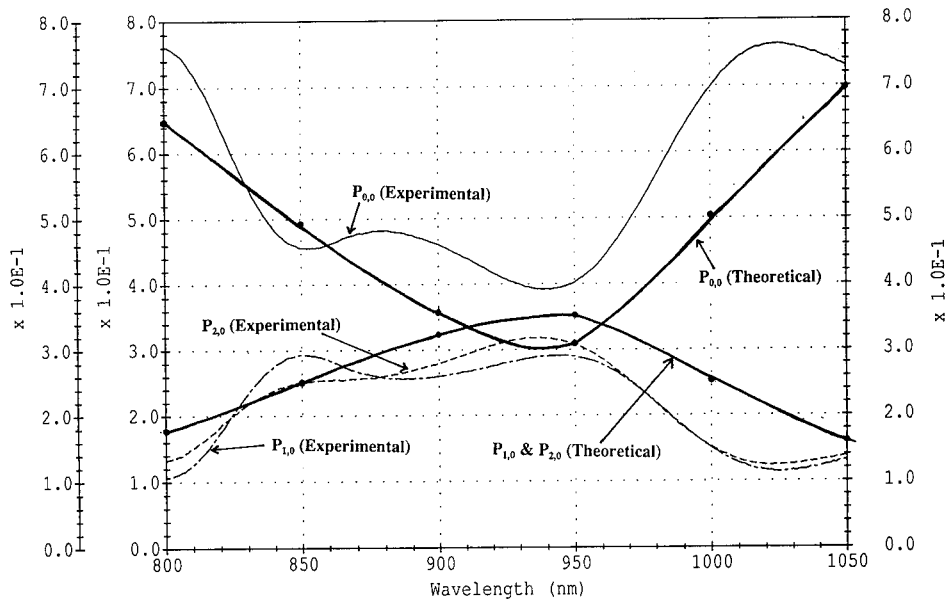


Figure 8. Experimental power coupling efficiency in comparison with the theoretical results ($2w = 5.0\mu m$, $2s = 5.0\mu m$, $5L_m = 6.0\mu m$, $d = 3.5\mu m$).

The device exhibits a wavelength-flattened characteristic over wide wavelength range about 150 nm. Since the structure is symmetric with respect to the central waveguide, theoretically, the optical power in two outer waveguides should be equal. However, the experimental results show a little difference between two outer waveguides. This is because

the input optical field is not exactly aligned to the middle of centre waveguide. Overall, the experimental results show quite good agreement with the theoretical results. The device presented here can be used as a 5 dB optical power splitter from about 830 nm to 980nm wavelength region. Also, the above mentioned procedure can be extended to the desired wavelength region by simply changing the waveguide parameters of the coupler.

CONCLUSION

K⁺/Na⁺ ion-diffused three core optical coupler has been analysed for optical power splitters with wavelength-flattened characteristics over wide wavelength range. It has been shown that the discretionary power splitting ratio can be obtained by properly regulating the device parameters. Based on the theoretical analysis, 5 dB splitter has been fabricated with good power splitting ratio. This kind of devices will find useful applications in optical signal processing networks, particularly in the systems working with multiplexed optical signals. Also, the device fabrication procedure is low-cost and batch production is possible.

ACKNOWLEDGEMENT

The authors wish to thank Dr. I. Skinner for fruitful discussions on this project and Dr. E. Gauja for photolithography processing. Financial support from the National Sciences Foundation, USA and from the School of Electrical Engineering, UNSW, Australia is gratefully acknowledged.

REFERENCES

1. Z. Weissman, A. Hardy, and E. Marom, Mode dependent radiation loss in Y-junction and directional couplers, *IEEE J. Quantum Electron.* QE-25:1200 (1989).
2. K. Al-hemyari, F. Doughty, C. D. W. Wilkinson, A. H. Kean, and C. R. Stanley, Optical loss measurement of GaAs/GaAlAs single-mode waveguide Y-junctions and waveguide bends, *J. Lightwave Technol.* 11:272 (1993).
3. A. Takagi, K. Jinguji, and M. Kawachi, Design and fabrication of silica-based waveguide-type (3X3) directional couplers with two identical outer waveguides, *Jpn. J. Appl. Phys.* 31:1618 (1992).
4. H. A. Haus and C. G. Fonstad, Jr, Three-waveguide couplers for improved sampling and filtering, *IEEE J. Quantum Electron.* QE-17:2321 (1981).
5. J. P. Donnelly, N. L. DeMeo, Jr, and G. A. Ferrante, Three-guide optical couplers in GaAs, *J. Lightwave Technol.* LT-1:417 (1983).

6. J. P. Donnelly, Limitation of power-transfer efficiency in three-guide optical couplers, *IEEE J. Quantum Electron.* QE-22:610 (1986).
7. J. P. Donnelly, H. A. Haus, and N. Whitakel, Symmetric three-guide optical couplers with nonidentical centre and outside guides, *IEEE J. Quantum Electron.* QE-23:401 (1987).
8. A. Hardy and W. Streifer, Coupled mode solutions of multiwaveguide systems, *IEEE J. Quantum Electron.* QE-22:528 (1986).
9. K. Kishioka and G. L. Yip, A novel three-wavelength demultiplexer utilizing the two- and three-guide couplers, *J. Lightwave Technol.* 11:234 (1993).
10. D. Yevick and B. Hermansson, Efficient beam propagation techniques, *IEEE J. Quantum Electron.* 26:109 (1990).
11. G. B. Hocker and W. K. Burns, Mode dispersion in diffused channel waveguides by the effective index method, *Appl. Opt.* 16:113 (1977).
12. J. Crank, "The Mathematics of Diffusion," Oxford University Press, Ely House, London (1967).
13. H. C. Cheng and R. V. Ramaswamy, Symmetric directional coupler as a wavelength multiplexer-demultiplexer: Theory and experiment, *IEEE J. Quantum Electron.* 27:567 (1991).
14. A. Miliou, H. Zhenguang, H. C. Cheng, R. Srivastava, and R. V. Ramaswamy, Fiber-compatible K^+-Na^+ ion-exchanged channel waveguides: Fabrication and characterization, *IEEE J. Quantum Electron.* 25:1889 (1989).
15. G. Hewa-Gamage and P. L. Chu, Single band and multi-band optical waveguide wavelength filters using ion-exchange process, *in: this issue* (1994).

SINGLE BAND AND MULTI-BAND OPTICAL WAVEGUIDE WAVELENGTH FILTERS USING ION-EXCHANGE PROCESS

G. Hewa-Gamage and P. L. Chu

Optical Communications Group
University of New South Wales
Sydney 2052
Australia

INTRODUCTION

Optical wavelength filters are very important devices for optical communication systems. More recently, the application of optical frequency filters in soliton transmission systems has been reported^{1,2}. Over a decade ago, LiNbO₃ waveguide filters were very popular³. This was mainly due to the fact that the filter could be made tuneable by simply varying the applied voltage. However, it suffered from the disadvantage that its refractive index does not match that of the fibre. Also, an InGaAsP-InP integrated optics wavelength filter was proposed and demonstrated⁴, but its fabrication technique is more complex hence device cost is very high. In recent years, ion exchanged waveguides have been developed⁵. As a results, a filter design based on ion-exchange process has been proposed^{6,7}. These designs are based on co-propagating waves in parallel waveguide structure. The two waveguides are made synchronous at a particular wavelength so that only the propagating wave at that wavelength may be coupled into the adjacent waveguide. In the parallel coupler scheme, however, considerable crosstalk may occur if the two waveguides are closely coupled. Also in the parallel coupler filter, the tolerance for the coupling length is very strict and any deviation from the exact coupling length may introduce additional crosstalk. Furthermore, the spectral response of parallel coupler has large sidelobes.

It has been suggested that a taper may be introduced at the input and output ports of the parallel coupler to eliminate the crosstalk⁸. The taper structure has also been employed to suppress the sidelobes of the filter response⁹. It has recently been shown that this structure can also be used to improve the length tolerance of the filter¹⁰. Furthermore, by cascading two or more optical couplers, it is possible to construct optical wavelength bandpass filters with small sidelobes¹¹.

In this paper, we show that a bandpass filter consisting of a length of parallel waveguide coupler followed by a tapered velocity coupler in K^+/Na^+ ion-exchanged glass can be constructed. There is an excellent agreement between the theoretical and experimental results. In addition, we show that a wavelength filter consisting of two cascaded parallel couplers followed by a tapered velocity coupler exhibits considerably narrow bandwidth with very small sidelobes. With this structure, it is also possible to design filters with multiple passbands.

THEORETICAL ANALYSIS

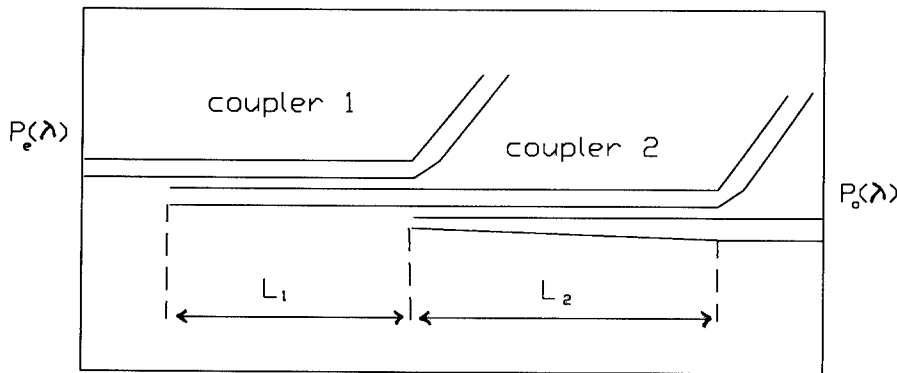


Figure 1. Schematic representation of optical wavelength bandpass filter structure.

A schematic diagram of the proposed wavelength filter is shown in Figure 1. It consists of a length L_1 of parallel waveguide coupler followed by a length L_2 of tapered velocity coupler. This tapered velocity coupler consists of two closely coupled waveguides, one has constant width and other has an increasing width. The refractive index profile in the depth direction for both waveguides can be the same. On the other hand, the two waveguides in the parallel coupler can be identical in waveguide width and refractive index. The propagation constant

β_u of each uniform waveguide can be calculated by means of Marcatili's analysis¹² with some modification for ion-exchanged waveguides. It is a function of operating wavelength as well as the waveguide dimensions and refractive indices. On the other hand, the propagation constant β_t of the tapered waveguide is also a function of the longitudinal z axis as well as the wavelength and waveguide dimensions. The calculation of β_t can be facilitated by dividing the tapered waveguide into successive sections of uniform waveguides with constant width and length Δz . The waveguide width of successive section increases according to the taper rate. This is called the multiple elemental segments approach¹³. The filter action of the complete structure relies on the combination of the frequency responses of the parallel coupler and the tapered coupler. The upper cut-off wavelength of the filter is given by the condition,

$$N_{eff}(\lambda) = n_b(\lambda) \quad (1)$$

where, $n_b(\lambda)$ wavelength dependent refractive index of the substrate and $N_{eff}(\lambda)$ is the effective index of the waveguide and is given by,

$$N_{eff}(\lambda) = \beta_u \lambda / 2\pi \quad (2)$$

The lower cut-off wavelength of the filter is determined by the slope of the rising edge of the wavelength response of the tapered velocity coupler¹³. This slope is related to the taper angle of the waveguide.

To model the filter structure shown in Figure 1, the solutions to the standard coupled mode equations for parallel coupler¹⁴ are used. Neglecting the exponential term, the complex field amplitudes a_1 and a_2 in each waveguide of the parallel coupler can be expressed as,

$$a_1(z) = a_1(0) \cos\left(\frac{C}{F} z\right) + iF \left[a_2(0) + \frac{\delta}{C} a_1(0) \right] \sin\left(\frac{C}{F} z\right) \quad (3a)$$

$$a_2(z) = a_2(0) \cos\left(\frac{C}{F} z\right) + iF \left[a_1(0) - \frac{\delta}{C} a_2(0) \right] \sin\left(\frac{C}{F} z\right) \quad (3b)$$

where, $\delta = (\bar{\beta}_1 - \bar{\beta}_2)/2$ and other variables are as defined in Reference 14.

Although Eqs. (3) are used to analyse a parallel waveguide coupler, the multiple elemental segments approach is used to analyse a tapered velocity coupler. Therefore, the field amplitudes at position $z + \Delta z$ where Δz is an elemental increase in z are given by,

$$a_1(z + \Delta z) = a_1(z) \cos\left(\frac{C \Delta z}{F(z)}\right) + iF(z) \left[a_2(z) + \frac{\delta(z)}{C} a_1(z) \right] \sin\left(\frac{C \Delta z}{F(z)}\right) \quad (4a)$$

$$a_2(z + \Delta z) = a_2(z) \cos\left(\frac{C \Delta z}{F(z)}\right) + iF(z) \left[a_1(z) - \frac{\delta(z)}{C} a_2(z) \right] \sin\left(\frac{C \Delta z}{F(z)}\right) \quad (4b)$$

where, $\delta(z) = \{\beta_u - \beta_l(z)\}/2$ and $F(z) = \left[1 + \left(\frac{\delta(z)}{C}\right)^2\right]^{-1/2}$. C is the coupling coefficient

between two parallel waveguides having lateral dimensions equal to the average lateral dimensions of the tapered waveguide and it is assumed to be constant along the waveguide for small tapering^{15,16}.

Applying Eqs. (3) and (4) throughout the whole filter structure, we can obtain the wavelength response of the output power at one of the arms of the tapered velocity coupler. Figure 2 shows the power coupling efficiency $\eta(\lambda)$ of a filter where $\eta(\lambda)$ is defined as,

$$\eta(\lambda) = \frac{P_o(\lambda)}{P_e(\lambda)} \quad (5)$$

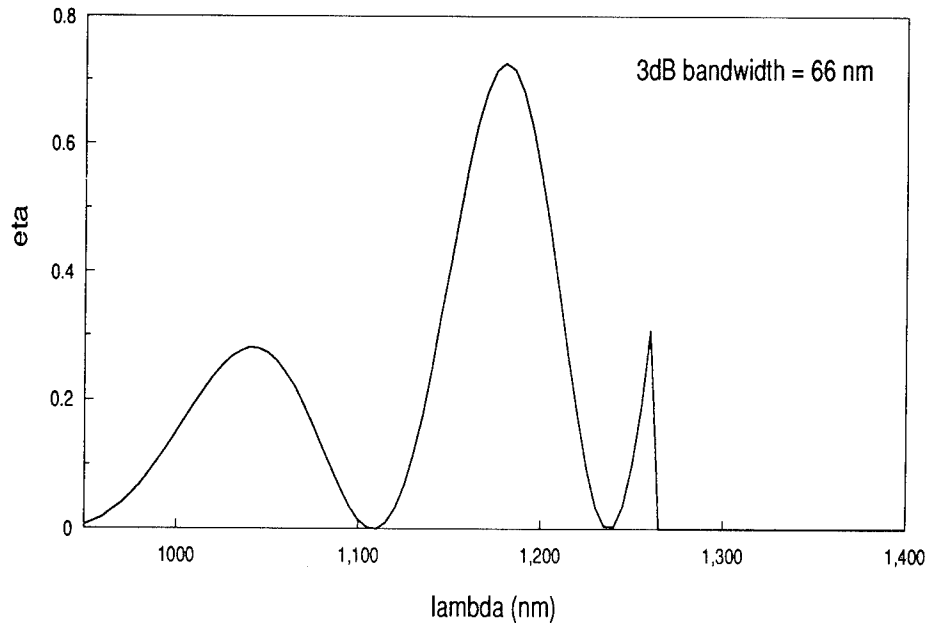


Figure 2. Power coupling efficiency of single bandpass optical wavelength filter made with cascaded two optical couplers (Theoretical).

The filter considered here has the following parameters corresponding to the TE mode:- Waveguide surface refractive index change, Δn_s is 0.009, substrate refractive index, n_b , at $\lambda = 0.6328 \mu\text{m}$ is 1.52 and cover refractive index, n_c is 1.0.

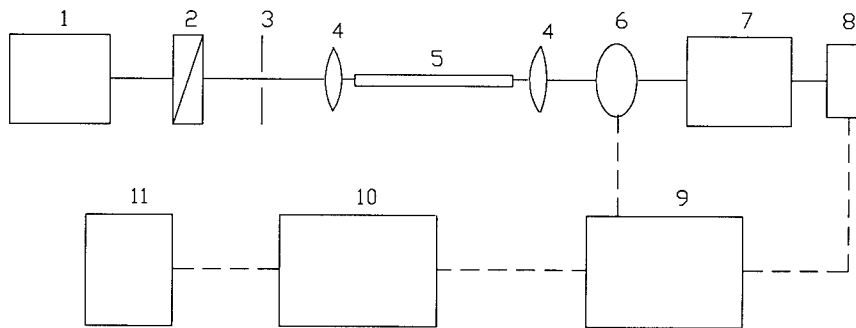
Coupler 1 (uniform):- Waveguide width, w is $10.5 \mu\text{m}$, waveguide depth, d is $2.8 \mu\text{m}$, waveguide separation, s is $2.7 \mu\text{m}$ and interaction length, L is 31 mm.

Coupler 2 (tapered):- Uniform waveguide width, w is $10.5 \mu\text{m}$, tapered waveguide: initial width, w_i is $8.5 \mu\text{m}$, final width, w_f is $11.5 \mu\text{m}$, waveguide depth, d is $2.8 \mu\text{m}$, waveguide separation, s is $3.8 \mu\text{m}$ and interaction length, L is 32 mm.

The centre wavelength of this filter is 1180 nm with a bandwidth of 66 nm and sidelobes occur at 1030 nm and 1250 nm respectively. Both sidelobes have amplitudes at about 30% of the peak value at centre wavelength.

EXPERIMENTAL RESULTS

A wavelength filter based on the structure of Figure 1 has been fabricated on glass substrate using the K^+/Na^+ ion-exchange technique¹⁷. The parameters of the waveguides are the same as given in the theoretical simulation.



1-white light source, 2-polarizer, 3-pinhole, 4-lens, 5-waveguide filter, 6-chopper, 7-monochromator, 8-photodetector, 9-lock-in amplifier, 10-personal computer, 11-printer.

Figure 3. Experimental set-up for the characterisation of optical wavelength bandpass filter.

The optical output spectrum of the filter is obtained by employing the experimental set-up shown in Figure 3. Using this set-up the polarised white light is launched into the device and output beam is focused into the monochromator through the small slit. The monochromatic light is then detected by the germanium detector and feed into the lock-in-amplifier which is synchronized with the chopping frequency. Amplified signal is then collected by the personal computer and the processed signal is printed by a laser printer.

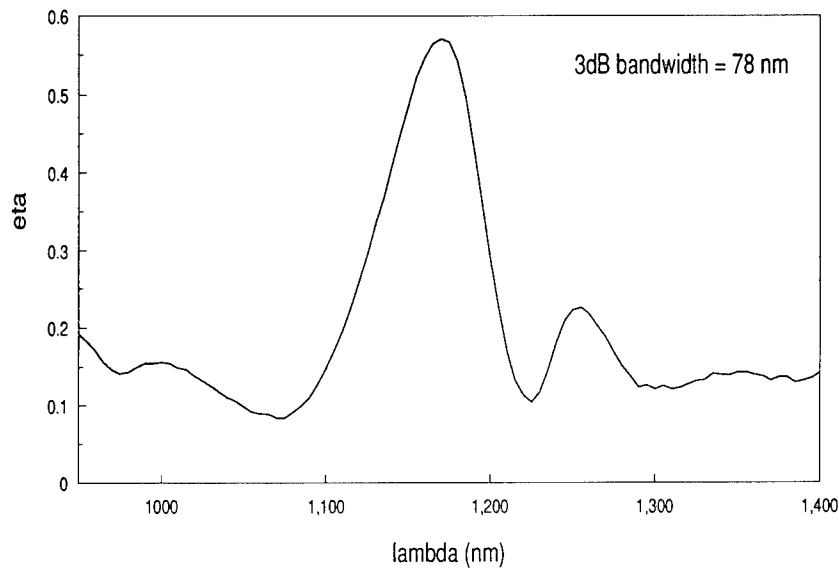


Figure 4. Power coupling efficiency of single bandpass optical wavelength filter made with cascaded two optical couplers (Experimental).

The measured wavelength response of the coupling efficiency of this filter for TE mode is shown in Figure 4. It can be seen that the centre wavelength is at 1170 nm which agrees with that of the theoretical filter. The sidelobes occur at 1000 nm and 1250 nm respectively. The amplitude of the sidelobe at 1000 nm is 15% of that of the main lobe while the amplitude of the sidelobe at 1250 nm is 22%. The 3 dB bandwidth is 78 nm as compared to 66 nm from the theory.

THREE-COUPLER FILTERS

We can now generalise the theory to three-coupler filters. These filters consist of two parallel couplers followed by a tapered coupler. The function of the two parallel couplers is to produce a wavelength response function with narrow but periodic passbands. The tapered velocity coupler is then used to select a particular passband for output. It also has the function

of narrowing the passband further and suppressing the sidelobes. Thus Figure 5 shows a design of a three-coupler filter that gives a 3 dB bandwidth of 46 nm centred at 1300 nm with sidelobe amplitudes of 7% of main lobe. The parameters of this filter for TE mode are,

$$\Delta n_s = 0.009, n_b = 1.52 (\lambda = 0.6328 \mu\text{m}), n_c = 1.0$$

Coupler 1 (uniform):- $w = 10.0 \mu\text{m}, d = 3.15 \mu\text{m}, s = 1.0 \mu\text{m}, L = 15.5 \text{ mm}$

Coupler 2 (uniform):- $w = 10.0 \mu\text{m}, d = 3.15 \mu\text{m}, s = 1.5 \mu\text{m}, L = 9.7 \text{ mm}$

Coupler 3 (tapered):- $w = 10.0 \mu\text{m}, w_i = 9.0 \mu\text{m}, w_f = 11.0 \mu\text{m}, d = 3.15 \mu\text{m},$
 $s = 3.9 \mu\text{m}, L = 9.0 \text{ mm}$

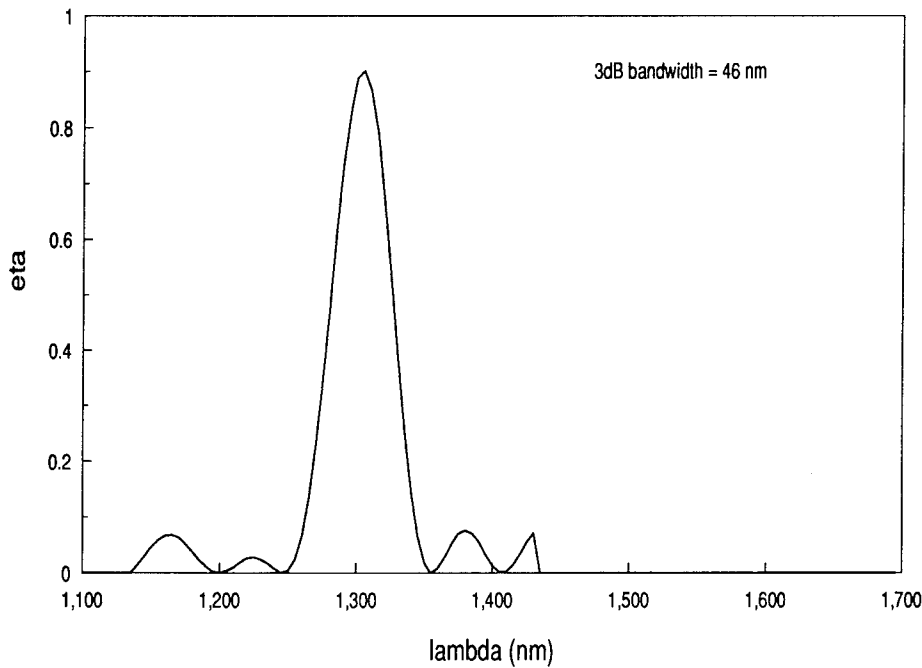


Figure 5. Power coupling efficiency of single bandpass optical wavelength filter designed with cascaded three optical couplers (Theoretical).

The three-coupler filter can also be designed to exhibit multiband characteristic. Figure 6 shows a filter with passbands at 1300 nm and at 1520 nm. The 3 dB bandwidth at 1300 nm is 46 nm and at 1520 nm is 42 nm. The sidelobe amplitudes are also around 7% of the main lobe. The parameters of this filter are,

$$\Delta n_s = 0.009, n_b = 1.52 (\lambda = 0.6328 \mu\text{m}), n_c = 1.0$$

Coupler 1 (uniform):- $w = 10.0 \mu\text{m}, d = 3.65 \mu\text{m}, s = 1.0 \mu\text{m}, L = 15.5 \text{ mm}$

Coupler 2 (uniform):- $w = 10.0 \mu\text{m}, d = 3.65 \mu\text{m}, s = 1.5 \mu\text{m}, L = 9.7 \text{ mm}$

Coupler 3 (tapered):- $w = 10.0 \mu\text{m}, w_i = 9.0 \mu\text{m}, w_f = 11.0 \mu\text{m}, d = 3.65 \mu\text{m},$
 $s = 4.2 \mu\text{m}, L = 13.5 \text{ mm}$

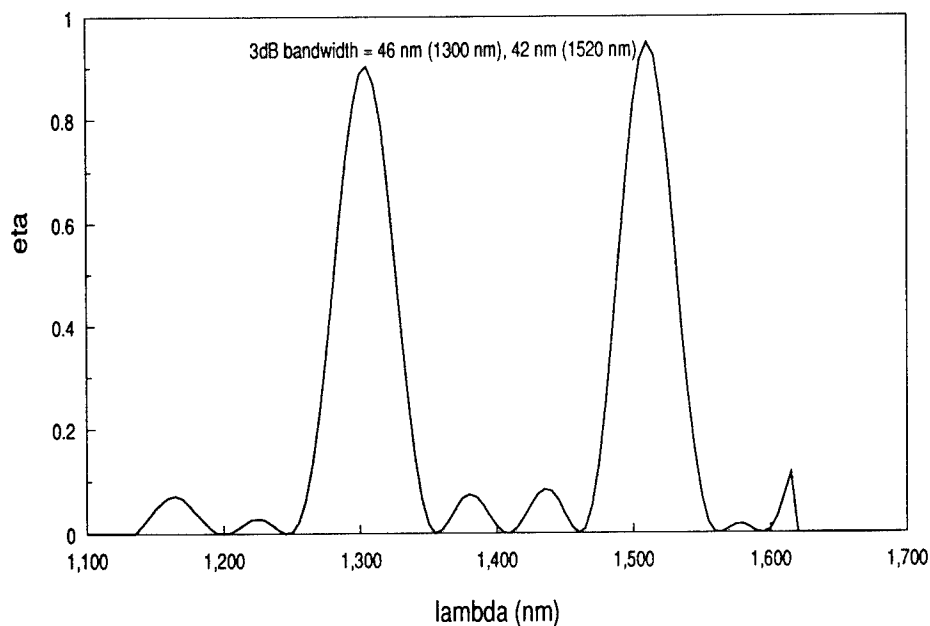


Figure 6. Power coupling efficiency of double bandpass optical wavelength filter designed with cascaded three optical couplers (Theoretical).

CONCLUSION

A combination of one or two parallel couplers followed by a tapered coupler can function as a single bandpass or multi-bandpass wavelength filters. Such filter has been fabricated using ion-exchanged optical waveguides. There is a good agreement between the theoretical and experimental results.

ACKNOWLEDGMENT

The authors wish to thank Dr. I. Skinner for valuable discussion and Dr. E. Gauja for photolithography processing.

REFERENCES

1. H. A. Haus, Molding light into solitons, *IEEE Spectrum* 30:48 (1993).
2. A. Mecozzi, J. D. Moores, H. A. Haus, and Y. Lai, Soliton transmission control, *Opt. Lett.* 16:1841 (1991).
3. R. C. Alfiness, Guided-wave devices for optical communication, *IEEE J. Quantum Electron.* QE-17:946 (1981).
4. B. Broberg, B. S. Lindgren, M. G. Oberg, and H. Jiang, A novel integrated optics wavelength filter

- in InGaAsP-InP, *J. Lightwave Technol.* LT-4:196 (1986).
5. R. Srivastava and R. V. Ramaswamy, Ion-exchanged waveguides: current status, *in: SPIE Vol.1583 Integrated Optical Circuits* (1991).
 6. H. C. Cheng and R. V. Ramaswamy, Symmetrical directional coupler as a wavelength multiplexer-demultiplexer: Theory and experiment, *IEEE J. Quantum Electron.* 27:567 (1991).
 7. I. S. Mauchline and G. Stewart, Fabrication of buried channel waveguides in K⁺-Na⁺ ion-exchanged glass and their application to notch filters, *Opt. Lett.* 18:1801 (1993).
 8. H. A. Haus and N. A. Whitaker, Jr., Elimination of cross talk in optical directional couplers, *Appl. Phys.* 44:1 (1985).
 9. R. C. Alferness and P. S. Cross, Filter characteristics of codirectionally coupled waveguides with weighted coupling, *IEEE J. Quantum Electron.* QE-11:843 (1978).
 10. W. P. Huang, B. E. Little, and S. K. Chaudhuri, Optical wavelength filter with tapered couplers, *IEEE Photon. Technol. Lett.* 3:809 (1991).
 11. G. Hewa-Gamage and P. L. Chu, Single band and multi-band optical waveguide wavelength filters, *in: Proc. of the Eighteenth Australian Conference on Optical Fibre Technology*, IREE Australia, Edgecliff (1993).
 12. E. A. J. Marcatili, Dielectric rectangular waveguide and directional coupler for integrated optics, *Bell Syst. Tech. J.* 48:2071 (1969).
 13. R. A. Betts and G. Hewa-Gamage, Broadband polarisation independent tapered optical couplers, *in: Proc. of the Fifteenth Australian Conference on Optical Fibre Technology*, IREE Australia, Edgecliff (1990).
 14. A. W. Snyder and J. D. Love, Cross-talk, *in: Optical Waveguide Theory*, Chapman and Hall, New York (1983).
 15. M. G. F. Wilson and G. A. Teh, Tapered optical directional coupler, *IEEE Trans. Microwave Theory Tech.* MTT-23:85 (1975).
 16. R. B. Smith, Analytic solutions for linearly tapered directional couplers, *J. Opt. Soc. Am.* 66:882 (1976).
 17. A. Miliou, H. Zhenguang, H. C. Cheng, R. Srivastava, and R. V. Ramaswamy, Fiber-compatible K⁺-Na⁺ ion-exchanged channel waveguides: Fabrication and characterization, *IEEE J. Quantum Electron.* 25:1889 (1989).

SYNTHESIS OF OPTICAL INTERCONNECTS AND LOGIC GATES

Lakshman S. Tamil¹ and Arthur K. Jordan²

¹Erik Jonsson School of Engineering and Computer Science, and
Center for Applied Optics, The University of Texas at
Dallas, Richardson, TX 75083, U.S.A.

²Remote Sensing Division, Naval Research Laboratory,
Washington, D.C. 20375, U.S.A.

OPTICAL INTERCONNECTS

The first part of this paper presents a method for designing guided wave optical interconnects with reduced clock skew, applicable in a chip-to-chip or intra chip situation. The interconnect consists of a multimode trunk waveguide and a set of single mode branch waveguides each of which couples one mode out of the trunk waveguide (see Fig.1). The graded-index guided wave interconnects can effectively reduce clock skew by suitable design of the refractive index profiles [1],[2]. This design is accomplished by properly tailoring the propagation constants of the guided modes to provide equal propagation times to a set of detectors. The scheme presented in this paper employs several optical channels, each having a different refractive index profile. This includes a main multimode channel and several single-mode waveguides coupled to the main line. Total system design takes into account the problem of clock skew as well as efficient coupling between the trunk and branch waveguides. An inverse scattering technique that provides the design parameters of an optoelectronic guided-wave structure from the prescribed transmission characteristics has been used to design the interconnect. This technique is contrary to the traditional techniques which require iterative adjustments of the design parameters to achieve the required transmission characteristics.

Optical Interconnect Circuit

The interconnect network is to be mounted on a GaAs wafer as shown in Fig.1. The goal of the interconnect circuit is to deliver a pulse from the source to each of the detector points on the wafer simultaneously. The circuit consists of N detectors or chips at points $P_{(1)}...P_{(N)}$ connected by a network of integrated optical waveguides consisting

of a N -mode trunk line feeding N branches, which are generally of a different design from the trunk.

Denoting the refractive index of the waveguide cladding (assumed, for simplicity, to be the same on both sides of the guiding layer) by n_2 , a pulse impressed upon a given mode with propagation constant β travels at the group velocity v_g , where

$$\frac{1}{v_g} = \frac{d\beta}{d\omega} = \frac{\omega}{\beta} \frac{n_2^2}{c^2}, \quad (1)$$

so that a pulse traverses a given length L in time

$$\tau = \frac{\omega}{\beta} \frac{n_2^2}{c^2} L. \quad (2)$$

Here, ω denotes the angular frequency of the radiation, and c is the vacuum velocity of light. Consider a clock pulse launched into the interconnect at point S . The time for a given mode to propagate from S to a designated $P_{(m)}$ is

$$\tau_m = \frac{\omega}{\beta_m} \frac{n_2^2}{c^2} L^{(m)} \text{ sec.}, \quad m = 1, \dots, N, \quad (3)$$

where $L^{(m)}$ is the distance from the source to $P_{(m)}$, and β_m is the propagation constant of the mode delivering the signal to $P_{(m)}$.

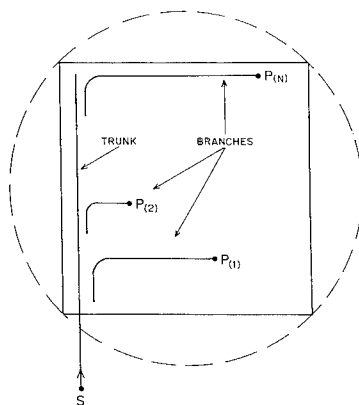


Figure 1. The guided-wave optical interconnect. Refractive index profiles are designed so that pulse launched from point S reaches each of the points $P(1), P(2), \dots, P(N)$ simultaneously.

For the purposes of this analysis, the important quantities are the total distances from the source to the points $P_{(m)}$. Arranging these in order of increasing length,

$$L_N > L_{N-1} > \dots > L_1, \quad (4)$$

so that $L_N = \max \{L^{(m)}\}$, $L_1 = \min \{L^{(m)}\}$, the points $P_{(1)} \dots P_{(N)}$ will be synchronized if the propagation constants satisfy

$$\frac{\beta_2}{\beta_1} = \frac{L_2}{L_1}; \quad \frac{\beta_3}{\beta_2} = \frac{L_3}{L_2}; \quad \dots; \quad \frac{\beta_N}{\beta_{N-1}} = \frac{L_N}{L_{N-1}}. \quad (5)$$

This provides us with a set of N propagation constants

$$\beta_1 < \beta_2 < \dots < \beta_N \quad (6)$$

which must be supported as propagating modes within the interconnect. The propagation constants themselves are restricted to the range

$$k_0 n_2 < \beta_m < k_0 n_{max}, \quad (7)$$

where n_{max} is the maximum core refractive index, and n_2 the refractive index of the cladding.

The design of the interconnect circuit consists of two interrelated parts. The first concerns the design of the refractive index profile for the multimode trunk waveguide, based upon the spectrum generated in Eq.(5). The second involves the design of the branch waveguides, each of which must efficiently couple off the appropriate mode from the trunk and deliver it to the designated point.

Transform Technique

Inverse scattering theory provides a frame work whereby the refractive index profile can be reconstructed from a set of eigen values selected *a priori*. We employ here the method of transformations known as Darboux or Crum-Krein transformations to obtain multimode potentials suitable for refractive index design in optical interconnects. The transform procedure is a technique which allows for the construction of N - mode potentials by specifying *a priori* a set of bound state eigenvalues, derived from the set $\{\beta_1, \beta_2, \dots, \beta_N\}$ via $k^2 \equiv k_0^2 n_2^2 - \beta^2$

$$k_m \in \{i\kappa_1, i\kappa_2, \dots, i\kappa_N\}, \quad (8)$$

where

$$\kappa_N \geq \kappa_{N-1} \geq \dots \geq \kappa_1 > 0. \quad (9)$$

The following discussion does not constitute proof of the transformation method, for which interested readers are referred to reference [3]. Rather, it outlines the practical steps necessary to construct a particular class of potentials which suit the purposes of refractive index profile design.

In the method outlined here, we are adding the N bound states to some chosen initial potential designated $v_0(x)$ which is assumed to contain no bound states. As additional input data, we require the explicit form of the Jost solutions $f_{\pm}^b(k, x)$ associated with $v_0(x)$.

Defining the N linear combinations of the Jost solutions as

$$\gamma_m \equiv (-1)^{m+1} f_+^b(i\kappa_m, x) + \rho_m f_-^b(i\kappa_m, x) \quad m = 1, \dots, N, \quad (10)$$

where ρ_m is an arbitrary positive definite parameter, the corresponding N - mode potential is simply:

$$v_N(x) = v_0(x) - 2 \frac{d^2}{dx^2} \ln W(\gamma_1, \dots, \gamma_N). \quad (11)$$

In the above equation, the quantities $W()$ denote Wronskians, i.e.,

$$W(\gamma_1, \gamma_2, \dots, \gamma_N) \equiv \begin{vmatrix} \gamma_1 & \gamma_2 & \dots & \gamma_N \\ \gamma_1' & \gamma_2' & \dots & \gamma_N' \\ \vdots & \vdots & \ddots & \vdots \\ \gamma_1^{(N-1)} & \gamma_2^{(N-1)} & \dots & \gamma_N^{(N-1)} \end{vmatrix}, \quad (12)$$

whose rows consist of functions $\gamma_1 \dots \gamma_N$ differentiated with respect to x from zero to $N - 1$ times. Equation(12) clearly illustrates the manner in which the N bound states are progressively added in stages represented by rows and columns of the Wronskian.

To demonstrate the procedure used here, we have used the data set $\{\beta_1, \beta_2, \beta_3, \beta_4, \beta_5\} = \{1.01034, 1.03202, 1.05369, 1.07611, 1.09752\}$ and have reconstructed the refractive index profile shown in Fig.2. We assume here $n_2 = 3.0$ and $\lambda = 0.9\mu m$. The eigenvalues are equally spaced and all $\rho_m = 1$. The resulting refractive index profile is symmetric about the origin and provides a smooth single channel. If near-degeneracies are introduced into the spectrum, splits will occur in the refractive index profile. The nature and extent of the splits will depend upon the number of modes involved.

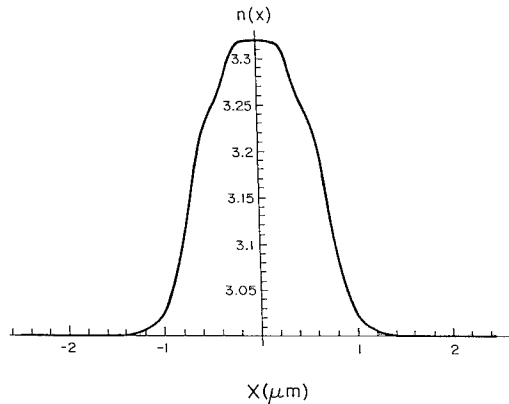


Figure 2. The smooth symmetric trunk refractive index profile resulting from evenly spaced eigenvalues and $\rho_m = 1$ for all m .

This example illustrates the application of the reconstruction procedure to typical spectra compatible with GaAs technology, with resulting refractive index profiles which are symmetric and well-behaved. It is clear from our analysis that a material such as AlGaAs [4], with a large variation in refractive index as a function of mole fraction, is well suited to the proposed interconnect since it allows for a relatively large spread of propagation constants, and consequently, greater flexibility in placement of chips on the wafer.

As a check of our algorithm, one hundred data points representing the value of the refractive index profile shown in Fig.2 were used as input to a finite-difference algorithm, solving the wave equation of the direct problem whose output consisted of the corresponding five propagation constants. Results of this direct solution are $\{1.01054, 1.03218, 1.05377, 1.07614, 1.09752\}$ showing excellent agreement with the exact propagation constants.

It was possible to design an interconnect consisting of a multimode trunk waveguide coupled to several single mode branch waveguides, each of which delivers a selected mode to a detector, and by exploiting the group velocity dispersion inherent in multimode waveguides, it was possible to select a set of propagation constants such that each of the modes can be delivered to its assigned detector simultaneously, eliminating clock skew.

The synthesis of waveguides with prescribed propagation constants is the key to the design of this interconnect. Consequently, an inverse scattering algorithm was required to reconstruct the refractive index profile which would support guided modes with this preselected spectrum. It was determined that the method of transformations provided a flexible, efficient means of generating the multimode trunk refractive index profiles suited to our use. These profiles are continuous and decay rapidly in the transverse direction, making them well-suited to practical systems.

By manipulating the normalization constants, it was possible to take full advantage of the possibilities of the transformation method. In particular, it was possible to efficiently couple the trunk waveguide and each of the branch waveguides, despite the fact that the

trunk and branches consisted, in general, of different refractive index profiles. This analysis resulted in a formulation of waveguide coupling coefficients in terms of the scattering data pertaining to the corresponding potentials. It is emphasized that this formulation is completely general and applicable to any waveguide systems in which the weak coupling approximation is valid [5].

In addition, it was found that proper manipulation of the normalization constants guaranteed trunk refractive index profiles which were symmetric and, under certain circumstances, free from large index gradients. However, it is clear that in general, the freedom of choosing unequal lengths for clock distribution is gained at the cost of the complexity of the waveguide profile.

OPTICAL LOGIC GATES

The second part of the paper discusses the synthesis of optical logic gates (AND, OR and NOT) using nonlinear periodic and aperiodic guidedwave structures. Future communication technology requires the ability to process and transmit large amounts of data. Optics provides an excellent means for handling vast amounts of data but the data rate is limited by the data processing electronics used in the front and rear ends of the communication system. The inherent speed limitation of electronics and the conversion of electrons to photons and vice versa that are required in present systems decrease the processing and the transmission speeds. The development of all optical logic gates, which are the building blocks for the switching and processing operations of optical signals provides the most promising answer to this problem. In this paper all optical intensity controlled logic gates are demonstrated using nonlinear periodic and aperiodic waveguiding structures. Intensity controlled bistability was first reported by Winful, Marburger, and Garmire [6]. Much work has been done since then in the area of intensity controlled switching using nonlinear periodic waveguiding structures such as multiple quantum wells and super lattice structures. Here, we are applying the bistability property of the nonlinear periodic and aperiodic waveguiding structures to develop AND, OR and NOT logic gates.

Nonlinear periodic medium can be characterized by coupled nonlinear differential equations. If the forward travelling wave is denoted by A_s^+ with phase $+\beta_s z$ and the reverse travelling wave is denoted by A_s^- with a phase $-\beta_s z = \beta_l z$, the phase matching condition is $2\beta_s - \frac{2\pi}{\Lambda} = 0$, and can be satisfied by an appropriate choice of Λ , the spatial perturbation period, which couples the forward and backward traveling waves. Now an equation that describes the coupling of forward traveling wave to the backward traveling wave can be written as

$$\begin{aligned} \frac{\partial A_s^+}{\partial z} + \frac{\omega}{\beta_s} \frac{n_0^2(\omega)}{c^2} \frac{\partial A_s^+}{\partial t} = -j \frac{n_0 n_2}{c^2} \frac{\omega^2}{2\beta_s} \left(|A_s^+|^2 + 2|A_s^-|^2 \right) A_s^+ \\ - j \frac{n_0 n_1}{c^2} \frac{\omega^2}{2\beta_s} A_s^- e^{-j2\Delta\beta z} \end{aligned} \quad (13)$$

where $\Delta\beta = \beta_s - \frac{\pi}{\Lambda}$.

A similar equation representing the coupling of backward traveling wave to forward traveling can be written by interchanging the superscripts + and - in the above equation

and making appropriate sign changes in the phase and the phase match condition

$$\begin{aligned} \frac{\partial A_s^-}{\partial z} - \frac{\omega}{\beta_s} \frac{n_0^2(\omega)}{c^2} \frac{\partial A_s^-}{\partial t} = +j \frac{n_0 n_2}{c^2} \frac{\omega^2}{2\beta_s} \left(|A_s^-|^2 + 2|A_s^+|^2 \right) A_s^- \\ + j \frac{n_0 n_1}{c^2} \frac{\omega^2}{2\beta_s} A_s^+ e^{j2\Delta\beta z} . \end{aligned} \quad (14)$$

Equations (13) and (14) are same as those obtained in references [6]-[8].

The exact solutions for Eq. (13) and Eq. (14) can be obtained using the method of Armstrong et al. [9]. Since this is difficult even for the simplest case, we have used here a numerical method based on finite differences and absorbing boundary conditions to solve the nonlinear coupled mode equations.

AND Gate

The AND gate conceived here consists of a Y shaped coupler with two inputs and an output. The power in the two inputs are combined by the coupler and the combined output is fed into a nonlinear periodic waveguide whose output is the output of the AND gate as shown in Fig.3.

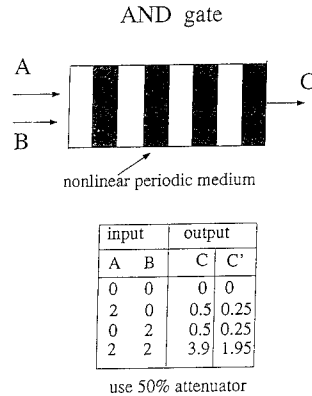


Figure 3. AND gate made up of a Y branch coupler and a nonlinear periodic waveguiding structure. A and B are the inputs and C is the output. C' is the output after 50% attenuation.

The nonlinear coupled differential equations (13) and (14) can be solved numerically to obtain the intensity dependent input - output characteristics of the nonlinear periodic waveguide. For a nonlinear constant $\gamma = 0.1$, coupling constant $\alpha = 0.5$, detuning $\Delta\beta = 0$, and normalized propagation length $L = 4$ the input-output amplitude relationship is shown in Fig.4.

Let the inputs of the AND gate be denoted by A and B and the output be denoted by C. The logical 1 and 0 are denoted respectively by amplitude values greater than 1 and 0.5. For discussion here, let us fix the input values of logical 0 to have the amplitude value 0 and logical 1 have the amplitude value 2.0. For logic operation 0-0, the combined output of the coupler has amplitude value 0. The output amplitude of the periodic waveguide for an input amplitude 0 is 0. After a 50% attenuation that is purposely introduced at the end of periodic waveguide, the amplitude output for logic AND operation 0-0 is 0 which denotes the logical value 0.

For logic AND operations 0·1 and 1·0, the combined output amplitude of the coupler is 2 which in turn is the input to the periodic nonlinear waveguide. From Fig.4 we see that the output of the periodic waveguide will be a normalized amplitude 0.5. After passing through a 50% attenuation, the output amplitude of the logic gate is 0.25 denoting a logic 0. For the logic AND operation 1·1, the output amplitude at the coupler is 4, that translates to an output amplitude 4 at the nonlinear waveguide which after 50% attenuation yields 2 corresponding to logic 1. The attenuator can be adjusted according to the dynamic range of the input-output characteristics.

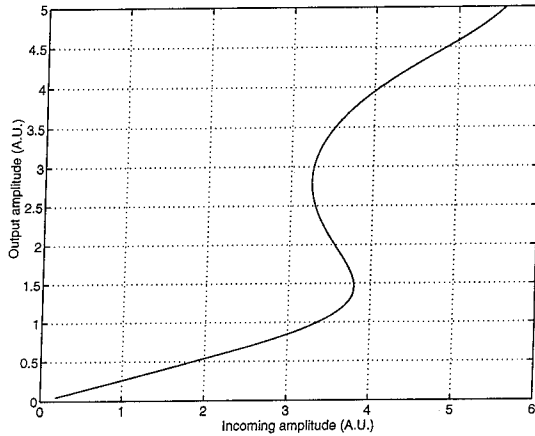


Figure 4. Input-output characteristics of a nonlinear periodic structure used for AND gate operation.

OR Gate

The logic operation OR cannot be achieved using a periodic structure, however studying the input-output characteristics of a nonlinear aperiodic structure suggests that the OR operation can be realized. The most fortunate aspect of this is that the aperiodic structures are compatible with the periodic structures studied earlier. They can be fabricated as multiple quantum well structures with varying thickness using molecular beam epitaxy techniques. Linear aperiodic transmission structures have been proposed earlier to compensate dispersion in high data rate fiber communication systems.

A linear chirped dielectric filter can be described by the following coupled mode equations [10]

$$\frac{dA_m^+}{dz} = \kappa A_m^- e^{-2i \int (\beta_{m0} - \frac{\pi}{\Lambda(z)}) dz}, \quad (15)$$

$$\frac{dA_m^-}{dz} = \kappa A_m^+ e^{2i \int (\beta_{m0} - \frac{\pi}{\Lambda(z)}) dz}, \quad (16)$$

where κ is the coupling coefficient β_{m0} is the propagation constant and $\Lambda(z)$ is the spatial frequency of the grating.

Letting $\Delta\beta(z) = \beta_{m0} - \frac{\pi}{\Lambda(z)}$, the coupled mode equations of the nonlinear aperiodic structure can be written using Eqs.(13) and (14) as :

$$\frac{\partial A_m^+}{\partial z} + \frac{n_0}{c} \frac{\partial A_m^+}{\partial t} = -j\gamma (|A_m^+|^2 + 2|A_m^-|^2) A_m^+ - j\alpha A_m^- e^{-j2 \int \Delta\beta(z) dz} \quad (17)$$

and

$$\frac{\partial A_m^-}{\partial z} - \frac{n_0}{c} \frac{\partial A_m^-}{\partial t} = j\gamma (|A_m^-|^2 + 2|A_m^+|^2) A_m^- + j\alpha A_m^+ e^{+2j \int \Delta\beta(z) dz} \quad (18)$$

where $\gamma = \frac{n_2 \beta_m}{2n_0}$ and $\alpha = \frac{n_1 \beta_m}{2n_0}$.

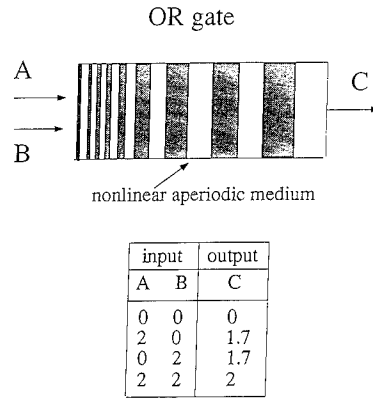


Figure 5. OR gate made up of a Y branch coupler and a nonlinear aperiodic waveguiding structure. A and B are the inputs and C is the output.

Using the two equations described above, the function of the OR gate can be simulated. Figure 5 shows the waveguiding structure with aperiodic dielectric variation that can be used as OR gate and Fig.6 shows the input-output characteristics of that structure.

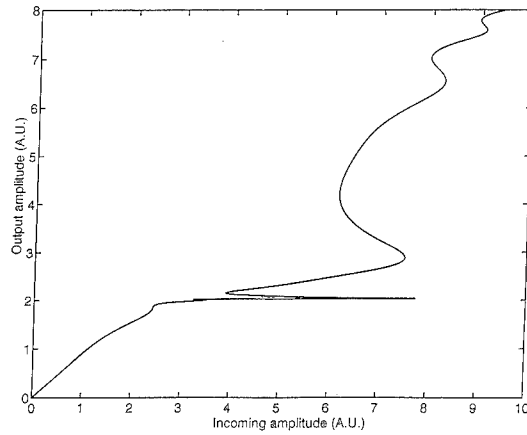


Figure 6. Input-output characteristics of a nonlinear aperiodic structure used for OR gate operation.

We have chosen a nonlinear constant $\gamma = 0.1$, a coupling constant $\alpha = 1.5$, an aperiodicity $-2z$, and a detuning $\Delta\beta = -1$. The propagation length is $L = 2$.

We see in Fig.6 a region where the output amplitude almost remain the same for varying input amplitudes and the threshold point. The width of this region can be controlled by the aperiodicity, detuning, propagation length, and the coupling constant. For the design of OR gate, this region is used for the logic Hi or 1.

We will again set the discrimination point as < 0.5 and > 1.0 amplitude values for logic 0 and logic 1 respectively. For logic operation 0+0 the output of the logic gate is lower than the amplitude value 0.5 denoting 0 logic value. For logic operations 1+0, 0+1 or 1+1, assuming an input amplitude value of 0 for logic value 0 and an input amplitude value of 2 for logic value 1, the output of the logic gate is an amplitude value 2 denoting logic value 1. The output of this OR gate can be cascaded with a tunable attenuator that may be tuned to provide the right amplitude values, a necessary feature to achieve cascability of these logic gates as well as large fan out.

NOT Gate

The realization and the operation of the NOT gate will be discussed in two parts. In the first part we discuss the realization of NOT gate using Y-junctions and nonlinear periodic waveguide and in the second part we verify by simulation the actual working of the NOT gate using the beam propagation method.

In the design of AND and OR gates we have used the transmission properties of the nonlinear periodic/apperiodic waveguiding structure whereas in designing NOT gate we will be using the reflection characteristics of the nonlinear periodic structure. The proposed structure for NOT gate is shown in Fig.7.

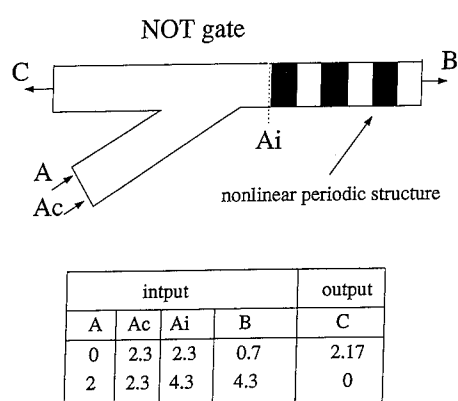


Figure 7. NOT gate made up of a Y branch coupler and a nonlinear periodic waveguiding structure. A is the input and C is the output of the NOT gate. Ac is an auxiliary input of constant amplitude.

A is the input to the device and C is the output of the device; Ac is a constant auxiliary input. The powers at the input and auxiliary input are combined using a Y junction coupler and the power at Ai is assumed to be sum of the input and auxiliary input powers. This assumption is valid and will be proved later using simulation.

When the input at the gate is logic 0 (Low), the amplitude at Ai is 2.3 assuming 0 amplitude input for logic zero and 2.3 amplitude for the constant auxiliary input. From the input-output characteristics of the nonlinear periodic structure shown in Fig.4 the transmitted output amplitude at B of the gate is 0.7. The output arm of the NOT gate is C and hence we need to compute the power reflected by the periodic structure and collected at C. The amplitude output is approximately 2.17, corresponding to logic 1 (Hi). Now let us assume that the input to the logic gate is logic 1 (Hi), that is an input amplitude of 2.0. The amplitude at Ai is 4.3, which yields a high transmissivity of 4.3 at the end of the nonlinear periodic structure. Computing the reflected output at C, one obtains an amplitude value approximately zero, denoting logic 0 (Low).

We have made here two assumptions that all input powers appear at the input of the nonlinear periodic structure (Ai) and that all the reflected power is collected at the output of the NOT gate. The assumptions can be proved to be true by proper design of the branch couplers. Using beam propagation method [11], we have shown that all the input powers appear at the input of the nonlinear periodic structure. Similar simulation shows that almost all the reflected power is collected at the logic gate output. Though there are scattered fields throughout the waveguide, the power returned to the input arm is negligible. This is important for continuous operation of the NOT gate.

Acknowledgments

The authors thank Drs. Duncan Mills and Yisheng Yu for many helpful discussions.

REFERENCES

- [1] L. S. Tamil, "Optical Interconnect: Design using inverse scattering approach," Center for Applied Optics, University of Texas at Dallas, Richardson, Research report: UTD/CAO-24, June 1991.
- [2] D. W. Mills and L. S. Tamil, "Synthesis of Guidedwave Optical Interconnects," *IEEE J. Quantum Electron.*, vol. 29, pp. 2825–2834, 1993.
- [3] P. Deift and E. Trubowitz, "Inverse scattering on the line," *Comm. Pure and Appl. Math.*, vol. 32, pp. 121–251, 1979.
- [4] S. Adachi, "GaAs, AlAs, and AlGaAs material parameters for use in research and device applications," *J. Appl. Phys.*, vol. 58, no. 3, 1985.
- [5] D. W. Mills and L. S. Tamil, "Coupling in multilayer optical waveguides using scattering data," *J. Lightwave Technol.*, vol. 12, pp. 1560–1568, 1994.
- [6] H. G. Winful, J. H. Marburger and E. Garmire, "Theory of bistability in nonlinear distributed feedback structures," *Appl. Phys. Lett.*, vol. 35, pp. 379–381, 1979.
- [7] H. G. Winful and R. Zamir, "Modulational instability in nonlinear periodic structures: Implication for 'gap solitons'," *Appl. Phys. Lett.*, vol. 58, pp. 1001–1003, 1991.
- [8] C. M. de Sterk, "Simulation of gap soliton generation," *Phy. Rev. A*, vol. 45, pp. 2012–2018, 1992.
- [9] J. A. Armstrong and N. Bloembergen, "Interaction between light waves in a nonlinear dielectric," *Phy. Rev.*, vol. 27, pp. 1918–1939, 1962.
- [10] L. S. Tamil, Y. Li, J. M. Dugan and K. A. Prabhu, "Dispersion compensation for high bit rate fiber communication system," *Appl. Opt.*, vol. 33, 1697–1706, 1994.
- [11] L. S. Tamil and Y. Yu, "A beam propagation technique to analyze integrated photonic circuits," *Micro. and Opt. Lett.*, vol. 5, pp. 617–621, 1992.

MODELLING OF A VERSATILE ALL-OPTICAL MACH-ZEHNDER SWITCH

Gijs J.M. Krijnen^{1,4}, Alain Villeneuve², George I. Stegeman¹
Stewart Aitchison³, Paul V. Lambeck⁴ and Hugo J.W.M. Hoekstra⁴

¹ CREOL, University of Central Florida
12424 Research Parkway Suite 400, Orlando, Florida 32826

² COPL et Dept. de Physique, Université Laval
Ste-Foy, Quebec, Canada, G1K 7P4

³ Dept. of Electronics and Electrical engineering
University of Glasgow, G12 8QQ, Glasgow, United Kingdom

⁴ Lightwave Devices Group, MESA Institute, University of Twente
P.O. Box 217, 7500 AE Enschede, the Netherlands

ABSTRACT

In this paper we describe a new nonlinear Mach-Zehnder interferometer with bimodal branches and asymmetric Y-junctions. Using various modelling techniques we show that this device can be used for an array of all-optical switching functions including wavelength, pulse-length and polarisation insensitive switching and conversion.

INTRODUCTION

High bit rate communication systems of the future will demand ultra fast devices for routing, amplification, polarisation-rotation and wavelength-conversion of optical signals as well as for performing logical functions. Without doubt it is a great benefit when all this can be done completely in the optical domain. In this paper we describe a device that can perform such functions. It is based on a Nonlinear Mach-Zehnder Interferometer (NMI) with bimodal branches and it exploits cross-phase modulation (XPM) of two co-propagating modes of different order. The advantages of the new concept over one using XPM of orthogonal polarised modes of monomode waveguides [1] are polarisation independence (while maintaining phase insensitivity), reduced switching power and reusable control signals.

In this paper we describe the geometry of this new device and exemplify it by a design in AlGaAs technology. The use of various modelling tools such as Coupled Mode Analyses (CMA), Nonlinear Effective Index Method (NEIM), Finite Difference Mode Solving (FDMS) in two dimensions and spatial and temporal Beam Propagation Methods (BPM) will be discussed. It will be shown that these various techniques enable the modelling of all major spatial and temporal aspects of this device.

A NEW DESIGN BASED ON NONLINEAR MACH-ZEHNDER INTERFEROMETERS

Interferometric measurements have always played an important role in free-space optical measurements. Small changes in the optical path length can be measured with sub-wavelength accuracy (at least in principle). In integrated optics, interferometric applications such as optical sensors and electro-optic amplitude modulators, are often of the Mach-Zehnder interferometer (MI) type (see Figure 1).

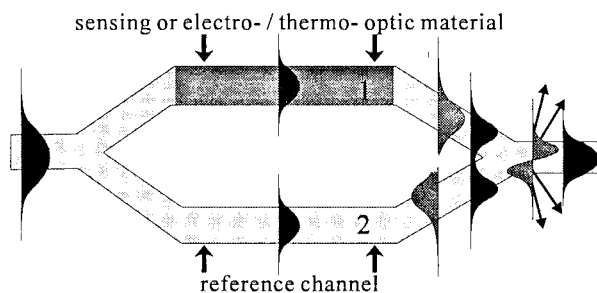


Figure 1: Example of an integrated optic Mach-Zehnder interferometer.

In this kind of interferometer, first introduced by Martin [2], one power-splitting Y-junction at the entrance of the structure is used for equal division of the incoming power over two monomode branches. During passage through these branches the two beams undergo phase changes which depend on the phase-velocity of the beams. At the output of the structure the modes of both channels are combined by means of a symmetric Y-junction. This combination of modes at the output will in general produce both the fundamental and first-order modes of the output section with a distribution that depends on the phase difference of the two combining modes. When the output waveguide is monomode the first-order mode is converted to radiation modes and only the fundamental mode emerges from the device. When an MI is used as an optical sensor, one branch (2) normally provides a reference signal whereas the other branch is sensitive to a measurand so that the light in that channel will experience a measurand dependent phase-change [3]. When using a MI as an electro- or thermo- optic modulator both channels induce phase-changes, but of opposite sign, which reduces either the required device length or the switching voltage by a factor of 2 relative to modulation in one channel only.

The Nonlinear Mach-Zehnder Interferometer (NMI) was introduced by Haus et al. [1][4]. In this NMI, see Figure 2, the branches contain third-order nonlinear materials and modulation in one (or two branches) is achieved by using cross-phase modulation (XPM) by additional control signals (P_c^1 and P_c^2) which are injected through Y-junctions. The nonlinear phase changes of the probe signals are resolved as (control-power dependent) ampli-

tude changes by interference in the output section. When using two control and one probe signals, logical switching ports of the XOR and AND type can be made.

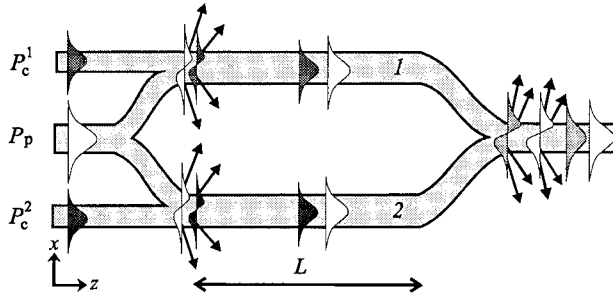


Figure 2: Schematic of the Nonlinear Mach-Zehnder Interferometer introduced in [1].

There are three drawbacks to the Nonlinear Mach-Zehnder Interferometer:

- 1) Since the branches of the interferometer are monomode the control and probe input(s) are necessarily fundamental modes inside the branches. Hence, when the inputs are polarised along the same direction there is no XPM but only an interferometric generation of the modes at the input of the branches. Therefore the control and signal inputs have to be perpendicularly polarised. Mannenberg et al. [5] proposed an implementation aimed at circumventing the interference of control and probe by using additional semiconductor laser-amplifiers but this necessitates the use of gain material and electrode patterning.
- 2) Also because the branches are monomode it is not possible to have 100% conversion of the inputs to the modes of the branches. For a perfect symmetrical Y-junction the control and the probe inputs fundamentally lose 50% of their power. Asymmetric Y-junctions can selectively improve the throughput of one input at the expense of the other.
- 3) Since probe and control power follow the same path to the output a polariser is needed to distinguish between both signals. Although this is not a major objection for experimental work, it is not favourable for an integrated optic implementation.

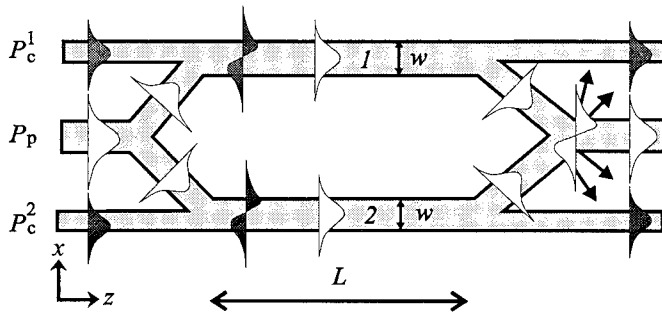


Figure 3: Left: Schematic of a NMI with monomode branches exploiting cross-polarised beams.
Right: Schematic of the new design with bimodal branches allowing for equi-polarised beams.

In the device-concept introduced here the drawbacks of the NMI are circumvented by a combination of asymmetrical mode-selective Y-junctions and bimodal branches (see Figure 3). Like the NMI this structure has three mono-mode input waveguides, the two outer being

control inputs and the centre being a probe input. The centre Y-junction following the probe input is symmetrical and divides the probe input equally over branches 1 and 2. The two outer Y-junctions are asymmetrical and designed to selectively launch the probe and control input into the fundamental and first-order modes of the branches respectively. This is achieved by giving these Y-junctions dissimilar input waveguides and small branching angles which cause the modes of the wider and smaller inputs to convert adiabatically into the fundamental and first order modes of the bimodal branches respectively [6]. This selective mode launching has no fundamental restrictions on the efficiency which means that the 50% losses can be avoided. Due to the mixing of modes of different order, which are distinguished by different propagation constants, there is no interferometric dependence on the phase differences between control and probe inputs, provided that the length of the branches (L) is much longer than the beat length of the modes ($=\pi/(\beta_p-\beta_s)$). Generally this beat length is on the order of tens of microns for slab waveguides and hundreds of microns for channel waveguides so that it will not form any limitation on the device implementation. At the output section three more Y-junctions are identified. The two outer asymmetric Y-junctions serve as mode splitters and remove the control modes from the branches. This cannot be omitted since otherwise the control modes end up in the centre output giving rise to a deteriorated interference resulting in reduced modulation depths. The centre Y-junction is again symmetric and combines the two fundamental modes of the branches. The in-phase parts will add and form the fundamental mode of the centre waveguide. The out-of-phase parts will generate the first-order modes of the output. For a monomode output this first-order mode is lost to radiation modes. Alternatively, for a bimodal output the first-order mode can be separated from the fundamental by another mode-splitting Y-junction and serve as an inverted output. This output can be exploited in cascaded devices or it can serve as a reference signal in sensor applications.

CMA ANALYSIS

To gain a basic understanding of the NMI a CMA analysis is carried out. To this end several assumptions are made. These assumptions will be verified later. The first assumption is that the Y-junctions in the input and output sections work perfectly and independently of the power in the modes. With this assumption the device operation is entirely determined by the interaction of the modes in the two branches. The second assumption is that the interaction between the modes comprises AC-Kerr cross- and self-modulation only, i.e. nonlinear coupling causing power exchange between signal and pump-modes is neglected. The third assumption is that the nonlinear effects are small, i.e. the linear index profiles dominate the waveguiding. Finally, it is assumed that the two branches of the NMI are identical.

With the assumptions above the analysis of the proposed new NMI is straightforward. The coupled-mode equations can be derived by inserting the nonlinear polarisation into the Maxwell equations and collecting the terms at fundamental frequency ω (it is assumed that no accidental large third harmonic generation is present). The propagating modes in the branch are written in the usual form:

$$\overline{E_i}(x,y,z,t) = \frac{1}{2} (a_i(z)E_i(x,y)e^{j(\omega t - \beta_i z)} + \text{c.c.}) \overline{e_x} \quad (1)$$

where it is assumed that the fields are quasi-TE polarised. The cases of quasi-TM and mixed polarisation are treated analogously. In the context of an implementation of an NMI by means of etched thin film waveguides the subscript i denotes the lateral mode-order

where the transverse mode-order is assumed to be zero for all modes. $E_i(x,y)$ is the modal-field distribution of the quasi TE_{0i} mode normalised to a power transport of 1 W. It is a real function of x and y in the limit of no loss. The power carried by the mode is equal to $a_i a_i^* = |a_i|^2$. Due to the assumption of small nonlinearity the Slowly Varying Envelope Approximation (SVEA) can be applied implying that the second-order derivative of $a(z)$ with respect to z can be neglected. Hence, the coupled-mode equation applying to one branch for mode i in the presence of mode j is written in the form:

$$-j \frac{\partial a_i}{\partial z} = a_i |a_i|^2 Q_{iiii} + 2a_i |a_j|^2 Q_{ijij} + a_j^* a_i^2 Q_{ijij} e^{-j(\beta_i - \beta_j)z} + a_i^* a_j^2 Q_{ijij} e^{-j2(\beta_j - \beta_i)z} + 2a_j |a_i|^2 Q_{ijij} e^{-j(\beta_j - \beta_i)z} + a_j |a_j|^2 Q_{ijij} e^{-j(\beta_j - \beta_i)z} \quad (2)$$

where the indices i and j are either 0 or 1 but unequal. The Q 's in equation (2) are given by the nonlinear overlap integrals [7]:

$$Q_{ijkl} = \frac{3\omega\epsilon_0}{4} \int_{x=-\infty}^{\infty} \int_{y=-\infty}^{\infty} \chi_{xxxx}^{(3)} E_i(x,y) E_j(x,y) E_k(x,y) E_l(x,y) dx dy \quad i,j,k,l \in \{0,1\} \quad (3)$$

The first and second term on the right hand side of equation (2) represent respectively the self- (SPM) and cross- (XPM) phase modulation of the modes. The last four terms of (2) are z -dependent and act like induced gratings. In general, these terms will only give rise to phase-mismatched mode-coupling causing fast oscillations with small modulation. These terms are dropped in accordance with the assumptions made above. For convenience, in the subsequent discussion the indices ii and jj will be contracted to i and j respectively. Examination of (2) shows that by neglecting the last four terms on the right-hand side, all coefficients of the remaining terms are real. Moreover, due to the assumption that there is no power exchange $|a_i|^2 = P_i$ and $|a_j|^2 = P_j$ are constant so that (2) can be integrated easily:

$$a_i(z) = a_i(0) e^{-j(Q_{ii}P_i + 2Q_{ij}P_j)z} \quad (4)$$

Insertion of (4) in (1) leads to the following formula for the power-dependant propagation constant of mode i :

$$\beta_i(P_i, P_j) = \beta_i(0) + Q_{ii}P_i + 2Q_{ij}P_j \quad (5)$$

Note that the change in propagation constant is independent of the modal-power distribution when $2Q_{ij} = Q_{ii} = Q$ i.e. $\Delta\beta = Q(P_i + P_j)$. This feature can be used beneficially to make the NMI independent of the performance of the Y-junctions (since the injected signal and pump powers will be almost completely converted to either the fundamental or first-order mode of the branches). Because of the assumption that the pump-power is equally divided over both branches by the middle Y-junction of the input section, P_0 is $P_p/2$. Hence the expressions for the power-dependant propagation constants read:

$$\beta_0^n(P_p, P_c^n) = \beta_0^n(0) + Q_{00}^n \frac{P_p}{2} + 2Q_{01}^n P_c^n \quad (6)$$

where the superscript n denotes the branch number of the branch. After propagation over a length L through the branches the accumulated phase difference (ϕ) between the two fundamental modes is:

$$\phi = L [\beta_0^1 - \beta_0^2] = L \left[\beta_0^1(0) - \beta_0^2(0) + \frac{P_p}{2}(Q_{00}^1 - Q_{00}^2) + 2Q_{01}^1 P_c^1 - 2Q_{01}^2 P_c^2 \right] \quad (7)$$

For identical branches and equal splitting of the probe power equation (7) reduces to:

$$\phi = 2LQ_{01} [P_c^1 - P_c^2] \quad (8)$$

In the output section the signal-modes are removed from the branches and the fundamental (or probe) modes are combined. The combined field is given by:

$$\begin{aligned} E_0(x) &= \sqrt{\frac{P_p}{2}} [E_0^1(x) + E_0^2(x) e^{-j\phi}] \\ &= \sqrt{\frac{P_p}{2}} [\{E_0^1(x) + E_0^2(x)\} \cos(\phi/2) + j\{E_0^1(x) - E_0^2(x)\} \sin(\phi/2)] e^{-j\phi/2} \\ &= \sqrt{P_p} [E_0^o(x) \cos(\phi/2) + jE_1^o(x) \sin(\phi/2)] e^{-j\phi/2} \end{aligned} \quad (9)$$

where the time dependence and a constant arbitrary phase factor have been omitted for simplicity. The field distributions $E_0^1(x)$, $E_0^2(x)$, $E_0^o(x)$ and $E_1^o(x)$ in equation (9) are the normalised field profiles of the fundamental mode of branches 1 and 2 and the fundamental and the first-order (system) modes of the output section. In equation (9) use has been made of the fact that the sum of the fundamental modes profiles of two identical waveguides forms the fundamental (symmetric) mode of the combined waveguide structure whereas the difference of both mode-profiles forms the first-order (antisymmetric) mode. For reasons of normalisation of the field profiles a factor of $\sqrt{2}$ is necessarily added. The power appearing in the fundamental mode at the output is given by:

$$P_0^o = P_p \cos^2(\phi/2) \quad (10)$$

The signal-power needed for switching the output from, say, 100% to 0% is given by the requirement that ϕ must be equal to π :

$$\phi = 2LQ_{01} [P_c^1 - P_c^2] = \pi \quad (11)$$

For only one input (say P_c^1) the switching power is given by:

$$P_s = \frac{\pi}{2LQ_{01}} \quad (12)$$

According to this first order analysis the probe power, the wavelength and the polarisation direction of pump and probe, may be arbitrarily chosen although Q_{01} (see equation (3)) will slightly depend on these quantities. Hence, the same device enables modulation, amplification, and wavelength and polarisation conversion and it can be used as a logical port as well [1].

A NMI IN AlGaAs TECHNOLOGY

Waveguide design and modelling

In the recent past interesting all-optical switching results have been obtained in AlGaAs waveguide structures with bandgap energies that are slightly larger than two times the photon energy. In these structures there is virtually no 2 photon absorption enabling long effective interaction lengths at still reasonable nonlinearities expressed by a good (<0.5) figure of merit T [8].

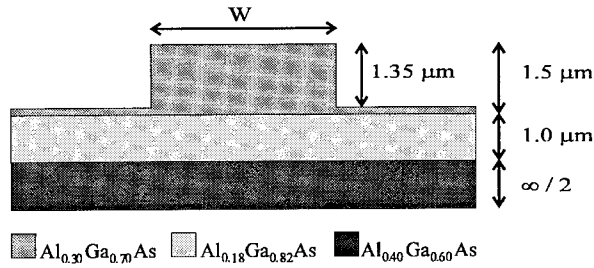


Figure 4: Sample waveguide structure in AlGaAs technology. The width W is variable.

The basic structure used in this study is shown schematically in Figure 4. In this study the etch-depth is fixed but the waveguide width W is variable to allow for different optical functions of the NMI. The waveguide consists a 40% Al substrate, a 1.0 μm thick 18% Al film layer and a 1.5 μm thick 30% Al cladding layer, etched down to 0.15 μm adjacent to the waveguides. With these Al-concentrations the bandgap energy is a little higher than 2 times the photon energy at 1.55 μm wavelength, thus virtually eliminating two-photon absorption while still retaining reasonable nonlinearity ($\approx 3.6 \cdot 10^{-20} \text{ m}^2/\text{V}^2$) [8]. The linear and nonlinear refractive indices were calculated as a function of Al concentration and wavelength using the model described in [9] and [10] respectively.

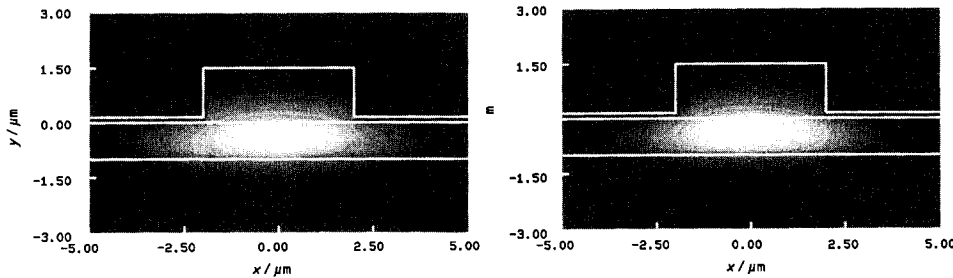


Figure 5: Field profile of a 4 μm wide waveguide calculated by the FDMS (left) and NEIM (right)

The field profiles and the nonlinear coefficients of the fundamental quasi TE_{00} and TE_{01} modes are calculated by a semi-vectorial Finite Difference Mode Solver (FDMS) [11] and the Nonlinear Effective Index Method (NEIM) [12]. Figure 5 shows the field profiles of the fundamental mode of a 4 μm wide waveguide calculated by the FDMS (left) and the NEIM (right).

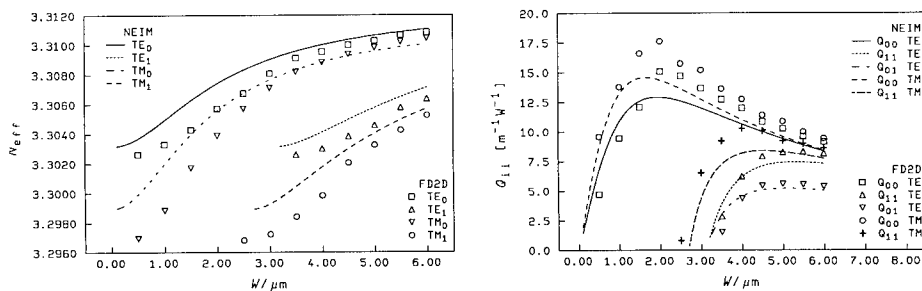


Figure 6: Effective indices (left) and nonlinear coefficients (right) as a function of waveguide width. Calculations by the FDMS and by the NEIM show very good agreement.

Clearly the agreement between both profiles is very good and minor deviations are only found around the etched corners where the field profile is already small compared to the field in the centre. The good agreement is verified by the overlap of both profiles which is >99%. Figure 6 shows that not only the field profiles but also the effective indices and the nonlinear coupling coefficients as calculated by the FDMS and by the NEIM are in very good agreement.

Spatial 2D BPM analysis

Since the waveguides can be sufficiently accurately modelled by the NEIM, further spatial properties of the NMI are investigated by means of a 2D Enhanced Finite Difference Beam Propagation Method (EFDBPM) [13] including Transparent Boundary Conditions (TBC) [14]. Using approximate expressions [15] the Y-junctions are designed to have a mode selectivity better than 20 dB which is obtained for a branching angle ≤ 0.15 degrees in combination with a width of 2 and 2.5 μm for the small and wide branches respectively. The mode selectivity calculated by means of EFDBPM is 24 dB, in good agreement with the simple approximations. A branch to branch separation of 20 μm is found to give sufficient decoupling (≈ -60 dB) of the modes in the two branches of the NMI.

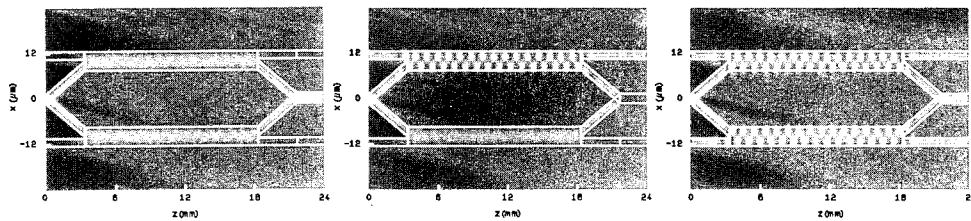


Figure 7: Intensity of the propagating light as calculated by EFDBPM. Left: $P_p=50$ W, $P_c^1=P_c^2=0$. Centre: $P_p=50$ W, $P_c^1=P_c^2=17.5$ W, $P_c^2=0$. Right: $P_p=50$ W, $P_c^1=P_c^2=P_c^3=17.5$ W.

The CW performance of a 2.5 cm long structure having 1.5 cm long 5.0 μm wide branches was analysed by means of EFDBPM calculations. P_p was fixed at 50 W. Figure 7 displays the intensities for no control input (left) one control input (centre) and 2 control inputs (right). Clearly when one input is present the probe transmission is completely switched off. For two inputs it is switched on again demonstrating the potential for all-optical logic.

Figure 8 left show the calculated probe transmission versus variations in P_c^1 between 0 and 50 W, showing strong modulation that leads to almost no probe transmission (0.2 %) for $P_c^1=17.5$ W. Note that a power-swing of 50 W at the output is obtained by an input power-swing of only 17.5 W, i.e. there is amplification.

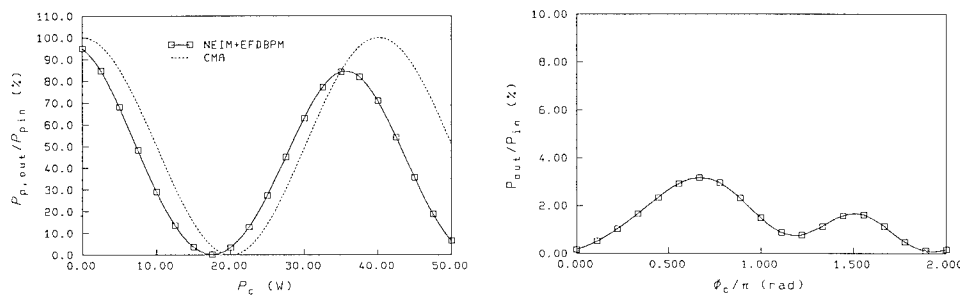


Figure 8: Probe transmission vs. P_c^1 (left) and vs. ϕ_c (right) for $P_c^1=50$ W.

The dotted line in Figure 8 left is obtained from the CMA expressions (8) and (10) with the nonlinear coupling coefficient calculated from the field profile obtained by FDMS. The good agreement means that the performance of the Y-junctions is good enough to allow for the assumptions made above. Figure 8 right shows the probe transmission as a function of the phase of the control (ϕ_c) at fixed $P_p=50$ and $P_c^1=17.5$ W. The modest peak of 3.2% at $\phi_c=2\pi/3$ demonstrates the phase-insensitivity of the device.

TEMPORAL BPM ANALYSIS

Due to the good performance of the Y-junctions, resulting in a very good agreement between CMA and the EFDPM results (Figure 8 left), the CMA can be used to study temporal effects as well. Since the interaction of the probe and control signals takes place almost solely in the branches, it is sufficient to model the temporal interaction of two pulses in one waveguide in the presence of SPM and XPM. This is done using a split-step Fourier method [16]. The influence of temporal pulse walk-off (caused by different effective group indexes (n_g)) and group velocity dispersion (GVD) are taken into account too. To this end the refractive indices according to the model of [9] are used in wavelength dependent NEIM calculations thus including both the effects of material dispersion and waveguide dispersion. The obtained values of n_g for the fundamental (3.4356) and first order mode (3.4419) indicate that the pulse walk-off length is large enough (2.4 cm for 0.5 ps long pulses) to be of no real concern for this design. Furthermore it turns out that the GVD is dominated by material dispersion. Values of ≈ 0.89 (ps)²/m are found for both the fundamental and first order modes with waveguide GVD well below 5% of the total GVD.

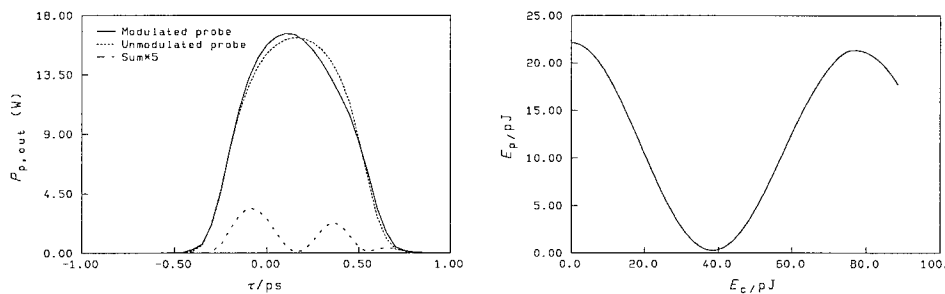


Figure 9: Left: pulse profiles after 1.5 cm propagation. Right: probe vs. control energy.

Figure 9 left shows 500 fs long Gaussian probe pulses ($P_{peak}=25$ W) after 1.5 cm propagation without (solid line) and with (dotted line) a co-propagating 2 ps long, 150 fs delayed, Gaussian control pulse ($P_{peak}=21$ W). The sum of both (dashed line), resembling the output of the NMI, is almost vanishing ($<1.5\%$ pulse energy) showing that complete switching without pulse break-up is possible. Figure 9 right shows the output probe energy (E_p) versus the input control energy (E_c). Conditions are the same as for Figure 9 left. Obviously, for this combination of pulse lengths and delay a very usable modulation depth of 18 dB is obtained with output pulses devoid of pulse break-up. Also note that the output probe pulse width is much shorter than the width of the control pulse, i.e. the device is capable of performing pulse-width conversion.

CONCLUSIONS

In conclusion we have introduced a new Nonlinear Mach-Zehnder interferometer. The use of bimodal branches and asymmetric Y-junctions enables the exploitation of cross-phase modulation of arbitrarily polarised beams of different mode-order. Even for equi-polarised inputs the resulting switch is to a large degree insensitive to variations in the phase-difference of control and probe inputs. Hence it allows not only for phase, wavelength and polarisation insensitive switching but also wavelength, polarisation and pulse-length conversion. Using realistic materials and geometry parameters we found that complete switching of very short (0.5 ps) pulses with moderate power (<25 W) is possible.

ACKNOWLEDGEMENTS

The research of GK has been made possible by a fellowship of the Royal Netherlands Academy of Arts and Sciences.

REFERENCES

- [1] A. Lattes, H. Haus, F. Leonberger and E. Ippen, An ultrafast all-optical gate, *IEEE J. Q. Elect.*, 19, 1983, pp 1718.
- [2] W. Martin, A new waveguide switch/modulator for integrated optics, *Appl. Phys. Lett.*, 26, 1975, p 562.
- [3] H. Kreuwel, Planar waveguide sensor for the chemical domain, PhD. thesis, University of Twente, 1988.
- [4] H. Haus and N. Whitaker Jr., All-optical logic in optical waveguides, *Phil. Trans. R. Soc. Lond.*, A313, , 1984, p 311.
- [5] G. Manneberg, M. Kull and S. Lindquist, An all-optical amplifier for terahertz AM signals, a proposal, *J. Lightw. Techn.*, 5, 1987, p 236.
- [6] W. Burns and F. Milton, Mode conversion in planar dielectric separating waveguides, *IEEE J. Q. Elect.*, 11, 1975, p 32.
- [7] Y. Silberberg and G. Stegeman, Nonlinear coupling of waveguide modes, *Appl. Phys. Lett.*, 50, 1987, p 801.
- [8] A. Villeneuve, C. Yang, G. Stegeman, C. Lin and H. Lin, Nonlinear refractive index and two-photon absorption near half the band gap in AlGaAs, *Appl. Phys. Lett.*, 62, 1993, p 2465.
- [9] S. Adachi, Optical dispersion relations for GaP, GaAs, GaSb, InP, InAs, InSb, $\text{Al}_x\text{Ga}_{1-x}\text{As}$ and $\text{In}_{1-x}\text{Ga}_x\text{As}_y\text{P}_{1-y}$, *J. Appl. Phys.*, 66, 1989, p 6030.
- [10] M. Sheik-Bahae, D. Crichton Huntings, D. Hagan, E. van Stryland, Dispersion of bound electronic nonlinear refraction in solids, *IEEE J. Q. Elect.*, 27, 1991, p 1296.
- [11] E. Schweig and W. Bridges, *IEEE Trans. Microw T. Techn.*, 32, 5, 1984, p 531.
- [12] G. Krijnen, H. Hoekstra and P. Lambeck, A new method for the calculation of propagation constants and field profiles of guided modes of nonlinear channel waveguides based on the effective index method, *IEEE J. Lightw. Techn.*, 12, 1994, p 1550.
- [13] H. Hoekstra, G. Krijnen and P. Lambeck, New formulation of the beam propagation method based on the slowly varying envelope approximation, *Opt. Comm.* 97, 1993, p 301.
- [14] G. Hadley, Transparent boundary conditions for beam propagation, *Opt. Lett.* 16, 1991, p 624.
- [15] G. Krijnen, H. Hoekstra, P. Lambeck and T. Popma, Simple analytical description of performance of Y-junctions, *Elect. Lett.*, 28, 1992, p 2072.
- [16] See for example: G. Agrawal, Nonlinear fiber optics, Academic press, ISBN 0-12-045140-9.

A GUIDE/ANTIGUIDE STRUCTURE FOR IMPLEMENTING SELF-IMAGING WAVEGUIDE BEAMSPLITTERS

Tristan J. Tayag[†] and Garnett W. Bryant[‡]

[†]Army Research Laboratory
2800 Powder Mill Road
Adelphi, Maryland 20783-1197

[‡]National Institute of Standards and Technology
Gaithersburg, Maryland 20899

INTRODUCTION

Optical beamsplitting forms a critical function in applications such as antenna remoting, cable television (CATV) distribution, and telecommunications. In each of these areas, the input and outputs to the splitting device typically consist of optical fibers. A Y-branching tree of fused fiber splitters is sufficient for small numbers of splitters, N . For $N \geq 16$, however, fused fiber splitters are impracticable and fiber-pigtailed integrated optical splitters appear more viable. Desired characteristics of integrated optical (IO) beamsplitters include robustness in fabrication tolerance, ease of manufacture, fabrication techniques implementable in a variety of material systems, insensitivity to polarization, uniformity in splitting ratios, low insertion loss, and compact size. Previous designs of IO beamsplitters used cascaded Y-junction branches [1] or evanescent field couplers [2]; but, more recently, computer-generated waveguide holograms [3], radiative power splitters [4], [5], and self-imaging beamsplitters [6] have been demonstrated. To achieve all the desired device characteristics, we argue that the self-imaging approach holds the greatest promise.

Self-imaging in planar optical waveguides was first demonstrated by Ulrich and Ankele [7]. In this early demonstration, self-imaging was demonstrated along the transverse dimension of the waveguide with both the transverse and lateral dimensions of the guide supporting multiple modes. The waveguide consisted of an immersion fluid sandwiched between a pair of fused quartz plates. More practical self-imaging beamsplitters were demonstrated recently in the semiconducting material systems by Heaton et al. in GaAs [6] and by Ferreras et al. in InP [8]. Both research groups used reactive ion etching (RIE) to etch deep vertical sidewalls completely through the guiding layer of a slab waveguide. In this way, the requisite reflective sidewalls were formed in the multimode propagation region of the device.

The use of RIE to etch deep vertical sidewalls through the entire guide layer of the slab waveguide results in a number of drawbacks. First, etching through the guide layer increases both the device insertion loss and polarization crosstalk due to scattering from sidewall roughness [9]. Insertion loss in these devices is typically calibrated with respect to an adjacent channel waveguide fabricated with the same process. The reported insertion loss values therefore are somewhat conservative, since the adjacent channel waveguides themselves are significantly lossy. Second, it is very difficult to fabricate deep vertical sidewalls in important waveguide material systems such as LiNbO_3 and LiTaO_3 . The highest reported etch rate selectivity between LiNbO_3 and a metal mask is about 10:1 using low pressure CF_4 planar sputter etching [10]. For the required etch depths of about $3\text{ }\mu\text{m}$, vertical sidewalls are difficult to achieve due to mask edge erosion.

In this paper, we present a novel guide/antiguide structure to realize self-imaging waveguide beamsplitters. The guide/antiguide structure overcomes the shortcomings of previous self-imaging implementation techniques by offering reduced insertion loss, lower polarization crosstalk, ease of manufacture, and implementation in a wide range of waveguide material systems, including LiNbO_3 and LiTaO_3 . Experimental data on the GaAs/AlGaAs material system are presented that demonstrate the concept. Insertion loss, polarization crosstalk, and splitting ratio uniformity data are presented for 1×16 beamsplitters.

GUIDE/ANTIGUIDE TECHNIQUE

Under certain conditions, self-imaging can be formed in multimode, laterally confined planar optical waveguides. An illuminated input object will excite the lateral modes supported by the waveguide. Since these lateral modes travel with distinctly different phase velocities, the modes become dephased. Self-images of the object are formed when the superposition of the modes in the image plane matches the original modal distribution in the object plane. This condition occurs at observation planes where the accumulated phase differences among the excited modes are integral multiples of 2π , which allows the excited modes to constructively interfere and reproduce the input object's modal distribution.

Moreover, multiple self-images are formed at observation planes that are between the single self-image planes. If the multimode region is center-fed, only its symmetrical lateral modes are excited. In this case, the input power is uniformly split among the multiple self-images. A compact, uniformly distributed beamsplitter can be fabricated in this way using self-imaging techniques.

The resolution, contrast, and very presence of self-imaging in waveguide beamsplitters depends on the number of lateral modes that contribute constructively to the image [11]. This in turn is dependent on the degree of confinement of the lateral modes. It is well-known that the ridge waveguide structure provides adequate confinement in strip-line waveguides. The guide/antiguide structure extends this concept for application to self-imaging beamsplitter devices.

Consider the mode index versus guide-layer-thickness plot of an asymmetric waveguide structure shown in Figure 1. The inset shows the GaAs guide layer bounded above by air and below by $\text{Al}_{0.06}\text{Ga}_{0.94}\text{As}$. For guide layer thicknesses less than the fundamental mode cut-off thickness of about $0.5\text{ }\mu\text{m}$, no modes are supported by the guide and an "antiguide" region is formed. For guide layer thicknesses between 0.5 and $1.6\text{ }\mu\text{m}$, the transverse waveguide forms a "guide" region which supports a single TE mode and a single TM mode.

A cross-sectional view of the transverse waveguide structure is shown in Figure 2. A tapered step in the guide layer thickness exists at the interface between the guide

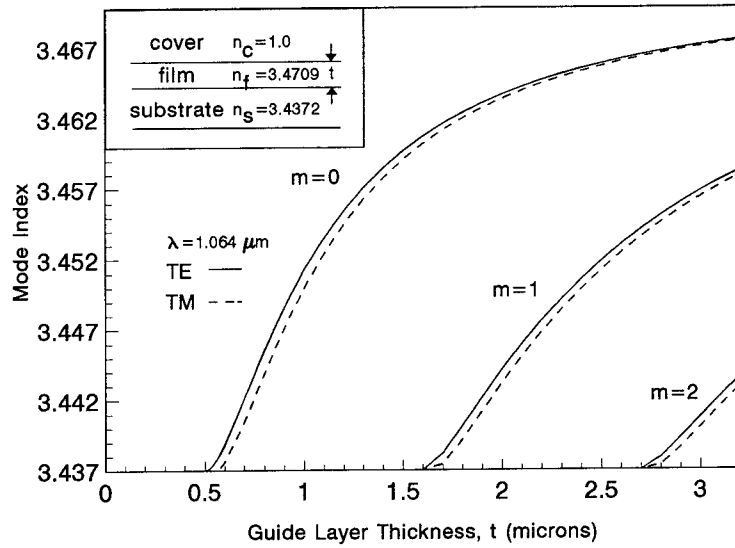


Figure 1. Mode index versus guide layer thickness for an asymmetric GaAs/AlGaAs slab waveguide.

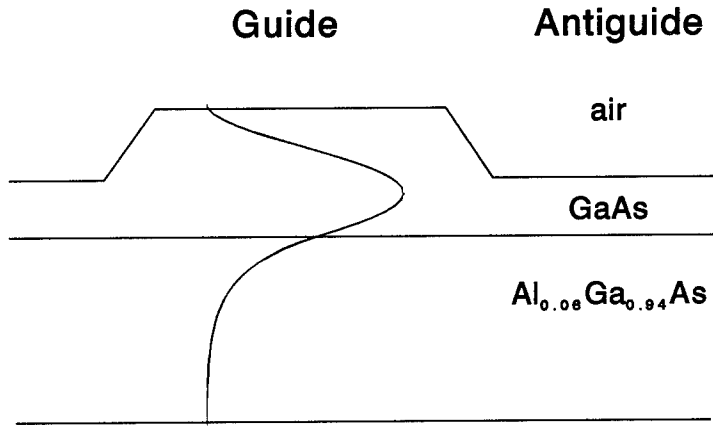


Figure 2. Cross-sectional view of a guide/antiguide self-imaging beamsplitter.

and antiguide regions. A mode supported in the guide region incident at the guide/antiguide interface undergoes total internal reflection (TIR) if its angle of incidence is greater than the critical angle for TIR,

$$\theta_c = \arcsin(n_s/N), \quad (1)$$

where n_s is the larger of the bulk indices of the two materials adjacent to the guide layer and N is the mode index of the guided mode [12]. Under this condition, the incident mode is totally internally reflected *regardless* of the thickness of the taper region.

For incidence angles smaller than the critical angle, the light is unable to propagate as a guided mode in the antiguide region and is radiated from the edge of the taper into the substrate. In the proposed beamsplitter structure, however, the input ridge waveguide that feeds the multimode propagation region is constructed from the same

guide/antiguide structure as the multimode propagation region. The numerical aperture of the input ridge waveguide defines the smallest incidence angle encountered at the multimode region's guide/antiguide interface. Therefore, incidence angles radiated by the input ridge waveguide into the multimode region by definition meet or exceed the condition for TIR.

The guide/antiguide structure of the self-imaging beamsplitter provides well-confined modes in the multimode propagation region. Since this structure does not require the guide layer thickness in the antiguide region to be zero, low excess loss and polarization crosstalk are expected due to reduced sidewall scattering. However, if the guide layer is completely removed in the antiguide region, the modes in the multimode region are more tightly confined. Thus, a greater number of modes are supported and contribute to the formation of the self-images. In the following section, we demonstrate self-imaging using the guide/antiguide structure for an antiguide layer thickness just at cut-off. The mode cut-off thickness in the antiguide layer is thus shown to be a sufficient condition for the realization of self-imaging beamsplitters using the guide/antiguide structure.

FABRICATION AND CHARACTERIZATION

Self-imaging beamsplitters were fabricated on the GaAs/AlGaAs slab waveguide structure shown in the inset of Figure 1. The structure was grown by molecular beam epitaxy (MBE) with a lower $\text{Al}_{0.06}\text{Ga}_{0.94}\text{As}$ cladding layer thickness of $3\text{ }\mu\text{m}$ and a GaAs guide layer thickness of $1\text{ }\mu\text{m}$. Splitters with splitting ratios ranging from 1×2 through 1×16 were designed based on the approach put forth by Heaton et al. [6]. Ar ion milling through a photoresist mask was used to define the guide/antiguide beamsplitter structure in the slab waveguide. The output rib array for a 1×16 splitter is shown in the SEM micrograph of Figure 3. In Figure 4 is shown the sloping sidewalls of a single ridge waveguide. The etch depth is at the mode cut-off thickness of $0.5\text{ }\mu\text{m}$ and the sidewall slant is 54 degrees relative to the waveguide surface.

Linearly polarized $1.064\text{ }\mu\text{m}$ light was endfire coupled with a $20\times$ microscope objective into the input guide. The output guides were imaged first onto a CCD detector and then onto a scanning slit detector to characterize splitter uniformity. Data for a 1×16 splitter are shown in Figure 5. Above is an image of the output facet positioned

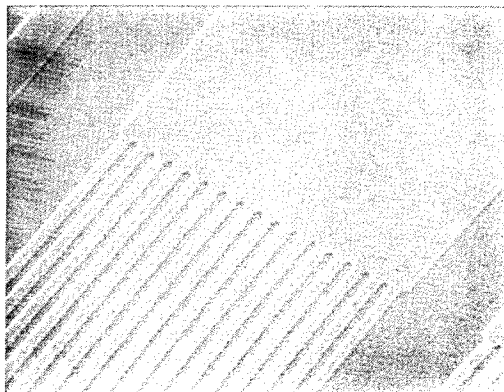


Figure 3. SEM micrograph of the output ridge array in a 1×16 beamsplitter. The multimode region width is $80.8\text{ }\mu\text{m}$ and the output ridge guide width is $2.8\text{ }\mu\text{m}$.

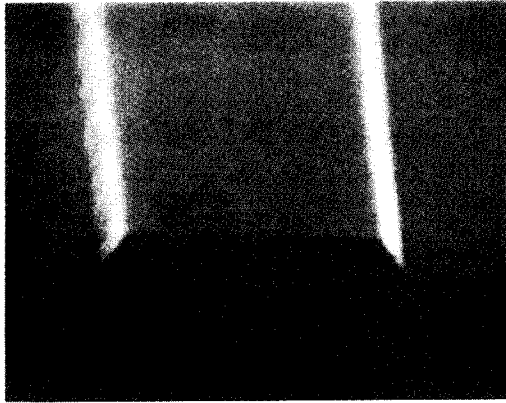


Figure 4. SEM micrograph of a ridge waveguide. The etch depth is $0.5\ \mu\text{m}$ and the sidewall slope is 54 degrees relative to the waveguide surface.

at the ridge waveguide array and below is the normalized intensity versus position data collected with a scanning slit detector.

For the 1×16 splitters made, the splitting ratio uniformity was typically $\pm 15.4\%$. The best case was $\pm 7.8\%$. Polarization crosstalk for either input polarization state was typically lower than $-25\ \text{dB}$. Device insertion loss was calibrated with respect to an adjacent ridge waveguide with typical device loss of about $3.5\ \text{dB}$.

To demonstrate that self-imaging indeed was occurring in the multimode propagation region, some devices were fabricated with no output ridge waveguide array. The output facet was positioned at the end of the multimode region. Data for a 1×16 splitter without an output waveguide array is shown in Figure 6. Typical uniformity in this case was $\pm 8.5\%$ with a best case value of $\pm 5.0\%$. Again polarization crosstalk was down around $-25\ \text{dB}$ and the typical insertion loss was about $0.8\ \text{dB}$.

DISCUSSION

A guide/antiguide structure for implementing self-imaging beamsplitters has been proposed and demonstrated. This technique offers potentially lower insertion losses than previously demonstrated techniques. The insertion losses measured in this work were calibrated against an adjacent ridge waveguide. In many cases, the insertion loss in the adjacent ridge waveguide was actually *greater* than that in the splitter. This is attributed to greater interaction of the guided mode with the sidewalls in the straight-through waveguides. The major loss mechanism in the splitter is misalignment of the output waveguide array with the image plane. A $\pm 0.25\ \mu\text{m}$ deviation in the design width of the multimode region results in a $\pm 10\ \mu\text{m}$ variation in the length of the multimode region needed for a given $1\times N$ split. Careful characterization of the guide region's mode index and calibration of the resist and etch processes will minimize this insertion loss.

All the devices characterized exhibited polarization crosstalk lower than $-20\ \text{dB}$ for both TE-to-TM and TM-to-TE conversion. As a comparison, the crosstalk was also measured in the straight-through waveguides. These typically had crosstalk which was

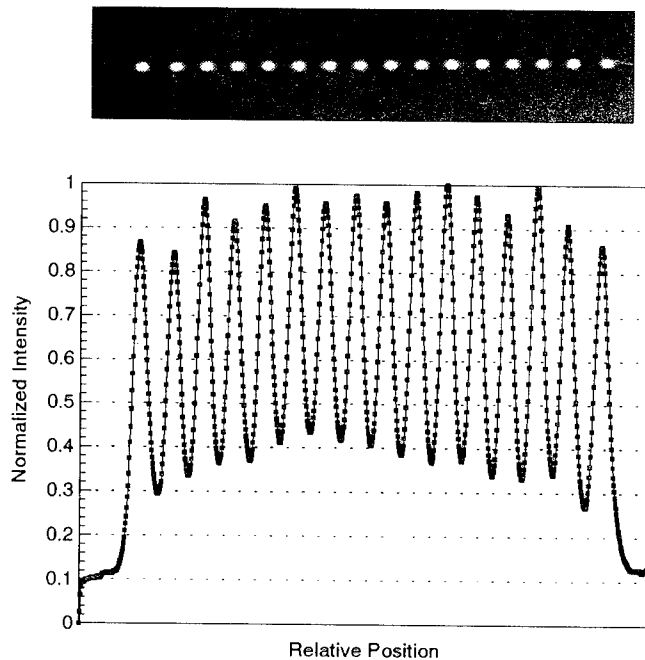


Figure 5. Imaged output facet at the output ridge array and scanning slit detector data for a 1×16 guide/antiguide self-imaging beamsplitter for TM polarized input. The dimensions of this device are a width of $80.8 \mu\text{m}$, a length of $1,337.6 \mu\text{m}$, and input/output ridge guide width of $2.8 \mu\text{m}$. The output ridge array pitch is $5 \mu\text{m}$. Insertion loss is 2.2 dB, splitting ratio uniformity is $\pm 7.8\%$, and polarization crosstalk is -25.3 dB .

about 5 dB greater than that in the splitters. Again, this is attributed to the greater sidewall scattering in the straight-through waveguides.

Competitive splitter uniformity values are achievable with self-imaging in comparison with other techniques such as radiative splitters [4] and cascaded Y-junctions [1]. For a 1×16 waveguide splitter with an output waveguide array, the best reported splitting uniformity for radiative splitters is $\pm 10.5\%$ [13]; for self-imaging splitters $\pm 4\%$ [6]; and for this work $\pm 7.8\%$.

In comparison with previously demonstrated self-imaging beamsplitter implementation techniques, the guide/antiguide structure offers ease of manufacturability in a wide range of waveguide material systems. All that is required is one step etching through a photoresist mask. The etching can be performed with either a wet or dry process, since sloped sidewalls do not present a problem. This simple manufacturing process uniquely offers the capability of implementing self-imaging beamsplitters in LiNbO_3 and LiTaO_3 material systems.

Significant areas of active research include integration of self-imaging beamsplitters with active waveguide components, development of techniques for efficient and stable fiber-optic pigtailling, and investigation of novel device structures based on guided wave self-imaging. Recently, integration of lasers, gratings, modulators, and amplifiers with a radiative combiner was reported [14]. The device architecture formed a novel WDM source. Pigtailling of fiber-optic arrays to waveguide beamsplitters has shown efficiency

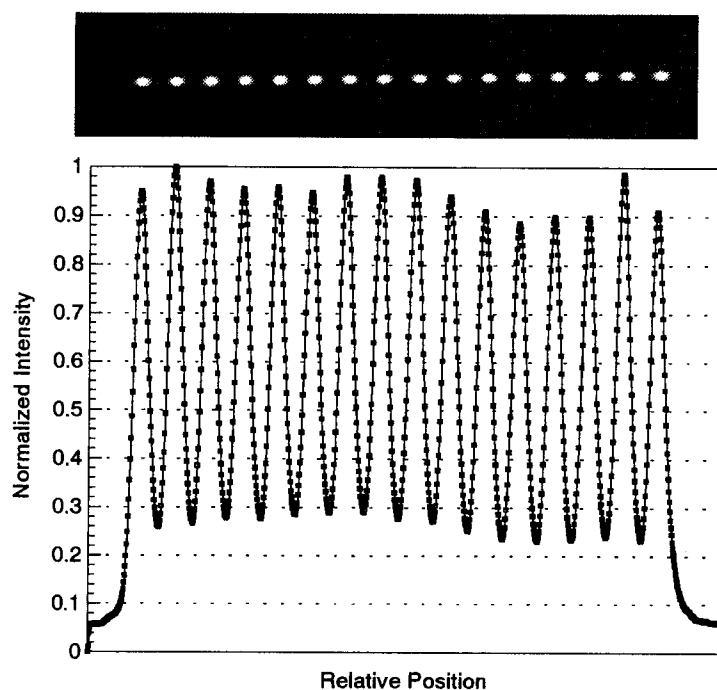


Figure 6. Imaged output facet at the multimode region's image plane and scanning slit detector data for a 1×16 guide/antiguide self-imaging beamsplitter for TM polarized input. The dimensions of this device are a width of $80.8 \mu\text{m}$, a length of $1,346.1 \mu\text{m}$, and input/output ridge guide width of $2.8 \mu\text{m}$. The output ridge array pitch is $5 \mu\text{m}$. Insertion loss is 1.8 dB, splitting ratio uniformity is $\pm 5.0\%$, and polarization crosstalk is -25.0 dB .

and long-term stability under severe environmental conditions [15], [16]. Multiple component integration and fiber pigtailling are critical stages to be overcome if waveguide devices are to come to fruition.

Because of its manufacturability and flexibility, guided wave self-imaging lends itself to a host of novel device structures. Proposed structures include generalized $N \times N$ Mach-Zehnder switches [17], phase diversity receivers [18], and WDM sources and demultiplexers.

ACKNOWLEDGEMENTS

The authors gratefully acknowledge MBE waveguide growth by Dr. Richard Leavitt of the Army Research Laboratory and funding support from the U.S. Army CECOM.

REFERENCES

- [1] M. Kawachi, "Silica waveguides on silicon and their application to integrated-optic components," *Opt. Quantum Electron.*, vol. 22, pp. 391–416, 1990.
- [2] E. A. J. Marcatilli, "Dielectric rectangular waveguide and directional coupler for integrated optics," *Bell Syst. Tech. J.*, vol. 48, pp. 2071–2102, 1969.

- [3] J. Saarinen, J. Turunen, and J. Huttunen, "Volume diffraction effects in computer-generated guided-wave holography," *Appl. Opt.*, vol. 33, pp. 1035-1042, 1994.
- [4] M. Zirngibl, C. Dragone, C. H. Joyner, M. Kuznetsov, and U. Koren, "Efficient 1×16 optical power splitter based on InP," *Electron. Lett.*, vol. 28, pp. 1212-1213, 1992.
- [5] H. Takahashi, K. Okamoto, Y. Ohmori, "Integrated-optic 1×128 power splitter with multi-funnel waveguide," *IEEE Photon. Technol. Lett.*, vol. 5, pp. 58-60, 1993.
- [6] J. M. Heaton, R. M. Jenkins, D. R. Wight, J. T. Parker, J. C. H. Birbeck, and K. P. Hilton, "Novel 1-to-N way integrated optical beam splitters using symmetric mode mixing in GaAs/AlGaAs multimode waveguides," *Appl. Phys. Lett.*, vol. 61, pp. 1754-1756, 1992.
- [7] R. Ulrich and G. Ankele, "Self-imaging in homogeneous planar optical waveguides," *Appl. Phys. Lett.*, vol. 27, pp. 337-339, 1975.
- [8] A. Ferreras, F. Rodriguez, E. Gomez-Salas, J. L. de Miguel, and F. Hernandez-Gil, "Design and fabrication of a InP/InGaAsP multimode power splitter," in *1993 Tech. Dig., Integrated Photonics Research*, vol. 10, paper IME4, Palm Springs, 1993.
- [9] R. J. Deri, E. Kapon, and L. M. Schiavone, "Scattering in low-loss GaAs/AlGaAs rib waveguides," *Appl. Phys. Lett.*, vol. 51, pp. 789-791, 1987.
- [10] P. S. Chung, C. M. Horwitz, and W. L. Guo, "Dry etching characteristics of LiNbO_3 ," *Electron. Lett.*, vol. 22, pp. 484-485, 1986.
- [11] R. Ulrich and T. Kamiya, "Resolution of self-images in planar optical waveguides," *J. Opt. Soc. Am.*, vol. 68, pp. 583-592, 1978.
- [12] R. Ulrich and R. J. Martin, "Geometrical optics in thin film light guides," *Appl. Opt.*, vol. 10, pp. 2077-2085, 1971.
- [13] U. Koren, M. G. Young, B. I. Miller, M. A. Newkirk, M. Chien, M. Zirngibl, C. Dragone, B. Glance, T. L. Koch, B. Tell, K. Brown-Goebeler, and G. Raybon, " 1×16 photonic switch operating at $1.55 \mu\text{m}$ wavelength based on optical amplifiers and a passive combiner," *Appl. Phys. Lett.*, vol. 61, pp. 1613-1615, 1992.
- [14] M. G. Young, U. Koren, B. I. Miller, M. A. Newkirk, M. Chien, M. Zirngibl, C. Dragone, B. Tell, H. M. Presby, and G. Raybon, "A 16×1 wavelength division multiplexer with integrated distributed Bragg reflector lasers and electroabsorption modulators," *IEEE Photon. Technol. Lett.*, vol. 5, pp. 908-910, 1993.
- [15] K. Kato, K. Okamoto, H. Okazaki, Y. Ohmori, and I. Nishi, "Packaging of large-scale integrated-optic $N \times N$ star couplers," *IEEE Photon. Technol. Lett.*, vol. 4, pp. 348-351, 1993.
- [16] Y. Hibino, F. Hanawa, H. Nakagome, N. Takato, T. Miya, and M. Yamaguchi, "High reliability silica-based PLC 1×8 splitters on Si," *Electron. Lett.*, vol. 30, pp. 640-642, 1994.
- [17] R. M. Jenkins, J. M. Heaton, D. R. Wight, J. T. Parker, J. C. H. Birbeck, G. W. Smith, and K. P. Hilton, "Novel $1 \times N$ and $N \times N$ integrated optical switches using self-imaging multimode GaAs/AlGaAs waveguides," *Appl. Phys. Lett.*, vol. 64, pp. 684-686, 1994.
- [18] E. C. M. Pennings, R. J. Deri, R. Bhat, T. R. Hayes, and N. C. Andreadakis, "Ultra-compact integrated all-passive optical 90 degree hybrid using self-imaging," in *Proc. of the 18th European Conf. on Opt. Comm.*, vol. 1, pp. 4611-464, 1992.

STRAINED-LAYER SUPERLATTICES FOR POLARIZATION-INSENSITIVE INTEGRATED WAVEGUIDE APPLICATIONS

Dhrupad A. Trivedi and Neal G. Anderson

Department of Electrical and Computer Engineering
University of Massachusetts at Amherst
Amherst, MA 01003

INTRODUCTION

Quantum well intermixing has emerged as a new method to define waveguides in semiconductors. Selected regions in a semiconductor quantum well structure are altered using dielectric cap disordering, laser induced disordering or impurity induced disordering (IID) thus creating a refractive index discontinuity at the diffusion boundary. The chief advantage of using multiple quantum wells in disordered structures is that it is possible to control the electronic and optical properties of multiple-quantum wells and superlattices by varying the layer widths and compositions. This creates great potential for designing waveguides, since quantum-size effects and strain effects can be used to obtain a range of superlattice designs which display desirable characteristics such as polarization insensitivity to the propagating light. Also, since IID provides a way to create waveguides in superlattices using conventional IC processing techniques, it is an attractive process to be considered for fabricating optoelectronic integrated circuits.

One of the potential applications of the IID technique is to create low-loss waveguides for interconnecting components on OEIC's. Such waveguides can be used to construct passive components which can be used in conjunction with other integrated optoelectronic and photonic components. For such applications the waveguide should have a low optical absorption coefficient to ensure low loss and high electrical resistance to isolate the integrated waveguide from other components. One of the ways to achieve high electrical resistance is to use electrically neutral impurities such as Fluorine (Marsh 1992), rather than electrically active impurities such as Si, or Zn, which simultaneously reduces free carrier absorption and increases electrical resistivity.

In this work we use a sophisticated model for designing the optical properties of strained-layer superlattices which can be used to form waveguides using quantum well disordering. The approach involves evaluating the dielectric constants of the superlattice

from first principles using a theoretical approach that combines the K-p and tight-binding methods for obtaining the superlattice bandstructure and optical matrix elements throughout the Brillouin zone. Superlattices are designed to have an operating wavelength of 1.55 microns, closely lattice match InP and are suitable for neutral disordering. The disordered region is modeled as a bulk alloy.

THEORETICAL MODEL FOR SUPERLATTICE OPTICAL PROPERTIES

The theoretical model used to obtain the optical properties of the strained layer superlattices combines the superlattice K-p model with a superlattice tight-binding calculation to obtain the dielectric constants for the superlattice from first principles. The K-p model is most valid at the superlattice zone center while the tight-binding calculation provides results which are more accurate than the K-p model further out in the zone.

The real and imaginary parts of the dielectric constant ($\epsilon = \epsilon_1 + i\epsilon_2$) can be expressed as :

$$\epsilon_2(\omega) = \frac{4\pi^2 e^2}{m^2 \omega^2} \sum_{c,v} \int_{BZ} \frac{2dk}{2\pi^3} |\mathbf{p} \cdot \mathbf{M}_{cv}|^2 \delta(E_c(\mathbf{k}) - E_v(\mathbf{k}) - \hbar\omega) \quad (1)$$

$$\epsilon_1(\omega) = 1 + \frac{8\pi^2 e^2}{m^2} \sum_{c,v} \int_{BZ} \frac{2dk}{2\pi^3} \frac{|\mathbf{p} \cdot \mathbf{M}_{cv}|^2}{\hbar} \frac{1}{[E_c(\mathbf{k}) - E_v(\mathbf{k})]^2 - \hbar^2 \omega^2} \quad (2)$$

where e is the electron charge, m is the electron mass, ω is the frequency, $\hbar = h/2\pi$, where h is the Planck's constant, \mathbf{k} is the wavevector, E_c, E_v are the energy levels of the conduction state and the valence state respectively, and \mathbf{M}_{cv} is the interband optical matrix element connecting those two states. \mathbf{p} is the polarization vector of the radiation. The summation is carried out over all possible subband transitions and throughout the first Brillouin zone. From a knowledge of the band structure of the system and the matrix elements, the complex dielectric constants of the superlattice can thus be evaluated as functions of the frequency and polarization of radiation. Note that in case of a superlattice, the summation in the above expressions for the dielectric constant must be carried out over all the minibands of the superlattice under the appropriate selection rules. Using electromagnetic theory it is possible to obtain expressions for the absorption coefficient (α), refractive index (n) and the extinction coefficient (κ) as a function of the photon energy

$$(n + i\kappa)^2 = \epsilon_1 + i\epsilon_2 \quad (3)$$

$$\alpha = \omega \epsilon_2 / nc \quad (4)$$

where, ω is the frequency of radiation, and c is the velocity of light in free space.

To carry out the integration in Equation 2 throughout the zone while retaining the accuracy at the zone center the integration space is divided into two regimes; one where the tight-binding model is used and the other where the K-p model is used. The K-p model is used for states which are bound in at least one layer while the tight-binding model is used for states which are unbound in both superlattice layers. This is schematically shown in Figure 1 for a typical type I superlattice configuration.

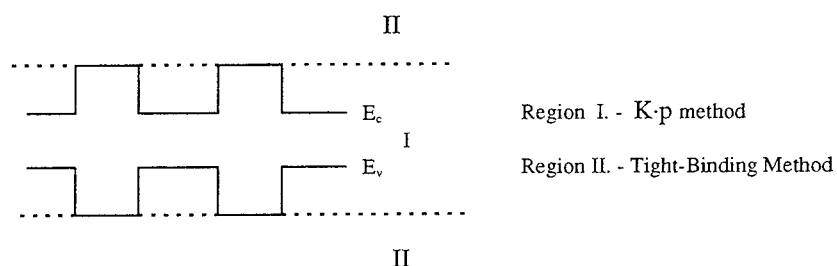


Figure 1 : A pictorial representation of the integration scheme used to calculate the dielectric constants for a superlattice

While there is a discontinuity in the two bandstructures at the transition point from regime I to regime II, this does not show up prominently in the dielectric constant which is obtained after integration over the full-zone bandstructure. The matrix elements used in the calculations of the dielectric constants are obtained from the K-p or the tight-binding model depending upon the regime of integration. Matrix elements for the K-p method are obtained in terms of the overlap of the superlattice envelope functions and bulk matrix elements (Baliga 1994). The matrix elements for the tight-binding method are obtained in terms of known K-p matrix elements using a recently developed method (Lew and Ram-mohan 1992). This method connects the optical matrix elements to elements of the tight-binding Hamiltonian matrix.

Details of the K-p method and results obtained therefrom for two material systems have been published elsewhere (Baliga 1994). The tight-binding treatment is based on a supercell calculation using only nearest neighbor interactions. It uses the sp^3s^* basis set of atomic orbitals and interaction parameters used are same as those obtained from the calculation of bulk bandstructure using the tight-binding method. The tight-binding Hamiltonian is numerically solved to obtain the allowed energy levels for a given value of the superlattice wavevector. Details of the formalism for obtaining optical properties will be presented in an upcoming publication.

DESIGN OF SUPERLATTICES FOR DISORDERED WAVEGUIDES

The two superlattice systems chosen for the study are the InGaAs-InAlGaAs and the InGaAs-InGaAsP systems. These systems were chosen since they have transition energies in the 1.55 micron range, and allow for the growth of strain balanced superlattices while allowing for the design of the transition energies using strain and quantum size effects. Also, it was recently shown experimentally by Marsh (1992) that these two material systems were strong candidates for neutral impurity disordering. All the cases considered for this study satisfy the following criteria :

- The structures are closely lattice matched to InP. In some cases, the net strain in the structure is minimized, with successive layers alternately under compression and tension. Superlattice-to-substrate matching allows for the growth of superlattices which are relatively defect free and thus provide better waveguiding properties.

- No individual layer exceeds the critical thickness limitations which are present due to strain in the structure.
- The superlattices are chosen so as to have a band structure configuration which leads to nearly equal values for the TE and TM refractive indices.

The superlattices in this study are designed to have optical gaps of 0.85 eV at 300K for all the InGaAs-InAlGaAs structures and 0.9 eV at 300K for all of the InGaAs-InGaAsP structures. Since the operating energy(wavelength) is considered to be 0.8 eV (1.55 micron) for both the systems, it assures a small band-to-band absorption at the operating wavelength. The topmost heavy-hole and light-hole bands are close to each other in energy and within 5 meV of the desired optical gaps in all the cases. This provides the conditions suitable for obtaining optical constants which are similar for TE as well as TM polarizations (i.e. polarization insensitivity). Sets of structures meeting these criteria are described in Tables I and II.

Table 1 : Superlattices studied for the InGaAs-InAlGaAs system

Case	In _{x_a} Ga _{1-x_a} As Thickness	x _a	In _{1-x_b-y_b} Al _{x_b} Ga _{y_b} As Thickness	x _b	y _b
I	50 Å	0.53	50 Å	0.08	0.43
II	100 Å	0.46	50 Å	0.05	0.39
III	150 Å	0.46	50 Å	0.35	0.12

Table 2 : Superlattices studied for the InGaAs-InGaAsP system

Case	In _{x_a} Ga _{1-x_a} As Thickness	x _a	In _{x_b} Ga _{1-x_b} As _{1-y_b} P _{y_b} Thickness	x _b	y _b
IV	50 Å	0.45	50 Å	0.17	0.41
V	50 Å	0.45	100 Å	0.24	0.56
VI	50 Å	0.45	150 Å	0.25	0.56

These cases are chosen to illustrate the flexibility allowed in the design of such superlattices. For the first material system the well width changes while the barrier width is held constant, whereas, for the second material system the well width is held constant while the barrier width is progressively increased. In both cases the layer compositions are chosen to obtain the desired optical gap and proximity of the topmost light- and heavy-hole bands. The superlattice in-plane lattice constants match InP to within 0.5 % for all of the cases studied here.

RESULTS

Calculated optical constants are shown for the InGaAs-InAlGaAs superlattices in Figure 2 and for the InGaAs-InGaAsP superlattices in Figure 3 for both TE and TM polarizations. Recall that the operating point is designed to be around 0.8 eV for both systems. This point is 50 meV or 100 meV below the electronic bandgap for the two material systems, ensuring that the band to band absorption is eliminated at the operating

wavelength. Values of the refractive index for the superlattices at the operating point are shown in the Tables 3 and 4 along with the calculated refractive index of the disordered superlattice treated as a bulk alloy. The refractive index of the alloy is computed in terms of linear interpolation of the refractive indices of the constituent binaries weighted by their composition fractions. Refractive index discontinuities at the as-grown/disordered interfaces ($\Delta n \%$) are shown in Table 3 and 4 alongside the superlattice refractive indices. The TE and TM refractive indices of the as-grown superlattices are well within 1% of one another for the cases considered. Note that in the first material system, while all the cases studied have the same electronic bandgap, the refractive index for the superlattice labeled Case III is higher than the other two and provides the largest refractive index difference with reference to the disordered alloy. Similarly, for the second material system Case IV provides the largest refractive index step.

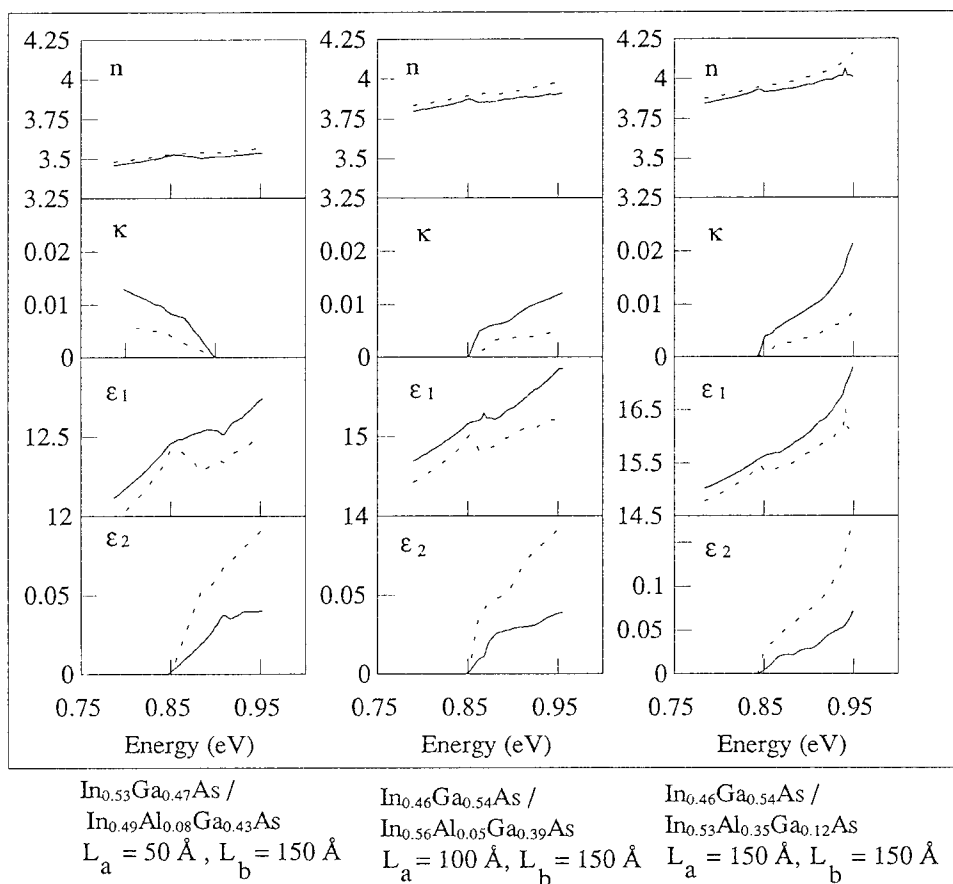


Figure 2 : Plots of the refractive index (n), extinction coefficient (κ) and the real (ϵ_1) and imaginary (ϵ_2) parts of the dielectric constant for InGaAs-InAlGaAs superlattices, closely lattice matched to InP at 300 K, for TE (solid line) and TM (dashed line) polarizations. L_a is the well width and L_b the barrier width for the superlattice.

Table 3 : Results obtained for the InGaAs-InAlGaAs system

	Refractive index of superlattice at 0.8 eV	Refractive index of disordered region at 0.8 eV	Index step Δn (%)
Case I	3.466	3.422	1.3
Case II	3.806	3.427	9.9
Case III	3.859	3.432	11.1

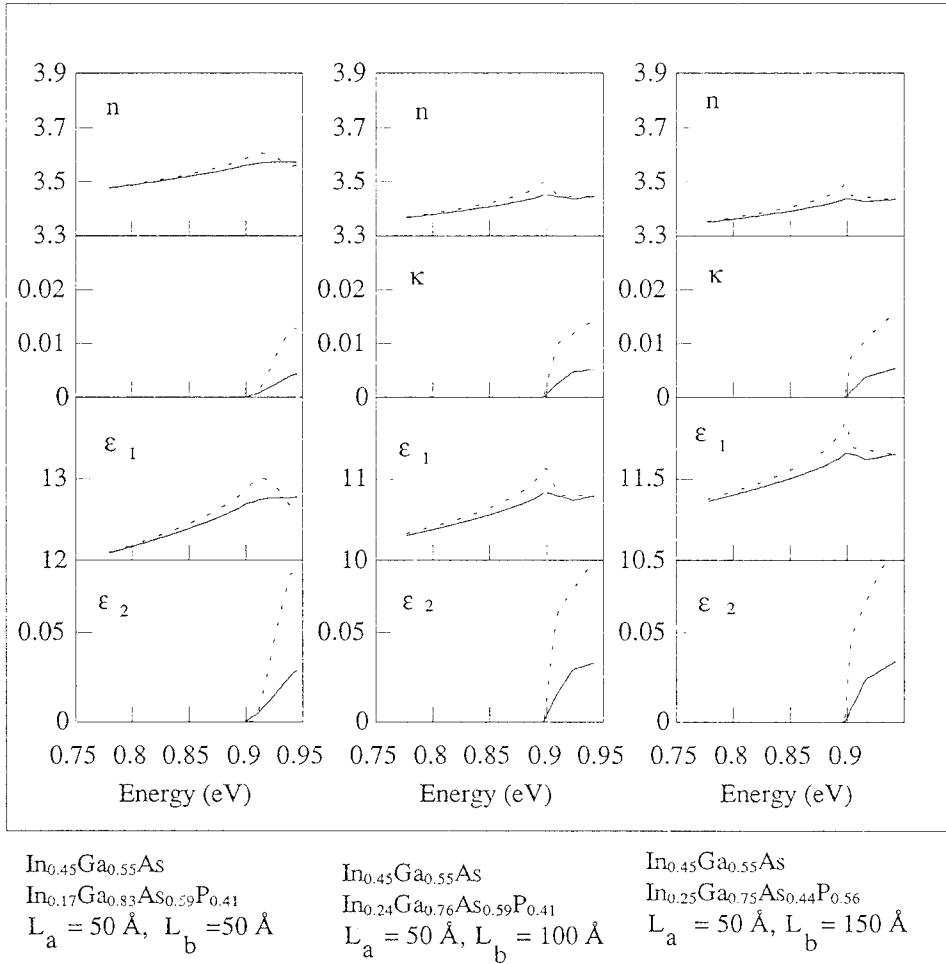


Figure 3 : Plots of the refractive index (n), extinction coefficient (κ) and the real (ϵ_1) and imaginary (ϵ_2) parts of the dielectric constant for InGaAs-InGaAsP superlattices, closely lattice matched to InP at 300 K, for TE (solid line) and TM (dashed line) polarizations. L_a is the well width and L_b the barrier width for the superlattices.

Table 4 : Results obtained for the InGaAs-InGaAsP system

	Refractive index of SL at 0.8 eV	Refractive index of disordered region at 0.8 eV	Index step Δn (%)
Case IV	3.488	3.340	4.2
Case V	3.377	3.293	2.5
Case VI	3.362	3.275	2.6

SUMMARY AND CONCLUSIONS

A sophisticated model was developed for calculating superlattice optical properties. This model can be used to design the optical properties of strained-layer superlattices to yield structures which best meet the requirements such as polarization insensitivity to propagating light in superlattice based disordered waveguides. In this work, we have used this model to design and study strained-layer InGaAs-InAlGaAs and InGaAs-InGaAsP superlattices for polarization insensitive waveguides.

Choosing a superlattice with energy band structure that has nearly merged light- and heavy-hole bands favors conditions which lead to polarization insensitivity. In the cases studied here it is possible to make the TE and TM refractive indices almost equal by proper choice of the layer widths and compositions. However, a merged band configuration does not necessarily lead to polarization insensitivity as TE and TM refractive indices are closest when the light-hole subband is slightly above the heavy-hole subband. Also, in actual waveguides, the TM modes are loosely confined as compared to the TE modes thus requiring higher TM refractive indices for polarization insensitive waveguiding. Thus, to design polarization-insensitive waveguides, it would be necessary to design superlattices with band-structure configurations where the topmost light-hole subband was energetically higher than the heavy-hole subband by a small amount (~ 1 to 10 meV).

REFERENCES

- Baliga, A, Trivedi, D. and Anderson, N.G., 1994, "Tensile strain effects in quantum-well and superlattice band structures", *Physical Review B*, 49:10402
- Lew Yan Voon, L.C., Ram-mohan, L.R., 1992, "Tight-Binding Representation of Optical Matrix Elements : Theory and Applications ", *Physical Review B*, 47: 15500
- Marsh, J.H, 1992, in " Waveguide Optoelectronics" edited by J. H. Marsh and R. M. De La Rue, Kluwer Academic Publishers, Boston

POWER COUPLING EFFICIENCY FOR ELECTRO-OPTIC DIRECTIONAL COUPLER SWITCH

T. Wongcharoen*, B.M.A. Rahman and K.T.V. Grattan

City University
Department of Electrical, Electronic and Information Engineering
Northampton Square, London EC1V 0HB, U.K.

INTRODUCTION

The investigation of coupling between optical waveguides is important for many directional coupler-based devices. Optical directional couplers, made from electro-optic materials, are the basis of several guided-wave devices including switches and modulators. The refractive index of the waveguide material changes due to the applied modulating field, which in turn affects the propagation constants of the two individual guides, the phase matching between them and the coupling length. When the change of refractive indices in the two guides are not identical due to unequal change of refractive indices in two coupled guides, then the power transfer efficiency deteriorates due to lack of phase matching between the guides. All these effects, combined together, change the total power transfer from one guide to another as a function of the applied potential, for switches and modulators.

MODAL SOLUTION BY FINITE ELEMENTS

The finite element method¹ has already been established as one of the most powerful methods to obtain modal solutions for a wide range of optical waveguides. In the finite element method, the region of concern is subdivided into a patchwork of a number of subregions called elements. These elements each can be of various shapes, such as triangles or rectangles or even having curved sides and they can be of various sizes, to suit the device to be modelled. Using many elements, any cross-section with a complex boundary and various refractive index profiles can be accurately approximated. Each element can also have a different loss or gain factor, different anisotropy or different nonlinearity, so a wide range of practical waveguides can be considered. The vector \mathbf{H} -

* On leave from Bangkok University, Thailand.

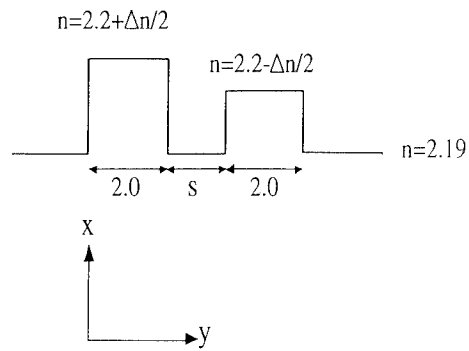


Figure 1 Schematic diagram of the structure representing an electro-optic directional coupler switch.

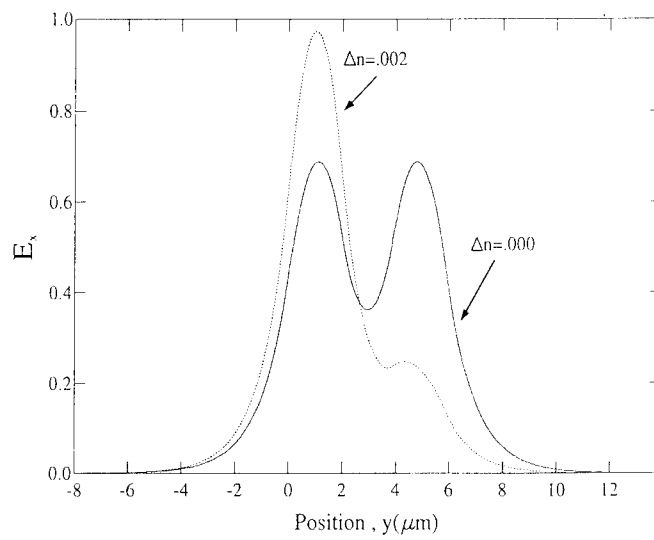


Figure 2. Variation of the field profiles for the first TE supermode, for $\Delta n = 0.0$, and 0.002 .

field formulation, which has been extensively used for the solution of a variety of optical waveguide problems, can be written as² :

$$\omega^2 = \frac{\int (\nabla \times H)^* \cdot \hat{\epsilon}^{-1} (\nabla \times H) d\Omega + \alpha \int (\nabla \cdot H)^* (\nabla \cdot H) d\Omega}{\int H^* \cdot \hat{\mu} H d\Omega} \quad (1)$$

The second part in the numerator imposes divergence conditions of the field in a least squares sense and eliminates possibility for spurious solutions. The above equation, being a vector formulation, this is "exact-in-the-limit", and particularly suitable for dielectric waveguides as the magnetic field is naturally continuous over the waveguide cross-section. In this formulation, $\hat{\epsilon}$ can be tensor, so the formulation is applicable to consider electro-optic and acousto-optic effects in optical waveguides and directional couplers. This method can provide accurate propagation constants and modal field profiles for isolated guides and supermodes for coupled structures even when the guides are strongly coupled or nonidentical³.

THE COUPLED MODE APPROACH

Once the modal properties of the isolated modes and supermodes are known, then the power transfer efficiency between the guides can be calculated by using the coupled mode approach. Recently there has been extensive research work to improve the traditional coupled mode approaches, among them the research of Hardy and Streifer,⁴ Marcanti⁵ and Chuang⁶ can be mentioned. In this work, first the accurate propagation constants and transverse modal field profiles are obtained by using the finite element method. Then the mode overlap, C_{ij} , and the coupling coefficients, K_{ij} , are calculated from the modal field profiles using the coupled mode approach. Finally the power transfer efficiency is calculated from the various coupling parameters.

RESULTS

In this example, a titanium-diffused LiNbO₃ electro-optic directional coupler switch is considered together with its simplified equivalent planar structure, as shown in Fig. 1. The unperturbed guides are 2 μm wide and with the refractive index 2.2, when no modulation is applied. The separation region between the guides is s μm wide with a refractive index in this region and as well as in the two cladding regions of 2.19. The operating wavelength is 1.3 μm . In this work it is assumed that when a positive modulation field is applied, the refractive index in the left guide is increased by $\Delta n/2$ and decreased by an equal amount in the right guide due to the opposite sign of the electric field, and the guides are no longer identical. Although the refractive index change due to the electro-optic effect, Δn_i , can be tensor and proportional to the modulating field components, the variational formulation given by equation (1) can handle this, but in this planar example only an isotropic refractive index change is considered.

The electric field profiles for the first TE supermode are shown in Fig. 2 for $\Delta n = 0$ and 0.002 when the guide separation, s , is 1.9 μm . When no modulation is applied, $\Delta n = 0$, the two guides are identical and the even and odd supermodes are symmetrical and antisymmetrical respectively. The even supermode for identical coupled guides is shown

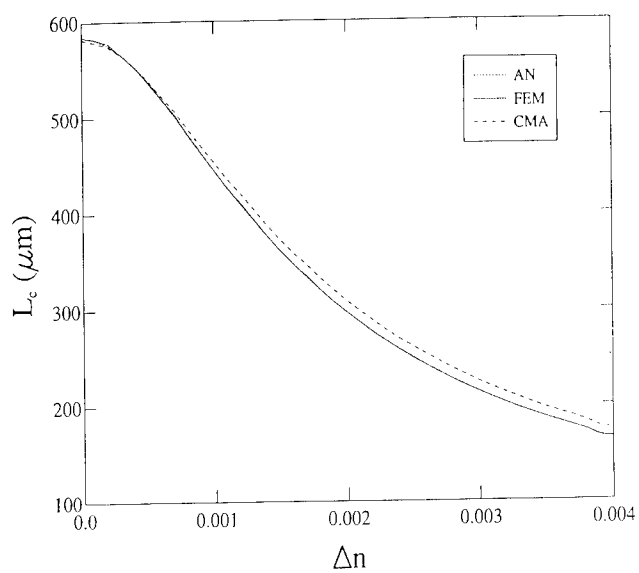


Figure 3. Variation of the coupling length with Δn , using different procedures.

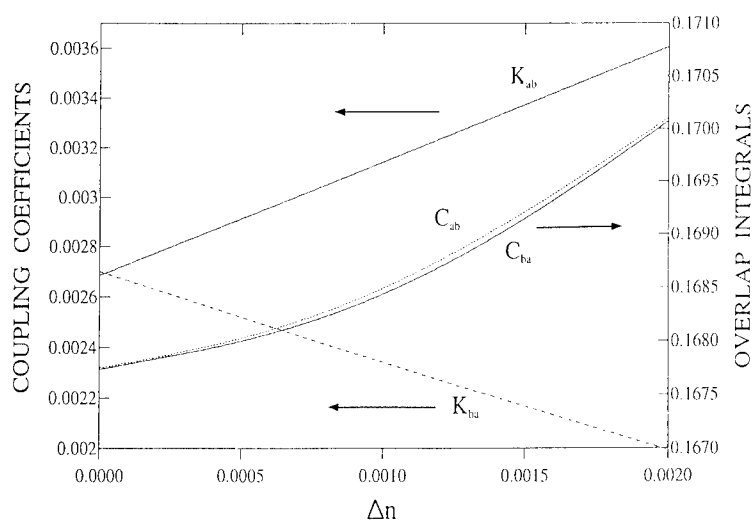


Figure 4. Variation of the coupling coefficients and overlap integrals with Δn .

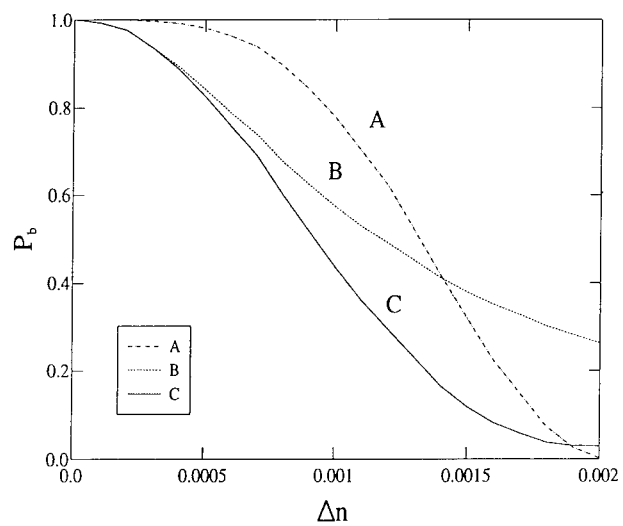


Figure 5. Variation of power transfer for three different situations.

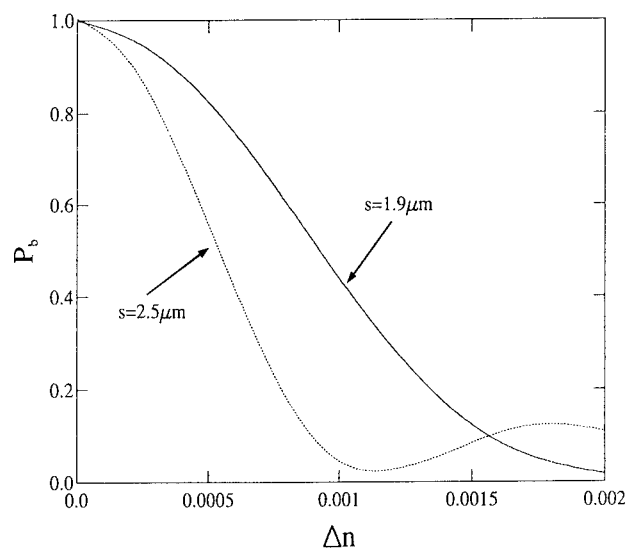


Figure 6. Variation of power transfer for two separation distances between the guides.

for $s = 1.9 \mu\text{m}$. However, when a modulation is applied, it can be observed that the first supermode is the deformed even-like mode with more power confined in the left guide which has a higher refractive index than the right guide. Similarly the second odd-like supermode will be more confined in the right guide, which is not shown here. This deformation is more prominent when the guide separation, s , is increased.

The coupling length decreases with the applied modulation since the propagation constant difference, $\Delta\beta$, between the two isolated waveguides increases. Propagation constants of two supermodes can also be calculated from the unperturbed modes of the two isolated guides using the coupled mode approach. Fig. 3 shows that the coupling length variations with Δn using the analytical method [AN], the finite element method [FEM] and using the coupled mode approach [CMA]. The analytical results and the finite element results are identical and cannot be distinguished one from another. The results using the coupled mode approach⁶ [CMA] shows slight disagreement. It can be observed that the coupling length is $296 \mu\text{m}$ when $\Delta n = 0.002$ compared to $583 \mu\text{m}$ at $\Delta n = 0$.

Fig. 4 shows the variation of the coupling coefficients, K_{ab} and C_{ab} by applying the coupled mode approach⁶. It can be noticed at $\Delta n = 0$, $K_{ab} = K_{ba}$, whereas when Δn increases K_{ab} increases and K_{ba} decreases. It may also be observed that C_{ab} and C_{ba} both increase with $|\Delta n|$ and C_{ab} and C_{ba} are slightly different.

Fig. 5 shows the power transfer efficiency between the guides under three different situations. The first, which is approximate and termed, *A*, neglects the phase mismatch ($\Delta\beta$) but considers only the effect of the coupling length (L_c) change due to the applied modulation. It can be seen that almost 100% power transfer occurs from guide *a* to guide *b* when $\Delta n = 0$. However, as Δn increases to 0.002, the power transfer from guide *a* to guide *b* is very small. This is due to the fact that at this situation the coupling length is nearly half of the coupling length at $\Delta n = 0$, so the power moves back to guide *a* as the total length is now twice the coupling length. In the second approximate case, *B*, the maximum power transfer is calculated when the device length is adjusted to be identical with the coupling length for all values of Δn . In this case, only the effect of phase mismatching between two isolated guides is considered. It can be observed that almost 100% power transfer occurs from guide *a* to guide *b* when $\Delta n = 0$ but again less power transfer is possible as Δn increases. In case *C*, as in the practical situation, the device length is fixed at $L=L_{co}$, L_{co} being the coupling length when no modulation is applied and also in this case the effect of phase mismatching is considered. The power transfer between guide *a* to *b* is always less than the maximum power transfer as shown by curve *B*. This result agrees with that of Chuang⁶. Fig. 6 illustrates the faster switching properties when the separation length, s , is increased when both coupling length and phase mismatching is considered. This is due to the fact that two isolated modes lose their synchronism faster because of reduced modal interactions. However, it should also be noted that with a larger waveguide separation, s , the device length will be longer and fabrication tolerances may be more critical.

CONCLUSION

The finite element analysis has been seen to provide accurate results for weakly or strongly coupled identical or nonidentical waveguides. Here the results are restricted to the TE modes in planar waveguides to enable a comparison of our results with other published work but it can be stressed that this numerical procedure is equally valid for hybrid modes in coupled waveguides with two dimensional confinement, anisotropic refractive indices

and diffused profiles. The application of coupled mode theory, along with the accurate eigenvectors and eigenvalues obtained by the finite element method, can provide the power transfer ratio between such practical coupled waveguides. Important applications are in the design of directional coupler-based devices, including passive and active filters, modulators and switches incorporating electro-optic, elasto-optic and nonlinear phenomena.

REFERENCES

1. B.M.A. Rahman, F.A. Fernandez, and J.B. Davies, "Review of finite element method for microwave and optical waveguides", *Proc. IEEE*. **79** :1142 (1991).
2. B.M.A. Rahman and J.B. Davies, "Finite-element solution of integrated optical waveguides", *J. Lightwave Technol.* **LT-2** :682 (1984).
3. B.M.A. Rahman, T. Wongcharoen, and K.T.V. Grattan, "Finite element analysis of nonsynchronous directional couplers", *Fiber and Integrated Optics*. **13** :331 (1994).
4. A. Hardy and W. Streifer, "Coupled mode theory of parallel waveguides", *J. Lightwave Technol.* **LT-3**: 1135 (1985).
5. E. Marcatili, "Improved coupled-mode equations for dielectric guides", *IEEE J. Quantum Electron.* **QE-22** : 988 (1986).
6. S.L. Chuang, "Application of the strongly coupled-mode theory to integrated optical devices", *IEEE J. Quantum Electron.* **QE-23** : 499 (1987).

DESIGN OPTIMIZATION AND FABRICATION OF A WIDENED X-BRANCH DEMULTIPLEXER BY ION-EXCHANGE IN GLASS

G. L. Yip and L. J. M. Babin

Guided-Wave Photonics Laboratory
Department of Electrical Engineering
McGill University
3480 University Street
Montreal, Quebec H3A 2A7

ABSTRACT

To achieve high performances of guided-wave photonic devices, design optimization is very important. For accurate designs, detailed information on the characteristics of slab and channel guides fabricated in specific substrates must be known in relation to their fabrication conditions to obtain accurate index profile models for these waveguides, which often form the basic units in more complicated waveguide structures used in devices. To illustrate the design methodology, this paper will present the design optimization, fabrication and measurement of a widened X-branch demultiplexer by ion-exchange in glass. The use of the index profile modelling by the effective index method (EIM) and a finite difference vector beam propagation method (FD-VBPM) to simulate the device function will be discussed. A comparison between the theoretical and experimental results will be made to demonstrate the effectiveness of the design methodology presented.

1. INTRODUCTION

Research activities in realizing planar guided-wave photonic devices fabricated by the technologies of ion-exchange in glass^{1,2} (Izawa and Nakagome, 1972; Giallorenzi et al., 1973) and Ti-diffusion in LiNbO_3 ³ (Schmidt and Kaminow, 1974) substrates have been progressing since the early 1970's. Both technologies involve diffusion processes and promise great signal processing capabilities in optical fiber communication and sensor systems such as power division, wavelength division, multiplexing, demultiplexing, modulation, switching, polarization splitting and so on. However, design optimization is very important to achieve high performances of guided-wave photonic devices. For accurate designs, namely, designs that can predict the performances of subsequently

fabricated devices with a reasonable accuracy, characteristics of slab and channel guides fabricated in specific substrates must be investigated in detail to establish their intimate relations with the fabrication conditions since these simple structures often form the basic units in more complicated waveguide structures used in devices. A knowledge of these relations, along with mathematics, then equip the device designers with the necessary tools to achieve design optimization. As an illustrative example, this paper will present the design optimization, fabrication and measurements of a widened X-branch demultiplexer by ion-exchange in glass. The design methodology^{4,5} involving the use of the index profile modelling by the effective index method (EIM)⁶, combined with a two-dimensional finite-difference vector beam propagation method (2-D FD-VBPM)⁷ will be presented. A comparison between theoretical and experimental results will be made to demonstrate the effectiveness of this design methodology. Although experimental work on a similar device was reported previously by others⁸, the design aspect has not yet been elaborated on before.

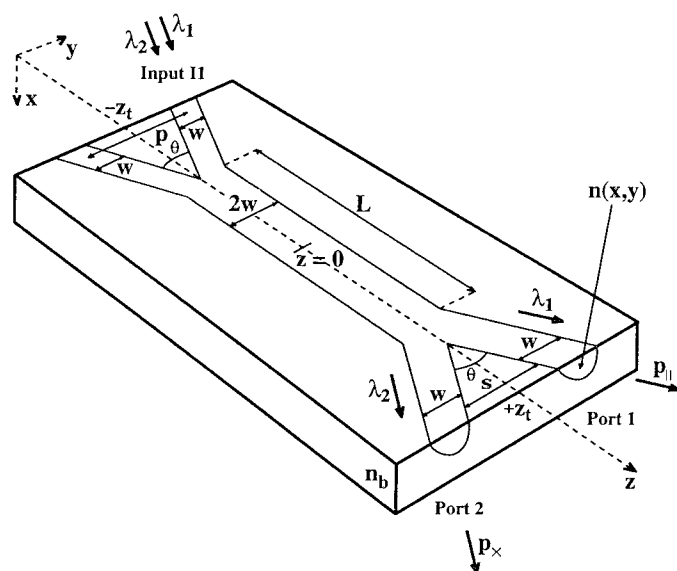


Figure 1. Widened X-branch

2. PRINCIPLE OF OPERATION

The device configuration is shown in Figure 1. It consists of input and output waveguides in the form of two identical tapered directional couplers of length l_t connected adiabatically to a two-mode waveguide of length L . Each channel guide in the tapered region has a width $2w$. This device works on the principle of interference between the two normal modes (TMI)⁹, supported by the structure, namely, the symmetric mode Ψ_s and the anti-symmetric mode Ψ_a . In the tapered regions ($z < -L/2$ or $z > L/2$), the symmetric and anti-symmetric modes can be considered as two different combinations of the two fundamental modes of the two input channel guides taken separately¹⁰. The two propagation constants β_s and β_a for Ψ_s and Ψ_a depend on the spacing between the two input or output branches and, hence, on z . In the central waveguide, the propagation constants β_s and β_a are constant over the length L . Due to mode orthogonality, Ψ_s and

Ψ_a do not exchange energy along the entire device. However, since $\beta_s \neq \beta_a$, the two modes accumulate a relative phase difference $\Phi = \int (\beta_s - \beta_a) dz$ along the device length. The power output at port 1 and 2 are given by¹⁰

$$\text{At output port 1 } (y > 0), P_1 = P_{in} \cos^2(\Phi/2) \quad (1)$$

$$\text{At output port 2 } (y < 0), P_x = P_{in} \sin^2(\Phi/2) \quad (2)$$

where P_{in} (normalized to unity) is the input power at port 1 for either λ_1 (1.31 μm) or λ_2 (1.55 μm) as shown in Figure 1. The operating conditions required for wavelength demultiplexing are¹¹:

$$\Phi(\lambda_1) = \Delta\beta_c(\lambda_1)L + 2\Phi_t(\lambda_1) = m\pi \quad (3)$$

$$\Phi(\lambda_2) = \Delta\beta_c(\lambda_2)L + 2\Phi_t(\lambda_2) = (m-1)\pi \quad (4)$$

where $\Delta\beta_c = \beta_s - \beta_a$ over the central region, whereas $\Phi_t = \int_{z_1}^{z_2} \Delta\beta_t(z) dz$ over either tapered region, z_1 and z_2 being either $-L/2$ and $-L/2$ or $L/2$ and $L/2$ and $\Delta\beta_t(z) = \beta_s(z) - \beta_a(z)$. If m is an even integer, we can show, using Eqns. (1) and (2), that $P_1(\lambda_1) = 1$, $P_x(\lambda_1) = 0$ and $P_1(\lambda_2) = 0$, $P_x(\lambda_2) = 1$. Hence, the light at λ_1 is channelled into the output port 1 while that at λ_2 into the output port 2. If m is an odd integer, the situation is reversed. In either case, wavelength demultiplexing can be achieved. The extinction ratios (ER) at both wavelengths are defined and calculated as:

$$ER(\lambda) = 10 \log |P_x(\lambda)/P_1(\lambda)| = 10 \log |\tan^2(\Phi/2)| \quad (5)$$

3. MODELLING AND DESIGN SIMULATION

The propagation characteristics of dielectric waveguides are critically dependent on the index profiles. Hence, the first step in a numerical simulation and design would be to determine as accurately as possible the index profiles $n(x, y)$ for the two basic structures which make up the present device, namely, a two-mode waveguide in the central region and a directional coupler configuration in each tapered region. For both cases, the ion-exchange diffusion equation, Eqn. (6), was solved numerically, with the specified fabrication conditions: diffusion temperature T and time t , using a three-level finite-difference scheme¹².

$$\frac{\partial C}{\partial t} = \frac{\partial}{\partial x} \left(\frac{D_k}{1-\alpha C} \frac{\partial C}{\partial x} \right) + \frac{\partial}{\partial y} \left(\frac{D_k}{1-\alpha C} \frac{\partial C}{\partial y} \right) \quad (6)$$

with $C = C_k/C_0$ and $\alpha = 1 - D_k/D_0$, where C_k and D_k are the concentration and self-diffusion coefficients of the incoming ions while C_0 and D_0 are those of the outgoing ions in the glass prior to the exchange. For the $K^+ \leftrightarrow Na^+$ ion-exchange used in our fabrication, the values of D_k for K^+ -ions at 1.152 and 1.523 μm can be obtained from our previous experimental characterizations of the planar waveguides by K^+ -ion exchange in soda-lime glass¹³ as shown in Table 1.

Table 1. Measured surface index change Δn_s and the effective diffusion constants D_e at $T=385^\circ\text{C}$.

Δ (μm)	Δn_s^{TE} ($\times 10^{-3}$)	Δn_s^{TM} ($\times 10^{-3}$)	D_e^{TE} (m^2/sec) ($\times 10^{-16}$)	D_e^{TM} (m^2/sec) ($\times 10^{-16}$)
1.152	8.56 ± 0.11	10.05 ± 0.36	10.33	10.04
1.523	8.57 ± 0.26	10.34 ± 0.24	11.53	11.27

The value of D_k at $1.31 \mu\text{m}$ can be calculated by interpolation. α has been determined to be 0.998^{14} . The refractive index distribution $n(x,y)$ is assumed to be proportional to the concentration distribution $c(x,y)$. Hence,

$$n(x,y) = n_b + \Delta n_s \cdot c(x,y) \quad (7)$$

where n_b is the substrate index and $\Delta n_s = n_s - n_b$ the surface index change, n_s being the surface index after ion-exchange. Given $n(x,y)$, we could then solve the wave equation, using the numerical Runge-Kutta (R-K) method, in the depth problem of the effective-index method (EIM) to establish the lateral effective-index profile of the whole structure as depicted in Figure 2.a, neglecting side-diffusion and in Figure 2.b, including side-diffusion effects. In the central region, a

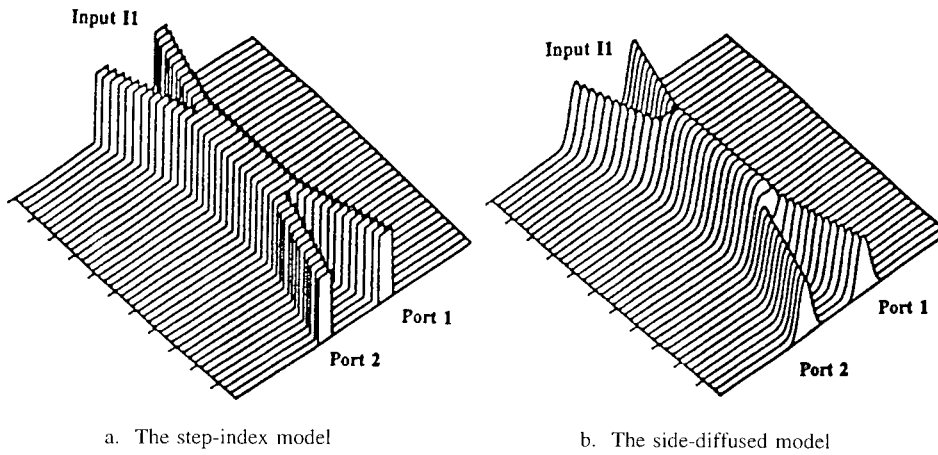


Figure 2. Lateral effective index for the widened X-branch

good analytical fitting function can be used as given in Eqn. (8), whereas, for the directional coupler in the tapered region, a good analytical approximation is given by Eqn. (9),

$$N_{\text{eff}}(x) = N(x) = n_b + \frac{[N(0) - n_b]}{2} \cdot \frac{\text{erf} \frac{x+w/2}{H} - \text{erf} \frac{x-w/2}{H}}{H} \quad (8)$$

where H is a fitting parameter and $H=0.7(D_k t)^{1/2}$ in the present problem.

$$N_{\text{eff}}(x)=N(x+p/2)+N(x-p/2)-n_b \quad (9)$$

With $N_{\text{eff}}(x)$ thus established, a 2-D FD-VBPM⁷ was applied to the side-diffused model in Figure 2.b to simulate the device function, employing the transparent boundary condition¹⁵. In order to calculate the propagation constants β_s , β_a required to satisfy Eqns. (3) and (4) in the design, a procedure due to Feit and Fleck¹⁶ was used. The BPM fields generated in our finite-difference scheme were used to compute the correlation function $P(z)$ by numerical integration. Fourier transforming $P(z)$ along z with a FFT algorithm produced the corresponding modal power spectrum $P(\beta)$. Locating the two peaks in $P(\beta)$ then yielded β_s and β_a . The calculations to find $\Delta\beta_c$, $\Delta\beta_i$, Φ_c , Φ_i followed. It is important to point out that $\Delta\beta_c$ depends on the wavelength λ , the waveguide width $2w$, hence w , the waveguide diffusion depth d [$d=(D_k t)^{1/2}$], hence t . The phase shift Φ_i also depends on these parameters, but, in addition, also the branching angle θ significantly. Hence, $\Delta\beta_c$ can be expressed as $\Delta\beta_c(\lambda, w, t)$ and Φ_i as $\Phi_i(\lambda, w, t, \theta)$. If m, w and θ are fixed and λ_1 and λ_2 set to 1.31 and 1.55 μm , respectively, t can be determined from Eqns. (3) and (4) by a root-search technique. The length L can then be determined from Eqn. (3) or (4). By adjusting the various device parameters, optimized device performance data such as the extinction ratios ER at λ_1 and λ_2 can be chosen in an iterative process. Two typical simulations are shown in Figure 3 for the TM modes, where the two-mode interference is evident in the central region while some radiation losses can be seen to occur in the tapered regions. The nearly optimized data indicated in Figure 3

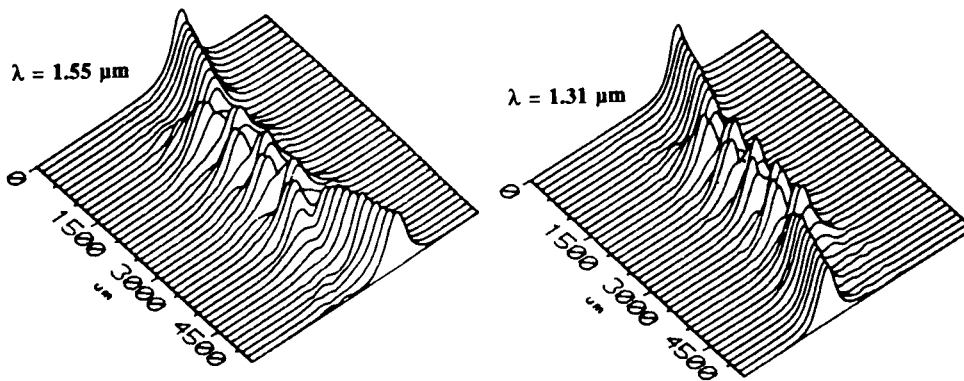


Figure 3. BPM simulations for TM modes
 $w=5.8 \mu\text{m}$, $t=275 \text{ min}$, $L=2930 \mu\text{m}$, $\theta=0.5^\circ$, $\text{ER}(1.31 \mu\text{m})=\text{ER}(1.55 \mu\text{m})=-35 \text{ dB}$

yield a theoretical ER of 35 dB for each wavelength. Numerical results show that most of the phase shift needed to effect wavelength demultiplexing is achieved over the central device region, the contribution from Φ_i over either tapered region being very small. The dependence of the device's performance on the two-mode interference over the central region makes the device very sensitive to fabrication errors in the optimized design parameters. An example is given in Figure 4 of the rapid decrease in its extinction ratio due to a fabrication error of $\Delta(2w)$ in the central waveguide width.

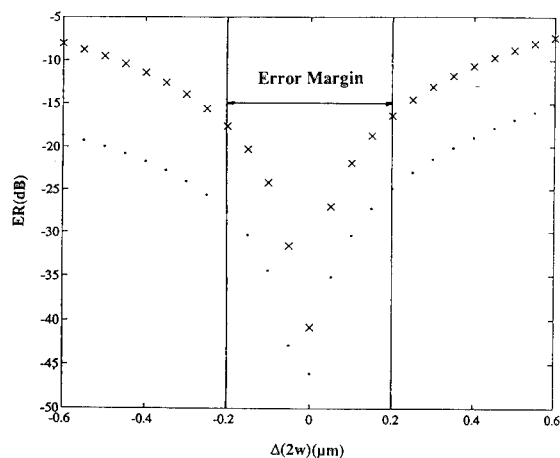


Figure 4. Extinction ratio $ER(\lambda)$ vs. error on width $\Delta(2w)$
 xxx $\lambda=1.31 \mu\text{m}$... $\lambda=1.55 \mu\text{m}$
 TM modes: $w=6.0 \mu\text{m}$, $t=257 \text{ min}$, $L=3100 \mu\text{m}$, $\theta=0.05^\circ$

The device is also polarization sensitive. Hence, a device optimized for the TM mode is not optimized for the TE mode and vice versa. The radiation loss can be calculated from $P_{\text{rad}}=1-(P_{\text{I}}+P_{\text{X}})$ and expressed in dB as $L_{\text{R}}=10 \log(1-P_{\text{rad}})$. Due to the page limitation, the presentation of this section must, regrettably, be very brief. For a more detailed exposition, the readers are referred to the listed references or the chapter on "Design Methodology for Guided-Wave Photonic Devices" in a forthcoming book¹⁷.

4. FABRICATION AND MEASUREMENT

Following the nearly optimized design data obtained as described above, a photomask with four sets of design data as shown in Table 2 was designed and made. The device samples were fabricated by a standard single-step $\text{K}^+\text{-Na}^+$ ion-exchange process at 385°C for diffusion times ranging from 220 to 280 minutes, yielding a diffusion depth d around $4 \mu\text{m}$. The fabricated device samples were experimentally

Table 2. Measurement results on the device samples
 TM modes, $\theta=0.5^\circ$. Theoretical $ER=-35 \text{ dB}$.

w (μm)	L (μm)	t (min)	ER (1.31 μm) (dB)	ER (1.55 μm) (dB)
6.0	3100	255	20	15
5.8	2930	270	20	>20
5.6	2710	280	15	18
5.9	2710	220	15	20

characterized by coupling an input laser beam at 1.31 and 1.523 μm , respectively, through a fiber into the input port I1 and observing the output light at port 1 and port 2 in an IR

vidicon camera, connected to an oscilloscope as shown in Figure 5, hence yielding the measured ER values as presented in Table 1. Considering the tight fabrication tolerances of the device parameters due to the TMI operation principle, illustrated in Figure 4, there appears to be a good agreement between the theoretical design and experimental results. It should be pointed out that in the device design calculations at $1.55\text{ }\mu\text{m}$ the index and diffusion coefficient data used as shown in Table 1 were, however, obtained at $1.523\text{ }\mu\text{m}$, using a HeNe laser. The subsequent measurement of the ER's of the fabricated devices were carried out with a semi-conductor laser diode at $1.55\text{ }\mu\text{m}$. Strictly speaking, the data used in the BPM simulations should be obtained by extrapolation at $1.55\text{ }\mu\text{m}$ to improve the agreement between the theoretical and measured ER's. Also, due to the nonlinearity of our Hamamatsu IR camera, the actual ER's could be higher.

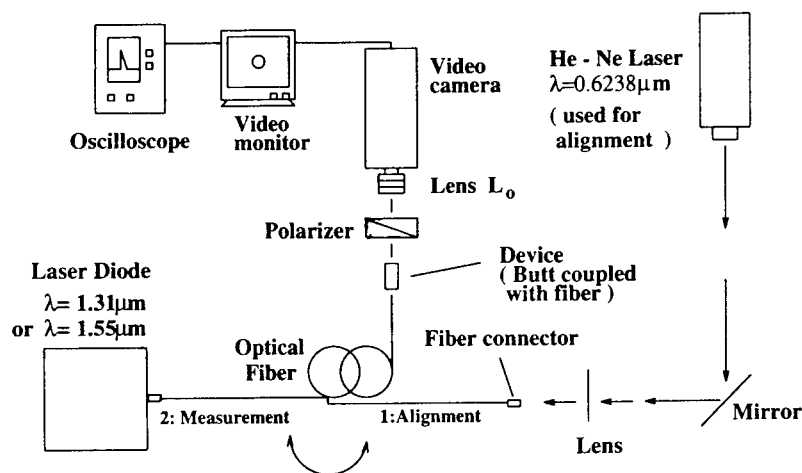


Figure 5. Measurement setup

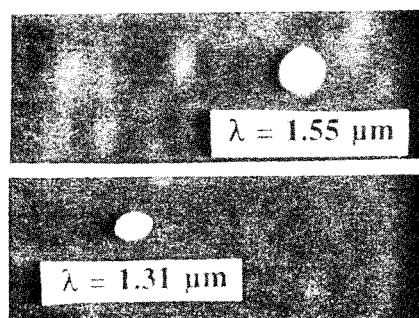


Figure 6. Output spots at end facet
TM modes: $w=5.8\text{ }\mu\text{m}$, $t=275\text{ min}$, $\theta=0.5^\circ$, $L=2930\text{ }\mu\text{m}$

5. CONCLUSIONS

The design optimization and experimental implementation of a widened X-branch demultiplexer by $K^+ \leftrightarrow Na^+$ ion-exchange in glass has been carried out. Our initial attempt has demonstrated a reasonably good agreement between theoretical and measured extinction ratios. Further improvements in design calculations, fabrication and measurement are clearly possible. The ion-exchange technology has matured to a stage where design-optimized glass waveguide devices are realizable in the laboratory to save device researchers and engineers much experimental effort in achieving high performing devices. The design methodology presented here is also applicable to guided-wave devices by other diffusion-related technologies such as Ti-indiffusion and proton-exchange in $LiNbO_3$ or $LiTaO_3$ substrates. Active research efforts are going on in improving the numerical accuracy and efficiency of the BPM algorithms to extend their applications in the analysis and design of wide-angle structures.

6. ACKNOWLEDGEMENTS

The research reported here was supported by a NSERC (Natural Sciences and Engineering Research Council, Canada) operating grant. L. Babin was a recipient of a graduate fellowship from Marseille, France (1991-1993). The authors would like to thank Alexandra Yip for typing this paper.

7. REFERENCES

1. T. Izawa and H. Nakagome, "Optical waveguides formed by electrically induced migration of ions in glass plates", *Appl. Phys. Lett.*, vol. 21, pp. 584-586, 1972.
2. T.G. Giallorenzi, E.J. West, R. Kirk, R. Ginther, and R.A. Andrews, "Optical waveguides formed by the thermal migration of ions in glass", *Appl. Opt.*, vol. 12, pp. 1240-1245, 1973.
3. R.V. Schmidt and I.P. Kaminow, "Metal-diffused optical waveguides in $LiNbO_3$ ", *Appl. Phys. Lett.*, vol. 25, pp. 458-460, 1974.
4. G.L. Yip, "Characterization, modelling and design optimization of integrated optical waveguide devices in glass", in: "Glasses for Optoelectronics II," G.C. Righini, ed., *SPIE Proceedings*, vol. 1513, pp. 26-36, 1991.
5. G.L. Yip, "Simulation and design of integrated optical waveguide devices by the BPM", in: "Integrated Optical Circuits," K.K. Wong, ed., *SPIE Proceedings*, vol. 1583, pp. 240-248, 1991.
6. H. Kogelnik, "Theory of optical waveguides", in: "Guided-Wave Optoelectronics," T. Tamir, ed., Springer Verlag, Heidelberg, 1988.
7. W.P. Huang, C.L. Xu, S.T. Chu, and S.K. Chaudhuri, "The finite-difference vector beam propagation method: analysis and assessment", *IEEE J. of Lightwave Technol.*, vol. 10, pp. 295-305, 1992.
8. C.D. Bernadi, S. Morasca, and D. Scarano, "Low loss, high performance integrated optic wavelength demultiplexers fabricated by K^+Na^+ ion exchange on glass," in: "Integrated Optics and Optoelectronics," K.K. Wong, ed., *SPIE Proceedings*, vol. 1177, pp. 155-161, 1989.
9. A. Neyer, "Electrooptic X-switch using single mode $LiNbO_3$ channel waveguides", *Electron. Lett.*, vol. 19, pp. 553-554, 1983.

10. R.A. Forber and E. Marom, "Symmetric directional coupler switches", *IEEE J. of Quantum Electron.*, vol. 22, pp. 911-919 1986.
11. Y.C. Chung, J.C. Yi, S.H. Kim, and S.S. Choi, "Analysis of a tunable multi-channel two-mode-interference wavelength division multiplexer/demultiplexer", *IEEE J. of Lightwave Techno.*, vol. 7, pp. 766-777, 1989.
12. J. Albert and G.L. Yip, "Wide single-mode channels and directional coupler by two-step ion-exchange in glass", *IEEE J. of Lightwave Techno.*, vol. 6, pp. 552-563, 1988.
13. G.L. Yip, K. Kishioka, F. Xiang, and J.Y. Chen, "Characterization of planar optical waveguides by K⁺-ion exchange in glass at 1.152 and 1.523 μm ", in: "Integrated Optical Circuits", K.K. Wong, ed., *SPIE Proceedings*, vol. 1583, pp. 14-18, 1991.
14. R.H. Doremus, "Ion exchange in glass", in: "Ion-Exchange, Vol. 2," J.A. Marinsky, ed., Dekker, New York 1969.
15. G.R. Hadley, "Transparent boundary condition for beam propagation", *Opt. Lett.*, vol. 16, pp. 624-626, 1991.
16. M.D. Feit and J.A. Fleck, "Computation of mode eigenfunctions in graded-index optical fibers by the propagation beam method", *Appl. Opt.*, vol. 19, pp. 2240-2246, 1980.
17. G.L. Yip, "Design methodology for guided-wave photonic devices", in: "Handbook of Photonics," M.C. Gupta, ed., CRC Press, Boca Raton, FL (To appear in 1995).

RECENT PROGRESS IN THE DEVELOPMENT OF TRAVELING WAVE LiNbO₃ MODULATORS

W. K. Burns

Naval Research Laboratory
Code 5671
Washington DC 20375

INTRODUCTION

Traveling wave electro-optic devices were first proposed by Kaminow(1) for bulk devices and demonstrated in LiNbO₃ waveguide modulators by Izutsu et al(2,3) in 1977. The basic concepts for broadband operation of phase velocity matching between the optical and the microwave wave, impedance matching between the microwave waveguide and external electrical connectors, low Ohmic losses in the microwave waveguide, etc. were well known at the outset. What was not immediately possible was the realization of these ideal conditions due to the intrinsic index of refraction and dielectric constants of LiNbO₃ and the limitations of what seemed like reasonable electrode geometries at the time. This paper will review how these limitations were overcome and show the recent rapid progress that has been made in the development of low drive voltage, broadband LiNbO₃ modulators.

EARLY WORK

Typical microwave effective indices for coplanar electrode structures on early LiNbO₃ devices were close to 4, whereas optical indices were ~2.2, indicating the difficulty of obtaining velocity matching. For coplanar strip(CPS) electrode structures impedances of ~50Ω could be obtained, but for coplanar waveguide(CPW) electrodes values closer to ~25Ω were more typical. Nevertheless by 1983 a 17GHz bandwidth modulator was reported(4), using a CPS electrode structure on a Mach Zehnder interferometer. Typical electrode structures of this era were electroplated gold, ~3-4μm thick.

Given the difficulties of obtaining true velocity matching, workers investigated approaches to obtain artificial velocity matching, which had earlier been proposed for bulk devices. The general idea was to design a periodic electrode structure which reversed the sign of the electric field, and thus the sign of the electrical phase, when the electrical and optical phase difference became negative. This periodic reversal kept the two signals in phase, avoiding the phase walkoff which otherwise must eventually occur. Artificial velocity matching was proposed(5,6) using periodic and non-periodic phase reversed electrode structures, and demonstrated for periodic structures in (7). The use of periodic structures resulted in bandpass responses, whereas the use of non-periodic structures was shown to result in a broader, or enhanced, bandwidth response. Non-periodic devices were extended to employ electrode patterns based on the Barker codes, to provide a flat, broadband response, and operation to 40GHz was reported(8). This remarkable device provided the first broadband operation comparable to today's devices. The negatives of the non-periodic electrode structure approach were a penalty in drive voltage, compared to a truly velocity matched device(true for periodic structures also), and a nonlinear phase response.

VELOCITY MATCHING

The initial electrode designs were based on analytic models, based on conformal mapping techniques, which could not account for SiO₂ buffer layers or metal film thickness. It was the tailoring of the thicknesses of these layers, in conjunction with the specific electrode design, which proved to be essential for true velocity matching. The accurate modeling of such effects required numerical methods such as the finite element technique.

This approach was used by Seino, et al(9,10) who showed with CPS structures that the use of thick buffer layers(~1μm) and thick electrode layers(>10μm) could substantially reduce the microwave effective index towards the optical index while maintaining a near 50Ω impedance and low drive voltages.

The effect of the thicker buffer and electrode layers can be explained as follows(11): In quasi-static analysis, the mode of wave propagation in coplanar lines is assumed to be pure TEM. Transmission characteristics are then calculated from the values of two capacitances, one(C_a) for a unit length of the electrode configuration with the dielectric substrate replaced by air, and the other(C) for a unit length of the electrode with the dielectric present. Values of the characteristic impedance Z and the phase constant β are written in terms of these capacitances as :

$$Z = \frac{1}{c(CC_a)^{\frac{1}{2}}} \quad (1)$$

$$\beta = \beta_o \left(\frac{C}{C_a} \right)^{\frac{1}{2}} \quad (2)$$

where $\beta_0 = \omega/c$, and c is the free space velocity of electromagnetic waves. The effective index n_{eff} is then given by β/β_0 . C and C_a are, in first order, a function of the narrow electrode width(S) to gap width(W) ratio(S/W), for the CPW or CPS structure used. When the analytic analysis is carried out for LiNbO_3 , the mode effective index is ~ 4 for a typical structure, compared to the optical LiNbO_3 index of ~ 2.2 . Thus the task of the adjustment of the layer thicknesses is to decrease n_{eff} by decreasing C and increasing C_a . Increasing the buffer layer thickness decreases C by putting more of the field in the SiO_2 , which has a lower dielectric constant than LiNbO_3 . Increasing the electrode thickness increases C_a because it moves more of the field out of the dielectric and into the air, effectively increasing the area of the air capacitor. As these changes are made one must also be concerned with the impedance which depends on the product of C and C_a . Fine tuning is done by adjusting the geometry(S/W ratio), assuming the design structure can be built in practice. Finally one must also be concerned with the electro-optic overlap, which determines drive voltage, and which is reduced by increasing the buffer layer thickness.

Similar results with CPW structures were obtained by using a shielding plane above the electrode structure instead of the thick electrode(12), also with a thick buffer layer. In this case only a thin electrode($\sim 4\mu\text{m}$) was used, but the air capacitance was increased by the presence of a grounded shielding plane placed $\sim 6\mu\text{m}$ above the electrodes. These approaches(10,12) resulted in $\sim 20\text{GHz}$ bandwidth devices but were plagued, at least in the case of (10), by unaccounted for microwave losses which were not eliminated until full consideration of substrate geometry and the interplay between guided and substrate modes was made(13).

As an aside to the electrode structure design problem posed above, it is interesting to note that between the constraints of the dielectric constant of LiNbO_3 , the desire to reduce drive voltage, and the ability to make fine line, thick electrode structures, there is very little room to achieve a velocity matched structure. This is evidenced by the fact that for the devices reported in refs. 9, 10, 12, 14, and 16, the electrode widths are within 7-9 μm and the electrode gaps are all 15 μm , i.e. they are all very close to the same design.

MICROWAVE LOSS

The microwave loss problem reported by Seino, et al(10) precluded operation beyond 20GHz for their device, although the velocity match should have allowed operation to much higher frequencies. Not all workers have reported similar effects, as evidenced by the 40GHz bandwidth reported in (8). It was proposed in (13) that such losses were due to a coupling between the fundamental coplanar waveguide mode and a substrate mode, as predicted earlier in the microwave literature. Such coupling can occur when the effective index of the substrate mode is larger than that of the coplanar mode. Phase match is achieved in the process by a tilt of the substrate mode wavevector relative to the axial direction of the coplanar mode and leakage occurs to both sides of the coplanar guide. This model was shown to be able to account for the variation in frequency of the loss dips with geometry in (10), and was shown to be in reasonable agreement with experiments in which the frequency of the initial loss dip was varied by varying the substrate thickness. This work pointed to one way to eliminate this microwave loss problem, i.e. modify the substrate dimensions so that the loss creating mode coupling only occurs at sufficiently

high frequencies as to be beyond the device bandwidth limited by other effects. For a CPW structure on a 0.25mm thick substrate electrical operation to 40GHz was demonstrated without mode coupling losses(13). By using this approach combined with the thick electrode and thick buffer velocity matching technique, optical operation to 40GHz was also demonstrated with a 5V half-wave voltage(14).

CURRENT PERFORMANCE

Finally, bandwidth has been extended to 50GHz(15), by the use of a somewhat shorter(1cm) electrode structure, and even 75GHz(16), by the use of a etched ridge structure in the LiNbO₃ which simultaneously achieves velocity and impedance matching. The latter device was able to break the constraint of the high LiNbO₃ dielectric constant by physically removing material, and the authors used this extra degree of freedom to do a better job of impedance matching for a CPW structure while maintaining velocity match. They achieved a device impedance of 47 Ω with a microwave n_{eff} of 2.20, with the constraint of electrical input through a probe, rather than a connector interfaced device. They simultaneously achieved a low 5V half-wave voltage.

FUTURE PROGNOSIS

It seems clear that the major problems of true velocity matching and loss control have been solved and probably most of the obtainable performance improvements in these devices have been achieved. However, having said that, it also seems clear that considerable improvement is still available and remains to be done. In the case of the device of (16) RF packaging is an issue. This paper illustrates the problem of designing broadband horns which can couple between a connector and the active part of the device, while maintaining constant impedance. In general packaging of broadband devices is more complicated than low frequency devices because high dielectric constant material must be kept away from the substrate in order to avoid microwave losses by creating an extended waveguide for lossy substrate modes. The mounting of very thin substrates in thermally stable, fiber coupled packages has yet to be demonstrated and will be challenging. Although in the development of broadband devices drive voltage has generally been a secondary consideration, the reduction of drive voltage is of great interest for greater efficiency in applications. For an exact velocity match, and negligible electrode losses, this can be achieved simply by increasing electrode length. Unfortunately electrode losses are not negligible, and the trade-off between achievable velocity match and electrode length has not yet been demonstrated. Clearly issues of reproducibility in fabrication will be an issue here, as the velocity match will have to be well controlled to take advantage of a longer device length.

Regardless of the above list of challenges, enormous improvements in broadband, low voltage devices have been made and prototype devices now exist for applications. It seems clear that they will have a broad impact in a variety of areas including microwave links over optical fiber, high frequency electric field sensors, antenna remoting(the ability to provide optical links to remote antennas), and instrumentation.

Although this paper has concerned itself with LiNbO₃ devices only, it behooves one to keep an eye on similar development in other material systems. Progress has also been impressive in semiconductor devices and in devices made with organic polymer thin films. Each material system has its own advantages and disadvantages and the lead in terms of performance has tended to oscillate with time and perhaps with the exact characteristics important to the user. Since all these devices are new availability may be the most important characteristic right now. Which system will prevail in the long run is still an open question, but to date LiNbO₃ remains a very viable contender.

ACKNOWLEDGMENTS

The author appreciates many helpful discussions with and the contributions of his coworkers, G. K. Gopalakrishnan, C. H. Bulmer, R. W. McElhanon, and A. S. Greenblatt.

REFERENCES

1. I. P. Kaminow and J. Liu, "Propagation characteristics of partially loaded two conductor transmission line for broadband light modulators," *Proc. IEEE* **51**, 132-136(1963).
2. M. Izutsu, Y. Yamane, and T. Sueta, "Broadband traveling wave modulator using a LiNbO₃ optical waveguide", *IEEE J. Quantum Electron.* **QE-13**, 287-290(1977).
3. M. Izutsu, T. Itoh, and T. Sueta, "10 GHz bandwidth traveling wave LiNbO₃ optical waveguide modulator," *IEEE J. Quantum Electron.* **QE-14**, 394-395(1978).
4. C. M. Gee, G. D. Thurmond, and H. W. Yen, "17 GHz bandwidth elector-optic modulator," *Appl. Phys. Lett.* **43**, 998-1000(1983).
5. R. C. Alferness, S. K. Korotky, and E. A. J. Marcetili, "Velocity-matching techniques for integrated optic traveling wave switch/modulators," *IEEE J. Quantum Electron.* **QE-20**, 301-309(1984).
6. D. Erasme and M. G. F. Wilson, "Analysis and optimization of integrated-optic traveling-wave modulators using periodic and non-periodic phase reversals," *Optical and Quantum Electron.* **18**, 203-211(1986).
7. D. Erasme, D. A. Humphreys, A. G. Roddie, and M. G. F. Wilson, "Design and performance of phase reversal traveling wave modulators," *J. Lightwave Tech.* **6**, 933-936(1988).
8. D. W. Dolfi, M. Nazarathy, and R. L. Jungerman, "40 GHz electro-optic modulator with 7.5 V drive voltage", *Electron. Lett.* **24**, 528-529(1988).
9. M. Seino, N. Mekada, T. Namiki, and H. Nakajima, "33-GHz-cm broadband Ti:LiNbO₃ Mach-Zehnder modulator," *Tech. Dig. ECOC'89*, paper ThB22-5(1989).
10. M. Seino, N. Mekada, T. Yamane, Y. Kubota, and M. Doi, "20-GHz 3dB-bandwidth Ti:LiNbO₃ Mach-Zehnder modulator," *Tech. Dig. ECOC'90*, paper ThG1-5(1990).
11. K. C. Gupta, R. Garg, and I. J. Bahl, "Microstrip Lines and Slotlines," Artech House, Dedham, Mass.,(1979).
12. K. Kawano, T. Kitoh, H. Jumonji, T. Nozawa, and M. Yanagibashi, "New traveling-wave electrode Mach-Zehnder optical modulator with 20 GHz bandwidth and 4.7 V driving voltage at 1.52 μ m wavelength", *Electron. Lett.* **25**, 1382-1383(1989).
13. G. K. Gopalakrishnan, W. K. Burns, and C. H. Bulmer, "Electrical loss mechanisms in traveling wave LiNbO₃ optical modulators", *Electron. Lett.* **28**, 207-208(1992).
14. G. K. Gopalakrishnan, C. H. Bulmer, W. K. Burns, R. W. McElhanon, and A. S. Greenblatt, "40 GHz low half-wave voltage Ti:LiNbO₃ intensity modulator", *Electron. Lett.* **28**, 826-827(1992).
15. D. W. Dolfi and T. R. Ranganath, "50 GHz velocity matched broad wavelength LiNbO₃ modulator with multimode active section", *Electron. Lett.* **28**, 1197-1198 (1992).

-
16. K. Noguchi, H. Miyazawa, and O. Mitomi, "75 GHz broadband Ti:LiNbO₃ optical modulator with ridge structure", Electron. Lett. 30, 949-951(1994).

INTEGRATED MAGNETOOPTIC BRAGG CELL MODULES AND APPLICATIONS *

Chen S. Tsai

Department of Electrical and Computer Engineering and the Institute for
Surface and Interface Science (ISIS)
University of California
Irvine, CA 92717

ABSTRACT

Non-collinear magneto-optic (MO) Bragg interactions between guided-optical waves and magnetostatic waves (MSWs) in Yttrium Iron Garnet-Gadolinium Gallium Garnet (YIG-GGG) waveguides have resulted in guided-wave MO Bragg cells in analogy with guided-wave acousto-optic (AO) Bragg cells. Recently, such MO Bragg cells have been miniaturized and integrated with ion-milled waveguide lenses to realize integrated optic device modules. In this paper, an up-to-date review on these integrated MO Bragg cell modules and some of their potential applications, and further research and development required are presented.

I. INTRODUCTION

Guided-Wave Magneto-optics is concerned with MO interactions between the guided-optical waves and the MSWs in a suitable magnetic substrate such as the YIG-GGG waveguides. MSWs are slow-propagating electromagnetic waves that result from propagation of electron spin precession around a DC (bias) magnetic field in a thin-film of ferromagnetic material such as YIG on GGG substrate. MSWs have their energy confined in a small depth beneath the ferromagnetic film, and can be readily and efficiently generated by applying a microwave signal to a short-circuited metallic strip deposited directly on it or brought over it with a small separation. The carrier frequency of the MSW can be tuned, typically from 0.5 to higher than 20 GHz, by simply varying the DC magnetic field. MO interactions result from the moving optical gratings induced by the MSW through the Faraday and Cotton-Mouton effects¹ in a manner similar to guided-wave AO interactions in which the surface acoustic wave (SAW) induces moving optical gratings through the photoelastic effect². In a noncollinear coplanar interaction geometry^{1, 3} a portion of an incident light is Bragg diffracted and mode-converted as a result. The Bragg-diffracted light, which carries a frequency shift identical to the frequency of the MSW, is scanned on the plane of the waveguide as the carrier frequency of the MSW is varied. The intensity of

* This work was supported by the ONR, UCMICRO Program, and New Focus, Inc.

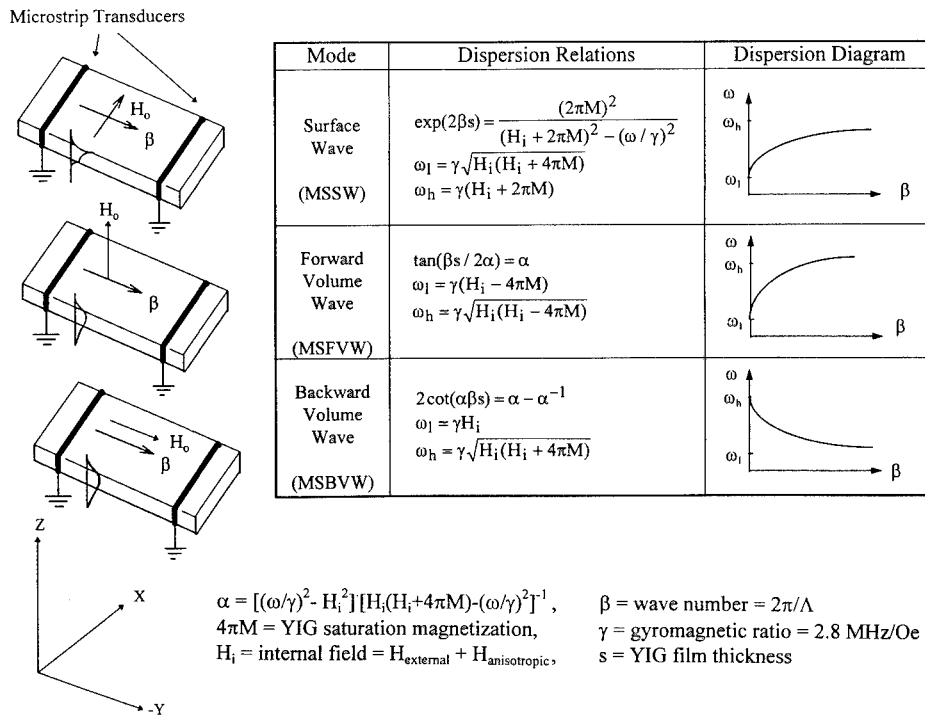


Figure 1. Excitation and propagation of magnetostatic waves in YIG film.

the diffracted light is directly proportional to the power of the MSW for a certain range of microwave drive power. It is to be noted that the aforementioned three characteristics of MO Bragg diffraction are similar to that of AO Bragg diffraction. Consequently, essentially all of the guided-wave AO Bragg devices that have been realized² can also be facilitated using guided-wave MO Bragg diffraction.

II. EXCITATION AND PROPAGATION CHARACTERISTICS OF MSWs

As indicated in the Introduction, MSWs are slow-propagating electromagnetic waves having dispersive frequency-wave number (ω - K) relations that are functions of both the carrier frequency and the DC magnetic field. There exists three distinct modes for the MSWs, namely, magnetostatic surface wave (MSSW), magnetostatic forward volume wave (MSFVW), and magnetostatic backward volume wave (MSBVW). Microstrip transducers are commonly used for their excitation. The required orientations for the microstrip transducer and the DC magnetic field for excitation of each of the MSW modes in a YIG film are depicted in Fig. 1. The corresponding dispersion relations and diagrams are also provided in the figure. It is to be noted that both the lower and the upper frequency bounds (ω_l and ω_h) increase with the DC magnetic field and that ω_l for the MSBVW is higher than that of the MSSW and the MSFVW by about $\gamma 4\pi M$ in which γ is the gyromagnetic ratio (2.8 MHz/Oe) and M is the saturation magnetization of the YIG film. For the commonly used YIG samples, this frequency differential is about five GHz. Also, while the direction of group velocity is the same as the phase velocity for both the MSSW and the MSFVW, the group velocity of the MSBVW is in a direction opposite to that of the phase velocity.

It is relatively simple to facilitate efficient and wideband excitation of the MSWs using the microstrip transducers. Figure 2 shows an example that provides an insertion loss (conversion of RF power to MSW power) of about -10 dB and a -3 dB bandwidth greater

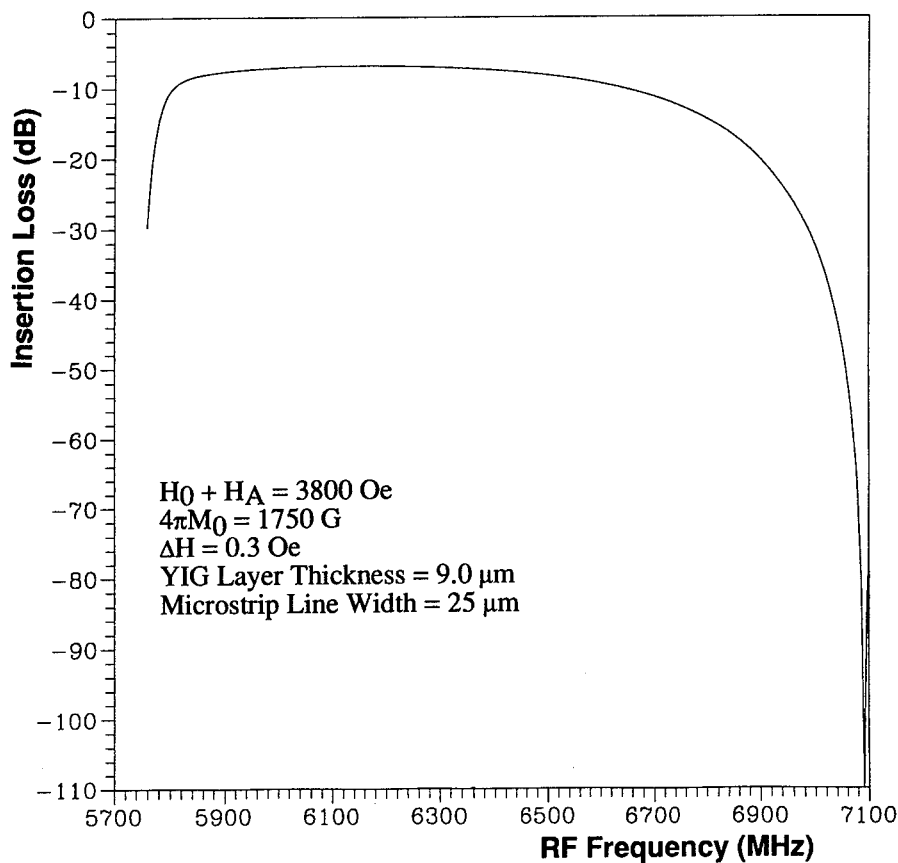


Figure 2. Calculated frequency response of microstrip transducer insertion loss.

than 1.0 GHz. Figure 3 shows the corresponding dispersion diagram for the same range of carrier frequency, indicating a wide range of variations in the wavenumber and the corresponding wavelength for the MSFVW. The dispersion diagram also shows a very large range of phase velocity, e.g., one to three orders of magnitude higher than that of the SAW is associated with the MSFVW. Consequently, the MSW transit time and thus the speed of the resulting MO space switches and scanners will be one to three orders of magnitude higher than their AO counterparts.

III. BASIC MAGNETOOPTIC BRAGG CELL GEOMETRY AND WORKING PRINCIPLE

Figure 4 shows the interaction geometries for noncollinear coplanar guided-wave MO Bragg diffraction, depicting the distinct directions of the DC magnetic field (H_0) for the three cases that involves, respectively, the MSSW, MSFVW, and MSBVW. As stated in the Introduction, propagation of the MSW generated by the input microstrip transducer induces moving optical diffraction gratings in the YIG-GGG waveguide through the Faraday and Cotton-Mouton effects. Portions of the input guided-light wave, incident upon the gratings at Bragg angle, is diffracted and frequency-shifted, and propagates at the Bragg angle with respect to the gratings in the plane of the waveguide. The intensity of the Bragg-diffracted light is directly proportional to the power of the MSW for a range of relatively low power. The diffracted light is scanned on the plane of the waveguide as the carrier frequency of the MSW is varied. It is important to note that in contrast to guided-

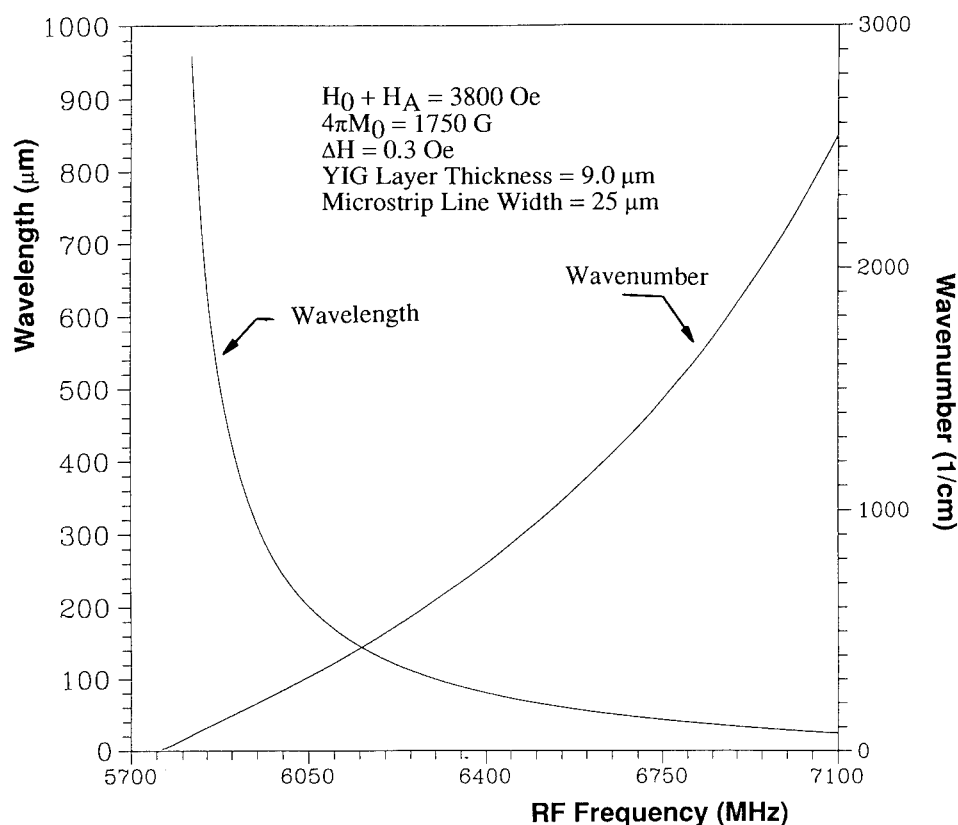


Figure 3. Computer-generated wavenumbers and wavelengths of MSFVW in pure YIG waveguide.

wave isotropic AO Bragg diffraction, the output angle of the diffracted light does not vary linearly with the carrier frequency of the MSW as a result of the dispersive property of the MSW. Also, for the same reason the diffracted light is scanned on the plane of the waveguide as the DC magnetic field is varied, while the carrier frequency of the MSW remains fixed. In analogy with the AO Bragg cells, the resulting devices are called the MO Bragg cells.

IV. RECENT ADVANCES

A. Analysis for Design of High-Performance MO Bragg Cells

A detailed coupled-mode analysis on guided-wave MO Bragg interaction in a practical four-layer YIG/GGG structure as shown in Fig. 5 was carried out recently⁴. This analysis has identified the key device parameters and the guidelines for design and realization of high-performance guided-wave MO Bragg cells. Only the two most important device performance parameters, the diffraction efficiency and the interaction bandwidth, are discussed here. Figures 6 and 7 show sample calculations based on this analysis. First, we note that a maximum MO Bragg diffraction efficiency of 12% was previously measured in a device that utilized a 0.5 cm interaction length in a Bi-doped YIG/GGG waveguide⁵. The required RF drive power was 2.0 watt. Thus, Fig. 6 suggests that at the same RF drive power density the corresponding diffraction efficiency will be increased to about 44 and 85%, respectively, when the interaction length is enlarged by a factor of two and three.

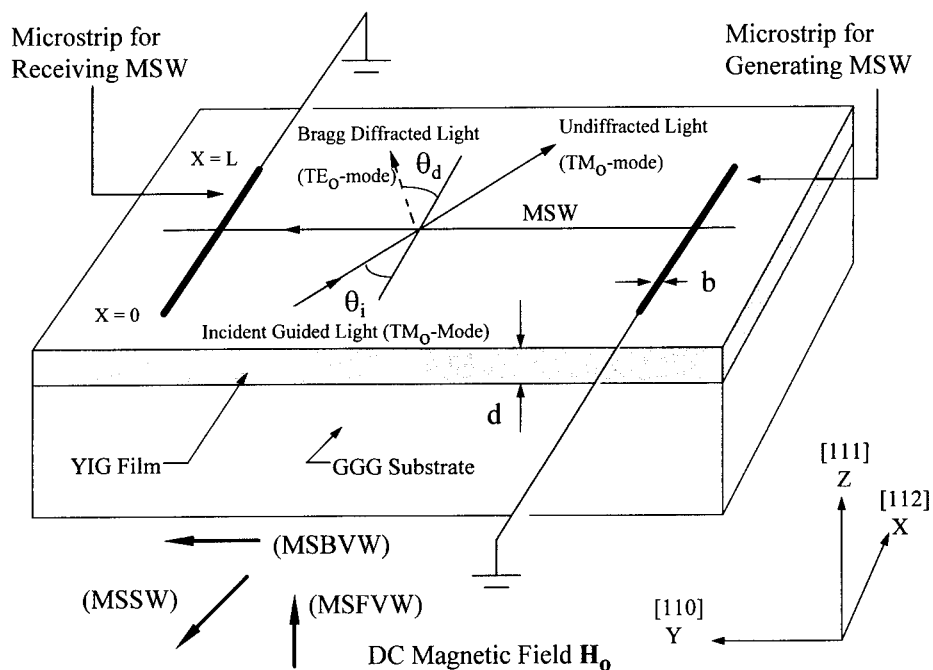


Figure 4. Noncollinear coplanar guided-wave magneto-optic Bragg diffraction from magnetostatic waves in YIG-GGG substrate.

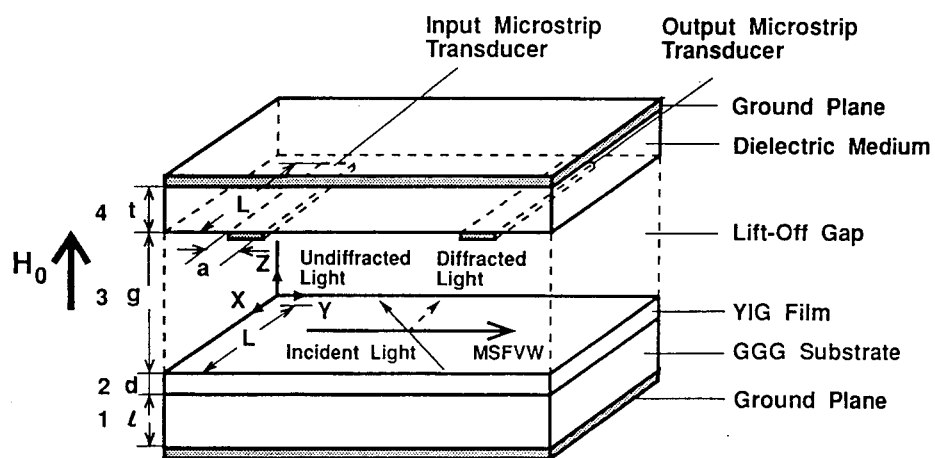


Figure 5. The YIG-GGG layered structure for MSFVW and guided-wave magneto-optic Bragg diffraction.

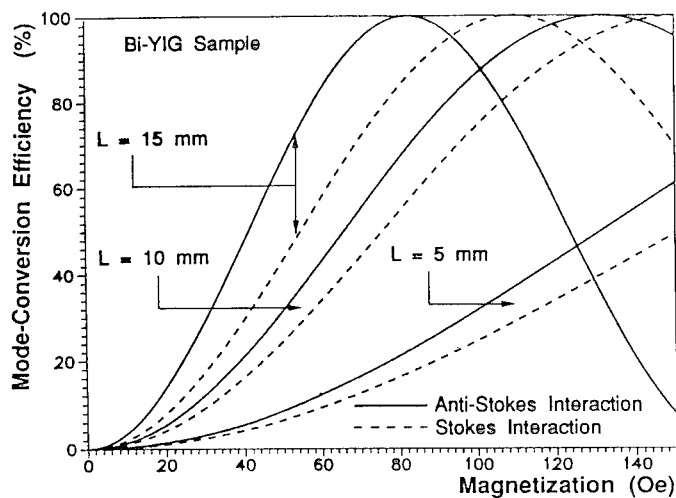


Figure 6. Mode conversion (Bragg diffraction) efficiency of guided-wave magnetooptic Bragg diffraction versus RF magnetization of the MSFVW.

Figure 7 shows that with a commonly used YIG layer thickness of about $3.25 \mu\text{m}$, the MO Bragg bandwidths of 300, 850, and 1,500 MHz, respectively, will be obtainable with the width of microstrip transducer equal to 50, 15, and $10 \mu\text{m}$. Thus, a device bandwidth of one gigahertz and higher is achievable as previously demonstrated⁶.

B. Miniaturized MO Bragg Cells

It is clear that in order to facilitate real-world applications of the guided-wave MO Bragg cells technologies for their miniaturization, integration and packaging must be

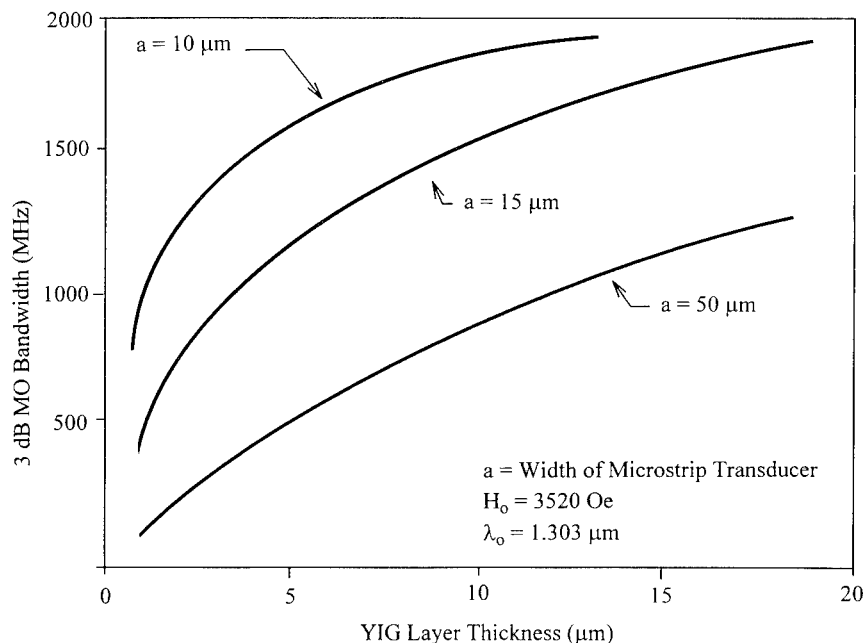


Figure 7. Calculated magnetooptic Bragg bandwidth versus YIG layer thickness with the width of microstrip transducer as a parameter.

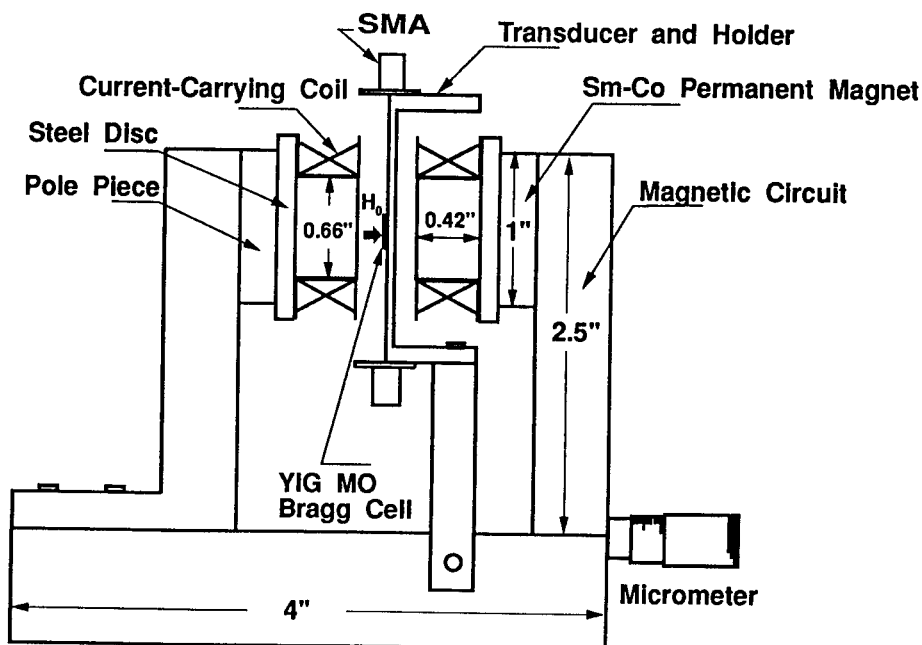


Figure 8. Compact magnetic circuit used in realization of magneto-optic Bragg cell modules.

devised and developed. Toward this goal the first miniaturized device modules using a pair of small permanent magnets together with a pair of current-carrying coils in a compact magnetic circuit were realized recently⁷. Figure 8 shows a sketch of the compact magnetic circuit that has been realized. The pair of permanent magnets, each 1" X 1" X 0.25" in size, were made of samarium-cobalt (Sm-Co). The pole pieces of smaller cross-sectional area were used to concentrate the magnetic flux and provide a uniform magnetic field in the air gap where the MO Bragg cell sample was inserted. The current-carrying coils were wound on nylon robins and placed around the pole pieces in order to facilitate electronic tuning of the magnetic field in the air gap. Using this simple but compact magnetic circuit, a uniform DC magnetic field (H_0) at the gap was readily varied from 1600 to 4126 Oe. The corresponding tuning range for the carrier frequency of the MSFVWs was measured to be from 2.0 to 12.0 GHz. For example, as shown in Fig. 9 the measured changes in the DC magnetic field (ΔH_{0e}) induced by a current of 0.85 amp was as high as 2446 Oe at an air gap of 6.16 mm. These current-controlled changes in the DC magnetic field provided a carrier frequency tuning bandwidth as high as 6.85 GHz. Clearly, even larger changes in the DC magnetic field, and thus larger tuning bandwidths for the carrier frequency could be obtained at a smaller air gap.

i. Compact MSFVM-based MO Bragg Cell. Both pure and Bi-doped YIG-GGG waveguide samples having, respectively, 4.2 and 3.5 μm YIG layer thickness were used in the construction of compact MSFVW-based MO Bragg cell modules. Measurements of performance characteristics were carried out at an optical wavelength of 1.303 μm using the setup and procedure previously reported^{3, 5, 6}. The measured performances were comparable to those obtained using a bulky electromagnet. For example, the measured diffraction efficiency at a carrier frequency of 7.6 GHz for a Bi-doped YIG Bragg cell was 7.14% at an RF drive power of 28.2 dBm (660 mW) or a corresponding calculated MSFVW power of 20 mW⁷. A dynamic range of 40 dB⁵ was also reproduced. However, for RF drive powers higher than 28.2 dBm, some deviation

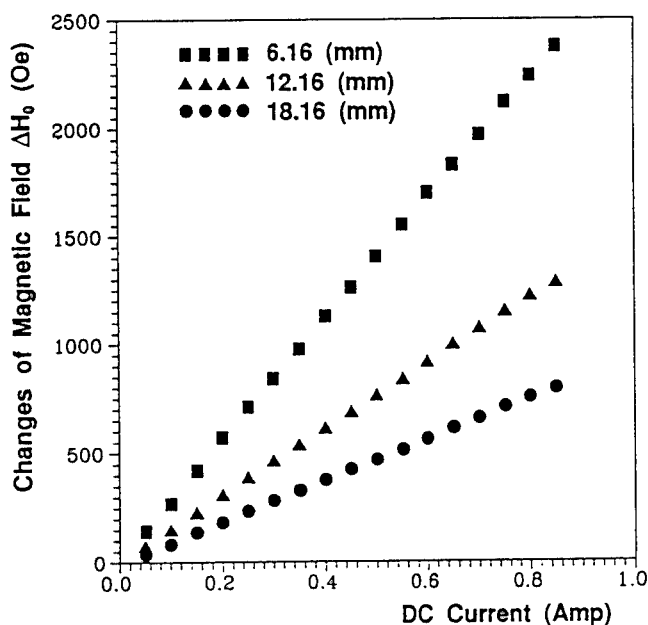


Figure 9. Measured changes of magnetic field induced by current-carrying coils versus direct current at three different air gaps.

from linearity between the diffraction efficiency and the RF drive power was observed. Based on the theoretical predictions⁴, compact MO Bragg cell modules with even higher carrier frequency, larger range of tunable carrier frequency, higher diffraction efficiency, and smaller physical size can be constructed. The compact MSFVW-based MO Bragg cells have been used to demonstrate applications in light beam scanning and RF spectral analysis.

ii. Compact MSBVW-based MO Bragg Cell. The compact magnetic circuit described previously was also utilized to construct miniaturized MSBVW-based MO Bragg cell module⁸. First, it is to be noted that the direction of the DC magnetic field required for excitation of the MSBVW as depicted in Fig. 4 necessitated a considerably greater gap between the two pole pieces. However, as stated in Section II, the lower bound frequency of the MSBVW is higher than that of the MSFVW by about $\gamma 4\pi M$. For pure YIG and Bi-YIG samples, we have $4\pi M = 1750$ Oe and 1800 Oe, respectively, and the corresponding $\gamma 4\pi M$ are 4.90 GHz and 5.04 GHz.

For example, the center carrier frequencies of the MSBVWs were measured to be 4.78 and 6.10 GHz, respectively, at the DC magnetic fields of only 1,000 and 1,900 Oe⁸. Such relatively low magnetic fields were readily provided by the compact magnetic circuit at the gap greater than 0.8 cm. Thus, it was possible to insert the MO Bragg cell sample of adequate dimensions into the air gap of the same magnetic circuit to realize miniaturized MSBVW-based MO Bragg cell modules.

The resulting MSBVW-based MO Bragg cells in both pure and Bi-doped YIG-GGG samples have demonstrated wide-angle light beam scanning from the UHF band (< 2 GHz) to the X-band (> 10 GHz). The measured performances of the MSBVW-based MO Bragg cells, including the center frequency and its tuning range and the corresponding tuning range of the dc magnetic field, the location of the first passband, the diffraction efficiency, the microwave drive power, and the light beam scan angle were found to be superior to that of the MSFVW-based MO Bragg cells.

V. INTEGRATED MO BRAGG CELL MODULES

Aside from the miniaturization of the magnetic circuit as described in Section IV.B, it is also essential to incorporate a collimation-focusing waveguide lens pair in a common YIG-

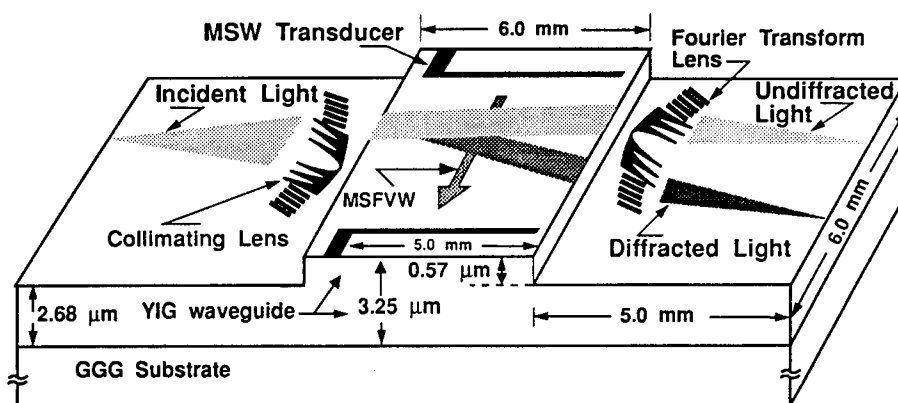


Figure 10. Integrated magneto-optic Bragg cell module in Bi-doped YIG-GGG tapered waveguide structure.

GGG substrate. As in integrated AO device modules⁹, such lens pair is required in a variety of integrated MO device modules such as RF signal processors, optical space switches and scanners¹⁰, and optical frequency shifters and modulators¹¹. Recently, an ion-milled collimation-focusing lens pair^{12, 13} was integrated with a MO Bragg cell in a common YIG-GGG taper waveguide substrate $6.0 \times 16.0 \text{ mm}^2$ in size to realize an integrated MO Bragg cell module (see Fig. 10)¹⁴.

Flat hybrid waveguide lenses which combine analog Fresnel and chirp gratings were devised and fabricated earlier in GaAs, LiNbO₃ and YIG-GGG waveguide substrates using ion-milling technique^{12, 15, 16}. Such ion-milled lenses had provided both high throughput efficiency and near diffraction-limited focal spot size for a light beam propagating within a small angle from the lens axis. However, when the light beam propagated at a larger angle from the lens axis the overall performance was significantly degraded due to the high degree of coma incurred. Recently, a curved hybrid lens in which the hybrid lens lies on a parabolic contour rather than a straight line (as used in the flat hybrid lenses) was devised to greatly reduce the coma¹³. Furthermore, such curved hybrid lenses were recently formed in a tapered YIG-GGG waveguide structure to accommodate simultaneously the requirements for large MO Bragg bandwidth and high lens throughput, and thus facilitated the realization of integrated MO Bragg cell modules¹⁴ as depicted in Fig. 10. The initial layer thickness of the Bi-doped YIG waveguide $6.0 \times 16.0 \text{ mm}^2$ in size was 3.25 μm . The two end regions of the tapered waveguide were ion-milled down to 2.68 μm in several steps in order to produce a gradual transition, and thus ensure a high transmission for the light beam. The curved hybrid lenses with 4.0 mm focal length and 0.8 mm aperture were then fabricated onto the two end regions (each 5.0 mm in length) using the ion-milling technique. The measured focal spot profiles obtained at 1.3 μm wavelength from the curved hybrid lenses show practically no coma with sidelobe levels lower than 12.3 dB from the main lobe for the incident light angle up to ± 3.5 degrees from the lens axis. An MO Bragg cell was subsequently constructed by incorporating a microstrip line transducer in the central region of the tapered waveguide. The compact magnetic circuit described previously in Section IV was used to provide the required DC magnetic field for saturation of the YIG layer as well as excitation and tuning of the carrier frequency of the MSFVWs ranging from 2 to 12 GHz. Typically performance figures such as a bandwidth of 260 MHz at the center carrier frequency of 10.0 GHz, a diffraction efficiency of 2.0% at one watt RF drive power, and a dynamic range of 30 dB were measured with the resulting integrated MO Bragg cell module. Again, the device module was used to demonstrate light beam scanning and switching, and RF spectral analysis.

VI. NOVEL APPLICATIONS

In comparison to their AO counterparts, the unique advantages associated with the MO Bragg cell modules are: 1) A much larger range of tunable carrier frequencies (0.5 to 20

GHz and higher) may be obtained by varying the DC magnetic field. Such high and tunable carrier frequencies with the MO devices allow direct processing at the carrier frequency of wideband RF signals and, thus, eliminate the need for indirect processing via frequency down-conversion as is required with the AO devices^{17, 18}. 2) A large MO bandwidth may be realized by means of a simpler transducer, and 3) Much higher and electronically tunable modulation/switching and scanning speeds are achievable because the velocity of propagation for the MSWs can be higher than that of the SAWs by one-to three-orders of magnitude. Consequently, a variety of unique applications in the areas of real-time RF signal processing and optical communications such as the following are anticipated: 1. Electronically tunable RF spectral analysis at X-band and beyond³, 2. Multicarrier frequency demultiplexing¹⁹, 3. Nanosecond optical space switching²⁰, and 4. High-speed wideband optical frequency shifting and modulation¹¹.

VII. CONCLUSION

A number of significant advances have been made most recently in MSW-based guided-wave magneto-optics. These advances include growth of high-quality pure YIG-GGG waveguides and quality improvement in Bi-doped YIG-GGG waveguides, design and fabrication of efficient and wideband transducers for MSWs, theoretical analysis on noncollinear coplanar guided-wave MO Bragg diffraction, realization of compact MO Bragg cells, realization of ion-milled waveguide lenses and integration with the MO Bragg cell, and demonstration of their applications in light beam modulation and scanning/switching and RF spectral at the X-band. Thus, a new class of optical devices called MO Bragg cells which are potentially capable of providing desirable features similar to that of the now prevalent AO Bragg cells, but with potentially superior performance characteristics, have been realized. These advances have paved the way for realization of a variety of MSW-based integrated MO device modules, such as high-speed optical scanners, optical space switches, tunable carrier frequency band RF spectrum analyzers, and correlators. It may also be possible to realize tunable optical filters similar to AO tunable filters²¹.

Finally, to expedite realization of the aforementioned integrated optic device modules and their applications, further advances such as those listed in the following are needed: 1. schemes for enhancement of MO Bragg diffraction efficiency, and thus reduction of the RF drive power requirement for the resulting MO Bragg cell modules, 2. development of robust coupling techniques between the YIG-GGG waveguide and the laser and/or the photodetector, and 3. development of packaging technology for the integrated MO device modules.

REFERENCES

1. (a) C.S. Tsai, Hybrid integrated optic modules for real-time signal processing, in "Proc. of NASA Optical Information Processing Conference II," *NASA Conference Publication* . 2302: 149-164 (1983); (b) C.S. Tsai, D. Young, W. Chen, L. Adkins, C.C. Lee, and H. Glass, "Noncollinear Magneto-optic Interaction of Guided-Optical Wave and Magnetostatic Surface Waves in YIG/GGG Waveguides," *Appl. Phys. Lett.* 47: 651-654 (1985).
2. See, for example, C.S. Tsai, Guided-wave acoustooptic Bragg modulators for wide-band integrated optic communications and signal processing," *IEEE Trans. on Circuits and Systems*. CAS-26: 1072-1098 (1979); C.S. Tsai, Guided-Wave Acousto-Optics, in: "Springer Series in Electronics and Photonics, Vol. 23," C.S. Tsai, ed., Springer-Verlag (1990).
3. See, for example, the many references cited in C.S. Tsai and D. Young, Magnetostatic-forward-volume wave-based guided-wave magneto-optic Bragg cells and applications to communications and signal processing," *IEEE Trans. on Microwave Theory and Techniques*. 38: 560-573 (1990).
4. Y. Pu and C.S. Tsai, RF magnetization of magnetostatic forward volume waves in a YIG-GGG layered structure with application to design of high-

- performance guided-wave magneto-optic Bragg cells, *International Journal of High-Speed Electronics*. 2: 185-208 (1991).
5. D. Young and C.S. Tsai, X-band magneto-optic Bragg cells using bismuth-doped yttrium iron garnet waveguides, *Appl. Phys. Lett.* 55: 2242-2244 (1989).
 6. D. Young and C.S. Tsai, GHz bandwidth magneto-optic interaction in YIG-GGG waveguide using magnetostatic forward volume waves, *Appl. Phys. Lett.* 53: 1696-1698 (1988).
 7. C.L. Wang, Y. Pu and C.S. Tsai, Permanent magnet-based guided-wave magneto-optic Bragg cell modules, *IEEE J. Lightwave Tech.* 10: 644-648 (1992).
 8. Y. Pu, C.L. Wang, and C.S. Tsai, Magnetostatic backward volume wave-based guided-wave magneto-optic Bragg cells and application to wide-band lightbeam scanning, *IEEE Photonics Technology Letters*. 5: 462-465 (1991).
 9. See, for example, the many references cited in C.S. Tsai, Integrated Acousto-optic Circuits and Applications, *IEEE Trans. Ultrasonics, Ferroelectrics and Frequency Control*. 39: 529-554 (1992).
 10. C.S. Tsai and D. Young, "Wideband scanning of guided-lightbeam and RF spectral analysis using magnetostatic forward volume waves in a YIG-GGG waveguide, *Appl. Phys. Lett.* 54:196-198 (1989).
 11. Y. Pu and C.S. Tsai, Wideband integrated magneto-optic frequency shifter at X-band, *Appl. Phys. Lett.* 62: 3420-3422 (1993).
 12. T.Q. Vu, C.S. Tsai, D. Young and C.L. Wang, Ion-milled lenses and lens arrays in yttrium iron garnet-gadolinium gallium garnet waveguides, *Appl. Phys. Lett.* 55: 2271-2273 (1989).
 13. C.L. Wang, Y. Pu, and C.S. Tsai, High-performance curved hybrid lenses in YIG-GGG waveguide, (to be published).
 14. C.L. Wang and C.S. Tsai, Integrated magneto-optic Bragg cell modules in YIG-GGG taper waveguide, (To be published *IEEE Photonics Technology Lett.*).
 15. T.Q. Vu, J.A. Norris, and C.S. Tsai, Planar waveguide lenses in GaAs using ion milling, *Appl. Phys. Lett.* 54: 1098-1100 (1989).
 16. T.Q. Vu, J.A. Norris, and C.S. Tsai, Formation of negative index-change waveguide lenses in LiNbO₃ using ion milling, *Opt. Lett.* 13: 1141-1143 (1989).
 17. G.D. Xu and C.S. Tsai, Integrated acousto-optic modules for interferometric RF spectrum analyzers, *IEEE Photonics Technology Lett.* 3: 153-155 (1991).
 18. (a) Y. Abdelrazek, C.S. Tsai, and T.Q. Vu, An integrated optic RF spectrum analyzer in a ZnO-GaAs-AlGaAs waveguide, *J. Lightwave Tech.* 8: 1833-1837 (1990); (b) T.Q. Vu, C.S. Tsai, and Y.C. Kao, Integration of curved hybrid waveguide lens and photodetector array in a GaAs waveguide, *Appl. Opt.* 31: 5246-5254 (1992).
 19. C.S. Tsai, Integrated acousto-optic and magneto-optic device modules for on-board processing and switching of microwave signals, *Proc. of American Institute of Aeronautics and Astronautics Conf. on Satellite Communication Systems*, San Diego, CA., February 28 - March 5, 1994.
 20. C.S. Tsai and P. Le, A 4 X 4 nonblocking integrated acousto-optic space switch, *Appl. Phys. Lett.* 60: 331-333 (1992); Also, A.K. Roy and C.S. Tsai, A 8 X 8 symmetric nonblocking integrated acousto-optic space switch module in LiNbO₃, *IEEE Photonics Tech. Lett.* 4: 731-734 (1992).
 21. See, for example, the many references cited in A. Kar-Roy and C.S. Tsai, Integrated acousto-optic tunable filters using weighted coupling, *IEEE J. Quantum Electron.* 30:1574-1586 (1994).

HIGH-SPEED WIDEBAND INTEGRATED MAGNETO-OPTIC FREQUENCY SHIFTER AND MODULATOR *

Chen S. Tsai and Yuan Pu [†]

Department of Electrical and Computer Engineering and
Institute for Surface and Interface Science
University of California at Irvine
Irvine, CA 92727

ABSTRACT

Improvements on a novel optical frequency shifting and modulation scheme that utilizes a single noncollinear conplanar guided-wave magneto-optic (MO) Bragg diffraction from magnetostatic waves (MSW) in a yttrium-iron-garnet/gadolinium-gallium-garnet (YIG/GGG) waveguide is reported. The scheme ensures constancy in the output angle of the frequency-shifted light beam, irrespective of the amount of frequency shift, through synchronous tuning of the carrier frequency of the microwave drive signal and the bias magnetic field using an electronic synchronizer. A curved hybrid waveguide lens was incorporated in the same waveguide substrate to enhance integration. The device operating at the optical wavelength of 1.302 μm and the microwave carrier frequency at X-band has demonstrated desirable characteristics such as large frequency shift (6-12 GHz), large tunable bandwidth (2-4 GHz), good dynamic range (31 to 34 dB), and high tuning speed ($\approx 10 \mu\text{s}$).

I. INTRODUCTION

Integrated optic frequency shifters and modulators that provide high-speed electronically tunable frequency-shifted light, are needed in fiber optic communication and sensor systems¹⁻³. A number of schemes that utilize acousto-optic (AO) effects for producing such frequency-shifted light sources were reported previously⁴⁻¹¹. The unique and important feature of the Bragg-type AO frequency shifters lies in their inherent single-sideband suppressed-carrier property. However, the guided-wave AO frequency shifters that utilize a single AO Bragg diffraction in a planar waveguide substrate are incapable of

* This work was supported by the ONR, UC MICRO Program, and New Focus, Inc.

[†] Applied Materials, Inc.

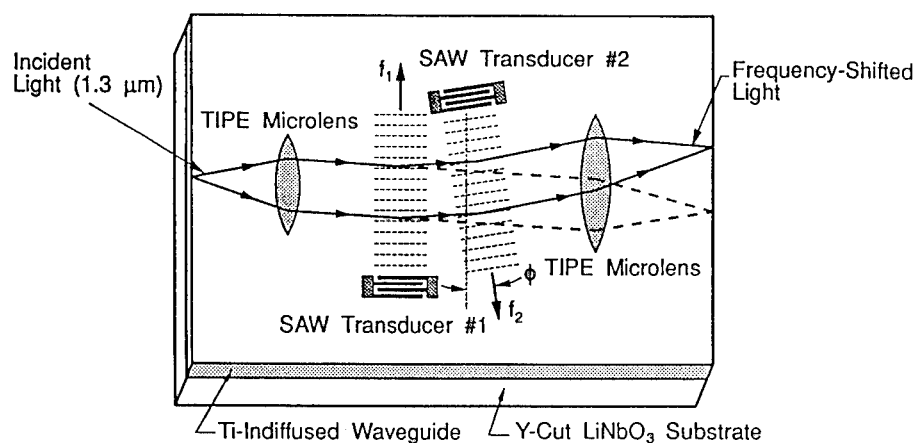


Figure 1. Integrated acoustooptic frequency shifters utilizing tilted AO Bragg cells in cascade. a) Baseband device: $\phi = \text{SAW transducer tilt angle} = \theta_{B2} + \theta_{B1}$; b) passband device: $\phi = \theta_{B2} - \theta_{B1}$.

providing the frequency-shifted light propagating at a fixed angle, irrespective of the amount of frequency shift. This undesirable drawback results from the fact that as the RF drive frequency for the surface acoustic waves (SAW) is varied, the periodicity of the photoelastically-induced optical diffraction gratings, and thus the corresponding output angle of the Bragg-diffracted light are varied accordingly. Consequently, the frequency-shifted light would miss the core of single-mode optical fibers.

Recently, a scheme using two guided-wave AO Bragg diffractions in cascade as shown in Fig. 1 was devised to provide the frequency-shifted light propagating at a fixed angle, irrespective of the amount of frequency shift^{12,13}. Using such a scheme, two distinct types of Bragg-type AO frequency shifters, namely, baseband and passband devices, have been realized. As shown in the inset of Fig. 1, for the baseband devices¹³ the tilt angle (ϕ) between the transducers for generating counter-propagating SAWs is set equal to the sum of the two Bragg angles (θ_{B1} and θ_{B2}) at the two SAW center frequencies (f_{10} and f_{20}). In practice, it is most convenient to set the two center frequencies identical. Thus, in operation a frequency shift of $2\Delta f$ (from the carrier frequency of the incident light) is produced in the diffracted light by varying the two drive frequencies (f_1 and f_2) by $+\Delta f$ and $-\Delta f$, respectively. Similarly, for the passband devices¹² the tilt angle between the transducers is set equal to the difference of the two Bragg angles at the two SAW center frequencies. A frequency shift of $(f_1 + f_2)$ is carried in the diffracted light when the two drive frequencies are set at f_1 and f_2 . Thus, in operation a tuning of frequency shift by $2\Delta f$ in the diffracted light is accomplished by varying the two drive frequencies by the same amount Δf . The scheme just described has demonstrated its capability for wideband tuning of the frequency shift.

Clearly, the aforementioned scheme is equally applicable to guided-wave MO Bragg diffraction^{14,15} for generation of wideband electronically tunable frequency-shifted light propagating at a fixed angle. In this paper we present a new and novel optical frequency shifting scheme which utilizes only a single MO Bragg diffraction¹⁶ as shown in Fig. 2. This scheme utilizes the dispersive property of the magnetostatic waves (MSW) in which the frequency-wave number (ω - k) plot is not a straight line and is also a function of the DC (bias) magnetic field. In other words, as the carrier-frequency of the MSW is varied the corresponding periodicity of the magnetically-induced optical diffraction gratings, and thus the output angle of the diffracted light can be made unchanged by varying synchronously the bias magnetic field.

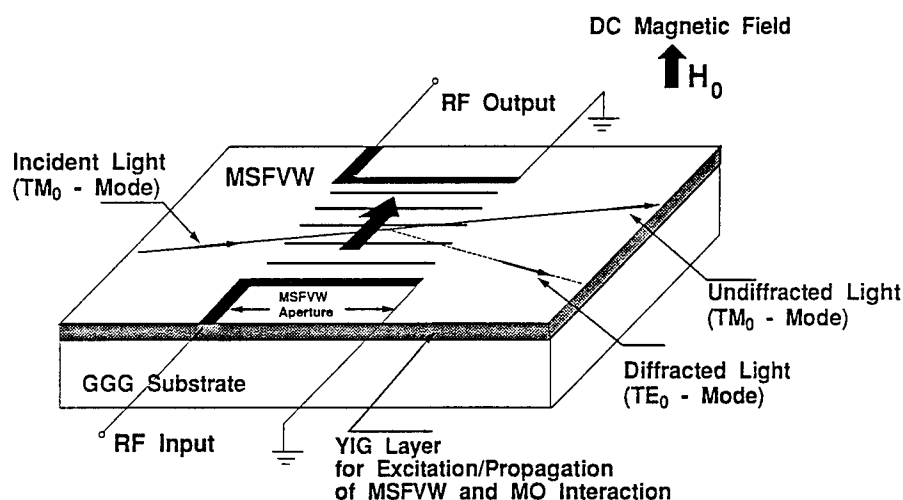


Figure 2. Guided-wave noncollinear magneto-optic (MO) Bragg diffraction from magnetostatic forward volume waves (MSFVW) in YIG waveguide.

II. DEVICE ARCHITECTURE AND WORKING PRINCIPLE

The components and architecture of the integrated MO frequency shifter that has been realized is shown in Fig. 3. The synchronous tuning between the microwave carrier frequency and the bias magnetic field was accomplished by a specially designed electronic synchronizer. The reference voltage from a sweep oscillator, which is proportional to the carrier frequency of the microwave used to excite the magnetostatic forward volume waves (MSFVW), is fed into the synchronizer. The synchronizer converts linearly the reference voltage into a current which is then used to activate a pair of current-carrying coils in a compact magnetic circuit¹⁷ to facilitate the required synchronous tuning of the bias magnetic field. The MO Bragg cell sample described in Sect. III was inserted into the airgap of the compact magnet circuit such that the bias magnetic field was perpendicular

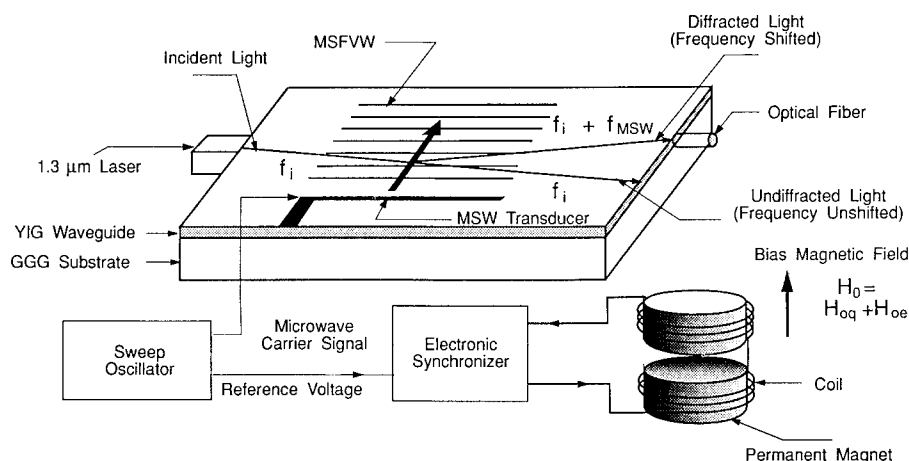


Figure 3. Electronically tunable wideband integrated magneto-optic frequency shifter.

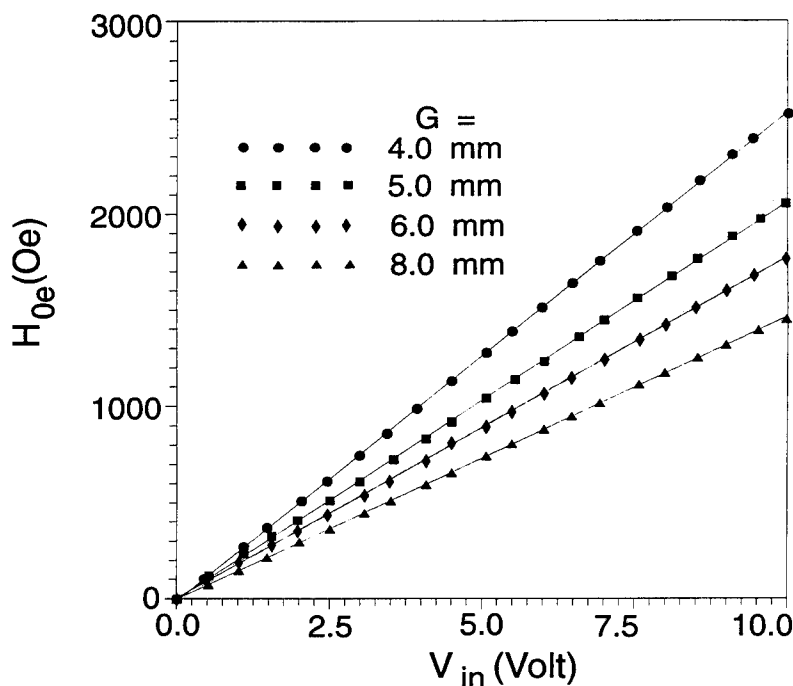


Figure 4. Electrically induced magnetic field (H_{Oe}) versus input voltage of synchronizer V_{in} as a function of air gap between the current-carrying coils (G).

to the waveguide sample for excitation of the MSFVW. The bias magnetic field consists of two components: The quiescent component H_{Oq} provided by a pair of samarium-cobalt (Sm-Co) permanent magnets and the electrically tuned component H_{Oe} produced by the current-carrying coils. Tuning of the former was accomplished by changing the air gap (G) between the permanent magnets using a micrometer, while tuning of the latter was obtained by varying the current through the coils.

In operation, an X-band sweep oscillator was used as the microwave carrier frequency generator and also to provide the reference voltage. The reference voltage was always varied linearly from 0 to 10 V for the range of carrier frequency sweep set. The maximum output current and the bandwidth of the electronic synchronizer were, respectively, 0.5 A and 1 MHz. At an air gap of 4.0 mm, a tuning range for H_{Oe} by as much as 2,500 Oe was obtained. As shown in Fig. 4, a high degree of linearity between the variation of the bias magnetic field and the reference voltage was accomplished. Thus, for a given but fixed wave number (K) of the MSFVW or periodicity of the resulting diffraction gratings, synchronous tuning between the total bias magnetic field and the microwave carrier frequency could be readily facilitated. In other words, the output angle of the MO Bragg-diffracted light can be made fixed, irrespective of the amount of frequency shift.

III. INTEGRATED MO BRAGG CELL SAMPLE

The geometry and dimension of the MO Bragg cell sample that integrates an MO Bragg cell with an ion-milled curved hybrid waveguide lens is shown in Fig. 5. The size of

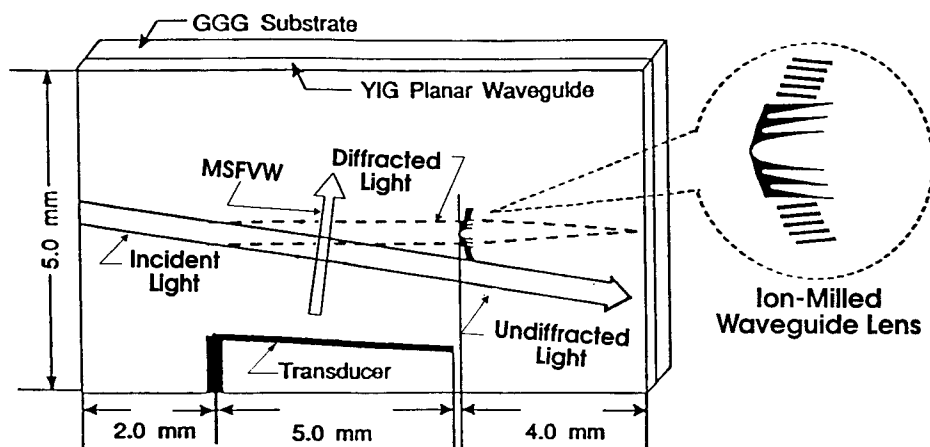


Figure 5. Geometry of integrated magneto-optic frequency shifter.

the bismuth-doped YIG-GGG planar waveguide substrate was $6 \times 10 \text{ mm}^2$ and the thickness of the YIG waveguide layer was $8.8 \text{ }\mu\text{m}$. The saturation magnetization ($4\pi M$) and the anisotropy field (H_a) of the YIG sample were 1800 and 250 Oe, respectively. A pair of microstrip line transducers with an aperture of 5mm and a strip width of $50 \text{ }\mu\text{m}$, and a separation of 5mm was fabricated on a $254 \text{ }\mu\text{m}$ thick alumina chip. The chip was then flipped and bonded onto the surface of the YIG-GGG waveguide. An incident light beam at $1.302 \text{ }\mu\text{m}$ was edge-coupled from the left edge of the YIG-GGG waveguide and converted to guided-mode. The guided light propagated at Bragg angle from the wavefront of the MSFVW which induced moving optical gratings through Faraday rotation and Cotton-Mouton effects^{14,15}. The resulting Bragg-diffracted light would carry a frequency shift. The waveguide lens placed after the MO interaction region, was used to focus the frequency-shifted light onto the right edge of the waveguide. The axis of the lens was oriented orthogonally to the side edges of the waveguide. The incident light was aligned at a proper angle such that the frequency-shifted light was incident upon the lens along the lens axis.

The pattern of the ion-milled curved-hybrid lens¹⁸ is shown in the inset of Fig. 5. It combines analog Fresnel gratings (central region) with Bragg chirp gratings (two outer regions) to extend the lens aperture without sacrificing the diffraction efficiency. This combination also allows a significant relaxation in the fabrication requirement as compared to a purely analog Fresnel lens. The inclusion of the curved contour in the bottom edge of the lens serves to reduce significantly the coma at off-axis focus, and thus enabling a larger angular field of view be accomplished¹⁸.

The measured performances of the waveguide lens are a throughput efficiency of about 25% and a 3dB angular field of view of about 3.0 degrees. The profile of the focused light spot was measured by a beam scanner. The measured 3dB diameter of the focused spot was $3.1 \text{ }\mu\text{m}$ which is comparable to the diffraction limit as determined by the lens aperture and the $1.302 \text{ }\mu\text{m}$ light wavelength involved, namely, $2.0 \text{ }\mu\text{m}$. It is to be noted that this focus spot size is much smaller than the core size of a typical single-mode fiber to be used to couple out the frequency-shifted light from the output edge of the YIG-GGG waveguide.

IV. MEASURED PERFORMANCE

Continuous tuning and wideband operation of the resulting integrated MO frequency shifter was accomplished at various microwave carrier frequency ranges. In the

experiments, the constancy of the output angle of the frequency-shifted light was first verified and characterized by measuring the deviation of the output light beam position with a photodetector mounted on a movable optical stage.

The performance of the frequency shifter module has been measured and characterized. For example, tunable bandwidths as large as 2.35 and 3.56 GHz have been achieved at the center carrier frequencies of 11.03 and 6.03 GHz, respectively. The maximum deviations of the output angle of the frequency-shifted light measured in the two frequency ranges are 2.0×10^{-4} and 2.5×10^{-4} radians, which are well within the tolerance limitation for efficient edge-coupling with a single-mode optical fiber. Thus, the constancy of the propagation direction of the diffracted light, irrespective of the amount of frequency shift, was clearly demonstrated. The MO diffraction efficiency was measured to be 8.5% of an RF drive power of 28 dBm. A linear dynamic range of about 30dB was also measured. The tuning speed of the device as determined by the response time of the current-carrying coil was measured to be around 10 μ s.

Finally, an indirect optical heterodyne detection scheme was employed to measure the frequency shift in the Bragg-diffracted light. In this measurement, two RF carrier frequencies at f_1 and f_2 were applied simultaneously to the transducer of the MO frequency shifter. The two resulting frequency-shifted light were then mixed in the detector. Since the difference between the two carrier frequencies could be readily tuned around convenient but relatively low frequencies, a photodetector with a small but sufficient bandwidth, namely 300 MHz in this experiment, could be used to provide a higher detection sensitivity. This indirect heterodyne scheme not only increased the S/N ratio in the heterodyne signal, but also significantly simplified the experimental set-up. As a matter of fact, one of the diffracted light beams in this indirect approach could be considered as the reference light in a direct heterodyne detection scheme. For example, a frequency spectrum at 55 MHz was detected in the Bragg-diffracted light when the two carrier frequencies applied to the transducer were $f_1 = 5.184$ GHz and $f_2 = 5.239$ GHz. The heterodyned spectrum at the frequency of $f_2 - f_1 = 55$ MHz shows that the frequency shift in the Bragg-diffracted light of the integrated MO frequency shifter is indeed identical to the drive carrier frequency of the MSFVW.

V. CONCLUSION

A novel MSW-based integrated MO frequency shifter/modulator at 1.3 μ m wavelength has been constructed and tested. The device possesses single-sideband suppressed carrier property, and is capable of providing large frequency shift (10 GHz and beyond), large bandwidth (4 GHz and beyond) high tuning speed (10 μ s or faster), and good dynamic range (31 dB or higher). Ultimate realization of such integrated optic devices and their applications require development of robust coupling techniques between the YIG-GGG waveguide and the laser and/or the optical fiber.

REFERENCE

1. R.F. Cahill and E. Udd, "Phase-Nulling Fiber-Optic Laser Gyro," *Opt. Lett.*, **4**, 93 (1979)
2. S. Ezekiel and S.R. Balsamo, "Passive Ring Resonator Laser Gyroscope," *Appl. Phys. Lett.*, **30**, 478 (1977)
3. J.L. Davis and S. Ezekiel, "Closed-Loop, Low-Noise Fiber-Optic Rotation Sensor," *Opt. Lett.*, **6**, 505 (1981)

4. K. Nosu, S.C. Rashleigh, H.F. Taylor, and J.F. Weller, "Acousto-Optic Frequency Shifter for Birefringent Fiber," *Electron. Lett.*, **19**, 816 (1983)
5. W.P. Risk, R.C. Youngquist, G.S. Kino, and H.J. Shaw, "Acousto-Optic Frequency Shifting in Birefringent Fiber," *Opt. Lett.*, **9**, 309 (1984)
6. R.C. Youngquist, J.L. Brooks, and H.J. Shaw, "Birefringent-Fiber Polarization Coupler," *Opt. Lett.*, **8**, 656 (1983)
7. B.Y. Kim, J.N. Blake, H.E. Engan, and H.J. Shaw, "All-Fiber Acousto-Optic Frequency Shifter," *Opt. Lett.*, **11**, 389 (1986)
8. C.S. Tsai, "Guided-Wave Acoustooptic Bragg Modulators for Wide-Band Integrated Optic Communications and Signal Processing," *IEEE Trans. Circuits Sys.*, **CAS-26**, 1072 (1979)
9. C.S. Tsai, C.L. Chang, C.C. Lee, and K.Y. Liao, "Acousto-Optic Bragg Deflection in Channel Optic Waveguides," *1980 Topical Meeting on Integrated and Guided-Wave Optics*, Technical Digest of Post-Deadline Papers, pp. PD7-1 to -4, IEEE Cat. No. 80CH1489-4QEA
10. C.S. Tsai, C.T. Lee, and C.C. Lee, "Efficient Acousto-Optic Diffraction in Crossed Channel Waveguides and Resultant Integrated Optic Module," *1982 IEEE Ultrasonic Symposium Proc.*, 422-425, IEEE Cat. No. 82CH1823-4
11. C.S. Tsai and Q. Li, "Wideband Optical Frequency Shifting Using Acousto-Optic Bragg Diffraction in a LiNbO₃ Spherical Waveguide," *Proc. of 5th International Conference on Integrated Optics and Optical Fiber Communication*, pp. 129-132, Venezia, Italy, Oct. 1-4, 1985, Istituto Internazionale Delle Comunicazioni Compagnia Dei Librai Editrice, Genova, Italy
12. C.S. Tsai and Z. Y. Cheng, "Novel Guided-Wave Acoustooptic Frequency Shifter Scheme Using Bragg Diffractions in Cascade," *Appl. Phys. Lett.*, **54**, 24 (1989)
13. Z.Y. Cheng and C. S. Tsai, "A Baseband Integrated Acoustooptic Frequency Shifter," *Appl. Phys. Lett.*, **60**, 12 (1992)
14. C.S. Tsai and D. Young, "Magnetostatic-Forward-Volume-Wave-Based Guided-Wave Magneto-optic Bragg Cells and Applications to Communications and Signal Processing," *IEEE Trans. Microwave Theory and Technol.* **MTT-38**, 560 (1990)
15. Y. Pu and C. S. Tsai, "RF Magnetization of Magnetostatic Forward Volume Wave in a YIG-GGG Layered Structure with Application to Design of High-Performance Guided-Wave Magneto-optic Bragg Cells," *International Journal of High Speed Electronics*, **2**, 185 (1991)
16. Y. Pu and C. S. Tsai, "Wideband Integrated Magneto-optic Frequency Shifter at X-Band," *Appl. Phys. Lett.*, **62**, 3420-3422 (1993)
17. C.L. Wang, Y. Pu and C. S. Tsai, "Permanent Magnet-Based Guide-Wave Magneto-optic Bragg Cell Modules," *IEEE J. of Lightwave Technology*, **10**, 644 (1992)
18. Y. Pu, C. L. Wang and C. S. Tsai, "Ion-Milled Curved Hybrid Waveguide Lenses," (To be published)

GaAs VLSI-COMPATIBLE OEIC TECHNOLOGY: DESIGN FOR A QUANTUM WELL n-i-p-i PHASE MODULATOR

Steffen D. Koehler and Elsa M. Garmire

University of Southern California
Center for Laser Studies and
National Center for Integrated Photonic Technology
University Park, DRB-17
Los Angeles, CA 90089-1112

INTRODUCTION

Monolithic opto-electronic integrated circuits (OEIC's), combining integrated optics and very large scale integrated (VLSI) electronics on one chip, provide advantages over separate optics and electronics by increasing speed and density, as well as reducing interconnects, cross-talk, and alignment complications. When the entire wafer undergoes all stages of crystal growth and device processing, economies of scale are introduced. In the University of Southern California's MOSIS program, the cost for experimental GaAs VLSI fabrication is approximately \$450/mm². The physical dimensions of integrated optics switches and modulators therefore drive the cost. The project discussed here was motivated to seek the lowest possible physical dimensions, subject to the other requirements of VLSI-compatible integrated optics.

Prof. C. Fonstad of MIT has suggested GaAs-based OEIC's in which the optical components are grown after completion of the VLSI components [1]. This approach is based on the fact that standard GaAs VLSI electronics is now a relatively mature technology, capable of much more complexity than the optical components. Standard VLSI is more cost-effective and readily available than custom-designed post-optics VLSI fabrication; it can be guaranteed and tested by standard methods. Furthermore, since GaAs MESFET VLSI processing requires long, high-temperature anneals (typically 1 hour at 800° C), if photonic components are grown first, diffusion may occur in their abrupt junctions, such as quantum wells and p-n junctions. Finally, because photonic waveguide devices tend to have vertical profiles on the order of several μm , post-growth VLSI processing requires considerable planarization before high-resolution photolithography can be performed.

The disadvantage of growing and fabricating photonic components after VLSI processing is that all steps must take place at temperatures that do not damage the VLSI. For GaAs-based technology, this limits temperatures is approximately 500° C over 3 hours. Higher growth and processing temperatures significantly degrade the stability of GaAs MESFET devices [2]. This temperature constraint limits the concentration of aluminum in AlGaAs, since MBE growth of more aluminum requires higher growth temperatures. Preliminary device designs described here assume aluminum concentrations $\leq 10\%$.

Our design effort was motivated by the desire to create a waveguide modulator with minimized device length and drive voltage, consistent with the requirement that such a modulator could be grown on top of GaAs VLSI. This effort has led to design rules that can be used in a number of applications.

DESIGN CONSTRAINTS FOR OEIC MODULATORS

The design analysis will focus on phase modulators that may be used, for example, in a Mach-Zehnder configuration to modulate 1.06 μm Nd:YAG microchip lasers. Similar modulators can also be used in a directional coupler configuration to achieve switching between waveguides, such as could be used in full-duplex transmitter/receiver chip applications. Absorption modulators would face a subset of the design issues encountered here.

The design constraint on total device area is 100 μm x 400 μm , originally defined by the research effort of Fonstad [3]. To allow space for etched turning mirrors and beamsplitters in a Mach-Zehnder configuration, the phase modulator may not be longer than ~ 300 μm . This severe constraint requires as large an index change as possible. Enhancement of the index change occurs near the band edge in semiconductors, where resonant electro-refraction can be larger than the linear electro-optic effect. Further enhancement occurs when quantum wells (QW's) utilize the Quantum Confined Stark Effect (QCSE). We will assume here near-resonant electro-refraction in QW's.

GaAs-based VLSI MESFET circuitry cannot supply unlimited power; for high-impedance loads (such as electro-optic modulators), voltages on the order of 3 V are available. We will show that these design constraints can be met by using QW's within a n-i-p-i structure [4]. This structure requires careful design to ensure the highest possible frequency response. Our analysis predicts -3 dB response at >300 MHz: fast enough for many switching applications, but not fast enough to compete with direct laser modulation.

Materials

All designs here consider GaAs substrates, since GaAs VLSI is now a mature technology. The QW's will be composed of strained InGaAs, and cladding layers will be composed of $\text{Al}_x\text{Ga}_{1-x}\text{As}$, with $x \leq 10\%$, although the design methodology is also applicable to other compositions. The designs presented here are for modulation at 1.06 μm , but are easily convertible to 0.98 μm , the wavelength of strained-layer InGaAs lasers.

N-i-p-i vs. P-i-n Tradeoff

In planning for a modulator, we investigated both p-i-n and n-i-p-i structures. The p-i-n's have higher speeds, while the n-i-p-i's can operate at the same voltage in much shorter lengths [5]. The trade-off question is whether the decreased frequency response of the n-i-p-i structure may be tolerated in order to increase the voltage-length product.

The modulator structure that we have investigated is shown in Figure 1a. Note that for n-i-p-i device, electrical contacts can be made only at the sides of the doped layers; this is the origin of relatively large RC time constants. The n-i-p-i has the advantage, however, that high internal electric fields can be generated (by using very thin i regions) and still obtain large optical confinement within the waveguide (by using several such i regions). We shall see that carrier depletion in the n and p regions is not negligible, however, and plays a large role in determining the actual electric field across the thin intrinsic regions.

Linear electro-optic effects tend to cancel in a n-i-p-i because of the alternating direction of the internal field. However, for quadratic effects such as the QCSE, the index changes add. Furthermore, because a n-i-p-i waveguide can be made arbitrarily thick while still operating at low voltage, it is possible to design a structure that butt-couples directly to an optical fiber. For all of these reasons, we chose to investigate the n-i-p-i/p-i-n modulator trade-off.

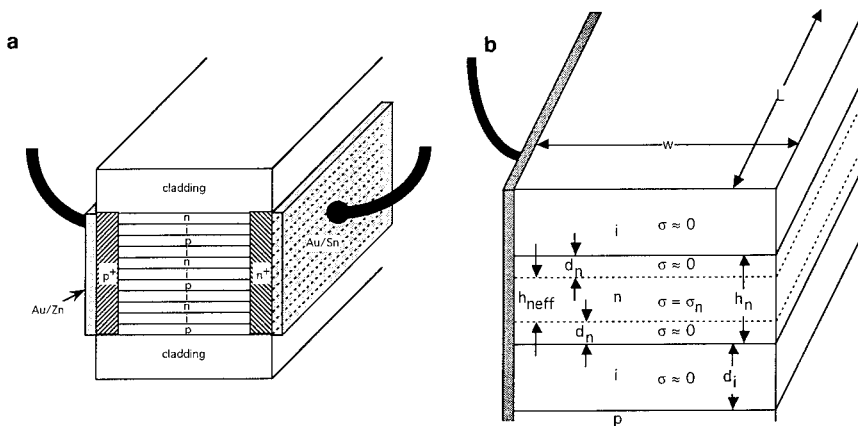


Figure 1. (a) Selective contacts to a n-i-p-i modulator. The cross-hatched n^+ and p^+ regions are counter-doped by ion implantation to provide better contact to the n and p layers. (b) End view of an n region of a n-i-p-i modulator. The n-type ohmic contact on the left is shown, but the p-type (rectifying) contact on the right is not, for clarity, since it ideally makes no electrical contact. A similar figure for p-doped regions could be drawn with the other contact shown. Light travels out of the plane of the paper, so the width of the device is w and the length is L . The width of the n-doped region is h_n , and d_n is the extent of each of the depletion regions into the n region.

Selective Contacts

A unique challenge posed by n-i-p-i's is selective contact to the n- and p-type layers, which must be made from the sides, as shown in Figure 1. (In a p-i-n structure, this is not a problem because the entire top and bottom surfaces of the doped layers are exposed, and broad area contacts can be used.) The elegant shadow mask technique [6] requires specialty MBE growth of the n-i-p-i structures. However, ordinary n-i-p-i material can use selective lateral contacts made by judicious choice of the contact metals [5,7] in a geometry such as that shown in Figure 1a without the cross-hatched p^+ and n^+ layers. It is known that Au/Sn makes a good ohmic contact with n-type GaAs, but makes a rectifying contact with p-type GaAs; conversely, Au/Zn makes good ohmic contact with p-type GaAs and rectifying contact with n-type GaAs [7].

Figure 1a includes counter-doping to decrease contact resistance and provide better selectivity. This is done by ion implantation after the original material has been grown and etched into a waveguide mesa. A potential drawback is that counter-doping limits the concentration of the grown dopants to less than the ion implantation doping.

MODULATOR STRUCTURE FIGURE OF MERIT

We shall define a structure figure of merit, F_m , based on the phase change that can be achieved for a given applied voltage. This requires knowledge of three things: the dependence of the QW refractive index on the internal field, the optical confinement factor, and the dependence of the internal field on the applied voltage. These three factors are discussed here.

QW Refractive Index as a Function of Internal Field

We will assume a strained InGaAs/GaAs QW composition that we have already shown is suitable for 1.06 μm phase modulators [8], using 100 Å $\text{In}_{0.13}\text{Ga}_{0.87}\text{As}$ MQW's. This composition provides approximately 100 meV detuning of the exciton peak from the

wavelength to be modulated, suitable to limit absorption loss in a 300 μm length to -0.5 dB, while being close enough to the band edge to provide reasonably large QCSE. We have also fixed the GaAs barrier widths at 100 Å.

It has been shown that, this far from the exciton resonance, the QCSE is mostly quadratic with internal electric field [9]. We therefore define a quadratic coefficient, s , such that

$$\Delta n = \frac{1}{2} n^3 s E^2, \quad (1)$$

where n is the QW refractive index and E is the internal electric field across the i region. From our experimental results [8], $s = 3.6 \times 10^{-15} \text{ cm}^2/\text{V}^2$. Note that this s value is defined for the QW only, where the modulation takes place. To calculate the effective index seen by a guided light wave, it is necessary to calculate the QW filling factor.

Optical Confinement Factor

Much of the light is not contained in the QW's, which are the only source of QCSE modulation. Light also sees the GaAs QW barriers and the $\text{Al}_x\text{Ga}_{1-x}\text{As}$ waveguide cladding layers above and below the guiding region. We must therefore calculate the fraction of light in the well, which is called the optical confinement factor, Γ . There are three contributions to Γ : the fraction of the light confined within the waveguide (γ_1), the fraction of the light in the guide that is also in the intrinsic regions (γ_2), and the fraction of the light in the intrinsic regions that is also in the QW's (γ_3). The overall confinement factor is the product of these three contributions:

$$\Gamma = \gamma_1 \gamma_2 \gamma_3. \quad (2)$$

Each of these confinement factors is calculated by taking the fraction of the integrated intensity of the guided mode in the appropriate regions. In the computation of γ_1 , it is necessary to define a refractive index for the waveguiding region. We assume the weighted average indium content, accurate for sufficiently low quantities of indium [10].

Internal Field

Carrier depletion in the n and p regions will enlarge the distance over which the potential drops and decrease the thickness of the conductive electrodes. This distance can be calculated from the electric field across the i region of an ideally abrupt p - i - n junction:

$$E = \frac{e n}{\epsilon} \frac{-d_i + \sqrt{d_i^2 - 2 \frac{\epsilon \Phi}{e n} (1 + \frac{n}{p})}}{(1 + \frac{n}{p})}, \quad (3)$$

where n is the donor doping density, p is the acceptor doping density, e is the elementary charge, ϵ is the dielectric constant, and Φ is the sum of the applied voltage, V_{applied} , and the built-in potential, V_0 , which is given by

$$V_0 = \frac{-E_g}{e} + \frac{k_B T}{e} \ln \left[\frac{1}{2np} \left(\frac{k_B T}{\pi \hbar^2} \right)^3 (m_e^* m_h^*)^{3/2} \right], \quad (4)$$

where k_B is Boltzmann's constant, T is the absolute temperature, \hbar is Plank's constant normalized to 2π , m_e^* is the electron effective mass, and m_h^* is the reduced hole effective mass. The derivation for V_0 assumes nondegenerate doping; for the dopings considered in this paper, the error from this assumption is on the order of 1%.

ALGORITHM FOR OPTIMIZATION

The aim is to maximize the phase change per volt applied in a QCSE waveguide phase modulator, consistent with the frequency response and compatibility requirements. Figure 2 shows the algorithm developed for the optimization. For any specified number of i layers, the design parameters that must be varied are doped layer concentration, doped layer thicknesses, and intrinsic layer thickness. These parameters, along with the number of i layers, determine the internal electric field and the optical confinement factor. It is necessary to perform a calculation that will determine the structure figure of merit, F_m , given by the product of the optical confinement factor and the change in the internal field squared as a result of 1 V applied reverse bias (if the QCSE is purely quadratic; if not, the proper functional form of the electric field must be included).

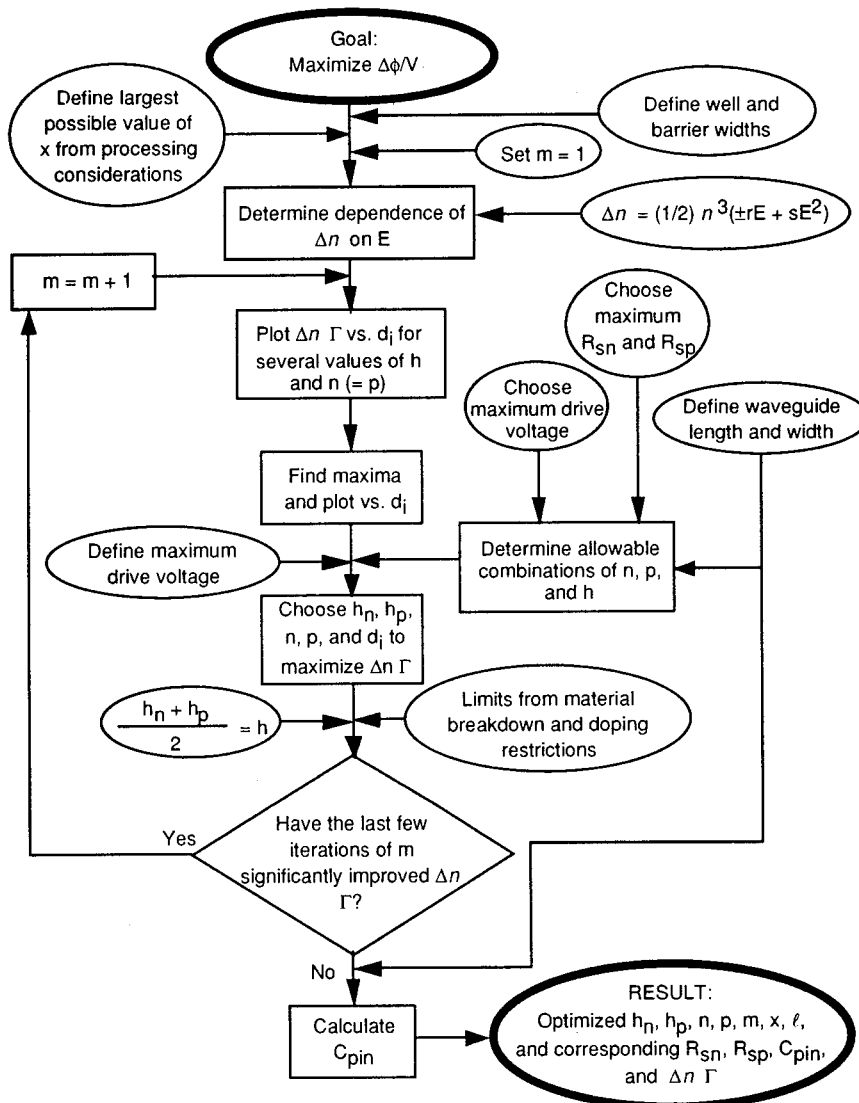


Figure 2. Algorithm for design of a waveguide modulator to minimize drive voltage (and length).

It is intuitively clear that, in terms of F_m , the n and p layers should be doped as highly as possible and grown as thin as possible (so-called δ -doping), since any finite thickness will reduce optical confinement (only the QW's are useful for modulation) and any finite doping density runs the risk of carrier depletion, uncovering charge and allowing some potential to drop across the doped regions.

However, for the modulator to be practical, its RC time constant must be suitably small. Therefore, the doped layer parameters cannot be chosen without calculating the effective resistivity and capacitance of the device at every step. This is the reason for the complicated flow diagram needed in the optimization. We will find that carrier densities on the order of $1 \times 10^{18}/\text{cm}^3$ and doped layer thicknesses on the order of 1000 Å will provide a suitable trade-off between speed and modulation figure of merit.

The parameters used in the optimization process are defined in Table I.

Table I. Definitions for parameters use in the optimization process.

d_i	Thickness of one intrinsic region ¹	h	Average doped layer thickness ²
d_w	Width of one QW	h_n	Thickness of one n-doped layer
b	Barrier thickness between adjacent QWs	h_p	Thickness of one p-doped layer
ℓ	Number of QWs in one intrinsic region	n	Carrier density of n-doped layers
m	Number of intrinsic regions in device structure	p	Carrier density of p-doped layers
x	Concentration of Al in $\text{Al}_x\text{Ga}_{1-x}\text{As}$ waveguide cladding layers		

$$^1 d_i = \ell d_w + (\ell + 1) b$$

$$^2 h = (h_n + h_p) / 2.$$

Electrical Limitations to the Choice of Doped Layer Parameters

The need to apply contacts to the edges of the doped regions causes significant sheet resistance if doping concentrations are too low and/or the doped regions are too thin. In the extreme limit of channel pinch-off, where the doped regions become entirely depleted of majority carriers, they would be almost non-conductive. On the other hand, doping concentrations cannot be arbitrarily high because of possible conflicts with contact schemes, such as counter-doping. In addition, free carrier loss may be unacceptable. Finally, very high doping with very thin intrinsic regions causes high built-in fields across the device. This, added to the large applied fields, can lead to a roll-off of the modulation [11] or breakdown of the material.

Sheet resistance. The resistance of a layer of doped material depends on the dimensions of the layer as well as its conductivity. Figure 1b shows a typical doped layer for a n-i-p-i modulator, including the depletion on either side. Note that the electrical signal must travel a distance w through the n region to completely form the electric field across the i region. The conductivity of the n region is σ_n , except in the depletion regions, where $\sigma \approx 0$. Thus, the effective electrical thickness of the n region is

$$h_{\text{neff}} = h_n - 2 d_n, \quad (5)$$

for $h_n > 2 d_n$, and similarly for the p regions. The width of the depletion region is

$$d_n = \frac{-d_i + \sqrt{d_i^2 - \frac{2 \epsilon \Phi (1 + \frac{n}{p})}{e n}}}{1 + \frac{n}{p}}, \quad (6)$$

and the resistance of a single n region becomes,

$$R_{sn} = \frac{w}{L (h - 2d_n) \sigma_n}, \quad (7)$$

where w is the *electrical* path length and L is the *electrical* path width.

Since R_{sn} increases as the depletion d_n increases, it is clear that sheet resistance increases with applied reverse bias. Higher doping concentrations not only decrease d_n , but also increase σ_n , thereby decreasing R_{sn} . Note that if reverse bias is sufficient (i.e. at the pinch-off voltage), a thin doping layer may become entirely depleted (i.e. $h_{eff} = 0$). Similar results hold for the p layers. The conductivity is given by $\sigma_n = e \mu_c n$, where μ_c is the electron mobility. For GaAs, μ_c is typically on the order of 3000 cm²/V sec (the hole mobility $\mu_h \approx 175$ cm²/V sec). [The exact mobilities are within $\pm 50\%$ of these values for all the doping concentrations considered in here.]

R_{sn} and R_{sp} increase reverse bias voltage until the pinch-off voltage (which depends on doped layer concentration and thickness) is reached. In order to limit our modulator design to practical sheet resistances, we have arbitrarily chosen to limit the sheet resistance to less than 200 Ω when a 5 V reverse bias is applied. At this point, dimensions for the modulator must be chosen. We use $L = 300 \mu m$ and $w = 7 \mu m$.

We can combine equations (3), (6), and (7) to specify the doped layer thicknesses that meet the $R_{sn} \leq 200 \Omega$ requirement for a given doping concentration. Assuming that $n = p$,

$$h_n = \frac{w}{L e \mu_c R_{sn}} + \sqrt{d_i^2 - \frac{4 \epsilon (V_0 - V_{rb})}{e n}} - d_i, \quad (8)$$

(and similarly for h_p , substituting μ_h for μ_c and p for n). Applying equation (4) for V_0 and inserting the parameters $h = 1000 \text{ \AA}$, $d_i = 1000 \text{ \AA}$, and $V_{rb} = 5 \text{ V}$ and the appropriate constants for GaAs, equation (8) gives $h_n \geq 730 \text{ \AA}$ and $h_p \geq 1180 \text{ \AA}$ when $n = p = 10^{18}/\text{cm}^3$.

Limits to Doping From Selective Contacts. External contacts may also limit the maximum doping concentration used for the device. If counter-doped contacts are used, the ion implanted concentration must be significantly greater than the grown doping concentration. Ion implantation causes damage to the host material, which must be removed by thermal annealing. Higher implantation concentrations require hotter and longer anneal periods, and therefore the maximum concentration is limited by the thermal requirements of the sample. Our investigations have shown that $2 \times 10^{18}/\text{cm}^3$ Si implanted into GaAs to a depth of 4000 \AA causes damage that may be removed by annealing for 30 sec. at 500 $^\circ\text{C}$, which is well within VLSI constraints.

Limits to Built-In Field. As the i region becomes thinner, the built-in field (defined in the absence of an applied field) increases. This means that to achieve large modulation depths at moderate internal fields, a combination of forward and reverse modulation may be necessary, since if only reverse bias modulation is used, the internal fields might have to become too large. Thus, it is necessary to know the built-in field for any trade-off analysis.

The Optimization Process

We now turn our attention to predicting V_π using the optimization process. The task, diagrammed in Figure 2, proceeds as follows:

Specify composition of waveguide and cladding layers. The design of QW's in the waveguide is determined by maximizing the index change from the QCSE without introducing too much loss from electro-absorption. Initial calculations are performed with a design placing the QW excitonic resonance 100 meV above the wavelength to be modulated. This introduces a loss on the order of -1 dB/mm. If further loss can be tolerated, an excitonic resonance closer to the desired wavelength will increase the QCSE. For example, operating 50 meV away from the exciton will introduce approximately -3 dB of loss in a 300 μm length, but double the index change. QW and barrier widths are set by the need to choose the energy of the exciton.

Cladding composition is chosen with $x \leq 0.1$ because of the low temperature growth constraints mentioned in the introduction. We ran the analysis for $x = 0$ and $x = 0.1$.

Initialize the number of i regions: $m = 1$. The value of m will be incremented until optimization is completed. We will find that n-i-p-i performance is improved by increasing m , although this improvement is marginal after $m \approx 6$.

Specify the index change parameter, s . The value of s within the QW from QCSE (equation 1) is determined by the chosen wavelength. We use as our example the TE polarization for a device previously reported [8], which consisted of 11 InGaAs QW's separated by 200 \AA GaAs barriers. From those data, we can infer nearly pure quadratic behavior with $s = 3.6 \times 10^{-15} \text{ cm}^2/\text{V}^2$.

Vary the thickness of the i region assuming a fixed 1 V reverse bias. We must calculate $F_m = \Gamma \Delta(E^2)$ (which is proportional to the effective index change) as a function of d_i for varying doped layer density, n (set equal to p), and average doped layer thickness h . Ensuring less than 200 Ω resistance at 5 V means that $d_p \approx 1250 \text{ \AA}$ and $d_n \approx 750 \text{ \AA}$.

Figure 3 shows F_m as a function of the intrinsic layer thickness for various number of i regions. Few i layers result in poorer optical confinement and generally have poorer modulation figures of merit. When $m > 6$, however, there is very little improvement in the modulation figure of merit. The exception is the result at $m = 1$ (a single p-i-n layer), which implies that the overall best figure of merit is produced by a single intrinsic layer with the thinnest possible thickness. This, of course, would cause a very high internal field and a thin guided mode (that is not compatible with external input/output coupling). The poorer performance of n-i-p-i structures at small intrinsic layer thickness is due to the poorer QW confinement factor ("waste" of light in the thicker doped regions).

Add linear electro-optic effect if necessary. The analysis so far is for QCSE only. An odd number of i layers allows some linear electro-optic effect (LEO) that must be added to the QCSE (adjacent i layers cancel out).

Include the fact that QW's discretize values of d_i . Recall that $d_i = \ell d_w + (\ell - 1)b$, where ℓ is the number of QW's in the i layer. In our example, both d_w and $b = 100 \text{ \AA}$. Thus, for $d_i = 700 \text{ \AA}$, $\ell = 4$.

We have performed calculations as in Figure 3 for the optimum doped layer thicknesses and carrier concentrations, allowing for several cladding layer compositions. The results are shown in Table 2. We have also listed the built-in and maximum internal fields. Since the behavior of QCSE modulators at fields above 250 kV/cm has not yet been reported in the literature, we choose device designs with fields not too far above this value, provided a large sacrifice in V_π need not be made.

So far, we have only considered the reverse biased characteristics of a phase modulator. It is possible, however, to apply a forward bias to the diodes. In this fashion, an index change of opposite sign can be applied to the device, at the expense of increased electrical current. Providing some forward bias to one arm of a Mach-Zehnder interferometer, while reverse biasing the other, introduces the prospect of operating at voltages below the V_π values specified in Table 2.

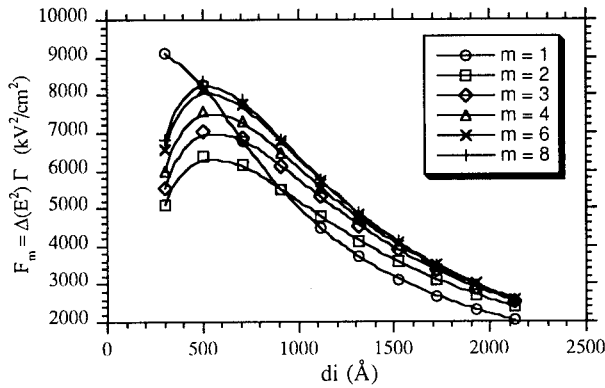


Figure 3. Figure of merit $F_m = \Delta(E^2) \Gamma$ vs. d_i for various numbers of intrinsic regions (m) as a result of 1 V applied. If n is purely quadratic in E (no linear component such as LEO), then this plot is proportional to $\Delta\phi$ vs. d_i . For this example, $h = 1000 \text{ Å}$, $n = p = 10^{18}/\text{cm}^3$, and $x = 0.10$. Note that there are different peak positions for F_m depending on m . The value $m = 1$ corresponds to a p-i-n structure.

Calculate frequency response. Next, we calculate the capacitance and sheet resistance of each intrinsic and doped layer, respectively, using the method shown in the next section. The results are included in Table 2. Considering all the factors discussed above, we choose the optimum case as $\ell = 4$ (700 Å intrinsic layer thickness), which we predict enables a V_π in 300 μm of 3 V with a frequency response of 360 MHz, at a maximum internal field of 372 kV/cm. This requires an $x = 10\%$ $\text{Al}_x\text{Ga}_{1-x}\text{As}$ cladding, an acceptable concentration for low temperature MBE growth.

Table 2. Values of V_π (assuming $L = 300 \text{ μm}$) for a proposed waveguide phase modulator. E_0 is the built-in field, E_π is the field necessary to achieve $\Delta\phi = \pi$, and f_c is the critical frequency. The structure has the constants $d_w \approx 100 \text{ Å}$, $b = 100 \text{ Å}$, $h_n = 750 \text{ Å}$, $h_p = 1250 \text{ Å}$, and $n = p = 10^{18}/\text{cm}^3$, and $R_{\text{source}} = 50 \text{ Ω}$. The values shown are scaled from measurements of a p-i-n modulator [8] and account for free-carrier absorption losses [12].

m	ℓ	d_i (Å)	x	V_π	Mode diameter (μm)	E_0 (kV/cm)	E_π (kV/cm)	f_c (MHz)	loss (dB/mm)
6	2	500	0.1	2.8	1.2	211	491	305	2.7
6	3	7000	0.1	2.8	1.3	168	416	327	2.0
6	4	900	0.1	3.0	1.4	138	372	358	2.0
6	5	1100	0.1	3.3	1.4	116	344	391	1.8
6	6	1300	0.1	3.6	1.5	100	324	420	1.8
6	4	900	0.0	4.5	3.6	138	470	325	1.2
6	5	1100	0.0	4.6	3.3	116	419	351	1.2
6	6	1300	0.0	4.7	3.2	100	383	359	1.3
1	2	500	0.1	3.1	1.2	211	515	2830	2.8
1	3	700	0.1	3.5	1.2	168	465	3130	2.2
1	4	900	0.1	3.9	1.2	138	430	3480	2.1
1	8	1700	0.1	5.4	1.1	78	342	2901	2.0
1	8	1700	0.0	7.1	2.9	78	417	5270	2.1

FREQUENCY RESPONSE

We now turn our attention to the frequency response of a n-i-p-i modulator, defined by its critical frequency, f_c . The frequency response in a QCSE modulator is limited by the speed with which a voltage can be applied to the intrinsic region. Thus, f_c is determined solely by the electrical resistance, inductance, and capacitance of the device.

Figure 4 shows a circuit diagram for a n-i-p-i modulator based on the geometry of Figure 1b. Since the sheet resistances and capacitances are distributed along the width of the waveguide, we divide them into g sections for ease of analysis with a Spice simulation. Thus, there are g resistors in each doped layer, each with value R_s/g ; capacitors are similarly divided. The circuit ignores inductances, and it assumes that the p-i-n and p-n junctions are reverse biased with no current leakage paths (i.e. infinite shunt resistance). The voltage supply output resistance (usually $50\ \Omega$) is given by R_{source} , and the capacitances of the rectifying junctions between the contacts and the regions of opposite doping are given by C_{pn} .

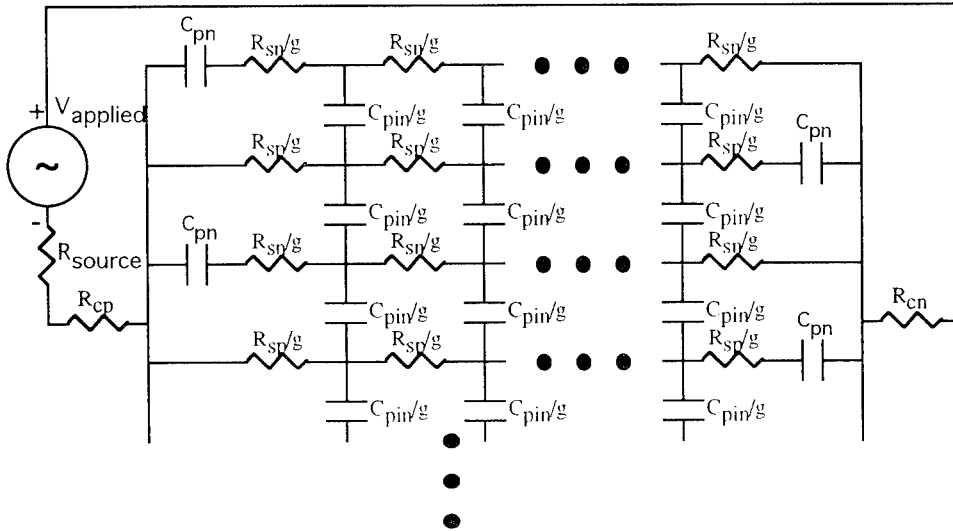


Figure 4. Circuit diagram for a reverse-biased waveguide n-i-p-i modulator, with distributed resistances and capacitances split into g divisions. The circuit does not account for inductance or diode leakage.

The values for R_s and C_{pin} are determined by the specific design parameters that we have chosen. R_{sn} and R_{sp} are calculated using equation (7), and $C_{pin} \approx \epsilon A / (d_i + d_n + d_p)$, where the area $A = wL$. We calculate C_{pn} for the counter-doped scheme assuming $n = p = 10^{18}/\text{cm}^3$ and a counter-doping of $2 \times 10^{18}/\text{cm}^3$. In this case, the capacitance area $A_n = (h_n - 2d_n)L$ and $A_p = (h_p - 2d_p)L$ in all but the outermost doped layers. For the values considered here, C_{pn} is less than 50 fF, and therefore we will approximate C_{pn} as an open circuit. Finally, if good ohmic contacts are made, R_c may be negligible for both sides of the device.

This circuit accurately models the device in the limit as g approaches ∞ . We evaluated the effect of g on the predicted frequency response and found that $g = 1$ had f_c within a factor of 3 of $g = 5$, while $g = 4$ had f_c only 20% below $g = 5$.

The effect of changing the number of i layers, m , on the frequency response is fairly small (less than 20% going from $m = 6$ to $m = 8$), since the individual i regions, while electrically in parallel, are mostly decoupled from each other through the large sheet resistance.

CONCLUSION

Table 2 shows that a half-wave modulation voltage of under 3 V is possible with a frequency response of over 300 MHz and internal fields that are under 375 kV/cm. The modulation voltage can be reduced further, and the frequency response increased, by operating closer to the exciton resonance (with attendant higher optical loss). Even further voltage reduction can be achieved by including some forward bias swing. Adding such factors should drop the voltage requirement to under 2 V, which would speed the devices up to ~600 MHz. Experimental efforts are presently underway to demonstrate such a modulator.

ACKNOWLEDGMENTS

This work was supported by ARPA through the National Center for Integrated Photonic Technology, based at the University of Southern California. The authors wish to thank Hughes Research Laboratories for extensive assistance, particularly discussions with Drs. A. Kost, T.C. Hasenberg, D. Yap, and R.G. Wilson.

REFERENCES

- [1] C.G. Fonstad, Jr., National Center for Integrated Photonic Technology research program.
- [2] K.V. Shenoy, C.G. Fonstad, Jr., and J.M. Mikkelsen, "High-temperature stability of refractory-metal VLSI GaAs MESFET's," *IEEE Electron Device Lett.*, vol. 15, pp. 106-108, 1994.
- [3] K.V. Shenoy, P.R. Nuytens, C.G. Fonstad, Jr., G.D. Johnson, W.D. Goodhue, and J.P. Donnelly, "Optoelectronic VLSI circuit fabrication," *IEEE LEOS Annual Meeting 1993 Conf. Proc.*, San Jose, CA, OM2.3, pp. 433-434.
- [4] A. Kost, E. Garmire, A. Danner, and P.D. Dapkus, "Large optical nonlinearities in a GaAs/AlGaAs hetero n-i-p-i structure," *Appl. Phys. Lett.*, vol. 52, pp. 637-639, 1988.
- [5] G.W. Yoffe, J. Bräbich, F. Karouta, W.C. van der Vleuten, L.M.F. Kaufmann, and J.H. Wolter, "Low-voltage hetero-nipi waveguide modulators with GaAs/AlAs quantum wells," *Appl. Phys. Lett.*, vol. 63, pp. 1456-1458, 1993.
- [6] K.H. Gulden, X. Wu, J.S. Smith, P. Kiesel, A. Höfler, M. Kneissl, P. Riel, and G.H. Döhler, "Novel shadow mask molecular beam epitaxial regrowth technique for selective doping," *Appl. Phys. Lett.*, vol. 62, pp. 3180-3182, 1993.
- [7] K.W. Goossen, J.E. Cunningham, and W.Y. Yan, "GaAs-AlAs low-voltage refractive modulator operating at 1.06 μm ," *Appl. Phys. Lett.*, vol. 57, pp. 744-746, 1990.
- [8] T.C. Hasenberg, S.D. Koehler, D. Yap, A. Kost, and S.D. Koehler, "All-Binary InAs/GaAs Optical Waveguide Phase Modulator At 1.06 μm ," *IEEE Photon. Technol. Lett.*, (accepted for publication in October, 1994)
- [9] J.S. Weiner, D.A.B. Miller, and D.S. Chemla, "Quadratic electro-optic effect due to the quantum-confined Stark effect in quantum wells," *Appl. Phys. Lett.*, vol. 50, pp. 842-844, 1987.
- [10] J. Krauss and P.P. Deimel, "Calculation of the propagation constant of optical modes in multiquantum-well structures," *IEEE J. Quantum Electron.*, vol. 26, pp. 824-826, 1990.
- [11] J.E. Zucker, I. Bar-Joseph, G. Sucha, U. Koren, B.I. Miller, and D.S. Chemla, "Electrorefraction in GaInAs/InP multiple quantum well heterostructures," *Electron. Lett.*, vol. 24, pp. 458-459, 1988.
- [12] H.C. Casey, Jr. and M.B. Panish, *Heterostructure Lasers, Part A: Fundamental Principles*, p. 175, New York: Academic Press, 1978.

DESIGN AND ANALYSIS OF SURFACE-NORMAL FABRY-PEROT OPTICAL MODULATORS IN THE NEAR INFRARED (InGaAs/GaAs) AND BLUE-GREEN (ZnCdSe/ZnMgSSe) REGIONS

S. K. Cheung¹, W. Huang¹, F. Jain¹, R. Sacks² and T. Grudkowski²

¹U-157, Electrical and Systems Engineering Department
University of Connecticut, Storrs, CT 06269-3157

²United Technologies Research Center, 411 Silver Lane
East Hartford, CT. 06108

INTRODUCTION

Optical modulators using quantum confined Stark effect (QCSE) have been investigated by a number of investigators since the reporting of the nonlinear excitonic effect in multiple quantum wells (MQWs) by Miller et al.¹ Current research on Multiple Quantum Well (MQW) Fabry-Perot (FP) optical modulators/switches has attracted a great deal of attention² because of their surface-normal configurations are particularly suitable for two-dimensional (2D) matrix manipulation and image processing. They are compatible with fiber optics and large-scale interconnection systems based on the hypercube topology. Previous works^{2,3} in MQW FP modulators have concentrated using photoabsorptive effects in symmetric and asymmetric FP structures. Unlike these modulators, we present high contrast symmetric Fabry-Perot optical modulators (SFPs) in which tuning is achieved by enhancing the electrorefractive effect inside the MQW cavity. We have demonstrated⁴ a SFP, which consists of an InGaAs/GaAs MQW cavity sandwiched between two AlAs/GaAs quarter-wave dielectric mirrors, to exhibit a contrast ratio of 30.8 dB with a Stark effect tuning range of 10 nm as a function of externally applied voltage. A dynamic range of 37.8 dB has been achieved in nontunable FP modulator structures.

This paper presents the optical characterization of the InGaAs/GaAs MQW layers in the SFPs using the Variable Angle Spectroscopic Ellipsometry (VASE). It provides a direct method to measure optical constants, field-induced changes in refractive index and extinction coefficient, and the location and the shift of the excitonic resonance for the design of Fabry-Perot optical modulators operated in the near infrared region. Comparison between calculated and experimental results of the high contrast InGaAs-GaAs MQW SFPs is presented. The methodology developed for the InGaAs-GaAs SFPs is used to design high contrast ZnCdSe-ZnSSe MQW optical modulators⁵ operated in the blue-green

region. We have simulated ZnCdSe-ZnSSe MQW modulators and would present designs to achieve high contrast performance.

DESIGN OF FABRY-PEROT MULTIPLE QUANTUM WELL OPTICAL MODULATORS

For III-VI and II-VI MQW layers, the operation of the Fabry-Perot MQW optical modulators can be described by the two effective interfaces method or the split filter analysis⁶ as shown in Figure 1. The reflection coefficients of the top (denoted by 1) and bottom (denoted by 2) mirrors are described by:

$$r_1' = |r_1'| \exp(i\phi_1) \quad (1)$$

$$r_2 = |r_2'| \exp(i\phi_2). \quad (2)$$

where ϕ_1 and ϕ_2 are the phase terms of the reflection spectra of the top and bottom DBRs, respectively. Variables t_1 , t_2 , r_1' and r_2 (viewed from the spacer) are the transmittance and reflectance of the top and bottom DBRs. By considering the MQW cavity as the spacer which is bounded by interfaces 1 and 2 with reflectivities defined by the top and bottom DBRs, respectively, the dispersive transmittance of the SFPM can be described by the Airy sum function as:

$$T(\lambda) = \frac{T_{\max}(\lambda)}{1 + F(\lambda) \sin^2(\beta)} \quad (3)$$

where

$$\beta(\lambda) = \frac{1}{2} \left[2\delta_c(\lambda) - (\phi_1(\lambda) + \phi_2(\lambda)) \right] \quad (4)$$

and

$$\delta_c(\lambda) = \frac{2\pi n_{MQW} d_c \cos(\theta_{in})}{\lambda}. \quad (5)$$

The system finesse of the SFPM is expressed by $F(\lambda)$. The MQW cavity parameters δ_c , n_{MQW} and d_c depict the phase shift, complex effective refractive index and the cavity thickness, respectively. The phase matching condition between the two mirrors and the MQW cavity is determined by $\beta(\lambda)$. If a FP mode in the first-order high-reflectance zone is chosen as the wavelength of operation, the optimization of T_{\max} and β at the FP resonance yields the design parameters of the SFPMs. The design parameters such as the periods p and q of the top and bottom GaAs/AlAs DBRs can be obtained by maximizing the transmittance at the wavelength of operation $\lambda_0 = \lambda_{design}$, i.e.,

$$\frac{\partial^2}{\partial p \partial q} T_{\max}(p, q)|_{\lambda_0} = 0. \quad (6)$$

For transmittivity $\geq 90\%$, it is found that the p and q (periods of the top and bottom GaAs/AlAs DBRs, respectively) are related by: $q \cong p + 3.5$. The choice of p and q is related to the half width and half maximum⁷ (HWHM) of the FP mode, $\Delta\lambda_{HWHM}$.

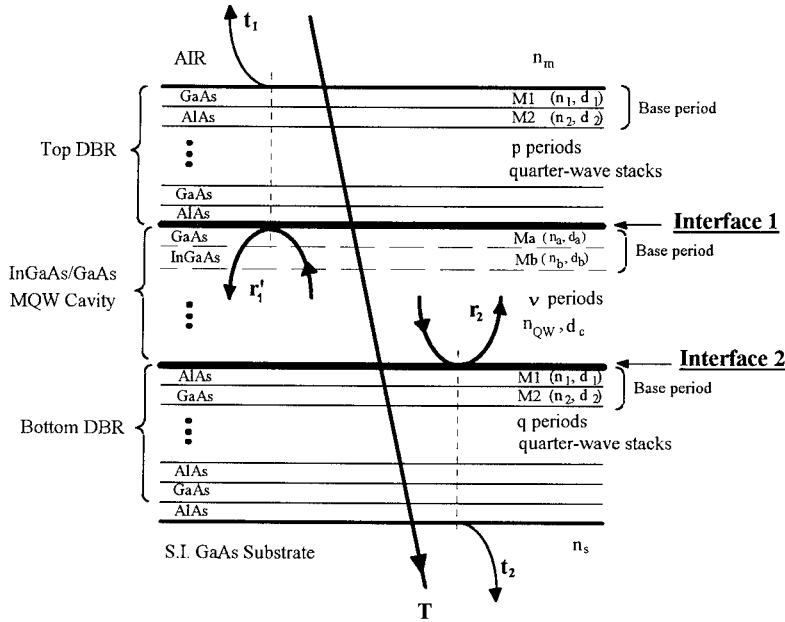


Figure 1. The two effective interfaces method.

For a FP mode centered at $\lambda_0 = \lambda_{design}$, $\Delta\lambda_{HWHM}$ is given by:

$$\Delta\lambda_{HWHM}|_{\lambda_0} = \lambda \frac{1 - \sqrt{R'_1(\lambda)R'_2(\lambda)}}{\left[R'_1(\lambda)R'_2(\lambda) \right]^{1/4} \left(\frac{2\pi n_{QW}d_c}{\lambda} - \lambda \frac{\partial \phi(\lambda)}{\partial \lambda} \right)} \bigg|_{\lambda=\lambda_0} \quad (7)$$

Simultaneously, the corresponding phase matching condition occurs at $\beta(\lambda_{design}) = m\pi$ and determines the cavity thickness and the location of the active Fabry-Perot mode. Although matching the phases between the two DBRs and the MQW cavity gives the theoretical location of the wavelength of operation and the cavity thickness, the uniformity of the grown layers in the top and bottom DBRs affects their phase changes and results in a shift of the wavelength of operation. In practice, the thickness of the MQW cavity is determined by assigning an integral value to m such that a sufficient dynamic range is obtained for the SLM. By choosing the FP mode at λ_{design} under normal incidence, the thickness of the MQW cavity is obtained by:

$$d_c(\lambda_{design}) = \frac{\lambda}{2\pi n_{QW}(\lambda)} \left[m\pi + \frac{\phi_1(\lambda) + \phi_2(\lambda)}{2} \right] \bigg|_{\lambda=\lambda_{design}} \quad (8)$$

Besides, the number of periods of the DBRs in the SFPs operated in the reflection mode can be obtained using the relation: $T + R = 1$.

It is important to obtain either theoretically or experimentally the field-induced changes of refractive index and absorption coefficient in the MQW cavity for device design and application. The following two sections will present the theoretical as well as experimental methodology used in our design.

FIELD-INDUCED CHANGES OF ABSORPTION COEFFICIENT AND INDEX OF REFRACTION IN MQWs

The total absorption coefficient of the MQW structure can be approximated^{8,9} by adding the contributions due to the interband and exciton transitions:

$$\alpha_{QW} \cong \alpha_{hh}^{cv} + \alpha_{hh}^{ex} + \alpha_{lh}^{cv} + \alpha_{lh}^{ex}, \quad (9)$$

where the excitonic absorption (α_{hh}^{ex} and α_{lh}^{ex}) is dominated by the exciton ground state, and is expressed as:

$$\alpha_{lh, hh}^{ex}(\omega) \cong \sum_{lh, hh} \frac{e^2 \hbar^2 \omega \tilde{P}_{cv} \rho_{hh, lh}^{TE, TM}}{n_0 c \epsilon_0 m_e^* (\hbar \omega)^2 L_z} \left| \langle \varphi_{cl}(z) | \varphi_{vl}(z) \rangle \right|^2 |\mathfrak{Y}_1(0)|^2 \Gamma(E_{ex} - \hbar \omega). \quad (10)$$

Here $\mathfrak{Y}_1(0)$ is the wave function of the exciton at $\rho = 0$, E_B^{ex} is the exciton binding energy. The absorption coefficient for the interband free electron-hole transition is described by:

$$\alpha_{hh, lh}^{cv}(\omega) = \sum_{lh, hh} \frac{e^2 m_r^* \omega \tilde{P}_{cv}}{6 \epsilon_0 c n_0 m_e^* L_z (\hbar \omega)^2} \sum_{n'n} \left| \langle \varphi_{cn'}(z) | \varphi_{vn}(z) \rangle \right|^2 I_{n'n}(\hbar \omega) \quad (11)$$

with

$$I_{n'n}(\hbar \omega) = \int_0^\infty dE \rho_{hh, lh}^{TE, TM}(E) S(E) \Gamma(E) \quad (12)$$

and

$$E_{ex} = E_g + \epsilon_1^e + \epsilon_1^h - E_B^{ex}, \quad (13)$$

where $\epsilon_1^{e,h}$ labels the electron and hole energies, and m_e^* represents the effective mass of electron. The functions $\rho_{hh, lh}^{TE, TM}(E)$, $S(E)$, $\Gamma(E)$ stand for the polarization factor, Sommerfeld enhancement factor and the Gaussian broadening line shape, respectively. The electron and hole wave functions in the confined structure are represented by $\varphi_{cn', vn}(z)$. With an applied external field, the transition energy between the electrons and heavy holes is reduced relative to their unperturbed states. This introduces a red shift in the exciton peak. In addition, the overlap integral, the exciton wave function, and the binding energy are modified in the presence of the electric field. Consequently, the absorption coefficient changes and so does the refractive index as they are related by the Kramers-Kronig transform¹⁰. Although the presence of the strain in the MQW layers affects the energy bands discontinuity and modifies the optical constants, we assume small strain effect in our calculations.

OPTICAL CHARACTERIZATION OF InGaAs/GaAs MQW STRUCTURES USING VARIABLE ANGLE SPECTROSCOPIC ELLIPSOMETRY (VASE)

Variable Angle Spectroscopic Ellipsometry (VASE) is a surface analytical technique which can be used to determine the optical properties, layer thickness, alloy composition, growth quality and morphology of thin film heterojunctions, MQWs or superlattice structures. By treating the MQW as a single layer, the effective optical constants of the MQW structure can be obtained using VASE. Ellipsometry measurements of parameters such as ψ and Δ yield the effective optical constants for a multilayer structure through the Fresnel coefficients derived from the boundary conditions of electromagnetic theory for given values of angle of incident¹¹.

A pseudomorphic $\text{In}_{0.2}\text{Ga}_{0.8}\text{As}/\text{GaAs}$ MQW samples (MBE#1816) was grown by MBE to study their optical properties. The MBE#1816 sample, which contains 47 periods of $46\text{\AA}-\text{In}_{0.2}\text{Ga}_{0.8}\text{As}/96\text{\AA}-\text{GaAs}$ MQWs (not intentionally doped) grown on a $0.19\text{ }\mu\text{m}$ n+GaAs buffer, has an overall MQW thickness (excluding the buffer and the substrate) $\sim 6770\text{\AA}$. This MQW thickness is well within the penetration depth of the probing beam of the VASE in the wavelength range of $800\text{--}1000\text{ nm}$. The carrier concentration in the n+GaAs buffer is $\sim 1 \times 10^{18}/\text{cm}^3$. The thickness of the n+GaAs substrate is taken to be $\sim 502\text{ }\mu\text{m}$. The indium content and the thickness of the MQWs are obtained from RHEED and DCXRD, respectively. The effective refractive index, n , and the extinction coefficient, k , of the InGaAs/GaAs MQWs for the sample MBE#1816 are sketched in Figure 2. There is a rapid change (~ 0.02) of the refractive index from 970 nm to 1000 nm . This is attributed to the excitonic effect and it occurs in the region where the excitonic absorption peak is observed ($\sim 973\text{ nm}$).

The effect of the electric field on the optical parameters in the InGaAs/GaAs layers is obtained using the VASE technique by applying a voltage in the crystal growth direction across the MQWs. Figure 3 (a) and (b) depict the changes

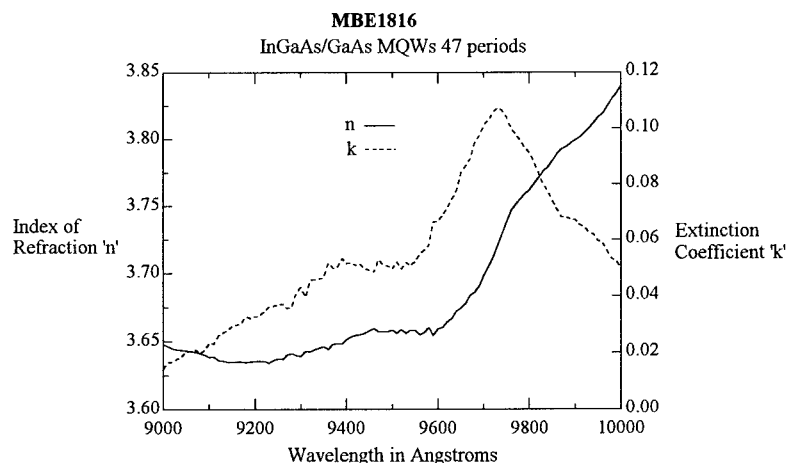


Figure 2. The measured effective refractive index n , and the extinction coefficient k of the InGaAs/GaAs MQWs for sample MBE#1816.

of absorption coefficient ($\Delta\alpha$) and the refractive index (Δn) versus wavelength for several applied voltages of: 2V, 4V, 8V and 16V. The corresponding electric field strengths are $\sim 30\text{ kV/cm}$, 60 kV/cm , 118 kV/cm and 236 kV/cm . Both the $\Delta\alpha$ - and Δn -spectra have

positive and negative regions which denote a possible red-shift and blue-shift operations, respectively. It is found that both spectra are flattened out for an electric field larger than 118 kV/cm (or 8 V) applied voltage due to high-field ionization and field-induced tunneling of the electron-hole pairs. For applied voltages falling between 0 V to 8 V, the device displays a regular and predictable response, i.e., the changes increase with external field.

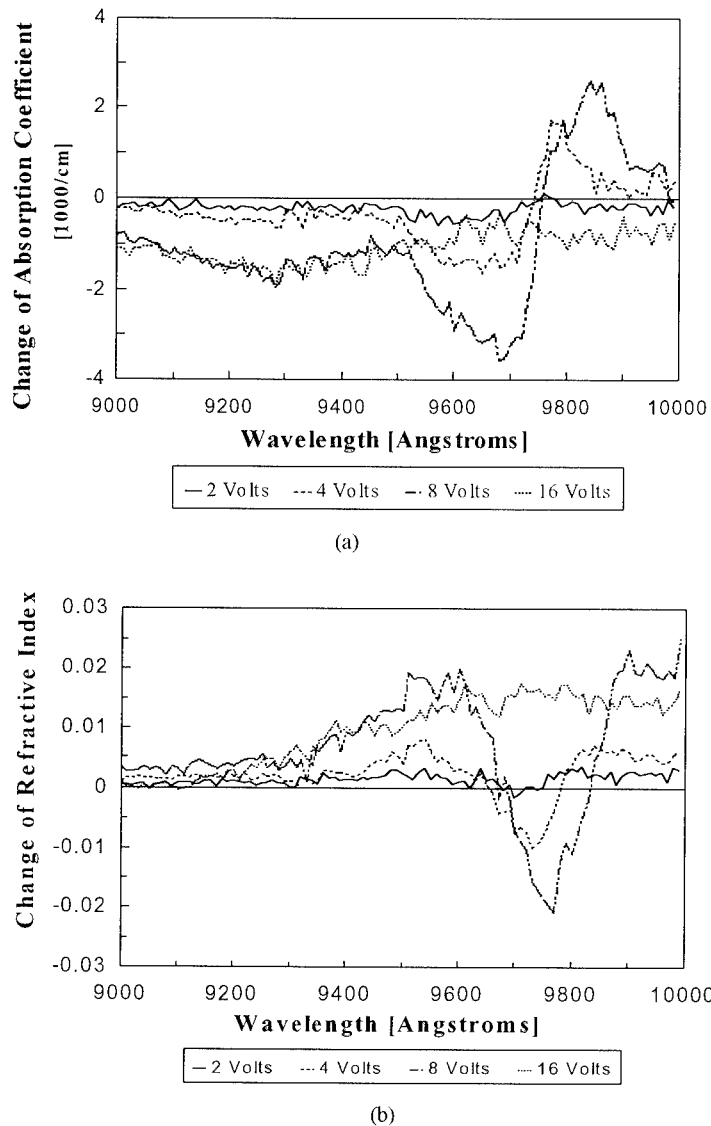


Figure 3. The field-induced changes of the optical constants ($\Delta\alpha$ and Δn) of the InGaAs/GaAs MQW measured by VASE. (a) $\Delta\alpha$ versus λ ; and (b) Δn versus λ .

The two maxima (at $\sim 3700 \text{ cm}^{-1}$ and 2800 cm^{-1}) of the $\Delta\alpha$ -spectra are at $\sim 970 \text{ nm}$ and $\sim 985 \text{ nm}$ when 8 V bias is applied. In this particular case, the peaks of index changes, which are ~ 0.02 , are located at $\sim 977 \text{ nm}$ and $\sim 990 \text{ nm}$ for the 8 volt bias. For electro-refractive operation, the choice of the operation wavelength is, therefore, to maximize the index change and minimize the absorption.

TUNABLE SYMMETRIC FABRY-PEROT MQW MODULATORS IN THE NEAR INFRARED REGIONS

Figure 4 shows a schematic configuration of the Fabry-Perot InGaAs/GaAs MQW optical modulator (sample MBE#1576). The modulator consists of a 50.5-period (51Å)-In_{0.18}Ga_{0.82}As/(333Å)-GaAs MQW cavity which is confined by two quarter-wave dielectric mirrors (DBRs) M1 and M2. The top dielectric mirror has 12-period of (697Å)-GaAs/(805Å)-AlAs in the form of [GaAs|AlAs|...|AlAs]. The bottom mirror consists of 15.5-period of (805Å)-AlAs/(697Å)-GaAs in the form of [AlAs|GaAs|...|AlAs]. The InGaAs/GaAs MQW cavity is modeled as a single layer with effective thickness 1953.3 nm and index $n=3.764$ as obtained from sample MBE1816. The modulator structure was fabricated on a $\sim 0.3 \mu\text{m}$ n+-GaAs buffer which was deposited on a S.I. GaAs substrate. In order to provide a uniform perpendicular electric field, a 100Å-gold thinfilm was evaporated on the surface of the modulator to supply the bias. The 100Å-gold thinfilm is near transparent in the NIR region. The n+ buffer layer is contacted by etching a via where an Au/Ge/Ni ohmic contact layer is deposited. An external voltage is applied across the n+GaAs buffer layer and the top Schottky barrier contact to supply the perpendicular electric field for the modulation of the device.

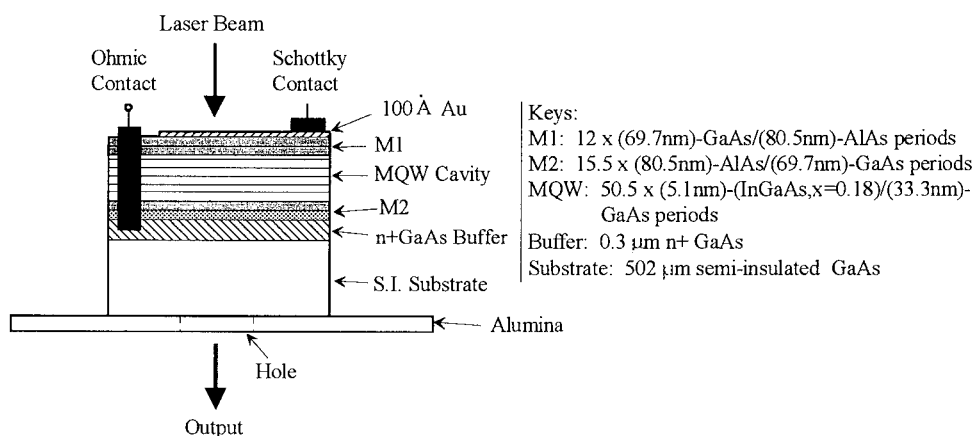


Figure 4. A schematic configuration of the Fabry-Perot MQW optical modulator.

Figure 5 (a) compares the transmission spectra of the Fabry-Perot modulator between the experimental and theoretical results. The mismatch of the Fabry-Perot mode is introduced by the additional 100Å gold layer which causes a fluctuation of the thickness in the structure. The on/off contrast ratio as a function of the bias voltage (ΔV) for the modulator MBE#1576 operated at 978 nm is shown in Figure 5 (b). A contrast ratio of 1200:1 had been observed for an applied voltage of ~ 25 volts. The measured insertion loss of the modulator at 974 nm is 12.5 dB while the measured FWHM is 8.7 Å compared to 7 Å calculated. There is a slight offset ~ 1.8 nm of the Fabry-Perot modes between the calculation and experiment results. The curve shows a gentle slope before 16 V and then displays a slightly drop of the contrast ratio MBE#1576 when ΔV approaching ~ 16 volts. This occurs when the exciton absorption peak of the InGaAs-GaAs MQW cavity is overlapping and passing the wavelength of operation at 978 nm. It is observed that the on-off contrast is enhanced by the Fabry-Perot structure due to its narrow FWHM and the

modal shift of the Fabry-Perot resonance. Although the imperfect surface of the layers, the optical constants, and the measurement error could contribute to the attenuation; the high insertion loss at the wavelength of operation is mainly caused by: (1) the absorption of the additional gold film, (2) the thickness fluctuations (include the effect of the gold film) of the effective mirrors that result a phase mismatch between the mirrors and the InGaAs/GaAs MQW cavity, and (3) the overlapping of the Fabry-Perot mode and the excitonic absorption peak. In order to achieve high contrast operation, it is advised that the wavelength of operation of the device is chosen close to and on the longer wavelength side of the excitonic resonance, most likely within the 3 dB of the excitonic resonance. By choosing the wavelength of operation further away from the excitonic peak could improve the insertion loss and yield better performance, since the modal shift is depend on Δn .

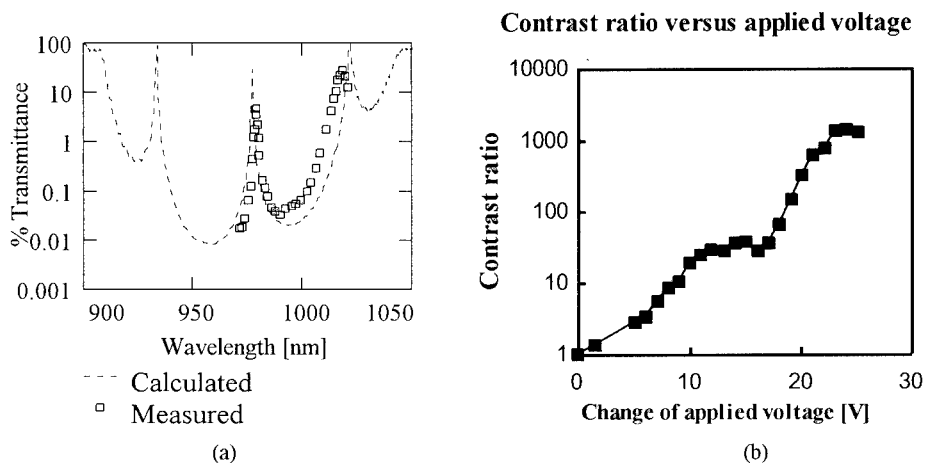


Figure 5. (a) The comparison of the transmission spectra for the tunable InGaAs/GaAs MQW Fabry-Perot optical modulator between the experimental and theoretical results. (b) The contrast ratio as a function of the change of applied voltage (ΔV) for the modulator MBE#1576 operated at 978 nm.

ZnSe-BASED MQW MODULATORS IN THE BLUE-GREEN REGIONS

The methodology developed for the InGaAs-GaAs SFPMs is used to design high contrast ZnCdSe-ZnSSe MQW optical modulators operated in the blue-green region. Computations on optical absorption and refractive index of $(80\text{\AA})\text{-Zn}_{0.8}\text{Cd}_{0.2}\text{Se}/(80\text{\AA})\text{-ZnS}_{0.06}\text{Se}_{0.94}$ quantum well were performed⁵ in order to study the performance of II-VI modulators. As the compressive strain in the ZnCdSe layer removes the band degeneracy of the heavy and light holes, it is observed that the absorption peaks of the heavy and light holes are well resolved. By incorporating the band to band transitions into the excitonic absorption, the changes of refractive index of the quantum well due to externally applied field exhibit negative values as shown in Figure 6. The magnitude of these changes are comparable to those in III-V materials. Figure 7 shows the transmittance of a ZnCdSe/ZnSSe MQW cavity structure consisting of ZnSe/ZnMgSSe DBR mirrors. For transmittivity $\geq 90\%$, the top and bottom p and q periods of the ZnSe/ZnMgSSe DBRs are related by: $p \approx q + 10$ using Equation (6). In this case, we choose the top and bottom DBR mirrors to be 32 periods and 40.5 periods of $(46.1\text{nm})\text{-ZnSe}/(48.3\text{nm})\text{-ZnMgSSe}$ layers, respectively. The MQW cavity has ~ 125 periods of $(80\text{\AA})\text{-ZnCdSe}/(80\text{\AA})\text{-ZnSSe}$.

The overall thickness of the device is $\sim 8.8 \mu\text{m}$. Assuming a ZnSe substrate, a contrast ratio of ~ 350 at 510 nm is obtained for a change of externally applied field of $\Delta E=120 \text{ kV/cm}$. The drawback of this modulator is that the field-induced shift of $\sim 3\text{-}3.5 \text{ nm}$ is relatively smaller than the InGaAs-GaAs MQW devices.

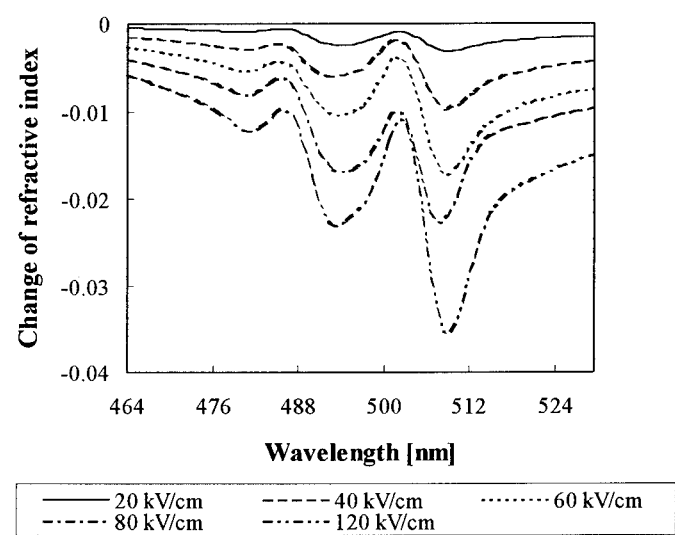


Fig. 6. The change of refractive index as a function of externally applied field of the (80Å)-Zn_{0.8}Cd_{0.2}Se/(80Å)-ZnS_{0.06}Se_{0.94} quantum well.

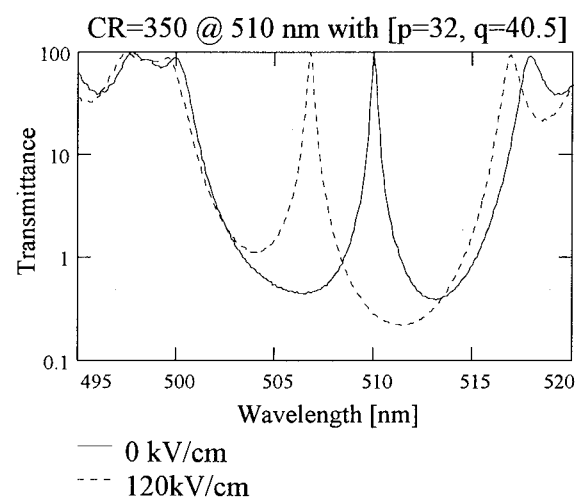


Fig. 7. The performance simulation of a ZnCdSe-ZnSSe QW modulator with a contrast ratio 350 operated at 510 nm.

CONCLUSIONS

We have presented the design methodology and experimental results on electrorefractive InGaAs/GaAs MQW symmetric Fabry-Perot modulators operated in the near infrared region (~ 980 nm). The optical parameters of the InGaAs/GaAs MQW are obtained using VASE technique in our design. The design technique has been extended to ZnCdSe/ZnSSe MQW modulators operated in the blue-green region. A contrast ratio of 350 at 510 nm is computed for a 125 periods MQW [(80Å)-ZnCdSe/(80Å)ZnSSe] Fabry-Perot modulator using 32 (top) periods and 40.5 periods (bottom) of (46.1nm)-ZnSe/(48.3nm)-ZnMgSSe DBRs. By adjusting the thickness of the DBRs and MQW layers, the modulators can be operated at different wavelength region.

It is observed that the contrast ratio of the ZnSe-based MQW modulators is relatively lower than that of the InGaAs/GaAs MQW devices. This is attributed to their smaller index difference between low-high index layers in the DBR mirrors. Therefore, a larger difference between the period for the top and bottom DBR mirrors is expected. In addition, the small modal shift due to externally applied fields indicates the need of thicker MQW cavity. As a result, II-VI devices are expected to be thicker compared to III-V devices in order to achieve the same magnitude of high contrast ratio.

ACKNOWLEDGMENTS

This work has been partly supported by the SDIO/ONR contract and the Connecticut Department of Economic Development and the National Science Foundation grants.

REFERENCES

1. D.A. B. Miller, D.S. Chemla, T.C. Damen, A.C. Gossars, W. Wiegmann, T.H. Wood, and C. A. Burrus, Electric field dependence of optical absorption near the band gap of quantum-well structures, *Phys. Rev. B* 32, 32, 1043:1060 (1985).
2. R. H. Yan, R. J. Simes, and L. A. Coldren, Analysis and design of surface-normal Fabry-Perot electrooptic modulators, *IEEE J. of Q.E.*, 25., 2272:2280 (1989).
3. R. Jin, G. Khitrova, H.M. Gibbs, C. Lowry, and N. Peyghambarian, *Appl. Phys. Lett.*, 59, 3216 (1991).
4. S. Cheung, F. Jain, R. Sacks, D. Cullen, G. Ball and T. Grudkowski, High contrast Fabry-Perot optical modulator using quantum confined Stark effect tuning in InGaAs-GaAs multiple quantum well cavity, *Appl. Phys. Lett.*, 63, 3, 296:298 (1993).
5. F. Jain, W. Huang, R. LaComb, C. Chung, G. Drake, "Optical modulators using quantum confined Stark effect in ZnSe based multiple quantum well structures, *J. of Crystal Growth*, 138, 709:713 (1994).
6. A. Thelen, "Design of Optical Interference Coatings," McGraw-Hill, NY (1989).
7. H.M. Liddell, "Computer-Aided Techniques for the Design of Multiplayer Filters", Adam Hilger Ltd., Bristol (1981).
8. J. Micallef, E.H. Li, and B.L. Weiss, Exciton optical absorption in disordered strained InGaAs/GaAs single quantum well, *Superlattices and Microstructures*, 13, no. 3, 315:322 (1993).
9. Y. Kan, H. Nagai, M. Yamanishi and I. Suemune, Field effects on the refractive index and absorption coefficient in AlGaAs quantum well structures and their feasibility for electrooptic device applications, *IEEE. J. of Q.E.*, 23, 2167:2180 (1987).
10. D.C. Hutchings, M. Sheik-Bahae, D.J. Hagan, and E.W. Van Stryland, Kramers-Kronig relations in nonlinear optics, *Opt. and Quant. Elect.*, 24, 1:30 (1990).
11. R.M.A. Azzam and N.M. Bashara, "Ellipsometry and Polarized Light", Elsevier Science Publishing Company, NY (1989).

OPTICAL PHASE MODULATION OF A QUANTUM WELL-DIELECTRIC SLAB WAVEGUIDE

H.L. Cui¹, C.D. Hechtman², E. Lenzing³, and B.S. Perlman³

¹*Department of Physics and Engineering Physics*

²*Department of Electrical Engineering and Computer Science
Stevens Institute of Technology, Hoboken, New Jersey 07030*

³*U.S. Army Research Laboratory, Fort Monmouth, New Jersey 07703*

INTRODUCTION

A new type of optical waveguide based on a planar dielectric slab with quantum wells containing mobile charge carriers on the boundaries of the slab is proposed and analyzed. It is shown that the effective index of refraction of the waveguide can be modulated by a large amount (20%) by simply charging or depleting the quantum wells of carriers in the case of a CoSi₂-Si metallic quantum well-heterostructure. We calculate the effective dielectric constant of such a structure, which consists of thin layers ($\sim 30\text{\AA}$) of CoSi with an extremely high carrier concentration ($\sim 4 \times 10^{22} \text{ cm}^{-3}$) on top and bottom of a Si substrate. We demonstrate that substantial modulation in the effective index of refraction can be achieved between the two limiting cases of carrier concentration in the quantum wells, namely, total depletion and almost metallic density. More importantly, we show that even a fractional change in the density of carriers in the quantum wells results in changes in the effective dielectric constant large enough phase shifting purposes. For example, our calculation indicates that a moderate increase in the carrier density, from $2 \times 10^{15} \text{ cm}^{-2}$ to $3 \times 10^{15} \text{ cm}^{-2}$, will result in about 20% increase in the effective index of refraction, making this structure potentially useful for modulating the phase of the guided waves. The required change in the surface charge density can be easily achieved with the application of a back-gate voltage, so that the effective Schottky barrier height is changed, leading to depletion of carriers.

BACKGROUND

The ability to vary the optical refractive index and/or the optical absorption coefficient of semiconductors is essential in integrated optoelectronics. The operation of

some of the most important components of integrated optics, such as phase shifters, frequency modulators and switches, requires controlled perturbation of the refractive index and/or the optical absorption coefficient. Such a perturbation is usually induced by electric fields or carrier injection, or a combination of both. Changes in the optical constants arise due to electric-field-related effects (electro-optical effects, birefringence, electroabsorption, Franz-Keldysh effect)¹⁻⁷, carrier-induced effects such as band-filling (Burstein-Moss effect)⁸⁻¹¹, band-gap renormalization/shrinkage¹², and free-carrier absorption (plasma effect)¹³, *etc.* In addition to these bulk effects, it is also possible to exploit boundary effects in modulating guided electromagnetic waves, as we will demonstrate in the present paper. We analyze here a new type of optical waveguide/phase shifter that employs quantum wells of tunable carrier density as the boundaries of a dielectric slab waveguide^{14,15}. We calculate the effective index of refraction of such a structure based on a CoSi₂-Si heterostructure, which consists of a thin layer of CoSi₂ with extremely high carrier concentration¹⁶⁻¹⁹, on top of a Si substrate.

FORMULATION

We consider a dielectric waveguide consisting of a slab of dielectric constant ε_2 , with planar boundaries that are quantum wells confining mobile charge carriers parallel to the $y-z$ plane, situated at $x = \pm d$. The space outside of the slab is assumed to have dielectric constant ε_1 . For simplicity we assume that the quantum wells are of infinite depth, and have negligible width. In the following we will examine the propagation characteristics of all the guided modes of such a guiding structure.

The electromagnetic fields of the guided wave will have the spatial-temporal dependence $\sim e^{i(\omega t - \beta z)}$, which, upon substitution into the Maxwell's equations, leads to, for transverse magnetic (TM) modes,

$$B_y = \frac{\omega \varepsilon_i}{\beta} E_x, \quad (1)$$

and

$$E_z = -\frac{i}{\omega \varepsilon_i} \frac{\partial B_y}{\partial x}, \quad (2)$$

with $i = 1, 2$. It is straightforward to obtain the guided-wave solutions for this structure. In the case of even TM modes one has $B_y(x) = B_y(-x)$, thus the fields inside the slab are

$$E_x = A e^{i(\omega t - \beta z)} \cos qx, \quad (3)$$

$$B_y = A \frac{\omega \varepsilon_2}{\beta} e^{i(\omega t - \beta z)} \cos qx, \quad (4)$$

$$E_z = A \frac{i q}{\beta} e^{i(\omega t - \beta z)} \sin qx, \quad (5)$$

and outside the slab they are

$$E_x = B e^{i(\omega t - \beta z) - p(x-d)}, \quad (6)$$

$$B_y = B \frac{\omega \varepsilon_1}{\beta} e^{i(\omega t - \beta z) - p(x-d)}, \quad (7)$$

$$E_z = B \frac{i p}{\beta} e^{i(\omega t - \beta z) - p(x-d)}. \quad (8)$$

The unknown amplitudes A and B can be eliminated employing the boundary conditions that at $x = d$

$$E_z(x = d+) - E_z(x = d-) = 0, \quad (9)$$

and

$$\varepsilon_1 E_x(x = d+) - \varepsilon_2 E_x(x = d-) = \rho_s. \quad (10)$$

The surface charge density $\rho_s = en_s$ (n_s is the surface density of carriers in the quantum well) is related to the surface polarizability χ through the relation

$$\rho_s = -\chi \nabla \cdot \mathbf{E}. \quad (11)$$

Combining the above equations one readily obtains

$$\left(\frac{\varepsilon_1}{p} - \chi \right) \tan qd = \frac{\varepsilon_2}{q}, \quad (12)$$

along with the dispersion relation (from the wave equation)

$$(pd)^2 + (qd)^2 = (\varepsilon_2 - \varepsilon_1)(k_0 d)^2, \quad (13)$$

where $k_0 = \omega/c$ is the wavenumber in free space. As usual, the propagation constant β is given by the relation

$$\beta^2 = \varepsilon_2 k_0^2 - q^2 = \varepsilon_1 k_0^2 - p^2, \quad (14)$$

which must be real for a propagating mode to exist.

For odd TM modes the analysis is essentially the same, except that the fields must satisfy the condition $B_y(x) = -B_y(-x)$, which leads to the dispersion relation

$$\left(\frac{\varepsilon_1}{p} - \chi \right) \cot qd = -\frac{\varepsilon_2}{q}. \quad (15)$$

In the cases of transverse electric (TE) modes, the surface charge enters the field equations through the boundary condition on the magnetic field, in the form of surface current density J_s , which is related to the charge density by the equation of continuity. Parallel to the discussion of TM modes, we obtain similar dispersion relations for the TE modes, which are also affected by the surface charges. For even TE modes, one has

$$q \tan qd - p = k_0^2 \chi, \quad (16)$$

and for odd TE modes, one has

$$-q \cot qd - p = k_0^2 \chi. \quad (17)$$

The dispersion relations obtained here reduce to the well-known expressions^{20,21} for a dielectric slab of dielectric constant ε_2 embedded in a medium of dielectric constant ε_1 , when the surface polarizability χ is set to zero. However, for a finite surface polarizability, as in the present case of a polarizable two-dimensional electron (or hole) gas confined in the quantum well at the surface of the slab, the mode dispersion relation will be different from that of a simple dielectric slab waveguide. Furthermore, the degree of this difference depends on the magnitude of the surface polarizability, which in turn depends on the density of carriers in the quantum well. This is to say that if one can effectively control the carrier density in the quantum well, the propagation characteristics of the guided wave can in turn be effectively controlled. We have numerically solved for the propagation characteristics for various carrier concentrations

in the quantum well to show how this modulation of propagation is manifested, and how much modulation is to be expected.

In our numerical calculation we employ the dynamic, nonlocal two-dimensional free carrier polarizability^{22,23} for carriers of mass m , charge e , and surface density n_s , at a temperature T ($\chi = \chi_1 + i\chi_2$)

$$\chi_1(k, \omega) = G \int_0^1 \frac{dx}{2(1-x)^{1/2}} \left(\frac{\eta_-}{\exp[\xi_F(\eta_-^2 x - \alpha)] + 1} + \frac{\eta_+}{\exp[\xi_F(\eta_+^2 x - \alpha)] + 1} \right), \quad (18)$$

$$\chi_2(k, \omega) = G \int_0^\infty \frac{dx}{2\sqrt{x}} \left(\frac{1}{\exp[\xi_F(x + \eta_-^2 - \alpha)] + 1} - \frac{1}{\exp[\xi_F(x + \eta_+^2 - \alpha)] + 1} \right), \quad (19)$$

where $G = 2mn_s e^2 / k_F k^3 \hbar^2$,

$$\eta_\pm = \frac{k}{2k_F} \pm \frac{m\omega}{\hbar k_F k},$$

$$\xi_F = E_F / k_B T,$$

and

$$\alpha = E_f / E_F.$$

E_f is the temperature-dependent Fermi energy, E_F is its value at $T = 0$ K. They are determined by electron surface density n_s :

$$E_f = k_B T \ln[\exp(E_F / k_B T) - 1],$$

$$E_F = \pi \hbar^2 n_s / m.$$

and $k_F = (2mE_F)^{1/2} / \hbar = (2\pi n_s)^{1/2}$ is the Fermi wavenumber. In our calculation we take $T = 300$ K. However, for the surface charge density pertaining to CoSi₂ films, we expect $E_F / k_B \sim 10^4$ K, so temperature effect is not significant.

RESULTS

Our numerical results are displayed in the figures, where the effective index of refraction of the guiding structure, defined as $n_{eff} = \beta / k_1$, with $k_1 = k_0 \sqrt{\epsilon_1}$, is shown as a function of the dimensionless quantity d/λ (λ is the wavelength) for various surface charge densities in the surface layer. Typical high quality CoSi₂ films have $n_s \sim 5 \times 10^{15} \text{ cm}^{-2}$, which leads to a drastic increase in n_{eff} in the frequency range investigated, as shown in the figures.

In Figure 1 the dependence of the effective index of refraction on the dimensionless inverse wavelength is exhibited, for various surface charge densities. The percentage increase in n_{eff} is shown in Figure 2, defined as $(n_{eff} - n_{eff}(\text{slab})) / n_{eff}(\text{slab})$, indicating that a moderate increase in n_s , say from $2 \times 10^{15} \text{ cm}^{-2}$ to $3 \times 10^{15} \text{ cm}^{-2}$, will result in about 20% increase in n_{eff} , making this structure an effective device for modulating the phase of the guided waves. We should point out that such a change in the surface charge density can be easily achieved with the application of a back-gate voltage, so that the effective Schottky barrier height²⁴⁻²⁸ is changed, leading to depletion of carriers. A simple estimate shows that in order to decrease the carrier density by about 20%, the depletion length should be a few Å, for a 30 Å-film of CoSi₂. For a typical Schottky barrier height of 0.6 eV, this requires an additional gate voltage of about a fraction of a volt. For a 20% reduction in carrier density, a 20% reduction in the effective index of refraction can be expected. With this modulation in n_{eff} , a phase shift of π can be

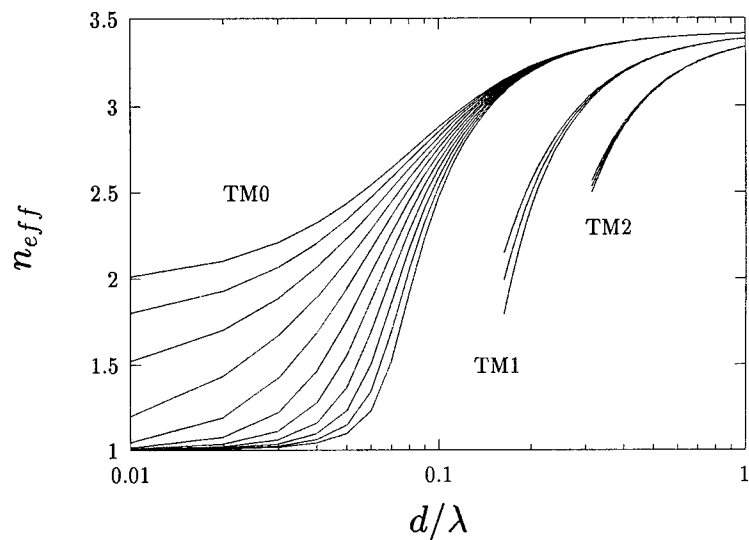


Figure 1 Effective index of refraction n_{eff} of a CoSi₂/Si slab dielectric waveguide, as a function of the dimensionless quantity d/λ , for various carrier densities in the CoSi₂ layer, for the first three TM modes. The curves correspond to (from bottom) $n_s = (0, 1, 2, 3, 4, 5, 6, 7, 8, 9, 10) \times 10^{15} \text{ cm}^{-2}$ for the TM0 mode and $n_s = (0, 5, 10) \times 10^{15} \text{ cm}^{-2}$ for TM1 and TM2 modes. Other parameters are $\varepsilon_1 = 1$, $\varepsilon_2 = 11.7$, $d = 1 \mu\text{m}$.

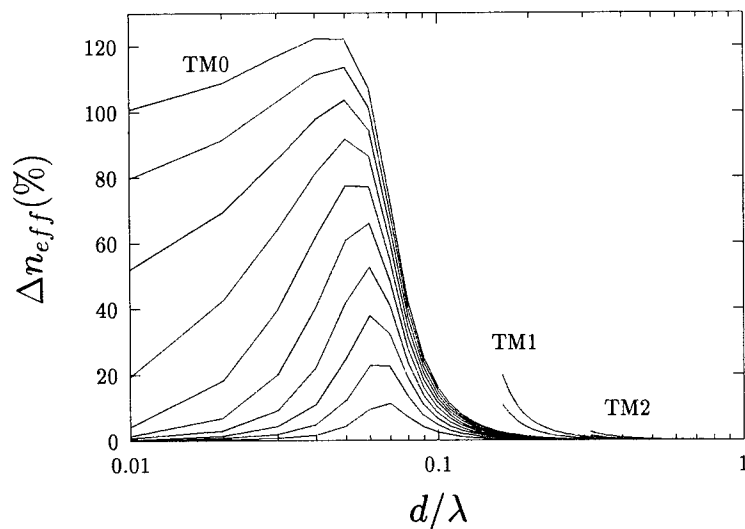


Figure 2 Percentage difference between the effective index of refraction n_{eff} of the CoSi₂/Si slab dielectric waveguide and that of a Si slab dielectric waveguide without the CoSi₂ layers on the boundaries ($n_s = 0$), for the first three TM modes. The curves correspond to (from bottom) carrier densities in the CoSi₂, $n_s = (1, 2, 3, 4, 5, 6, 7, 8, 9, 10) \times 10^{15} \text{ cm}^{-2}$ for the TM0 mode and $n_s = (5, 10) \times 10^{15} \text{ cm}^{-2}$ for TM1 and TM2 modes. Other parameters are the same as in Figure 1.

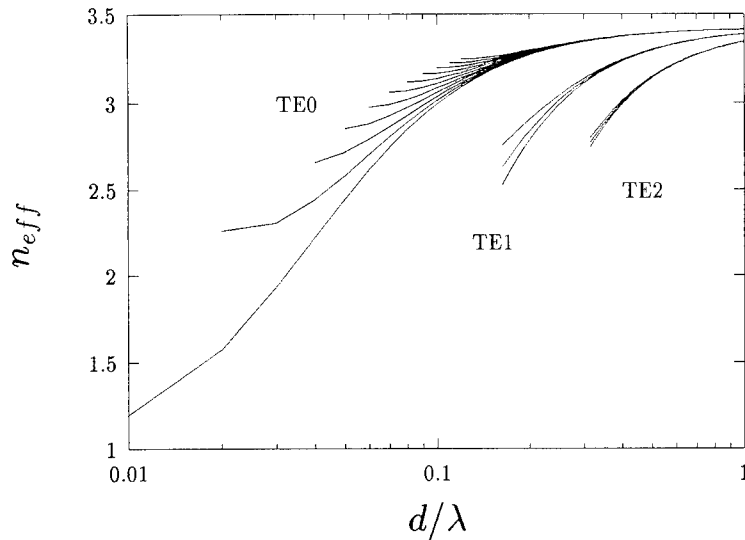


Figure 3 Effective index of refraction n_{eff} of a CoSi₂/Si slab dielectric waveguide, as a function of the dimensionless quantity d/λ , for various carrier densities in the CoSi₂ layer, for the first three TE modes. The curves correspond to (from bottom) $n_s = (0, 1, 2, 3, 4, 5, 6, 7, 8, 9, 10) \times 10^{15} \text{ cm}^{-2}$ for the TE0 mode and $n_s = (0, 5, 10) \times 10^{15} \text{ cm}^{-2}$ for TE1 and TE2 modes. Other parameters are $\varepsilon_1 = 1$, $\varepsilon_2 = 11.7$, $d = 1 \mu\text{m}$.

obtained for a structure of length less than ten times the wavelength of the guided wave. It is apparent from Figure 1 that this phase shifter will be most effective for wavelengths a few times the slab thickness. With a slab of $1 \mu\text{m}$ thick, the required structure length is $\sim 10 \mu\text{m}$, for a π phase shift to obtain. The TE modes are similarly subject to modulations of effective index of refraction. However, in addition to the change in the effective index brought about by the change of the surface charge density, the cutoff frequencies for TE modes are also affected. These are clearly evident in Figure 3.

SUMMARY

In conclusion, we have shown that the introduction of mobile charge carriers into a surface layer (in the form of quantum wells) of a dielectric slab waveguide can modify the boundary conditions of the guided waves, thus leading to modification of the effective index of refraction of the guiding structure. A concrete example is given in the case of a CoSi₂/Si waveguide, which we showed to be promising in realizing such a modulator structure.

REFERENCES

1. J.P. van der Ziel and A.C. Gossard, J. Appl. Phys. **49**, 2919 (1978).
2. D.A.B. Miller, J.S. Weiner and D.S. Chemla, IEEE J. Quan. Electron. **QE-22**, 1816 (1986).
3. F.R. Ore, and X. Chen, IEEE J. Quan. Electron. **QE-26**, 532 (1990).
4. J.S. Weiner, D.A.B. Miller, D.S. Chemla, T. Damen, C.A. Burrus, T.H. Wood, A.C. Gossard, and W. Wiegmann, Appl. Phys. Lett. **47**, 1148 (1985).

5. J.S. Weiner, D.S. Chemla, D.A.B. Miller, H.A. Haus, A.C. Gossard, W. Wiegmann, and C.A. Burrus, *Appl. Phys. Lett.* **47**, 664 (1985).
6. See for example, K. Seeger, *Semiconductor Physics*, (Springer, Berlin, 1982), pp.319-324.
7. S. Schmitt-Rink, D.A.B. Miller, and D.S. Chemla, *Phys. Rev.* **B35**, 8113 (1987).
8. E. Burstein, *Phys. Rev.* **93**, 632 (1954).
9. T.S. Moss, G.J. Burrell, and B. Ellis, *Semiconductor Opto-electronics*, (Wiley, New York, 1973).
10. F. Stern, *Phys. Rev.* **A133**, 1653 (1964).
11. P.A. Wolff, *Phys. Rev.* **126**, 405 (1962).
12. R.A. Abram, G.N. Childs, and P.A. Saunderson, *J. Phys. C: Solid State Phys.* **17**, 6105 (1984).
13. A.D. Yaskov, *Sov. Phys. -Semicond.* **17**, 937 (1983).
14. F. Huang, S. Cai, and Y. Zhu, *J. Phys. D: Appl. Phys.* **21**, 375 (1988).
15. H.L. Cui, C.D. Hechtman, and N.J.M. Horing, *J. Phys. D: Appl. Phys.* **26**, 1032 (1993).
16. M. Wölfel, M. Schulz, J. Ionally, and P.J. Grunthaner, *Applied Physics A* **50**, 177 (1990).
17. J.C. Hensel, R.T. Tung, J.M. Poate, and F.C. Unterwald, *Phys. Rev. Lett.* **54**, 1840 (1985).
18. J.M. Phillips, J.L. Batstone, J.C. Hensel, and M. Cerullo, *Appl. Phys. Lett.* **51**, 1895 (1987).
19. F. Nava, K.N. Tu, E. Mazzega, M. Michelini, and G. Queriolo, *J. Appl. Phys.* **61**, 1085 (1987).
20. J.F. Lotspeich, *Appl. Opt.* **14**, 327 (1975).
21. A. Yariv, *Optical Electronics*, (Holt, Rinehart and Winston, New York, 1985).
22. F. Stern, *Phys. Rev. Lett.* **18**, 546 (1967).
23. X.L. Lei, J.L. Birman, and C.S. Ting, *J. Appl. Phys.* **58**, 2270 (1985).
24. R.W. Fathauer, T.L. Lin, P.J. Grunthaner, P.O. Andersson, J.M. Iannelli, and D.N. Jamieson, *J. Appl. Phys.* **64**, 4082 (1988).
25. L. Magaud-Martinage, D. Mayou, A. Pasturel, and F. Cyrot-Lackmann, *Surf. Sci.* **256**, 379 (1991).
26. L. Haderbache, P. Wetzol, C. Pirri, J.C. Peruchetti, D. Bolmont, and G. Gewinner, *Thin Solid Films* **184**, 365 (1990).
27. J. L. Everaert, R.L. Van Meirhaeghe, W.H. Laflere, and F. Cardon, *Semicond. Sci. Technol.* **5**, 60 (1990).
28. G.J. van Gurp, *J. Appl. Phys.* **46**, 4308 (1975).

CHARACTERIZATION OF OPTICAL MODULATORS FOR APPLICATION IN LIGHTWAVE LINKS AT CERN

M. Glick,¹ F. Vasey,² G. Stefanini,² P. Duthie,³ N. Green,³
A. Moseley,³ D. Robbins,³ D. Streames-Smith,³ N. Try,³ R. Cingolani⁴,
and the RD23 collaboration

¹Institute for Micro and Optoelectronics, EPFL Lausanne (CH)

²CERN, Geneva (CH)

³GEC-Marconi (UK)

⁴MSDLE/University of Lecce (I)

Optoelectronic solutions are being investigated for analog signal transmission in experiments in the Large Hadron Collider (LHC) to be built at CERN.^{1,2,3,4} The goal of the RD-23 project is to develop modulator arrays to be mounted on silicon and microstrip gas chamber detector hybrid modules and the development of transceiver arrays (lasers couplers photodiodes) in hybrid or monolithic form to be mounted on readout modules at the back end of the link (Fig. 1). Other goals include identification and measurement of radiation hard fibers and multi-way optical connectors. Digital optical links are used for transferring timing and trigger signals. These links may use some of the components developed for analog transfer .

There are severe constraints on the devices to be put in the "front-end", the high radiation region which strongly influence the modulator and package design (Fig. 2). The requirements include low power dissipation (mW per channel), radiation hardness (10Mrad and a neutron fluence of 10^{14} n/cm² over 10 years), peak signal to noise greater than 100:1, low mass, and small size (footprint approximately 10 mm x 8 mm, with a height of about 6 mm). The bandwidth requirement is less than 100 MHz. The modulators must be optimized for operation in magnetic fields of 2 T or 4 T and still give usable response at zero field for testing purposes. Modulator specifications are also, in part, determined by the particular detector under consideration. Operation at liquid argon temperature (85 K) may also be required. The wavelengths of 1.3 μ m and 1.5 μ m are preferred for increased radiation resistance.

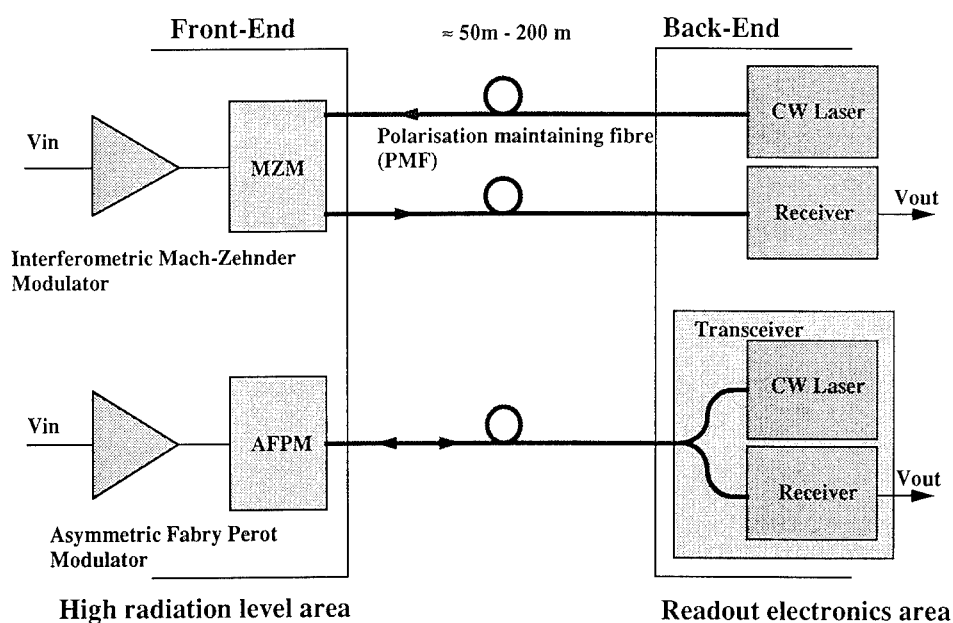


Fig. 1. Schematic of the lightwave link with both waveguide and reflective modulator alternatives.

The development of semiconductor modulators for LHC has focused on the InP based asymmetric Fabry-Perot (AFPM) vertical cavity device developed at GEC-Marconi Materials Technology, UK^{5,6} in conjunction with systems integrator GEC-Marconi Defense Systems. Mach-Zehnder interferometric modulators in lithium niobate, as developed in the first year of the program¹ achieve very good linearity and large dynamic range but also lead to major constraints. No scheme to perform polarization control at an affordable cost in such a large system has been found. In addition the on-chip splitting for multi-channel devices leads to a relatively large device length that is difficult to fit in the detector hybrids. It was concluded

that the Mach-Zehnder modulator on Ti:LiNbO is not a cost effective solution for volume application in LHC experiments. However, the 16-channel array developed in this

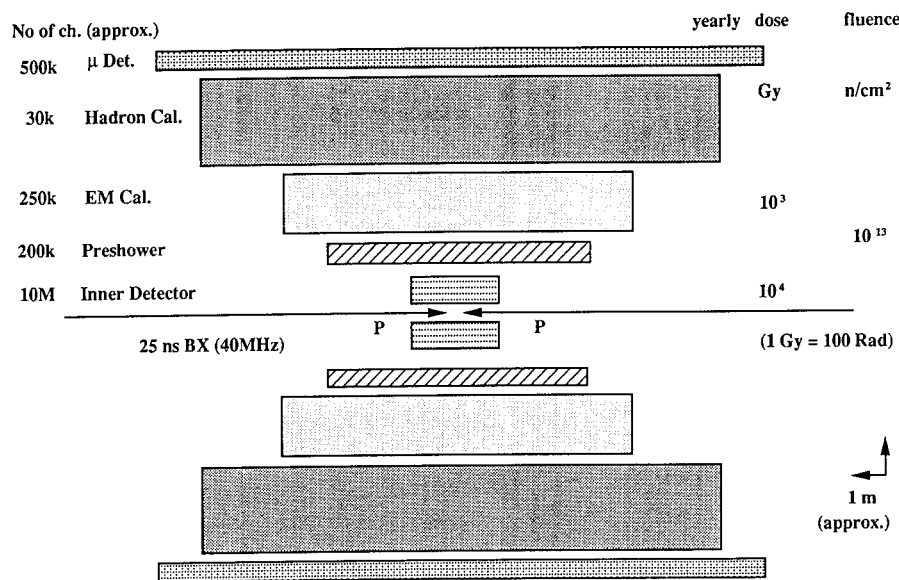


Fig. 2 Schematic of the Large Hadron Collider detector, indicating approximate number of channels and radiation levels for each separate detector

program has found application in the NA-52 experiment, where it will be used to transfer the analog signals from a set of Cherenkov counters at the target to the counting room over a distance of 350 m with a bandwidth of DC to 300MHz.

The AFPM modulator, although less linear and with a smaller dynamic range than the waveguide interferometric modulator, can meet the requirements necessary for the LHC application. The AFPM is polarization insensitive. It requires only one input/output fiber, as it is a device that works in reflection mode. It also allows the fabrication of very compact arrays and is much simpler to interface to optical fibers than waveguide devices.

The characteristics of the reflective AFPM modulators have been investigated on pigtailed arrays fabricated by GEC-Marconi Materials Technology (GMMT). The structures are based on a linear array of 8 channels with active multiquantum well areas of 30 μm diameter on 125 μm pitch. Since the pitch of the fibers is a ribbon is 250 μm every other element is used so that each packaged device contains four pigtailed channels. The first prototypes used a trial assembly technique in which the single mode fiber ribbon was interfaced to the modulators through the transparent substrate using relay microlenses. The typical transfer function of an AFPM is shown in Fig. 3. The laser power launched in the modulator pigtail is ≈ 65 μW at a wavelength of λ = 1538 nm. The central region of the

transfer function shows linear response with an integral non-linearity contained within $\approx 2\%$ of full scale for input signals in the range of ± 1.5 V relative to the half point bias. The full linear input range corresponds to a reflectance change of $\delta R \approx 10\%$.

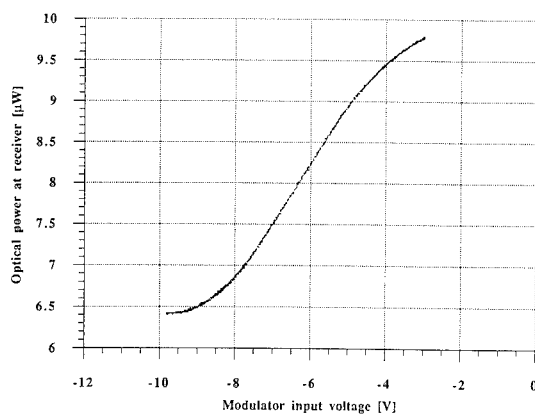


Fig. 3 Transfer function of the asymmetric Fabry Perot modulator

A novel assembly technique has recently been developed at GMMT, in which the fibers are butt-coupled to the modulators through the thinned substrate. This provides improved thermal stability, lower losses and cost-effective assembly suitable for volume production (Fig. 4).

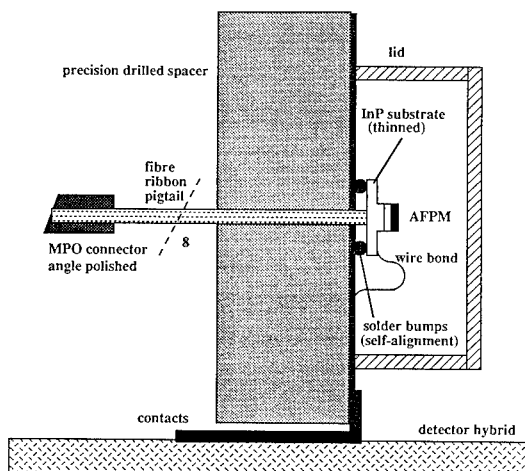


Fig. 4 Schematic of the butt coupled asymmetric Fabry-Perot modulator array

As mentioned above, the LHC modulators will be expected to perform in a particularly harsh environment and must be tested for their response in magnetic fields and under irradiation.

The particle tracking detector operates within a magnetic field to bend the particle tracks enabling their sign and momenta to be differentiated. The modulators must operate in relatively high magnetic fields (up to 4 T) and still give usable response at zero field for testing purposes. The direction of the magnetic field may be at an arbitrary orientation to the well growth direction. To confirm the small effect on the quantum wells expected by theory, several samples of varying well width (5 nm to 11.5 nm) have been measured in magnetic fields up to 8 T and 12 T. Measurements to 12 T were obtained at room temperature in a warm bore superconducting solenoid with the magnetic field B parallel to the well growth direction⁷. Measurements to 8 T at cryogenic temperatures were obtained with the magnetic field oriented both parallel and perpendicular to the growth direction⁸. The exciton shift with magnetic field should not depend on temperature. The results for the same sample for the magnetic field parallel to the well growth direction are in agreement within experimental error.

The results of the exciton shift for samples with well widths of 6.5 nm and 11.5 nm at 4 K for both magnetic field directions are shown in Fig.5. In both samples the diamagnetic exciton shift is larger when the field is parallel to the growth direction. This is consequence of the delocalization of the exciton wavefunction in the plane of the quantum well, where the cyclotron motion occurs. A smaller shift is expected for the field perpendicular to the growth direction, as the cyclotron motion occurs along the growth axis and the exciton wavefunction feels the lateral boundaries of the InP barriers. This enhanced localization results in the observed reduction of the diamagnetic shift. For an arbitrary field direction the shift of the exciton absorption peak should be along a linear extrapolation between the two field directions. The comparison of the two samples reveals that the total diamagnetic shift is larger in the wider well sample. This is again a consequence of the reduced localization of the exciton in the 11.5 nm well.

A well width of 6.5 nm is near optimal width for the device. At 4 T for the 6.5 nm quantum wells a shift of 2.6 meV was obtained at a temperature of 4 K. The shift measured for the field perpendicular to the growth direction is 0.2 meV. Exciton shifts of this order measured are not expected to significantly change the reflectivity properties of the devices, therefore, a special design is not necessary for the devices that will be subjected to the magnetic fields

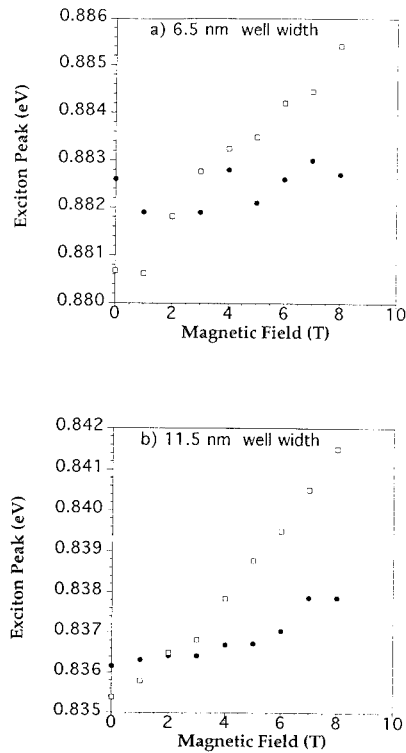


Fig. 5 The results of the exciton shift for samples with well widths of 6.5 nm and 11.5 nm at 4 K. The empty squares (□) represent measurements taken with the magnetic field oriented parallel to the well growth direction. The filled dots (●) are for the magnetic field perpendicular to the growth direction.

Modulator structures and optical fibers have been recently exposed to gamma irradiation in a ^{60}Co cell. The accumulated dose was 20Mrad with a dose rate of 205krad /hr. Reflectance spectra were measured before and after irradiation, while the leakage current was monitored throughout the irradiation and recovery periods.

Gamma irradiation does not induce any measurable effect in reflectance modulation. Leakage current (at a voltage bias of 7 V) increased to a saturation level of 100 nA in some devices, while it was not affected in others. Full recovery was observed in all cases. Previous measurements of neutron irradiation (fluence of 1.3×10^{14} neutrons/cm²) showed virtually no change in the modulator reflectance characteristics. The results obtained so far indicate that the AFPM structures are capable of withstanding the most severe radiation constraints at LHC without any significant degradation in optical and electrical performance.

Irradiation measurements will be extended to the new butt coupled devices, including the in situ monitoring of the optical properties during exposure.

Work is underway to optimize the cavity design and an integrated transceiver is being developed. Field tests in particle beams are planned. Low temperature studies of the AFPM modulators for application in the liquid argon detectors is being undertaken.

Lightwave analog links based on optical modulators can find high volume application at colliders for high energy physics experiments. The technologies developed in this context have potential for application in industry (process control in hostile environments) and other physics experiments. A Ti:LiNbO Mach-Zehnder modulator array developed for LHC has already found application in another experiment (NA-52), and the NESTOR deep water neutrino experiment is now investigating the use of optical modulators.

This work is part of the CERN DRDC project RD-23.

REFERENCES

- ¹Status Reports on the RD-23 Project "Optoelectronic analogue signal transfer for LHC detectors", CERN/DRDC 94-38, October 1994 and CERN/DRDC 93-35, August 13, 1993.
- ²C. Da Via, G. Stefanini, J. Dowell, I. Kenyon, M. Haben, K. Webster, M. Glick, F.K. Reinhart, G. Hall, T. Akesson, G. Jarlskog, S. Kröll, A. Baird, P. Sharp, J. Davies, N. Green, A. Moseley, W. Stewart, T. Young, "Lightwave analogue links for LHC detector front ends", Nucl. Instr. Meth A 344, 199-211 (1994).
- ³M. Glick et al, Conference on Lasers and Electro-Optics, Anaheim Ca. May 1994, CTuD3.
- ⁴C. DaVia et al, European Conference on Lasers and Electro-optics, Amsterdam, August 1994, CThH4
- ⁵C.J.G. Kirby, M.J. Goodwin, A.J. Moseley, D. J. Robbins, M.Q. Kearly, J. Thompson, "Low-voltage InGaAs/InP multiple quantum well reflective Fabry-Perot modulators for optical communications at microwave frequencies" IEE Proceedings 139,249, 1992.
- ⁶A.J. Moseley, M.Q.Kearly, M.J. Goodwin, D.J. Robbins, J. Thompson, A.K. Wood, C.J.Gorves-Kirkby, N.Carr, N. Maung and D. Clewitt, "8-channel InGaAs/InP quantum well asymmetric Fabry-Perot modulator hybridised with foundry VLSI silicon CMOS drive circuits", Elec. Lett. 28, 1658, (1992).
- ⁷M. S. Haben, "Applications of Optoelectronics in High Energy Physics", PhD Thesis, University of Birmingham, UK (1993).
- ⁸M. Glick, R. Cingolani, R. Rinaldi, D. Greco, P. V. Giungo, L. Calcagnile, P. Prete, "Summary of the results of magnetotransmission experiments performed on the InGaAs/InP MQW samples grown at GEC Marconi Material and Technology," internal report July, 1994.

Periodic Waveguide Structures - 101 Varieties!

by

R. C. Alferness
AT&T Bell Laboratories
Crawford Hill Laboratory
Holmdel, New Jersey 07733

Throughout the evolution of the field of integrated optics/photonic integration, periodic structures have played a key role. The early grating couplers, fine pitch Bragg gratings, acousto-optic and electro-optic phase-matched TE \leftrightarrow TM conversion, periodic domain reversal for efficient second harmonic generation, grating-assisted coupling in vertically stacked InP waveguides, periodic electrodes for velocity matched modulators.....the list goes on and on. As evident from this partial list, the impact of periodic structures extends over a wide range of device functions. While 101 may be an exaggeration, it is not too far off! In this talk we examine the enabling capabilities offered by periodic structures in integrated optics. We note the common features that characterize these devices in spite of their generally widely differing functions. While we include both back and forward coupled devices, because of time limitations, we focus on coarse period structures and deal mostly with couple mode devices - that brings the 101 number down to manageable levels! As a particular example, we conclude by reviewing our recent work on the vertical coupler filter and its application to widely tunable lasers and photonic circuits.

Conceptually, these devices are characterized by two waveguide modes, typically with different effective indices, that interact through a periodic coupling coefficient [1]. The modes can, for example, represent those of different waveguides or orthogonal polarizations in a single waveguide. The wavelength of maximum interaction is, of course, defined by the phase match condition (1)

$$\frac{N_1}{\lambda_0} - \frac{N_2}{\lambda_0 (+)} = \frac{1}{\Lambda} \quad (1)$$

where the $-(+)$ corresponds to forward coupling/coarse period (backward coupling/fine period) interactions. This phasematch condition results in a bandpass wavelength dependent coupling between modes. Examination of the phasematch condition gives the well known result that fine (Bragg) grating devices provide narrowband filters whose center wavelength is relatively insensitive to the waveguide indices while coarse grating devices are broadband, but quite tunable. For relatively weak coupling the filter response, coupling efficiency versus wavelength, is proportional to the Fourier Transform of the coupling coefficient along the propagation direction.

The wide variety of devices results from the number of ways the waveguide modes, their geometries, the coupling effect and the periodicity can be chosen. Material birefringence provides an excellent method of achieving two modes of different effective index in a same waveguide. By employing the electro-optic effect (e/o) an e/o mode converter results [2]; use an acousto-optic effect and you have an acousto-optic driven device. With a strongly birefringent material (so that $N_2 - N_1$ is large) like lithium niobate the response is highly wavelength dependent. Add polarization splitters and combiners and you have a tunable filter; add a diversity structure and you have a polarization independent tunable filter [3,4].

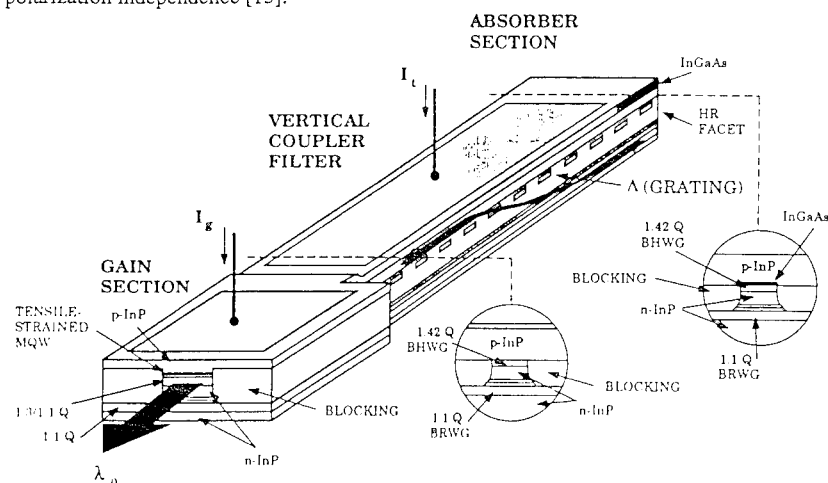
While we generally assume that polarization conversion (TE \leftrightarrow TM) in planar devices requires a non-diagonal electro-optic or acousto-optic coupling element, recently it has been achieved passively in InP - again with a periodic structure [5]. In this case a periodic laterally asymmetric waveguide induces slight rotation of the principle axis to passively provide the TE \leftrightarrow TM coupling. The weak birefringences result is a relatively broadband TE \leftrightarrow TM well suited for integrated coherent receivers.

The Fourier Transform relation between the filter response and the coupling coefficient provides important flexibility in shaping the response of this class of devices. Reducing sidelobes and

broadening the response by appropriately weighting the coupling coefficient or chirping the period are well known. Other examples include skipping sections of the grating. This can be done in tunable e/o filters to allow tuning electrodes access to the waveguide. The additional satellite filter bands introduced can be designed out of the wavelength range of interest [6]. Alternately, one can design the sampling, as demonstrated with Bragg gratings [7], to achieve a response of multiple, closely spaced filter bands, useful for broadly tunable DBR lasers.

In fact, periodic structures can be used to provide phase-matching between electrical and optical modes as implemented in phase-reversed traveling-wave optical modulators. The electrical frequency response of these devices mimic the wavelength response of their filter counterparts [8,9].

In wavelength drop/add devices for channel separation it is convenient to couple between spatially separate waveguide modes. Again both backward [10] and forward [11] coupling options have been demonstrated. Vertical stacking of non-identical waveguides in InP is particularly attractive because of the large index difference that can be achieved and the suitability for monolithic integration. The resulting grating-assisted vertical coupler filter is an attractive element for a variety of photonic circuits including a widely tunable laser [Fig. 1] which we describe [12]. As a tunable filter, the VCF is polarization dependent. However, once again the solution is to go periodic - in this case doubly periodic to achieve polarization independence [13].



REFERENCES

1. S. E. Miller, Bell Syst. Tech. J. **48**, 2189 (1969).
2. R. C. Alferness and L. L. Buhl, Opt. Lett. **5**, 473 (1980).
3. W. Warzanskyj, et al, Appl. Phys. Lett. **53**, 13 (1988).
4. D. A. Smith, et al, Appl. Phys. Lett., **56**, 209 (1990).
5. Shani, et al, Appl. Phys. Lett., **59**, 1278 (1991).
6. F. Heismann and R. C. Alferness, IEEE J. of Quant. Elect., **QE-24**, 83 (1987).
7. V. Jayaraman, et al, IEEE Photon. Tech. Lett., **5**, 489, (1993).
8. R. C. Alferness, et al, IEEE J. of Quant. Elect., **QE-20**, 301 (1984).
9. M. Nazarathy and D. Dolfi, IOOC'87, paper TUQ37, Reno, Nevada.
10. T. L. Koch, et al, IEEE J. of Quant. Elect., **QE-23**, 889 (1987).
11. R. C. Alferness, et al, Appl. Phys. Lett., **55**, 2011 (1989).
12. I. Kim, et al, Appl. Phys. Lett., **64**, 2764 (1994).
13. F. Heismann, et al, Appl. Phys. Lett., **64**, 2335 (1994).

WAVEGUIDE GRATING ROUTER COMPONENTS FOR WDM NETWORKS

Ivan P. Kaminow

AT&T Bell Laboratories
Crawford Hill Laboratory
Holmdel, NJ 07733-0400

I will describe several unique wavelength routing components, both passive and active, and their applications in WDM networks. These components are all based on a novel NxN optical multiplexer.

Dragone proposed the NxN optical multiplexer, based on a phased waveguide array, that is lossless in the ideal design limit. He demonstrated¹ an efficient silica-on-silicon multiplexer based on such a waveguide grating array accessed at input and output through two integrated star couplers². Independently, Smit proposed an optical phased array dispersive element, and demonstrated³ a 1xN demultiplexer. These multiplexers can also be regarded as wavelength or optical frequency routers. Passive silica waveguide grating routers (WGR) have applications in long haul, transparent and local access WDM networks.

A number of interesting wavelength multiplexing functions, such as multifrequency lasers, filters and receivers operating over a wide optical frequency band, can be realized by combining the passive router with active elements. The passive semiconductor WGR has been demonstrated by Zirngibl et al⁴. The active devices described in⁵ have recently been demonstrated experimentally by Zirngibl and Joyner^{6,7}.

The operation of the router is illustrated schematically in the figure. N input optical waveguides enter an MxM star coupler, where $M \geq N$, so that a fraction of the inputs may not be connected. The signal from any of the N input ports is distributed over the M outputs of the star to the array inputs. The array of M waveguides, whose lengths ℓ_i progressively decrease by a fixed amount $\ell = (\ell_i - \ell_{i+1})$, connects the input star to a similar output star. It is convenient to express ℓ in terms of the number q of guide wavelengths, λ/n , where n is the waveguide (group) index

$$\ell = q(\lambda/n) = q(c/fn) \quad (1)$$

and $\lambda = c/f$. If $\ell=0$, then, by symmetry, light of any optical frequency f entering the top input port (1) would exit at the conjugate (bottom) output port (N) of the router. However, if $\ell \neq 0$, the light will exit at a different port as determined by ℓ and f, due to the progressive phase delay $\phi = 2\pi f n \ell / c$ introduced by the waveguide array across the entrance to the output star. At frequencies for which ϕ is an integer times 2π , light entering any input port again appears at the conjugate output port.

The transmission function from a given input port to a given output port is illustrated in the figure. As f increases by $c/n\ell$, ϕ increases by 2π and the transmission function repeats with period or free spectral range

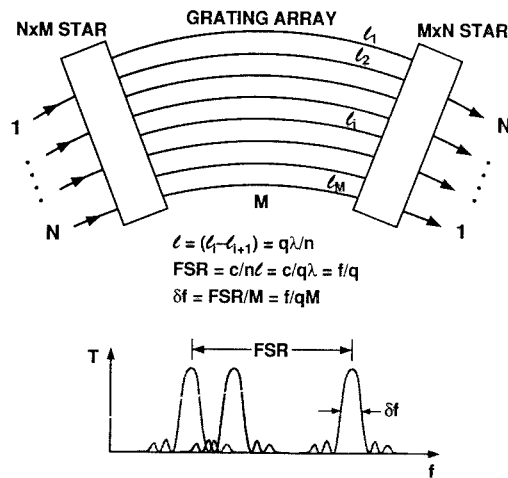


Figure 1. Operation of the router.

$$FSR = c/n\ell = f/q \quad (2a)$$

and the transmission peaks occur at

$$f = qc/n\ell, \quad q \text{ an integer.} \quad (2b)$$

At $\lambda = 1500\text{nm}$, $f=200\text{ THz}$. The design FSR, determined by the operating spectrum of the optical frequency-division multiplexed (OFDM) system, is typically $\sim 2\text{ THz}$, which may be the gain width of an amplifier or the tuning range of a semiconductor laser. Thus, the order q is approximately 100, which is difficult to achieve with conventional gratings.

The resolution of the device, which operates as a generalized Mach-Zehnder interferometer or, alternatively, as a generalized grating of order q , is determined by M

$$\delta f = FSR/M = f/qM, \quad (3)$$

where δf is the minimum resolvable separation between adjacent channel peaks within an FSR. Adjacent channels can be accessed by incrementing by unity one of the M inputs of the input star or one of the M outputs of the output star.

REFERENCES

- [1] C. Dragone, C. A. Edwards and R. C. Kistler, "Integrated optics NxN multiplexer on silicon", *IEEE Photonics Tech. Letters*, Vol. 3, No. 10, pp. 896-899, (October 1991).
- [2] C. Dragone, C. H. Henry, I. P. Kaminow and R. C. Kistler, "Efficient multichannel integrated optics star coupler on silicon", *IEEE Photonics Tech. Letters*, Vol. 1, No. 8, pp. 241-243, (August 1989).
- [3] A. R. Vellekoop and M. K. Smit, "Four-channel integrated-optic wavelength demultiplexer with weak polarization dependence", *Journal of Lightwave Technology*, Vol. 9, No. 3, pp. 310-314, (March 1991).
- [4] M. Zirngibl, C. H. Joyner, L. W. Stulz, Th. Gaiffe and C. Dragone, "Polarisation independent 8x8 waveguide grating multiplexer on InP", *Electronics Letters*, Vol. 29, No. 2, pp. 201-202, (January 1993).
- [5] B. Glance, I. P. Kaminow and R. W. Wilson, "Applications of the integrated waveguide grating router", *Journal of Lightwave Technology*, Vol. 12, No. 6, pp. 957-962 (June 1994).
- [6] M. Zirngibl and C. H. Joyner, "A 12-frequency WDM laser based on a transmissive waveguide grating router", *OFC '94*, PD16.
- [7] M. Zirngibl and C. H. Joyner, "A high performance, 12 wavelength optical multi-channel controller", *IPR '94*, PD2.

DISTRIBUTED FEEDBACK CHANNEL DROPPING FILTERS

Hermann A. Haus, Jay N. Damask, and Mohammad J. Khan

Department of Electrical Engineering
and Computer Science
Research Laboratory of Electronics
Massachusetts Institute of Technology
Cambridge, MA 02139

ABSTRACT

Passive, Quarter-Wave Shifted Distributed Feed-Back (QWS-DFB) resonators can act as transmission filters either singly, or in cascade. Equivalent circuits can be developed which predict the filter characteristics near the center of the stopband. The performance of recently fabricated filters is described.

QWS-DFB resonators side-coupled to a signal waveguide, can couple out one channel, without disturbing other channels within the bandgap of the DFB structure. Cascades of such filters have potential application to Wavelength Division Multiplexing (WDM). The theory of such structures, their equivalent circuits and predicted responses are presented.

Side-coupled active Gain Distributed Feedback resonators have desirable properties in that they enhance the responses at chosen resonances in comparison with the undesirable ones. They provide another means for channel dropping. Their performance is compared with that of QWS-DFB resonators.

1. INTRODUCTION

Distributed feedback was proposed by Kogelnik et al. in 1972^[1]. The first realization of such a structure was done with an interferometrically produced gain grating in a dye film^[2]. With advances in fabrication technology, index gratings can be etched. Distributed Feedback (DFB) laser diodes are now standard for communications applications.

A uniform DFB index grating structure exhibits transmission resonances on the two sides of the stopband. If used as the resonator structure for a diode laser, the lasing may occur in either one of the two resonances next to the stopband. The resonance frequency is selected by spurious reflections from the two ends of the structure and is thus difficult to control. From a given wafer, about half the laser diodes operate on one side of the stopband, the other half on the other side. If a quarter wave shift (QWS) is introduced at the middle of the grating, a high-Q resonance occurs at the center of

the stopband^[3]. If used as the laser diode resonator structure, the laser selects only this operating frequency, a distinct advantage. The central resonance of a quarter wave shifted DFB structure has the added advantage that the grating corrugation obeys the Bragg condition and is maximally reflecting. Cascades of QWS-DFB resonators can realize useful filter responses as first demonstrated with Surface Acoustic Wave Resonators^[4]. Recently, the fabrication technology has advanced sufficiently that such structures can be realized for optical filters.

A QWS-DFB resonator side-coupled to a "signal" waveguide can act as a channel dropping filter^[5]. At MIT we are pursuing the design and fabrication (in a silicon-nitride, silicon-dioxide, silicon material system) of passive filter structures of this type^[6,7].

Active or Gain DFB structures have been recently fabricated^[8]. They offer an alternate approach to channel dropping. Whereas reinjection of the signal into the bus by a receiver, using the QWS-DFB resonators, requires three resonant structures^[5], one of them active, channel dropping filters that use gain gratings can pick up a signal and reinject it using one simple uniform (unshifted) gain grating. Another interesting property of active resonators is that they provide much greater mode discrimination than passive structures. The mode discrimination can be used to suppress crosstalk.

2. THE REFLECTION FILTER AND THE QUARTER-WAVE SHIFTED RESONATOR

A cosinusoidal variation of the height of an optical waveguide of period Λ causes coupling of the forward to the backward wave, if Λ is close to half the wavelength of a waveguide mode. With reference planes at the maximum cross section of the cosinusoidally varying height of the guide, the equations of coupling between the forward and backward waves are^[9]

$$\frac{dA}{dz} = -j\delta A - j\kappa B \quad (2.1)$$

$$\frac{dB}{dz} = j\delta B + j\kappa A \quad (2.2)$$

where A is the envelope of the forward wave, B that of the backward wave, δ is the normalized frequency deviation from the Bragg frequency ω_0 ,

$$\delta \equiv \frac{\omega - \omega_0}{v_g} \quad (2.3)$$

with v_g the group velocity, ω_0 the frequency at which the waveguide wavelength is equal to 2Λ . The grating coupling strength is represented by κ which is real and positive when the reference planes are picked in the stated manner. An imaginary κ corresponds to a gain grating, namely a cosinusoidal variation of gain (negative gain is loss) along the waveguide.

The actual forward and backward waves a and b have the dependence

$$a(z, \omega) = A(z, \omega) e^{-j\frac{k_g}{2}z} \quad (2.4a)$$

$$b(z, \omega) = B(z, \omega) e^{j\frac{k_g}{2}z} \quad (2.4b)$$

When equations (2.1) and (2.2) are solved with a reflection coefficient Γ_0 assumed at $z = 0$, one finds:

$$\Gamma(z) = -\frac{1 + \Gamma_o[(\gamma/j\kappa) \coth \gamma z + (\delta/\kappa)]}{\Gamma_o - [(\gamma/j\kappa) \coth \gamma z - \delta/\kappa]} \quad (2.5)$$

With $\Gamma_o = 0$, the grating is matched at one end. The grating is reflecting in the stopband. In the passband, there are transmission resonances to either side of the stopband, the width of these resonances get wider and wider as one deviates in frequency to either side of the stopband.

A transmission resonance of a grating filter can be produced in the center of the stopband by introducing a quarter wave shift into the center of the grating. This is easily understood if one asks for the resonance in an infinite grating made up of two semi-infinite grating sections separated by a quarter wave shift. A wave $\exp -\kappa z$ in the right half of the grating has a reflection coefficient $\Gamma = -j$. The reflection coefficient of a wave $\exp +\kappa z$ in the left half of the grating is $\Gamma = j$. The quarter wave section matches these two reflection coefficients to each other. The reader will recognize the analogy of this resonance with a local electron energy state in a crystal due to a defect.

The external Q can be evaluated by simple perturbation theory^[9]. The external Q of the two ports, $i = 1, 2$, at distance ℓ from the center is

$$\frac{1}{Q_{ei}} = 2\kappa v_g e^{-2\kappa\ell} \quad (2.6)$$

If one constructs an equivalent L, C circuit for the resonator, the external Q 's of the equivalent circuit are given by

$$\frac{1}{Q_{ei}} = \frac{Y_o}{\omega_o C} \quad (2.7)$$

where Y_o is the characteristic admittance of the transmission line. The transmission

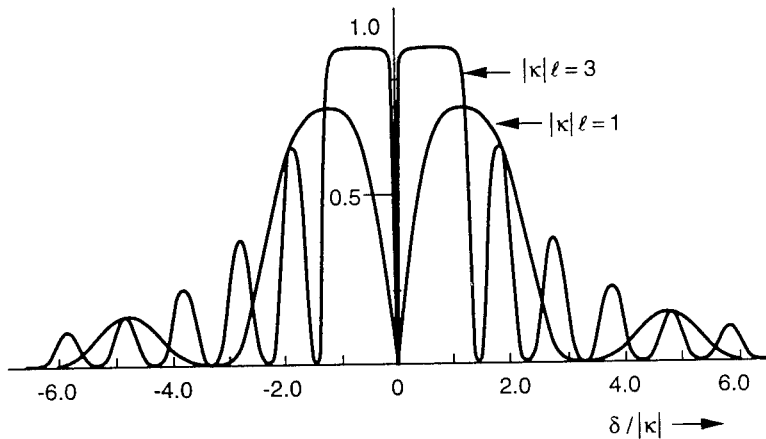


Figure 1. Transmission of quarter-wave shifted DFB structure.

characteristic of the quarter wave shifted resonator is as shown in Fig. 1 for varying values of $\kappa\ell$. The center resonance is Lorentzian, and its width is accurately predicted by the external Q computed above for $\kappa\ell > 1$. The structure is reflecting over the remainder of the stopband, gradually providing less and less reflection with increasing deviation from the stopband. There are other low Q resonances outside the stopband.

In collaboration with Prof. H. Smith's group at MIT, DFB transmission filters

have been fabricated in silica using Spatial-Phase-Locked E-Beam Lithography^[6]. Figure 2 shows the experimentally realized and theoretically predicted transmission characteristic of a QWS - DFB resonator. The resonator is constructed by stitching together 9 EBL fields to a precision of ≤ 10 nm. There are 128 grating corrugations per field, and the grating period is 513 nm. The grating strength, κ , is 73 cm^{-1} . The waveguide loss and loss due to the presence of the grating are estimated to be $0.53 \pm 0.05 \text{ dB/cm}$ and $< 1 \text{ dB/cm}$, respectively. The linewidth of the resonator is limited by the 0.1 nm resolution of the spectrometer. The plot on the left superimposes the measured data with a coupled-modes calculation of the resonator where the Fabry-Perot resonances have been included. Since the agreement is so good, the measured data was then filtered on a computer to give an indication of the resonance response for AR coated facets.

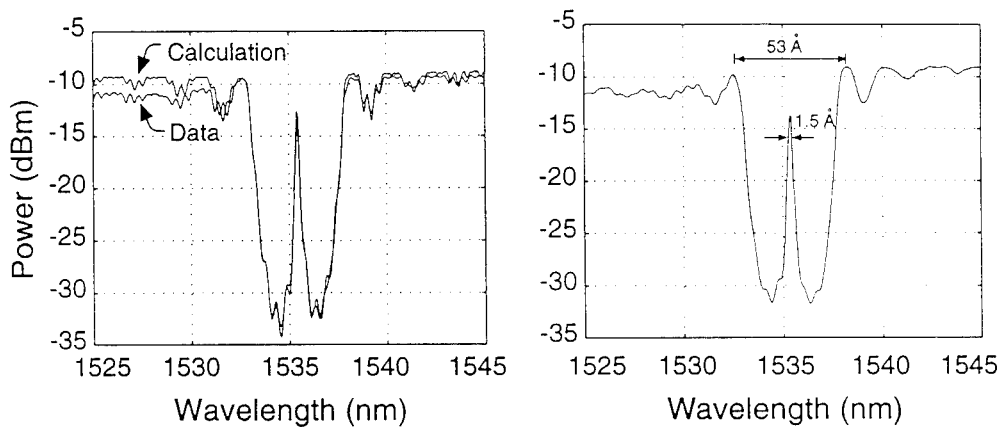


Figure 2. (Left) Overlay of experimental transmission spectrum of a quarter-wave shifted resonator along with a coupled-modes calculation (including facet effects) of the response. The measured linewidth is limited by the 0.1 nm resolution of the spectrometer. (Right) A replot of the measured data from the left figure where the Fabry-Perot fringes are digitally filtered out. This spectrum gives an indication of the spectral response when the facets are AR coated.

The experimental sensitivity is limited to -30 dB by the “white light” background of the broadband source. Otherwise, the agreement is excellent.

3. SIDE-COUPLED QUARTER WAVE SHIFTED RESONATORS

When a QWS-DFB resonator is coupled through its evanescent fields to an adjacent waveguide, power incident in the waveguide within the transmission peak of the resonator is transferred from the waveguide to the resonator. Within the remainder of the stopband of the grating, the effect of the resonator on the waveguide can be kept small. Thus, a cascade of such resonators tuned to different frequencies can serve as taps for different frequency channels of signals propagating in the waveguide.

We now turn to the analysis of such structures. In addition to the DFB equations for the resonator grating waveguide α , there are propagation equations for the side-coupled waveguide β . In order to take advantage of the symmetry of the structure, we assume that the quarter-wave gap is placed so that the central reference plane falls into nodes of the sinusoidal grating corrugation as shown in Fig. 3. If we take the reference planes at integer multiples of Bragg wavelength away from the center, the coupling coefficient κ is referred to new reference planes calling for a multiplier j .

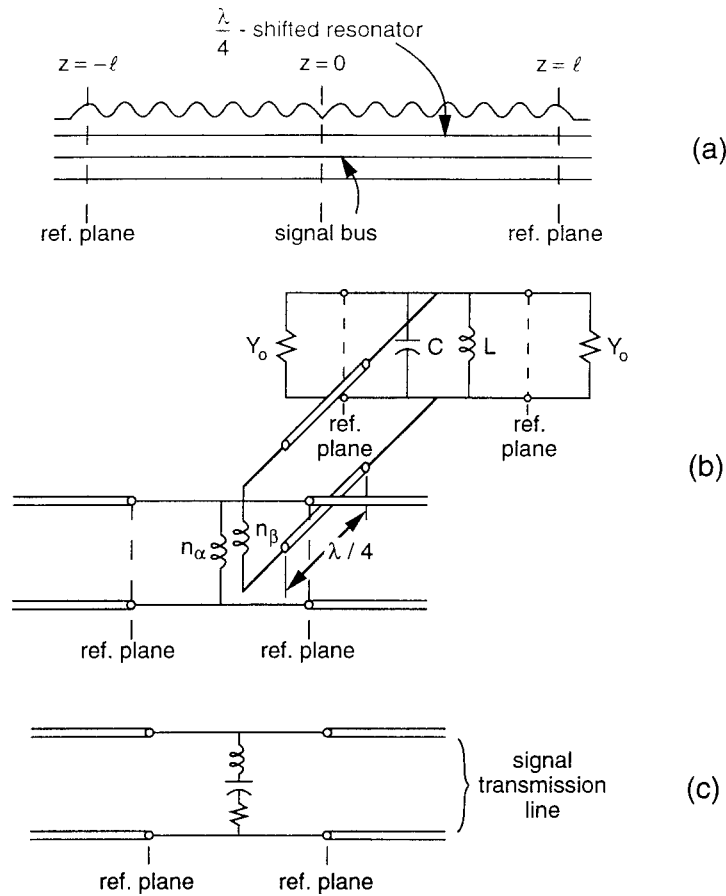


Figure 3. (a) The choice of reference plane for side-coupled, quarter wave shifted distributed feedback resonator. (b) and (c): Equivalent Circuit for side-coupled resonator.

Thus, the equations become:

$$\frac{dA_\alpha}{dz} = -j\delta A_\alpha - \kappa B_\alpha - j\mu A_\beta \quad (3.1)$$

$$\frac{dB_\alpha}{dz} = j\delta B_\alpha - \kappa A_\alpha + j\mu B_\beta \quad (3.2)$$

$$\frac{dA_\beta}{dz} = -j\delta A_\beta - j\mu A_\alpha \quad (3.3)$$

$$\frac{dB_\beta}{dz} = j\delta B_\beta + j\mu B_\alpha \quad (3.4)$$

Generally, μ must be much smaller than κ if the Q of the structure is to be high, so that an expansion of the solutions in orders μ/κ can be meaningful. To zeroth order the resonator is uncoupled, and, at the center of the band ($\delta = 0$), its field is of the form $A_0 \exp(\pm \kappa z)$ decaying away from the central reference plane.

To develop an equivalent circuit that contains electrical elements one must define equivalent voltages and currents. This is done in analogy with Transmission Line theory by defining the "voltage"

$$V = A + B \quad (3.5)$$

and the "current" I

$$I = Y_o(A - B) \quad (3.6)$$

V is the normalized electric field and I is the normalized magnetic field and Y_o is a normalizing admittance.

At the center of the band ($\delta = 0$), with (3.1)-(3.4) rewritten in terms of the equivalent voltages and currents

$$\frac{d}{dz}V_\alpha - \kappa V_\alpha = -j\mu Z_o I_\beta \quad (3.7)$$

$$\frac{d}{dz}Z_o I_\alpha + \kappa V_\alpha = -j\mu V_\beta \quad (3.8)$$

$$\frac{d}{dz}V_\beta = -j\mu Z_o I_\alpha \quad (3.9)$$

$$\frac{d}{dz}Z_o I_\beta = -j\mu V_\alpha \quad (3.10)$$

The equations are pairwise decoupled. The resonator solution has $I_\alpha = 0$ and thus (3.7) and (3.10) can be solved independently. Even here, perturbation theory is helpful since it gives physical insight into the physical processes. The structure is symmetric. When the resonator is terminated symmetrically, symmetric and antisymmetric excitations in the sidecoupled waveguide give all the necessary information. Suppose we start with the resonance in a long ($\kappa\ell \gg 1$) almost closed QWS-DFB structure and couple its field to the sidecoupled waveguide. The "voltage" distribution V_α in the resonator is symmetric. The field being symmetric, it leads to a symmetric "voltage" at symmetric reference planes at $z = \pm\ell$ in the waveguide. From (3.10) we see that a symmetric V_α leads to an antisymmetric I_β . Since V corresponds to the electric field, I to the magnetic field, we find that the magnetic field in the waveguide is antisymmetric for a symmetric electric field distribution, as it should be. Since $V_\beta = 0$, the electric field in the waveguide is zero at the reference plane. A perfect standing wave exists in the waveguide with its H -field maxima at the reference planes.

A symmetric excitation of V_β does not couple to the resonant mode. The field in the waveguide is essentially unperturbed by the presence of the resonator.

The symmetric and antisymmetric solutions in the waveguide can be used to construct new solutions. In particular, we are interested in the case when the waveguide is terminated in a match on the right hand side. We add the symmetric and antisymmetric solutions to obtain a pure traveling wave on the right hand side, and find that the traveling wave is zero at $z = \ell$, and a perfect standing wave exists at $z = -\ell$. The structure is perfectly reflecting with no throughput. The equivalent circuit must be a resonant circuit coupled via a transformer into the "signal" waveguide as shown in Fig. 3. The resonator presents an open-circuit across its terminals.

Since it appears as a short across the signal transmission line, there is a quarter wave section of transmission line inserted as shown. The product LC is clearly equal to the inverse square of the resonance frequency, $1/\omega_o^2$. The transformer ratio can be evaluated by perturbation theory. If we start with the resonant field in the resonator and ask for the power escaping from the resonator into the signal waveguide for a given peak amplitude A_o in the resonator, we may use (3.3) to find A_β and thus the signal amplitude escaping into the waveguide:

$$A_\beta = -2j\frac{\mu}{\kappa}A_o \quad (3.11)$$

From (3.4) we find that B_β is of the same magnitude. The power escaping from the

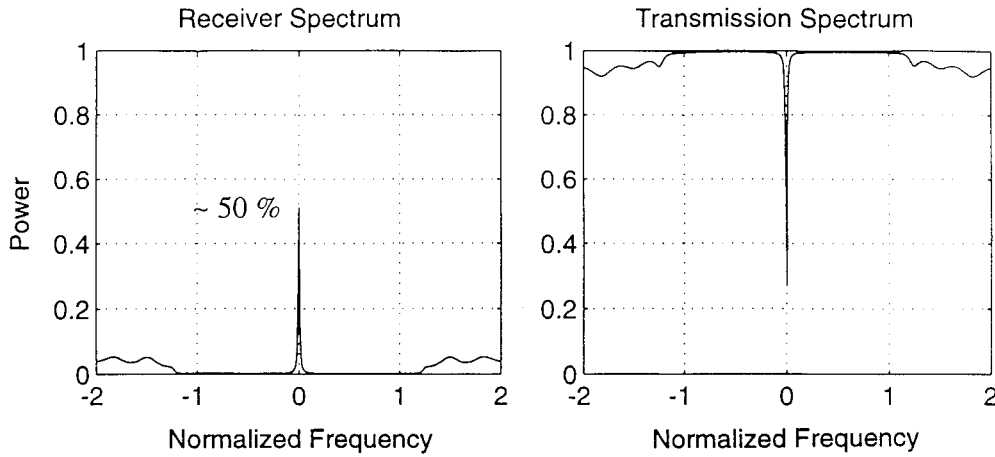


Figure 4. Power transfer and transmission spectra of a channel-dropping filter constructed with a single resonator.

resonator into the right hand waveguide is:

$$P_e = 4 \left| \frac{\mu}{\kappa} \right|^2 |A_o|^2 \quad (3.12)$$

The peak voltage in the equivalent circuit is set $V_o = 2A_o$. Then, equating the energy storage in the equivalent circuit to that in the resonator, we find for C :

$$C = \frac{1}{2\kappa v_g} Y_o \quad (3.13)$$

The power into the two sides of the waveguide from the equivalent circuit is

$$P_e = 2 \left| \frac{n_\alpha}{n_\beta} \right|^2 \left| \frac{V_o}{2} \right|^2 Y_o \quad (3.14)$$

In this way one finds the transformer ratio

$$\left| \frac{n_\alpha}{n_\beta} \right|^2 = 4 \frac{\mu^2}{\kappa^2} \quad (3.15)$$

If the resonator is coupled to one or two loads, one may evaluate the escaping power analogously. Such loads appear as additional conductances in parallel in the equivalent circuit of Fig. 3b. If the load is adjusted to maximize the power delivered to it, one finds from the equivalent circuit that, under this condition, one half of the incident power is delivered to the load, one quarter is transmitted and one quarter is reflected. In this way, we have developed the equivalent circuit for the central resonance of a sidecoupled resonator. Figure 4 shows the transmission, reflection, and coupled power computed from the full coupled mode equations (3.1)-(3.4). One sees the prediction of the maximum power delivery confirmed. One also sees that the transmitted power is unaffected off resonance and within the stopband of the grating.

If one wants to deliver all of the incident power to the resonator load, one requires a second resonator placed so that it presents an open circuit at the reference plane of the first resonator. When this is done, the responses are as shown in Fig. 5.

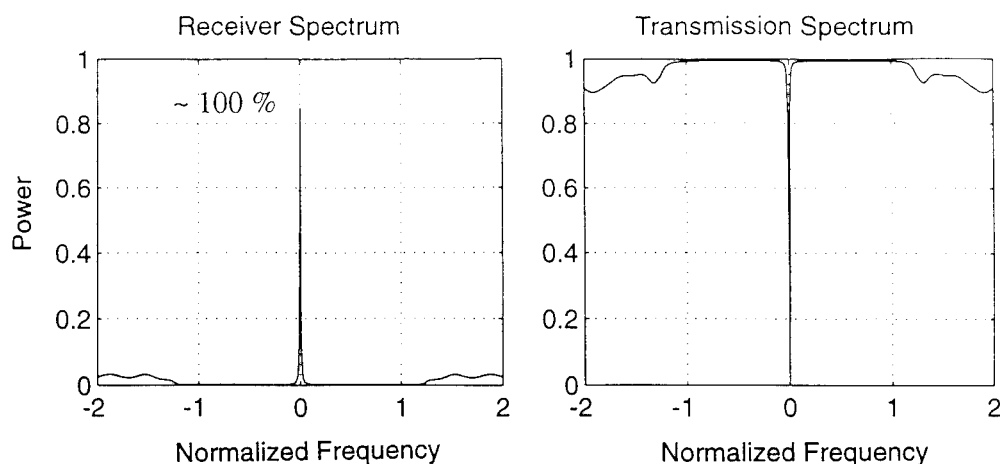


Figure 5. Power transfer and transmission spectra of a channel-dropping filter constructed with two resonators. The peak power transfer is not 100% because energy escapes from the two ends of the second side-coupled resonator

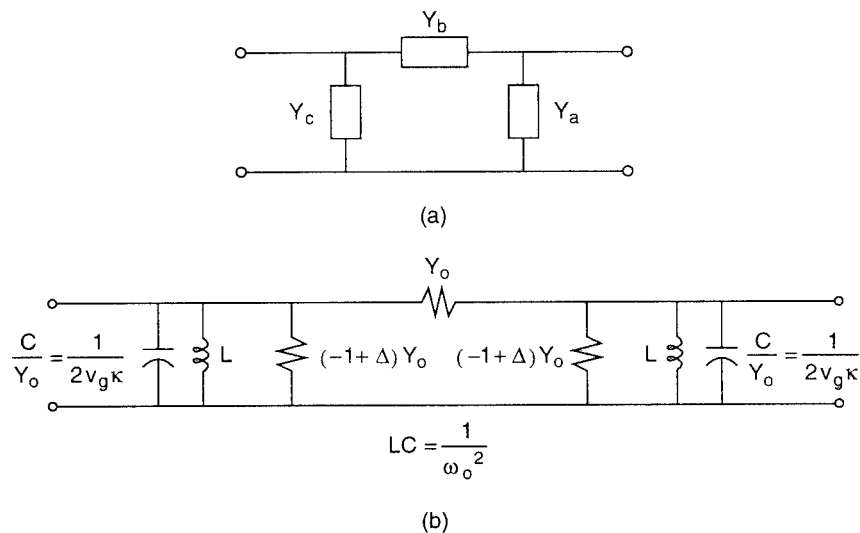


Figure 6. Equivalent circuit for uniform gain grating structure.

4. THE GAIN DISTRIBUTED FEEDBACK RESONATOR

Next we study the gain distributed feedback resonator. As mentioned earlier, the coupling coefficient is now pure real when referred to the peak of the gain "corrugation." The equations for the amplitudes A and B in the structure are:

$$\frac{dA}{dz} = -j\delta A + \kappa B \quad (4.1)$$

and

$$\frac{dB}{dz} = j\delta B - \kappa A \quad (4.2)$$

If the reflection coefficient at $z = 0$ is Γ_0 , the reflection coefficient at z can be

evaluated as before:

$$\Gamma(z) = \frac{(1 - \frac{\beta-\delta}{j\kappa}\Gamma_o)e^{-j\beta z} - (1 + \frac{\beta+\delta}{j\kappa}\Gamma_o)e^{j\beta z}}{(-\frac{\beta+\delta}{j\kappa} - \Gamma_o)e^{-j\beta z} - (\frac{\beta-\delta}{j\kappa} - \Gamma_o)e^{j\beta z}} \quad (4.3)$$

In particular, for $\Gamma_o = 0$, one finds that $\Gamma = \infty$ when $\beta\ell = -\pi/2$. The structure is an oscillator at the threshold of oscillation.

The frequency of the oscillation can be moved by changing the reflection coefficient at the right end of the structure. When the value of $\Gamma_o \neq 0$ is presented to the right hand side of the structure by an appropriate device, the structure oscillates for $\beta\ell = \pi/2$. The "frequency" of oscillation δ_o is

$$\delta_o = -j\kappa\Gamma_o \quad (4.3)$$

As $|\delta|$ increases from zero, and $\beta\ell$ is kept fixed at $\pi/2$, smaller and smaller values of κ are needed to maintain oscillation threshold. If the gain is through carrier injection, the current supply to the grating can be decreased.

How can this occur, since the grating becomes detuned when $\delta_o \neq 0$ and thus the grating effectiveness decreases? The answer lies in the nature of the gain of a GDFB structure. A pure traveling wave does not experience gain, since a GDFB grating alternates gain with loss and a traveling wave averages the two. A standing wave of proper spatial phase, with intensity maxima at the gain portions of the grating, and intensity minima at the loss portions, experiences net gain. The structure with $\kappa\ell = \pi/2$, matched at its two ends, oscillates with net gain by virtue of the standing wave pattern that forms at and near the center of the structure. At either end the net gain goes to zero. When a reflection is introduced near one of the ends of the structure, a standing wave pattern extends over a greater portion of the grating and thus the net gain goes up, allowing the frequency to shift, inspite of the fact that the effectiveness (phase matching) of the grating is decreased.

For the development of the equivalent circuit, we use again equivalent voltages and currents as in (3.7)-(3.10). Since we consider only symmetric structures, we can again look at symmetric and antisymmetric excitations of the structure and develop from these equations expressions for the equivalent circuit of a symmetric twoport.

For the case when $\beta\ell = \frac{\pi}{2} - \Delta$, with Δ small, i.e. the resonator close to threshold and small frequency deviations $\delta/\kappa \ll 1$, one finds for Y_a and Y_b of Fig. 6a^[10]:

$$Y_a \approx -(1 - \Delta)(1 - j\frac{\delta}{\kappa})Y_o \quad (4.8)$$

$$Y_b \approx (1 - \frac{j\delta}{\kappa})Y_o \quad (4.9)$$

Y_b has a positive conductance. These findings are very suggestive. A symmetric excitation puts the standing wave maxima of the electric field at the positions of the gain segments. Hence, a symmetric excitation uncovers a negative conductance $G = -(1 - \Delta)Y_o$. Conversely, an antisymmetric excitation displaces the standing wave of the electric field so that its maxima fall on the loss segments of the structure, the conductance accessed by this excitation is positive. The imaginary parts of the admittances are responsible for the bandwidth limiting. We recognize that the admittance of a parallel GLC circuit near resonance is, approximately

$$Y = G + 2j\Delta\omega C \quad (4.10)$$

with $G = -(1 - \Delta)Y_o$ and

$$C = \frac{1}{2v_g\kappa} Y_o$$

The complete equivalent circuit is shown in Fig. 6b. The contribution $-j\delta/\kappa$ to Y_b is ignored since $|\delta/\kappa| \ll 1$.

5. THE SIDE-COUPLED GAIN DISTRIBUTED FEEDBACK RESONATOR

The equations of coupling to the waveguide are

$$\frac{dA_\alpha}{dz} = -j\delta A_\alpha + \kappa B_\alpha - j\mu A_\beta \quad (5.1)$$

$$\frac{dB_\alpha}{dz} = j\delta B_\alpha - \kappa A_\alpha + j\mu B_\beta \quad (5.2)$$

$$\frac{dA_\beta}{dz} = -j\delta A_\beta - j\mu A_\alpha \quad (5.3)$$

$$\frac{dB_\beta}{dz} = j\delta B_\beta + j\mu B_\alpha \quad (5.4)$$

The reference planes are moved back to the maxima of the corrugation. In this manner, one may again slice the structure with a symmetry plane at the center (there is no quarter wave shift!) and solve for symmetric and antisymmetric solutions. A symmetric excitation in the resonator (i.e. the resonance, or laser operation at threshold) couples to a symmetric voltage-, antisymmetric current-excitation in the waveguide. An antisymmetric voltage-excitation in the waveguide couples negligibly to the resonator to first order in μ/κ . We find entirely analogously to Section 3 that for $\kappa\ell = \pi/2$ the structure acts as a short at the center frequency, $\delta = 0$. Hence, we conclude that the equivalent circuit must be as shown in Fig. 7, where we have omitted the component in the resonator equivalent circuit excited only by antisymmetric excitations (that are too weak when attempted from the signal waveguide) and where we still allow for slight deviations from $\kappa\ell = \pi/2$. The transformer ratio is evaluated as before by assuming an excitation in the resonator and evaluating the power escaping in the two directions into the waveguide. For a voltage V_o across the equivalent circuit of Fig. 7, the power is found to be given by (3.14). Equating this power to computed from (5.3) and (5.4) for sinusoidal distributions of A_α and B_α , we find for the transformer ratio as before:

$$\left| \frac{n_\alpha}{n_\beta} \right|^2 = 4 \frac{\mu^2}{\kappa^2} \quad (5.5)$$

thus completing the determination of the equivalent circuit.

The responses obtained from the equivalent circuit and the full analysis are shown in Fig. 8. One should point out that the responses of the side-coupled GDFB structure show remarkable differences from those of a passive side coupled quarter wave shifted resonator^[10]. First of all, the latter structure permits only one half of the power in the bus to be coupled to the resonator. In the present case, amplification is present. It is possible to adjust the gain so that the power flow in the main bus is hardly changed, the output power from the resonator is an amplified version of the signal in the bus. Thus, this structure permits cascading, with access to the same channel by filters further down along the bus.

If the resonator is detuned by providing an appropriate reflection from one of its two ends, the filter can be tuned. We shall not develop here the equivalent circuit for a detuned filter.

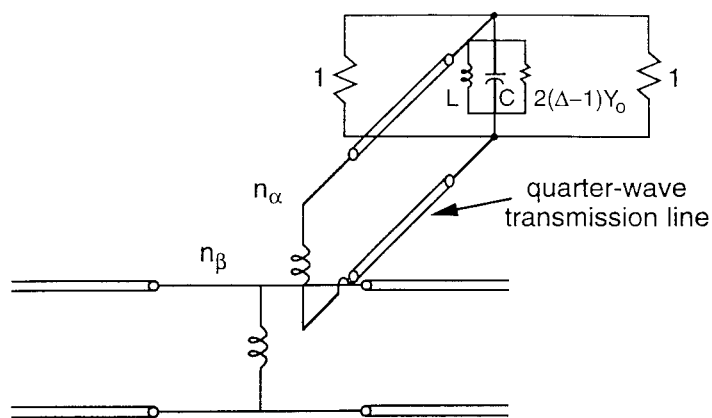


Figure 7. Equivalent circuit of side-coupled gain grating.

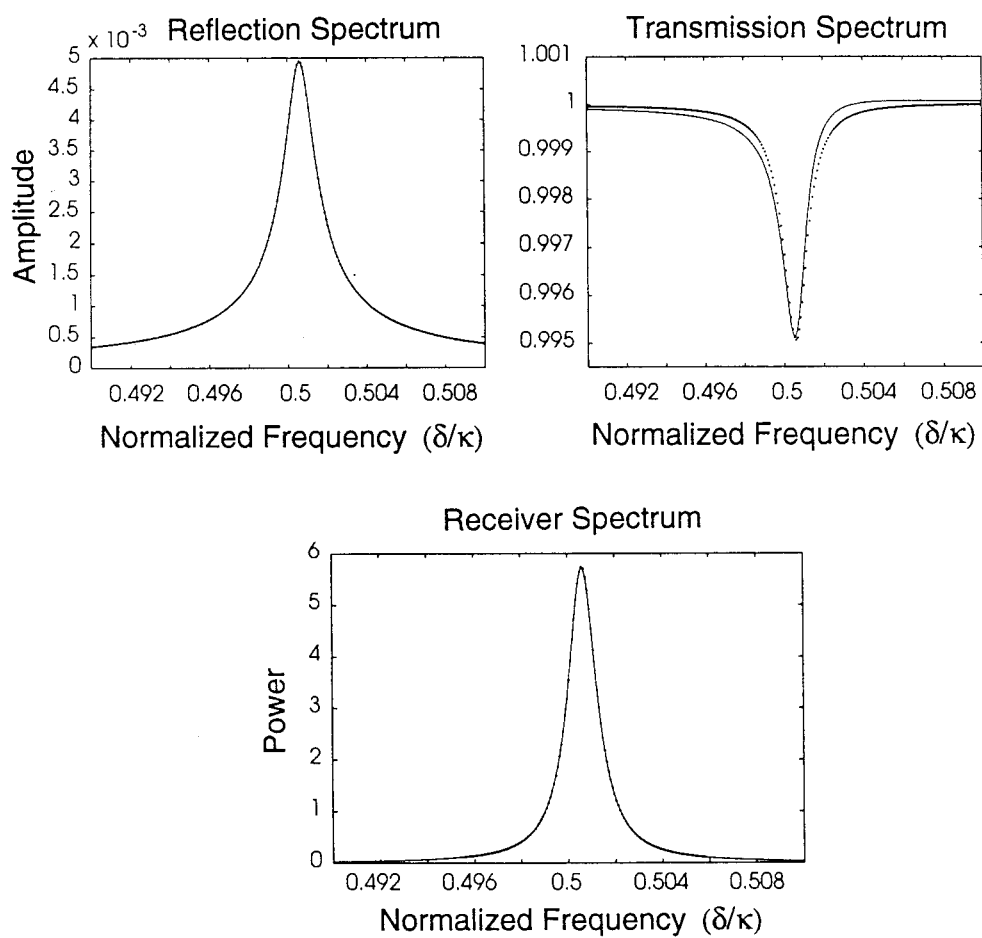


Figure 8. Responses computed from equivalent circuit (solid line) and coupled mode analyses (dotted line); (Left) Reflected amplitude; (Right) Transmitted amplitude; (Lower) Received power; $\mu/\kappa = 0.002$, $\Delta = 0.001$, $\delta_o/\kappa = 0.5$.

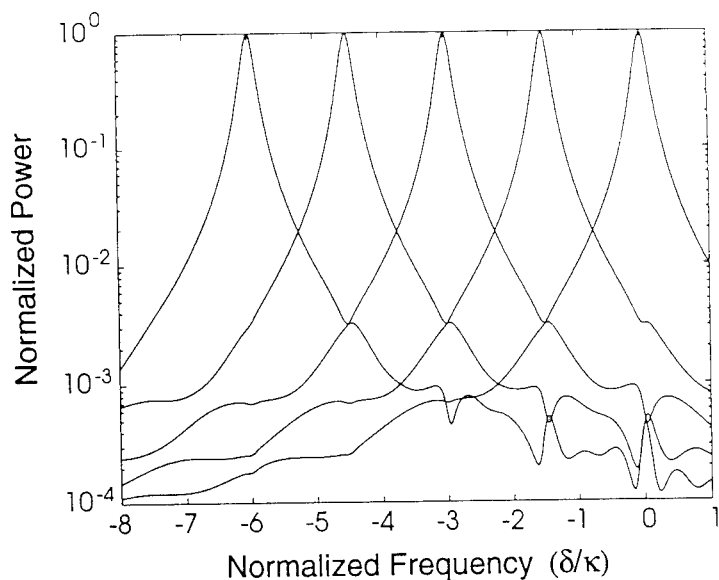


Figure 9. Normalized received power for five 10 GHz filters spaced 68 GHz apart; $\kappa = 35 \text{ cm}^{-1}$.

The channel dropping filters can be practical only if they exhibit acceptable crosstalk characteristics. We have mentioned in the introduction that active filters can discriminate against undesirable responses by providing sufficient gain. This shows clearly in the response of the filter cascade. Figure 9 shows the response of a cascade of five on-resonance filters, of 10 GHz bandwidth each, spaced by 6.8 times their bandwidth. The transmitted signal experiences small dips at and near the center frequency of each filter. The received power does not have gain in the case given here, because the value of 35 cm^{-1} for κ with a bandwidth of 10 GHz constrained the design so as not to provide gain. The crosstalk is -24 dB at center frequency of each filter. This crosstalk level could be improved if κ values greater than 35 cm^{-1} could be assumed.

ACKNOWLEDGMENTS

This work was supported in part by the University of California NCIPT Subcontract Grant 542383 and the Joint Services Electronic Program DAAL03-92-C-0001.

REFERENCES

1. H. Kogelnik and C. V. Shank, "Coupled-Wave theory of distributed feedback lasers," *J. Appl. Phys.* 43:2327 (1972).
2. D. C. Flanders, H. Kogelnik, R. V. Schmidt, and C. V. Shank, "Grating filters for thin-film optical waveguides," *Appl. Phys. Lett.* 24:194 (1974).
3. H. A. Haus and C. V. Shank, "Antisymmetric taper of distributed feedback lasers," *IEEE J. Quantum Electron.* QE-12:532 (1976).

4. H. A. Haus and R. V. Schmidt, "Transmission response of cascaded gratings," *IEEE Trans. Sonics Ultrasonics* SU-24:94 (1977).
5. H. A. Haus and Y. Lai, "Narrow-band optical channel dropping filter," *J. Lightwave Tech.* 10:57 (1992).
6. J. N. Damask, J. Ferrera, V. V. Wong, H. I. Smith, and H. A. Haus, "Limitations and solutions for the use of integrated $\lambda/4$ -shifted distributed Bragg resonators in wavelength-division multiplexing applications," International Symposium on Integrated Optics: Nanofabrication Technologies and Device Integration, W. Karthe, ed., SPIE 2213:137 (1994).
7. V. V. Wong, J. Ferrera, J. N. Damask, J. M. Carter, E. E. Moon, H. A. Haus, and H. I. Smith, "Spatial-phase-locked electron-beam lithography and x-ray lithography for fabricating first-order gratings on rib waveguides," *J. Vac. Sci. Technol.* November/December 1994.
8. Y. Luo, Y. Nakano, K. Tada, T. Inoue, H. Hosomatsu, and H. Iwaoka, *Integrated Optics and Optical Fiber Communication (IOOC'89)* (Kobe, Japan, July 18-21, 1989, post-deadline paper 20PDB-2, pp. 39-42).
9. H. A. Haus, in: "Waves and Fields in Optoelectronics," Prentice-Hall, Englewood Cliffs, NJ (1984).
10. H. A. Haus and M. J. Khan, "Gain distributed feedback filters," submitted to *IEEE Journal of Lightwave Technology*.

Periodically Segmented Waveguides

A. Hardy, Z. Weissman, D. Nir and S. Ruschin
Faculty of engineering, Tel Aviv University
Ramat Aviv 69978, ISRAEL

1 Introduction

Periodically segmented waveguides (PSW, see Fig. 1) have attracted considerable attention recently. They were first used for second harmonic generation (SHG) in $Rb : KTiOPO_4$ [1, 2]. Currently, KTP PSWs are the most efficient waveguide frequency doublers, with conversion efficiencies of $800 \frac{\%}{W_{cm^2}}$ reported [3]. Apart from its excellent phase-matching capability in KTP, the PSW has some interesting linear waveguiding properties. In particular, a PSW with an index difference Δn and a duty cycle η (see Fig. 1) acts essentially as a continuous waveguide with an index difference $\Delta n' = \eta \Delta n$ [4, 6]. However, the PSW is also a high-order grating, and as such can couple light to either radiation (resulting in an exponential decay factor α of the propagating mode) and/or back-reflection (if the wavelength of operation is near a Bragg resonance).

The fact that Δn can be modified by segmentation enables realization of some novel waveguide devices which require different - or spatially varying - Δn 's on the same chip. Examples are mode taper, asymmetric directional coupler filter and wavelength demultiplexer [5, 6]. Using this technique, the realization is quite simple: it can be achieved via proper design of the geometrical layout of the device - without modifying the specific waveguide fabrication process. Thus the PSW is a generic type of waveguide device, which can be employed for various types of applications.

Here we review our research results on this topic. The following sections deal with basic properties of the PSW, linear applications and SHG.

2 Characteristics of PSW

The PSW is a kind of lens waveguide. At the same time, it is also a kind of waveguide grating. The specific properties of the PSW, as well as the methods that can be used

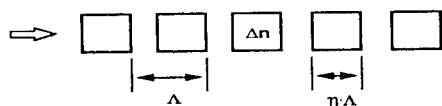


Figure 1: Periodically segmented waveguide (PSW)

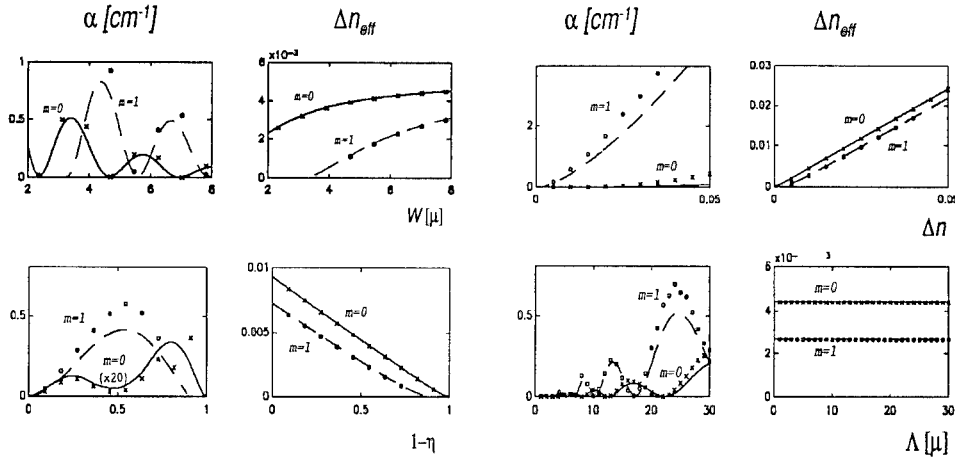


Figure 2: Eigenvalues of a Periodically segmented waveguide. Dots represent BPM results, and curves represent coupled mode results (for α) or solution of the TE eigenvalue equation for the respective nonperturbed (averaged) waveguide (for Δn_{eff}). Parameter values: $width = 7\mu$, $\Delta n = 0.01$, $n_0 = 1.85$, $\lambda = 0.85\mu$, $\eta = 0.5$.

to analyse it, are derived from these two different perspectives. In a detailed analysis, one is mainly interested in the eigenvalues and eigenfunctions of the guided modes in a PSW. In view of the above, two types of methods are used in this section: a beam propagation method (BPM) and a coupled mode method [6].

2.1 Analysis

The simplest PSW to analyse is the step-index 2D PSW, for which nonperturbed modal solutions are found easily, and BPM calculation are not excessively time consuming. We thus consider this type of waveguide first.

eigenvalues As mentioned above, the PSW combines index averaging with an inherent radiation loss. The typical PSW design problem would thus be as follows: For a specific fabrication process (i.e. a specific Δn profile), how can a waveguide with a desired index difference $\Delta n' = \eta \Delta n$ be designed for minimal losses? With this goal in mind, the complex eigenvalues ($\beta \equiv \frac{2\pi(n_0 + \Delta n_{eff})}{\lambda} - i\alpha$) were calculated as a function of various parameters of the wave and the waveguide (width, period, duty-cycle, index difference, wavelength and guided-mode order m). The results are given in Fig. 2. The main observations with respect to these graphs are the following:

- Δn_{eff} of a PSW (as calculated by BPM) is indeed equal to that of a continuous waveguide, with an averaged index difference, $\Delta n' = \eta \Delta n$. In particular, the effective index is independent of the period, and is roughly linear with the duty cycle.
- The loss factor α is very sensitive to the values of the various parameters. In particular, α increases monotonously with Δn and oscillates with W, Λ, η and also with λ . Note that for some specific sets of values, α almost vanish.

- The BPM results coincide with those of the TE eigenvalue equation (with respect to Δn_{eff}) and are in good agreement with those of the mode coupling analysis (with respect to α).

These results indicate that the available design parameters are sufficient to minimize the PSW loss, for a desired value of the modified Δn . We now turn to examine some of these results more closely.

The loss parameter α is related to overlap integrals (over the perturbation region) between the propagating guided modes and some of the radiation modes which are connected by an inverse grating vector. Modifying the grating parameters may change the propagation direction of these radiation modes, and with it also the number of lobes they have within the perturbation region. Thus α oscillates as λ , Λ , η and W are varied. These oscillations are most interesting in the context of the grating period Λ , as very low losses can occur even at relatively long periods. In this range the k -value of the grating ($k = \frac{2\pi}{\Lambda}$) is small, so that the dominant first-order radiation-mode has only few lobes within the waveguide cross-section, which results in larger overlap with the guided mode. That in turn results in increasing radiation loss and also in increasing distance between consecutive minima of α . Intuitively, one can expect that long periods would incur large diffraction losses.

The effect of the duty cycle η on α is also interesting. In this case, we choose a grating period of $22\mu m$, for which the loss is minimal (see Fig. 2). Evidently, α remains very low over the entire range of η . Note that for the limits of continuous waveguide ($\eta = 1$, i.e. ideal mode) and homogeneous medium ($\eta = 0$, i.e. plane-wave) the loss becomes zero - as should be expected.

eigenfunctions A guided mode eigenfunction of a PSW is a periodic function of z , which oscillates along the route of propagation. In practice, however, the oscillations are very small, and the modal beam can be considered to have an approximately uniform cross section, equal to that of the (truly uniform) mode of the respective nonperturbed waveguide. Naturally, the beam width is increased as the duty cycle η is reduced. These properties are particularly interesting in the context of channel PSWs, and they are considered in more detail below.

2.2 Experiments

To verify the above theoretical results, experiments have been carried out in *KTP*, proton exchanged (PE) *LiNbO₃*, annealed proton exchanged (APE) *LiNbO₃* and *Ti : LiNbO₃* waveguides.

Index averaging Effective index of PSW was measured in *KTP* [9], *PE : LiNbO₃* [8] and *APE : LiNbO₃* [7], using prism coupling and back reflection of a tunable source. Some of the waveguides were in fact two dimensional while others were three dimensional. The periods used in these measurements were relatively short ($3 - 6\mu$). All of these measurements clearly supported the averaged index model.

Modal eigenfunctions The increase of the modal spot with reduced duty cycle is a direct result of index averaging. Near fields were measured in *Ti : LiNbO₃* [10], for various periods and duty-cycles. Some of the modal contours are given in Fig. 3.

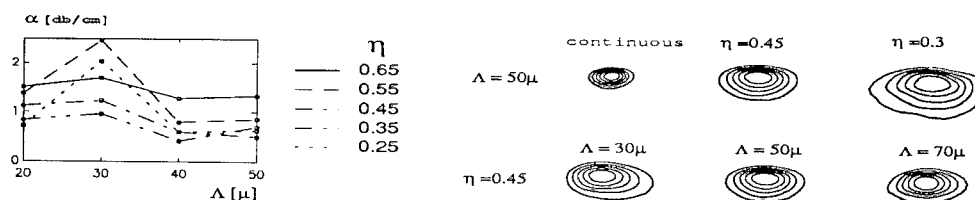


Figure 3: Measured loss coefficients (left) and modal contours (right) in $Ti : LiNbO_3$ channel PSWs.

Radiation loss To determine the loss factor α , measurements were carried out in $Ti : LiNbO_3$ channels [10]. To induce significant (and thus measurable) losses, long periods (tens of microns) were used. Results are given in Fig. 3, as a function of the period, with the duty cycle as a parameter.

The measured radiation loss is maximal at $\Lambda = 30\mu$, for all duty cycles. This type of behavior is in agreement with the theoretical predictions above. To further understand these results, the waveguides were modelled by a 2D step-index PSW. To take into account the air-substrate interface, the radiation loss was calculated for the antisymmetrical depth mode of the doubled thickness waveguide, using the coupled mode method described in [6]. In this model two types of radiation loss mechanisms were taken into account: segmentation loss and surface loss. The second mechanism is related to the periodic relief created on top of the surface due to diffusion of the segments. The total loss is taken as the sum of these two components, as described in Fig. 4.

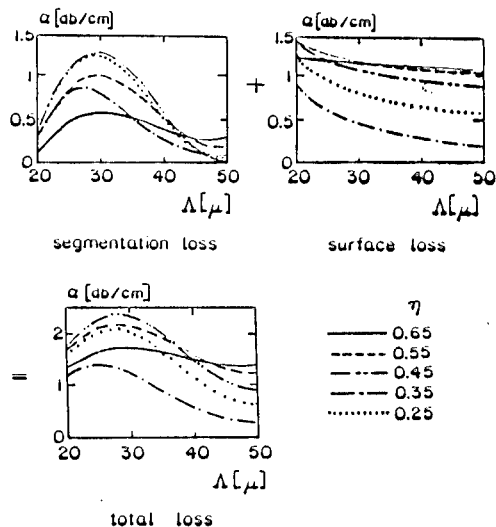


Figure 4: Propagation losses in $Ti : LiNbO_3$ channel PSWs: modelling results.

The similarity between theory and experiment is evident. Note the different patterns of the two loss mechanisms: whereas the segmentation loss oscillates with Λ , the surface

loss decreases monotonically. This is due to the fact that relief thickness is considerably smaller than $\frac{\lambda}{n}$, whereas the slab thickness is considerably larger than the $\frac{\lambda}{n}$. As a result, the transverse periods of relevant radiation modes are much larger than the surface perturbation but much smaller than the segmented perturbation. Thus, on the surface the overlap between guided and radiation modes decreases monotonously, whereas in the waveguide region it has an interference-like pattern.

3 Linear applications of PSW

As seen above, waveguide segmentation enables a reduction of Δn to $\Delta n' = \eta \Delta n$. Because segmentation is realized at the lithography level, the technique is completely independent of the specific waveguide fabrication process (e.g diffusion, deposition, etc.). This practical advantage can be utilized for several configurations, which so far required multi-step fabrication processes of various kinds. Two examples are described schematically in Fig. 5.

Mode expanders are widely used in integrated optics, to obtain efficient in/out coupling. Whereas lateral tapering is simple, depth tapering typically requires a considerable effort. Waveguide segmentation can be used for that purpose [5, 6], as described in Fig. 5. In this scheme, the averaged index difference (over a period) is reduced towards the fiber end, and the width is increased, to a point where the mode mismatch becomes minimal. To allow some tolerance in edge processing (polishing or cleaving) the taper section is augmented by a regular segmented I/O section at the fiber end. The technique is applicable, in principle, to any type of waveguide - subject to the amount of radiation loss caused by segmentation.

As an example, consider coupling of a silica fiber (with a 10μ wide gaussian mode) to an InP strip waveguide, with $\Delta n = 0.085$ and $W_{out} = 1.5\mu$, at $\lambda = 1.55\mu$. The large mode mismatch between the fiber and waveguide leads to coupling loss of $4dB$. By using a PSW mode taper section, 400μ long, in which the duty cycle is reduced to $\eta = 0.31$ at the fiber side, and the waveguide is widened to $W_{in} = 7\mu$, with a period $\Lambda = 3\mu$, the coupling loss is reduced to $0.6dB$.

If two neighbouring waveguides have different dispersion curves that intersect at a particular wavelength, they can form a frequency selective device, such as an asymmetric directional coupler (see Fig. 5) or an asymmetric Y junction. In particular, by using two PSWs with different widths and duty cycles, the wavelength of intersection and (to some extent) its slope can be determined. Consider, for example, two silica waveguides with thickness of 3μ , $\frac{\Delta n}{n} = 0.75\%$, widths of 6μ and 2μ , as described in Fig. 5. Whereas the narrow waveguide is continuous, the wider waveguide is segmented to $\eta = 0.69$, at $\Lambda = 10\mu$. The two dispersion curves intersect at $\lambda_0 = 1.415\mu$.

If we now put these two waveguides in parallel, 4μ apart, they would form an asymmetric directional coupler filter. At $\lambda = \lambda_0$ the two coupler arms are phase matched, resulting in a complete power transfer at $L = 8mm$. On the other hand, at $\lambda = 1.5\mu$, the arms are at phase mismatch and there is no net power transfer. Thus this coupler may be used as a filter, with a center wavelength λ_0 .

4 SHG in PSW

The search for compact, coherent, blue light sources have been intensive in the recent decade, for various applications, such as high density optical memories, reprography,

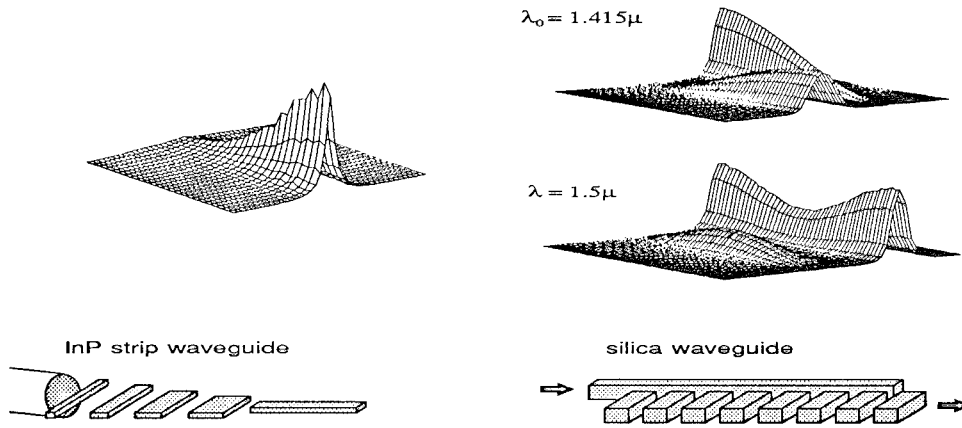


Figure 5: Wave intensity evolution in an InP strip PSW mode expander (left) and a Silica PSW directional coupler (right). The parameters are given in the text.

etc. There has been a good progress in frequency doubling of GaAs laser via SHG in a waveguide. PSW's play an important role in this progress.

PSW's can be used for two purposes: first, to obtain quasi phase matching (QPM) of the SHG. Second, to lock the semiconductor laser to the QPM wavelength, by using the selective reflection property of the PSW, operating in a Bragg-resonant QPM scheme (termed below as B-QPM), to obtain a stable doubling operation. In the rest of this paper the SHG in a B-QPM is considered in some detail [13].

4.1 Bragg-resonant, quasi phase matched SHG

The basic problem with the B-QPM approach is that high reflection at ω largely reduces the harmonic conversion, precisely at the operating wavelength of the laser. This is demonstrated in the right pair of graphs of Fig. 6, which describes an experiment in *Rb : KTP* segmented waveguides. The waveguides in this experiment were superperiodic, with $M=2$, meaning that a unit cell is made of two segments, i.e. it is composed as follows: $[l_{d1}, l_{u1}, l_{d2}, l_{u2}], [l_{d1}, \dots], \dots$, where l_d, l_u represent length of segment and gap, respectively. The specific waveguide used here had $[l_{d1}, l_{u1}, l_{d2}, l_{u2}] = 2.6\mu, 1.4\mu, 2.7\mu, 1.4\mu$, which results in $\Lambda_{QPM} = 4.05\mu$. The waveguide length was 5.5mm, and the normalized nonresonant (i.e. for $\lambda_q \neq \lambda_b$) conversion efficiency was $500 \frac{\%}{Wcm^2}$.

The waveguide was excited by a TM polarized $TiAl_2O_3$ laser, and was heated to obtain the required coincidence $\lambda_q = \lambda_b$. The left part of the figure shows the spectra of the IR transmission and the forward SHG in a nonresonant situation, for the TM_{00} mode. In a nonresonant situation the SHG curve has the usual phase-matching bell-shape ($\approx 3\text{\AA}$ wide). At $\lambda = \lambda_b$, the IR transmitted power was mostly in the TM_{01} mode, which indicates close to zero transmission of the TM_{00} mode, primarily due to reflection, which was roughly 85%. The reflection was in the 35th order of the superperiodic grating.

The right part of the figure shows the forward and backward SHG in a resonant situation. In this case, a spectral valley appears at the center of the QPM curve, due to high IR reflection. At the center of the valley (where the laser would eventually

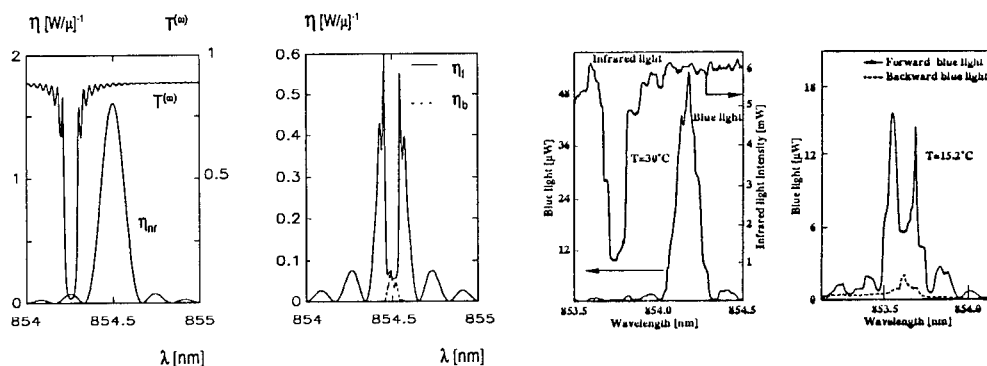


Figure 6: Bragg-resonant QPM SHG in a KTP PSW: experimental results (left) and calculated results (right), for a nonresonant and resonant situations.

operate), the conversion efficiency is about 10% of the nonresonant value. In another sample, the IR reflectivity was lower ($\approx 70\%$), and the relative efficiency was higher ($\approx 20\%$).

To analyze the waveguide operation, a new QPM theory was developed [12] as none of the theories published so far apply to a resonant situation. In fact, linear index modulation was considered in these theories only with respect to phase matching per se. Furthermore, in these cases, the relevant guided modes were taken into account, but most of the higher order grating waves driven by these modes were ignored. The effect of these waves is particularly important with respect to radiation losses and reflection in the periodic waveguide.

By definition, both harmonics have Bragg resonances at $\lambda = \lambda_q = \lambda_b$. Thus, with the exception of few specific values of the duty cycle - for which κ_L^ω and/or $\kappa_L^{2\omega}$ are nulled (e.g. for a duty-cycle of 0.5, at an even Bragg order, $\kappa_L^\omega = \kappa_L^{2\omega} = 0$) - both harmonics theoretically have peak reflections precisely at the QPM peak. Due to higher Δn and better confinement at 2ω , $\kappa_L^{2\omega}$ is normally larger than κ_L^ω , even though the reflection order is twice higher for 2ω . These properties should result in a forbidden band around λ_q , in which the forward and backward conversion efficiencies, η_f and η_b , are practically nulled.

The practical situation, however, is considerably less severe: the results of Fig. 6 indicate a very low linear reflection at 2ω (though we were not able to measure it directly). The main reason appears to be random variations in the domain boundaries, which - due to the shorter wavelength - reduce the reflection at 2ω much more than at ω . Since the above formulation does not account for such random variations, their effect was included indirectly, by arbitrarily reducing $\kappa_L^{2\omega}$ to a very low value (while keeping κ_L^ω as is). The calculated results are given in the lower part of Fig. 6. The similarity with the experimental results is evident. Note, however, that the measured harmonic conversion at the center of the hole is higher than calculated - partly due to the effect of the random boundary variations on the reflectivity at ω . Note also that the reflection line at ω is wider in the experiment than in theory - which may also be due to such random variations.

5 Conclusion

Periodically segmented waveguides are useful for various applications in integrated optics. Their properties include tailorable index profile, linear Bragg reflection and (in some cases) Quasi phase matching for frequency conversion devices. They can be combined (e.g. in the form of B-QPM SHG device) or used separately - depending on the design parameters. The PSW is a generic waveguide geometry, in the sense that it is applicable to any type of waveguide. In practice, the applicability to a specific type of waveguide would depend on a variety of factors, including the amount of radiation loss, the required lithographical accuracy, and others.

Acknowledgements: We thank M. Katz, D. Eger and M. Oron from Soreq research center, for providing the experimental SHG results. The research at Tel Aviv University was partly supported by a grant from the Israel Academy of Arts and Sciences.

References

- [1] J.D. Bierlein et al, *Appl. Phys. Lett.*, **56**, 1725, 1990.
- [2] C.J. Van der Poel, J.D. Bierlein, J.B. Brown and S. Colak, *Appl. Phys. Lett.*, **57**, 2074, 1990.
- [3] D. Eger, M. Oron, M. Katz and A. Zussman, *Appl. Phys. Lett.*, **64**, 3208, 1994.
- [4] L. Li and J.J. Burke, *Opt. Lett.*, **17**, 1195, 1992.
- [5] Z. Weissman and A. Hardy, *Electron. Lett.*, **28**, 1514, 1992.
- [6] Z. Weissman and A. Hardy, *J. Lightwave Technol.*, **11**, 1831, 1993.
- [7] K. Thyagrajan, C.W. Chien, R.V. Ramaswamy, H.S. Kim and H.C. Cheng, *Opt. Lett.*, **19**, 880, 1994.
- [8] P. Baldi, M.R. Shenoy, S. Nouh, M.P. De Micheli and D.B. Ostrowski, *Opt. Comm.*, **104**, 308, 1994.
- [9] D. Eger, M. Oron and M. Katz, *J. Appl. Phys.*, **74**, 4298, 1993.
- [10] D. Nir, Z. Weissman, S. Ruschin and A. Hardy, *Opt. Lett.*, **19**, 1994.
- [11] Shinozaki, T. Fukunaga, K. Watanabe and T. Kamijoh, *J. Appl. Phys.*, **71**, 22, 1992.
- [12] Z. Weissman and A. Hardy, *Proc. SPIE*, **2212**, 307, 1994.
- [13] Z. Weissman, A. Hardy, M. Katz, M. Oron and D. Eger, "Second harmonic generation in resonant, quasi phase matched, periodically segmented waveguides", submitted to *Opt. Lett.*

GUIDED WAVE DEFLECTORS USING GRATINGS WITH SLOWLY-VARYING GROOVE DEPTH FOR BEAM SHAPING

Nandakumar Ramanujam, James J. Burke, and Lifeng Li

*Optical Sciences Center
University of Arizona
Tucson, AZ 85721, USA*

INTRODUCTION

Thin film waveguides with periodic surface variation are important components in integrated optical devices. These waveguide-grating structures provide the means for efficient coupling of light into and out of such films. They can also be used for the mutual coupling of guided waves, resulting in interesting phenomena such as polarization conversion, deflection, and reflection [1,2].

We report here our work on a guided wave deflector which incorporates a finite aperture Bragg grating with an adiabatic variation of the groove depth as shown in Fig. 1. Earlier investigations of noncollinear coupling between planar waveguide modes using finite aperture gratings have revealed that the scattered wave has a lateral (in the plane of the waveguide) amplitude profile that is different from that of the incident wave [3-6]. This deformation of the lateral profile is undesirable in many applications such as optical data storage in which a collimated Gaussian beam is desired at the objective lens. The beam deformation is also unacceptable in cases where additional planar optics such as mode index lenses are to be employed in cascade. However, reshaping of the beam is important not only for these purposes but also for some mode-matching applications in which the coupling efficiency is to be optimized.

We will present the differential equations that describe the interaction of modes of planar waveguides in the noncollinear grating geometry, and discuss approximate analytical solutions for the case of nonuniform grating groove depth. This approximate formulation is then used to solve the inverse problem of determining the particular grating depth variation that will reshape the lateral amplitude profile and hence rectify the beam deformation. The analytical result, which will be shown to be valid only for limiting cases, will be augmented by numerical optimization techniques to satisfy the design criteria of deflection efficiency and beam shape.

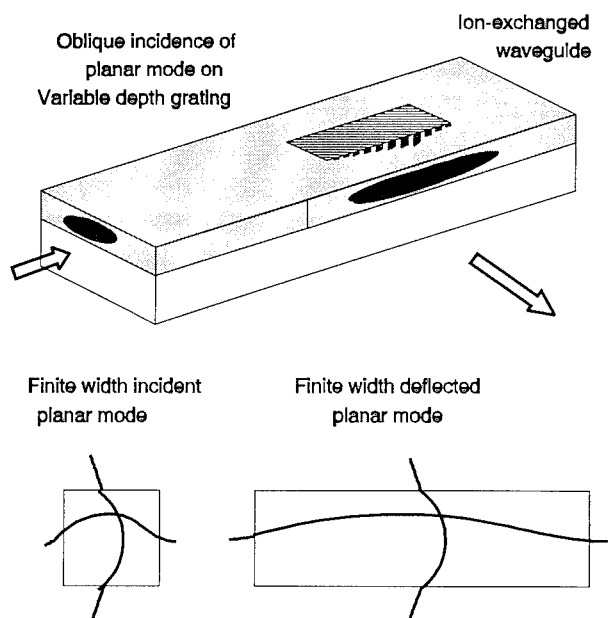


Fig. 1 Deflection of finite width planar waveguide mode by finite aperture surface-relief grating. Deformation of lateral field is corrected by grating's adiabatic groove depth variation, thus producing a Gaussian profile.

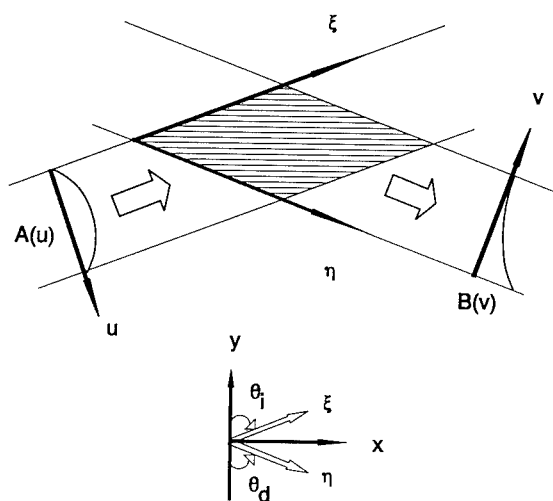


Fig. 2 Top view of noncollinear coupling geometry using a finite aperture waveguide-grating with uniform groove depth. Deformation of deflected beam is depicted.

NONCOLLINEAR GRATING COUPLING

Derivation Of The Coupled Equations

Our analysis of the noncollinear grating coupling of guided waves follows the work of Svidzinskii [3] closely. We begin by defining the coupling geometry as shown in Fig. 2. The grating grooves run parallel to the x -direction, and in this particular case, the finite grating aperture is defined by the region of overlap of the incident and deflected modes. This type of coupling geometry is more realistic than the semi-infinite grating structure (with infinitely long grating grooves), which has been employed traditionally to analyze these types of problems [7,8]. In general, the grating aperture can be of an arbitrary shape but we shall focus on the geometry shown without any loss of generality.

We analyze the modal interaction using coupled mode theory, with the assumption that the corrugated grating is a weak periodic perturbation of the waveguide-cover interface. This assumption is reasonable in the case of shallow surface-relief gratings with small index contrast between the waveguide surface and the cover (as is the case with glass ion-exchanged waveguides).

The waveguide modal fields are first transformed to the grating coordinate system, resulting in five non-zero components for the electric and magnetic fields for the transverse electric (TE) and transverse magnetic (TM) polarized modes. The transverse components of the fields in the grating region are then described in terms of an expansion over a complete, orthogonal basis set of forward- and backward-propagating modes of the unperturbed waveguide. The phase variation of the fields is expressed by the factor $\exp[+i(\vec{\beta} \cdot \vec{r} - \omega t)]$. The longitudinal components of the fields follow directly from Maxwell's equations. We can conveniently neglect the unbound modes as well as the backward-propagating modes of the waveguide because phasematching constraints dictate that negligible power is coupled to these modes in this type of noncollinear guided wave interaction.

Following the standard procedures outlined in coupled mode analysis [9], and considering only a phasematched interaction between two modes, we arrive at a set of coupled equations,

$$\begin{aligned} \sin\theta_i \frac{\partial A(x,y)}{\partial x} + \cos\theta_i \frac{\partial A(x,y)}{\partial y} &= i e^{+i\delta x} \kappa B(x,y) \\ \sin\theta_d \frac{\partial B(x,y)}{\partial x} - \cos\theta_d \frac{\partial B(x,y)}{\partial y} &= i e^{-i\delta x} \kappa^* A(x,y) \end{aligned} \quad , \quad (1)$$

that describe the interaction between the incident and deflected modes in the grating region (see also Fig. 2). The coefficients A and B correspond to the slowly-varying amplitudes of the incident and deflected modes, respectively. Close examination of these equations reveals that the first terms on the left hand side can be dropped if the grating extends to infinity along the x -direction and the planar modes are of infinite width. In this case, we obtain the familiar coupled equations that are used to describe noncollinear coupling in semi-infinite gratings. The $\cos\theta$ factor is sometimes lumped with the coupling coefficient [8],

$$\kappa = \frac{\omega}{4} \int_{-\infty}^{+\infty} \vec{E}_i^*(z) \cdot (\Delta\epsilon(z))_m \cdot \vec{E}_d(z) dz \quad , \quad (2)$$

which is a measure of the rate of mutual conversion of the waves. The term, $\Delta\epsilon$, represents the m th order Fourier component of the surface perturbation for a medium with a diagonal permittivity tensor. The degree of angle and wavelength mismatch in this resonant interaction is represented by the detuning factor, $\delta = \vec{\beta}_d - \vec{\beta}_i + m\vec{K}$, where m is the grating order and K is the magnitude of the grating vector. This interaction is assumed to be phasematched when δ is approximately zero. The coupling coefficient is the parameter of interest for the rest of our work here. It is well-known that for shallow surface-relief gratings, the coupling coefficient is linearly proportional to the grating groove depth [10]. Hence, by modulating the groove depth, we can in effect adiabatically vary the coupling strength across the grating. It should be noted that polarization conversion effects come into play when guided waves are obliquely incident upon the grating.

The Characteristic Coordinate System

If the problem of interest is similar to that shown in Fig. 2, where the grating region is defined by the overlap region of finite-width planar modes, we can make some significant simplifications by transforming the problem to the characteristic coordinate system. This terminology derives from the fact that the boundaries of the grating are delineated by the so-called characteristics of the boundary value problem [11]. The characteristics in this case are defined by the directions ξ and η , corresponding to the paths along which the incident and deflected modes are evolving. This in essence changes the boundary value problem to an initial value problem for which the initial conditions are specified at $\xi=0$ and $\eta=0$. At $\xi=0$, we project the incident field onto the entrance aperture to obtain one of the initial conditions, and at $\eta=0$, we assume that the deflected or scattered field is zero because there are no sources in the system. With a straightforward coordinate transformation, we obtain a new set of coupled equations:

$$\frac{\partial A(\xi, \eta)}{\partial \xi} = +i\kappa B(\xi, \eta) \quad , \quad (3a)$$

$$\frac{\partial B(\xi, \eta)}{\partial \eta} = +i\kappa^* A(\xi, \eta) \quad . \quad (3b)$$

These equations can of course also be written as a second-order hyperbolic partial differential equation,

$$\frac{\partial^2 A(\xi, \eta)}{\partial \xi \partial \eta} + |\kappa|^2 A(\xi, \eta) = 0 \quad , \quad (4)$$

for which analytical solutions are available using an appropriate Reimann's function [3,11] when the coupling coefficient is constant (or, equivalently, when the grating is of uniform depth and fixed periodicity). These characteristic coupled equations can also be solved numerically using explicit finite-differencing techniques [4] and the results are identical to those obtained analytically. In Fig. 3a, we show the evolution of an initially uniform incident field along the length (ξ direction) of a grating with a rectangular aperture and a constant coupling coefficient. In Fig. 3b, the deflected field evolution along the η direction of the same grating is depicted. From these plots, it is clear that for finite aperture gratings, the coupling of the incident and

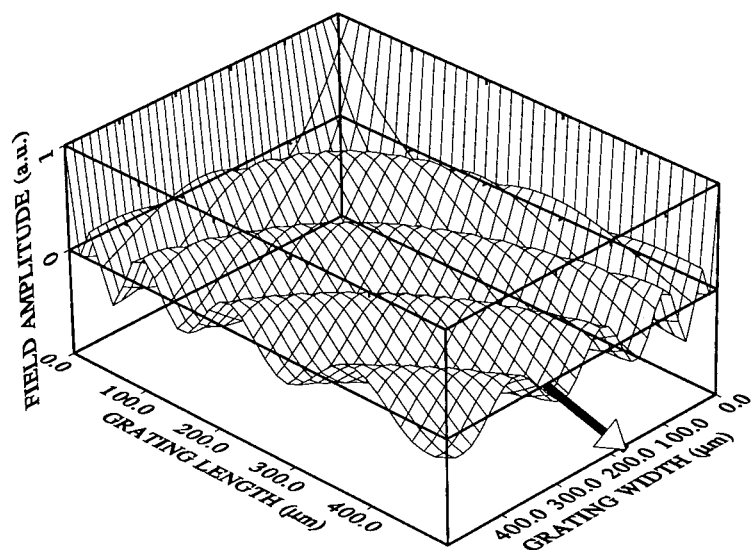


Fig. 3a Evolution of uniform incident field along direction indicated by arrow. Grating size is $500\text{ }\mu\text{m}$ by $500\text{ }\mu\text{m}$, and $\kappa = 0.03\text{ }\mu\text{m}^{-1}$. Field was computed using an explicit finite-differencing algorithm.

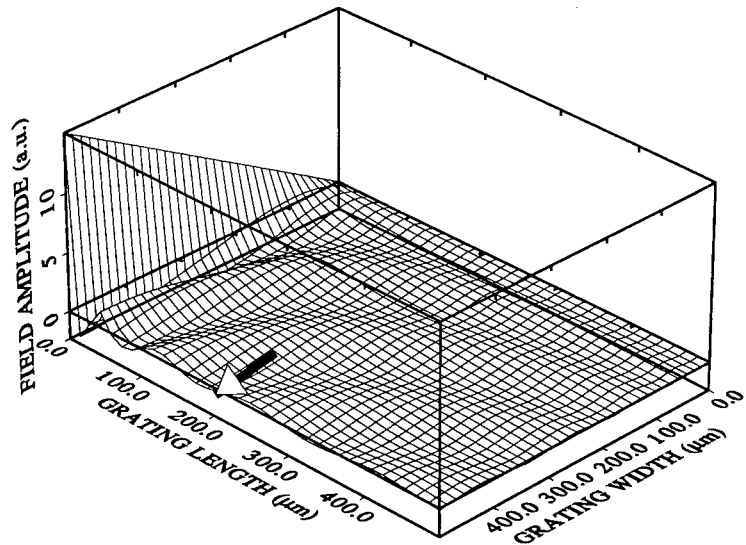


Fig. 3b Evolution of deflected field along direction indicated by arrow. Grating parameters are the same as in Fig. 3a. Note the strongly asymmetric output field distribution.

scattered fields in the grating region results not only in power exchange but also in a transformation of the angular spectrum. As a consequence, the lateral amplitude profile of the deflected field at the exit aperture is significantly different from the uniform incident field at the entrance aperture. In fact, the profile is grossly asymmetric with most of the energy being concentrated near one end of the exit aperture.

MODULATION OF THE COUPLING COEFFICIENT

The Weak Coupling Approximation

The analytical solution of the characteristic coupled equations becomes more complicated if the coupling coefficient is no longer uniform. This is the case if the grating depth is non-uniform or if the grating period is not constant. These changes to the grating can be represented mathematically in terms of a complex, position-dependent coupling coefficient, $\kappa(\xi, \eta)$, where the magnitude represents any adiabatic variation of the grating groove depth, and the phase represents a chirped grating period [12]. For our applications, we chose to examine a constant-period grating with a slow groove-depth variation along the ξ direction, represented by $\kappa_0(\xi) = |\kappa(\xi)|$. Part of the difficulty in obtaining a rigorous analytical solution is due to the fact that Eqs. (3a) and (3b) are not separable. If we turn again to Reimann's method for characteristic problems, a suitable Reimann's function for this modified partial differential equation is not easily found. Certainly, the coupled equations can still be solved numerically as before using finite-differencing but this provides a solution to the forward problem only, where the deflected and transmitted fields can be computed given a particular coupling coefficient distribution. However, if we wish to solve the inverse problem where we need to determine the particular coupling coefficient distribution that will yield a desired deflected field profile, the numerical technique alone is inadequate. In such cases, an analytical solution is preferred. To attain this end, we will make some judicious, simplifying approximations, based on a physically intuitive model.

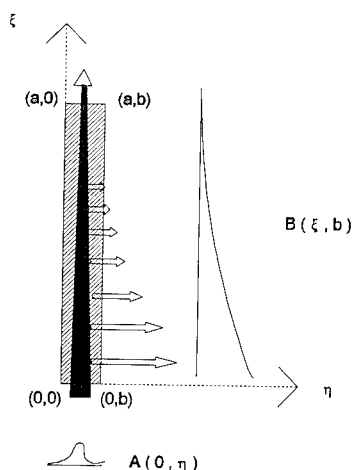


Fig. 4 Schematic of a very narrow grating of length a , width b , and weak coupling strength.

Consider for now the narrow grating shown in Fig. 4. An incident field is scattered by the grating into a specific direction dictated by phasematching considerations. If the grating is narrow (along the η direction), then the deflected field has little opportunity to couple back to the incident field (which is evolving along the ξ direction). This simple single-scattering model presumes weak coupling between the modes. Therefore, we could equivalently widen the grating but still restrict the strength of coupling so that the degree of recoupling or secondary scattering is effectively negligible. This translates mathematically into a decoupling of Eqs. (3a) and (3b). Formally, this is similar to the physical mechanism governing the interaction of fields in input/output grating couplers where recoupling between scattered and incident fields is not present [13]. Upon integration of Eq. (4b) with respect to η , with the assumption that the incident field, $A(\xi, \eta)$, is a slowly-varying function of η , the deflected field becomes:

$$B(\xi, b) \approx i\kappa^*(\xi) b A(\xi, \bar{\eta}) \quad , \quad (5)$$

where $A(\xi, \bar{\eta})$ is the root-mean-square (RMS) strength of the incident field along the length of the grating. By substituting this result into Eq. (4a), we find, as expected, that the incident field is defined by:

$$A(\xi, \bar{\eta}) = A(0, \bar{\eta}) \exp \left[-b \int_0^\xi |\kappa(\xi')|^2 d\xi' \right] \quad . \quad (6)$$

Very simply, the incident field decays exponentially as power leaks out along the η direction, as per our model. Then, by substituting Eq. (6) into Eq. (5), we can obtain an expression for the deflected field which depends on the grating coupling coefficient and the incident (RMS) field strength,

$$A(0, \bar{\eta}) = \sqrt{\frac{1}{b} \int_0^b |A(0, \eta)|^2 d\eta} \quad . \quad (7)$$

The Inverse Problem

Our aim, however, is to determine the coupling coefficient distribution that will yield a deflected beam with a desired lateral amplitude profile. We therefore define a deflectivity distribution,

$$\rho(\xi) = \left| \frac{B(\xi, b)}{A(0, \bar{\eta})} \right| = b\kappa_0(\xi) \exp \left[-b \int_0^\xi \kappa_0^2(\xi') d\xi' \right] \quad , \quad (8)$$

which we shall specify to be Gaussian and centered about the midpoint of the exit aperture (at $\eta=b$), i.e., $\rho(\xi) = \exp[-(\xi-a/2)^2/2\sigma^2]$. This equation can then be recast in the form of a differential equation, which we readily recognize to be a Bernoulli equation [14]:

$$\frac{d\kappa_0}{d\xi} = b\kappa_0^3 + \kappa_0 \left(\frac{1}{\rho} \frac{d\rho}{d\xi} \right) \quad (9)$$

After some algebraic manipulation, we obtain the expression:

$$\kappa_0(\xi) = \frac{\exp[-(\xi - \frac{a}{2})^2 / 2\sigma^2]}{\sqrt{b\sqrt{\pi}\sigma \left[\left(\frac{1+T}{1-T} \right) \operatorname{erf}\left(\frac{a}{2\sigma}\right) - \operatorname{erf}\left(\frac{2\xi-a}{2\sigma}\right) \right]}} \quad (10)$$

for the coupling coefficient function that will yield a deflected field with a Gaussian-like lateral profile. The parameter:

$$T = \left[\frac{A(a, \bar{\eta})}{A(0, \bar{\eta})} \right]^2 = \int_0^b |A(a, \eta)|^2 d\eta / \int_0^b |A(0, \eta)|^2 d\eta \quad (11)$$

is a necessary boundary condition for the problem and represents fractional power transmissivity through the grating. It follows then from power conservation that the deflection efficiency is $1-T$.

To verify our analytical result based on the weak coupling approximation, we incorporated the coupling coefficient function into our finite-difference scheme and allowed the fields to evolve. Figure 5a clearly shows that the deflected field has the desired Gaussian shape for its lateral amplitude distribution. The other important design criterion that has to be met is the deflection efficiency. For a grating which had been designed to produce a deflection efficiency of 0.05, we find that the numerical scheme results in a deflection efficiency of 0.02. This result is satisfactory and indicates that, in the weak coupling limit, our analytical theory is indeed valid. However, when the coupling is stronger, our analytical theory begins to break down. For example, when we design a grating with a deflection efficiency of 0.99, we numerically obtain an efficiency of only 0.47. In addition, we note that the Gaussian profile is very slightly asymmetric (see Fig. 5b). We conclude that although the approximate theory made possible analytical solutions, its validity was limited to the weak coupling regime.

NUMERICAL OPTIMIZATION

Clearly, the usefulness of such a beam-shaping deflector depends on how well the design targets for deflection efficiency and beam profile are met. In view of the limitation of the approximate theory, we developed an algorithm for numerically improving the deflection efficiency while maintaining the desired deflected beam shape.

In this algorithm, we use the coupling coefficient function that is obtained analytically as an initial estimate for our numerical scheme. We express this function as a superposition of Chebyshev polynomials of finite order (20 is often sufficient), and determine the coefficients for these polynomials. We then incorporate this coupling coefficient function into our finite-difference scheme and propagate the fields. Our optimization is complete if the deflected field,

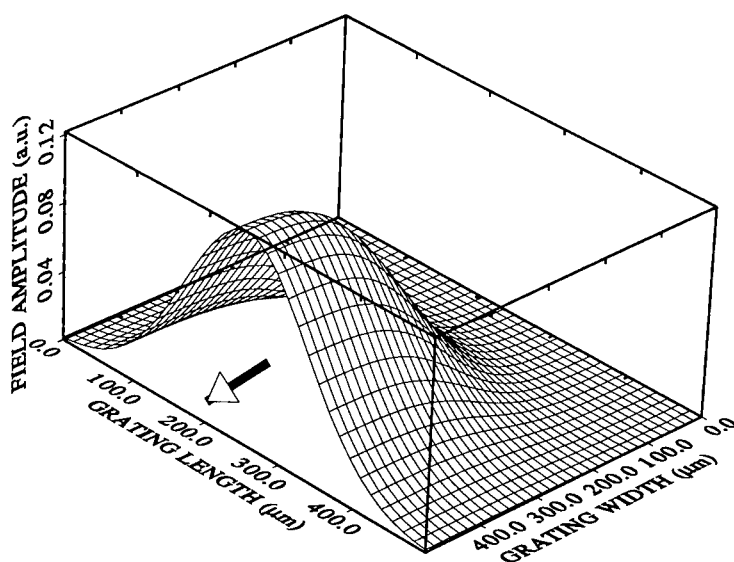


Fig. 5a Evolution of deflected field in a grating with adiabatic groove depth variation. Grating size is 500 μm by 500 μm , and $\kappa = 6 \times 10^{-4} \mu\text{m}^{-1}$ at deepest point. Deflection efficiency is 0.02.

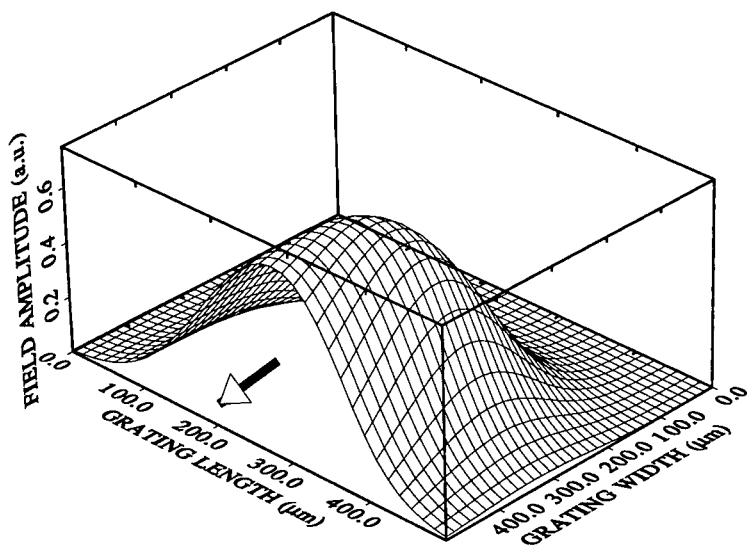


Fig. 5b Evolution of deflected field in a grating with adiabatic groove depth variation. Grating size is the same as in Fig. 5a, but $\kappa = 5.5 \times 10^{-3} \mu\text{m}^{-1}$ at deepest point. Deflection efficiency is 0.47.

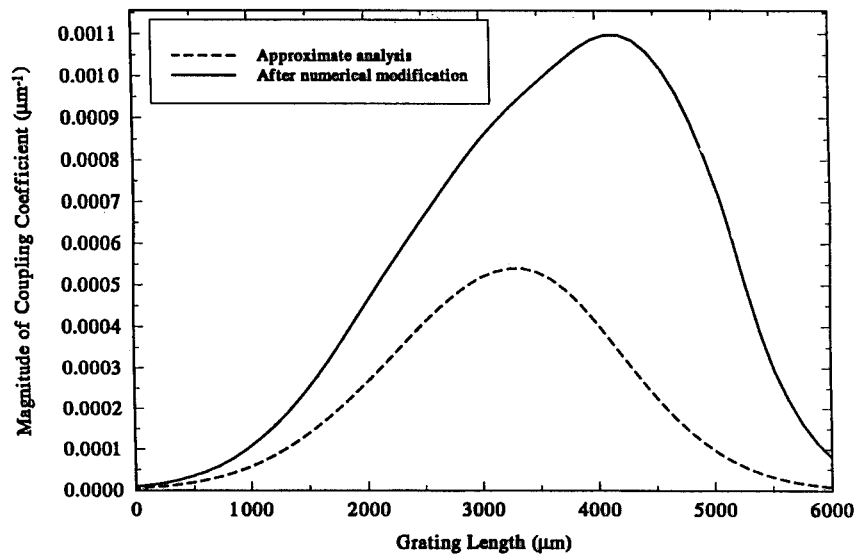


Fig. 6a Numerical optimization of analytically-derived coupling coefficient using Downhill Simplex minimization method and finite-difference propagation algorithm. Grating size is 6mm by 1mm.

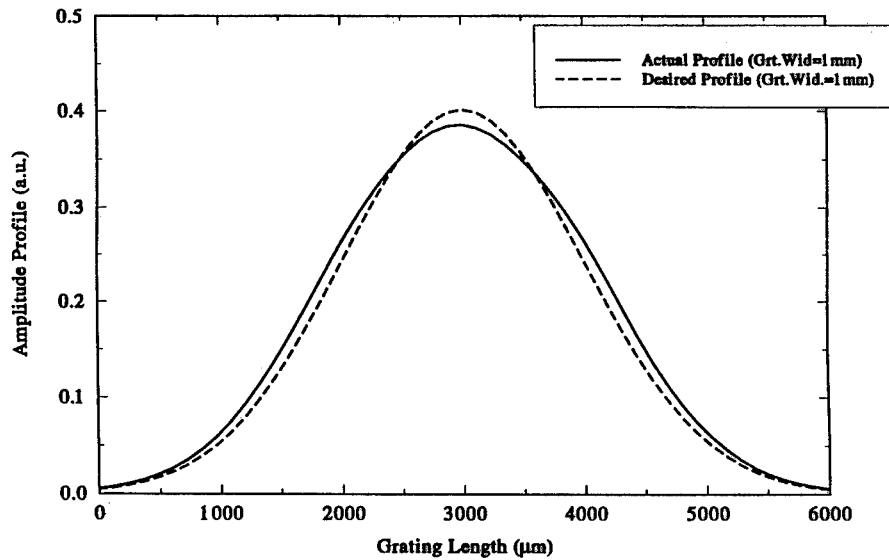


Fig. 6b Deflected beam with Gaussian-like profile and desired deflection efficiency of 0.65 is obtained after numerical optimization. Grating size is same as in Fig. 6a.

which results from the numerical propagation, meets the shape and deflection efficiency criteria that we set. If not, we vary the coefficients of the Chebyshev polynomials to obtain in essence a modified coupling coefficient function, and recompute the deflected field. This algorithm has been implemented using the standard Downhill Simplex minimization method [15], where the function to be minimized is the square of the relative error between the numerically computed deflected field profile and the desired field profile. A measure of the deflection efficiency is implicit in the magnitude of the deflected field distribution.

Our results indicate that this algorithm efficiently generates the correct coupling coefficient distribution (see Fig.6a) to satisfy our design requirements for deflection efficiency and beam shape. In our test case, the analytically derived coupling coefficient function was modified until the deflection efficiency of 0.65 was obtained (see Fig.6b). The optimization algorithm required 86 minutes on an HP Apollo series 735 workstation for a 300 x 50 computational grid. It appears that the analytical result based on the weak coupling approximation was significant in generating a suitable starting point for the optimization routine. In fact, in the absence of the initial analytical estimate for the coupling coefficient, which is surprisingly similar to the final result, the numerical algorithm does not even converge. In principle, this method can be applied to designing beam-shaping deflectors with arbitrarily high deflection efficiency.

SUMMARY

We have discussed the theory of the finite aperture grating deflector, and derived an analytical result for the required adiabatically-varying grating groove depth to obtain a desired lateral amplitude profile for the deflected field using a physically intuitive model. We have discussed the limitations of the theory due to the weak coupling approximation and demonstrated an algorithm through which the design criteria of deflection efficiency and beam shape can be met. This technique can be extended to the design of grating deflectors that generate other continuous, slowly-varying beam profiles such as the sine-squared function.

Our fabrication of this device in Potassium-Sodium ion-exchanged planar waveguides (in Soda-Lime and BK7 glasses) is underway. Plans to extend the theory, design and experiment to coupling between channel waveguides, in which the issue of mode-matching to attain high deflection efficiency is critical, are also in progress.

ACKNOWLEDGEMENTS

This research was supported by the Advanced Technology Program of the U.S. Department of Commerce through a grant to the National Storage Industry Consortium.

REFERENCES

- [1] T. Tamir, in *Integrated Optics*, T. Tamir, ed. (Springer-Verlag, Berlin 1975).
- [2] H. Nishihara, M. Haruna, and T. Suhara, *Optical Integrated Circuits* (McGraw-Hill, New York 1989).
- [3] K.K. Svidzinskii, Sov. J. Quantum Electron., **10**(9), 1103 (1980).
- [4] J. Van Roey and P.E. Lagasse, Appl. Opt., **20**(3), 423 (1981).
- [5] A.M. Belin, K.K. Svidzinskii, and G.M. Turbina, Sov. J. Quantum Electron., **12**(9), 1153

(1982).

- [6] L.M. Walpita and C.W. Pitt, *Appl. Opt.*, **23**(19), 3434 (1984).
- [7] K. Wagatsuma, H. Sakaki, and S. Saito, *IEEE J. Quantum Electron.*, **15**(7), 632 (1979).
- [8] L.A. Weller-Brophy and D.G. Hall, *IEEE J. Quantum Electron.*, **6**(6), 1069 (1988).
- [9] H. Kogelnik, in *Guided-Wave Optoelectronics*, T. Tamir, ed. (Springer-Verlag, Berlin 1988).
- [10] W. Streifer, D. Scifres, and R.D. Burnham, *IEEE J. Quantum Electron.*, **11**(11), 867 (1975).
- [11] R. Courant and D. Hilbert, Chpt. 5 in *Methods of Mathematical Physics Vol. II* (Interscience, New York 1962).
- [12] H. Kogelnik, *Bell Sys. Tech. J.*, **55**(1), 109 (1976).
- [13] K.A. Bates, L. Li, R.L. Roncone, and J.J. Burke, *Appl. Opt.*, **32**(12), 2112 (1993).
- [14] M. Tennenbaum and H. Pollard, *Ordinary Differential Equations* (Harper & Row, New York 1963).
- [15] W.H. Press, B.P. Flannery, S.A. Teukolsky, and W.T. Vetterling, *Numerical Recipes: The Art Of Scientific Computing* (Cambridge Univ. Press, Cambridge 1986).

WAVEGUIDE COUPLING GRATINGS: ATTRACTIVE FEATURES AND DANGEROUS PITFALLS

Olivier Parriaux,¹ Vladimir A. Sychugov,² Alexander V. Tishchenko²

¹CSEM Swiss Center for Electronics and Microtechnology Inc.,
CH-2007 Neuchâtel, Switzerland

²Institute of General Physics,
Moscow 117942, Russia

I INTRODUCTION

Grating coupling is the waveguide access technology which in principle allows for the integration of the access function together with the integrated optical processing functions on a monolithic planar substrate. The fundamental merit of grating coupling technology is its geometrical and, to a large extent, its technological compatibility with the planar processes which define the integrated signal processing waveguide circuit. However, poor coupling efficiency, highly dispersive character, absence of user friendly modelling tools, fabrication difficulties have long prevented this technology from being implemented into practical sensor and microsystem designs. Most of these difficulties are being overcome and grating couplers are envisaged as part of commercial system applications. This contribution will review the points where recent technological progress are decisive, illustrate for the future users some attractive features of waveguide coupling gratings and also underline for the designer some of the traps that may be encountered.

The subject of corrugation coupling gratings has been treated since the beginning of Integrated Optics¹ since trapping light into waveguides necessarily implies coupling it to and from the outside world. Grating coupling is not the only access technology. For laboratory use, prism excitation is the most convenient technique whereas in communication components such as lithium niobate modulators and passive power splitters, fibre pigtailling is the most efficient approach which in addition is polarization and wavelength independent. Grating coupling is bound to be used in sensors and microsystems where cost, compactness, multifunctionality, planarization are prime prerequisites. They may also become useful for non-linear effects; but this is not the subject of the present paper.

I.1 Direct Writing of Coupling Gratings

The main technological progress allowing fabricability concerns the writing and the transfer of the grating patterns. Writing technology has experienced a big jump ahead since the introduction of electron beam pattern generators (BPG) in most maskshops. BPGs enable the direct writing of submicron gratings achieving complex functions. Variable dose or variable energy writing gives freedom on the groove profile which can then be cheaply reproduced with high fidelity by replication technologies² such as embossing and casting. More than 40% input coupling efficiency has been achieved by means of a blazed focusing grating into a strip polymer waveguide³. A recent significant progress in e-beam technology is the capability of writing smooth grating lines in a vector scan mode⁴ which leads to low aberration and low

loss curved gratings. Figure 1 is the comparison between two writing strategies of a focusing grating. Both are electron microscope pictures of the same grating. The grating of Fig. 1a) was written by means of a ZBA 23H BPG whereas that of Fig. 1b) was written by means of a LION LV1 BPG⁴, both produced by Jenoptik Jena. Although the visual aspects are strikingly different, the optical function performance is less affected and the use of a ZBA-like machine is still recommended when the writing time is a subject of concern.

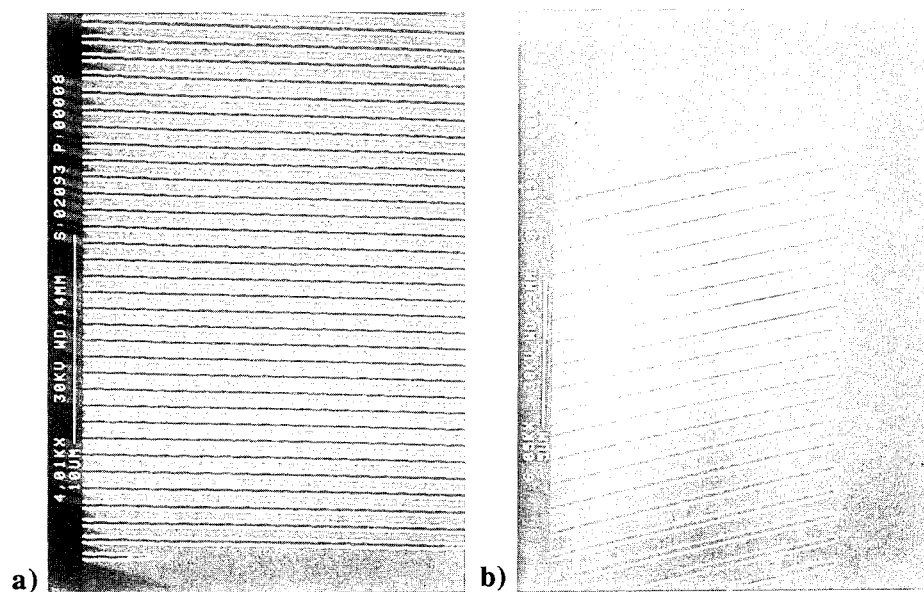


Figure 1. Optical microscope picture of a curved grating directly written in an e-beam resist, grating area 1mm². a) by means of a ZBA 23H, variable shape beam, address size 50 nm, writing time 4 min. b) by means of a vector scan LION LV1 machine⁴, Gaussian beam, address size 10 nm, writing time 20 min.

1.2 Photolithographic Transfer of High Spatial Frequency Gratings

The photolithographic mask transfer of high spatial frequency gratings is another technological step where important progress have been made. An expensive e-beam chromium photomask must be cheaply transferrable for cost effective grating devices. The early proposed photolithographic scheme under oblique incidence^{5,6} has been further developed⁷ in particular for the transfer of the grating mirrors of DFB lasers⁸. An important practical feature that has been recently revealed by extensive theoretical and experimental results is the large tolerance on the oblique incidence transfer conditions. The same angle of incidence can be used for the high contrast transfer of variable pitch gratings, curved gratings, gratings of different spatial frequency and radial gratings. The transfer technique can be operated with a laser or a filtered and polarized standard Hg lamp. Figure 2 is the grey-tone copy of two colour pictures representing two illuminated arrays of 16 400 x 400 μm grating patches of periods 0.3 μm and 0.4 μm (Fig. a) and b) resp) transferred into a thin resist film on a metal substrate. The gratings are very uniform and the grooves are open down to the metal substrate.

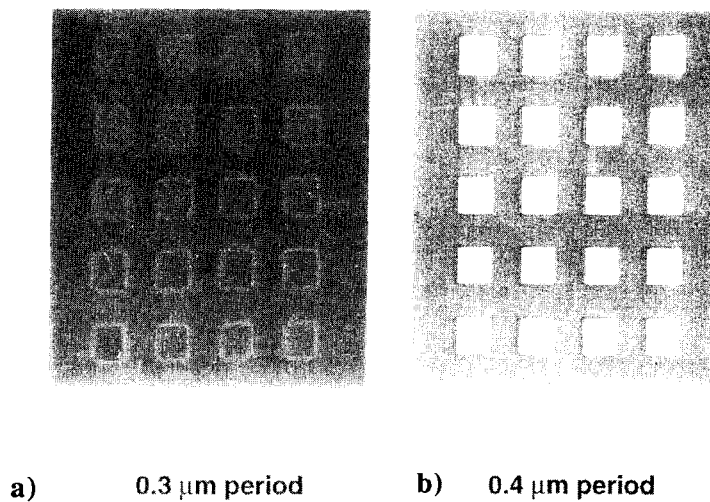
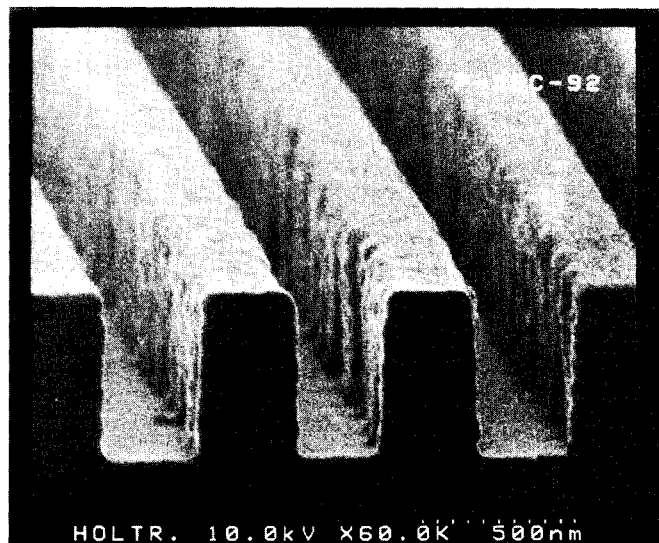


Figure 2. Optical binocular picture of an array of transferred submicron gratings showing good uniformity⁷; a) 0.3 μm period; b) 0.4 μm period.

Another, quite generic, photolithographic technique rests on a holographic principle⁹. The hologram of a chromium mask is first recorded; then a writing laser beam reconstructs the image of the mask on a resist coated substrate placed in proximity in a scan mode by means of a machine very similar to conventional proximity transfer aligners. There are no limitations as to the polarization, the spatial frequency and the orientation of the grooves. Periodic as well as non periodic features can equally be transferred. Figure 3 shows the SEM picture of a high aspect ratio rectangular groove of 0.6 μm period transferred into a thick photoresist film.

Figure 3
SEM picture of a 0.6 μm period rectangular grating obtained by holographic mask transfer⁹.



I.3 CAD Tools

Another difficulty has been the poor input coupling efficiency generally obtained from a grating which has not been carefully designed: a number of possible diffraction orders are generally involved and some surprises can be encountered in the coupling coefficient dependence on the opto-geometrical parameters. There are no simple mental concepts allowing the anticipation of the properties of a given coupling structure. It is even more difficult to design a grating structure exhibiting a set of desired features. Such difficulty can now be overcome thanks to a few available, practical modelling tools^{10, 11}. The examples of coupling grating features and possible pitfalls described hereafter will be treated by means of existing codes that have been further developed and tested within the frame of a BRITE project¹². Such tools are based on the Fourier-Rayleigh approximation which has been shown to be sufficient for most practical cases of interest¹² and are capable of simulating practical coupling configurations involving a finite size coupled beam of arbitrary orientation and polarization, and a finite area grating. The kind of coupling structures considered is illustrated in figure 4.

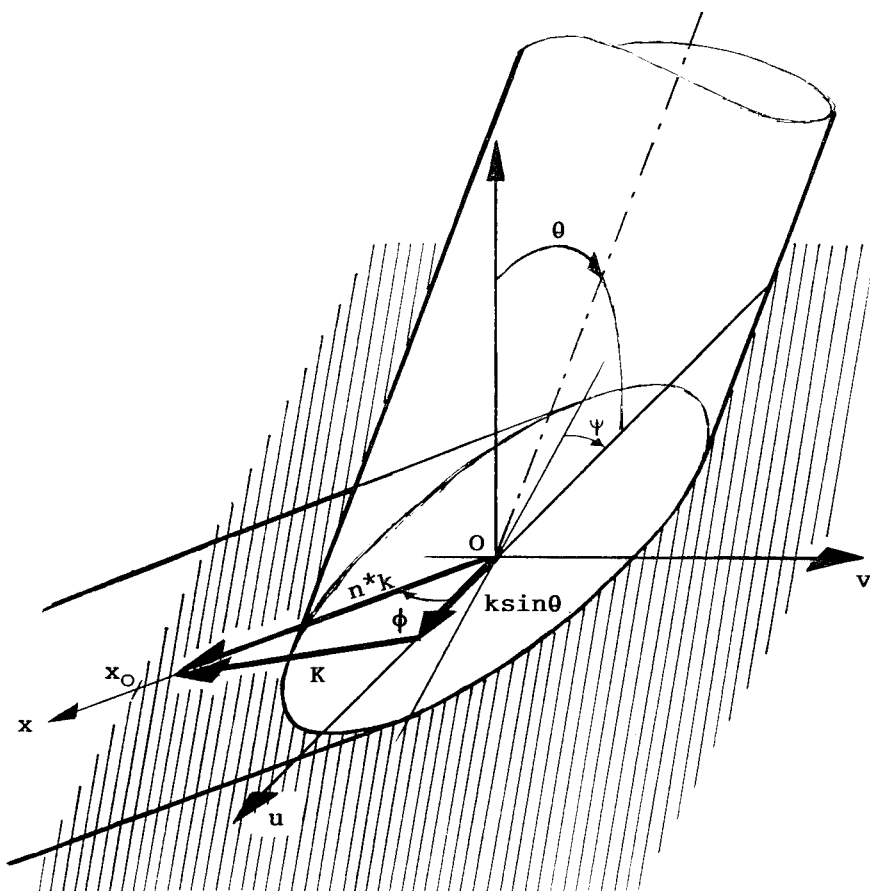


Figure 4. General non-collinear waveguide coupling grating configuration. ψ is the orientation of the grating edge. ϕ is the direction of the coupled guided beam.

II Matching the Incident Beam with the Coupling Grating: Some Rules

The practical problem of coupling a limited cross-section free space wave into a planar waveguide by means of a finite size grating amounts to optimally managing the power coupled in and the power coupled out by the grating. In the collinear case, where the direction of the coupled waveguide mode and the grating vector K coincide and lie in the incidence plane, a maximum power coupling efficiency of about 80 % can be obtained if the incident beam has a Gaussian field amplitude profile and if the grating is uniform¹³. Such maximum coupling situation is governed by two relationships¹⁴ linking the opto-geometrical quantities w (half-width of the incident Gaussian field distribution), θ (the incidence angle), x_0 (the distance between the beam axis impact in the grating area and the grating front edge) and the important quantity α (the field radiation loss coefficient) which characterizes the waveguide grating:

$$\alpha w = 0.68 \cos \theta \quad (1)$$

$$\alpha x_0 = 0.5 \quad (2)$$

Expressions (1) and (2) establish the relationship between the incident beam geometry via w , the relative position in space of the beam and the finite size grating via θ and x_0 , and the waveguide grating strength via α . As an approximate rule in cases where the incidence is not too far from normal, we can state that x_0 must be roughly equal to w and that both must be equal to $1/2\alpha$.

The radiation loss coefficient α is a fundamental quantity. Some insight in its physical content can be gained by looking at its analytical expression obtained under the Rayleigh approximation¹⁵ in the simple but practically very relevant case of a step index waveguide profile of substrate, guide and cover index n_1 , n_2 , n_3 and thickness h , propagating a TE mode, the grating being defined at the guide-cover interface:

$$\alpha = \left(\frac{k\sigma}{2} \right)^2 \frac{n_2^2 - n^*{}^2}{n^* h^*} \frac{(n_2^2 - n_1^2) \{ N_3 N_2^2 + N_1 [N_3^2 + (n_2^2 - n_3^2) \cos^2(N_2 k h)] \}}{[N_2^2 + N_3 N_1]^2 - (n_2^2 - n_3^2)(n_2^2 - n_1^2) \cos^2 N_2 k h} \quad (3)$$

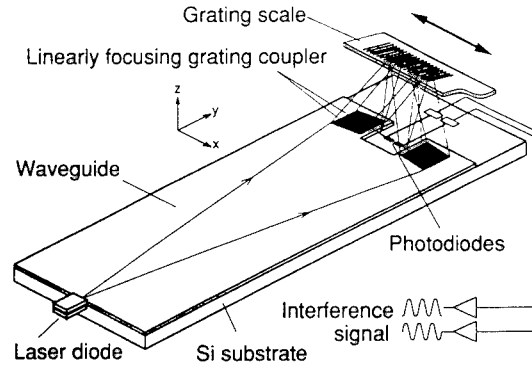
where

$N_i = \sqrt{n_i^2 - (n^* - \lambda / \Lambda)^2}$, $k = 2\pi / \lambda$. λ is the wavelength in vacuum, n^* is the TE mode effective index and h^* is the effective waveguide thickness. 2σ is the peak to peak grating depth.

Expression (3) reveals several interesting features of α which are discussed in more details elsewhere¹⁵: α depends on the square of the corrugation depth (2σ), it increases with the modal field confinement and it depends on how the radiated waves interfere in the cover material via the cosine terms.

What has been said so far concerns collinear coupling. A number of practically foreseeable situations, however, will impose a non-collinear coupling configuration as illustrated in figure 5 in the application case of a moving grating displacement readout head¹⁶. In this more general case of non-collinear coupling, a third condition must be satisfied which concerns the orientation of the front edge of the grating area¹⁷.

Figure 5
Example of non-collinear grating coupling applied to the interferometric readout of a translation encoder¹⁶.



This additional condition can be simply understood from the meaning of the collinear coupling event where the incident Gaussian beam of half-width w makes an angle θ with the normal of the waveguide grating plane. Let us consider figure 4 again. The coordinate system (u, v) is centred at the impact point O of the incident beam axis. u is arbitrarily directed in the plane of incidence. The incident field distribution $E(u, v)$ in the grating plane is a Gaussian given by

$$E(u, v) = E_0 \exp \left\{ -\frac{1}{w^2} (u^2 \cos^2 \theta + v^2) \right\} \quad (4)$$

Consequently, the equi-amplitude incident field traces in the grating plane are ellipses with their major axis directed along the u -coordinate. The direction of the coupled guided mode is set by the angle ϕ which results from the synchronism condition

$$\cos \phi = (n^*{}^2 + \sin^2 \theta - K^2 / k^2) / 2 n^* \sin \theta \quad (5)$$

where $K = 2\pi/\Lambda$ is the grating spatial frequency. Λ is the grating period defined orthogonally to the grating grooves. x is the axis of the waveguide coupled beam. All straight lines parallel to x and intersecting the u axis at ordinate u_0 make a slice in the field distribution $E(u, v)$. Using expression (4), the field distribution along these lines is

$$E(u_0, v) = E_0 \exp \left\{ -\frac{1}{w^2} \left[\left(u_0 - \frac{v}{\tan \phi} \right)^2 + v^2 \right] \right\} \quad (6)$$

These are all Gaussian functions having the same half-width w_ϕ along x :

$$w_\phi = w / \sqrt{1 - \cos^2 \phi \sin^2 \theta} \quad (7)$$

The locus of the positions in the (u, v) plane of the field maxima in the set of Gaussian profiles with u_0 as a parameter is a straight line making an angle ψ (all angles are defined counter-clockwise) with axis u . ψ is obtained by cancelling the derivative of $E(u_0, v)$ relative to v . This yields the expression

$$\operatorname{tg} \psi \operatorname{tg} \phi = -\cos^2 \theta \quad (8)$$

As from now, the problem is the same as in the collinear case: for a maximum power coupled into the waveguide, the grating front edge must be a straight line of angle ψ linking the maxima of the Gaussian profiles, and located at distance x_0 away from the latter along direction x . It is useful to point out that the straight line of angle ψ given by expression (8) is also the line joining the two intersection points between the equi-amplitude ellipses and their tangents of orientation ϕ . This gives a simple geometrical definition of the optimum grating front edge orientation.

The set of three conditions for maximum coupling in the non-collinear case are therefore:

$$\alpha w = 0.68 \sqrt{1 - \cos^2 \phi \sin^2 \theta}$$

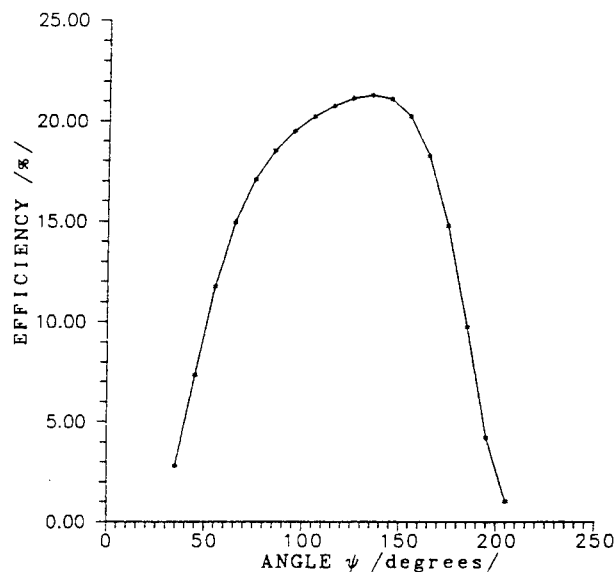
$$\alpha x_0 = 0.5 \quad (9)$$

$$\operatorname{tg} \psi \operatorname{tg} \phi = -\cos^2 \theta$$

The radiation coefficient α in the general non-collinear case is a complicated expression involving both polarizations which can be found elsewhere^{18,19,20}. However, the computer assisted design tool¹⁰ described above finds the optimum excitation configuration satisfying all three expressions (9) and provides itself with the necessary intermediate results such as α .

Figure 6 illustrates how critical is the direction ψ of the gratings front edge for the achievement of a high power coupling efficiency. There is a maximum of 21% power coupling into the propagating TE₀ mode from an incident beam having a TE polarization relative to the incidence plane. Leaving the period, beam and waveguide characteristics unchanged, the orientation ψ of the front edge is rotated around the point located at distance x_0 from the coordinate centre O in the direction of maximum coupling ϕ . It appears that the condition on ψ is not sharply critical: there is in the considered case an angular tolerance range of about 90°. Outside this range the efficiency falls off rapidly.

Figure 6
Coupling efficiency of a semi-infinite grating versus the grating front edge orientation ψ .
Waveguide thickness $h = 0.5 \mu\text{m}$.
Cover, waveguide, substrate index: 1, 1.66, 1.52. Wavelength: 633 nm. Sinusoidal grating of period 618 nm and depth 50 nm. Gaussian beam of half-width $w = 346 \mu\text{m}$, incidence angle $\theta = 45^\circ$, axis located at distance $x_0 = 310 \mu\text{m}$ from the grating front edge in the direction $\phi = 26.83^\circ$ of the guided mode for maximum coupling. The grating vector is at 45° relative to the incidence plane.



As from now on, we will go through a number of examples of coupling gratings exhibiting practically attractive as well as dangerous features. All cases will be analysed by means of existing codes¹⁰ or by specific programs all based on the Fourier-Rayleigh approximation. The set of examples given hereafter is just a selection of possibly interesting functional structures amongst known grating elements. It is likely that additional, yet unknown features, will be unveiled as soon as flexible modelling tools, associated with simple mental concepts, can be used. This statement rests on the assumption that much can be expected from a structure associating a diffractive element, or feedback element, with a transverse resonator which a waveguide is.

III High-Efficiency TM-TE Beam Expander

High efficiency grating coupling from a narrow free space beam to an enlarged guided wave can be a practically interesting element since a single periodic corrugation would combine the beam coupling function with that of beam expansion. This could thus spare the necessary beam expanding pair of lenses which are difficult elements to integrate. Quite a few coupling configuration are possible which can give rise to beam expansion: actually any non-collinear grating coupler provides some expansion of the incoming beam. However, the coupling efficiency is generally very low and there is just one very interesting case¹⁹ that was revealed by using the CAD tool developed by the authors¹⁰. This case is represented in figure 7. A TM free space Gaussian beam of half-width w impinges on the corrugation grating from the air side at a large angle of incidence θ . The spatial frequency vector K of the grating is oriented so as to synchronously excite the TE_0 guided mode of a slab waveguide in a direction which is normal to the incidence plane.

Figure 7
Grating coupling geometry of a high-efficiency TM-TE beam expander.

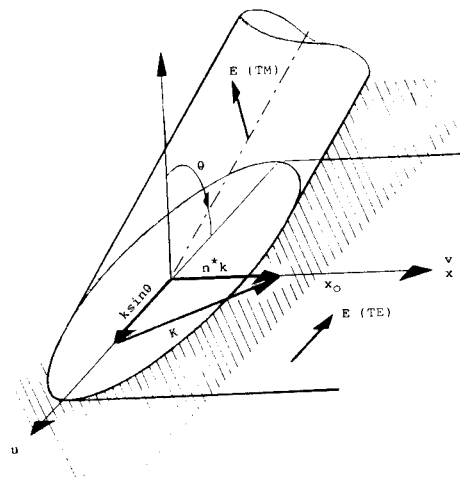
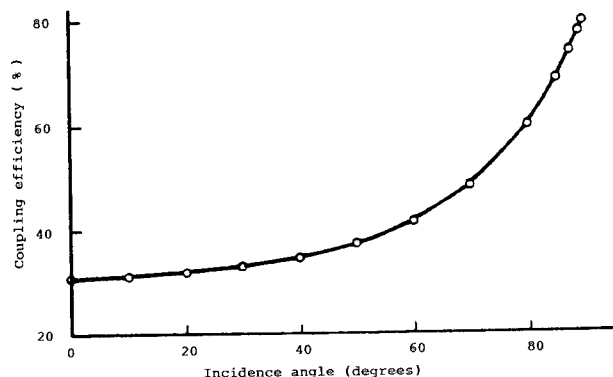


Figure 8
Power coupling efficiency of the TM-TE beam expander versus the angle of incidence. The synchronism condition is always satisfied. Gaussian index profile with 0.07 index increase, 0.4 μm depth. $\lambda = 633\text{nm}$.



As figure 8 shows in the case of a high guidance ion-exchanged waveguide on glass with a shallow sinusoidal corrugation grating of 10 nm depth, the coupling efficiency is very high, increases with increasing incidence angle θ and reaches the maximum 80 % at grazing incidence.

This example of a TE-TM mode converter beam expander illustrates how useful it may be to get off the limited configuration of collinear grating coupling. Waveguide conical diffraction allows for a more complex optical functionality. Non-collinear coupling can find useful practical applications as shown in figure 5 where grating antennae can be advantageously used in a moving grating displacement sensor^{16,21} where they achieve all at once waveguide coupling, linear focusing, beam redirecting and give an elegant solution to the topological problem of this type of interferometric sensor performing in a reflection configuration. The functional complexity allowed by non-collinear coupling, and also its geometrical complexity render a realistic modelling tool indispensable as soon as the engineering of a device is concerned as it is the case now in the fields of displacement sensors and various pickup devices^{22,23}.

IV Waveguide Grating Polarizer

A lot has been published on waveguide polarizers based on the resonant coupling between the TM waveguide mode and the TM plasmon mode at the waveguide side of a metal film deposited at the waveguide surface through a thin low index buffer layer located between the waveguide surface and the metal film²⁴. The resonant coupling only affects the TM mode which experiences a strong attenuation whereas the TE waveguide mode propagates almost unaffected under the metal film. A differential attenuation of -40dB between TM and TE modes can easily be achieved²⁵.

This approach suffers two limitations: first it does not allow for polarization separation. Secondly, only the TM mode power can be suppressed. This is one of the difficulties of the more general problem of guided wave polarization optics. It has long been known that waveguide coupling grating can give a simple solution to the TE mode filtering out²⁶ and, in some applications cases, to waveguide polarization splitting. This feature was experimentally demonstrated long ago²⁷. The TE waveguide polarizer is represented in figure 9. The waveguide structure considered here is a single mode ion exchanged glass substrate with a 0.01 index increase ERFC profile of 3 μm depth. The wavelength is 0.8 μm . The grating is made by etching a 2.4 index TiO_2 film of 50 nm thickness. The polarizing effect occurs for high spatial frequency corrugation gratings which would radiate the guided waves essentially contra-directionally in the substrate only. The remarkable feature is illustrated in figures 10 showing the field radiation loss coefficient of the TE_0 and TM_0 waves versus the radiation angle. In the presently considered waveguide structure the TM_0 radiation remains negligible up to period $\Lambda = 0.31 \mu\text{m}$, corresponding to a radiation angle of -45° degrees in the substrate whereas the TE_0 radiation loss coefficient remains steadily quite high. As an example, a 2.5 mm long grating leads to a TE radiation loss of -28 dB and a TM excess loss of -0.01 dB.

This polarization separation effect results from the dramatic fall of the TM mode radiation coefficient over an wide angular range. This can be understood as a Brewster condition for the -1 diffraction order of the grating²⁸. From this standpoint it is expected that the same effect will be present also in channel waveguides.

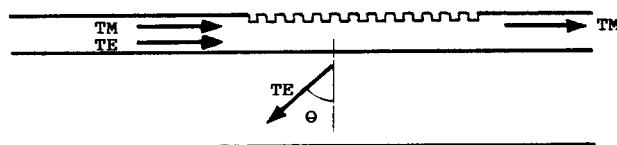


Figure 9
Sketch of a TM propagating, TE
out-filtering waveguide grating.

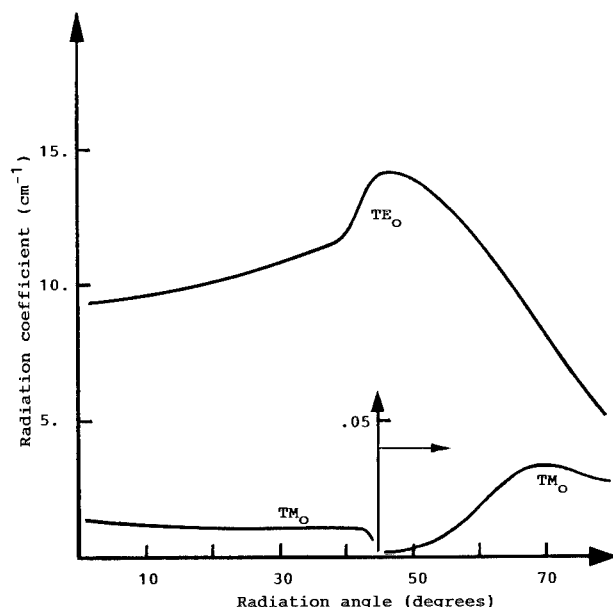


Figure 10. Field radiation loss coefficient of the guided TE₀ and TM₀ modes versus radiation angle. ERF waveguide profile with 0.01 index increase, $h = 3 \mu\text{m}$.

V Single-Order Coupling by Dual-Undulation Gratings

In most grating coupling configurations of practical interest, the incoming free space beam incidence is not too far from normal. This implies conversely that a guided wave radiates into both the substrate and the cover. For TE waves, and in the case of a single undulation gratings, the ratio of power radiated into the air (medium 1 of index n_1) and into the substrate (medium 3 of index n_3) is given by the approximate expression²⁹: $\alpha_1/\alpha_3 = N_1/N_3$, where α_i are the radiation loss coefficients into media 1 and 3. That is, in the case of an air cover and glass waveguide, no more than 40 % power radiates into the air. This places an unacceptable limit upon the incoupling efficiency from the air side which is the case most often met in practice.

A solution which was demonstrated experimentally^{30,31}, and a variant thereof recently³², is to use a grating waveguide with two corrugated boundaries. As illustrated in figure 11a) the double undulation is that of a high index film deposited on top of an existing waveguide as in ref. 31 or it can also be the two boundaries of a deposited step index waveguide³⁰ as illustrated in figure 11b). The total guided mode diffraction is the superposition of the diffracted radiation due to each undulation, in either outer medium, taking into account the phase shift between them. The resulting interference depends therefore on the relative position of the two undulations and on their amplitude σ_1 and σ_2 . Simplified design rules have been obtained in both cases of figures 11a)³³ and 11b)³¹. They give the depth σ_i of each corrugation under the requirement that the diffraction efficiencies are equal and the necessary phase shift between the two undulations in terms of the radiation angle and the index n_2 and thickness h of the waveguide layer.

In the case of a TE mode propagating in a step index waveguide with its two sides corrugated, a maximum radiation takes place in the cover in the -1st order if the following condition is satisfied:

$$\frac{\sigma_2}{\sigma_1} = N_2 \left\{ N_2^2 \cos^2 \Delta / 2 + N_1^2 \sin^2 \Delta / 2 \right\}^{-1/2} \sqrt{\frac{n_2^2 - n_1^2}{n_2^2 - n_3^2}} \quad (10)$$

where $\Delta = 2 k h N_2$

and if the phase shift φ between the two undulation is $\varphi = -m \pi + \arctan \frac{N_1}{N_2} (\tan \Delta / 2)$.

A remarkable feature of this solution is that it is non-resonant. It is of interferential nature, thus little sensitive in the geometrical characteristics of the double undulation. Radiation into the air of more than 95% was measured³¹ after a technological sequence of glass etching followed by isotropic high index film deposition, then ion beam etching under an angle. Extended results are still awaited from a technologically simpler and practically more applicable sequence of processes: glass etching followed by high index film deposition under an angle³².

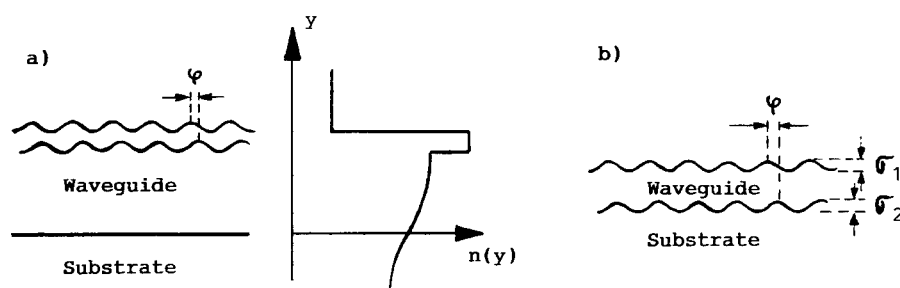


Figure 11. Sketch of a single-order, double-undulation waveguide grating. a): The corrugation is at the two sides of a high index film coating a diffused planar waveguide. b): The two sides of a step index waveguide are corrugated.

VI Substrate Enhanced Grating Efficiency

One of the most promising passive waveguide technologies is the CVD of silica based step index dielectric films on a single crystal silicon substrate. This approach is especially interesting for sensor and microsystem applications since it is fully compatible with microelectronics tools and processes. Submicron coupling grating technology can in principle also be implemented accordingly but the relevant low cost photolithographic technique is not ready yet or, if ready⁹, not widespread enough presently. Grating coupling into or from waveguides based on a silicon substrate benefits from a unique feature which is inherent to the very presence of a high index substrate. As illustrated in figure 12, the wave radiated into the silica buffer, and strongly reflected by the high index difference substrate-buffer interface, can be re-used to interfere with the wave radiated into the cover. Constructive interference in the cover gives rise to maximum radiation into the cover (usually air) and opens the way to the use of high efficiency flat optical antennae³⁴ as illustrated in figure 12a). Destructive interference into the cover leads to high efficiency power radiation into the silicon substrate towards a photodetector for applications which need integrated photoelectric detection as shown in figure 12b).

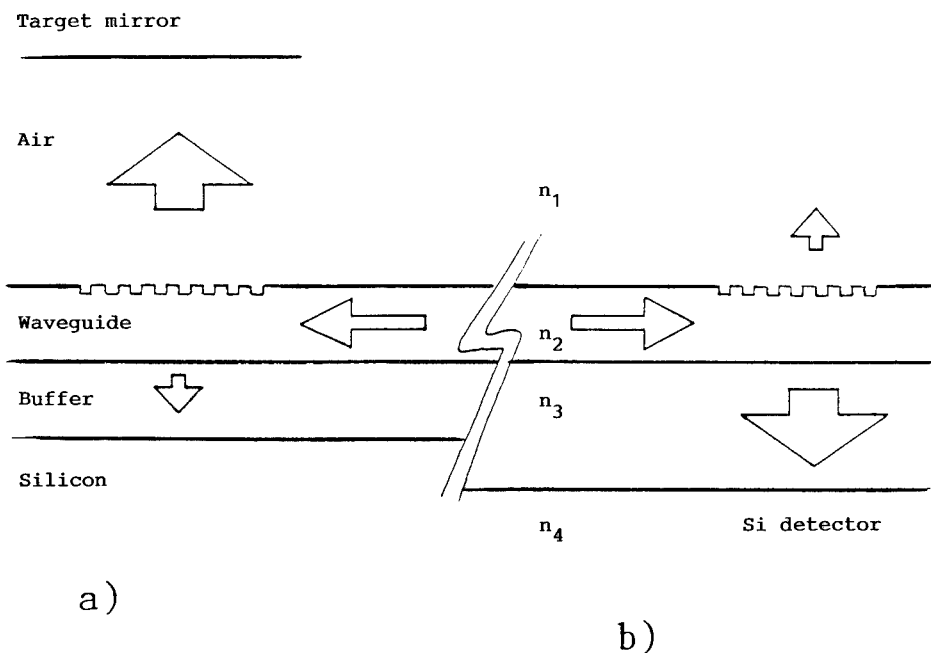
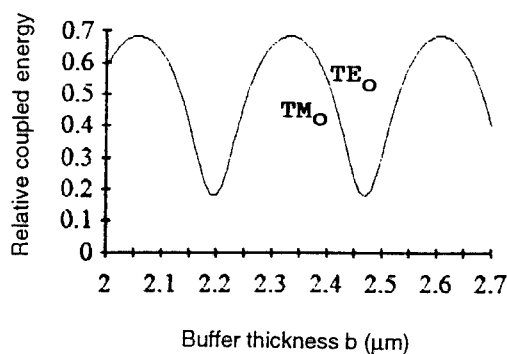


Figure 12. Waveguide grating based on a high-reflectivity substrate; a): High efficiency flat optical antenna; b): High-efficiency coupling into the substrate.

The interference condition depends in an oscillatory fashion on a number of structure parameters³⁵. The most important parameter is the buffer thickness b . Figure 13 illustrates the relative power coupled into the cover versus b . b is given reasonable values at which the gratingless waveguide mode does not leak into the silicon substrate. The relative power coupled into the silicon substrate is the complement to 1 of the curve of figure 13. The curve is practically identical for both TE_0 and TM_0 modes; the only difference is in the radiation loss coefficient which is larger for TE modes³⁶.

Figure 13
Relative power coupled from the waveguide grating of figure 12 into the air versus the buffer thickness in microns in the case of a large guidance silicon nitride waveguide ($n_2 = 2$), waveguide thickness $0.2 \mu\text{m}$, wavelength $0.8 \mu\text{m}$, fused quartz buffer ($n_3 = 1.46$) and silicon base ($n_4 = 4.6 + 0.003i$). With $\Lambda = 0.49 \mu\text{m}$, the radiation is close to normal.



The buffer thickness b giving maximum TE and TM radiation into the cover is given by³⁵:

$$b = \frac{-\phi + \tan^{-1}(X) + m\pi}{2kN_3} \quad (11)$$

The quantities Φ and X are long algebraic phase shift expressions which are given in ref. 35.

Simple closed form expressions for the maximum relative relative power P_c radiated into the cover material of index n_1 can be obtained in the case of close to normal radiation

$$P_c = n_1 / \left(n_1 + \frac{n_3}{n_4} n_3 \right) \quad (12)$$

As an example, the maximum power sent into the air from a structure composed of a silica buffer and a Si_3N_4 waveguide ($n_2 = 2$, $n_3 = 1.46$ and silicon index $n_4 = 4.6$) is 68 %.

The maximum relative power P_s coupled into the silicon substrate is given by

$$P_s = n_4 / (n_1 + n_4) \quad (13)$$

This amounts to 82 % for the same structure.

These figures reveal a very strong asset of silicon based technology: not only the very presence of the high index substrate allows coupling efficiencies which are acceptable for most applications but the grating technology is also very easy since it amounts to a simple etching of the waveguide material at a quite shallow depth of the order of 10 nm depending on the waveguide index.

VII Total Reflection from a Corrugated Waveguide Surface

Coupling of light into a waveguide by means of a grating is inherently associated with radiation out of the waveguide. Assuming excitation from the cover, as illustrated in figure 14, the wave radiated into the substrate by the first order of the grating is parallel to the uncoupled transmitted wave whereas the 1st order wave radiated into the cover is parallel to the specularly reflected incident beam. Therefore an interference takes place in the substrate and in the cover. The interference conditions depend on the waveguide coupling conditions which determine the amplitude and phase of the coupled, then re-radiated waves. The reflected and transmitted wave fields are π phase shifted. It follows that by an altering of the mode excitation conditions, eg the incidence angle, a destructive interference can be produced in the substrate which amounts to an abnormal total reflection of the incident wave³⁷. If the grating is at the substrate guide interface, it is also possible to obtain a condition for the cancelling of the specular reflection³⁸. Figure 15 illustrates the relative transmitted and reflected power versus the angle of incidence in the case of a corrugation grating mode in a parabolic profile waveguide. Both waveguide and grating are lossless.

Figure 14

Waveguide grating coupling configuration. θ_1 and θ_2 are the incidence and transmission angles, 2σ is the full grating depth, h the waveguide thickness.

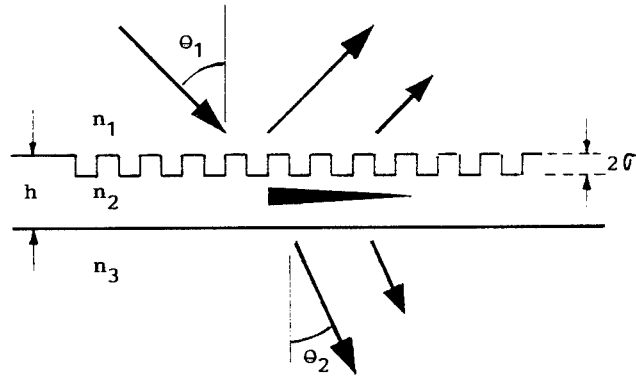
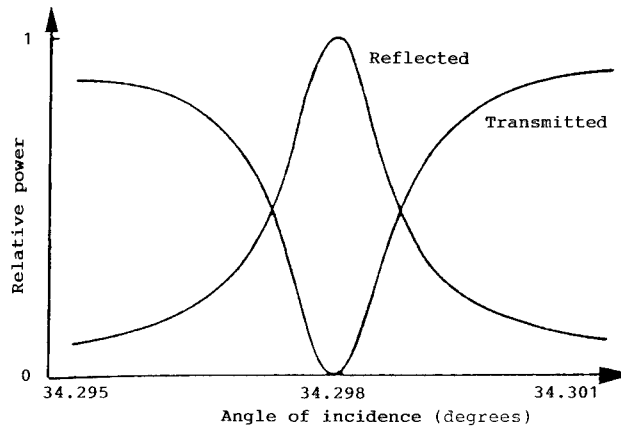


Figure 15

Relative reflected and transmitted power versus incidence angle θ_1 in degrees in the case of a parabolic profile glass waveguide of 0.01 index increase. $n_3 = 1.512$, $2\sigma = 40$ nm, $\lambda = 633$ nm. Curve a): relative reflection. Curve b): relative transmission.



Expression (14) gives the conditions that must be fulfilled for total abnormal reflection of a TE polarization from a step index waveguide³⁸:

$$\left(\frac{\lambda}{\Lambda} - n\right)^2 = (n_1 \sin \theta)^2 + (k^{-1} \text{Im}(\kappa))^2 \quad (14)$$

when $\alpha w \gg 1$

where $\kappa = \kappa' + i\kappa''$ is the second order intraguide coupling coefficient. Abnormal reflection is highly angle and wavelength sensitive. It can be used for highly selective wavelength filters. However, its angular sensitivity restricts its use. Due to the resonant character of waveguide excitation, abnormal reflection is approximately concentrated in the following angular $\Delta\theta$ and spectral range $\Delta\lambda$ ³⁹:

$$\Delta\theta = \lambda\alpha / 4\pi \cos \theta \quad \text{and} \quad \Delta\lambda = \Lambda\lambda\alpha / 4\pi \quad (15)$$

where α is the total field radiation loss coefficient and Λ the grating period. There are quite a few possible applications if significantly less than 100% reflection is tolerated, ie, when one wishes to tailor the reflectivity angular and wavelength spectra of a surface. As a rule, abnormal reflection takes place when $\alpha \gg \alpha_d$ where α_d is the total dissipative and scattering loss of

the waveguide grating. In addition, there is no abnormal reflection if $2w\alpha \ll 1$; there is abnormal reflection but no beam widening for $2w\alpha \gg 1$ and there is also beam widening when $2w\alpha$ is about 1.

The type of application where the highly angular and wavelength selectivity of close to 100 % abnormal reflectivity can best be exploited is in physical systems where stimulated light amplification takes place. Abnormal reflection also takes place at normal incidence. A waveguide grating can thus be the metal-less, single layer mirror of a laser. The feedback properties of such mirror, are unique: not only it provides a wavelength selective mirror, therefore temporal coherence, similarly to a dielectric multilayer, but it also provides a means of increasing the spatial coherence of the laser beam. This can be understood in figure 16 showing that the reflection mechanism is associated with a redistribution of the photons within the plane of the laser beam cross-section. This effect increases the homogeneity of the k-vectors of the stimulated photons as was demonstrated experimentally in the case of a dye laser⁴⁰.

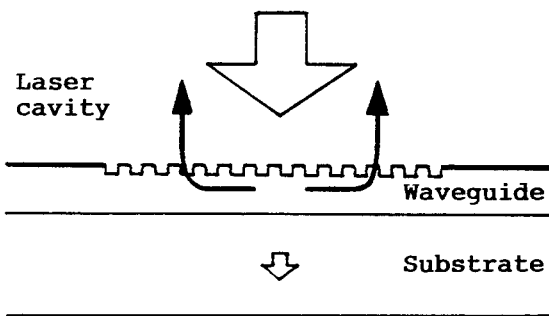


Figure 16
Abnormal waveguide grating reflector as the mirror of a laser with transverse redistribution of photons.

VIII Coupling Failure under Normal Incidence

The optogeometrical configuration of waveguide coupling under normal incidence is very attractive practically since it simplifies the relative alignment between the elements of an excitation head and makes it achievable by means of simple right angle machining. Besides, this geometry prevents any waste of power by second order radiation. Normal incidence is however a situation where interesting and unexpected effects can occur: one beneficial effect was described in section VII; it is the effect of abnormal reflection which also exists at normal incidence. One detrimental effect will be described here which can lead to catastrophic coupling failure. This is a consequence of the inherent feature of normal coupling that the condition for first order coupling synchronism at zero incidence angle is also the synchronism condition for second order intraguide coupling between the just coupled forward and backward propagating modes.

That such three wave coupling event may lead to some trouble can be inferred when considering the better known reciprocal problem of a distributed waveguide Bragg mirror using the second order of a grating to achieve reflection. The motivation for this was and still is that second order gratings are much easier to fabricate than first order ($0.4 \mu\text{m}$ period instead of $0.2 \mu\text{m}$ in the example of a DBR semiconductor laser at 1.3 or $1.55 \mu\text{m}$ wavelength). It was shown⁴¹ that a second order reflection grating radiates zero power at first order normally into the cover and substrate because the first order radiation of the forward and reflected guided waves are out of phase. Such situation exactly occurs only if the forward and backward waves in the grating have equal amplitude, ie, if the transmission of the grating mirror is zero,

ie, when the grating is sufficiently long. From the just described reciprocal case, one can infer that a situation may be encountered in the case of incoupling under normal incidence where a catastrophic coupling failure could take place.

In order to check on this intuition and to identify the conditions for coupling failure, the coupling efficiency of a waveguide grating versus the angle of incidence was first calculated under the hypothesis that the grating length L is adjusted to the optimum coupling value $L = 1/|\kappa|$ where κ is the second order intraguide coupling coefficient. $|\kappa|$ is slightly larger than the 1st order radiation coefficient α . Figure 17, curve a), shows the wavelength dependence of the coupling efficiency into the forward and backward modes under normal incidence with the incident Gaussian beam centered in the grating area. Although the maximum power is smaller by about 20 % than under non-normal incidence, the curve shows no peculiarity. If however the grating length is increased by a factor 3 to the right as sketched in the insert of figure 17, curve b), a dramatic coupling failure takes place in some wavelength range. This corresponds to the case where the left-propagating guided wave undergoes a cancelling interference with the reflection of the right-propagating coupled wave. This shows that corrugated waveguide excitation under normal incidence may be dominated by the second order intraguide coupling mechanism and lead to undesired coupling behaviour. Care should therefore be taken of the magnitude of the intraguide coupling coefficient in a given coupling structure relative to the size of the grating. A safe and optimum coupling under normal incidence of the two counter propagating modes is achieved by satisfying the condition $L = 2w$.

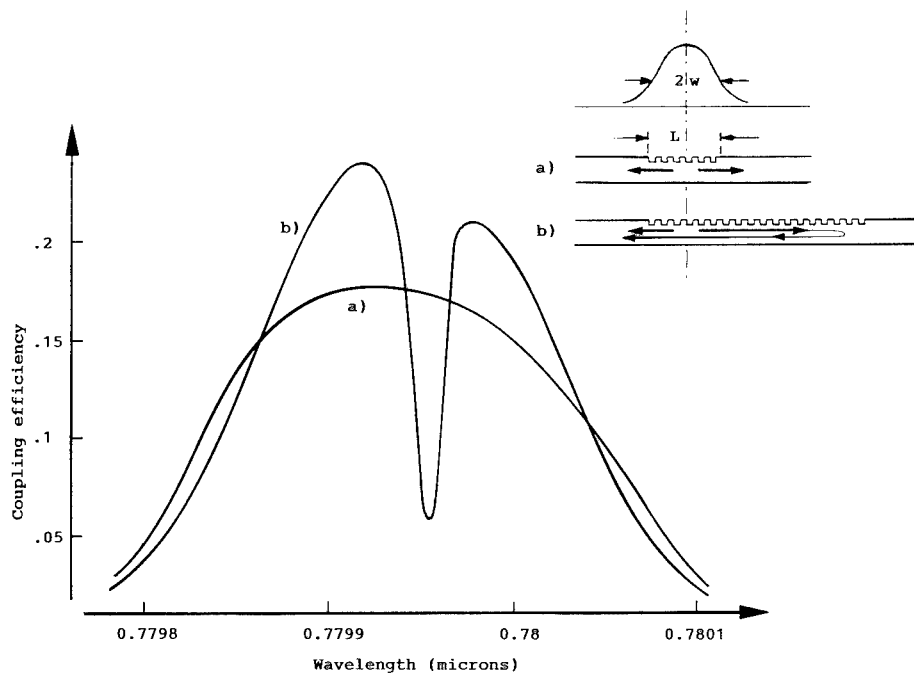


Figure 17. Power coupling efficiency under normal incidence into either guided mode. The coupling geometry is sketched in the insert.

a) The grating length is the optimum length of 2.2 mm. The waveguide is SiON on silica with substrate, guide, cover refractive index 1.46, 1.55, 1 resp., 1.243 μm thickness, propagating the TE_0 mode. The grating has rectangular grooves of 50 nm depth etched into the SiON layer and a period of 516.16 nm. The incident beam is a Gaussian of half-width $w = 1.1$ mm. The beam axis intersects the grating area at its middle point.

b) Same representation with grating length extended to 3 times the optimal length of 2.2 mm to the right. The left edge of the grating is still at 1.1 mm from the beam axis intersection.

IX Waveguide Dimensioning for High Radiation Coefficient

As mentioned in section II, the waveguide dimensions and index distribution can affect the radiation in two ways. First it is the amplitude of the modal field at the guide-cover interface which decides on the strength of the radiation coefficient. This factor is contained in the front term of expression (3) in the case of step index waveguides and TE modes. The condition for maximum field magnitude at the guide surface was obtained in a normalized form⁴² for the TE modes of a step index waveguide. For a given set of refractive indices there is an optimum h/λ ratio ensuring maximum radiation coefficient⁴³. The condition is rather tolerant towards larger waveguide thickness values h and is much more critical towards smaller values of h .

The second factor is only present in the case of waveguide profiles exhibiting sharp refractive index jumps at both interfaces because it results from interferences between radiated waves in the cover if the grating is at the guide-cover interface. This effect is accounted for in expression (3) by the cosine terms. High radiation coefficient means $N_2 kh = m\pi$, $m = 1, 2, 3$. This condition is in general not the same as the surface field maximum condition in the grating mentioned above. An easier understanding of the effect of this second condition is gained by considering close to normal incidence in which case $N_1 = n_i$ and the condition becomes

$$n_2 kh = m\pi \quad (16)$$

The cosine term gains a large importance in expression (3) in strong guidance cases typical of evanescent wave biochemical sensors⁴⁴ for instance. In the case of TiO_2 films on silica substrate and water solvent cover, the radiation coefficient can vary by as much as a factor 4 depending on whether expression (16) is satisfied or $n_2 kh = 2m\pi$.

X Guidance Strength and Radiation Coefficient

As can be inferred from expression (3) in the particular case of TE radiation from a step index waveguide, the radiation coefficient increases with the mode confinement term $1/h^*$. The radiation coefficient is the quantity which determines the scaling of the coupling geometry through expressions (9). Usually, the beam size $2w$ is given. The grating waveguide parameters, thus the radiation coefficient, must be matched accordingly to achieve maximum power coupling. This is not always possible however. For instance, in the case of a weak guidance such as in fibre compatible glass waveguides or $\text{Ti} : \text{LiNbO}_3$ waveguides, the radiation coefficient of a grating consisting of a corrugation of the guide surface hardly reaches 10 dB/cm regardless of the groove depth since there is a well known saturation effect. This implies that an efficient power incoupling would require a beam diameter and grating length of the order of 10 mm which is not desirable practically. This is why it is advisable in such cases to make the corrugation into a thin high index film deposited onto the waveguide. This has the effect of increasing the gratings dielectric perturbation, and to increase the electric field amplitude in the grating region. In doing so, the radiation coefficient of the very same waveguide structure can increase at least ten times for a grating depth of less than 100 nm as illustrated in figure 18a).

Much more attractive is the case of large guidance structures consisting of Si_3N_4 or TiO_2 or Ta_2O_5 on glass or silica. The confinement is so large, thus the field at the guide-cover interface so high, that a very shallow grating of a few nanometer depth causes a radiation rate which fits with a beam diameter of the order of 1 mm as illustrated in figure 18b). Moreover this case is much less polarization dependent than the loaded weak guidance case of figure 18a).

As a conclusion of this section, the matching between the beam size and the radiation coefficient of any particular waveguide technology must be carefully analysed in order to avoid disappointing coupling results or time consuming technology trial and error tests.

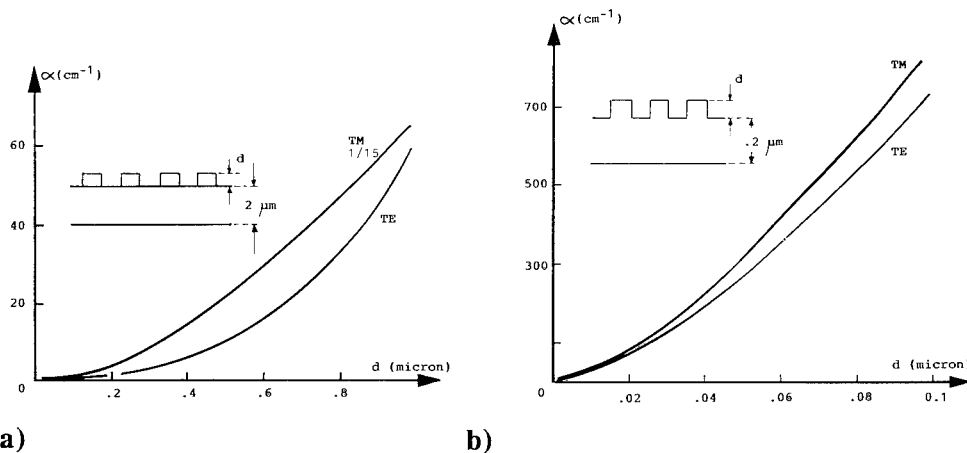


Figure 18. TE and TM radiation loss coefficient dependence on the guidance strength of the grating waveguide $\lambda = 0.8 \mu\text{m}$; $\Lambda = 0.5 \mu\text{m}$.
 a): dependence on the groove depth in a thin high index film ($n = 2.3$) deposited on a weak guidance step index waveguide of 0.01 index increase.
 b): dependence on the depth of a grating made at the surface of a large guidance tantalum oxide ($n_2 = 2.3$) waveguide.

XI Conclusion

A lot more could be said about coupling gratings. Worth mentioning would be double-frequency gratings for three wave couplers^{45,46}, tapered efficiency gratings⁴⁷ for radiation field shaping or for getting over the 80 % coupling efficiency limit, chirped and curved gratings⁴⁸ for light focusing, just to quote a few novel features. The aim of the present contribution is to identify and describe some of the practically most interesting features and some of the most problematic situations where the designer should pay attention. It is also to shed light onto a vast and not well known segment of the scientific literature on this subject and on the user friendly and physically enlightening modelling tools that have emerged from it. The Fourier-Rayleigh method is capable of accounting for most coupling cases of interest and for making the synthesis of functional grating elements. Further checking of the correctness, and assessment of the technological stability of the designed working point can then be made by applying safe vectorial methods and codes which are also available to the designer^{11,49}.

Now as the technology for submicron coupling grating fabrication is reaching its maturity and that high efficiency coupling can be readily achieved in silicon based waveguides, early commercial applications should emerge soon. An important difficulty for the generalized use of coupling gratings as a waveguide access element is its resonant character. A semiconductor laser source must be frequency selected, adjusted and locked to ensure the excitation synchronism condition, or the incident beam direction must be changeable. Both solutions amount to a significant cost threshold. Using a dispersion compensating grating is a very interesting solution⁵⁰ which however implies a decrease of efficiency and means renouncing monolithicity. It is why early products are likely to appear in application fields where the excitation and readout head can contain most part of the system cost as in pharmaceutical affinity tests and immunoassays⁵¹.

Low wavelength dependence applications are also foreseeable in the interferometric measurement of the movement of non-cooperative or smart cooperative targets. A very large field of applications can be that of optical pick up²³ and storage devices where waveguide gratings can help scale down the size and weight of existing devices.

REFERENCES

1. K.C. Chang, and T. Tamir, Simplified approach to surface-wave scattering by blazed dielectric gratings, *Applied Optics*, 19:282 (1980)
2. M.T. Gale, and L. Baraldi, Replicated microstructures for integrated optics, Int. Symposium on Integrated Optics, Lindau, Germany, 11-15 April 1994, paper 2213-01
R.E. Kunz, J. Edlinger, P. Sixt, and M. T. Gale, Replicated chirped waveguide gratings for optical sensing applications, Eurosensors VIII on Solid State Transducers, Sept. 25-28, 1994, Toulouse, Paper No. 72
3. R. Waldhäusl, E.-B. Kley, P. Dannberg, A. Bräuer, and W. Karthe, Grating couplers in planar polymer waveguides, *ibid.*, paper 2213-15
4. R. Plontke, A low energy electron exposure system for nanometric structures, NATO-Workshop on "Nanolithography: a Borderland between STM, EB, IB and X-Ray Lithography", Rome/Frascati, April 6-8, 1993
E.-B. Kley, Oberflächenprofile für Profilmasken der integrierte Optik und Mikrooptik, VDI-Berichte Nr 1102, 27-28 Oct. 1993, München
5. J.-L. A. Roumiguères, and M. Nevère, US Patent 4, 389, 094, June 21, 1993
6. T. Suhara, and H. Nishihara, Integrated optics components and devices using periodic structures, *IEEE J. of Quantum Electronics*, 22:845 (1986)
7. H. Vuillienet, L. Falco, O. Parriaux, and M. Nevère, Transfer of submicron period gratings by conventional chromium mask photolithography, Int. Symposium on Integrated Optics, Lindau, Germany, 11-15 April 1994, paper 2213-02.
8. M. Okai, S. Tsuji, N. Chinone, and T. Harada, Novel method to fabricate corrugation for a $\lambda/4$ -shifted distributed feedback laser using a grating photomask, *Appl. Phys. Lett.*, 55:415 (1989)
9. F. Clube, S. Gray, D. Struchen, and J.-C. Tisserand, Holographic mask aligner, *Optical Engineering*, 32:2403 (1993)
10. V.A. Sychugov, A.V. Tishchenko, M.S. Klimov, and O. Parriaux, CAD-Tool for integrated optic coupling gratings, Microsystem Technologies 90, Berlin, 10-13 Sept. 1990, Springer-Verlag, pp. 44-51
11. E. Glytsis, T. Gaylord, and D. Brundrett, Rigorous coupled-wave analysis and applications of grating diffraction, Critical Reviews Vol. CR49, SPIE press'93.
N. Cateau, and J.-P. Hugonin, Algorithm for the rigorous coupled-wave analysis of grating diffraction, *J. Opt. Soc. Am. A*, 11:1321 (1994)
12. BRITE EURAM II project "FOA" BE-5072
13. R. Ulrich, Efficiency of optical grating couplers, *J. Opt. Soc. Am.* 63:1449 (1973)
14. T. Tamir, in "Integrated Optics", T. Tamir, Ed., Vol. 7 of Topics in Applied Physics, Berlin: Springer-Verlag, 1979, p. 105
15. V.A. Kiselev, Diffraction coupling of radiation into a thin-film waveguide, *Sov. J. Quantum Electron.*, 4:872 (1975)
16. S. Ura, M. Shinohara, T. Suhara and H. Nishihara, Integrated-optic grating - scale - displacement sensor using linearly focusing grating couplers, *IEEE Photonics Technology Letters*, 6:239 (1994)
17. M.S. Klimov, V.A. Sychugov, A.V. Tishchenko and O. Parriaux, Optimization of optical waveguide grating couplers, *Fiber and Integrated Optics*, 11:85 (1992)
18. V.A. Sychugov, and A.V. Tishchenko, Change of polarization of light in a corrugated waveguide, *Sov. Phys. Lebedev Inst. Rep.*, No 8, 1979
M.S. Klimov, V.A. Sychugov and A.V. Tishchenko, Non-collinear geometry for highly efficient excitation of a corrugated waveguide, *Sov. J. Quantum Electron.*, 22:173 (1992)
19. M.S. Klimov, V.A. Sychugov, and A.V. Tishchenko, Corrugation waveguide excitation by Gaussian beam: general case, *Sov. Lightwave Commun.*, 1:85 (1991).
20. V.A. Sychugov, and A.V. Tishchenko, Light emission from a corrugated dielectric waveguide, *Sov. J. Quantum Electron.*, 10:1175 (1980)
21. A. Teimel, Technology and applications of grating interferometers in high-precision measurement, *Precision Engineering*, 14:147 (1992)
22. T.A. Strasser, and M.C. Gupta, Integrated optic grating-coupler-based optical head, *Appl. Opt.* 32:7454 (1993)

19. M.S. Klimov, V.A. Sychugov, and A.V. Tishchenko, Corrugation waveguide excitation by Gaussian beam: general case, *Sov. Lightwave Commun.*, 1:85 (1991).
20. V.A. Sychugov, and A.V. Tishchenko, Light emission from a corrugated dielectric waveguide, *Sov. J. Quantum Electron.*, 10:1175 (1980)
21. A. Teimel, Technology and applications of grating interferometers in high-precision measurement, *Precision Engineering*, 14:147 (1992)
22. T.A. Strasser, and M.C. Gupta, Integrated optic grating-coupler-based optical head, *Appl. Opt.* 32:7454 (1993)
23. S. Nishiwaki, J. Asada, and S. Uchida, Optical head employing a concentric-circular focusing grating coupler, *Applied Optics*, 33:1819 (1994)
24. O. Parriaux, S. Gidon, and F. Cochet, Fiber-optic polarizer using plasmon-guided wave resonance, ECOC'81, Copenhagen, pp. P6-1 - P6-4 (1981)
25. L. Li, G. Wylangowski, D.N. Payne, and R.D. Birch, Broad-band metal/glass single-mode fibre polarizers, *Electron. Lett.*, 22:1020 (1986)
26. A.M. Prokhorov, A.A. Spikhal'skii, and V.A. Sychugov, Emission of E and H waves from a corrugated section of a diffused waveguide, *Sov. J. Quantum Electron.*, 6:1211 (1976)
27. A.M. Prokhorov, A.A. Spikhal'skii, V.A. Sychugov, and A.A. Khakimov, Polarization effects in corrugated optical waveguide, *Sov. J. Quantum Electron.*, 8:1202 (1978)
28. A.M. Prokhorov, A.A. Spikhal'skii, and V.A. Sychugov, Brewster analogs in diffraction, *Sov. Tech. Phys. Lett.*, 4:23 (1978)
29. A.A. Zlenko, V.A. Kiselev, A.M. Prokhorov, A.M. Spikhal'skii, and V.A. Sychugov, *Sov. J. Quantum Electron.*, 4:839 (1975)
30. I.A. Avrutsky, A.S. Svakhin, and V.A. Sychugov, Interference phenomena in waveguides with two corrugated boundaries, *J. Modern Optics*, 36:1303 (1989)
31. I.A. Avrutsky, A.S. Svakhin, V.A. Sychugov, and O. Parriaux, High efficiency single order waveguide grating coupler, *Optics Letters*, Vol. 15:1446 (1990)
32. J.C. Brazas, S. Barry, J. Hirsh, L. Li, and A.L. McKeon, Optical waveguide gratings having double-surface corrugation for highly efficient input coupling, *Diffraction Optics: design, fabrication and applications*, Topical Meeting, Rochester, 6-9 June 94, p. 190
33. I.A. Avrutsky, A.S. Svakhin, V.A. Sychugov, and A.V. Tishchenko, Unidirectional coupling of radiation out of a composite dielectric waveguide, *Sov. J. Quantum. Electron.* 19:225 (1989)
34. O. Parriaux, Integrated optic displacement interferometers and flat optical antennae, *Technisches Messen*, 58:158 (1991)
35. A.V. Tikhomirov, B.A. Usievich, V.A. Sychugov, and O. Parriaux, Optimization and control of grating coupling to/from a silicon-based optical waveguide, submitted to *J. Lightwave Tech.*
36. A.V. Tikhomirov, B.A. Usievich, V.A. Sychugov, and O. Parriaux, Conditions for optimum grating coupling efficiency in silicon-based waveguide technologies, CLEO-Europe, Amsterdam, 28 Aug. - 2 Sept. 1994, p. 177.
37. G.A. Golubenko, A.S. Svakhin, V.A. Sychugov, A.V. Tishchenko, E. Popov, and L. Mashev, Diffraction characteristics of planar corrugated waveguides, *Optics & Quantum Electronics*, 18:123 (1986)
S.S. Wang, and R. Magnusson, Theory and applications of guided-mode resonance filter, *Applied Optics* 32:2606 (1993)
38. G.A. Golubenko, A.S. Svakhin, V.A. Sychugov, and A.V. Tishchenko, Total reflection of light from a corrugated surface of a dielectric waveguide, *Sov. J. Quantum Electron.*, 15:886 (1985)
39. I.A. Avrutsky, V.A. Sychugov, Reflection of a beam of finite size from a corrugated waveguide, *J. of Modern Optics*, 36:1527 (1989)
40. I.A. Avrutsky, G.A. Golubenko, V.A. Sychugov, and A.V. Tishchenko, Spectral and laser characteristics of a mirror with a corrugated waveguide on its surface, *Sov. J. Quantum Electron.*, 16:1063 (1986)
41. A.A. Zlenko, V.A. Kiselev, A.M. Prokhorov, A.A. Spikhal'skii, and V.A. Sychugov, Emission of surface light waves from a corrugated section of a thin-film waveguide, *Sov. J. Quantum Electron.* 5:1325 (1975)
42. O. Parriaux, and P. Dierauer, Normalized expressions for the optical sensitivity of evanescent wave sensors, *Optics Letters*, 19:508 (1994)

23. S. Nishiwaki, J. Asada, and S. Uchida, Optical head employing a concentric-circular focusing grating coupler, *Applied Optics*, 33:1819 (1994)
24. O. Parriaux, S. Gidon, and F. Cochet, Fiber-optic polarizer using plasmon-guided wave resonance, ECOC'81, Copenhagen, pp. P6-1 - P6-4 (1981)
25. L. Li, G. Wylangowski, D.N. Payne, and R.D. Birch, Broad-band metal/glass single-mode fibre polarizers, *Electron. Lett.*, 22:1020 (1986)
26. A.M. Prokhorov, A.A. Spikhal'skii, and V.A. Sychugov, Emission of E and H waves from a corrugated section of a diffused waveguide, *Sov. J. Quantum Electron.*, 6:1211 (1976)
27. A.M. Prokhorov, A.A. Spikhal'skii, V.A. Sychugov, and A.A. Khakimov, Polarization effects in corrugated optical waveguide, *Sov. J. Quantum Electron.*, 8:1202 (1978)
28. A.M. Prokhorov, A.A. Spikhal'skii, and V.A. Sychugov, Brewster analogs in diffraction, *Sov. Tech. Phys. Lett.*, 4:23 (1978)
29. A.A. Zlenko, V.A. Kiselev, A.M. Prokhorov, A.M. Spikhal'skii, and V.A. Sychugov, *Sov. J. Quantum Electron.*, 4:839 (1975)
30. I.A. Avrutsky, A.S. Svakhin, and V.A. Sychugov, Interference phenomena in waveguides with two corrugated boundaries, *J. Modern Optics*, 36:1303 (1989)
31. I.A. Avrutsky, A.S. Svakhin, V.A. Sychugov, and O. Parriaux, High efficiency single order waveguide grating coupler, *Optics Letters*, Vol. 15:1446 (1990)
32. J.C. Brazas, S. Barry, J. Hirsh, L. Li, and A.L. McKeon, Optical waveguide gratings having double-surface corrugation for highly efficient input coupling, *Diffraction Optics: design, fabrication and applications*, Topical Meeting, Rochester, 6-9 June 94, p. 190
33. I.A. Avrutsky, A.S. Svakhin, V.A. Sychugov, and A.V. Tishchenko, Unidirectional coupling of radiation out of a composite dielectric waveguide, *Sov. J. Quantum Electron.* 19:225 (1989)
34. O. Parriaux, Integrated optic displacement interferometers and flat optical antennae, *Technisches Messen*, 58:158 (1991)
35. A.V. Tikhomirov, B.A. Usievich, V.A. Sychugov, and O. Parriaux, Optimization and control of grating coupling to/from a silicon-based optical waveguide, submitted to *J. Lightwave Tech.*
36. A.V. Tikhomirov, B.A. Usievich, V.A. Sychugov, and O. Parriaux, Conditions for optimum grating coupling efficiency in silicon-based waveguide technologies, CLEO-Europe, Amsterdam, 28 Aug. - 2 Sept. 1994, p. 177.
37. G.A. Golubenko, A.S. Svakhin, V.A. Sychugov, A.V. Tishchenko, E. Popov, and L. Mashev, Diffraction characteristics of planar corrugated waveguides, *Optics & Quantum Electronics*, 18:123 (1986)
- S.S. Wang, and R. Magnusson, Theory and applications of guided-mode resonance filter, *Applied Optics*, 32:2606 (1993)
38. G.A. Golubenko, A.S. Svakhin, V.A. Sychugov, and A.V. Tishchenko, Total reflection of light from a corrugated surface of a dielectric waveguide, *Sov. J. Quantum Electron.*, 15:886 (1985)
39. I.A. Avrutsky, V.A. Sychugov, Reflection of a beam of finite size from a corrugated waveguide, *J. of Modern Optics*, 36:1527 (1989)
40. I.A. Avrutsky, G.A. Golubenko, V.A. Sychugov, and A.V. Tishchenko, Spectral and laser characteristics of a mirror with a corrugated waveguide on its surface, *Sov. J. Quantum Electron.*, 16:1063 (1986)
41. A.A. Zlenko, V.A. Kiselev, A.M. Prokhorov, A.A. Spikhal'skii, and V.A. Sychugov, Emission of surface light waves from a corrugated section of a thin-film waveguide, *Sov. J. Quantum Electron.* 5:1325 (1975)
42. O. Parriaux, and P. Dierauer, Normalized expressions for the optical sensitivity of evanescent wave sensors, *Optics Letters*, 19:508 (1994)
43. O. Parriaux, and P. Sixt, Sensitivity optimization of grating coupled evanescent wave immuno-sensors, to be published in *Sensors and Actuators B*
44. M. Heming, B. Danielzik, J. Otto, V. Paquet, and Ch. Fattinger, Plasma impulse CVD deposited TiO₂ waveguiding films: properties and potential applications in integrated optical sensor systems, *Mat. Res. Soc. Symp. Proc.* 276:117 (1992)
45. B. Geh, and A. Dorsel, Integrated optical grating scale readout employing a double grating, *Appl. Opt.*, 31:5241 (1992)
46. G. Voirin, P. Sixt, O. Parriaux, and Li Yan, Digitized dual-frequency coupling grating for waveguide displacement interferometry, CLEO-Europe, Amsterdam, 28 Aug. - 1 Sept. 1994, p. 339

47. K.A. Bates, Lifeng Li, R.L. Roncone, and J.J. Burke, Gaussian beams from variable groove depth grating couplers in planar waveguides, *Appl. Opt.*, 32:2112 (1993)
48. S. Ura, Y. Furukawa, T. Suhara, and H. Nishihara, Linearly focusing grating coupler for integrated-optic parallel pickup, *J. Opt. Soc. Am. A*, 7:1759 (1990)
49. M. Nevière, The homogeneous problem, in "Electromagnetic Theory of Gratings", R. Petit ed., Springer-Verlag, pp. 123-157 (1980)
50. D.L. Hetherington, R.K. Kostuk, and M.C. Gupta, Dispersion compensation for an integrated optic grating utilizing a transmission volume hologram, *Appl. Opt.*, 32:303 (1993)
51. R. J. Davies, and D. Pollard-Knight, An optical biosensor system for molecular interaction studies, *American Biotechnology Laboratory*, July 1993

INTEGRATED-OPTIC DISPLACEMENT SENSOR USING A PAIR OF GRATING COUPLERS

Shogo Ura, Toshiaki Suhara, and Hiroshi Nishihara

Faculty of Engineering,
Osaka University
Osaka, Japan

INTRODUCTION

Integration of optical interferometers for displacement sensing is very attractive because of its high resolution, high stability, device compactness, etc. In fact, there have been several reports¹⁻⁵ on integrated-optic devices for sensing mirror vibration/displacement along the direction of a sensing beam propagation with resolution of sub-micrometer. In an integrated-optic displacement/position sensor³, a focusing grating coupler has been integrated and displacement measurement with long working distance can be achieved without an external collimating lens. It has also been proposed that a grating coupler of double grating is applicable for another sensing configuration⁶, in which two beams are radiated with a small separation angle by the grating coupler from the waveguide and the displacement of a grating scale crossing the radiated beams is measured. We have proposed and demonstrated a new integrated-optic device⁷ for sensing the displacement of a grating scale. In the proposed sensor, the two beams are radiated separately from two grating couplers, diffracted by a grating scale and linearly focused onto integrated photodiodes (PDs). The use of the linearly focusing beams has an advantage in reduction of PD size, namely in reduction of ground noise and PD capacitance in comparison with a case⁶ using the beams without focusing. Another advantage is a possibility for sensing two-dimensional displacement by integrating two sets of the components on one substrate, since two focal lines can be crossed on a sensor head and used for sensing displacement along two directions independently⁸. In order

to construct the linearly focusing configuration, we modified a linearly focusing grating coupler (LFGC)^{9,10} to couple a diverging guided wave to a beam of conical wavefront in the air. In this paper, we describe the proposed integrated-optic grating-scale-displacement sensor and discuss the features.

DEVICE CONSTRUCTION AND OPERATION PRINCIPLE

A schematic view of the proposed integrated-optic sensor is illustrated in Fig. 1. The waveguide consists of a glass core layer and a SiO₂ buffer layer on a Si substrate, and a LFGC pair and a PD pair are monolithically integrated. The guided wave diverging from a butt-coupled laser diode is diffracted by the LFGCs to be two beams in the air and overlap with each other on the grating scale. The two beams are diffracted by a grating scale to the same direction normal to the scale plane and interfere on the PDs.

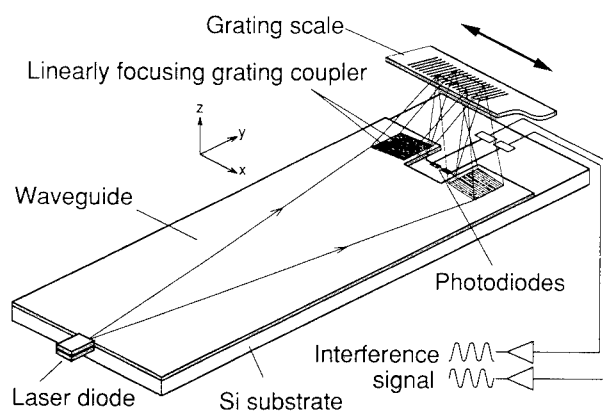


Fig. 1 Schematic view of the proposed integrated-optic device for sensing grating scale displacement.

Interference signal shows the grating scale displacement along the grating vector direction (x-direction). The diffracted beams are focused to a line parallel to x-axis on the PDs. Fig. 2 illustrates a diffraction scheme in a x-z plane including LFGCs, PDs and the grating scale. The guided wave is diffracted by the LFGC with an angle θ . The grating scale has a linear and uniform grating pattern. If the grating scale period Λ_s is $\lambda/\sin\theta$, both beams from the LFGCs are deflected to the same direction normal to the scale plane. The electric fields of the beams on the PDs depend on the scale displacement $\Delta\xi$ along x-direction and $\Delta\zeta$ along z-direction, and are expressed by

$$\widetilde{E}_L = E_0 \exp \left\{ j \left[- \frac{2\pi}{\Lambda_s} \Delta\xi + k (1 + \cos\theta) \Delta\zeta \right] \right\}, \quad (1)$$

$$\widetilde{E}_R = E_0 \exp \left\{ j \left[\frac{2\pi}{\Lambda_s} \Delta \xi + k (1 + \cos \theta) \Delta \zeta \right] \right\}, \quad (2)$$

where k is the wavenumber in free space. Phases vary in the opposite way to each other with respect to the $\Delta \xi$. The resultant interference intensity is given by

$$I = 2I_0 \left\{ 1 + \cos \left[\frac{4\pi}{\Lambda_s} \Delta \xi \right] \right\} = 2I_0 \left\{ 1 + \cos [2k \sin \theta \cdot \Delta \xi] \right\}, \quad (3)$$

and shows a cosinusoidal dependence upon $\Delta \xi$ while no dependence upon $\Delta \zeta$. Thus the sensor head constructs an optical interferometer by utilizing ± 1 st order diffraction of the grating scale, and the displacement $\Delta \xi$ is determined by the variation of the interference signal. The intensity does not depend on the grating scale displacement along y-direction since the grating pattern is uniform along y-direction.

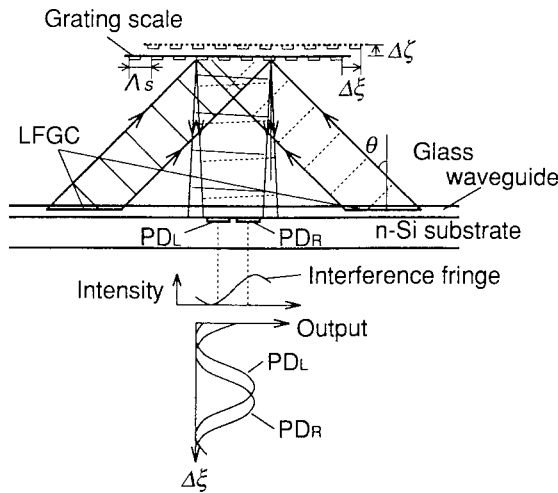


Fig. 2 Optical interferometer constructed by ± 1 st order diffraction of grating scale.

If the grating period Λ_s is set to be slightly shifted from $\Lambda_{s0} = \lambda / \sin \theta$, the directions of the two diffracted beams are splitted, resulting in an interference intensity distribution on the PDs along x-direction. A constant phase retardation is introduced in a output photocurrent variation against the other, so that the displacement direction can be discriminated by the phase relation.

LINEARLY FOCUSING FUNCTION AND SETTING TOLERANCE

A focusing function may reduce tolerance in grating scale setting. We compared the tolerance with those in no focusing and point focusing cases. The signal interference is insensitive to the grating scale vibration along y-direction, since the grating scale is uniform along y-direction. There are no difference of linearly focusing case from the other focusing cases in the tolerance of revolutions of grating scale on x-, y-, and z-axes. When a position error $\Delta \zeta$ to z-direction is present, the diffracted beams

shift to x-direction and the interference visibility V is determined by the overlap of the two beams. The beam shift causes a serious reduction of overlap for point focusing case, while it does not affect so much in no focusing or linearly focusing case. For an example, in which wavelength $\lambda = 0.8\mu\text{m}$, LFGC aperture $L_x = L_y = 0.2\text{mm}$, radiation tilt angle $\theta = 10^\circ$ and working distance $l_{WD} = 1.5\text{mm}$, the error $\Delta\zeta$ reducing V by 10% was calculated to be $\pm 6\mu\text{m}$ for a point focusing case and to be $\pm 58\mu\text{m}$ for the other cases. Thus there is no disadvantage on the tolerance in using a linearly focusing beam in comparison with the use of beam of no focusing.

EXPERIMENTAL RESULTS

The sensor was fabricated and the operation principle was confirmed. The LFGC has a modified and complicated grating line pattern to couple the diverging guided wave to the linearly focusing wave in the air, and the pattern was realized by the electron-beam (EB) direct writing method. Specifications of the fabricated device are listed in Table I, and the fabrication processes are illustrated in Fig. 3. A SiO_2 optical buffer layer, of which thickness was determined¹¹ to reduce the guided wave decay due to absorption by Si substrate and to maximize the power distribution ratio of the LFGC, was grown on an n-Si substrate by thermal oxidation and patterned for PDs by photolithography. Boron was diffused by using a spin-coated and patterned poly-Boron-film (PBF) into Si substrate to form p-n junctions. A Si-N layer deposited by plasma CVD, of which thickness was determined to optimize the radiation decay factor α to satisfy the condition¹¹ $\alpha L_y = 1$ for providing both the high efficiency and the large effective aperture of LFGC, was patterned by EB writing and RIE to form the LFGC grooves. A #7059 glass guiding layer was RF-sputtered on it. Windows were opened

Table I Specifications of the fabricated integrated-optic device

Light source	Laser diode		$\lambda = 0.79 \mu\text{m}$
Waveguide	Glass/SiO ₂ /Si single mode	Guiding layer	0.70 μm #7059glass
		Grating layer	0.041 μm Si-N
		Buffer layer	1.78 μm SiO ₂
		Mode index	$N = 1.534$
Linearly focusing grating coupler		Aperture	0.2 mm \times 0.3 mm
		Focal length	$f = 2l_{WD} = 2.8 \text{ mm}$
		Distance from LD	$r = 10 \text{ mm}$
		Output angle	5 deg
		Tilt angle	$\theta = 10 \text{ deg}$
		Period	0.53–0.57 μm
Photodiodes		Element size	90 μm \times 60 μm

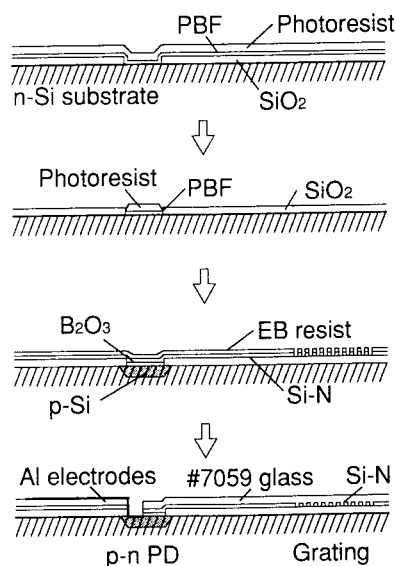


Fig. 3 Fabrication process of the device.

and Al electrodes were fabricated and wire-bonded. A SiO_2 layer on the rear face of the substrate was etched and Au was evaporated for another electrode for PDs. A waveguide end was cleaved and used for exciting a diverging guided wave. Microphotographs of the fabricated LFGCs and PDs are shown in Fig. 4. The LFGC has tilted, curved and chirped line/space pattern to give a linearly focusing beam with tilted radiation angle. The PD width of $60\mu\text{m}$ was wider than the LFGC focal line for accepting a range of error in grating scale angle revolved on x-axis. The waveguide is separated by an etched groove in order to avoid a direct propagation of the guided wave into the integrated PDs.

The characteristics of the LFGC were checked at first. The interference fringes, which is generated by two beams radiated by the LFGCs on the plane at the grating scale position, was observed by an objective lens and a CCD 2-D sensor. Fig. 5 shows a photograph of the obtained fringes. It was confirmed that linear and uniform

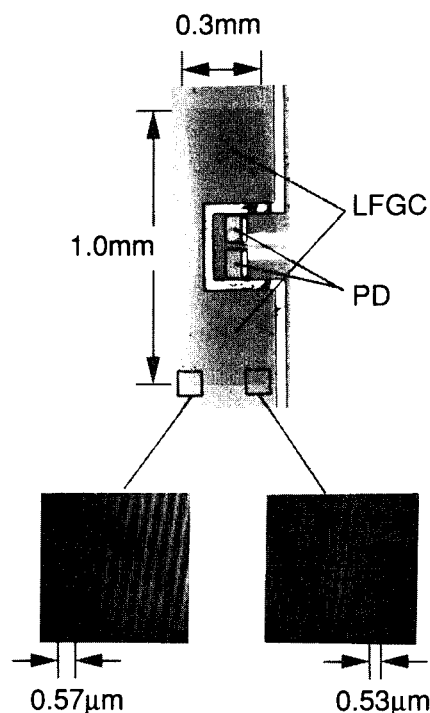


Fig. 4 Microphotographs of the fabricated LFGCs and PDs.

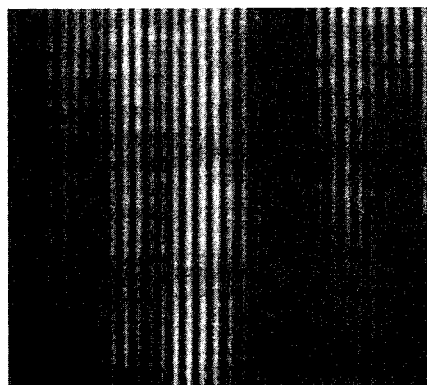


Fig. 5 Photograph of the interference fringes generated by two beams radiated by a pair of LFGC.

interference fringes with the designed period of $2.3\mu\text{m}$ were obtained. A grating scale of $4.6\mu\text{m}$ period was set and moved to x-direction as shown in Fig. 1 while output photocurrents were measured. Fig. 6 shows the dependence of the photocurrents on the displacement. It was confirmed that the photocurrent varied sinusoidally with the period of half of the grating scale period.

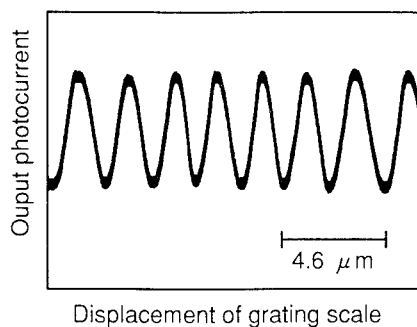


Fig. 6 Dependence of output photocurrent on grating scale displacement.

DISCUSSIONS

The features of the proposed and demonstrated device are summarized in Table II in comparison with interferometer sensing systems constructed by using conventional optics or integrated optics. The proposed device is essentially a grating scale reader or encoder. The measurement range is not limited by the light source coherence but by the scale length, while there is no advantage on the resolution because the grating scale

Table II Comparison of the proposed device with other optical interferometer displacement sensor/system

	conventional	integrated	proposed
configuration	Michelson	←	symmetric Machzehnder
range limits	coherent length of light source	←	grating scale length
units	wavelength	←	grating scale pitch
accuracy	excellent (gas laser)	depend (gas laser, LD)	fair
stability	poor	excellent	←
compactness	poor	depend (LD, gas laser)	excellent
applications	high accuracy positioning	←	encoder two-dimensional

pitch (a few micron typically) is longer than the wavelength. Optical paths of the interfering two beams are the same in the proposed device so that wavelength fluctuation tolerance is much larger than that of the others measuring the displacement along the sensing beam propagation direction. The sensing configuration, that is, the measurement of the scale displacement crossing the sensing beams, has a potential application to two dimensional displacement sensing by one-chip integrated-optic sensor head.

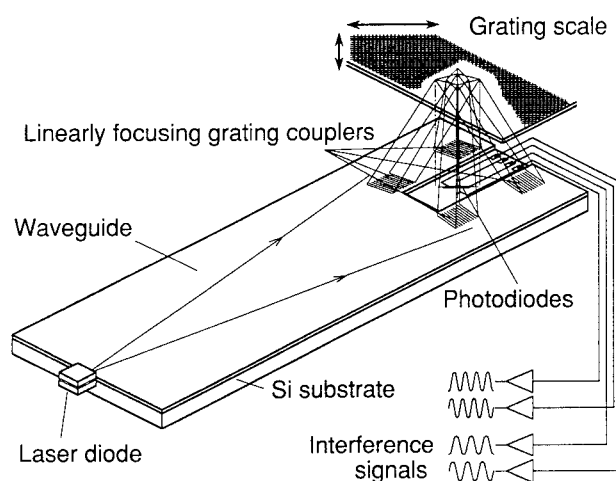


Fig. 7 Schematic view of an integrated-optic device for measuring two dimensional displacement of a grating scale.

Configuration of an integrated-optic device for measuring two dimensional displacement of a grating scale is shown in Fig. 7⁸. Two pairs of LFGCs and two pairs of PDs are integrated on a Si substrate to construct two crossed interferometers. The four beams are radiated from the four LFGCs, diffracted by a grating scale (which has two grating vectors crossed with each other) and focused to crossed two lines on the two PD pairs. By the same principle as discussed in this paper, each component of two dimensional displacement of the grating scale are measured independently and separately from the other component. We are now investigating design, fabrication and characterization of the device.

CONCLUSIONS

A new integrated-optic displacement sensor constructed by integrating a pair of LFGCs and a pair of PDs on a Si substrate was described with preliminary experimental results, and the features are discussed in comparison to other displacement sensing systems. Possibility of integration of two interferometer heads on one chip is one of the

most attractive points. The integration provides a very compact and stable system, namely, no alignment between two interferometers is needed for two dimensional measurement. Application fields of the device would be in machinery or plant automatization, in aerospace or marine engineering, as well as in robotics.

REFERENCES

1. M. Izutsu, A. Enokihara and T. Sueta, "Optical -waveguide microdisplacement sensor," *Electron.Lett.*, **18**, pp. 867-868, 1982.
2. P. Gidon, S. Valette and P. Schweizer, "Vibration sensor using planar integrated interferometer circuit on oxidised silicon substrate," *Int'l. Conf. Opt. Fiber Sensors '84*, Sept. 5-7, Stuttgart, paper P2.
3. S. Ura, T. Suhara and H. Nishihara, "Integrated-optic interferometer position sensor," *IEEE J. Lightwave Technolo.*, **7**, pp. 270-273, 1989.
4. H. Toda, M. Haruna and H. Nishihara, "Integrated-optic heterodyne interferometer for displacement measurement," *IEEE J. Lightwave Technolo.*, **9**, pp.683-687, 1991.
5. D. Jestel, A. Baus and E. Voges, "Integrated-optic displacement sensor in glass with 1 nm resolution," *Topical Meet. Integrated Photonics Research '91*, April 9-11, Monterey, CA, paper ThE2.
6. B. Geh and A. Dorsel, "Integrated optical grating scale readout employing a double grating," *Appl. Opt.*, **31**, pp. 5241-5245, 1992.
7. S. Ura, M. Shinohara, T. Suhara and H. Nishihara, "Integrated-optic grating-scale-displacement sensor using linearly focusing grating couplers," *IEEE Photon. Technolo. Lett.*, **6**, pp. 239-241, 1994.
8. S. Ura, T. Endoh, T. Suhara and H. Nishihara, "Linearly focusing grating couplers for sensing 2-dimensional grating-scale displacement," *Topical Meet. Int'l Comm. Opt.*, April 4-8, Kyoto, paper 7A-5, 1994.
9. A. Katzir, A. C. Livanos, J. B. Shellan and A. Yariv, "Chirped gratings in integrated optics," *IEEE J. Quantum Electron.*, **QE-13**, pp. 296-304, 1977.
10. S. Ura, Y. Furukawa, T. Suhara and H. Nishihara, "Linearly focusing grating coupler for integrated-optic parallel pickup," *J. Opt. Soc. Am. A*, **7**, pp. 1759-1763, 1990.
11. S. Ura, T. Suhara, H. Nishihara and J. Koyama, "An integrated-optic disk pickup device," *J. Lightwave Technolo.*, **LT-4**, pp. 913-918, 1986.

RIGOROUS GUIDED-WAVE SOLUTIONS FOR PLANAR GRATING STRUCTURES

T. Tamir and S. Zhang*

Polytechnic University
Electrical Engineering Dept.
Six Metrotech Center
Brooklyn, NY 11201.

Abstract: An exact solution is described for electromagnetic problems posed by dielectric-layer configurations that include planar gratings. Because it represents the modes guided by the grating structure in an implicit analytical form, this solution can readily clarify and accurately quantify the wave effects associated with the presence of the grating. Examples worked out for grating-assisted directional couplers reveal that design criteria based on approximate coupled-wave considerations may lead to operating conditions that are less than optimal.

INTRODUCTION

Planar gratings have been used extensively in dielectric-film configurations to construct couplers, lasers and other optoelectronic devices. The electromagnetic fields that play the major role in these applications have been investigated mostly by means of coupled-wave methods using perturbation arguments or other approximations.¹ However, these techniques may not yield sufficiently accurate data, and they are often unable to provide information on all the effects produced by the grating. For example, information available on radiation leakage is rather sparse,² and other details of the diffraction process are not easily explored in the absence of exact solutions.

We therefore present here a rigorous solution of the relevant electromagnetic problem, which applies to most grating profiles of practical importance. This solution utilizes a modal representations that was used in the past^{3,4} but extends it to a wider class of structures. Our formalism may account for any number of layers and it leads to simple but systematic algorithms for the numerical computations of all aspects of the wave diffraction process.

* On leave from the Hangzhou Institute of Electronics Engineering, Hangzhou, P.R. China.

THE FIELDS GUIDED BY A GRATING STRUCTURE

The electromagnetic problems usually posed by a grating configuration may involve either the scattering of waves incident upon the structure, or the guiding of (surface or leaky) modes along that structure. The latter situation is somewhat more difficult from a mathematical point of view, but we shall focus on it here because of its relevance to applications in the area of optoelectronics.

For this purpose, we consider the geometry shown in Fig. 1 which involves an arbitrary number of layered media indicated by subscripts $j = 0, 1, 2, \dots, J+1$. Of these, all media but one are homogeneous and therefore have fixed dielectric

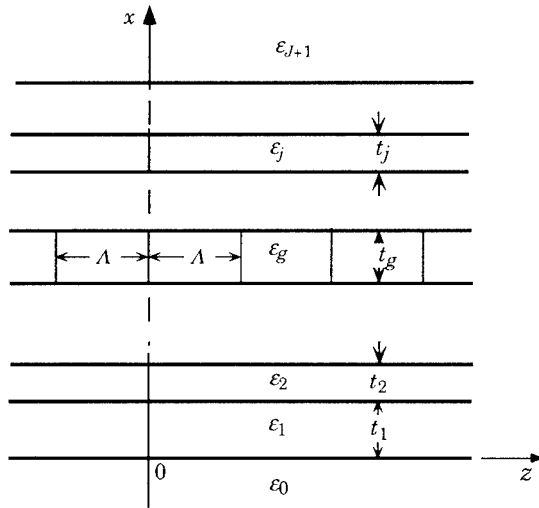


Fig. 1: Geometry of layered media containing a planar grating.

constants ϵ_j . The inhomogeneous medium (identified by some $j = g$) acts as a grating of height t_g because its permittivity exhibits a periodic variation $\epsilon(z) = \epsilon(z+\Lambda)$ with an average dielectric constant ϵ_g . All the layers are located between open substrate ($j = 0$) and cover ($j = J+1$) regions. The variation $\epsilon(z) = \epsilon(z+\Lambda)$ in the grating layer may be arbitrary provided that it does not change with x . Gratings having rectangular or sinusoidal (holographic) variations are special but important cases that comply with this condition. (It should be noted, however, that our approach applies to any number of such gratings if they all have the same periodicity Λ . A grating with an arbitrary x -dependent profile variation $\epsilon(x, z) = \epsilon(x, z+\Lambda)$ can then be treated by subdividing it into a number $l = 1, 2, \dots, L$ of layers that are sufficiently thin so that each one of them may be characterized by a variation $\epsilon_l(z) = \epsilon_l(z+\Lambda)$ that does not depend on x .)

It is convenient to use local coordinates x_j starting at the bottom and ending at the top of each layer so that $0 \leq x_j \leq t_j$; in the open regions, we take $x_0 = x$ in the substrate and $x_{J+1} = x - t_s$ in the cover, where t_s is the sum of all t_j . If a time dependence $\exp(-i\omega t)$ is assumed but suppressed, the fields in the homogeneous ($j \neq g$) regions are given by

$$E_j = \sum_n [f_{jn} \exp(ik_{jn}x_j) + r_{jn} \exp(-ik_{jn}x_j)] \exp(ik_{zn}z), \quad (1a)$$

$$H_j = \sum_n y_{jn} [f_{jn} \exp(ik_{jn}x_j) - r_{jn} \exp(-ik_{jn}x_j)] \exp(ik_{zn}z), \quad (1b)$$

where $k_{zn} = k_{z0} + 2n\pi/\Lambda$, $n = 0, \pm 1, \pm 2, \dots$ and $k_{jn} = \sqrt{(k_o^2 \epsilon_j - k_{zn}^2)}$ for all $j \neq g$. For guided waves as assumed here, we take $f_{0n} = 0$ in the substrate and $r_{J+1,n} = 0$ in the cover. The fields in the grating ($j = g$) region can be expressed in the form

$$E_g = \sum_m [f_{gm} \exp(ik_{gm}x_g) + r_{gm} \exp(-ik_{gm}x_g)] \sum_n a_{nm} \exp(ik_{zn}z), \quad (2a)$$

$$H_g = \sum_m y_{gm} [f_{gm} \exp(ik_{gm}x_g) - r_{gm} \exp(-ik_{gm}x_g)] \sum_n b_{nm} \exp(ik_{zn}z), \quad (2b)$$

where, for any given k_{z0} , the quantities k_{gm} , a_{nm} and b_{nm} are known as characteristic values of fields that satisfy the dispersion relation (for $t_g \rightarrow \infty$) inside the grating region only.⁴ In all cases, $E = E_y$, $H = H_z$ and $y_{jn} = k_{jn}/\omega\mu_o$ for TE modes, or $E = E_z$, $H = -H_y$ and $y_{jn} = \omega\epsilon_o\epsilon_j/k_{jn}$ for TM modes, with $\epsilon_j = \epsilon_g$ in the grating layer.

The expressions inside the square brackets of Eqs. (1) and (2) can be cast as "voltages" $\mathbf{v}_{xj} = \mathbf{v}_j(x_j)$ or "currents" $\mathbf{i}_{xj} = \mathbf{i}_j(x_j)$ in the column-vector form

$$\mathbf{v}_{xj} = \mathbf{E}_{xj} \mathbf{f}_j + \mathbf{E}_{xj}^{-1} \mathbf{r}_j \equiv \mathbf{E}_{xj} (\mathbf{1} + \mathbf{R}_{xj}) \mathbf{f}_j, \quad (3a)$$

$$\mathbf{i}_{xj} = \mathbf{Y}_j (\mathbf{E}_{xj} \mathbf{f}_j - \mathbf{E}_{xj}^{-1} \mathbf{r}_j) \equiv \mathbf{Y}_j \mathbf{E}_{xj} (\mathbf{1} - \mathbf{R}_{xj}) \mathbf{f}_j, \quad (3b)$$

where \mathbf{Y}_j and \mathbf{E}_{xj} are diagonal matrices with elements $\{\mathbf{Y}_j\}_{nr} = y_{jn} \delta_{nr}$ and $\{\mathbf{E}_{xj}\}_{nr} = \exp(ik_{jn}x_j) \delta_{nr}$, while \mathbf{R}_{xj} are square "reflectance" matrices obeying

$$\mathbf{R}_{xj} = \mathbf{E}_{t-x,j} \mathbf{R}_{tj} \mathbf{E}_{t-x,j}, \quad (4)$$

where, as defined through Eqs. (3), \mathbf{R}_{tj} consist of reflection factors r_{jn} looking up (along the $+x$ axis) at $x_j = t_j$ in the j -th layer. At the interface between two homogeneous regions, i.e., for all $j \neq g-1$ or g , the appropriate boundary conditions are

$$\mathbf{v}_{tj} = \mathbf{v}_{0,j+1}, \quad \mathbf{i}_{tj} = \mathbf{i}_{0,j+1}. \quad (5)$$

For the grating layer we have

$$\mathbf{v}_{t,g-1} = \mathbf{A} \mathbf{v}_{0g}, \quad \mathbf{i}_{t,g-1} = \mathbf{B} \mathbf{i}_{0g}, \quad (6a)$$

$$\mathbf{A} \mathbf{v}_{tg} = \mathbf{v}_{0,g+1}, \quad \mathbf{B} \mathbf{i}_{tg} = \mathbf{i}_{0,g+1}, \quad (6b)$$

where \mathbf{A} and \mathbf{B} are square matrices with elements $\{\mathbf{A}\}_{nm} = a_{nm}$ and $\{\mathbf{B}\}_{nm} = b_{nm}$. If these conditions are inserted into Eqs. (3) and (4), we can substitute out all but one vector \mathbf{f}_q , where q is any preferred value of j . We then get

$$(\mathbf{1} - \mathbf{R}_{0q} \mathbf{E}_{tq} \mathbf{R}_{tq} \mathbf{E}_{tq}) \mathbf{f}_q = 0, \quad (7)$$

where \mathbf{R}_{0q} consist of reflection factors r_{qn} looking down (along the $-x$ axis) at $x_q = 0$. For any given k_{z0} , Eq. (7) yields all the terms in \mathbf{f}_q provided a normalization condition is assumed. The appropriate values of k_{z0} for guided waves are those that cause the determinant of Eq. (7) to vanish, i.e.,

$$| \mathbf{1} - \mathbf{R}_{0q} \mathbf{E}_{tq} \mathbf{R}_{tq} \mathbf{E}_{tq} | = 0, \quad (8)$$

so that \mathbf{f}_q acts as an eigenvector. After applying Eqs. (3) and (4) to obtain all other \mathbf{f}_j ($j \neq q$) and all \mathbf{r}_j , the modal fields are determined at any point (x, z) by Eqs. (1) and (2). It is instructive to note that Eq. (8) is a secular relation in matrix form, which reduces to the familiar scalar form $1 - r_{0q} r_{tq} \exp(2ik_q t_q) = 0$ if no grating is present.

The above implies that the infinite but discrete (guided-wave) spectrum of k_{z0} is given by all $k_{z0} = \kappa_\nu = \beta_\nu + i\alpha_\nu$ ($\nu = 1, 2, \dots$), where κ_ν^2 denote the

eigenvalues of Eq. (7). Thus each κ_v represents the wavenumber of a field propagating as $\exp(i\kappa_v z)$ along the longitudinal direction z of the grating. In lossless situations and for sufficiently small periods Λ , a few $\kappa_v = \beta_v$ are real and correspond to purely bound (surface-wave) modes; all other (discretely countable but infinitely many) modes are evanescent. For larger Λ , every κ_v is generally complex and then refers to a quasi-bound (leaky-wave) mode if $|\beta_v| \gg \alpha_v > 0$; in that case, α_v denotes attenuation due to radiation away from the grating region. Solving Eq. (8) for κ_v thus automatically yields both the phase factor β_v and its attendant leakage-loss factor α_v for every guided mode.

For most applications, the parameters κ_v of interest are only those having values near $k_{z0} = k_{sv}$ where k_{sv} refer to wavenumbers of surface-wave modes along the same structure but with its periodicity removed, *e.g.*, by replacing the grating with a layer having a permittivity equal to the average value ϵ_g of $\epsilon(z) = \epsilon(z + \Lambda)$. The presence of the grating thus causes the (surface-wave) values of k_{sv} to change into the complex quantities κ_v discussed above. When using coupled-wave analysis or other methods, the modified values κ_v of k_{sv} are obtained in terms of β_v approximations only, with no estimate for corresponding α_v values. By contrast, the secular relation (8) can determine the full complex values of κ_v to any desired degree of accuracy. The importance of this exact approach is illustrated by the example discussed below.

POWER TRANSFER IN GRATING-ASSISTED DIRECTIONAL COUPLERS

A typical grating-assisted directional coupler is shown in Fig. 2, where two guiding layers ($j = 1$ and 4) are coupled by means of a rectangular-profile grating layer ($j = 3 = g$).

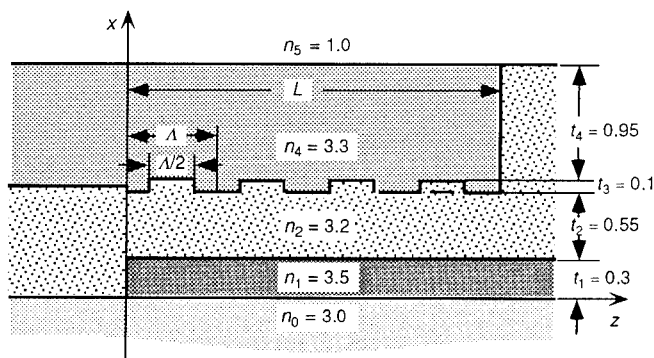


Fig. 2: Grating-assisted coupler for transferring power between the two planar guides having refractive indices n_1 and n_4 . All given lengths are in μm .

If the grating is absent, the layered structure supports two surface-wave TE modes (also referred to as supermodes¹ or compound modes⁵). Of these, one has an effective refractive index N_1 and its power is carried mostly inside the lower guide (with $j = 1$) while the other has an effective refractive index N_2 and its power is mostly inside the upper guide (with $j = 4$). Because the two guides are different, the dispersion curves of N_1 and N_2 do not intersect when plotted as a function of $k_o = 2\pi/\lambda$, where λ is the wavelength in vacuum. However, if a grating with vanishingly small height t_j is introduced, the N_2 curve may cross a curve

$N_1 + n\lambda/\Lambda$ for suitable values of the periodicity Λ and n , as shown in Fig. 3(a) by the solid lines for $n = -1$.

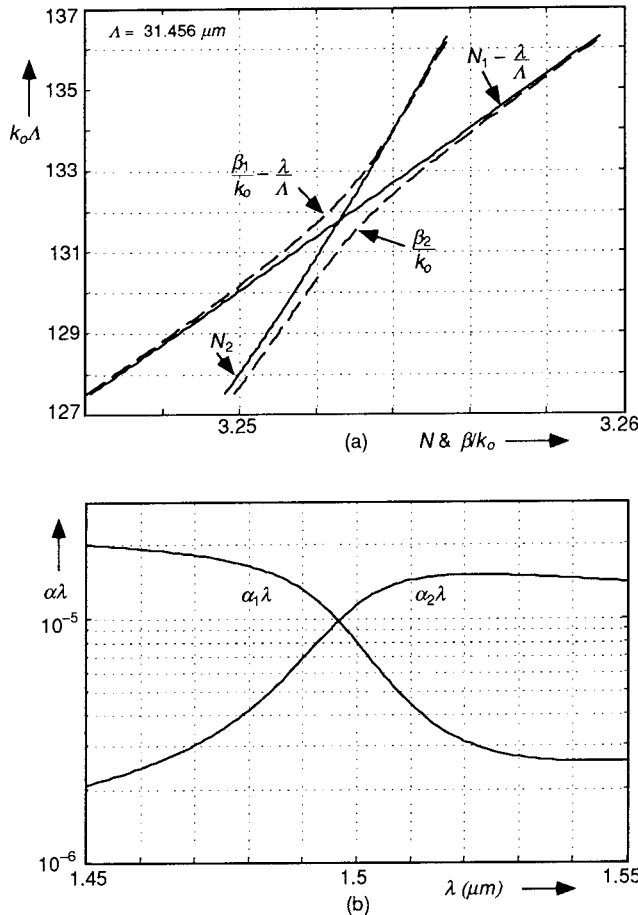


Fig. 3. Dispersion curves for the grating region $0 \leq z \leq L$ shown in Fig. 2: (a) variation of N if periodicity is absent (solid curves) and β/k_0 in the presence of periodicity (dashed curves); (b) attenuation $\alpha\lambda$.

For finite values of t_g , i.e., when the presence of periodicity can no longer be neglected, the solid-line dispersion curves are modified into those shown dashed in Fig. 3(a). The latter represent dispersion curves for the grating region $0 \leq z \leq L$ of Fig. 2, which are given by the real parts β_1 and β_2 of the complex values of κ_1 and κ_2 , respectively. We already discussed above that the imaginary parts α_1 and α_2 are then also automatically obtained. In the present example, those results are given in Fig. 3(b) which suggests that the leakage α for either mode is relatively small. However, the total attenuation αL may be quite large and possibly prohibitive in certain cases.

A more interesting result is revealed if the N_2 mode guided at $z < 0$ by the upper ($j = 4$) guide is incident from the left across the $z = 0$ plane in Fig. 1. To the right of $z = 0$, the energy of that mode splits almost evenly between the two modes given by κ_1 and κ_2 so that their superposed fields interfere. As z increases towards L , the net power then alternates from the upper to the lower guide and back over a beat length $B = \pi/|\beta_1 - \beta_2 - 2\pi/\Lambda|$. For design purposes, it is important to examine the behavior of this field as a function of the periodicity Λ .

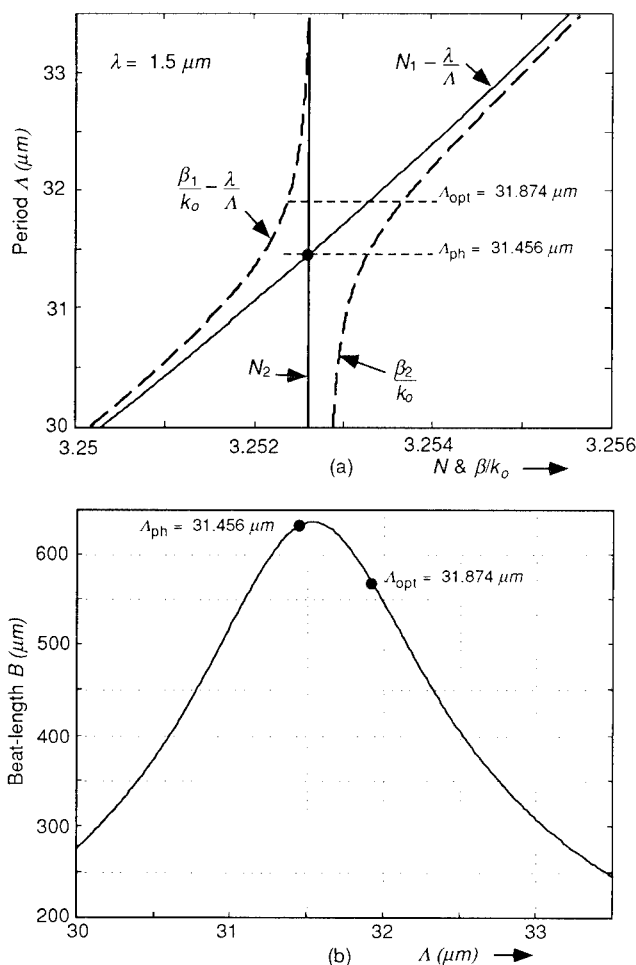


Fig. 4. Variation in terms of the period Λ for: (a) the phase factors β_1 and β_2 ; (b) the beat-length B .

We therefore show in Fig. 4 the variation with Λ for the dispersion curves and the beat length B . Because these results can be very accurately determined by means of the present approach, we observe that the maximum value of B in Fig. 4(b) occurs close to, but not exactly at, the phase-match period Λ_{ph} defined by the intersection point of the N curves in Fig. 4(a).

As a function of L , the power fed at $z > L$ into the N_1 mode of the lower guide can be found by using an overlap-integral calculation.¹ To assess the power-transfer process, we show in Fig. 5(a) the field intensities $|E_1|$ and $|E_2|$ along the cross-sectional distance x for the two modes belonging to κ_1 and κ_2 , respectively, when the phase-match condition $\Lambda = \Lambda_{\text{ph}}$ is satisfied. We then note that both curves exhibit peaks inside the guiding layers $j = 1$ and 4 . However, the field of mode 1 (shown solid) undergoes no phase change along x whereas that of mode 2 (shown dashed) changes sign. Owing to this behavior, these modes have been referred to⁵ as symmetric and anti-symmetric, respectively. We also note in that their fields $|E_1|$ and $|E_2|$ show peaks in Fig. 5(a) that have different values inside the guiding layers. As a result, the superposition of the two modes over a beat length B yields a resultant field that concentrates only

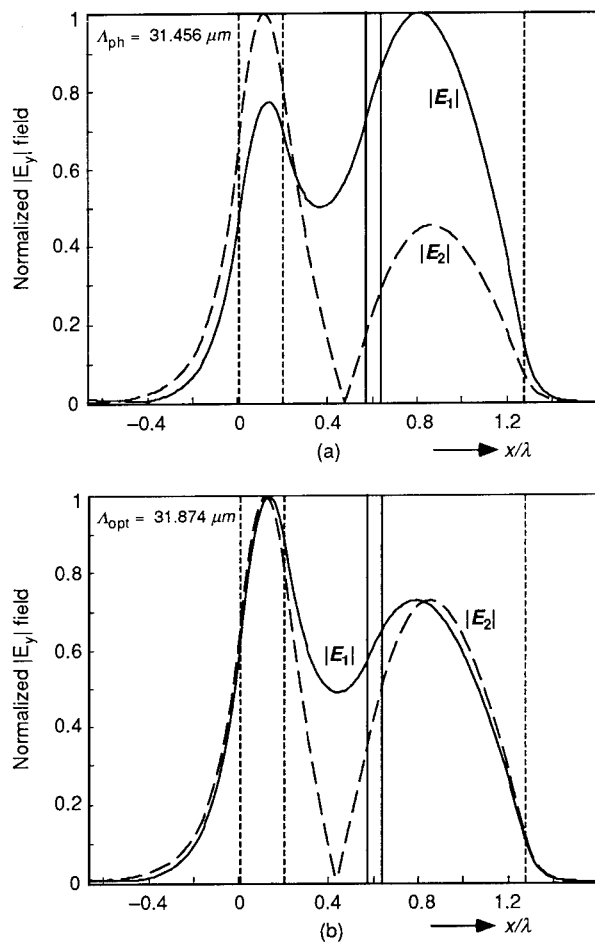


Fig. 5. Variation of electric field amplitude $|E|$ for the two modes at $z = 0$ in the grating region: (a) under phase-match conditions; (b) under optimum power-transfer conditions. Vertical lines refer to layer and grating boundaries shown shaded and solid, respectively.

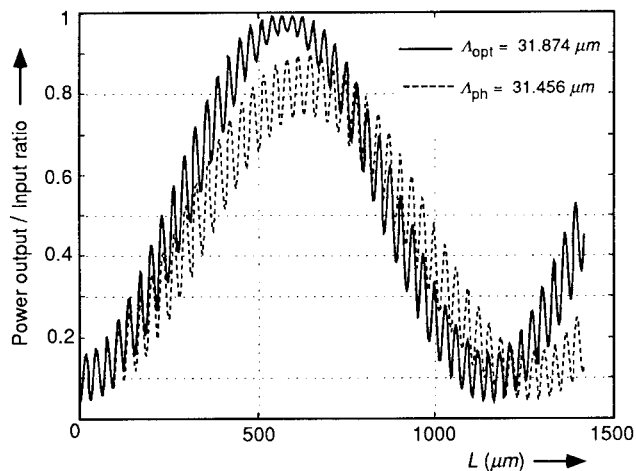


Fig. 6. Power transferred in the lower guide of Fig. 2 as a percentage of the power incident in the upper guide.

partly in the lower guide. Specifically, the power in the lower guide produced by this superposition is shown in Fig. 6 by the dashed line, which indicates that only about 90% power-transfer efficiency can be reached.

The power-coupling conditions can be improved by choosing a different periodicity $\Lambda = \Lambda_{\text{opt}}$ such that the peaks of $|E_1|$ and $|E_2|$ have equal values, as shown in Fig. 5(b). The determination of Λ_{opt} cannot be formulated analytically and must therefore be found by numerical inspection. The result is then given by the solid curve in Fig. 6 which shows that the goal of 100% power-transfer efficiency can be reached. In addition, we note that the fluctuations of the solid curve around its peak near 100% are smaller than those of the dashed curve around 90%. Hence the coupler is less sensitive on L if its periodicity is Λ_{opt} instead of Λ_{ph} . We therefore conclude that the phase-match condition $\Lambda = \Lambda_{\text{ph}}$ may not achieve best results for power-coupling purposes.

CONCLUDING REMARKS

We have presented a rigorous approach to the solution of problems involving a planar grating embedded in an arbitrary number of dielectric layers. In particular, we have formulated the modes guided by such configurations by deriving their dispersion relation and have obtained the fields of those modes at any point in terms of explicit analytic expressions. Because these fields represent exact solutions of the pertinent electromagnetic boundary-value problem, they can be used to explore every aspect of the diffraction effects produced by the grating.

To illustrate the utility of this rigorous approach, we have applied it to examine power transfer in a typical grating-assisted coupler involving two different (asynchronous) waveguides coupled by a grating. We have first shown that the power radiated transversely by such a coupler can be readily obtained in terms of a leakage attenuation factor derived from the exact dispersion relation. By then examining the power transferred from one waveguide of the coupler to the other one, we found that maximum power transfer occurs under conditions different from those satisfying a phase-match regime. Furthermore, the maximum-transfer situation also optimizes design conditions because power coupling is then less sensitive on the grating length. These results suggest that the rigorous approach can serve as a powerful tool in improving the performance of grating couplers and other periodic thin-film optical applications.

ACKNOWLEDGMENTS

This study was supported by the U.S. National Science Foundation and by the Chinese National Science Foundation. Some of the work was carried out while T. Tamir was on a Sabbatical leave at the AT&T Bell Laboratories, Holmdel, N.J.

REFERENCES

1. W.-P. Huang, "Coupled-mode theory for optical waveguides: an overview," *J. Opt. Soc. Am. A* **11**, 963-983 (1994).
2. D. Marcuse, "Radiation loss of grating-assisted directional coupler," *IEEE J. Quant. Electron.* **26**, 675-684 (1990).
3. S. T. Peng, T. Tamir and H. L. Bertoni, "Theory of periodic dielectric waveguides," *IEEE Trans. Microwave Theory & Tech.* **MTT-23**, 123-133 (1975).
4. H. L. Bertoni, L.-S. Cheo and T. Tamir, "Frequency-selective reflection and transmission by a periodic dielectric layer," *IEEE Trans. Ant. & Prop.* **37**, 78-83 (1989).
5. D. Marcuse, "Directional couplers made of nonidentical asymmetric slabs. Part II: Grating-assisted couplers," *J. Lightw. Tech.* **LT-5**, 268-273 (1987).

Cascading: Modelling a New Route to Large Optical Nonlinearities and All-Optical Devices

George Stegeman, Roland Schiek, Gijs Krijnen, William Torruellas, Mike Sundheimer and
Eric VanStryland

CREOL, University of Central Florida
12424 Research Parkway, Orlando, FL 32751

Curtis Menyuk

Dept. of Electrical Engineering, University of Maryland, Baltimore County
Catonsville, MD 21228-5398

Lluís Torner

Dept. of Signal Theory and Communications, Polytechnic University of Catalonia
P.O. Box 30002, 08080 Barcelona, SPAIN

Gaetano Assanto

Dipartimento di Ingegneria Eletttronica, University of Roma III
Via Eudossiana 18, 00184 ROMA-ITALY

INTRODUCTION

One of the attractive possibilities offered by nonlinear optics is the application of an intensity dependent refractive index to various all-optical switching, data processing and logic operations. Despite the concentrated effort made in searching for materials with large nonlinearities and low linear and nonlinear losses, the powers required for integrated optical waveguide device operation are still of the order of watts.

An intensity-dependent refractive index is not the only way to achieve the nonlinear phase shifts required for all-optical devices. It has been known since the early days of nonlinear optics that second order susceptibilities can lead to effects similar to third order

susceptibilities.[1] In fact for a single input wavelength this process requires both up conversion (second harmonic generation) and down conversion (the mixing of the generated second harmonic with the fundamental to produce photons at the fundamental wavelength). This is shown schematically in Fig. 1. The distance which a second harmonic photon travels before returning via down conversion to the fundamental beam is typically the coherence length, making this a non-local process. If the process is not phase-matched, i.e. $n(\omega) \neq n(2\omega)$ and the phase velocities are not equal, i.e. $v_1 \neq v_2$, then the photons returning to the fundamental are shifted in phase (relative to the fundamental beam) by $\Delta\phi \approx \pi - 2[n(\omega) - n(2\omega)]L\omega/c$. The π serves to conserve energy in this interaction. That is for the phase-matched case, the photons returning to the fundamental are π out of the phase with the fundamental which leads directly to pump depletion. The "nonlinear phase shift" associated with this cascading process is given by the index difference term. It is nonlinear because the number of second harmonic photons is proportional to the input fundamental intensity, and hence the induced phase shift is also proportional to the input intensity. Although this brief explanation has been limited to Type I phase-matching, it can easily be extended to Type II phase-matching, and in general other parametric processes.[2-4]

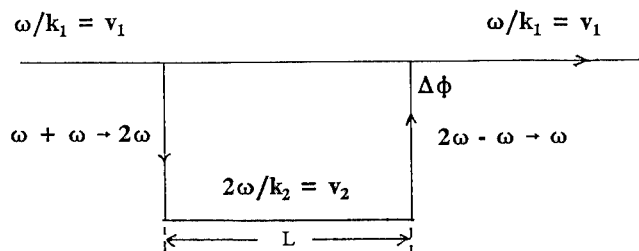


Fig. 1 Schematic diagram of the cascading process for producing phase shifts. L is typically the coherence length.

Until recently the phase-matchable second order nonlinearities were too small to make this effect useful. However, there has been considerable progress in developing new materials, and in finding new ways to phase-match existing materials for orientations with large second order susceptibilities. As a result it appears that effective nonlinearities available from cascading will be orders of magnitude larger than from the best third order materials. And in fact large effects have been observed experimentally.[5-8]

In this paper we will discuss some results obtained to date with the modelling of the cascading phenomenon. Although some of the effects predicted are reminiscent of third order effects, in fact one cannot just replace the third order nonlinearity by a new effective nonlinearity and find the true rich spectrum of phenomena available with cascading. Instead it is necessary to treat the up conversion and down conversion processes in detail. Here we will outline some of the interesting results that we have found.

CW CASCADING EQUATIONS - NONLINEAR PHASE SHIFTS

The equations needed to describe cascading are just those needed for describing any second order parametric mixing process. For the simplest case of cw second harmonic generation,[2]

$$\frac{d}{dz}a_{2\omega}(z) = -i\kappa(-2\omega; \omega, \omega)a_{\omega}^2(z)e^{i\Delta\beta z} - \alpha(2\omega)a_{2\omega}(z) \quad (1)$$

$$\frac{d}{dz}a_{\omega}(z) = -i\kappa(-\omega; 2\omega, -\omega)a_{2\omega}(z)a_{\omega}^*(z)e^{-i\Delta\beta z} - \alpha(\omega)a_{\omega}(z). \quad (2)$$

$$\kappa(-2\omega; \omega, \omega) = \frac{\omega d_{ijk}^{(2)}(-2\omega; \omega, \omega)e_i(2\omega)e_j(\omega)e_k(\omega)}{[2n_i(2\omega)n_j(\omega)n_k(\omega)c^3\epsilon_0]^{1/2}} \quad (3)$$

$$\kappa(-\omega; 2\omega, -\omega) = \frac{\omega d_{ijk}^{(2)}(-\omega; 2\omega, -\omega)e_i(\omega)e_j(2\omega)e_k(\omega)}{[2n_i(\omega)n_j(2\omega)n_k(\omega)c^3\epsilon_0]^{1/2}} \quad (4)$$

Here the wavevector mismatch is $\Delta\beta = 2k_{\text{vac}}(\omega)[n(2\omega) - n(\omega)]$, the complex field amplitudes $a(z)$ are normalized so that $|a(z)|^2$ is the intensity and the e_i 's are the field unit vectors. For the lossless case, far from any material resonances, and in the absence of coupling to other fields, these equations can be solved analytically in terms of Jacobi elliptic functions.[10] We used fourth order Runge-Kutta to numerically solve the coupled mode equations 1 and 2.

Some of the most interesting results are summarized in Figs. 2 and 3.[2] From the example in Figs. 2 with the smallest cumulative phase-mismatch it is clear that the phase shift of the fundamental occurs primarily when the second harmonic is converted back into the fundamental. This leads to the "plateau-like" behaviour in $\Delta\phi^{\text{NL}}$. Note, however, that large phase shifts are still possible for large detunings from phase-match for which the oscillations in the second harmonic power are smaller, but occur more frequently than for the almost phase-matched case. A similar behaviour was found for the variation in phase shift with increasing intensity. There it appears at large intensities that the phase shift may saturate. This is a misconception: The dependence of the $\Delta\phi^{\text{NL}}$ actually becomes linear in the field for large phase shifts. There is an optimum detuning for maximizing the phase shift. All of these results show clearly that this effect is non-local and behaves differently from phase shifts derived from the third order nonlinearity $\chi^{(3)}$. Therefore accurate modelling of this cascading phenomenon cannot be done just by assuming an appropriate $\chi_{\text{eff}}^{(3)}$.

Nevertheless, it is instructive to compare the magnitude of the effect relative to n_2 . By solving Eqns. 1 and 2 in the limit of negligible conversion to the harmonic,

$$\frac{d}{dz}\Delta\phi \approx n_{2,\text{eff}}k(\omega)I(\omega) \quad (5)$$

and finding the maximum phase shift condition leads to

$$n_{2,\text{eff}} \approx \text{sign}(\Delta\beta) \frac{4}{\epsilon_0 c} \frac{[d_{\text{eff}}^{(2)}]^2 L}{n^3 \lambda} \quad (6)$$

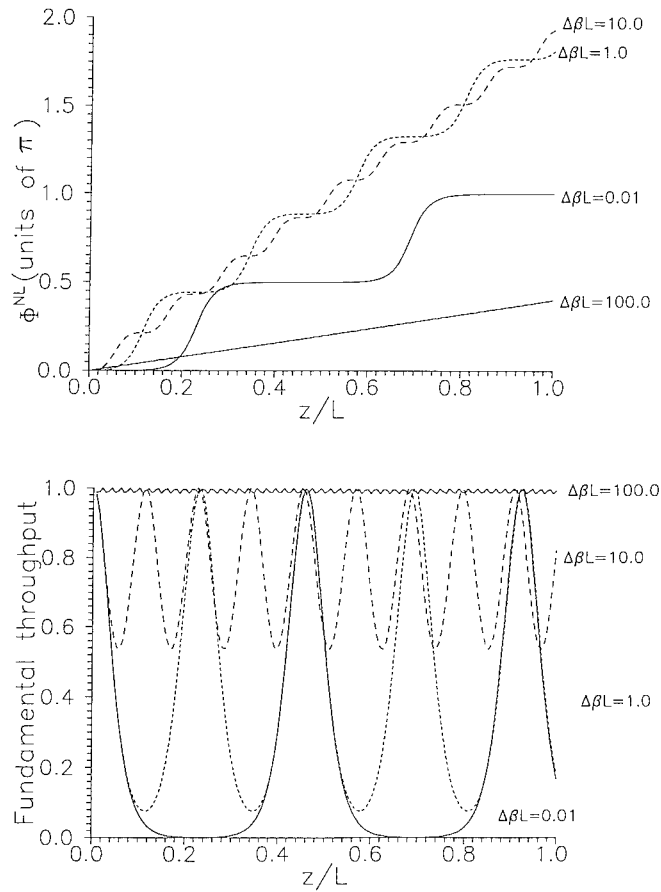


Fig. 2 The variation in (a) the nonlinear phase shift Φ^{NL} and (b) the fractional fundamental intensity $|a_\omega(z)|^2/|a_\omega(0)|^2$ with propagation co-ordinate z is shown for different wavevector detunings (normalized to π) $\Delta\beta L = 0.01, 1.0, 10.$, and 100 . Here $\kappa L = 4$ and $|a_\omega(0)|^2 = 25$.

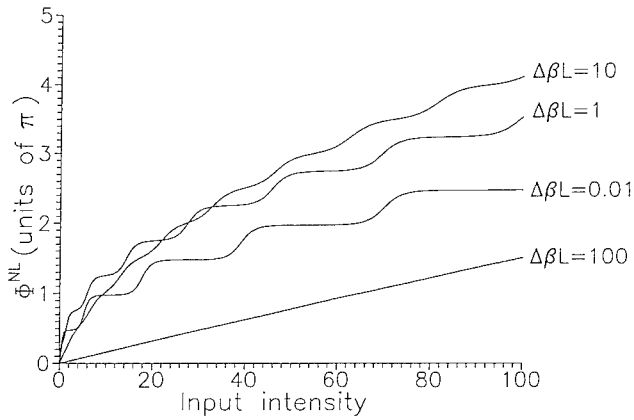


Fig. 3 The variation in the nonlinear phase shift Φ^{NL} versus input intensity for various wavevector detunings $\Delta\beta L$ (normalized to π) and $\kappa L = 4$.

Table 1 lists some values which might be possible, if all of the conditions for cascading can be satisfied. They should be compared with the largest known non-resonant nonlinearity, $2.2 \times 10^{-12} \text{ cm}^2/\text{W}$. Clearly there are exciting possibilities for very large effects.[9]

Table 1 **Effective, optimized, nonlinear coefficients n_2 via cascading for materials with representative d_{ij} .**

MATERIAL L= 1cm	d_{ij} pm/V	d_{ij} pm/V	$n_2(\text{effective})$ cm^2/W
LiNbO ₃	36		2×10^{-11}
LiNbO ₃		5.8	5×10^{-13}
MNA	165		7×10^{-10}
NPP		84	2×10^{-10}
DAST	600		6×10^{-9}

NPP N-(4-Nitrophenyl)-(L)-prolinol
MNA 2-Methyl-4-nitroaniline
DAST dimethyl amino stilbazolium tosylate

Because all-optical switching devices require nonlinear phase shifts, it is clear that they can all be implemented with cascading nonlinearities.[10] The generation of the second harmonic is an unwanted complication and effectively reduces the fundamental output.

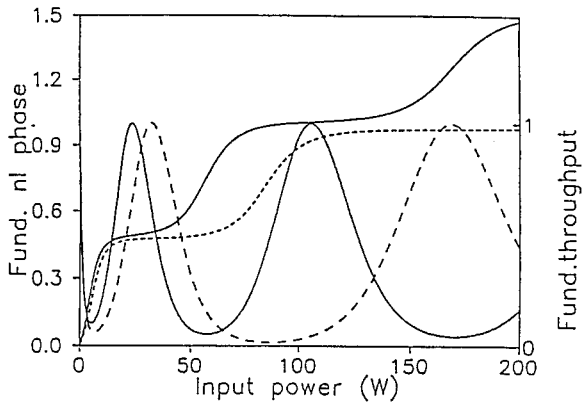


Fig. 4 The effect of "seeding" at the input with a 1% second harmonic signal on the nonlinear phase shift ϕ^{NL} versus normalized input intensity for various $\Delta\beta L$, i.e. accumulated phase mismatch. The slowly rising curves correspond to the phase shift and the oscillating curves to the throughput of the fundamental. Solid line- no seed. Dashed line - 1% seed.

One of the fascinating features of cascading is that there are new devices possible which are not feasible with third order nonlinearities. A distinctive aspect of this nonlinear process is that it

is coherent.[1,12] This has its disadvantages since the phase of the interacting waves must be stable. On the other hand, the outcome of a parametric process can be controlled by "seeding" it with a weak signal. An example of seeding with a weak second harmonic is shown in Fig. 4. Very large modulation can be achieved and in fact has been observed.[13]

OPTICAL TRANSISTOR

This last result suggests that an all-optical transistor might be possible. In Fig. 5 we sketch an interaction involving two orthogonally polarized input waves at ω , two ω -outputs and two effective nonlinear susceptibilities. The two fundamental waves are separately phase-matched to the same harmonic through different nonlinear coefficients. In the case of a strong cw pump and a weak signal carrying the information, the latter will affect the phase and amplitude of both outputs, with small signal gain and amplification at the expense of the pump wave. This is the prototype of an all-optical "common emitter" amplifier, with base and collector corresponding to cw and signal fundamental inputs, respectively.[14]

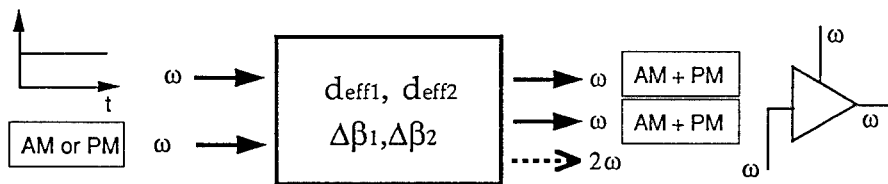


Fig. 5 An interaction allowing two orthogonally polarized fundamental waves to couple with the same SH-wave. The PM or AM signal will in general induce both PM and AM onto the "pump" fundamental, potentially with "small-signal" gain and amplification. No 2ω -inputs are involved.

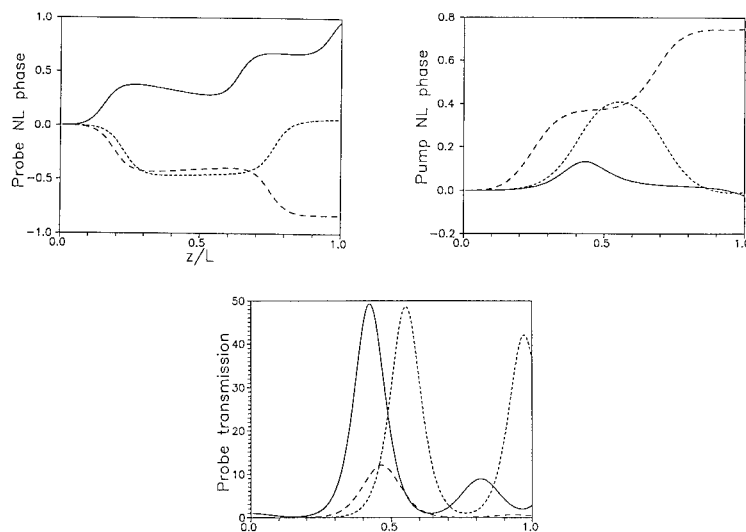


Fig. 6 Coherent interaction with a strong fundamental and a weak orthogonally polarized wave. a) Probe and b) pump nonlinear phases (units of π) and c) probe throughput versus normalized propagation distance for $|a_1(0)|^2=50$ (pump), $|a_2(0)|^2=1$, $\kappa_1 L=1$, $\kappa_2 L=2$, with $\Delta\beta_1 L=0.1\pi$ and $\Delta\beta_2 L=\pi$ (solid lines), $\Delta\beta_1 L=0.1\pi$ and $\Delta\beta_2 L=-0.1\pi$ (short dashes), $\Delta\beta_1 L=\pi$ and $\Delta\beta_2 L=0.1\pi$ (long dashes).

Fig. 6 shows some examples of energy transfer between the two fundamental beams versus propagation distance, assuming an intensity ratio of 50:1, $\kappa_2 L = 2\kappa_1 L = 2$ and various detunings $\Delta\beta_1$ and $\Delta\beta_2$ (see caption).[14] Graphed in Fig. 6c is the probe throughput normalized to its initial value at $z=0$. A substantial transfer of power takes place versus z , with the weak beam being amplified up to the level of the pump. Figs. 6a,b show the nonlinear phases vs z in both FF waves. The energy transfer from pump to second harmonic to probe imprints different signatures onto the phase evolution for differing initial wavevector mismatches.

SPATIAL SOLITONS

Another interesting application of cascading is to solitons. Although it might prove possible to find the appropriate materials to demonstrate and utilize temporal solitons, the right conditions are available for spatial solitons.[15-17] In fact, this effect has recently been demonstrated experimentally in LiNbO₃ slab waveguides. These spatial solitary waves have many interesting properties and are currently the subject of many theoretical investigations. The non-diffracting waves are different from spatial solitons generated via third order effects since both the fundamental and the second harmonic need to be mutually trapped. A numerical example is shown in Fig. 7. Some of the interesting features are listed below:

1. 0, 1 and 2 parameter families of stable spatial solitons exist;
2. Spatial solitons consist of coupled, mutually trapped, fundamental and second harmonic waves;
3. Some solutions are stationary, others are oscillating and energy can oscillate between the fundamental and second harmonic with propagation distance;
4. Spatial solitons can be excited by gaussian beams;
5. There are threshold powers for the existence of spatial solitons;
6. For "negative effective nonlinearities", bright spatial solitons can exist, but require "seeding" with an input second harmonic.

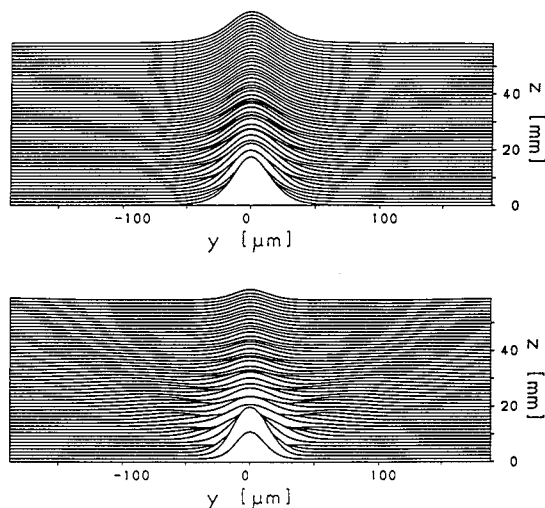


Fig. 7 Calculated self-trapping of a 40 μ m wide beam input with a sech spatial profile near wavevector matching, for propagation along the X-axis of LiNbO₃. The top and bottom curves show the spatial evolution along the propagation axis z of the fundamental and second harmonic beams respectively.

SUMMARY

Cascading of two second order parametric mixing interactions produces large nonlinear phase shifts. These shifts can be much larger than any available from third order nonlinear materials. And in fact all-optical devices are possible with cascading. However the spectrum of phenomena is much greater than for third order effects. One of the reasons is the coherence of the interactions which offers new possibilities in phase and amplitude modulation. New devices such as all-optical transistors appear feasible. Effects identified with third order nonlinearities such as solitons take on new features.

This research was supported by ARPA and ARO (DAAL03-91-C-0042).

REFERENCES

1. T.K. Gustafson, J.-P.E. Taran, P.L. Kelley and R.Y. Chiao, "Self-modulation of picosecond pulses in electro-optic crystals", *Opt. Commun.*, **2**, 17-21 (1970); E. Yablonovitch, C. Flytzanis, N. Bloembergen, "Anisotropic interference of three-wave and double two-wave frequency mixing in GaAs", *Phys.Rev.Lett.* **29**, pp.865-868(1972); Chr. Flytzanis and N. Bloembergen, "Infrared dispersion of third-order susceptibilities in dielectrics: retardation effects", *Quant. Electron.*, **4**, pp.271-300 (1976)
2. G.I. Stegeman, M. Sheik-Bahae, E. Van Stryland, G. Assanto, "Large nonlinear phase-shifts in second-order nonlinear-optical processes", *Opt.Lett.* **18**, pp.13-15(1993)
3. D. Hutchings, J.S. Aitchison, C.N. Ironside, "All-optical switching based on nondegenerate phase shifts from a cascaded second-order nonlinearity", *Opt.Lett.* **18**, pp.793-795(1993)
4. A.L. Belostotsky, A.S. Leonov, A.V. Meleshko, "Nonlinear phase change in type II second-harmonic generation under exact phase-matched conditions", *Opt.Lett.* **19**, pp.856-858 (1994).
5. N.R. Belashenkov, S.V. Gagarinskii, M.V. Inochkin, "Nonlinear refraction of light on second-harmonic generation", *Opt.Spectrosc.* **66**, pp. 806-808(1989)
6. R. DeSalvo, D.J. Hagan, M. Sheik-Bahae, G. Stegeman, E.W. Van Stryland, "Self-focusing and self-defocusing by cascaded second-order effects in KTP", *Opt.Lett.* **17**, pp.28-30(1992)
7. M.I. Sundheimer, Ch. Bosshard, E.W. Van Stryland, G.I. Stegeman, J.D. Bierlein, "Large nonlinear phase modulation in Quasi-Phase-matched KTP waveguides due to cascaded second-order processes", *Opt.Lett.* **18**, pp.1397-1399(1993)
8. D.Y. Kim, W.E. Torruellas, J. kang, C. Bosshard, G.I. Stegeman, P. Vidakovic, J. Zyss, W.E. Moerner, R. Twieg, G. Bjorklund, "Second-order cascading as the origin of large third-order effects in organic single-crystal-core fibers", *Opt.Lett.* **19**, pp.868-870 (1994).
9. B. Lawrence, M. Cha, J.U. Kang, W. Torruellas, G.I. Stegeman, G. Baker, J. Meth and S. Etemad, "Large Purely Refractive Nonlinear Index of Single Crystal P-Toluene Sulfonate (PTS) at 1600 nm", *Electron. Lett.*, **30**, pp. 447-8 (1994).
10. G.I. Stegeman, E.M. Wright, "All-optical waveguide switching", *Opt.Quant.Electron.* **22**, pp.95-122(1990)
11. G. Assanto, G.I. Stegeman, M. Sheik-Bahae, E. VanStryland, "A novel approach to all-optical switching based on second-order nonlinearities", *Proc. of "Nonlinear Optics: Materials, Fundamentals, and Applications"*, Lahaina, Maui, Hawaii, pap. PD11, pp.1-4, Aug. 1992; G. Assanto, G.I. Stegeman, M. Sheik-Bahae, E. Van Stryland, "All-optical switching devices based on large nonlinear phase shifts from second harmonic generation", *Appl.Phys.Lett.* **62**, pp.1323-1325(1993)
12. P. St.J. Russell, "Theoretical study of parametric frequency and wavefront conversion in nonlinear holograms", *IEEE J. Quant. Electron.*, **27**, pp.830-5 (1991).
13. D.J. Hagan, M. Sheik-Bahae, Z. Wang, G. Stegeman, E.W. Van Stryland, G. Assanto: "Phase

Controlled Transistor Action by Cascading of Second-Order Nonlinearities in KTP", Opt. Lett., **19**, pp. 1305-7 (1994).

14. G. Assanto, G.I. Stegeman, M. Sheik-Bahae and E. VanStryland, "Coherent Interactions for All-Optical Signal Processing via Quadratic Nonlinearities", J. Quant. Electron., under revision

15. M.J. Werner and P.D. Drummond, "Simulton Solutions for the Parametric Amplifier", J. Opt. Soc. Am. B, **10**, pp.2390-3 (1993).

15. L. Torner, C.R. Menyuk and G.I. Stegeman, "Excitation of Soliton-like Waves with Cascaded Nonlinearities", Opt. Lett., **19**, pp.1615-7 (1994).

16. R. Schiek, "Nonlinear refraction caused by cascaded second-order nonlinearity in optical waveguide structures", J. Opt.Soc. Am. B **10**, pp.1848-1854 (1993).

Nonlinear phase-shifts by cascading in the Čerenkov regime

Gijs J.M. Krijnen^{1,2}, William Torruellas¹, George I. Stegeman¹,
Hugo J.W.M. Hoekstra² and Paul V. Lambeck²

¹ CREOL, University of Central Florida
12424 Research Parkway Suite 400, Orlando, Florida 32826

² Lightwave Devices Group, MESA Institute
University of Twente, P.O. Box 217, 7500 AE Enschede, The Netherlands

ABSTRACT

We present Beam Propagation Method studies of Second Harmonic Generation and nonlinear phase-changes by cascading in the Čerenkov regime. It is shown that cascading in the Čerenkov regime can produce phase changes comparable to those obtained by guided mode - guided mode interaction. The signature of cascading, with both positive and negative phase-changes is observed when the core refractive indices are varied. Large phase-shifts with small loss of the fundamental are shown to be possible.

INTRODUCTION

The interest in $\chi^{(2)}$ -materials and related nonlinear wave-propagation effects has been driven for a long time by potential applications in efficient blue-light generation by Second Harmonic Generation (SHG) and electro-optical switching [1]. Recently additional interest has been raised by advances in organic $\chi^{(2)}$ -materials which promise large nonlinear phase-shifts by cascading of second order effects. In this scheme the up-conversion of a fundamental beam to its second harmonic and the subsequent down-conversion of the second harmonic to the fundamental due to a wavevector mismatch generates nonlinear phase changes on the fundamental beam [2][3]. This approach offers possibilities for tackling problems which have traditionally required third order nonlinearities: all optical switching [4].

From a practical point of view the interest in SHG has been dominated by guided mode - guided mode (here referred to as type A) interactions rather than by guided mode - radiation mode (type B) interactions (also called Čerenkov radiation) since the latter cause problems for the collection of the SHG light as well as for analytical investigations. Initial papers on cascading [2] naturally focused on type A interactions since these lent themselves to be tackled by Coupled Mode Analysis (CMA). One of the remarkable results of the CMA of second order cascaded processes is that both the magnitude and sign of the nonlinear phase-shifts can be tailored by choosing appropriate wavevector mismatches. In the case of type B interactions analytical relations are far more difficult to obtain due to the problems associated with normalisation of radiation modes and, thus, expressions for the nonlinear coupling coefficients are more difficult to derive. Numerical studies on type B interactions [5] have merely focused on the efficiency of SHG in structures in which both the index of the cladding and the core at 2ω ($n_{cl}^{2\omega}$ and $n_c^{2\omega}$ respectively) are larger than the effective index of the guided modes at ω (N_{eff}^ω).

In this paper we will describe a widely applicable method: the SHG Beam Propagation Method (SHG-BPM). This method is an extension of normal BPM's and offers a general approach to dealing with waves rather than with modes thereby circumventing the problems associated with depletion and non-normalisable radiation modes encountered in coupled mode approaches. Using the SHG-BPM we investigate the SHG efficiencies and nonlinear phase changes of type B interactions taking the nontrivial case $n_c^{2\omega} < N_{eff}^\omega < n_{cl}^{2\omega}$ into account too. We find that, depending on the quantity $\Delta n = n_c^{2\omega} - N_{eff}^\omega$, large phase changes (>360 degrees) and/or almost complete conversion (97%) are possible while maintaining small input powers and short interaction lengths.

NUMERICAL METHOD

The numerical method we use (here referred to as SHG-BPM) starts with the second order nonlinear polarisation that couples the two wavelengths [6]. Inserting this polarisation into the wave-equation using $\chi^{(2)}(\omega, \omega; 2\omega) = \chi^{(2)}(2\omega, -\omega; \omega) \equiv \chi^{(2)}$, applying the Slowly Varying Envelope Approximation (SVEA) and discretising the fields in the transverse (x -) direction the propagation equations are:

$$j \frac{\partial \bar{\psi}_f}{\partial z} = \mathbf{M}_f \bar{\psi}_f + \frac{1}{2n_0 k_0} \frac{\partial^2 \bar{\psi}_f}{\partial z^2} + \frac{k_0 \chi^{(2)}}{n_0} \bar{\psi}_f^* \bar{\psi}_s \quad (1a)$$

$$j \frac{\partial \bar{\psi}_s}{\partial z} = \mathbf{M}_s \bar{\psi}_s + \frac{1}{4n_0 k_0} \frac{\partial^2 \bar{\psi}_s}{\partial z^2} + \frac{k_0 \chi^{(2)}}{n_0} \bar{\psi}_f^2 \quad (1b)$$

where the subscripts f and s refer to the fields at ω and 2ω respectively, k_0 is ω/c , n_0 is a suitable background refractive index, $\bar{\psi}_f$, $\bar{\psi}_s$ are vectors representing the discretised field envelopes and \mathbf{M}_s and \mathbf{M}_f are tri-diagonal discretisation matrices. The equations are solved using a split-step approach; the first two linear operators are handled by an Enhanced Finite Difference Beam Propagation Method (EFDBPM) [7] whereas the third operator, which is given by the coupled differential equations

$$\begin{aligned} j \frac{\partial \psi_f^i}{\partial z} &= \alpha \psi_f^{i*} \psi_s^i \\ j \frac{\partial \psi_s^i}{\partial z} &= \alpha \psi_f^i \psi_f^i \end{aligned} \quad \alpha = \frac{k_0 \chi^{(2)}}{n_0}, i \in (0, m) \quad (2)$$

is solved pointwise for all m discretisation points. When integrating over small distances Δz in which $|\psi_f^i|$ can be assumed to be constant the eigenvalues of equation (2) become $\pm\alpha|\psi_f^i|$. The corresponding eigenvectors are:

$$\begin{bmatrix} \psi_{f1}^i \\ \psi_{s1}^i \end{bmatrix} = \frac{1}{\sqrt{2}} \begin{bmatrix} e^{-i\phi} \\ 1 \end{bmatrix} \quad \text{and} \quad \begin{bmatrix} \psi_{f2}^i \\ \psi_{s2}^i \end{bmatrix} = \frac{1}{\sqrt{2}} \begin{bmatrix} e^{-i\phi} \\ -1 \end{bmatrix} \quad (3)$$

where ϕ is the phase of ψ_f^i i.e. $\psi_f^i = e^{i\phi}|\psi_f^i|$. The accuracy of the numerical implementation of the solution of equation (2) is increased by taking three integration steps for each step of the EFDBPM. The accuracy of each of these three steps in turn is improved by solving $\psi_f^i(z+\Delta z)$ using the eigenvalues $\pm\alpha|\psi_f^i|$, followed by using the average of $\psi_f^i(z)$ and the first obtained approximation of $\psi_f^i(z+\Delta z)$ in the calculation of the eigenvalues in equation (3). In principle other BPM's can be used as well. Although equation (1) will be different, equation (2) can be solved in a similar way. Here the EFDBPM was chosen because of the high accuracy with which it calculates propagation constants. To keep calculation times reasonable and the accuracy of the simulations independent of the window size we used transparent boundary conditions [8]. This is extremely important since we are dealing with fields consisting primarily of radiation modes at 2ω .

In order to keep track of the amount of power contained in the field at ω we calculate the overlap of this field with the launched guided mode. In almost all cases this power is about equal to the total amount of power (i.e. the power of the fields at ω and 2ω together) at any propagation co-ordinate. Since the only loss of total power in the calculation is caused by outflow of radiation modes at 2ω the power that is converted to the field at 2ω can be calculated from the remaining guided mode power at ω .

NUMERICAL STUDIES

Simulated Structure

As an example we studied a 4.3 mm long slab-waveguide, with cladding refractive index $n_{cl}^\omega = 1.6875$, $n_{cl}^{2\omega} = 1.7100$, a 5 μm thick core with refractive index $n_c^\omega = 1.6992$ and a $\chi^{(2)}$ of 54 pm/V, at $\lambda_f = 1.32 \mu\text{m}$. This structure resembles to some extent the waveguide properties of a DAN fibre in which large nonlinear phase-shifts have been measured recently [9]. The effective indices of the fundamental and first order mode at ω are $N_0^\omega = 1.69672$ and $N_1^\omega = 1.69023$.

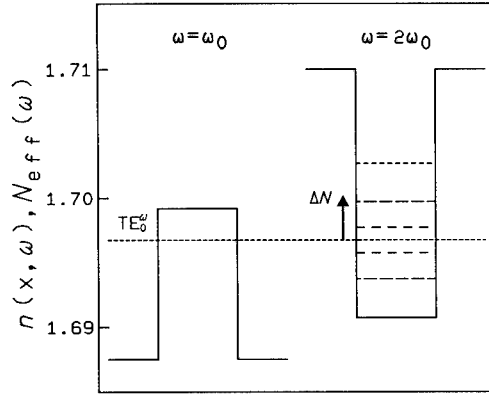


Figure 1: Graphical illustration of the structure used.

We investigate the system which is schematically shown in Figure 1. Either the TE_0^ω or the TE_1^ω mode is launched and the refractive index of the core at 2ω ($n_c^{2\omega}$) is varied around the value of the effective refractive index of the TE_i^ω ($i=0,1$) mode, i.e. $\Delta n \equiv n_c^{2\omega} - N_i^\omega$. In all calculations the stepsizes in the propagation (z -) and lateral (x -) directions were fixed at 1 and $\approx 0.1 \mu\text{m}$ respectively.

Launching the TE_0^ω mode

In the simulations that show appreciable SHG there is primarily a strong initial (i.e. at small propagation co-ordinate) conversion to 2ω followed by a steady outflow of power at 2ω . Simultaneously the TE_0^ω -mode is initially quickly depleted changing over to exponential decay at longer distances. This is illustrated in Figure 2 which was obtained for $\Delta n = 1 \cdot 10^{-3}$. In some simulations there are initial oscillations between the fields at ω and 2ω . However, these oscillations tend to damp out rather quickly.

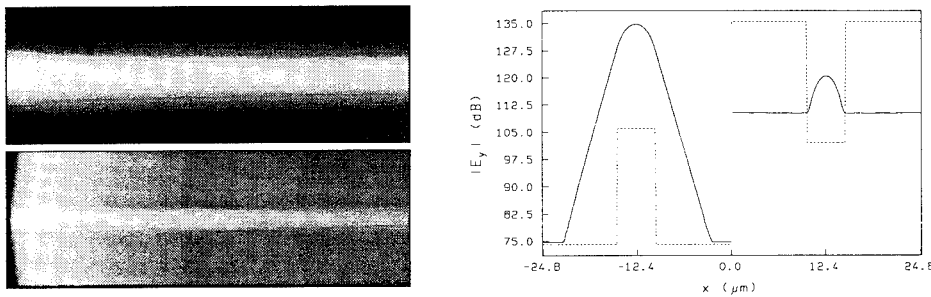


Figure 2: SHG-BPM results for launching the TE_0^ω mode and $\Delta n = 1 \cdot 10^{-3}$. Left: intensity profiles at ω (top) and 2ω (bottom). The profiles are plotted on a 60 dB scale and the figures correspond to an area of $25 \mu\text{m} \times 4.3 \text{ mm}$. Right: field profile at the output of the structure on a logarithmic scale. The field profiles at ω (left) and 2ω (right) are both shown. The dotted lines show the index profiles.

Figure 2 right shows the output fields at ω (left) and 2ω (right) on a logarithmic scale after 4.3 mm of propagation. The field at ω neatly corresponds to a guided mode since strong interaction with the field at 2ω only takes place in the first 1 or 2 mm.

By calculating the overlap integrals the nonlinear phase changes induced by cascading and the conversion to SHG are obtained. The depletion and nonlinear phase change of the TE_0^{ω} mode after 4.3 mm of propagation are shown in Figure 3 left and right respectively for an input power $P_{in}^{\omega}=8.5$ MW/m (corresponding to an equivalent input power of 30 W in the fibre-geometry). The results are plotted as a function of Δn . Clearly both the depletion (i.e. SHG efficiency) and the nonlinear phase change are strongly dependent on Δn and, moreover, the sign of the nonlinear phase shift can be positive as well as negative depending on Δn . The observed resonance behaviour is very similar to that obtained for type A interactions.

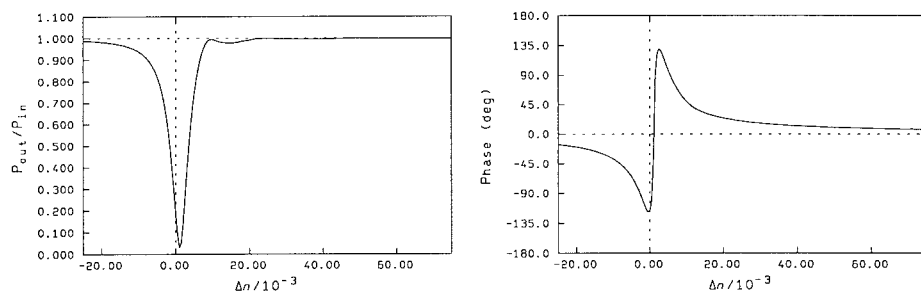


Figure 3: Power (left) and nonlinear phase change (right) of the TE_0^{ω} mode versus Δn .

The zero phase-shift and maximum depletion coincide but they do not coincide with $\Delta n=0$. Instead they are shifted to positive Δn ($\approx 1 \cdot 10^{-3}$) a result that we confirmed to not depend on either the accuracy of the EFDBPM calculations or on P_{in}^{ω} (confirmed by calculations at smaller P_{in}^{ω} not shown here). Apart from the deep dip at $\Delta n=1 \cdot 10^{-3}$, there are additional shallow dips at $\Delta n=12 \cdot 10^{-3}$ and $34 \cdot 10^{-3}$. Combining Figure 3 left and right it can also be seen that there exist Δn -values for which the depletion of the fundamental is very small whereas there is still appreciable nonlinear phase change. This is especially true for $\Delta n=9.5 \cdot 10^{-3}$ where almost 53 degrees phase-change is obtained at only 0.6% conversion.

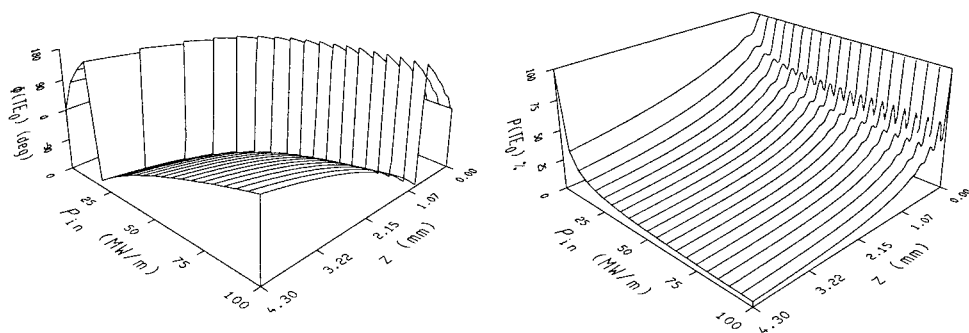


Figure 4: Phase changes modulus 360 degrees (left) and fraction of power in the TE_0^{ω} mode (right) as a function of input power (P_{in}^{ω}) and propagation distance (z) for fixed $\Delta n=2.5 \cdot 10^{-3}$.

Since nonlinear phase-changes by cascading are interesting for all-optical switching it is necessary to study the power dependent characteristics. Of course, the requirements for switching do not only include a large phase-change but also a large output power at ω .

Therefore the power-dependence of the depletion and nonlinear phase changes are investigated in a series of calculations with increasing input power.

A first choice for Δn is $2.5 \cdot 10^{-3}$ since this is the value for which the nonlinear phase change is maximum (see Figure 3 right). Figure 4 left displays the nonlinear phase change (unwrapped) by cascading as a function of P_{in}^{ω} and propagation distance. Clearly the nonlinear phase changes increase with increasing input power as well as with increasing propagation length. However, the growth of the phase changes with either length or input power slows down considerably with increasing length or power. The reason for this decreasing growth is evident from Figure 4 right. It shows the fraction of power remaining in the TE_0^{ω} mode as a function of P_{in}^{ω} and propagation distance (z). At low power depletion (i.e. SHG) is modest. However, on increasing the power the conversion becomes more complete leading to almost complete depletion of the TE_0^{ω} mode at $z=4.3$ mm. Therefore, since the phase-changes can only be acquired at the expense of converting, and losing, power to the second harmonic, there is no sustained growth of the nonlinear phase change i.e. depletion will decrease the effective length over which the nonlinear phase change is accumulated. Moreover, the large loss of input power makes this an unattractive scheme by itself. Since it is clear from Figure 4 that maximum phase change at high power is not necessarily obtained for the Δn value for which maximum phase change at lower power is found, it is interesting to take a value for Δn for which the losses are low while still having an appreciable nonlinear phase-change. As mentioned before, this is especially true for $\Delta n=9.5 \cdot 10^{-3}$.

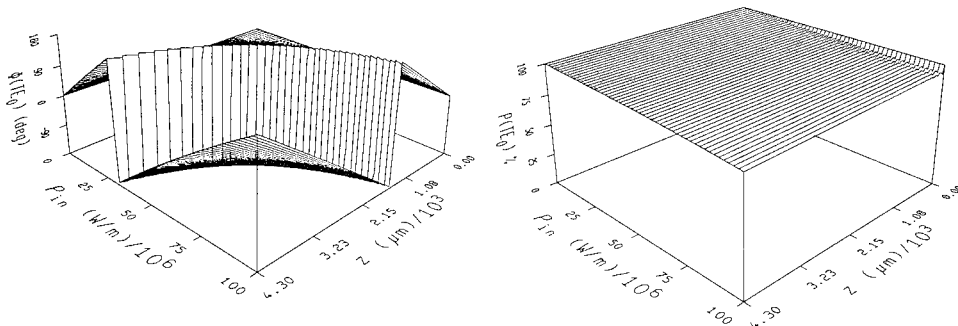


Figure 5: Phase changes modulus 360 degrees (left) and fraction of power in the TE_0^{ω} mode (right) as a function of input power (P_{in}^{ω}) and propagation distance (z) for fixed $\Delta n=9.5 \cdot 10^{-3}$.

Figure 5 left shows the nonlinear phase changes versus input power and propagation length for $\Delta n=9.5 \cdot 10^{-3}$. As for the case of $\Delta n=2.5 \cdot 10^{-3}$ the phase increases with input power as well as with length. However, in contrast to the case of $\Delta n=2.5 \cdot 10^{-3}$, the growth of the nonlinear phase-change does not show any significant decrease with distance. Instead it grows virtually linearly with both power and propagation length. Note that Figure 5 left shows a nonlinear phase-change of 360 degrees for an input power of 66 MW/m (which corresponds to about 230 W in the equivalent 4.3 mm long fibre). From Figure 5 right the virtual linear behaviour is easily understood since it shows that there is no strong depletion of the fundamental. Hence the power remains available for generation of more and more phase-shift as the mode propagates through the structure.

Because of the linear characteristics the nonlinear phase change can be expressed in degrees per meter of device length per W of input power. For the equivalent fibre structure this value is 360 degrees/Wm. Hence, 360 degrees phase change could be obtained by

inputting 10 W into a 10 cm long fibre. It is expected that even larger phase changes are obtainable with materials with larger $\chi^{(2)}$ and fibres with smaller core-size.

Launching the TE_1^0 mode

Comparable calculations were done for the case of launching the TE_1^0 instead of the TE_0^0 mode. The SHG-BPM results are illustrated in Figure 6 left for $\Delta n \equiv n_c^{2\omega} - N_1^0 = 1 \cdot 10^{-2}$. For this value of Δn there is considerable conversion of power to the 2ω field. The 2ω field profile differs strongly from those displayed in Figure 2 and, moreover, the field at 2ω is much smaller. Both features are especially well shown in Figure 6 right. It should be remarked though, that for $\Delta n = 1 \cdot 10^{-3}$, field profiles at 2ω similar to the 2ω profiles shown in Figure 2 are obtained. It shows that the field at 2ω is not necessarily proportional to the square of the fundamental field.

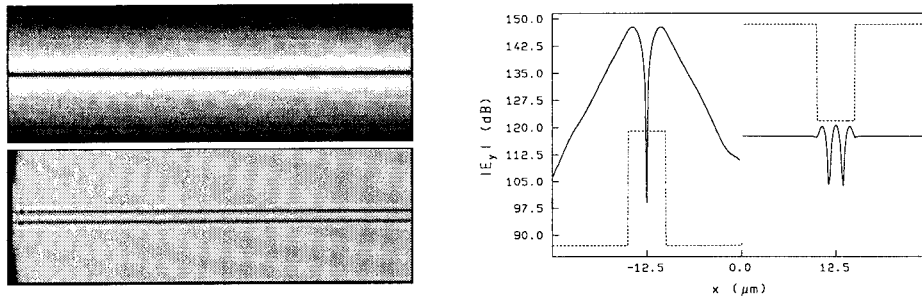


Figure 6: SHG-BPM results for launching the TE_1^0 mode and $\Delta n = 1 \cdot 10^{-2}$. Left: intensity profiles at ω (top) and 2ω (bottom). Details as for Figure 2.

The nonlinear phase change and depletion of the TE_1^0 mode at the output of the structure as a function of Δn are shown in Figure 7 left and right respectively. The input power was again $P_{in}^0 = 8.5$ MW/m.

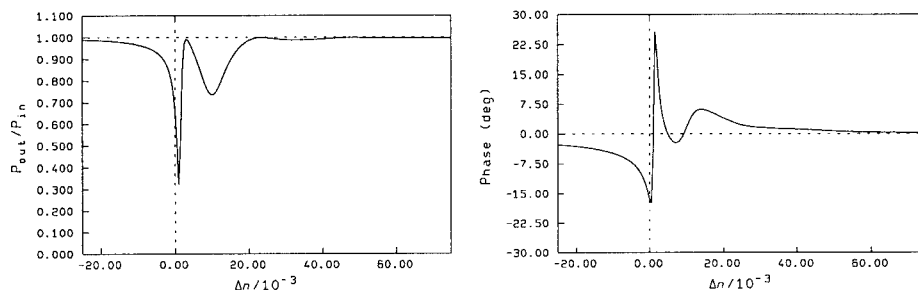


Figure 7: Power (left) and nonlinear phase change (right) of the TE_1^0 mode versus Δn .

As in the case of launching the TE_0^0 mode the nonlinear phase change and depletion are strongly dependent on Δn . Figure 7 left shows 3 distinct minima in the transmission curve (corresponding to three maxima in the SHG output) of the TE_1^0 mode at Δn -values of $1 \cdot 10^{-3}$ (32.3% transmission), $10 \cdot 10^{-3}$ (73.5%) and $32 \cdot 10^{-3}$ (98.7%). Note that these values are close to the values for which the minima are found when the TE_0^0 mode is launched. However, in contrast to that case the dip at $\Delta n = 1 \cdot 10^{-3}$ is less deep and sharper whereas the dip at $10 \cdot 10^{-3}$ is deeper and broader. Figure 7 right shows the nonlinear phase change. It is

seen to dependent strongly on Δn and its sign can again be positive or negative. However, the absolute values of the nonlinear phase changes are smaller than those obtained when launching the TE_0^0 mode. Furthermore it is noted that in this case (of launching the TE_1^0 mode) the nonlinear phase-changes consist of at least two superimposed resonances. In a future publication we will address the physical origin of the observed resonances and the particular Δn values for which these resonances occur.

Comparison of type A and type B interactions for cascading

To compare the results obtained for cascading in the Čerenkov regime to those obtainable with type A interactions a waveguide structure similar to the previous two cases but with $n_{cl}^{2\omega}=1.6975$ and $n_c^{2\omega}=1.6900$ is simulated. These refractive index values correspond to a $\Delta N=N_0^{2\omega}-N_0^\omega=3.0 \cdot 10^{-3}$ for which the nonlinear phase-change at 8.5 MW/m input power has a maximum of 306 degrees. Figure 8 left displays the nonlinear phase change by cascading as a function of P_{in}^ω and propagation distance. It shows that at fixed Δn the nonlinear phase change per oscillation of the power between the fields at ω and 2ω is more or less fixed giving the graph its staircase like appearance. However, as the input power increases, the number of oscillations increases and thereby the total nonlinear phase change at the output. Figure 8 right shows the transmission of the TE_0^0 mode versus P_{in}^ω and propagation distance. At low power (1 MW/m) there is already an appreciable amount of SHG. When increasing the power this conversion becomes more complete but at the same time the coherence length shortens causing an increasing number of oscillations within a fixed length. This means that the amount of power emerging from the waveguide in either the fundamental or the second harmonic is difficult to control since it is power dependent. These results are consistent with CMA analyses of type A interactions [2].

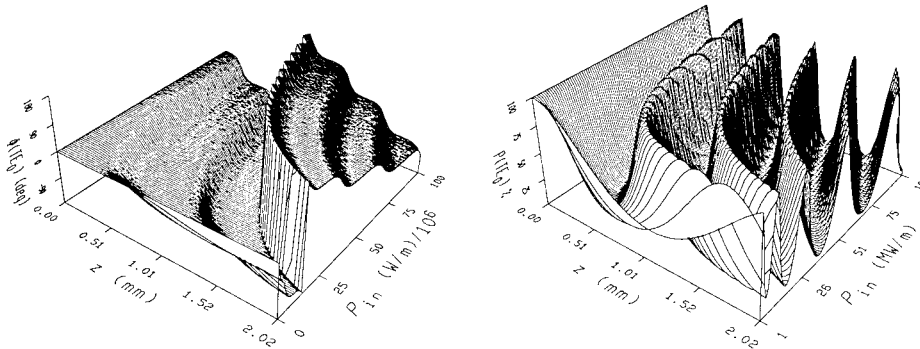


Figure 8: Nonlinear phase change modulus 360 degrees (left) and fraction of power in the TE_0^0 mode (right) as a function of input power and propagation distance for type A interactions (note that only the first 2.02 mm is shown).

Comparing type A and type B interactions, especially those shown in Figure 5 for $\Delta n=9.5 \cdot 10^{-3}$, it can be concluded that type B offers advantages in the form of a non-periodic behaviour with nonlinear phase changes which increase essentially proportional to the length and input power while losses of the fundamental field are only a few percent. However, type A interactions show nonlinear phase changes which are almost a factor of 6 larger than those obtained for type B at a given length and input power but at the expense of power-dependent periodic conversion. Taking larger detuning the modulation depth of the periodic conversion can be decreased but this on its turn will decrease the nonlinear phase

changes too. Hence eventually, both type of interactions may be comparable with type A interactions having the disadvantage of small periodic power conversion versus the disadvantage of small power loss for type B interactions.

CONCLUSIONS

In conclusion we have described a method for the calculation of the interaction of waves in $\chi^{(2)}$ -materials and devices. We have employed this method to investigate SHG and cascading in the Čerenkov regime. As in the case of type A interactions, type B interactions show interesting nonlinear phase changes which bear the signature of (type A) cascading. A proper choice of refractive indices can result in a system that is capable of producing large nonlinear phase changes (>360 degrees) at moderate losses (<6%) and moderate input power. Advantages of type B interactions are the absence of periodic conversion and the almost linear growth of the nonlinear phase-shift with power and propagation length.

ACKNOWLEDGEMENTS

It is with pleasure that we acknowledge the many fruitful discussions with Roland Schiek. The research of GK has been made possible by a fellowship of the Royal Netherlands Academy of Arts and Sciences.

REFERENCES

- [1] "Compact Blue-Green Lasers", OSA Technical digest Series, Santa Fe, New Mexico, (1992).
- [2] G. Stegeman, M. Sheik-Bahae, E. van Stryland and G. Assanto, "Large nonlinear phase shifts in second-order nonlinear processes", *Opt. Lett.* 18, pp. 13-15, 1993.
- [3] M.L. Sundheimer, Ch. Bosshard, E. Van stryland, G.I. Stegeman and J. Bierlein, "Large nonlinear phase modulation in quasi-phase-matched KTP waveguides as a result of cascaded second order processes", *Opt. Lett.* 18, pp. 1397-1399, 1993.
- [4] "Photonics in Switching", Edited by John E. Midwinter, Academic Press, London, 1993.
- [5] K. Chikuma, S. Umegaki, "Theory of optical second-harmonic generation in crystal-cored fibers based on phase matching of type radiation", *J.O.S.A.B.* 9, pp. 1083-1092, 1992.
- [6] A. Yariv and P. Yeh, "Optical Waves in Crystals", John Wiley & Sons, 1984.
- [7] H. Hoekstra, G. Krijnen and P. Lambeck, "New formulation of the beam propagation method based on the slowly varying envelope approximation", *Opt. Comm.* 97, pp. 301-303, 1993.
- [8] G. Hadley, "Transparent boundary conditions for beam propagation", *Opt. Lett.* 16, pg 624-626, 1991.
- [9] D. Kim, W. Torruellas, J. Kang, C. Bosshard, G. Stegeman, P. Vidakovic, J. Zyss, W. Moerner, R. Twieg and G. Bjorklund, "Second order cascading as the origin of large third-order effects in organic single-crystal-core fibers," *Opt. Lett.* 19, pp. 868-870, 1994.

ULTRASHORT PULSE PROPAGATION IN NONLINEAR PLANAR OPTICAL WAVEGUIDES

Govind P. Agrawal and Andrew T. Ryan

The Institute of Optics
University of Rochester
Rochester, NY 14627

INTRODUCTION

For many years, optical pulse propagation in fibers has been an area of intense investigation.¹ Apart from the obvious communication applications, optical fibers are important because they provide a simplified environment for studying the nonlinear effects. Two important consequences of the guiding nature of fibers are that diffractive effects can be eliminated from consideration and, perhaps more importantly, nearly constant pulse energies can be maintained over relatively long propagation distances due to the low loss in fibers. Thus, optical fibers are an excellent tool for studying the interplay of chromatic dispersion and optical nonlinearities, in particular the intensity-dependent refractive index or Kerr nonlinearity.¹

Planar waveguides are similar to fibers in the sense that there is still good field confinement. But since the confinement is only one-dimensional, it is possible to study the influence of diffractive effects on the field dynamics in the presence of the Kerr nonlinearity responsible for self-focusing or self-defocusing. This interplay is particularly interesting when the field is in the form of an ultrashort pulse, in which case not only do the dispersive and diffractive effects occur simultaneously but also the spatial behavior is coupled via the nonlinearity to the temporal behavior. This paper is devoted to studying the effects of such a spatio-temporal coupling in planar optical waveguides modeled as a dispersive nonlinear medium. We present the results of numerical simulations showing that, because of this spatio-temporal coupling, one can manipulate the pulse width in time with manipulation of the optical phase in space.

NONLINEAR SCHRÖDINGER EQUATION

The numerical simulations presented here are based on the nonlinear Schrödinger equation (NSE) which has long been a useful tool in describing nonlinear optical

phenomena.¹ The NSE is derived from Maxwell's equations for the case of an intensity-dependent (Kerr-type) index of refraction of the form $n(\omega) = n_0(\omega) + n_2 I$ (resulting in a cubic nonlinearity in the field dependence of the polarization), where the frequency-dependence of the linear index $n_0(\omega)$ stems from chromatic dispersion. We model pulse propagation with the NSE in the one-dimensional or waveguide approximation which consists of assuming that diffraction occurs in only one transverse direction, the field behavior in the other direction being determined by the structure of the waveguide. To simplify the model and broaden the applicability of the results, we normalize all of the variables including the field which is normalized so that its peak input value is unity. The coordinates are normalized as follows: transverse spatial coordinate $\xi = x/\sigma$ is normalized to the input beam width σ , temporal coordinate $\tau = [t - (z/v_g)]/T_0$ is the reduced time normalized to the incident pulse width T_0 , and propagation distance $\zeta = z/L_d$ is measured in units of the diffraction length $L_d = (2\pi/\lambda)\sigma^2$, where λ is the optical wavelength. The normalized NSE then takes the form²:

$$i \frac{\partial u}{\partial \zeta} + \frac{1}{2} \frac{\partial^2 u}{\partial \xi^2} - \frac{s}{2} \frac{\partial^2 u}{\partial \tau^2} + \text{sgn}(n_2) N^2 |u|^2 u = 0. \quad (1)$$

Here, the parameter $N^2 = (2\pi\sigma/\lambda)^2 n_0 n_2 I_0$ represents the strength of the Kerr nonlinearity. (It will be seen later that N corresponds to the soliton order.) The quantity $n_2 I_0$ is the maximum nonlinear index change for an input pulse of peak intensity I_0 and depending on the sign of n_2 , it can be either positive (self-focusing) or negative (self-defocusing). The parameter $s = L_d/L_D = (2\pi/\lambda)\sigma^2\beta_2/T_0^2$ is the ratio of the diffraction length to the dispersion length ($L_D = T_0^2/|\beta_2|$) and represents the relative strengths of dispersion and diffraction. Here β_2 is the group-velocity-dispersion (GVD) parameter defined as the second derivative of the propagation constant β of the waveguide mode and evaluated at the carrier frequency ω_0 . The s parameter can be either positive or negative, depending on whether the medium is normally ($\beta_2 > 0$) or anomalously ($\beta_2 < 0$) dispersive.

For a linear medium ($N = 0$), the NSE is a separable equation leading to solutions whose space- and time-domain features evolve independently of each other. The inclusion of the nonlinearity makes the NSE inseparable in ξ and τ , thereby coupling the behavior in the two domains together. It also makes analytical solutions extremely difficult to achieve, hence our numerical approach. We use the well-known split-step Fourier method¹ to model the evolution of an input Gaussian field of the form:

$$u(\xi, \tau, 0) = \exp\left(-\frac{\xi^2}{2} - \frac{\tau^2}{2}\right) \exp[i\phi(\xi)]. \quad (2)$$

Here we use $\phi(\xi)$ to represent the spatial phase modulation, typically assumed to be of the form $\phi(\xi) = \phi_0 \sin(2\pi p \xi + \delta)$. Although sinusoidal in appearance, in reality our spatial modulation frequencies are small enough ($p \approx 0.2$) that, depending on the phase shift δ , the modulation is either approximately linear (for $\delta = 0, \pi$) or quadratic (for $\delta = \pi/2$). The former has a prism-like effect useful for beam steering³ while the effect of the latter is lens-like and can be used to either focus ($\phi_0 > 0$) or defocus ($\phi_0 < 0$) the input field. Depending on the medium parameters n_2 and β_2 , lens-like spatial phase modulation may be used, via the spatio-temporal coupling provided by the nonlinearity, to control the width of the field

in the time domain (the pulse width). Since both β_2 and n_2 can be positive or negative, pulse propagation in waveguides can be classified in four different propagation regimes. These regimes have previously been investigated⁴ in the context of modulation instability where it was found that a cw beam can be modulationally unstable in the normal-dispersion regime in both the self-focusing and self-defocusing cases because of spatio-temporal coupling. It was also shown that the anomalous-dispersion regime of a self-defocusing medium was modulationally stable. We discuss the field behavior in each regime separately with an emphasis on the pulse and beam widths. However, before doing so it is useful to consider spatial and temporal solitons that are exact solutions of Eq. (1) under certain special conditions.

SPATIAL AND TEMPORAL SOLITONS

In order to better understand the effects of a self-focusing nonlinearity ($n_2 > 0$) we should first investigate solutions of the NSE under some simplified conditions. For a relatively wide pulse ($T_0 > 10$ ps) the dispersion length becomes much larger than the diffraction length such that $s \ll 1$. If we neglect the third term in Eq. (1), it takes the form:

$$i \frac{\partial u}{\partial \zeta} + \frac{1}{2} \frac{\partial^2 u}{\partial \xi^2} + \text{sgn}(n_2) N^2 |u|^2 u = 0. \quad (3)$$

For a self-focusing medium ($n_2 > 0$), this equation has exact solutions⁵ (known as spatial solitons) for integer values of N such that N represents the order of the spatial soliton. The fundamental soliton ($N = 1$) is characterized by an unchanging, hyperbolic secant profile $\text{sech}(\xi)$ occurring because the nonlinearity and the diffraction add phase curvatures of opposite sign to the field which exactly balance each other. Higher-order solitons ($N > 1$) do not maintain their shape consistently but return to it periodically with a period $\zeta = \pi/2$. In between these revivals, the FWHM of the beam passes through a minimum which gets narrower and closer to $\zeta = 0$ as the order of the soliton increases.

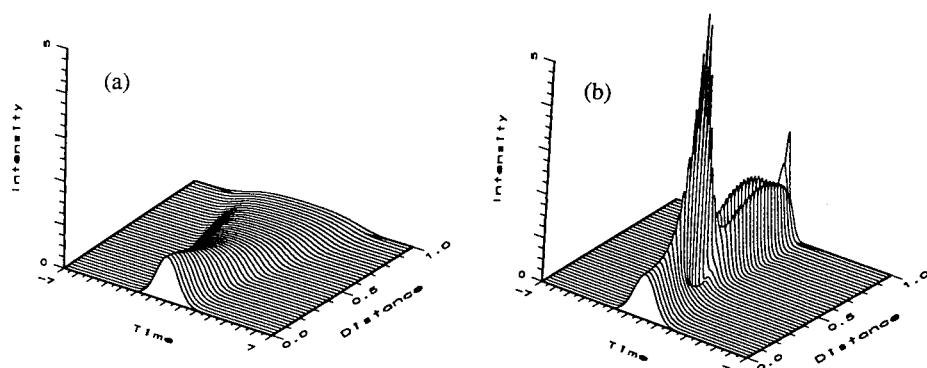


Figure 1. Pulse evolution in the case of (a) normal and (b) anomalous GVD for $N = 3$. Diffractive effects are ignored by assuming that $L_d \gg L_D$.

A similar situation occurs for relatively wide input beams for which the plane-wave approximation holds and the diffraction length becomes much larger than the dispersion length ($s \gg 1$). In this case we renormalize the NSE to the dispersion length. By dropping the diffractive term, Eq. (1) becomes:

$$i \frac{\partial u}{\partial \zeta'} - \text{sgn}(\beta_2) \frac{1}{2} \frac{\partial^2 u}{\partial \tau^2} + \text{sgn}(n_2) N'^2 |u|^2 u = 0. \quad (4)$$

Here $N'^2 = (2\pi/\lambda|\beta_2|)T_0^2 n_0 n_2 I_0$ and $\zeta' = z/L_D$ reflect the new normalization. If n_2 and β_2 have the same signs, puls-like soliton solutions of Eq. (4) do not exist (dark solitons are not considered here), and the pulse monotonically broadens as can be seen in figure 1(a). However, if n_2 and β_2 have the opposite signs, Eq. (4) becomes isomorphic to Eq. (3), except that it describes the temporal evolution of the field. The NSE then supports temporal solitons. Higher-order temporal solitons recover their input shape periodically, but go through an initial compression stage, an effect known as soliton-effect pulse compression.¹ Figure 1(b) shows the evolution of a third-order soliton. As seen there, even a nonlinearity as low as $N = 3$ can generate a significantly compressed pulse.

SELF-FOCUSING NONLINEARITY

For a narrow beam of ultrashort pulses, $L_d \approx L_D$ and $s \approx 1$. We can then make neither of the approximations discussed above and so must use Eq. (1) to describe the field evolution. One might guess that, since anomalous dispersion and diffraction both lead to field compression in the presence of the self-focusing nonlinearity, when both effects are included the degree of compression would increase. In fact it does, and for nonlinearities such that $N > 3/2$, eventually leads to spatio-temporal collapse of the pulse (in reality the wave collapse is averted by higher-order dispersion and self-steepening terms not included here). This is not surprising if we note that for $s < 0$, Eq. (1) is identical to the equation describing self-focusing of cw beams in bulk nonlinear media. Catastrophic self-focusing of cw beams when N exceeds a critical value is a well-known phenomenon.⁵

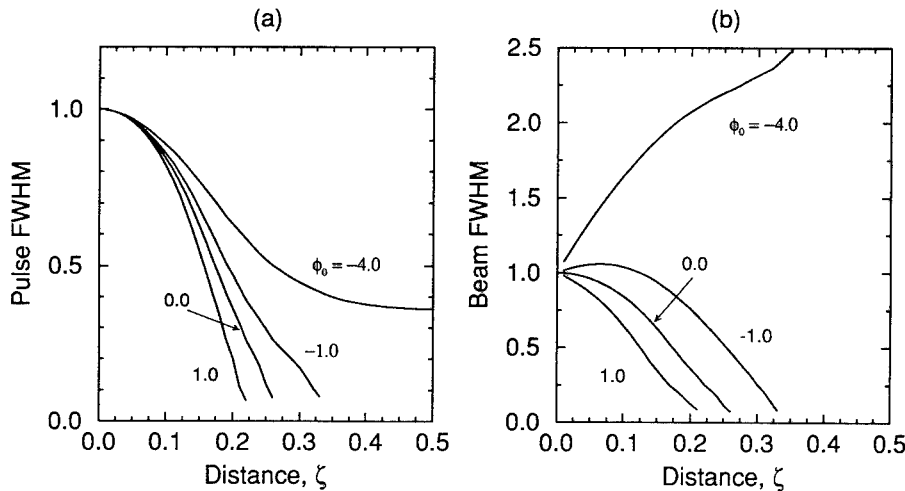


Figure 2. Effect of spatial phase modulation on (a) pulse width and (b) beam width as a function of propagation distance for $N = 3$ and $s = -1$. Note that catastrophic self-focusing does not occur for $\phi_0 = 4$.

To show how spatio-temporal coupling can be used to advantage, we apply a spatial phase modulation of the form $\phi(\xi) = \phi_0 \sin(2\pi p\xi + \delta)$ to the input field. In Fig. 2, we plot the pulse width and the beam width as a function of propagation distance for a

range of modulation amplitudes with $N = 3$ and $s = -1$. As seen there, a focusing modulation ($\delta = \pi/2$, $\phi_0 > 0$) can hasten the collapse while a defocusing modulation can either delay or eliminate it entirely depending on the modulation amplitude, with larger amplitudes being required to overcome larger nonlinearities. The noteworthy point here is that the time-domain behavior is altered with a spatial manipulation. The mechanism at work is fairly simple. The spatial phase modulation for $\phi_0 < 0$ merely spreads energy out (or helps concentrate it for $\phi_0 > 0$) from the center of the field thereby reducing (or enhancing) the nonlinearity-induced phase curvature of the field which is the cause of the collapse.

For normal dispersion and negligible diffraction (plane-wave approximation), the interaction of the dispersion and the nonlinearity leads to a monotonic pulse spreading as seen in Fig. 1(a). However, as shown in Fig. 3, the inclusion of the diffractive term can lead to a modest degree of pulse compression provided the nonlinearity is much stronger than the dispersion ($N^2 \gg s$). This feature can be understood by recalling that higher-order ($N > 1$) spatial solitons in waveguides undergo periodic beam narrowing (and a corresponding increase in intensity) and that the distance to the first minimum decreases as N increases. In the non-dispersive case ($s = 0$), an input pulse with $N > 1$ can be viewed as a continuous series of spatial solitons ranging from zeroth-order at the wings of the pulse to order N at its center. Since the center has the highest order, it will spatially narrow at a shorter distance than the wings. As a result, the pulse appears compressed because the center has become more intense while the wings have remained virtually unchanged.

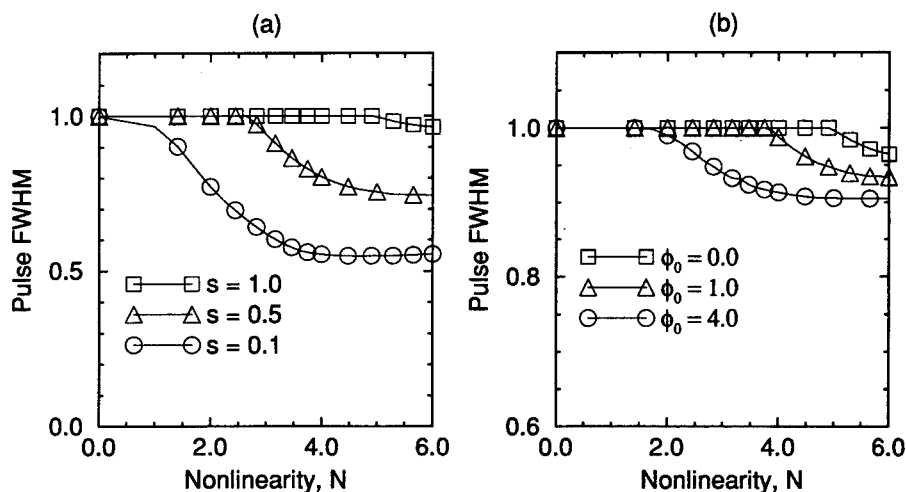


Figure 3. Effect of (a) normal dispersion and (b) spatial phase modulation on the minimum pulse width and plotted as a function of propagation distance for $N = 3$. Note the possibility of pulse compression even in the normal-dispersion regime of planar waveguides.

When normal dispersion is included for a focusing nonlinearity ($n_2 > 0$), the effect is to spread power from the peak of the pulse to the wings. For weak dispersion ($s \approx 0.1$) this effect is minimal compared to the spatial soliton effects; thus the compression is strongest [Fig. 3(a)]. As the strength of the dispersion is increased, the effect becomes more important, until at $s = 1$, a large nonlinearity ($N > 5$) is required to achieve even a minimal (5%) reduction in pulse width. We can again further exploit the spatio-temporal coupling with spatial phase modulation and either enhance or suppress the pulse

compression. As seen in Figure 3(b), the degree of pulse compression changes with both the modulation amplitude and the strength of the nonlinearity. Also note that with the spatial phase modulation, pulse compression can occur over a wide range of nonlinearities where it would not occur at all in its absence.

SELF-DEFOCUSING NONLINEARITY

In the self-defocusing case with the plane-wave approximation, the roles of the two dispersion regimes are reversed. The nonlinearity now works with anomalous dispersion and the pulse broadens exactly as it does in the normal-dispersion regime of a self-focusing medium [Fig. 1(a)]. Conversely, the normal-dispersion regime with a defocusing nonlinearity supports temporal solitons [Fig. 1(b)]. The picture becomes more interesting when we include diffraction. In the anomalous-dispersion regime, diffraction and dispersion work together to broaden the field in both dimensions. As seen in Fig. 4, the spatio-temporal coupling manifests itself by increasing the rate of pulse broadening when the diffractive effects are included. Spatial phase modulation in this case can slow the rate of pulse broadening, but at the price of broadening the beam spatially.

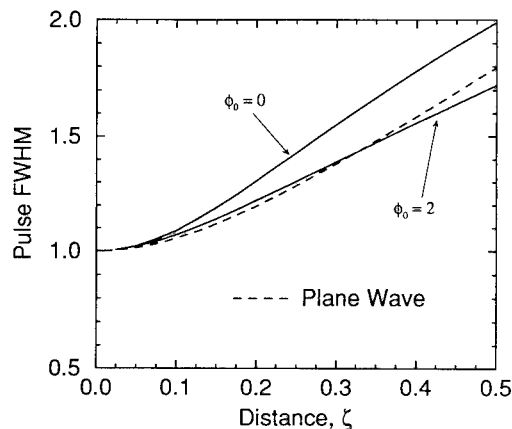


Figure 4. Pulse width as a function of propagation distance for $N = 3$ in a self-defocusing medium with anomalous dispersion with and without spatial phase modulation. Dashed curve shows the behavior when diffraction is ignored (plane-wave approximation).

In the absence of diffraction, the natural effect of normal dispersion interacting with the defocusing nonlinearity is to compress the pulse, the compression factor getting larger as the nonlinearity is increased. Similarly, cw simulations show that the effect of the diffraction is to broaden the beam. It is therefore not surprising that when the diffractive effects of a waveguide are included with a defocusing nonlinearity, the result is a more moderate pulse compression (rather than a wave collapse) as seen in Fig. 5(a). The reason for this is that although the dispersion and the nonlinearity are acting to bring energy in from the temporal wings of the field, the diffraction is using the nonlinearity to move energy out to the spatial wings thereby reducing the peak field strength and thus the pulse compression. The diffraction-induced beam spreading can be counteracted by imposing a spatial phase curvature on the input field which the diffraction must overcome before it can reduce the peak power. Thus, because of the spatio-temporal coupling we are again able to

enhance (or reduce) the pulse compression with spatial phase modulation. As seen in figure 5(a), by increasing the modulation amplitude to $\phi_0 = 2$, we can even achieve the same pulse compression as that obtained without diffraction.

Another interesting aspect of the spatio-temporal coupling occurring in the waveguide is the counterintuitive result that as the strength of the defocusing nonlinearity is increased, the spatial width of the field can be reduced (the beam can be focused!) as evidenced by the data in 5(b). To study the beam narrowing under weak diffraction, it was necessary to renormalize the NSE to the dispersion length. The parameter $s_d = 1/s = L_D/L_d$ appears in front of the diffractive term as a consequence of this renormalization. Figure 5(b) plots the minimum spatial FWHM of the field as a function of N' for a range of s_d values. This is similar to our earlier results which showed pulse compression in a self-focusing, normally dispersive medium (both n_2 and $\beta_2 > 0$). Except in this case it is a temporal soliton effect that brings energy to the center of the field faster than the diffraction can remove it. The analogy with our focusing nonlinearity results holds further in that if we use a temporal lens⁶ to put a quadratic temporal phase curvature on our input field (chirped pulse) we can reduce the spatial FWHM still further (obviously spatial phase modulation can also be used to reduce the beam width).

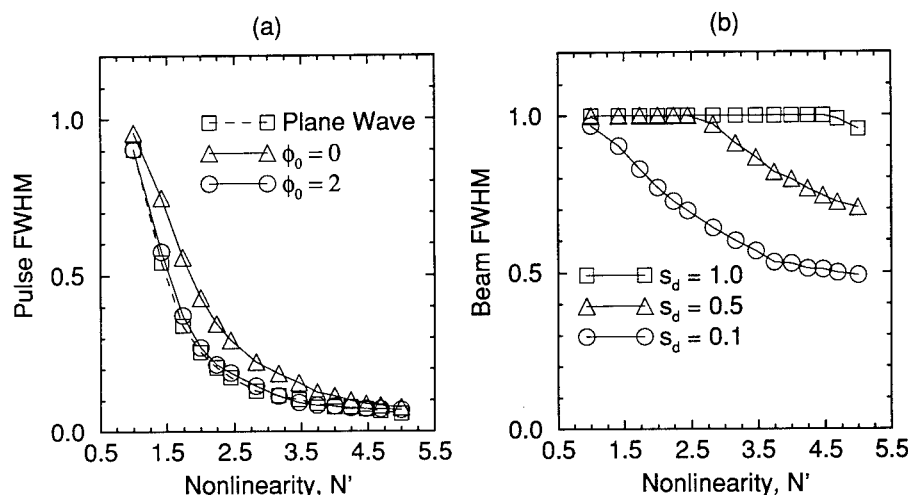


Figure 5. Effect of (a) anomalous dispersion and (b) spatial phase modulation on the on the beam width plotted as a function of N . Note the possibility of self-focusing even in a self-defocusing medium.

CONCLUSIONS

For ultrashort pulses travelling in a nonlinear planar optical waveguide we have presented two results that are both fundamentally interesting and seemingly contradictory. We have seen that in a waveguide with $n_2 > 0$ and $\beta_2 > 0$, a strong nonlinearity can bring energy in from the spatial wings of the field faster than the normal dispersion can move it to the temporal wings thus making pulse compression possible in the normal dispersion regime. We have also seen that with $n_2 < 0$ and $\beta_2 > 0$ a strong nonlinearity can bring energy in from the temporal wings faster than the diffraction can spread it to the spatial wings, making beam narrowing in a self-defocusing medium possible. The contradiction is resolved when we recall that we are speaking only of a reduction of the FWHM of either the temporal or spatial profile. In reality, while the peak increases in intensity the wings

become broader. Thus the beam or pulse narrowing is localized to the center of the field. In both cases the temporal or spatial variance increases monotonically. Nonetheless, with the use of a fast saturable absorber the temporal or spatial wings may be removed.

Another issue we have not addressed is the post-compression field evolution. It has been shown^{7,8} that pulses in a normally dispersive, self-focusing medium will split rather than collapse and we also observe the same behavior. In all of our simulations where we achieved pulse compression in a normally dispersive, self-focusing medium it was followed immediately by pulse splitting. Similarly, in the situations where we achieved beam narrowing in a defocusing medium it was immediately followed by beam splitting. In both cases, the compression was followed by rapid beam broadening if spatial phase modulation was used to achieve or enhance the compression. However, in the defocusing medium there was a large range of nonlinearities where significant pulse compression was achieved without beam splitting or spatial phase modulation suggesting the potential of device applications there.

ACKNOWLEDGEMENTS

The authors would like to thank the Cornell Theory Center for the use of their supercomputing facilities, Sun Microsystems for the color printer, and the US Air Force for a graduate fellowship. The research is supported in part by the U.S. Army Research Office.

REFERENCES

1. G.P. Agrawal, "Nonlinear Fiber Optics," 2nd ed., Academic Press, San Diego (1995).
2. A.T. Ryan and G.P. Agrawal, "Pulse compression and Spatial phase modulation in normally dispersive nonlinear Kerr media," to be published in Optics Letters.
3. A.T. Ryan and G.P. Agrawal, "Steering of optical beams in nonlinear Kerr media by Spatial Phase Modulation", *Opt. Lett.* 18:1795 (1993).
4. L.W. Liou, X.D. Cao, C.J. McKinstrie and G.P. Agrawal, "Spatio-temporal Instabilities in Dispersive Nonlinear Media," *Phys. Rev. A* 46:4202 (1992)
5. V.E. Zakharov and A.B. Shabat, "Exact theory of two dimensional self-focusing and one-dimensional self-modulation of waves in nonlinear media," *Sov. Phys. JETP* 34:62 (1972)
6. B.H. Kolner, "Space-time duality and the theory of temporal imaging," *IEEE J. Quantum Electron.* 30:1951 (1994)
7. J.E. Rothenberg, "Pulse splitting during self-focusing in normally dispersive media," *Opt. Lett.* 17:583 (1992)
8. P. Chernev and V. Petrov, "Self-focusing of short light pulses in dispersive media," *Opt. Comm.* 87:28 (1992)

$\lambda/4$ -SHIFTED NONLINEAR PERIODIC STRUCTURE: THEORY OF LOW-INTENSITY SWITCHING

Stojan Radic, Nicholas George, and Govind P. Agrawal

The Institute of Optics
University of Rochester
Rochester, NY 14627

INTRODUCTION

It is difficult to overemphasize the role that the $\lambda/4$ -shifted periodic structure has played in the design of linear distributed feedback (DFB) waveguides. First proposed by Haus and Shank¹, such structures have been used extensively in the fabrication of single-mode semiconductor lasers^{2,3} and narrow-bandpass filters^{4,5}. Most recently, $\lambda/4$ -shifted DFB devices have been successfully used for highly discriminative waveguide coupling⁶ leading to an entire new class of waveguide filters.⁷

In a view of the considerable interest that nonlinear DFB (NLDFB) structures have attracted over the past decade,⁸⁻¹² it is rather surprising that, to our knowledge, no explicit treatment of the $\lambda/4$ -shifted NLDFB device exists. Since the pioneering work of Okuda⁸ and Winful,⁹ a wide variety of applications using NLDFB structures have been studied in detail.¹⁰⁻¹² The change of the local refractive index due to a nonlinear medium response coupled with the strong dispersion of the DFB structure, gives rise to the novel phenomena such as slow energy transport in form of Bragg solitons and all optical switching and limiting. Unfortunately, in most cases of practical interest, the required input intensities are extremely high, rendering the proposed configurations difficult to realize. Designed nonuniformities^{13,14} in NLDFB proved to be moderately successful in lowering the field intensity requirements.

We propose the use of $\lambda/4$ -shifted NLDFB as a means to significantly reduce the intensities necessary to achieve all optical switching and limiting behavior. A linear $\lambda/4$ -shifted device is characterized by exceptionally strong electric fields in its center (phase shifting location) - a feature that should readily facilitate significant changes in local refractive index even for a moderate input intensities.

NONLINEAR COUPLED MODE METHOD

Consider the structure shown in Fig. 1. We assume that the waveguide allows only a single TE mode to propagate, neglecting any longitudinal field components (weakly guiding structure). The polarization of the field remains unchanged throughout the entire waveguide structure. Nonlinear response of the optical medium is given by Kerr-type nonlinearity: $n_{NL} \sim n^{(2)}|E|^2$. The variation of the effective linear index is given by:

$$n_{eff}(z) = n_0 + \Delta n \cos(2\beta_B z + \Omega); \quad \Omega = \begin{cases} \Omega_1, & z < 0 \\ \Omega_2, & z \geq 0 \end{cases} \quad (1)$$

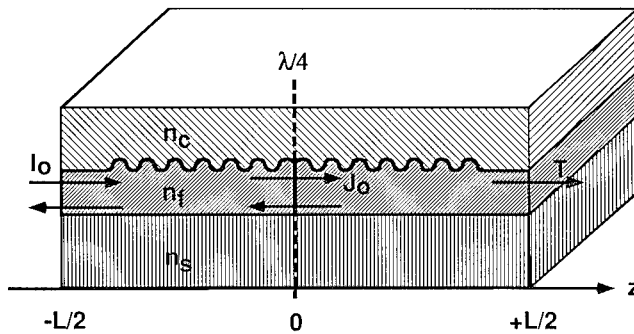


Figure 1. Geometry of $\lambda/4$ -shifted planar waveguide DFB device.

The transmission of the linear $\lambda/4$ -shifted DFB device is shown in Fig. 2, exhibiting nearly full transparency at the middle of the photonic stop-band. The central transmissive peak is characterized by a very narrow linewidth, a feature arising from the resonant nature of the $\lambda/4$ -shifted structure. A nonlinear device with an identical geometry should have the same transmission characteristics in the low-intensity limit when its nonlinearity can be neglected. However, as the input intensity of the device is increased, one would expect a change in the band structure, particularly at the zero-detuning position ($\Delta\beta L = 0$).

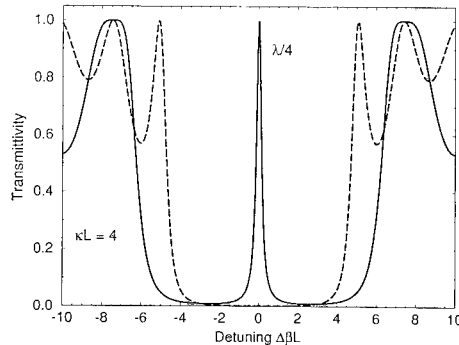


Figure 2. Transmission characteristics of linear $\lambda/4$ -shifted DFB device with $\kappa L = 4$.

In order to describe such a behavior, we start with the standard coupled-mode approach, by separating the field into its forward and backward propagating components:

$$E(z) = E_+(z)e^{i\beta z} + E_-(z)e^{-i\beta z}. \quad (2)$$

Making use of the standard slowly-varying envelope approach, one can derive the following nonlinear coupled-mode equations:

$$\frac{dE_+}{dz} = i\kappa E_- e^{-i(2\Delta\beta z - \Omega)} + i\gamma[|E_+|^2 + 2|E_-|^2]E_+ \quad (3a)$$

$$\frac{dE_-}{dz} = -i\kappa E_+ e^{i(2\Delta\beta z - \Omega)} - i\gamma[2|E_+|^2 + |E_-|^2]E_- \quad (3b)$$

The parameter $\kappa = \pi\Delta n/\lambda_B$ determines the linear coupling strength, $\gamma = \pi n_2/\lambda_B$ governs self- and cross-phase modulation, while $\Delta\beta = \beta - \beta_B$ is detuning from the Bragg frequency given by $\beta_B = 2\pi/\Lambda$. In order to solve the set of Eqs. (3a,b) in each DFB region, we write the counterpropagating field components by separating their magnitude and phase:

$$E_{\pm}(z) = |E_{\pm}(z)|e^{i\phi_{\pm}(z)} = A_{\pm}(z)e^{i\phi_{\pm}(z)} \quad (5)$$

By substituting Eq. (4) into Eqs. (3a,b), and separating its real and imaginary parts, we obtain the following set of equations:

$$\frac{dA_+}{dz} = \kappa A_- \sin\Psi, \quad (5a)$$

$$\frac{dA_-}{dz} = \kappa A_+ \sin\Psi, \quad (5b)$$

$$A_+ \frac{d\phi_+}{dz} = \kappa A_- \cos\Psi + \gamma(|A_+|^2 + 2|A_-|^2)A_+, \quad (6a)$$

$$A_- \frac{d\phi_-}{dz} = \kappa A_+ \cos\Psi + \gamma(|A_-|^2 + 2|A_+|^2)A_-. \quad (6b)$$

It can be immediately seen from the Eqs. (5a,b) that transmitted flux quantity defined as $A_T^2 = A_+^2 - A_-^2$ is conserved in each uniform region of the device. Furthermore, by using Eqs. (6a,b), one can find the second constant of motion in the form:

$$\Gamma = A_+(z)A_-(z)\cos\Psi(z) + [2\Delta\beta + 3\gamma A_-^2(z)]A_+^2(z)/(2\kappa). \quad (7)$$

The phase information implied by the quantity Ψ is given by:

$$\Psi(z) = 2\Delta\beta z + \phi_+(z) - \phi_-(z) - \Omega. \quad (8)$$

Non-reflective boundary condition at the right end of the structure ($z = L/2$) implies that transmitted flux is equal to the total forward flux at the output interface: $A_T^2 = A_+^2(L/2)$. A boundary condition at $z = L/2$, together with Eqs. (5) and (7) allows the construction of the forward flux equation within the second region of the device ($0 \leq z \leq L/2$):

$$\left(\frac{L}{2} \frac{dJ}{dz}\right)^2 = (J-T)[(\kappa L)^2 J - (J-T)(\Delta\beta L + 4J)^2] = Q(J). \quad (9)$$

The normalized parameters in Eq. (9) are defined as the forward flux $J = (A_+/A_c)^2$, transmitted flux $T = (A_-/A_c)^2$ and critical intensity $A_c^2 = 8\lambda n_0/3\pi n_2 L$. Eq. (9) can be regarded as the energy equation of the classical particle confined in the potential well $V = -Q(J)$, as shown in Fig. 3a. The allowed region for such particle ($J \geq 0$) is the rightmost region indicated in Fig. 3a.

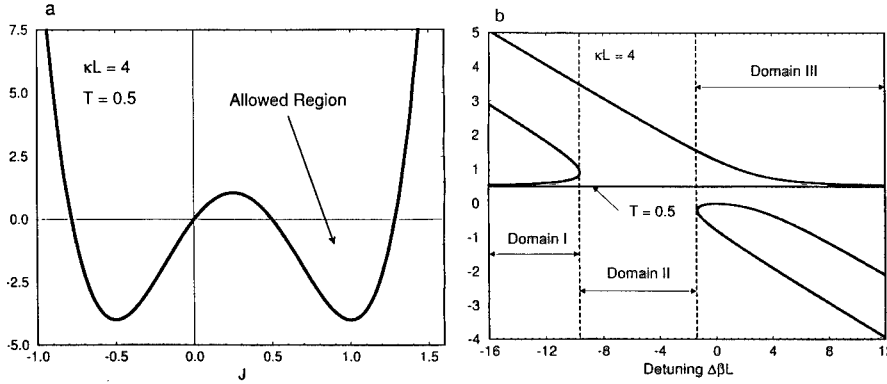


Figure 3. a) Potential well corresponding to a forward flux equation for a uniform NLDFB structure, given by Eq. (9) in text, b) Loci of zeros of forward flux equation in region 2, showing three different integration domains.

Integration of Eq.(9) depends upon the position of the zeros of the polynomial $Q(J)$, i.e. the turning points of the potential $V(J)$. Figure 3b shows a loci of these zeros for the different detuning domains in which Eq. (9) has to be integrated. In the special case of zero detuning ($\Delta\beta L = 0$), it can be shown that center-device forward flux can be calculated in form:

$$J_0 = T[1 + nd(\kappa Lx, 1/x)]/2. \quad (10)$$

The quantity x appearing in Eq. (10) is defined as $x = \sqrt{(2T/\kappa L)^2 + 1}$. To find the solution for the intradvice intensity in the first region ($-L/2 \leq z < 0$), we impose the following boundary condition at $z = 0$:

$$\lim_{\epsilon \rightarrow 0} E_z(0 - \epsilon) = \lim_{\epsilon \rightarrow 0} E_z(0 + \epsilon). \quad (11)$$

Condition (11) implies that the transmitted flux A_T^2 remains constant throughout the entire structure. The boundary condition at the device center, together with Eq. (5) allows us to relate the phase informations in two regions of the structure:

$$\lim_{\epsilon \rightarrow 0} \Psi(0 - \epsilon) = \lim_{\epsilon \rightarrow 0} \Psi(0 + \epsilon) - \Delta\Omega. \quad (12)$$

In the special case $\Delta\Omega = \pi$, it is possible to obtain a particularly simple expression for the forward flux within the first region ($-L/2 \leq z < 0$) by combining the Eqs. (5), (7) and (12):

$$\left(\frac{L}{2} \frac{dl}{dz}\right)^2 = (\kappa L)^2 l(l-T) - [8J_0(J_0-T) - 4l(l-T)]^2 = P(l). \quad (13)$$

The parameter l is defined as the forward flux in the first region: $l = A_+^2(z)/A_c^2$. J_0 is defined as $J_0 = J(0)$. Once again, the integration of Eq. (13) depends on the location of the turning points of the potential $Q(l) = -P(l) = -\prod_{i=1,4}(l-l_i)$. Similar to the integration domains shown for Eq. (9), three detuning domains are resolved for Eq. (13): 1) $l_1 > l_2 > l_3 \geq l_0 > l_4$; 2) $l_1 \geq l_0 > l_2$ and $l_4 = l_3$; and 3) $l_1 \geq l_0 > l_2 > l_3 > l_4$. For the most interesting case when $l_1 \geq l_0 > l_2 > l_3 > l_4$ (domain 3) one can explicitly integrate Eq. (13) to obtain the input intensity in the following form:

$$l_0 = l_3 - \frac{l_3 - l_2}{1 - \frac{l_1 - l_2}{l_1 - l_3} \text{sn}^2(v, k)}. \quad (14)$$

Argument v of the elliptic function $\text{sn}(v, k)$ is given by $v = F(\varphi, k) - u$, where φ , u and k are related to the intensities as:

$$\sin \varphi = \sqrt{\frac{(l_1 - l_3)(J_0 - l_2)}{(l_1 - l_2)(J_0 - l_3)}}, \quad (16)$$

$$u = 2\sqrt{(l_1 - l_3)(l_2 - l_4)}, \quad (17)$$

$$k = 2\sqrt{(l_1 - l_2)(l_3 - l_4)}/u. \quad (18)$$

TRANSMISSION AND SWITCHING CHARACTERISTICS

We now compare the transmissive characteristics of the $\lambda/4$ -shifted device to that of the uniform NLDFB that requires the switching intensities comparable to the critical intensity parameter A_c . In order to relate A_c to physical units, one might consider the case of a 1-mm long GaAs device with $\kappa L = 4$. The critical intensity parameter for such a device is $\sim \text{GW}/\text{cm}^2$, implying both serious intradevice thermal problems and the need for highly intensive optical sources. It is therefore of practical interest to reduce the operating input intensities to a values well below A_c .

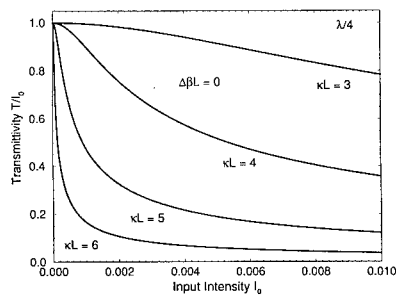


Figure 4. Zero detuning transmissive characteristics of $\lambda/4$ -shifted NLDFB device with $\kappa L=4$.

Figure 4 shows the zero detuning input-output characteristics of the $\lambda/4$ -shifted NLDFB for different coupling strengths: $\kappa L = 3, 4, 5$ and 6 . For the device with $\kappa L = 6$, one can transmit $\sim 100\%$ of the optical signal in low intensity limit ($I < 2 \times 10^{-4}$). By increasing the input intensity to $\sim 7 \times 10^{-4}$, the transmission drops to $\sim 20\%$, corresponding to the "OFF" state of the device. Upswitching is performed by reverse process, effectively making the $\lambda/4$ -shifted NLDFB a negative logic gate with a differential level of $\sim A_0/1000$.

Bistable behavior of the device is shown in Fig. 5a. Transmissive hysteresis appears at the detuning $\Delta\beta L \sim -0.3$ and for the input intensity of $I \sim 5 \times 10^{-3}$. The hysteresis depth and the switching efficiency are controlled by both the frequency detuning $\Delta\beta L$ and the input intensity parameter. As a reference, the input-output characteristics of the edge-tuned uniform NLDFB device is shown in Fig. 5b. The hysteresis indicating the bistable behavior appears at $I \sim 0.05$, i.e. at the input level that is approximately an order of magnitude higher than that of the $\lambda/4$ -shifted device.

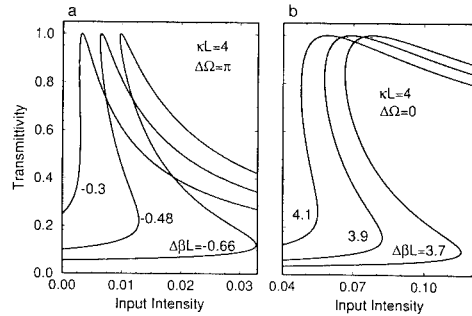


Figure 5. a) Transmissive characteristics of the $\lambda/4$ -shifted NLDFB for different detuning values $\Delta\beta$, b) Transmissive characteristics of edge-tuned uniform NLDFB with otherwise identical parameters.

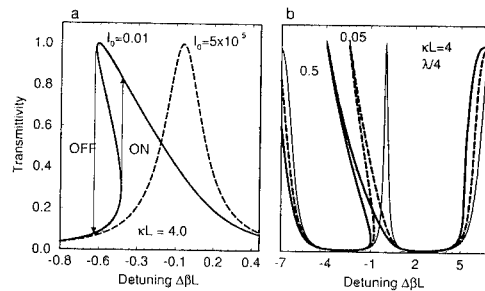


Figure 6. a) Transmissive peak behavior for small input intensities, b) Central peak is shifted for almost a third of the stop bandwidth as the intensity is increased to $I \sim 0.5$.

Shifting of the central transmissive peak location is shown in Fig. 6a, implying the possibility for the all-optical switching at low fixed input intensity, controlled by wavelength tuning of the optical carrier. Sensitivity of the central peak to the intensity change is shown in Fig. 6b. For the input intensity of $I \sim 0.1$, the central peak is shifted by $1/3$ of the stop-bandwidth, while band edges remain almost unaffected. To understand the reason behind high sensitivity of the central peak, we plot longitudinal distribution of the

forward flux in Fig. 7. In low intensity limit ($I \sim 0.001$) almost 100% of the input is transmitted, while for finite intensity input ($I \sim 0.013$) a large portion of the input flux is reflected back. Even for a low optical inputs, the center-device intensity is strong enough to considerably change the local refractive index of the phase-shifting region at $z = 0$. The change of the local index in turn changes the phase retardation properties of the central region, effectively destroying the resonance of the $\lambda/4$ -shifted structure at $\Delta\beta L = 0$.

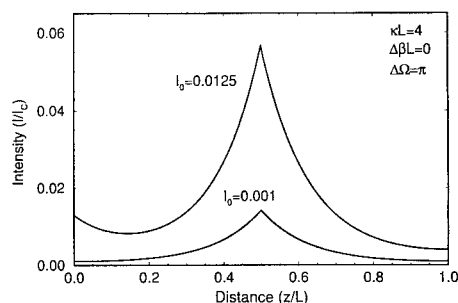


Figure 7. Longitudinal distribution of the intradevice intensity, indicating strong field at the phase-shifting location $z = 0$.

CONCLUSIONS

By analyzing the transmissive behavior of the $\lambda/4$ -shifted NLDFB we have demonstrated its potential superiority for low-intensity, all-optical switching applications. Switching intensities that are up to three orders of magnitude lower than those of the uniform NLDFB are predicted, greatly reducing the problems connected with high intensity optical sources and intradevice thermal damages. The analytic method derived here is readily applied to specific geometries such as the thin-film waveguide or the fiber-grating device. We believe that current advances in fabrication of highly nonlinear optical materials coupled with phase-shifted and nonuniform NLDFB design will result in a wide variety of practical, all-optical switching devices in the near future.

ACKNOWLEDGEMENTS

This research is sponsored in part by the U.S. Army Research Office, the National Science Foundation, and the New York State Science and Technology Foundation.

REFERENCES

1. H. A. Haus and C. V. Shank, "Antisymmetric taper of distributed feedback lasers," *IEEE J. Quantum Electron.* **QE-12**, 532-539 (1976).
2. K. Utaka, S. Akiba, K. Sakai and Y. Matsushima, " $\lambda/4$ -shifted InGaAsP DFB Lasers," *IEEE J. Quantum Electron.* **QE-22**, 1042-1051 (1987).
3. G. P. Agrawal and A. H. Bobeck, "Modeling of distributed feedback semiconductor lasers with axially-varying parameters," *IEEE J. Quantum Electron.* **QE-24**, 2407-2414 (1988).

4. M. Yamada and K. Sakuda, "Analysis of almost-periodic distributed feedback slab waveguides via a fundamental matrix approach," *Appl. Opt.* **26**, 3474-3478 (1987).
5. G. P. Agrawal and S. Radic, "Phase-shifted fiber Bragg gratings and their application for wavelength demultiplexing," *IEEE Photon. Technol. Lett.* **6**, 995-997 (1994).
6. H. Haus and Y. Lai, "Narrow-Band distributed feedback reflector design," *J. Lightwave Tech.* **9**, 754-760 (1991).
7. J. N. Damask and H. Haus, "Wavelength-division multiplexing using channel-dropping filters," *J. Lightwave Tech.* **11**, 424-428 (1993).
8. H. G. Winful, J. H. Marburger and E. Garmire, "Theory of bistability in nonlinear distributed feedback structures," *Appl. Phys. Lett.* **35**, 379-381 (1979).
9. M. Okuda and K. Onaka, "Bistability of optical resonator with distributed Bragg-reflectors by using Kerr effect," *Jpn. J. Appl. Phys.* **16**, 769 (1977).
10. W. Chen and D. L. Mills, "Optical response of nonlinear multilayer structures: Bilayers and superlattices," *Phys. Rev. B* **36**, 6269-6278 (1987).
11. D. N. Christodoulides and R. I. Joseph, "Slow bragg solitons in nonlinear periodic structures," *Phys. Rev. Lett.* **62**, 1746-1749 (1989).
12. H. G. Winful and G. I. Stegeman, "Applications of nonlinear periodic structures in guided wave optics," *Proc. SPIE* **517**, 214-218 (1984).
13. C. Martijn de Sterke and J. E. Sipe, "Launching of gap solitons in nonuniform gratings," *Opt. Lett.* **18**, 269-271 (1993).
14. H. A. Haus, "Matching of distributed-feedback structures," *Opt. Lett.* **15**, 1134-1136 (1992).

FREQUENCY CONVERSION IN Ti:LiNbO₃ CHANNEL WAVEGUIDES

Michael Čada¹, Jiří Čtyroký²

¹Technical University of Nova Scotia
Halifax, Canada

²Institute of Radio Engineering and Electronics
Academy of Sciences of the Czech Republic
Prague, Czech Republic

INTRODUCTION

Nonlinear optical effects based on the χ^2 nonlinearity (optical second harmonic generation, optical frequency mixing, parametric amplification and generation) in optical waveguides have been intensively studied from the very beginning of integrated optics¹⁻³. There were hopes that light confinement for relatively long distances in waveguides would help significantly reduce light power required for efficient nonlinear interaction. Materials for guided-wave optical nonlinear applications have to fulfil a number of requirements simultaneously: they should not only exhibit large nonlinearity but it must also be suitable for fabricating high-quality optical waveguides. Moreover, there must exist a way to fulfil the phase matching condition, and, last but not least, the mode field overlap of all three interacting modes has to be as high as possible for good efficiency of the nonlinear process. From just a few suitable materials, lithium niobate crystal is still one of the most promising choices.

Various configurations have been designed to reach phase matching in LiNbO₃. For birefringent phase matching⁴, suitably oriented Ti:LiNbO₃ waveguides are used, with fine tuning by temperature or wavelength. In the so called "Cherenkov" configuration, one of the interacting waves, usually the newly created wave, is radiated into the substrate in the form of radiation modes. Since radiation modes have continuous spectrum of propagation constants, the phase matching is fulfilled in quite a broad spectral range. The mode field overlap is, however, very small. Proton exchange fabrication technology seemed to be very promising for phase matching because it could change the 'effective birefringence' of the LiNbO₃ crystal⁵. However, it was found later that nonlinear properties are strongly reduced and propagation losses are increased after strong proton exchange. Very recently, a novel and very flexible method of quasi-phase matching has been successfully applied to difference frequency generation in LiNbO₃ waveguides⁶. In this case, a periodic structure of inverted ferroelectric domains is created in the crystal by titanium indiffusion that helps match the wave vectors of interacting modes. The waveguide is created after the domain inversion by annealed proton exchange. The periodic structure is photolithographically patterned and can

thus be varied in a broad range with good precision by the mask design. Another important advantage is that the largest nonlinear coefficient d_{33} of LiNbO₃ is fully utilized.

One of the promising applications of the χ^2 -based optical nonlinear effects in waveguides is optical frequency conversion. Thanks to the femtosecond response times, a very fast "all-optical" AND gate could be realized by the sum or difference frequency generation. Possible configurations of Ti:LiNbO₃ devices based on a non-conventional birefringent phase matching capable of operation in the optical communication windows around 1.55 μm and 1.3 μm are subject of this study.

THEORETICAL BACKGROUND

We first review briefly the nonlinear sum frequency generation in channel optical waveguides. In an (optically linear) weakly guiding channel waveguide with relative permittivity distribution $\bar{\epsilon}(x, y)$, any monochromatic electric field distribution of a mode has to fulfil the wave equation

$$\Delta_{\perp} \mathbf{E} + k^2(\bar{\epsilon} - N^2)\mathbf{E} = 0, \quad (1)$$

where N is the effective refractive index of a mode, and \mathbf{E} is the complex representation of the electric field vector. It is useful to normalize the dominant transverse components of electric and magnetic fields of the mode by

$$\mathbf{E}_{\perp m} = \sqrt{\frac{2Z_0}{N}} A_m \mathbf{e}_m(x, y), \quad \mathbf{H}_{\perp m} = \sqrt{2NY_0} A_m \mathbf{z}^0 \times \mathbf{e}_m, \quad Z_0 = \sqrt{\frac{\mu_0}{\epsilon_0}}, \quad Y_0 = \sqrt{\frac{\epsilon_0}{\mu_0}}, \quad (2)$$

where $\mathbf{e}_m(x, y)$ is the orthonormalized field distribution of the electric field of the m -th mode,

$$\int_{-\infty-\infty}^{\infty} \int_{-\infty-\infty}^{\infty} \mathbf{e}_m(x, y) \cdot \mathbf{e}_n^*(x, y) dx dy = \delta_{mn}, \quad (3)$$

\mathbf{z}^0 is the unit vector parallel to the waveguide axis, and A_m is the complex amplitude of a mode. With this normalization, power transmitted by the mode along the waveguide is given by $|A_m|^2$:

$$P_m = \frac{1}{2} \text{Re}(\mathbf{E}_m \times \mathbf{H}_m^*) = |A_m|^2. \quad (4)$$

As we will now introduce the nonlinearity, we have to use complex field representation with care. The origin of frequency mixing is in the nonlinear polarization term of the form

$$\mathcal{P}^{NL} = 2\tilde{\mathbf{d}}:\mathbf{E}\mathbf{E}, \quad (5)$$

where $\tilde{\mathbf{d}} = \epsilon_0 \tilde{\chi}^2$ is the tensor of the second-order nonlinearity of a waveguide medium, and \mathbf{E} is the real (time-dependent) vector of the electric field intensity. In the presence of two waves with pump and signal frequencies ω_p and ω_s , respectively, this expression contains a term with sum or difference frequency ω_c that acts as a source of these new waves. The wave equation should now be written in the time-dependent form

$$\Delta \mathbf{E} - \frac{1}{c^2} \frac{\partial^2}{\partial t^2} (\bar{\epsilon} \cdot \mathbf{E}) = \frac{1}{c^2} \frac{\partial^2}{\partial t^2} \left(\frac{2\tilde{\mathbf{d}}}{\epsilon_0} : \mathbf{E}\mathbf{E} \right). \quad (6)$$

This equation can be solved in the well-known slowly varying envelope approximation (SVEA). The solution will be looked for in the form

$$\mathbf{E} = \text{Re} \left\{ \sqrt{2Z_0} \sum_q \frac{1}{\sqrt{N_q}} A_q(z) \mathbf{e}_q(x, y) \exp[i(k_q N_q z - \omega_q t)] \right\}, \quad (7)$$

where $q = p, s$, and c stand for the pump, signal and converted waves, respectively, and A_q are expected to be slowly varying complex amplitudes of the waves. We explicitly assume that the converted wave has a sum frequency, *i.e.*, $\omega_c = \omega_p + \omega_s$. Substituting the expression (7) into the wave equation (6), neglecting the second derivatives of A_q that are small compared to $k_q^2 N_q^2 A$ and $2k_q N_q (\partial A / \partial z)$ (the key assumption for SVEA), separating terms with equal angular frequencies, and taking into account the orthonormality properties of the modes (3), we finally arrive to the coupled equations for the complex amplitudes A_q :

$$\begin{aligned} \frac{d A_p(z)}{d z} &= i k_p \frac{\sqrt{2Z_0} F}{\sqrt{N_p N_s N_c} \epsilon_0} A_c A_s^* \exp[i(k_c N_c - k_s N_s - k_p N_p)z], \\ \frac{d A_s(z)}{d z} &= i k_s \frac{\sqrt{2Z_0} F}{\sqrt{N_p N_s N_c} \epsilon_0} A_c A_p^* \exp[i(k_c N_c - k_s N_s - k_p N_p)z], \\ \frac{d A_c(z)}{d z} &= i k_c \frac{\sqrt{2Z_0} F}{\sqrt{N_p N_s N_c} \epsilon_0} A_s A_p \exp[i(k_s N_s + k_p N_p - k_c N_c)z]; \end{aligned} \quad (8)$$

here, d is the pertinent component of the tensor \mathbf{d} , and

$$F = \int_{-\infty-\infty}^{\infty} \int_{-\infty-\infty}^{\infty} e_p(x, y) e_s(x, y) e_c(x, y) dx dy \quad (9)$$

is the overlap integral of the dominant transversal components of electric fields of the modes. To solve the set of equations (8), we can use to our advantage the simple "non-depleted pump approximation": if the pump power is significantly stronger than the other two frequencies, $|A_p^2| \gg |A_s^2|, |A_c^2|$, we can take A_p as constant and solve only the last two equations (8) for A_s and A_c . This is now a set of linear equations, formally identical to those describing, *i.e.*, the guided-wave acoustooptic interaction:

$$\begin{aligned} \frac{d A_s(z)}{d z} &= i \kappa_s A_c \exp[i\Delta \beta z], \quad \kappa_s = i k_s \frac{\sqrt{2Z_0} F}{\sqrt{N_p N_s N_c} \epsilon_0} A_p^*, \\ \frac{d A_c(z)}{d z} &= i \kappa_c A_s \exp[-i\Delta \beta z], \quad \kappa_c = i k_c \frac{\sqrt{2Z_0} F}{\sqrt{N_p N_s N_c} \epsilon_0} A_p, \end{aligned} \quad (10)$$

where

$$\Delta \beta = k_c N_c - k_p N_p - k_s N_s \quad (11)$$

is the phase mismatch. Solving this set of equations with the boundary conditions $A_s(0) \neq 0$, $A_c(0) = 0$, we obtain the following expression for the power conversion efficiency from the signal into the converted wave

$$\eta(z) = \left| \frac{A_c(z)}{A_s(0)} \right|^2 = \frac{|\kappa_c|^2}{\gamma^2} \sin^2 \gamma z \approx |\kappa_c|^2 z^2 \left(\frac{\sin(\Delta \beta z/2)}{(\Delta \beta z/2)} \right)^2, \quad \gamma = \sqrt{(\Delta \beta/2)^2 + |\kappa_s \kappa_c|}. \quad (12)$$

The approximate equality can be shown to be valid with a few-percent error as long as the efficiency is lower than about 50%. From (12), it follows directly the condition of phase matching, too: the maximum conversion efficiency is obtained for zero phase mismatch:

$$\Delta \beta = k_c N_c - k_p N_p - k_s N_s = 0. \quad (13)$$

Then, for the waveguide of the length L , the efficiency of conversion from the signal into the sum frequency is

$$\eta = \frac{2k_c^2 L^2 Z_0}{N_p N_s N_c} F^2 \frac{d^2}{\epsilon_0^2} P_p, \quad (14)$$

where $P_p = |A_p^2|$ is the power of the pump wave.

ROTATED Z-CUT PHASE MATCHING IN Ti:LiNbO₃ WAVEGUIDES

Before we start to discuss the phase matching in detail, we briefly mention the dispersion properties of Ti:LiNbO₃ waveguides at the wavelengths of interest, *i.e.*, at approximately 1.55 μm , 1.3 μm and 0.707 μm (the sum frequency of both former ones). All these wavelengths have to propagate in the same channel waveguide simultaneously. It is therefore quite important to know, at least approximately, the number of modes supported by the waveguide at each wavelength. We have to realize that only the interaction of the type “ $o + o \rightarrow e$ ” can be used because of the normal dispersion and negative birefringence of Ti:LiNbO₃ waveguides. Thus, both “pump” (1.55 μm) and “signal” (1.3 μm) waves have to be ordinarily polarized while the “converted” (0.707 μm) wavelength has to be extraordinarily polarized. In Fig. 1 we show the calculated dispersion curves in terms of the differences $N_{\text{eff}} - n_{\text{sub}}$ versus the waveguide width for our typical Z-cut Ti:LiNbO₃ waveguides at these wavelengths. The graph corresponds approximately to waveguides fabricated by the diffusion of 85 nm thick titanium film for 8 h at 1025°C. The dispersion of both substrate and titanium-induced index change were considered in the calculation. It can be seen that the optimum waveguide width is around 7 μm ; the waveguide is single-mode at 1.55 μm , very weakly two-mode at 1.3 μm , and about 4 to 5 lateral modes (and two other modes corresponding to higher-order depth modes not shown in Fig. 1) are to be expected at 0.7 μm .

Both depth and lateral field distributions of fundamental modes are shown in Fig. 2. As it can be seen, the mode field overlap is quite good; the overlap integral calculated from (9) gives the value of $F = 82.9 \times 10^3 \text{ m}^{-1}$ for this case (note that the physical dimension of the orthonormalized field distribution $e(x, y)$ is m^{-1}).

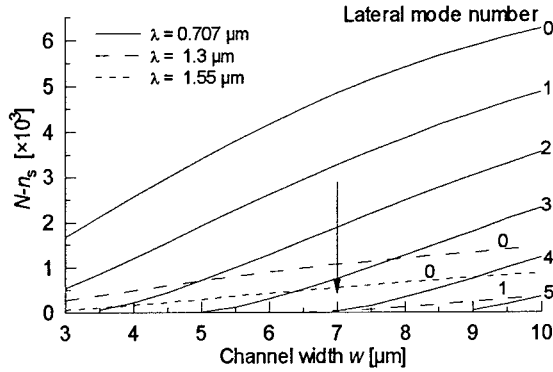


Figure 1: Dispersion curves of a Ti:LiNbO₃ waveguide at the pump, signal and converted wavelengths

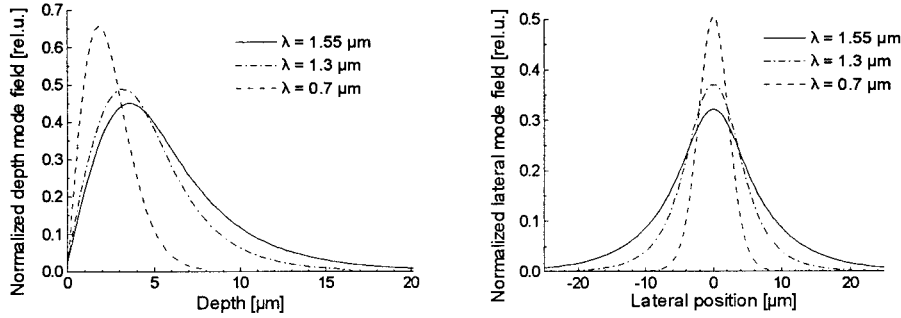


Figure 2: Depth and lateral field distributions of fundamental modes in Ti:LiNbO₃ optical waveguide

To get phase matching, the N_c at the sum frequency has to fulfil the condition (13). Its “theoretical” value is therefore

$$N_c^{\text{theor}} = \lambda_c \left(N_p / \lambda_p + N_s / \lambda_s \right). \quad (15)$$

It is clear that this value must lie between the extraordinary and ordinary (effective) indices N_c^e and N_c^o of modes in channels perpendicular to the optic axis, respectively, in order to be experimentally attainable by angled propagation. To avoid problems with strongly lossy leaky modes and/or polarization conversion in off-axis propagation on the X- or Y-cut LiNbO₃ substrates⁷, we suggest to use the rotated Z-cut substrate as shown in Fig. 3. In this case, both “pump” and “signal” waves are to be TE-polarized while the converted wave must be TM-polarized. The wavelength range in which the phase matching can be adjusted in this way is shown in Fig. 4. Here, the effective indices N_c^{theor} , N_c^e and N_c^o are calculated as a function of the signal wavelength, and the converted wavelength λ_c is also shown. It is seen from the figure that the phase matching is possible for signal wavelength larger than approximately 0.8 μm. In the next figure 5, there is shown the rotation angle needed for phase matching versus the signal wavelength. For the signal wavelength of 1.3 μm, the rotation by $\Theta_{\text{synchron}} = 34^\circ$ is required. In this case, the nonlinear coefficient is reduced to $d = d_{31} \cos \Theta_{\text{synchron}} = 0.829 d_{31}$. An estimation of the conversion efficiency from (14) with the

overlap factor $F = 82.9 \times 10^3 \text{ m}^{-1}$ for the waveguide length $L = 20 \text{ mm}$ gave the result of about $\eta \approx 20\%$ per one watt of the pump power.

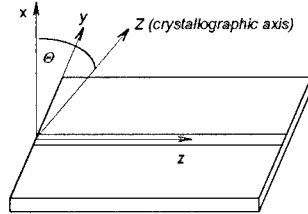


Figure 3: Rotated Z-cut for phase matching. Z is the optic axis of the LiNbO_3 crystal. Cartesian coordinates (x, y, z) are used for field calculation.

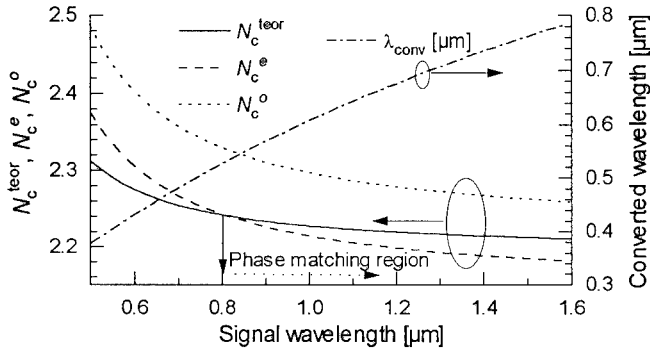


Figure 4: Wavelength range in which the phase matching by rotated Z-cut substrate is possible. The pump wavelength is $1.55 \mu\text{m}$.

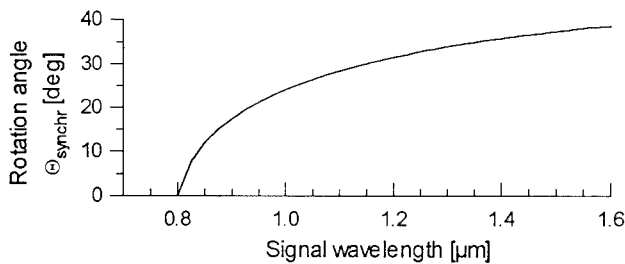


Figure 5: Phase matching angle Θ_{synchron} versus the signal wavelength

A very important parameter from the practical point of view is the wavelength selectivity of the frequency conversion. From the expression (12) it is seen that the conversion efficiency decreases with detuning from the phase-matching condition (13) according to sinc function. For the detuning of $\Delta\beta L = \pi$, the efficiency changes $(2/\pi)^2$ times, *i.e.*, is decreased by about 4 dB. Taking into account that the wavelength detuning may be both positive and negative, by differentiating (13) we obtain for the spectral width of the signal wavelength

$$\Delta\lambda_s \leq \lambda_s^2 \left/ \left(N_c - N_s - \lambda_s \left(\frac{\lambda_c^2}{\lambda_s^2} \frac{dN_c}{d\lambda_c} - \frac{dN_s}{d\lambda_s} \right) \right) \right. L \quad (16)$$

For the waveguide length of about 20 mm, the typical bandwidth is just below one nanometer. In real waveguides, the figure can be quite strongly influenced by longitudinal nonuniformities of the waveguides and, hence, by local deviations from the phase synchronism (the worse the waveguide, the broader the spectral curve, but the smaller the efficiency).

It is perhaps interesting to note that for a specific case of pump at 1.55 μm and λ_s around 0.8 μm , the phase matching may be obtained even for $\Theta = 0^\circ$, as can be seen from Figs. 4 and 5. The converted wavelength is then close to 0.530 μm . In this case, the full value of the nonlinear coefficient d_{31} is utilized. As a consequence, any of the crystal cuts X, Y, or Z may be used, if the channel direction and the polarization of the waves are chosen correspondingly. The estimated theoretical conversion efficiency in 20 mm long waveguide is higher than 30% per 1 W of the pump power. Experiments on X-cut Ti:LiNbO₃ waveguides confirmed these predictions and good agreement between theory and experiment was obtained.

CONCLUSIONS

Analysis of nonlinear frequency conversion of a signal at 1.3 μm by a pump at 1.55 μm in a channel Ti:LiNbO₃ waveguide was presented. Birefringent tuning of phase matching using rotated Z-cut substrate was suggested. This configuration is free of leaky-mode loss and/or of polarization conversion effects that are typical for off-Z-axis propagation in X- or Y-cut channel waveguides. The conversion efficiency in a 20 mm long waveguide was estimated to be about 5% per one watt of the pump power, with approximately 1 nm bandwidth of the signal wavelength. The very fast frequency up-conversion of the communication channels of 1.55 μm and 1.3 μm to the 0.8 μm band is advantageous for several reasons. One of them is the availability of very sensitive, low-noise and fast silicon detectors. An interesting possibility of frequency conversion of the signal around 0.8 μm with the pump at 1.55 μm in a standard (non-rotated) Ti:LiNbO₃ waveguide was predicted and is now being verified experimentally. Although the theoretical conversion efficiency cannot overcome that of the quasi-phase-matched arrangement because of the smaller nonlinear coefficient used, the extreme simplicity of the arrangement and the possibility to use longer waveguides are promising.

REFERENCES

1. A. Yariv: "Coupled-mode theory for guided-wave optics". IEEE J. Quantum Electron., vol. QE-9, p. 919, 1973
2. P. K. Tien: "Integrated optics and new wave phenomena in optical waveguides". Rev. Mod. Phys., vol. 49, p. 361, 1977
3. H. F. Taylor, A. Yariv: "Guided-wave optics". Proc. IEEE, vol. 62, p. 1044, 1974
4. W. Sohler, H. Suche: "Optical parametric amplification in Ti-diffused LiNbO₃ waveguides". Appl. Phys. Lett., vol. 37, p. 255, 1980
5. M. De Micheli: "Nonlinear effects in TIPE-LiNbO₃ waveguides for optical communications", J. Opt. Commun., vol. 4, p. 25, 1983
6. M. L. Bortz, D. Serkland, M. M. Fejer: "Near degenerate difference frequency generation at 1.3 μm in LiNbO₃ waveguides for application as an all-optical channel shifter". Proc. CLEO '94, Anaheim, May 8 - 13, 1994, p. 288
7. J. Čtyroký, M. Čada: "Generalized WKB method for the analysis of light propagation in inhomogeneous anisotropic optical waveguides". IEEE J. Quantum Electron., vol. QE-17, p. 1064, 1981

SPATIAL SOLITONS IN SUPERLATTICE WITH NEAR RESONANT NONLINEARITY

Chi Sheng Zhou¹ Changjun Liao² Chunji Lee²

¹Department of Physics

²Institute of Quantum Electronics
South China Normal University
Guangzhou 510631, China

Abstract: MQW waveguide with barrier thickness slowly decreasing along its length is analyzed to have enhanced adiabatic amplification which facilitate the spatial dark soliton evolution. The technique in a MOCVD system to grow tapered epitaxial layer is proposed that results in slowly widened reaction chamber design.

Key words: Waveguide, Multi-quantum well, Spatial soliton

1 INTRODUCTION

Spatial solitons have been extensively studied in recent years in many materials such as CS₂, ZnSe, SBN, GaAs, glass, DANS and artificial Kerr media due to the potential applications in areas of all optical switching, signal routing, planar spatial light modulation and optical interconnection. Both bright and dark spatial solitons have been observed^{1, 2}. A dual-frequency input signal have been used to generate a periodic array of dark spatial solitons via diabatic amplification in a Kerr-like medium³. A cylindrical lens was placed near the input face of the cell containing the liquid Kerr-like medium to produce an effective amplification. This kind of amplification is limited by the self-defocussing which is actually needed for the generation of the spatial dark solitons. One has to keep the input power close to the soliton level. We propose here the use of superlattice materials of the III-V semiconductor which are important materials in the opto-electronics device applications to produce spatial dark soliton array. The needed adiabatic amplification is from the geometric structure of the waveguides.

We deduce the evolution equation of soliton in multi-quantum well

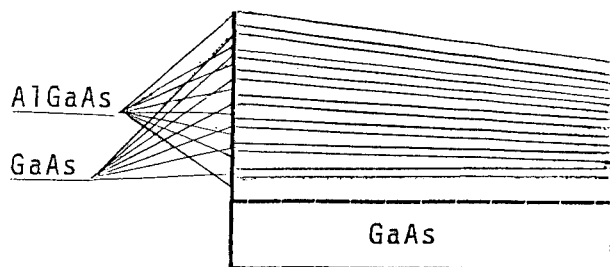


Figure 1. Schematic drawing of the superlattice.

waveguide with barrier thickness slowly decreasing. We find the adiabatic amplification enhanced by physical origin. The MOCVD technique has made possible growing a waveguide with slowly decreasing thickness along its length. The technique in a MOCVD system to grow a tapered epitaxial layer is also analyzed.

2 ENHANCED ADIABATIC AMPLIFICATION

The GaAs/AlGaAs superlattice has excitonic nonlinearity origin and fast response time⁴. It shows a negative nonlinear refractive index that is a decrease of the index with an increase in intensity. We can control the laser light to generate the needed densities of the excitons and electron-hole pairs which are responsible for the nonlinearity of the material and stable in the quantum well. When the excitation well below the absorption edge, the electric field of the coherent light induces a coherent polarization that persists only as long as the field is applied. The nonlinear polarization can couple various optical fields that new produced spatial components can interact with the excitation field in a manner of cross phase modulation resulting in self-defocussing effects.

The wave function in the quantum well penetrates into the barrier of the quantum well limited to about 20Å. The measurement of the exciton saturation has shown that up to densities at which the exciton peak bleaches significantly, single-QW and multi-QW behave similarly⁵. This suggests that long range Coulomb forces are effective within the same layer only. We can design a multi-QW with barrier thickness decreasing slowly along its length while keeping the well in same size as shown in Fig. 1.

The contribution of each pair of exciton to the nonlinear index is expressed by $\Delta n/N$, where Δn is the nonlinear index change and N is the number of the exciton pairs. $\Delta n/N = 3.8 \times 10^{-19}$ in the material of GaAs/AlGaAs multi-QW with well size of 76Å⁶. The number of the exciton pairs is proportional to the intensity of the input light for excitation far from saturation.

$$dN = D \mu I \quad (1)$$

where $D = D_0(1 + \epsilon z)$ is the cross section of the exciton generation, μ

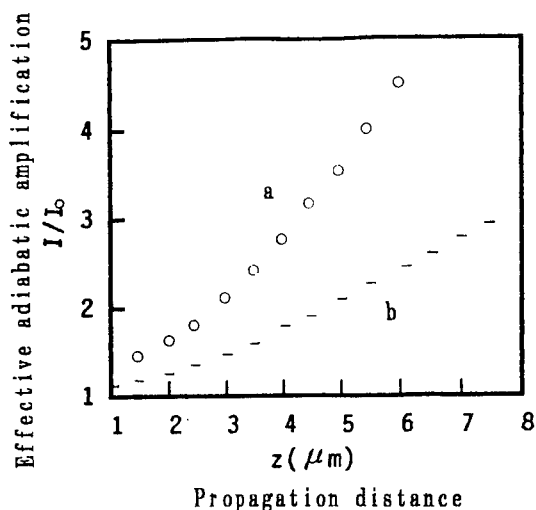


Figure 2. Effect adiabatic amplification with propagation distance.

is the factor of geometrical focussing. The exciton generation has two sources: one is from the increase in intensity due to the geometrical focussing, the other is from the increase of the cross section due to the increase of the quantum well density. The effective intensity change responsible for all the exciton generation is

$$dI/dz = (1 + \varepsilon z) \mu I \quad (2)$$

The coefficient of the effective gain is therefore $G = (1 + \varepsilon z) \mu$. There is also an amplification from physical origin that is due to an increase in the average index in the MQW waveguide. For example, 1.017 times increase in the GaAs/Al_{0.4}Ga_{0.6}As MQW waveguide in the designed structure here. Both the geometrical amplification and the physical amplification are belong to the adiabatic amplification, and the effective amplification is further increased due to the nonlinearity enhancement by the exciton generation cross section increase. The nonlinear Schrodinger equation describing spatial soliton evolution in the multi-QW waveguide with barrier thickness slowly decreasing is

$$i \partial A / \partial \xi + (1/2) \partial^2 A / \partial \eta^2 + A |A|^2 + i \mu (1 + \gamma \xi) A / 2 = 0 \quad (3)$$

where, $\gamma = \varepsilon z_d$, $\xi = z/z_d$, $\eta = x/a$. $z_d = ka^2$ is diffraction length, a is the width of the dark soliton. k is wave vector. For adiabatic transformation of the dual frequency signal into a stable array of dark soliton, the input signal intensity should be the order of, or less than that required for a fundamental soliton and the amplification should not be too large over a diffraction length. In the case we consider here the barrier thickness decreases from 176Å to 76Å in a length of 5 cm while keeping the well size of 76Å unchanged. The nonlinearity quantity $\Delta n/N$ in the MQW structure here is 5.8×10^{-19} , the same as the measured value for the uniform layered structure with same well

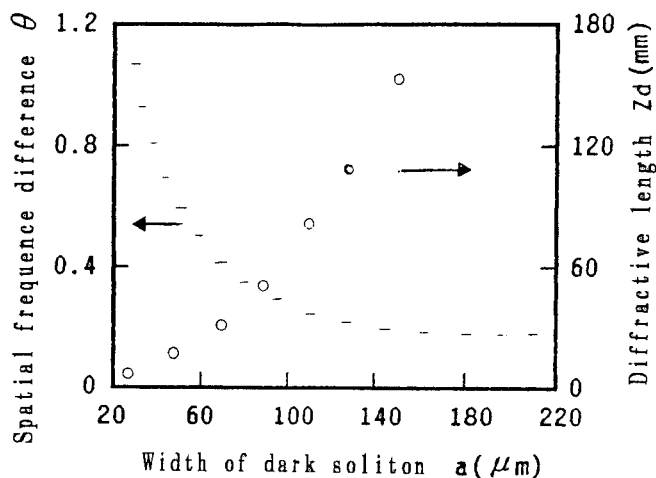


Figure 3. Diffractive length with width of dark soliton.

size. Supposing dual frequency signal were produced with two beam cross in the plane parallel to the layer of the quantum well structure, the interference stripe is normal to the layer. For the h-h excitation of 1s exciton and the input light of $0.84\mu\text{m}$ wavelength, with the incident light creates a density N of 1×10^{17} at the entrance surface, the density at the end side will rise to 1×10^{18} as shown in Fig. 2. The adiabatic amplification in the multi-QW waveguide with barrier thickness slowly decreasing is much larger than that in the waveguide with uniform barrier layer. The effective amplification is estimated to be 8.

The diffraction length and the spatial frequency difference via the width of the dark soliton are shown in Fig. 3. $A = E(x, z)/E_g$ is the normalized amplitude of the optical field in the waveguide. With the normalization factor $E_{\pi} = (n_0/n_2)^{1/2}/ka$, one can calculate for the peak power density of the bright background of the fundamental spatial dark soliton. It is possible to produce fundamental dark soliton with a semiconductor laser as the light source.

3 GROWTH DYNAMICS OF THE TAPERED LAYER

The MOCVD technology is now able to grow structures of MQW at will with atomic monolayer precision. The uniformity over a wafer of 4 inch can be made of less than 1% in a planetary rotation regime. The question is how to grow the tapered barrier layer. Under certain conditions, the growth rate is a function of H_2 carrier gas flow rate for the growth of GaAs⁷. We demonstrate that the growth rate of AlGaAs layer can also be controlled by H_2 carrier gas flow rate. Single control of the gas flow rate makes possible to grow tapered layer if the chamber designed keeps a distributed gas flow rate in the chamber and stops planetary rotation of the sample.

The low pressure condition of less than 5 Torr were selected to minimize gas phase reaction, reduce the mass transfer limitation, re-

sult in large diffusion coefficients. TMG, TEAl and arsine were chosen as the precursor materials. For large V/III ratios, the surface reaction of the III group appears to be self-limiting. We assume that the growth rate follows a simple bimolecular, separate sites Langmuir-Hinshelwood mechanism. The complex chemical reactions in the chamber were divided as the decomposition of the organometallic precursors, adduct formation, AlAs and GaAs deposition, and polymeric deposits formation. The steady state balance for gallium and aluminium can take the form:

$$P_{GO}-P_{Ga}-\tau k_{fg}P_{Ga}P_{As}+\tau k_{rg}P_C-\tau (S/V) R_n=0 \quad (4)$$

and

$$P_{AO}-P_{Al}-\tau k_{fa}P_{Al}P_{As}+\tau k_{ra}P_C-\tau (S/V) R_n=0 \quad (5)$$

where the first two terms represent the partial pressure difference between gallium and aluminium precursors in and out flow in the reacting volume respectively. P_{As} is the partial pressure of arsine and P_C is for the adduct complex. The subscript fg, rg of the rate constant k are for the forward and reversible reaction of gallium. k_{fa} , k_{ra} are for aluminium. τ is the residence time. The last term includes the loss of gallium and aluminium due to polymeric deposits which are small since the surface to volume ratio is small and will be neglected in the following. A similar balance over the adduct complex gives

$$P_{CO}-P_C+\tau (k_{fg}P_{Ga}+k_{fa}P_{Al})P_{As}-\tau (k_{rg}+k_{ra})P_C-\tau k_dP_C=0 \quad (6)$$

Where the first term represents adduct formed in the gas handling system which can be made zero. Therefore the P_C is actually equal to $\tau (k_{fg}P_{Ga}+k_{fa}P_{Al})P_{As}$. By adding (4), (5) and (6) together, we have:

$$P_{GO}+P_{AO}=(P_{Ga}+P_{Al}) (1+\tau k_fP_{As}+\tau^2 k_d^2P_{As}) \quad (7)$$

where an approximation has been made, $k_{fg}=k_{fa}=k_f$. Note that the large V/III ratio in the case we consider here, the equation (7) can be approximately expressed as:

$$P_{Ga}+P_{Al}=(P_{GO}+P_{AO}) / \tau k_tP_{As} \quad (8)$$

and the P_{As} can be taken as the partial pressure of the arsine precursor and

$$k_t=k_f+\tau k_r k_d \quad (9)$$

We assume that the growth rate follows a simple bimolecular, separate sites Langmuir-Hinshelwood mechanism and note that the residence time is inversely proportional to the carrier gas flow rate F, a simplified

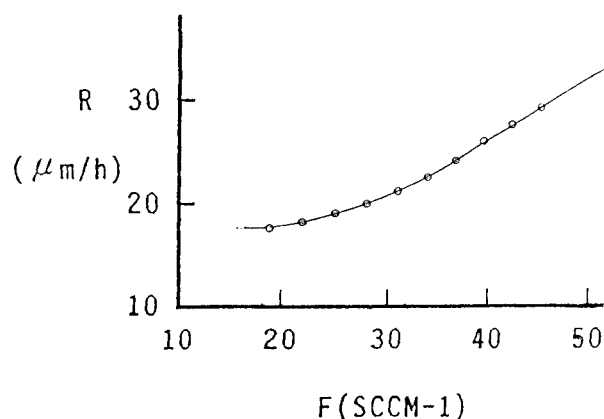


Figure 4. Growth rate R with gas flow rate F.

expression for the growth rate as a function of H_2 carrier flow rate (F) and temperature (T):

$$R = [FK_n K_1 (P_{Ga} + P_{Al}) / P_{As}] / [1 + FK_1 (P_{Ga} + P_{Al}) / P_{As}] \quad (10)$$

where K_n is the rate constant for the surface reaction producing AlGaAs. $L_1 = K_f / k_t$ and K is the absorption constant of gallium and aluminium.

$$K_n = K_{n0} \exp(E_{An} / R_T)$$

$$K_1 = K_{G0} \exp(E_{Gn} / R_T) \quad (11)$$

K_n and K_1 have to be determined by fit of the kinetic model of the experimental data. As an approximation calculation to show the dependence of the growth rate of the gas flow rate, we take $K_{n0} = 7$ cm/s and $K_{10} = 1.6 \times 10^{-8}$ (SCCM $^{-1}$) at the pressure of 1 Torr, with the growth temperature at 700°C. The dependence of the growth rate of the gas flow rate calculated is shown in Fig. 4.

4 DISCUSSION

During laminar flow passing the substrate both the alkyl partial pressure and the arsine pressure decrease while the ratio of V/\dot{V} keeps approximately constant. The carrier gas flow rate has a corresponding decrease also in a specially designed reaction chamber where the transverse size is gradually widened. A growth rate distribution along its length like that in Fig. 4 will make a corresponding tapered layer growth in a linearly widened chamber. While the reaction constants have to be determined experimentally, the growth rate depends on the carrier gas flow rate have been demonstrated experimentally⁷. By keeping low pressure growth condition, the uniform layer grows when the substrate is in a planetary rotation while a tapered layer grows

with no rotation. A structure as shown in Fig.1 will be made in this manner.

The evolution of dark spatial soliton in this MQW waveguide with barrier thickness slowly decreasing will be published elsewhere. The adiabatic amplifications reported up to date are still small. The enhancement is especially needed in practical case where there is always losses in the material.

REFERENCES:

1. C. T. Law and G. A. Swartzlander Jr., "Optical vortex solitons and the stability of dark soliton stripe", *Opt. Lett.* 18:586 (1993)
2. G. C. Duree, J. L. Shultz, and G. J. Salamo et al. "Observation of self-trapping of an optical beam due to the photorefractive effect", *Phys. Rev. Lett.* 71:533 (1993)
3. P. V. Mamyshev, C. Bosshard and G. I. Stegeman, "Generation of a periodic array of dark spatial solitons in the regime of effective amplification" in press in *J. Opt. Soc. Am. B* (1994),
4. H. M. Gibbs, S. S. Tarng, and J. L. Jewel et al., "Room-temperature excitonic optical bistability in a GaAs/GaAlAs superlattice relation" *Appl. Phys. Lett.* 41:221 (1982).
5. J. S. Weiner, D. C. Chemla, and D. A. B. Miller et al. "Highly anisotropic optical properties of single quantum well waveguides", *Appl. Phys. Lett.* 47:664 (1985).
6. N. Peyghambarian and H. M. Gibbs, in "Optical Nonlinearities and Instabilities In Semiconductors", Hartmut Hang Ed. Academic Press, pp. 302 (1988)
7. Thomas R. OMSTEAD, Penny M. VAN SICKLE and Klavs J. JENSEN; "Gas phase and surface reactions in the MOCVD of GaAs from triethylgallium, trimethylgallium and tertiarybutylarsine", *J. Crystal Growth*, 93:20-26 (1988).

COMPUTER-AIDED ANALYSIS AND DESIGN IN GUIDED-WAVE OPTOELECTRONICS

Wei-Ping Huang, Chenglin Xu

Department of Electrical and Computer Engineering
University of Waterloo
Waterloo, Ontario, Canada N2L 3G1

Brent Little

Department of Electrical Engineering
Massachusetts Institute of Technology
Cambridge, Massachusetts 02139, USA

1 Introduction

Computer-aided analysis and design, which are commonplace in electronic and microwave devices, are expected to play an important role in development of optoelectronic devices. So far, the development of optoelectronic devices has followed a traditional pattern of design, fabrication, test, and redesign. Such an approach has been fruitful in discovering and verifying novel concepts and designs in the early stage of the research. As the optoelectronic technologies become more mature and the optoelectronic devices are more close to development and production stages, the conventional approach may not be sufficient in terms of accuracy, efficiency, and cost.

As far as the optoelectronic devices based optical waveguides are concerned, Maxwell's equations that govern propagation and interaction of the electromagnetic waves are exactly known. In principle, given the refractive index profiles as well as the boundary conditions of an optical waveguide, the solutions of the Maxwell's equations or their equivalent wave equations will yield precise descriptions of the behaviors of the electromagnetic waves in the devices. The finite-difference time-domain (FDTD) technique,

which was developed in microwaves, is one of the methods to do so[1, 2]. Though exact, the FDTD requires enormous computer resources for most of the realistic optical guided-wave structures and is therefore limited in its usefulness for analysis and design in guided-wave optoelectronics. In comparison with microwaves, optical guided-waves have higher carrier frequency and thus narrower relative bandwidth. Also, the interaction between the optical guided-waves and the media is weak and consequently the device feature size is much larger than that of the optical wavelength. Hence, considerable simplifications are possible by proper consideration of the characteristics of the optical guided-waves.

2 Coupled-Mode Theory

One popular method in guided-wave optoelectronics is the coupled-mode theory (CMT)[3, 4]. Like the FDTD, the CMT originated from microwaves, but its adaption to optics has been very successful. Often considered as an approximate method, the CMT provides insightful and accurate description of the resonant-like interaction among different optical guided waves, which are weakly coupled but phase-matched. Therefore, it to great extent catches much of the key features of the guided-wave optoelectronics and is particularly useful in explorations of novel devices. In practice, the usage of the CMT requires the knowledge of the guided modes in some unperturbed waveguides. Since analytical solutions are known only for a few simple waveguide configurations, numerical solutions are necessary for most practical waveguide structures. Another shortcoming of the CMT is the radiation phenomena associated with optical guided-wave devices, which are made of weakly guided, open dielectric waveguides, are difficult to model rigorously in the CMT.

3 Beam Propagation Method

Another method which has increasingly gained popularity is the beam propagation method (BPM)[5, 6]. The conventional BPM was based on a split-step FFT algorithm and solved the one-way, paraxial scalar wave equations in frequency domain. Recently, several new algorithms based on finite-difference and finite-element methods have been developed which are able to treat nonparaxial and vectorial waves[7]. Unlike the FDTD, which simulates the wave propagation in time-domain and requires to store all the field values at each grid, the BPM models the wave propagation in frequency-domain and requires to store the field data over one cross-section only and keeps updating them while the wave propagates step by step longitudinally. Hence, the BPM is more efficient and requires less computer memory than the FDTD. Also, the BPM is more accurate and versatile than the CMT. One does not need to identify the perturbed/unperturbed structures and solve for the modes since both guided-wave and radiation are included in the BPM formulation. As a result, arbitrary index profiles can be modeled and radiation phenomena can be simulated. One disadvantage of the BPM is that the backward reflection is ignored. Since most optical guided-wave devices are weakly-guiding transversely and slowly-varying longitudinally, the reflection is usually weak and negligible, esp. for the distributed feed-back structures. Therefore, the BPM is more suitable for optical guided-wave devices.

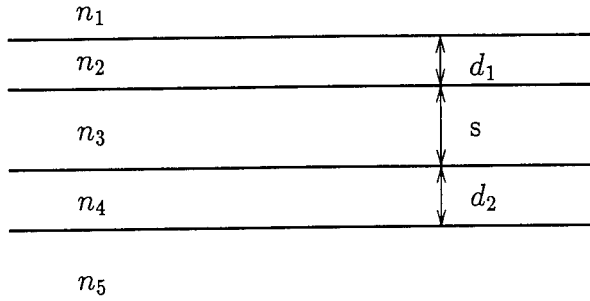


Figure 1: Schematic diagram of a parallel directional coupler/filter.

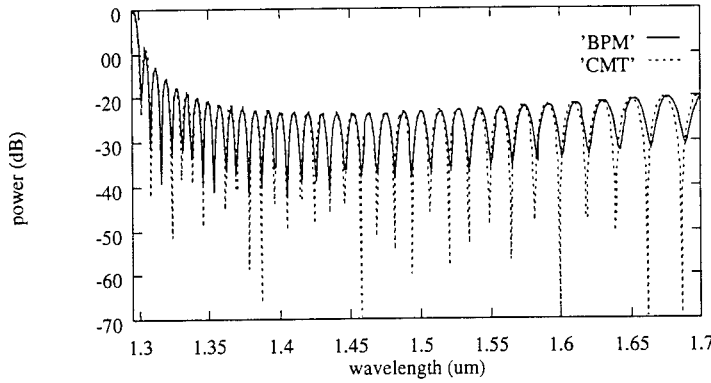


Figure 2: Spectrum of a parallel directional coupler/filter. Solid: BPM results; dashed: CMT results.

4 Applications

One of the typical guided-wave devices is the directional coupler/filter. As shown in Fig. 1, two dissimilar waveguides are placed in proximity and the interaction between the modes of the individual waveguides causes the power exchange between the two waveguides. The coupling can be synchronized and a complete power exchange can be achieved at the central wavelength λ_o , at which the two waveguides have the same propagation constants[8], i.e.

$$\beta_1(\lambda_o) = \beta_2(\lambda_o). \quad (1)$$

The guided modes of the two-dimensional coupler are well defined and, therefore, can be easily simulated by the CMT. In order to make a comparison, we simulate the structure with both the CMT and the BPM. The parameters we used in the simulation are: $n_1 = n_3 = n_5 = 3.2$, $n_2 = 3.4$, $n_4 = 3.304$, $d_1 = 0.3\mu m$, $d_2 = 1.0\mu m$, and $s = 1.35\mu m$. The device length is $L = 5mm$ and the central wavelength is $\lambda = 1.3\mu m$. Shown in Fig. 2 are the simulation results and the comparison. It is noted that the CMT result is in excellent agreement with the BPM result.

One may note that the spectrum of the parallel coupler/filter suffers high sidelobes, a phenomenon unwanted in practical applications. The sidelobes can be reduced by tapering the coupling between the waveguides as shown in Fig. 3. Theoretically, the sidelobes can be reduced to any desired level by optimizing the taper shape[10]. Both

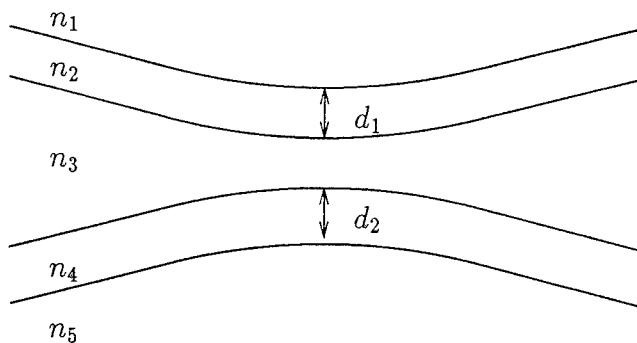


Figure 3: Schematic diagram of a tapered directional coupler/filter.

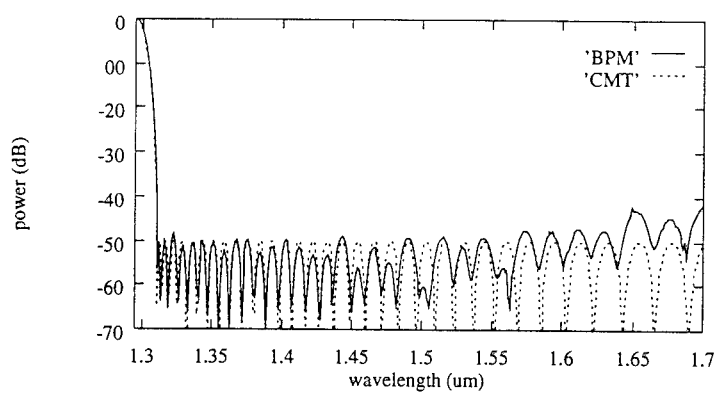


Figure 4: Spectrum of a tapered directional coupler/filter. Solid: BPM results; dashed: CMT results

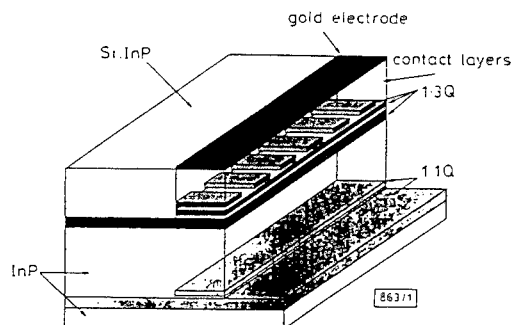


Figure 5: Schematic diagram of a grating assisted coupler/filter by AT&T Bell Labs.

the CMT and the BPM can be used as an optimization tool, but the CMT may be much more efficient since it is an analytical approach. Shown in Fig. 4 is a simulation results for a tapered structure with $-50dB$ sidelobes. Like the results shown in Fig. 2, the CMT and the BPM yield very similar results.

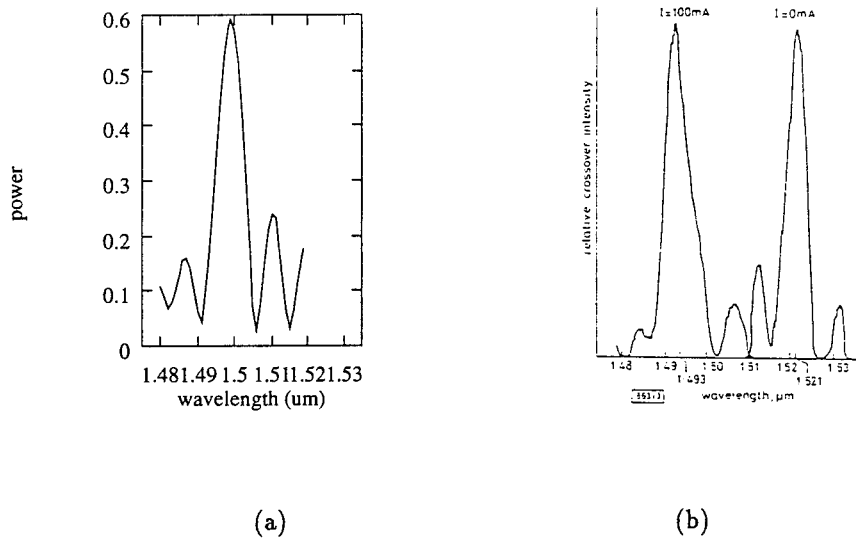


Figure 6: Spectrum of the grating-assisted coupler/filter. (a) BPM result; (b) Experimental result

If Eqn. 1 is not be satisfied at the central wavelength λ_o , complete power exchange can still be achieved by introducing a periodic grating. The phase-matching condition for the grating-assisted coupler is[9]

$$\beta_s(\lambda_o) - \beta_a(\lambda_o) = \frac{2\pi}{\Lambda}, \quad (2)$$

where β_s and β_a are the propagation constants of the symmetric-like and asymmetric-like modes of the coupler/filter, and Λ is the grating period.

In order to make a comparison with the experimental results, we choose a filter structure which is designed, fabricated, and tested by AT&T Bell Labs[11]. Shown in Fig. 5 is the schematic diagram of the structure. Light is input from the lower waveguide and coupled to the upper waveguide with the assistance of the grating on the top of the upper waveguide. Direct CMT simulation is difficult for this complicated structure since the guided modes is not available analytically. The BPM can, however, handle this problem easily since it does not require the knowledge of mode.

In our BPM simulation, we use the parameters published in Ref.[11]. The simulation result is shown in Fig. 6(a) and the experimental result from Ref[11] is shown in Fig. 6(b). We can see that the simulation results are in good agreement with the experimental data.

5 Conclusion

The computer-aided analysis and design in guide-wave optoelectronics has been reviewed. The characteristic of the optical guide-wave devices and the popular simulation tools have been introduced. The comparison between the CMT and the BPM has been made for a two-dimensional directional coupler/filter. Finally, a comparison with the published experimental result has been made.

References

- [1] K. Yee, Numerical solution of initial boundary value problem involving Maxwell's equations in isotropic media, *IEEE Trans. Antennas Propagat.*, AP-14:302 (1966).
- [2] S. Chu and S. K. Chaudhuri, A finite-difference time-domain method for the design and analysis of guided-wave optical structures, *J. Lightwave Technol.*, LT-5:1(1987).
- [3] S. E. Miller, Coupled wave theory and waveguide applications, *Bell Syst. Tech. J.*, 33:661(1954).
- [4] W. -P. Huang, Coupled-mode theory for optical waveguides: an overview, *J. Opt. Soc. Am. A.*, 11:963(1994).
- [5] M. D. Feit and J. Fleck Jr., Light propagation in graded-index optical fibers, *Appl. Opt.*, 17:3990(1978).
- [6] D. Yevick and B. Hermansson, Split-step finite-difference analysis of rib waveguides, *Electron. Lett.*, 25:461 (1989).
- [7] W. P. Huang, C. L. Xu, S. T. Chu, and S. K. Chaudhuri, The finite-difference vector beam propagation method: analysis and assessment, *J. Lightwave Tech.*, 10:295(1992).
- [8] D. Marcuse, Directional couplers made of nonidentical asymmetrical slabs. part I: Synchronous couplers, *J. Lightwave Tech.*, 5:113(1987).
- [9] W. P. Huang and H. A. Haus, Power exchange in grating-assisted couplers, *J. Lightwave Tech.*, 7:920(1989).
- [10] B. Little, C. Wu, and W. -P. Huang, Sidelobe suppression for optical wavelength filter, *Opt. Lett.*, submitted for published.
- [11] L. L. Buhl, R. C. Alferness, U. Koren, B. I. Miller, M. G. Young, T. L. Koch, C. A. Burrus, and G. Raybon, Grating-assisted vertical coupler/filter for extended tuning range, *Electron. Lett.*, 29:81(1993).

PARALLEL-PROCESSING FINITE-DIFFERENCE BEAM PROPAGATION METHODS

Husain M. Masoudi and John M. Arnold

Department of Electronics and Electrical Engineering
University of Glasgow
Glasgow G12 8LT, Scotland, UK

INTRODUCTION

The computational modelling of optoelectronic guided-wave devices in 3-dimensions is usually very demanding in terms of computer time because of the size of typical devices, which are generally much longer than a wavelength. In these circumstances, it is natural to turn to parallel processing implementations in order to achieve practical run times for realistic devices. Not all serial methods are readily adapted to the parallel environment, however, and care needs to be exercised in selecting the appropriate method for parallelisation. In general, for MIMD architectures one should seek to minimise the time spent in communicating between processors, and one is therefore led to prefer methods which can be localised onto separate processors. Finite-difference methods are intrinsically local in the configuration domain, and hence very suitable for parallel processing.

THEORY

The BPM algorithm is based on the parabolic approximation to the Helmholtz equation which can be expressed, for a scalar monochromatic electric field E in 3-dimensions, as

$$-2ikn_0 \frac{\partial E}{\partial z} = \frac{\partial^2 E}{\partial x^2} + \frac{\partial^2 E}{\partial y^2} + k^2(n^2 - n_0^2)E, \quad (1)$$

where k is the free-space wave number, n_0 is a reference refractive index and $n(x, y, z)$ is the refractive index profile, x and y are the transverse coordinates and z is the propagation direction. One way to describe the propagation of the field in (1) is to use the unconditionally

stable split operator which is second-order accurate with respect to the propagation coordinate z

$$E(x, y, z + \Delta z) = e^{i \frac{\Delta z}{2a} \partial_x^2} e^{i \frac{\Delta z}{2a} \partial_y^2} e^{i \frac{\Delta z}{a} d} e^{i \frac{\Delta z}{2a} \partial_x^2} e^{i \frac{\Delta z}{2a} \partial_y^2} E(x, y, z) + O((\Delta z)^3), \quad (2)$$

where

$$\begin{aligned} a &= 2kn_0 \\ d(x, y, z) &= k^2 [n^2(x, y, z) - n_0^2] \\ \partial_\rho^2 &= \frac{\partial^2}{\partial \rho^2} \quad (\rho = x, y) \end{aligned}$$

Here Δz is a small step in the propagation direction.

Fast Fourier Transform BPM (FFT-BPM)

In the FFT-BPM [1], the discretised field over the cross-section at z is transformed into Fourier space before being multiplied with operators representing transverse partial derivatives, then transformed back into configuration space before being multiplied with the operator containing the refractive index. This procedure exploits the fact that the transverse Laplacian operator is diagonal in Fourier space, with values equal to transverse wave numbers. The FFT numerical routine is used to link between the spectral space and the spatial space. Although the computation of the transverse Laplacian using Fourier space is highly accurate, nevertheless the use of the FFT restricts the overall efficiency of the algorithm in parallel implementations. This is because the FFT requires information from the entire spatial domain to compute each spectral frequency component, and this requires extensive and inefficient communications to take place between the processors. Also, even in serial implementation, the FFT requires $O(N \log_2 N)$ operations per transverse dimension per propagation step, whereas the corresponding count for FD methods is $O(N)$. Other methods based on the finite-difference approximation to approximate the transverse partial derivatives of the operator are much better to use than the FFT. Finite-difference methods are more efficient and more flexible (e.g. nonuniform mesh and radiation boundary conditions) than the FFT-BPM, and some are very well suited to the parallel environment.

Alternating Direction Implicit BPM (ADI-BPM)

The most popular BPM, the ADI-BPM [2], replaces the operators which contain the Laplacian with the relation

$$e^{i \frac{\Delta z}{2a} \partial_\rho^2} = \left[1 - i \frac{\Delta z}{4a} \partial_\rho^2 \right]^{-1} \left[1 + i \frac{\Delta z}{4a} \partial_\rho^2 \right] + O((\Delta z)^3). \quad (3)$$

Using the central-difference approximation to replace the partial derivatives in eq. (3) will lead to a large block-tridiagonal system of equations for each propagational step. This method

also requires the inversion of a matrix at every propagation step, which is generally not a very efficient process.

Real Space BPM (RS-BPM)

The Real Space method (RS-BPM) [3, 4] also uses the central-difference approximations with matrix splitting operators to approximate eq. (2), and can be written as

$$E(z + \Delta z) = \left\{ F \exp\left(i \frac{\Delta z}{a} U\right) F \right\} E(z) + O((\Delta z)^3) \quad (4)$$

where

$$F = e^{\alpha_y S_y^o} e^{\beta_y S_y^e} e^{\alpha_x S_x^o} e^{\beta_x S_x^e} e^{\alpha_x S_x^o}$$

$$U(x, y, z) = d(x, y, z) - \frac{2}{\Delta x^2} - \frac{2}{\Delta y^2}$$

$$\beta_p = i \frac{\Delta z}{2 a \Delta \rho^2} = 2\alpha_p$$

and Δx and Δy are the mesh sizes in the x and the y directions respectively. E in (4) is now a vector of the sampled values of the field on a mesh on the x - y plane. It is possible to choose the splitting in eq. (4) such that each of the matrices S^e and S^o is 2×2 block-diagonal. In this manner the computation of the operators is reduced to a simple analytical exponentiation of independent 2×2 matrices, which reduces the computational time by a large factor compared to the ADI-BPM. It is important to note that the RS-BPM is an explicit method, which means that operations on any spatial field point are local and therefore also highly parallel. This feature adds to the advantages of the RS-BPM algorithm compared to the ADI-BPM; the latter is an implicit method and will not gain as much if it is implemented on parallel computers because the computation of the inverse matrix in (3) is not localised.

Explicit Finite-Difference BPM (EFD-BPM)

An efficient and highly parallel finite-difference BPM is the explicit finite-difference method (EFD-BPM) [5, 6], which is based on applying the central-difference approximation directly to the parabolic equation. This method can be formulated, in a discretised fashion, as

$$E_{j,m}(z + \Delta z) = E_{j,m}(z - \Delta z) + 4\beta_x [E_{j-1,m}(z) + E_{j+1,m}(z)]$$

$$+ 4\beta_y [E_{j,m-1}(z) + E_{j,m+1}(z)] + i \frac{2\Delta z}{a} U_{j,m} E_{j,m}(z) \quad (5)$$

The indices (j, m) represent the mesh coordinates replacing the (x, y) transverse coordinates after discretisation. The application of eq. (5) is simply a multiplication of the input field with a very sparse matrix containing only five non-zero elements in each row, which makes the method very efficient. However, this algorithm is stable only if the following condition is satisfied:

$$\Delta z < 2kn_0 \left[\frac{4}{\Delta x^2} + \frac{4}{\Delta y^2} + k^2 |n_{j,m}^2 - n_0^2|_{\max} \right]^{-1}. \quad (6)$$

In addition to the high efficiency of the EFD-BPM, it is also highly parallel.

PARALLEL IMPLEMENTATIONS

We have implemented both of the explicit methods, the EFD-BPM and the RS-BPM, on a transputer array and a Connection Machine. The transputer array is a PARSYTEC super-cluster consisting of 64 IMS-T800 processors (MIMD architecture) each with 4 Mb of local memory. The Connection Machine is a CM-200 consisting of 16k (16,384) serial processors (SIMD architecture) with a total memory of 0.5 Gb.

As a preliminary example, in order to assess the speed-up and efficiency achievable by parallel implementation, we have modelled the propagation through a longitudinally uniform semiconductor rib waveguide [7, 8]. The explicit finite-difference method (EFD-BPM) achieves the largest speed-up in the SIMD implementation, with speed-up factors of the order 550 over the same method implemented serially having been observed. In the MIMD environment we have achieved 85% efficiency using the EFD-BPM, and higher efficiency around 94% using the RS-BPM, where efficiency is defined as the speed-up factor divided by the number of processors used. These figures relate to the time per propagation step, with transverse grids of 240×240 points. The RS-BPM, although slightly more efficient, is 6 times slower than the EFD-BPM. All of the parallel-processing performance indicators improve with increasing number of transverse grid points. Systematic tests have also been carried out to establish that the numerical accuracy and convergence of each method are retained in the parallel implementations. The accuracies deduced from convergence tests of the methods indicate that the EFD and RS methods produce comparable accuracy for the same longitudinal step-length Δz .

In order to further demonstrate the capabilities of the parallel implementation of the BPM, we have studied a specific problem in the theory of nonlinear guided waves, namely second-harmonic generation in a nearly-phase-matched semiconductor rib waveguide [9, 10], using the EFD-BPM on account of its superior speed. Because of the difference in phase velocities between the lowest-order guided modes at the fundamental and second-harmonic frequencies in semiconductor optical waveguides it is necessary to introduce quasi-phase-matching (QPM) by means of a grating in the active second-order susceptibility tensor coefficient $\chi^{(2)}(\omega, \omega)$ [11]. This grating is implemented explicitly in our model by switching the coefficient on and off periodically along the waveguide axis at the period required for QPM, given by $\Lambda = 2\pi/(k_2 - 2k_1)$ where k_1 and k_2 are the lowest-order guided-mode propagation coefficients at the fundamental and second-harmonic frequencies respectively. There is considerable current interest in the behaviour of this device when the grating period is slightly detuned from the exact QPM condition by an amount $\Delta k = k_2 - 2k_1 - 2\pi/\Lambda$, since the fundamental experiences an intensity-dependent phase shift in these circumstances [12]. The modelling here is a 3-dimensional parallel version of a calculation previously carried out in 2-dimensions serially [13]. Figure 1 shows the semiconductor rib waveguide geometry used for this calculation, which used a value of $\chi^{(2)}(\omega, \omega) = 300 \text{ pm V}^{-1}$ and a wavelength for the fundamental of $\lambda = 1.55 \text{ }\mu\text{m}$.

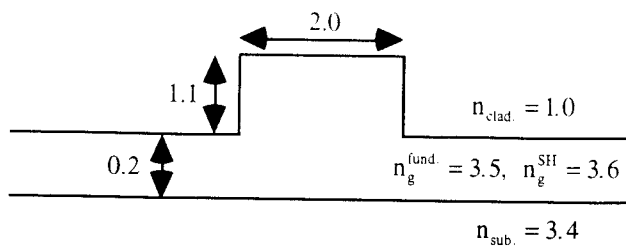


Figure 1: Semiconductor rib waveguide parameters

Figure 2 shows the periodic depletion and recovery along the device of the power in the guided mode at the fundamental frequency for a phase mismatch of $\Delta kL = 2\pi$, where L is the length of the device, taken to be $L = 1$ mm in this example. The input power to the waveguide in the fundamental is 81 W. The propagation of the parallel BPM algorithms over the full length of the device with a transverse mesh of 80×80 points and a longitudinal step length of $0.02484 \mu\text{m}$ (40250 steps) took about 4 minutes on the CM-200, and about 30 minutes on the 64-transputer array at 54% efficiency, which is equivalent to a serial execution time of 17.3 hours.

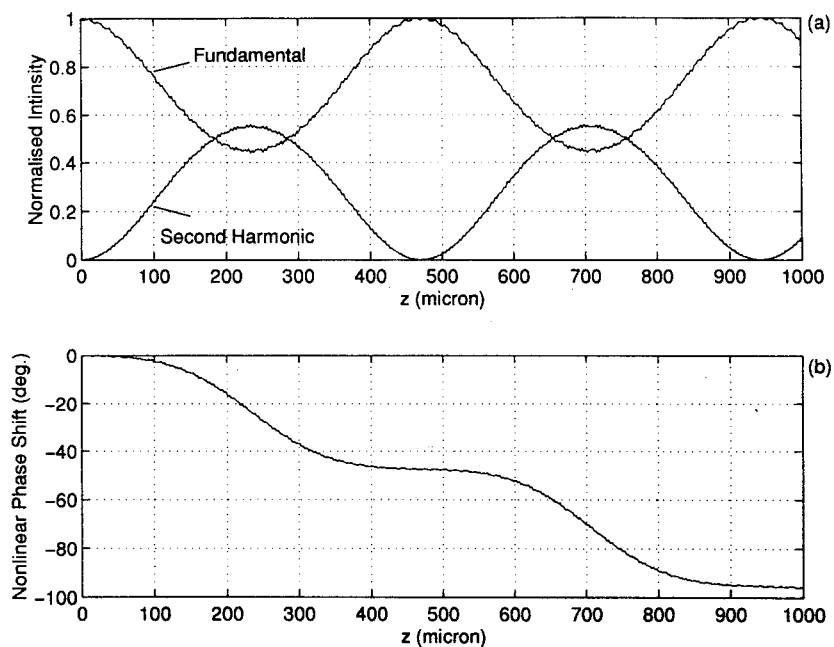


Figure 2: Power exchange between fundamental and second-harmonic and nonlinear phase change as functions of propagation distance for quasi-phase-matched semiconductor rib waveguide

CONCLUSIONS

We have demonstrated the application of parallel-processing techniques to the modelling of 3-dimensional waveguide geometries using finite-difference BPM techniques. The explicit finite-difference BPM is found to be particularly valuable in this respect, since its formulation is highly localised in the spatial domain and its execution involves only the multiplication of a vector by a sparse matrix at each propagation step. The principal disadvantage of the explicit method, which is shared by its parallel versions, is the fact that the stability constraint (6) must be satisfied, which renders the allowed longitudinal step length rather small. This could be improved by using higher-order finite-difference approximations to the transverse derivatives, allowing the transverse mesh size to be increased for a given accuracy and hence relaxing the longitudinal step length constraints. This and other methods which retain the parallelisability of the direct implicit method are currently being studied

ACKNOWLEDGEMENTS:

Mr. Masoudi would like to thank King Fahd University of Petroleum and Minerals (Saudi Arabia) for their support while he is at the University of Glasgow. Both authors would like to thank the University of Edinburgh Parallel Computing Centre for access to the Connection Machine. The work was partially supported by the Engineering and Physical Sciences Research Council under research grant GR/H82471.

REFERENCES

1. M. D. Feit and J. A. Fleck, "Analysis of rib waveguides and couplers by propagation beam method", *J. Opt. Soc. Am. A*, **7**, 73-79, 1990.
2. D. Yevick, "A guide to electric field propagation techniques for guided-wave optics", *Opt. Quan. Elect.*, **26**, 185-197, 1994.
3. H. DeRaedt, "Product formula algorithms for solving the time dependent Schrödinger equation", *Comp. Phys. Rep.*, **7**, 1-72, 1987.
4. J. Richardson, "Computational physics on the CM-2 supercomputer", *Phys. Rep.*, **207**, 305-320, 1991.
5. Y. Chung and N. Dagli, "An assessment of finite difference beam propagation method", *IEEE J. Quant. Elect.*, **26**, 1335-1339, 1990.
6. Y. Chung and N. Dagli, "Analysis of z-invariant and z-variant semiconductor rib waveguides by explicit finite difference beam propagation method with nonuniform mesh configuration", *IEEE J. Quant. Elect.*, **27**, 2296-2305, 1991.
7. H. M. Masoudi and J. M. Arnold, "Parallel beam propagation methods", *IEEE Phot. Tech. Lett.*, **6**, 848-850, 1994.
8. H. M. Masoudi and J. M. Arnold, "Parallel three-dimensional finite-difference beam propagation methods" accepted for publication in *Int. J. Num. Mod.*, 1994.
9. H. M. Masoudi and J. M. Arnold, "Parallel beam propagation method for the analysis of second harmonic generation", submitted to *IEEE Phot. Tech. Lett.*, 1994.
10. H. M. Masoudi and J. M. Arnold, "Modelling second-order nonlinear effects in optical waveguides using a parallel-processing beam propagation method", submitted to *IEEE J. Quant. Elect.*, 1994.
11. M. M. Fejer, G. A. Magel, D. H. Jundt, and R. L. Byer, "Quasi-phase matched second harmonic generation: tuning and tolerances", *IEEE J. Quant. Elect.*, **28**, 2631-2654, 1992.
12. R. DeSalvo, D. J. Hagan, M. Sheikh-Babae, G. Stegeman and E. W. Van Stryland, "Self-focusing and self-defocusing by cascaded second-order effects in KTP", *Opt. Lett.*, **17**, 28-30, 1992.
13. G. J. Krijnen, H. J. Hoekstra and P. V. Lambeck, "BPM simulations of integrated optic structure containing second order nonlinearity", *ECIO (Euro. Conf. Intg. Opt.)*, 5-4 to 5-5, 1993.

AN EXPLICIT AND STABLE FINITE DIFFERENCE BPM FOR APPLICATIONS TO DEVICE ANALYSIS AND DESIGN

Feng Xiang and Gar Lam Yip

Guided-Wave Photonics Laboratory
McGill University
Department of Electrical Engineering
3480 University Street
Montreal, Quebec, Canada H3A 2A7

INTRODUCTION

Recently, the beam propagation method (BPM) has been significantly improved after finite-difference schemes replaced the FFT scheme. There are two kinds of commonly used finite-difference schemes. One is the Crank-Nicolson method¹ in which a tri-diagonal matrix has to be found for a two dimensional (2-D) problem, followed by a matrix inversion for each propagation step. This scheme is stable and accurate. For a weakly guiding structure, a large step-size can be used with a reasonable accuracy. However, for a three dimensional (3-D) problem, the matrix becomes complicated, and its inversion is not easy to find. The other is simply based on an explicit (centred forward-difference) method². The latter method gives a very simple formulation for each propagation step, which is good for solving a three dimensional problem. However, its stability is critical. In order to keep the scheme stable, the propagation step has to be less than a certain size which usually must be very small and, in some cases, too small to be practical.

In this paper, we will present a different finite-difference scheme, based on the DuFort-Frankel method³ which is explicit and stable. It has the merits of both the above-mentioned methods. The scheme is not popular and not even mentioned in some mathematical books because it introduces an extra error proportional to the second-order derivative of the field with respect to the propagation direction. If the structure is weakly guiding as is the case in most integrated optical devices, this second-order derivative is small and can be neglected as usually done in deriving the paraxial wave equation. Since the scheme is explicit, it is particularly useful for 3-D problems. By incorporating the vector boundary conditions in the scheme, the scheme can work as a vector FD-BPM.

A so-call 'Leap-frog computation ordering' technique³ can be applied in the new scheme to save the computation time by half without any loss in accuracy. It has been found that the conventional transparent boundary condition⁴ (TBC) does not work well

in the scheme. Modified TBCs for both 2-D and 3-D will be presented.

A slab waveguide directional coupler has been taken as an example to compare the accuracy and computation time of the new scheme with other methods. 3-D results were obtained for a directional coupler formed by two channel surface waveguides on a glass substrate. Finally, as an illustration, the scheme was used to design a three-wavelength demultiplexer, which has two cascaded asymmetric Mach-Zehnders.

DUFORT-FRANKEL FINITE-DIFFERENCE SOLUTIONS

Assume the refractive index $n(x,y,z)$ to be piecewise uniform over the transverse cross section and vary slowly along z . Thus, in each uniform transverse medium, the vector wave equation can be approximated by

$$\nabla^2 E_t + n^2 k_o^2 E_t = 0 \quad (1)$$

where E_t is the transverse field component and k_o the free space wave number. Furthermore, we will neglect the possible coupling between the x and y polarizations and assume all the index interfaces are normal to the x -axis or the y -axis. Letting

$$E_t(x, y, z) = \phi(x, y, z) e^{-jn_r k_o z} \quad (2)$$

and making use of the slow variation approximation of $\phi(x, y, z)$ along z , the wave equation Eq.(1) can be reduced to the paraxial wave equation

$$2jk_o n_r \frac{\partial \phi}{\partial z} = \frac{\partial^2 \phi}{\partial x^2} + \frac{\partial^2 \phi}{\partial y^2} + k_o^2 [n^2(x, y, z) - n_r^2] \phi \quad (3)$$

where n_r is a reference refractive index. E_t in Eq.(2) can be either E_x or E_y . The relation between the second-order derivative of field ϕ and its centred finite-difference expression with respect to the propagation direction z is given by

$$\frac{\partial^2 \phi_{m,n}^k}{\partial z^2} = \frac{\phi_{m,n}^{k+1} - 2\phi_{m,n}^k + \phi_{m,n}^{k-1}}{\Delta z^2} + O(\Delta z^2 \frac{\partial^4 \phi_{m,n}^k}{\partial z^4}) \quad (4)$$

where $\phi_{m,n}^k = \phi(x=m\Delta x, y=n\Delta y, z=k\Delta z)$. Solving for $\phi_{m,n}^k$ in Eq.(4) and neglecting terms with orders higher than Δz^2 , we have

$$\phi_{m,n}^k = \frac{1}{2}(\phi_{m,n}^{k+1} + \phi_{m,n}^{k-1}). \quad (5)$$

This is called DuFort-Frankel approximation.

At first, let us consider $E_t = E_x$. For the derivative $\partial^2 \phi / \partial y^2$ normal to the direction of polarization, the electric fields are tangential to the possible index interfaces which may be crossed by the discretized field values in its finite-difference expression along y . The boundary conditions on E_x are automatically satisfied in the finite-difference approximation given by

$$\frac{\partial^2 \phi}{\partial y^2} = \frac{\phi_{m,n+1}^k - 2\phi_{m,n}^k + \phi_{m,n-1}^k}{\Delta y^2}. \quad (6)$$

For the derivative along the direction of the polarization, the finite-difference approximation has to be modified to satisfy the boundary conditions at an index interface which is given by⁵

$$\frac{\partial^2 \phi}{\partial x^2} = \frac{T_{m+1,n}^{kx} \phi_{m+1,n}^k - 2\phi_{m,n}^k \epsilon_{m,n}^{kx} + T_{m-1,n}^{kx} \phi_{m-1,n}^k}{\Delta x^2} \quad (7)$$

where

$$T_{m\pm 1,n}^{kx} = \frac{2n_{m\pm 1,n}^2}{n_{m\pm 1,n}^2 + n_{m,n}^2} \quad \text{at } z_k = k\Delta z, \quad (8)$$

$$\xi_{m,n}^{kx} = 1 - \left(\frac{1}{2}\right) \frac{n_{m+1,n}^2 - n_{m,n}^2}{n_{m+1,n}^2 + n_{m,n}^2} - \left(\frac{1}{2}\right) \frac{n_{m-1,n}^2 - n_{m,n}^2}{n_{m-1,n}^2 + n_{m,n}^2} \quad \text{at } z_k = \Delta z k. \quad (9)$$

Applying a center forward-difference approximation for $\partial\phi/\partial z$ and using Eqs.(5-7), the finite-difference solution of Eq.(3) for an x polarized field at z_{k+1} is given by

$$\begin{aligned} \phi_{m,n}^{k+1} &= \frac{1 - r(\xi_{m,n}^{kx} + \eta^2 - \alpha)}{1 + r(\xi_{m,n}^{kx} + \eta^2 - \alpha)} \phi_{m,n}^{k-1} + \frac{r}{1 + r(\xi_{m,n}^{kx} + \eta^2 - \alpha)} \\ &\times (T_{m+1,n}^{kx} \phi_{m+1,n}^k + T_{m-1,n}^{kx} \phi_{m-1,n}^k + \eta^2 \phi_{m,n+1}^k + \eta^2 \phi_{m,n-1}^k) \end{aligned} \quad (10)$$

where

$$\eta = \frac{\Delta x}{\Delta y}, \quad r = \frac{-j\Delta z}{n_r k_o \Delta x^2}, \quad \text{and} \quad \alpha = \frac{1}{2} k_o^2 \Delta x^2 (n^2 - n_r^2).$$

By a similar procedure, we can get the solution for a y polarized field $E_t = E_y$ at z_{k+1} given by

$$\begin{aligned} \phi_{m,n}^{k+1} &= \frac{1 - r(1 + \xi_{m,n}^{ky} \eta^2 - \alpha)}{1 + r(1 + \xi_{m,n}^{ky} \eta^2 - \alpha)} \phi_{m,n}^{k-1} + \frac{r}{1 + r(1 + \xi_{m,n}^{ky} \eta^2 - \alpha)} \\ &\times (\phi_{m+1,n}^k + \phi_{m-1,n}^k + \eta^2 T_{m,n+1}^{ky} \phi_{m,n+1}^k + \eta^2 T_{m,n-1}^{ky} \phi_{m,n-1}^k) \end{aligned} \quad (11)$$

where

$$T_{m,n\pm 1}^{ky} = \frac{2n_{m,n\pm 1}^2}{n_{m,n\pm 1}^2 + n_{m,n}^2} \quad \text{at } z_k = k\Delta z, \quad (12)$$

$$\xi_{m,n}^{ky} = 1 - \left(\frac{1}{2}\right) \frac{n_{m,n+1}^2 - n_{m,n}^2}{n_{m,n+1}^2 + n_{m,n}^2} - \left(\frac{1}{2}\right) \frac{n_{m,n-1}^2 - n_{m,n}^2}{n_{m,n-1}^2 + n_{m,n}^2} \quad \text{at } z_k = \Delta z k. \quad (13)$$

We can see that the solutions given by Eqs.(10) and (11) are explicit.

For a 2-D problem, $\partial/\partial y = 0$ which leads $\Delta y \rightarrow \infty$ and $\eta \rightarrow 0$. Eq.(10) is then reduced to

$$\phi_m^{k+1} = \frac{1 - r(\xi_m^k - \alpha)}{1 + r(\xi_m^k - \alpha)} \phi_m^{k-1} + \frac{r(T_{m+1}^k \phi_{m+1}^k + T_{m-1}^k \phi_{m-1}^k)}{1 + r(\xi_m^k - \alpha)} \quad \text{for } E_x \quad (14)$$

which is the same as the solution reported⁶ for a TM polarization in a 2-D problem. For the TE polarization, the solution can be simplified from Eq.(11) to be given by

$$\phi_m^{k+1} = \frac{1 - r(1 - \alpha)}{1 + r(1 - \alpha)} \phi_m^{k-1} + \frac{r(\phi_{m+1}^k + \phi_{m-1}^k)}{1 + r(1 - \alpha)} \quad \text{for } E_y. \quad (15)$$

It can be shown that the above two solutions are von Neumann stable if the refractive index is real and

$$\Delta z \leq \frac{n_r}{\sqrt{n^2 - n_r^2}} \Delta x \quad \text{where} \quad n(x, z) > n_r. \quad (16)$$

For $n(x, z) \leq n_r$, the scheme is unconditionally stable provided that $n(x, z)$ is real.

In addition to the finite-difference error of the conventional explicit or Crank-Nicolson methods, the new scheme introduces an extra error of the order of

$$\varepsilon \sim [(\Delta z/\Delta x)^2 + (\Delta z/\Delta y)^2] \partial^2 \phi_{m,n}^k / \partial z^2 \quad (17)$$

after using Eq.(5). It can be seen that if $\Delta z \leq (\Delta x, \Delta y)$, this extra error will be equivalent to the error of neglecting $\partial^2 \phi / \partial z^2$ in deriving the paraxial wave equation.

LEAP-FROG ORDERING OF CALCULATION

For the sake of convenience, the discussion will be given only for a 2-D problem. Taking a close look at Eqs.(14) and (15), it is not difficult to find that ϕ_m^k with an even number $m = 2, 4, \dots$, are independent of the previous field values ϕ_m^{k-1} with an even number $m = 2, 4, \dots$, and the next previous field values ϕ_m^{k-2} with an odd number $m = 1, 3, \dots$. Thus, we can have two independent sets of solutions indicated by circles and solid dots respectively in Fig.1. Usually, one set is enough, for example, the circles. Thus, the field values at the solid dots are not needed and the amount of computation time can be reduced by half without decreasing the accuracy. This is called the leap-frog ordering of calculation³. It is also valid for the solutions Eqs.(10) and (11) for a 3-D problem.

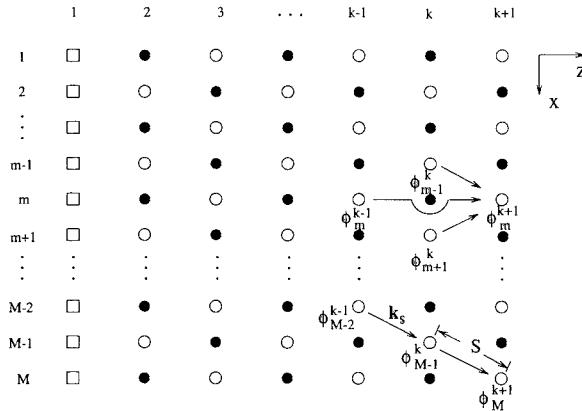


Fig.1 Leap-frog ordering of calculation, where the squares indicate the points having initial input field values.

TRANSPARENT BOUNDARY CONDITIONS

The conventional transparent boundary condition(TBC)⁴ can still be used in the present new scheme. However, the application of the conventional TBC may lead to numerical instability, manifested in the occurrence of parasitic waves at the boundaries, which will spread towards the center after further propagation steps. To eliminate this problem and to adapt to the data obtained at the diagonal grid points in a leap-frog scheme as outlined above, the following modified TBCs have been found for both 2-D and 3-D problems, after several other trials, to yield numerical stability.

$$\phi_M^{k+1} = \phi_{M-1}^k \left(\frac{\phi_{M-1}^k}{\phi_{M-2}^{k-1}} \right) \quad (18)$$

and

$$\phi_{M,n}^{k+1} = \phi_{M-3,n}^{k-2} \left(\frac{\phi_{M-1,n}^k}{\phi_{M-2,n}^{k-1}} \right)^3 \quad (19)$$

are the TBCs for 2-D and 3-D respectively. The grid points to be used in these expressions are located at the diagonal points from the boundary points such as $(M, n, k+1)$. For example, in the 2-D case, the two grid points to be used for a boundary point at $(M, k+1)$ are located at $(M-2, k-1)$ and $(M-1, k)$ as indicated in Fig.1. For a 3-D problem, Eq.(19) gives the value at the boundary normal to x axis and the grid points involved are on the plane $y = n\Delta y$. To ensure outgoing waves only, the imaginary part of $\log_e(\phi_{M-1}^k/\phi_{M-2}^{k-1})$ for 2-D or $\log_e(\phi_{M-1,n}^k/\phi_{M-2,n}^{k-1})$ for 3-D [N.B. $\phi_{M-1}^k = \phi_{M-2}^{k-1} \exp(-jk_s s)$, k_s is the wavenumber along the diagonal direction.] should be nagtive.

EXAMPLES AND COMPARISONS

A slab waveguide directional coupler has been taken as an example to illustrate the new scheme. The coupler has its waveguide index $n_1 = 1.5$, the surrounding medium index $n_2 = 1.3$, waveguide width $D = 0.5\mu m$, and the waveguide separation $S = 1.0\mu m$. The reference refractive index $n_r = 1.372$ is chosen to be the average effective index of the first and second order local modes. The wavelength λ is $1.5\mu m$ and the window size is $10\mu m$. Thus, Eq.(16) gives $\Delta z \leq 2.3\Delta x$ for stability. Assume $\Delta x = 0.05\mu m$. In the conventional explicit method², $\Delta z \leq n_r k_o \Delta x^2 / (2 + \alpha) = 0.0072\mu m$ for computational stability. In the new scheme, $\Delta z \leq \Delta x = 0.05\mu m$ is required to keep the extra error term insignificant which is about 7 times the step-size used in the conventional explicit scheme.

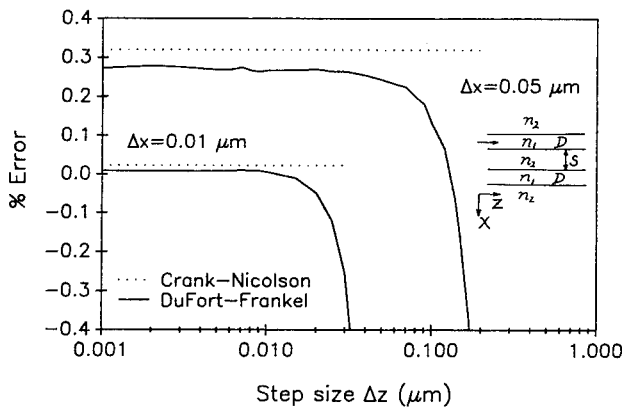


Fig.2 Percentage errors in the coupling length versus the step-size Δz . The other parameters are given in the text.

Fig.2 shows curves of the percentage error for the coupling length versus the propagation step-size Δz . It can be clearly seen that the error is mainly dependent on Δx when $\Delta z \leq \Delta x$ and the error increases dramatically for $\Delta z \geq 3\Delta x$. However, it is still reasonable for $\Delta z = 2\Delta x$ which is 14 times that allowed in the conventional explicit method. Although the propagation step-size is restricted by the stability requirement Eq.(16), the extra error term in Eq.(17) is the main reason for limiting the step-size according to our experiences. The coefficients in front of the field values on the right side of Eqs.(14) and (15) are slightly more complicated than those in the conventional explicit scheme². Without worrying about this minor difference, the new scheme with the leap-frog ordering technique can be about 27 times faster than the conventional explicit scheme in computation for this particular example. Comparing with the error in the Crank-Nicolson method, some improvement is shown in Fig.2 which may be due to

the use of the new transparent boundary condition Eq.(17). Letting $\Delta x = 0.01\mu m$ and hence $\Delta z = 2\Delta x = 0.02\mu m$ in both the new scheme and the Crank-Nicolson scheme, we performed the computations for the coupler with $40\mu m$ in length on a SUN SPARC station. The CPU times are 143 seconds and 730 seconds for the new and Crank-Nicolson schemes respectively, keeping it in mind that the step-size Δz in the Crank-Nicolson scheme is not subjected to the same limitation of $\Delta z = 0.02\mu m$. Fig.3 shows the field patterns of TM waves propagating along the directional coupler. The discontinuities of the transverse electric fields E_x at the waveguide boundaries are clearly visible. All the results obtained by using the new scheme, here, are based on the leap-frog ordering of calculation.

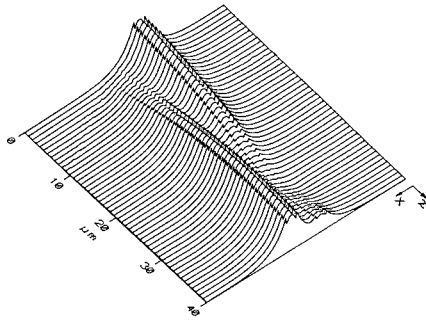


Fig.3 Field patterns of E_x for the TM waves propagating along the coupler, $\Delta x = 0.05\mu m$ and $\Delta z = 0.1\mu m$.

The second example is also a directional coupler but with two channel waveguides as shown in Fig.4. The device parameters are given in the figure caption. The computing window sizes are $50\mu m$ and $24.8\mu m$ along x direction and y direction respectively. The numbers of grid points along x and y are 251 and 125 which leads to $\Delta x = \Delta y = 0.2\mu m$. Fig.5 shows the input field E_x at the input plane $z=0$ obtained by effective index method for the left side channel waveguide. At $z = 555\mu m$ and $1110\mu m$, the field amplitude distributions are also shown in Fig.5. The total CPU time on a SUN SPARC station for the result at $z = 1110\mu m$ (one coupling length) is 2498 seconds if $\Delta z = 0.4\mu m$. Regrettably, we have not tested any other 3-D method yet to make a comparison.

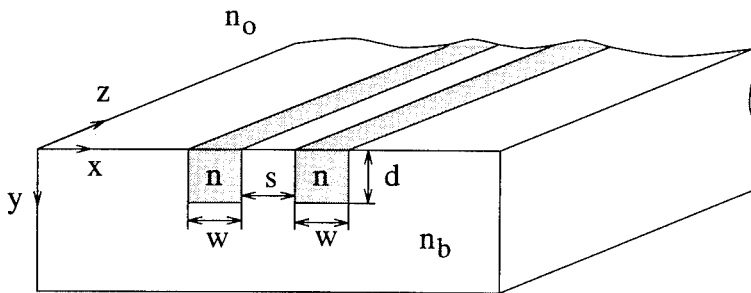


Fig.4 Schematic diagram of a channel waveguide directional coupler, where $n_0 = 1.0$, $n_b = 1.498$, $n = 1.508$, $W = d = S = 4.0\mu m$, and the wavelength $\lambda = 1.55\mu m$.

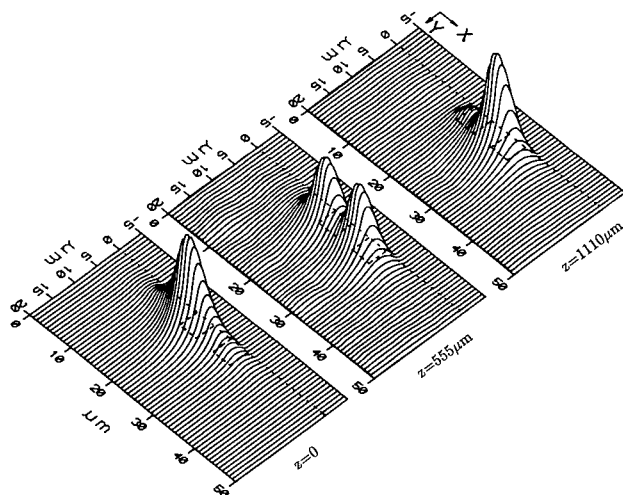


Fig.5 Field amplitude distributions in the channel waveguide directional coupler at different cross-sections with $\Delta x = \Delta y = 0.2 \mu\text{m}$, $\Delta z = 0.4 \mu\text{m}$, and $n_r = 1.4996$.

ANALYSIS AND DESIGN FOR A THREE-WAVELENGTH DEMULTIPLEXER

As an illustration, the new scheme was used to analyze and design a three-wavelength Mach-Zehnder wavelength demultiplexer for $\lambda_1 = 0.98 \mu\text{m}$, $\lambda_2 = 1.31 \mu\text{m}$, and $\lambda_3 = 1.55 \mu\text{m}$. The device consists of two cascaded Mach-Zehnder interferometers as shown in Fig.6.

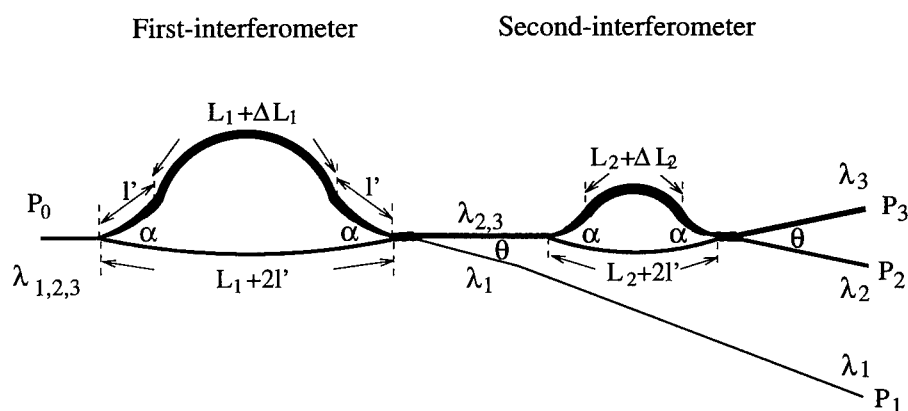


Fig.6 Configuration for a three-wavelength Mach-Zehnder wavelength demultiplexer.

Each Mach-Zehnder interferometer has a 3-db power divider which equally splits the input power into two interferometer arms. A 4-port hybrid coupler, formed by a 3-db power combiner and an asymmetric Y-branch mode splitter, is located at the end of each interferometer. The two arms of each interferometer are designed to be asymmetric not only in arm length but also in arm width such that a phase delay will be realized at the end. This phase delay is wavelength dependent. It is designed to be $(2M+1)\pi$ at λ_1 , $2N\pi$ at λ_2 , and $2K\pi$ at λ_3 for the first interferometer as shown in Fig.7,

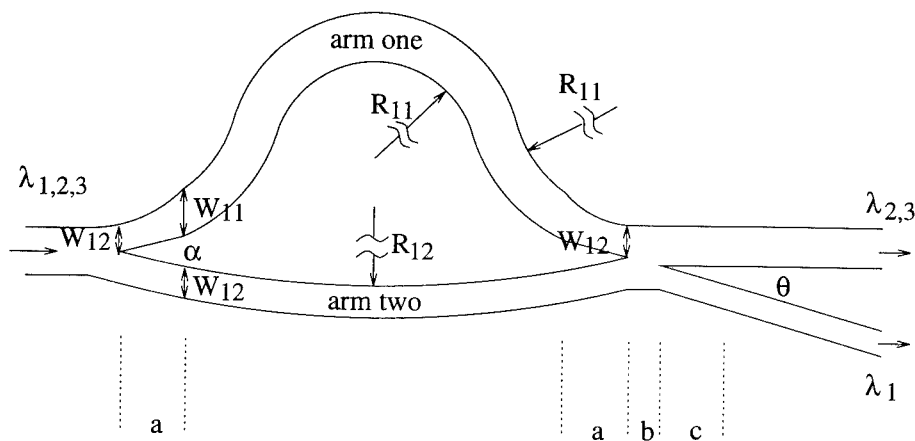


Fig.7 Geometry of the first interferometer, a: 3db power divider or combiner, b: two-mode region, and c: mode splitter.

where M, N , and K are integers. Thus, a second-order mode will be excited at the end of the first interferometer and enter the narrower branch of the following mode splitter at λ_1 . On the other hand, the first-order mode will be excited at the end and enter the wider branch of the mode splitter at both λ_2 and λ_3 . The second Mach-Zehnder similar to the first one (with the same l' , α , and θ) splits two wavelengths λ_2 and λ_3 from the wider branch of the previous mode splitter. The phase delays are designed to be $(2M' + 1)\pi$ and $2N'\pi$ at the end of the second interferometer for λ_2 and λ_3 respectively, where M' and N' are integers. The design is relatively easier and the details have been reported⁷.

A proper combination of the device parameters, such as the arm lengths, widths, and depth, are chosen to satisfy the phase conditions for each wavelength at the end of each interferometer. The depth of the two interferometers are chosen to be equal so that only one-step waveguide fabrication is needed. The device is assumed to be made in glass substrate by a purely thermal K^+ ion-exchange at temperature $T=385^\circ C$ ⁸. The index profile in the depth direction is Gaussian-like with 0.01 as the maximum index change at the waveguide surface for all three wavelengths. The glass indices are given by $n_b=1.5053$, 1.5011, and 1.4982 at λ_1 , λ_2 , and λ_3 respectively. The lateral index changes in the waveguide are assumed as step-like. The total length of the device made by K^+ ion-exchange in glass is about 1.5cm. The initial design was done by using the effective index method and the appropriate phase relations. The results were far from being optimized since there are waveguide branches and bendings involved in the device. The 2-D Dufort-Frankel FD-BPM was then recently used to optimize the design for this long device. Through many attempts, we reached a reasonable design. Its parameters are given as follows, the waveguide depth $D = 4.7\mu m$, $l' = 400\mu m$, $\alpha = 0.035$ rad, $\theta = 0.005$ rad, for the first interferometer: $M=5$, $N=4$, $K=3$, $L_1=2864\mu m$, $\Delta L_1 = 1.52\mu m$, $W_{11} = 7.0\mu m$, and $W_{12} = 4.0\mu m$, and for the second interferometer: $M'=2$, $N'=2$, $L_2 = 1880.0\mu m$, $\Delta L_2 = 0.90\mu m$, $W_{21} = 10.0\mu m$, and $W_{22} = 5.5\mu m$. The simulations are shown in Fig.8 and the extinction ratios are listed in Table 1.

Table 1 Extinction ratios

db	P_1	P_2	P_3
λ_1	0	< -30	-28
λ_2	-27	0	-25
λ_3	< -30	-29	0

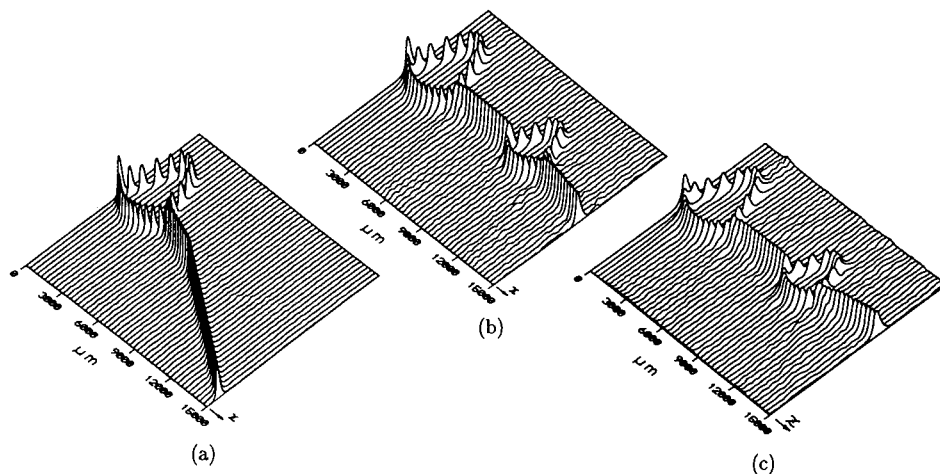


Fig.8 BPM simulations of a three-wavelength demultiplexer,
(a) $\lambda_1 = 0.98\mu\text{m}$, (b) $\lambda_2 = 1.31\mu\text{m}$, and (c) $\lambda_3 = 1.55\mu\text{m}$.

CONCLUSIONS

In conclusion, the scheme presented here is explicit and stable. The propagation step-size can be at least the size of the transverse grid which is much larger than that in the conventional explicit method, and, with the leap-frog ordering technique, the new scheme can be more efficient. Both 2-D and 3-D solutions have been presented. The method is good for a weakly guiding structure especially for a 3-D problem because of its easy implementation and saving in computing time.

Acknowledgments

The work was supported by the National Science and Engineering Research Council (Canada) through an operating grant. F. Xiang was a recipient of a McGill University Major Fellowship (1992-1993).

REFERENCES

1. Y. Chung and N. Dagli, "A assessment of finit difference beam propagation method", *IEEE J. Quautum Electron.*, vol. 26, no. 8, pp.1335-1339, 1990.
2. Y. Chung and N. Dagli, "Explicit finite difference beam propagation method: application to semiconductor rib waveguide Y-junction analysis", *Electron. Lett.*, vol.26, no.11, pp.711-713, 1990.
3. E.C. DuFort and S.P. Frankel, "Stability conditions in the numerical treatment of parabolic differential equations", *Math. and Other Aids to Comp.*, vol.7, no.41, pp.135-153, 1953.
4. G.R. Hadley, "Transparent boundary condition for beam propagation", *Optics Lett.*, Vol.16, no.9, pp.624-626, 1991.
5. W.P. Huang, C.L. Xu, S.T. Chu, and S.K. Chaudhuri, "A vector beam propagation method for guided-wave optics", *IEEE Photon. Technol. Lett.*, vol. 3, no.10, pp. 910-913, 1991.

6. F. Xiang and G.L. Yip, "An explicit and stable finite-difference 2-D vector beam propagation method", *IEEE Photon. Technol. Lett.*, vol.6, no.10, pp.1248-1250, 1994.
7. F. Xiang and G.L. Yip, "Asymmetric Mach-Zehnder wavelength demultiplexers", *GRIN Proceedings*, Paper C2, Kawasaki, Japan, Oct. 1993.
8. G.L. Yip, K. Kishioka, F. Xiang, and J. Y. Chen, "Characterization of planar optical waveguides by K^+ ion-exchange in glass at $\lambda = 1.152$ and $1.523\mu m$ ", *SPIE Proceedings*, vol.1583, pp.14-18, Boston, 1991.

AN OEIC CAD SYSTEM FOR PASSIVE AND ACTIVE PLANAR WAVEGUIDE CIRCUITS

Robert Amantea, Peter L. Demers, Michael Ettenberg, and Donald J. Channin

Solid State Device Research Division
David Sarnoff Research Center
Princeton , NJ 08540

INTRODUCTION

This work reports on the development of an integrated CAD system for optoelectronic devices and optoelectronic integrated circuits (OEICs). The work has two goals. The first goal is to establish a software environment that supports the designer both in its ease of use and in its capability to ultimately handle any optoelectronic design problem. The second goal is to provide the key software analysis and simulation tools to design basic OEICs and facilitate the development and use of tools made available from other design groups. Our approach offers significant advantages over conventional software. Specifically, we use a commercial visualization environment to bring a full complement of visualization tools and a consistent user interface to the problem along with the ability to operate the system over a network. We use hierarchical data structures so that a great deal of the specification of the problem is automatic thereby

increasing throughput by at least an order of magnitude over conventional methods. Finally, the layout and specification of the circuit and analysis are enhanced by the use of an iconic programming language that mimics the physical structure of the problem.

The complexity of optoelectronic devices and networks makes their analysis and design more difficult and time consuming than the corresponding electronic units. The problems are difficult to specify because they embody boundary conditions, material properties, geometry, and excitations. Analysis results are difficult to understand because much of the information is contained in two and three dimensional distributions.

Our solution uses the network analysis paradigm. Problem specification is broken down into material capture, geometry capture, and source specification. Computational modules are "tuned" to a problem to increase efficiency and accuracy and decrease development time. A commercial visualization environment, AVS¹, was selected to provide a consistent user interface, an iconic programming language, and a wide variety of output graphics.

Three numerical solvers are the processing engines of our approach. We use a finite difference two-dimensional eigenmode solver based on magnetic field components to find the true eigenmodes of arbitrary semiconductor waveguides. We use the finite difference beam propagation method (BPM) in two-dimensional format to solve for field propagation in passive and active planar waveguides. We use the effective index method to find the approximating modes for propagation in the BPM.

Two examples will be discussed, a beam splitter and a tapered laser amplifier. In the case of the tapered amplifier, a nonlinear version of the BPM is used to simulate the effects of pumped gain, carrier diffusion, antiguiding, current spreading, and material nonuniformity.

OVERVIEW OF THE OEIC CAD SYSTEM

A guided-wave simulation problem is specified by constructing a network of software modules that represents the problem to be solved. Such a network is composed of modules, macro modules, wires, and panels. A module is an independent computational process that is triggered when valid data is presented to its input ports, it is represented by a rectangular icon as shown in Fig. 1. A macro module is a collection of modules that have been encapsulated so that internal ports are hidden. They are distinguished by a blue panel box on the

right hand side of the module icon. Wires connect modules to one another and represent the data flow between them. They are color coded to show the type of data being passed. Panels are windows where the module parameters can be specified. They are opened by clicking in the panel box on the right hand side of the module.

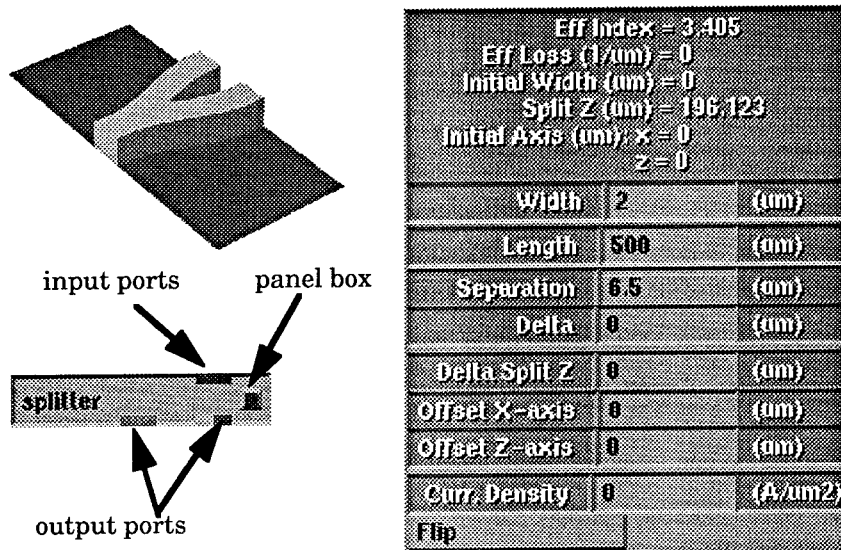


Figure 1. A ridge-guide splitter is represented by a geometry module. Its panel is used to specify its dimensions.

OEIC CAD modules are partitioned into four groups: material, geometry, processing, and visualization. This partition tracks the actual design and fabrication of an OEIC. The formulation of a OEIC simulation follows a top down methodology from materials through visualization. Data is accumulated at each level in the hierarchy and flows downward to the next level. Once specified, a parameter does not have to be specified again. This insures against errors and streamlines data input.

The material group of modules contains the substrate module, material layer modules, and modules to convert this information into effective index. At the substrate level we specify the basic properties of the material and the optical wavelength. As each layer is added we add to the specification layer properties such as composition and thickness. Finally the composite material is summarized as an effective index by a 1-dimensional eigenmode finder for layered materials.

The geometry group deals with boundaries, waveguides, and devices. The boundaries specify the physical extent of simulations. For now we are dealing with two dimensional regions where the lateral extent, i.e., the x direction, the longitudinal extent, i.e., the z direction, and the computational grid need to be specified. The transverse extent (y direction) is modeled by the effective index approximation. Straight and curved, uniform and nonuniform, passive and active waveguides also are specified.

ANALYSIS OF A BEAM SPLITTER

The beam splitter geometry is shown in Fig. 1. Its main dimensions are length, L , guide width, w , and the separation of its branches, s . Its location relative to the preceding waveguide or the source at $z=0$ is given by the offset parameters. The curved edges of the splitter are modeled by two circular arcs of opposite curvature placed end to end. The relationships between angular arc length, θ , radius of curvature, r , s , and L are given by the equations. The problem network is shown in Fig. 2.

$$s = \frac{L(1 - \cos \theta)}{\sin \theta} \quad \text{and} \quad r = \frac{L}{2 \sin \theta}$$

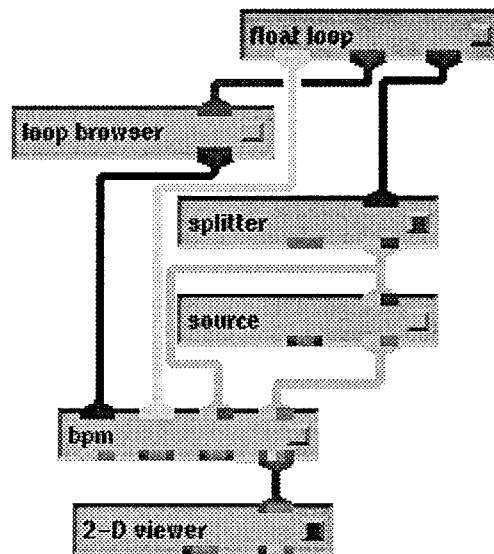


Figure 2. The problem network used to simulate light propagation in a beam splitter.

The float loop module is used to step through several values of the beam splitter separation, s . The float loop module also transmits a 'go' signal to the

bpm module to start a new simulation. The source module provides the initial field to the bpm. The loop browser module automatically increments file names so that bpm results are saved for each variation. The 2-D viewer module translates the calculated data into an image and renders the image on the CRT.

Several features of the OEIC CAD system are demonstrated in this problem network. First, the AVS software provides a means to connect any specified quantity to an input port of a module. Therefore, any quantity can be connected to the float loop module and stepped. Second, the splitter macro module encapsulates material and geometry information as shown in Fig. 3, thereby hiding some of the complexity of the problem.

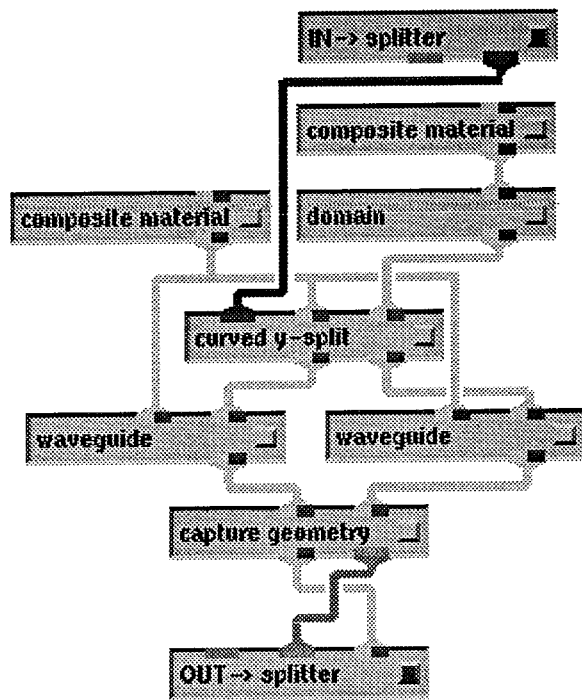


Figure 3. The splitter macro module expanded into its elements. The composite material modules specify the effective index of the different regions. The domain module specifies the simulation region and the numerical grid. The curved y-split module specifies the data for the beam splitter. The waveguide modules are used to extend the simulation so that we can see the evolution the field after leaving the splitter. The capture geomtry module translates all the material and geometry data into the format required by the bpm.

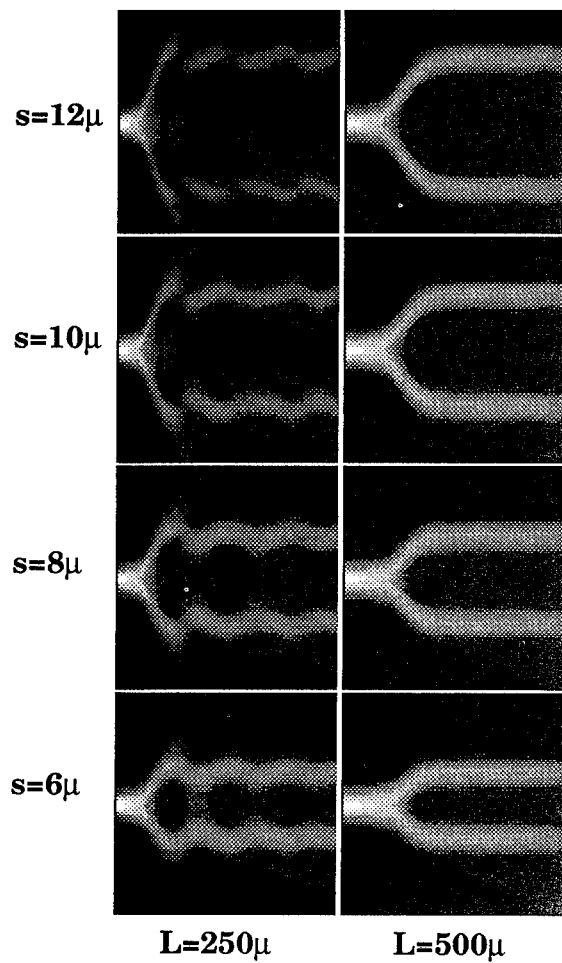


Figure 4: Parameters for this simulation are: smulation region= 20μ by 1000μ , splitter length= L , waveguide separation= s , waveguide width= 3μ , wavelength= 0.9μ , background effective index= 3.4 , ridge effective index= 3.45 . A short beam splitter generates higher order modes due to small radius of curvature. In severe cases ($L=250\mu$ and $s=12\mu$) most of the beam departs the guiding structure and is not transferred to the straight section of waveguide.

The bpm module performs a beam propagation analysis using the finite difference method applied to the Fresnel equation². Under the weak guide approximation, if the guiding geometry does not change too rapidly in the direction of propagation, the Helmholtz equation reduces to the Fresnel equation which is solved by the finite difference beam propagation algorithm. This approach puts significant restrictions on the applicability of the computational

model. Specifically, it restricts applicability to systems that have no significant reflections in the direct path of propagation. Although methods exist for taking these reflections into account, they are not considered here. Reflections at the lateral boundaries are accounted for through the use of the transparent boundary condition³

Results of these simulations is given in Fig. 4.

ANALYSIS OF A LINEARLY TAPERED LASER AMPLIFIER

In an active waveguide, where carriers are injected, the light and the carriers interact. This interaction is manifested as stimulated recombination and optical gain. Stimulated recombination detracts from the number of available carriers and its impact is modeled by a diffusion equation. Although diffusion is a 3-dimensional effect, we neglect diffusion effects in the transverse (y) and longitudinal (z) directions. It is justifiable to neglect the diffusion in the z direction since optical power and geometric structures change very slowly in that direction. We correct for lateral (x) ohmic spreading of the current in the cap layers between the contact and the active region so that $J(x)$ is computed at the active layer. Under these conditions, the diffusion equation in the active region is⁴

$$D \frac{d^2 N}{dx^2} = -\frac{J(x)}{qd} + \frac{N}{\tau_{nr}} + BN^2 + CN^3 + \frac{g\Gamma|E|^2}{\hbar\omega d},$$

where N is the density of free carriers, D is the carrier diffusion constant, d is the active layer thickness, $J(x)$ is the applied current density, τ_{nr} is the nonradiative recombination time, B is the spontaneous recombination coefficient, C is the Auger recombination coefficient, $g=aN-b$ is the optical power gain, a , is the gain coefficient, b is the transparency loss, and Γ is the confinement factor.

The optical gain introduced by the carriers is modeled in the wave equation by introducing a complex effective index. The Fresnel equation in the presence of loss, α , is

$$2jk_0 n_0 \frac{\partial \mathbf{E}}{\partial \mathbf{z}} = (\nabla_T^2 + k_0^2 (n^2 - n_0^2) - 2jk_0 n_0 \alpha) \mathbf{E}$$

We note that in the absence of lateral and transverse effects that this equation reduces to $\partial \mathbf{E} / \partial \mathbf{z} = -\alpha \mathbf{E}$, indicating that for positive α , the field decays as it propagates in the z direction. We define the complex differential effective index

$$\Delta n^2 = n^2 - n_o^2 - 2j \frac{n_o}{k_o} \alpha + 2\Gamma \frac{n_o}{k_o} (aRN + j(aN - b)),$$

where R is the antiguiding parameter, which is introduced to model the depression in the real part of the effective index due to an increase in carriers in the confinement layer. The factor 2 is necessary to convert the effect of the power gain $aN-b$ into that of a field amplitude gain.

Figure 5 shows the module network used to simulate propagation in a tapered laser amplifier and the resulting free carrier density. The problem network at the left is a simplified view of the modules required to perform the simulation. The “tapered amplifier” module is a macro-module composed of material modules and geometry modules connected together to specify the material properties and the geometry. The source supplies an eigenmode to the input of the geometry. The “bpm module” executes the nonlinear version of the BPM. The “3d viewer” is a macro-module composed of AVS supplied modules that separates the component of the data desired, maps it to a surface, applies color, and renders the result. Field intensity, phase, index, pumped carriers, and free carriers are all computed. The light enters from the left and propagates to the right.

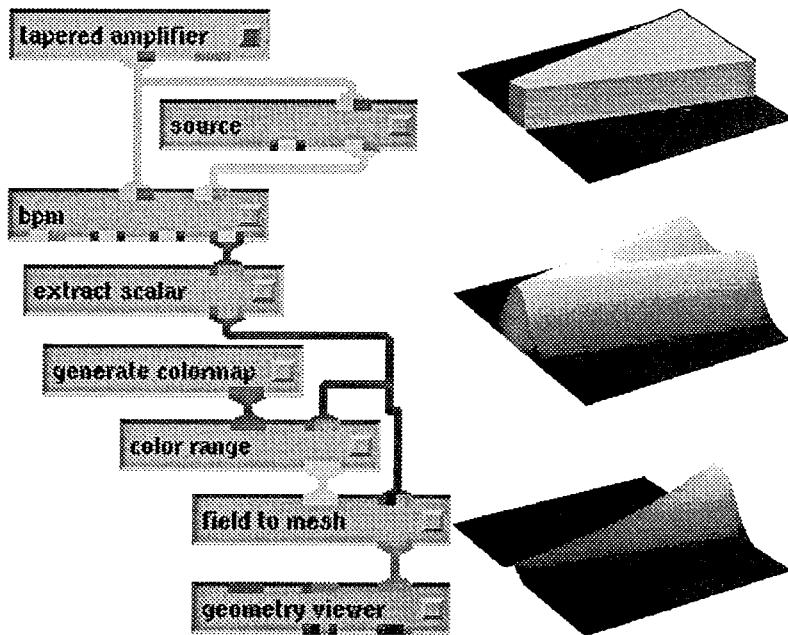


Figure 5. The problem network is shown with a tapered amplifier macro module that encapsulates the material and geometry modules. On the right we show the ridge guide

geometry, the carrier density, and the field intensity. As the field intensity grows, stimulated recombination reduces the carrier density.

CONCLUSIONS

We have built an OEIC CAD system based on a commercial off the shelf visualization software with a modular user interface that simplifies data input, increases throughput by an order of magnitude, minimizes required training, is easily extended, and is networkable. We have developed key computational modules, notably a linear and nonlinear finite difference beam propagation module, an one dimensional eigenmode module, and a two dimensional eigenmode solver.

ACKNOWLEDGEMENT

This work was supported by ARPA.

¹AVS is a trademark of Advanced Visual Systems Inc., Waltham MA.

²W.P. Huang, C.L. Xu, S.T. Chu, and S.K. Chaudhuri, The Finite Difference Vector Beam Propagation Method: Analysis and Assessment, IEEE J. Lightwave Technol., 10:295 (1992).

³G.R. Hadley, Transparent Boundary Conditions for the Beam Propagation Method, IEEE J. Quantum Electron., 18:363 (1992).

⁴G.R. Hadley, J.P. Hohimer, and A. Owyong, Comprehensive Modeling of Diode Arrays and Broad-Area Devices with Applications to Lateral Index Tailoring, IEEE J. Quantum Electron., 24:2138 (1988).

FINITE ELEMENT SOLUTION OF NONLINEAR OPTICAL WAVEGUIDES

B.M.A. Rahman, P.A. Buah and K.T.V. Grattan
City University,
Department of Electrical, Electronic and Information Engineering,
London EC1V 0HB, England.

INTRODUCTION

The propagation of light through nonlinear optical waveguides recently has stimulated considerable interest. These devices are capable of exhibiting a wide range of complex but very useful phenomena such as soliton emission¹ and photonic switching². Nonlinear waveguides can be analysed by studying either 'mode' characteristics (as an eigenvalue problem) or the propagation and evolution of waves (as an initial value problem). Both these approaches are complementary with their individual advantages and disadvantages. In this work, the application of the finite element method for both these approaches is reviewed.

MODAL SOLUTION

For waveguides with weak nonlinearity, the approach of a modal solution provides a fundamental step in understanding the behavior of wave propagation. Over the last decade there have been many approaches to obtain the modal solution of such nonlinear optical waveguides. Among them are the semianalytical technique³, the numerical⁴, the matrix method⁵, the variational⁶ and the finite element method⁶. The analytical approach³ takes into account the satisfaction of the field continuity conditions at the dielectric interfaces and then the solving of the power-dependent transcendental equations. This procedure and its variations have been used to obtain TE and TM modes in waveguides with various carefully chosen laws of nonlinearity, and its application has only been restricted to planar structures. Akmediev *et al.*⁴ have presented a numerical solution for a nonlinear optical waveguide with two-dimensional confinement and Ramdas *et al.*⁵ have used the matrix method to obtain modal solutions of nonlinear optical waveguides.

In the last two decades, the finite element method has been established as one of the most powerful and versatile numerical methods to characterize a wide range of optical waveguides using the vector **H**-field formulation⁷. In this approach, the optical waveguide cross-section is first suitably divided into a patchwork of triangles. These elements can be of different shapes and sizes and using many elements, and thus a complex waveguide with any

transversely varying permittivity $\epsilon(x,y)$ cross-section can be accurately represented. For optical waveguides, the simplest formulation is the use of scalar approximations but for a more accurate solution the vector full magnetic field (\mathbf{H}) formulation should be used. An attraction of this \mathbf{H} -field formulation for optical waveguides is that although ϵ is inhomogeneous and μ is homogeneous, all three components of the \mathbf{H} -field are continuous everywhere in the structure. One early difficulty with the spurious modes for the vector formulation in the finite element method (or almost any other) procedure can be avoided by adding a penalty term⁸. The augmented vector \mathbf{H} -field variational formulation with the penalty term is given by⁸:

$$\omega^2 = \frac{\int (\nabla \times \mathbf{H})^* \cdot \hat{\epsilon}^{-1} (\nabla \times \mathbf{H}) d\Omega + (\alpha / \epsilon_0) (\nabla \cdot \mathbf{H})^* \cdot (\nabla \cdot \mathbf{H}) d\Omega}{\int \mathbf{H}^* \hat{\mu} \mathbf{H} d\Omega} \quad (1)$$

where α is the dimensionless penalty parameter and the other terms are as defined by Rahman *et al.*⁸. The stationary solution of the above functional, after minimization with respect to the nodal field variables, yields a standard eigenvalue equation. This formulation has been widely used to characterize a wide range of practical linear optical waveguides and guided-wave devices.

However, in the nonlinear optical waveguide, its refractive index distribution depends on the field intensity profile, $\epsilon(x,y,|E|)$, and the field profile, $|E|$ in turn depends on the refractive index profile. Therefore in the finite element approach, a simple iterative scheme is adopted to seek a consistent modal solution. Modal analysis by finite elements provides an ideal framework to consider diverse nonlinear material laws, including saturable, higher-order nonlinearity and with material anisotropy or local loss or gain. Initially the waveguide problem is solved without considering a nonlinear contribution. The resulting field is scaled to the given power and then used to calculate the associated refractive index change by applying any given nonlinear law for ϵ . The new refractive index profile is employed to solve the waveguide problem again and the resulting new field profile is used to recalculate the nonlinear refractive index contribution for the next iteration. This iteration scheme is continued until a consistent and stable solution is obtained.

Since 1988, there has been considerable activity to find the modal solution of a planar structure^{9,6} using the finite element method. In the first example a scalar TE formulation is considered for a five-layer planar structure. A 1 μm thick linear film layer, b , with refractive index 1.57 is bounded by two identical 1 μm thick nonlinear cladding layers, a and c , with refractive index 1.55. The nonlinear coefficient n_2 in the two identical cladding layers is considered to be $10^{-9} \text{ m}^2/\text{W}$ and the operating wavelength is 0.515 μm . The three-layer structure is embedded in air with $n_0=1.0$. Although physical symmetry exists at the middle of the film layer, b , this was not imposed to achieve a flexible solution, where symmetry can be broken due to the noise or nonsymmetrical illumination and in the case of computer simulation due to the round-off errors. P_a , P_b , and P_c are the power carried by the three layers, a , b , and c , respectively, and although the power inconfinement in air claddings is also calculated, as these factors are extremely small they are not shown here. It can be observed that, at low total power, most of the power is carried by the middle layer, b . However, as the total power is increased, although P_b increases, its share of the total power decreases (i.e. the slope reduces) slowly until the threshold power, P_t , is reached. This reduced share is due to the fact that as refractive indices of two nonlinear cladding layers are increased with the total guided-power,

and so their shares of total power, in turn, are also increased. So far both the cladding layers *a* and *c* carry equal amount of power. However, the symmetry breaks down just above the threshold power, P_t .

In case of the computer simulation, if either the *a* or *c* layer has a slightly higher field value, that will increase its refractive index slightly more, which in turn draws out the field profile more towards that layer. This process continues until a stable solution is reached. In practice no device can be perfectly symmetrical, perfectly smooth or can be illuminated with a perfectly symmetrical excitation profile, and this lack of symmetry will allow the mode to move to one of the two nonlinear cladding layers. Sharp switching of power from guide *b* to *a* can be observed at this point. The threshold power increases if the height of the central guide *b* is increased. Beyond the threshold power, the optical power is mainly confined in one of these two nonlinear claddings. In our simulation, it can be seen that guide, *a*, is carrying a large share of power compared to guide, *c*. When the total power is reduced from above the threshold value, P_t , the power in layer *b*, P_b , again increases abruptly below the lower threshold value, P_r . It can be noted that for a total power value between P_r and P_t , two stable modal states are possible with high P_a/P_b power contrast ratios.

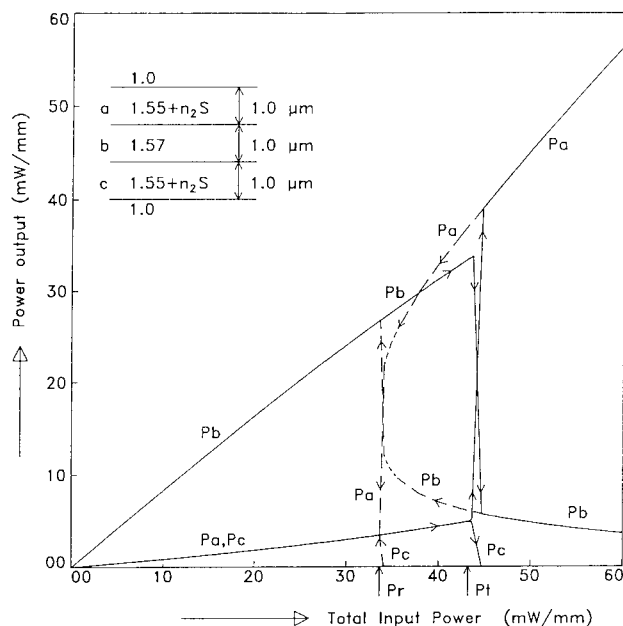


Figure 1. Variation of the optical parameters for multilayer nonlinear planar waveguide.

The finite element procedure has also been used to find modal solutions for nonlinear optical waveguides with two-dimensional confinement^{10,11,12}. Results for important optical parameters for a semiconductor waveguide incorporating a defocusing nonlinear MQW region are considered. The MQW active region consisted of 70 periods of InGaAs quantum well and InP barrier layers. The validity of the equivalent replacement refractive index for the MQW region earlier has been tested numerically¹². The equivalent height for the MQW region was 0.98 μm and its refractive index¹² was 3.25780 for the quasi-TE modes. Earlier it has also been tested¹³ that the use of the geometrical average of the nonlinear coefficient for a MQW region is a satisfactory approach and the average nonlinear coefficient for this example was $-0.857 \times 10^{-11} \text{ m}^2/\text{W}$. The rib width was 4 μm and the operating wavelength was 1.52 μm .

Figure 2 shows the variation of some important optical parameters with total power in normalized units. The unit value of the normalized power is 200 mW for the given nonlinear coefficient. It can be observed that the modal effective index decreases with the total power and the spot size increases. The power fraction carried by the active region also decreases with the total power due to the defocusing nonlinearity in this region.

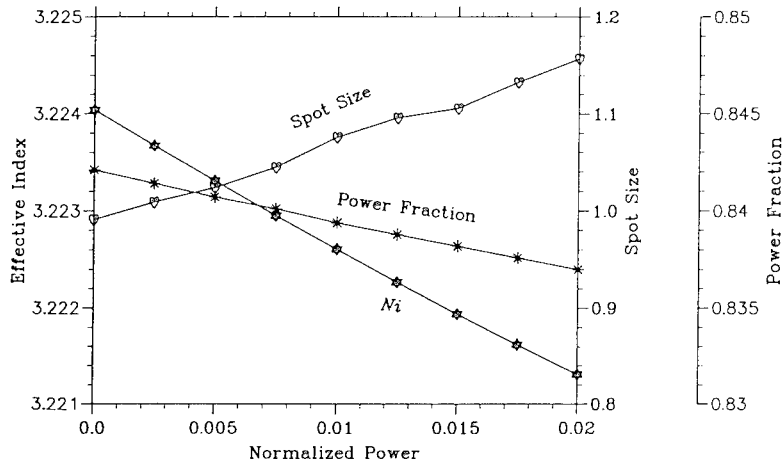


Fig. 2 Nonlinear characteristics of a MQW semiconductor rib waveguide.

PROPAGATION MODEL

As shown in the earlier section, the modal analysis has been successfully applied to solve z -independent nonlinear optical waveguide problems. However, the results must be interpreted with care, as the absence of linearity or superposition means that expansion in terms of modes is no longer appropriate. Besides the nonlinear effect, the complex nature of the novel integrated optical devices requires an algorithm capable of taking into consideration the nonuniform optical waveguides. For this task the beam propagation method¹⁴, based on the fast-Fourier transform has been commonly applied. As a result of the limitations of the classical BPM, many alternative algorithms have started to appear in the past 4 years, and among them is the efficient and versatile finite element-based approach¹⁵⁻¹⁸. Ignoring the group velocity dispersion for the propagation distance under consideration and applying the slowly varying amplitude approximation, the time-dependent wave equation for pulse propagation in a nonlinear integrated-optic waveguide that may exhibit a delayed nonlinear response is given by¹⁶

$$2jk_0\beta \left[\frac{\partial E}{\partial z} + \frac{n_i}{\beta v_i} \frac{\partial E}{\partial t} \right] + \frac{\partial^2 E}{\partial x^2} - k_0^2 [\beta^2 - (n_i^2 + \delta)] E = 0 \quad (2)$$

where k_0 is the wavenumber of the field in the vacuum, β is the effective index, n_i and v_i are the refractive index and the group velocity of the field in medium i and δ is the total nonlinear contribution to the refractive index. The response of the waveguide materials is approximated by the usual phenomenological Debye relaxation equation given by

$$\tau_D \frac{\partial \delta}{\partial t} = -\delta + \alpha_i |E|^2 \quad (3)$$

with τ_D representing the Debye relaxation time of the medium and α_i is the nonlinear coefficient of the i th medium. The finite element-based beam propagation algorithms are essentially based on the finite element discretization of the transverse domain and finite-differencing in the propagation direction.

A uniform nonlinear planar structure is considered to enable a study to be carried out of the evolution of lightwave along the propagation direction. The central linear film layer is $10 \mu\text{m}$ wide with refractive index 1.571. The substrate layer on the right is also linear with refractive index 1.569 but the cladding layer on the left is nonlinear with refractive index 1.57 and nonlinear coefficient $10^{-10} \text{ m}^2/\text{W}$. The operating wavelength was $0.633 \mu\text{m}$. Figure 3 shows the emission of CW solitons into the nonlinear cladding region.

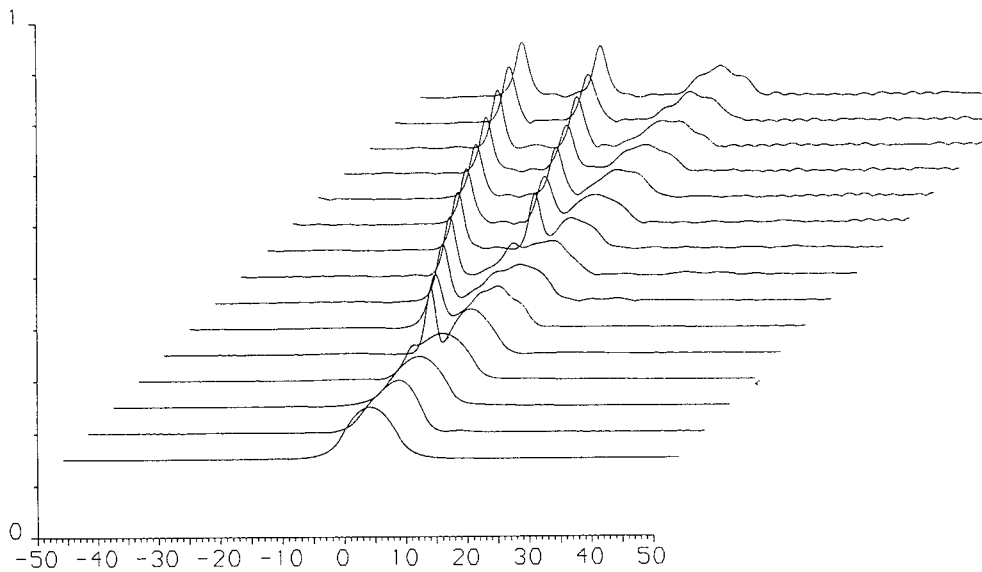


Figure 3 The emission and propagation of CW solitons.

In addition, the recently developed space-time marching split-step finite-element method¹⁶, which is an extension of the split-operator finite element method, has been applied, to include time to simulate pulse dynamics in nonlinear waveguides. The inclusion of the time dimension is necessary to study pulse propagation with a finite material response. The pulse propagation within a z -variant waveguide, such as a tapered waveguide, is presented. In this example, the incident field is composed of a strong TE₀ and a weak TE₁ mode. The spatial soliton excited in the nonlinear media beyond the thinner (output) end can follow a different route depending on the relative phases and amplitudes of the TE₀ and TE₁ signals respectively. Figure 4 shows the propagation demultiplexing of four light pulses in a nonlinear taper waveguide.

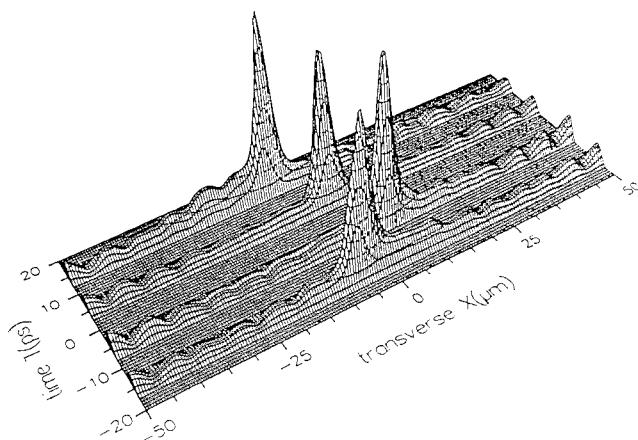


Figure 4 The excitation of four pulses for different excitation

CONCLUSIONS

The finite element method is well established as one of the most versatile methods to provide an accurate modal solution for uniform optical waveguides with arbitrary cross-section, index profiles, anisotropy and nonlinearity law. Recently the finite element approach has been extended to study pulse propagation through z -variant nonlinear optical waveguides with finite material response time. A number of attractive features such as adaptive mesh and mixed boundary conditions make this method computationally more efficient than the alternative numerical approaches. The modal and propagation solutions using the finite element method are complimentary in nature and many important and novel phenomena can be numerically investigated.

REFERENCES

- [1] HA Haus, *IEEE Spectrum*, **30**, p.48, 1993.
- [2] G.I. Stageman, E.M. Wright, N. Finlayson, R. Zandoni and C.T. Seaton, Third order nonlinear integrated optics, *J. Lightwave Tech.*, **6**, p.953, 1988.
- [3] C.T. Seaton, J.D. Valera, R.L. Shoemaker, G.I. Stageman, J.T. Chilwell, and S.D. Smith, Calculation of nonlinear TE waves guided by thin dielectric films bounded by nonlinear media, *IEEE J Quantum Electron.*, **21**, p.774, 1985.
- [4] N.N. Akmediev, R.F. Nabiev, and Yu. M. Popov, Angle dependent nonlinear modes of a cylindrical waveguides, *J. Opt. Soc. Am, B*, p.975, 1990.
- [5] MR Ramadas et al., *J. Lightwave Technol.*, LT-7, p.1901, 1989.
- [6] BMA Rahman, JR Souza, and JB Davies, Numerical analysis of nonlinear bistable optical waveguides, *IEEE Photonic Tech. Lett.*, **2**, p.265, 1990.
- [7] BMA Rahman, FA Fernandez, and JB Davies, Review of finite element methods for microwave and optical waveguides, *Proc. IEEE*, **79**, p.1442, 1991.

- [8] BMA Rahman and JB Davies, Finite element solution of integrated optical waveguides, *J. Lightwave Technol.*, LT-2, p.682, 1984.
- [9] K Hayata, N Nagai, and M Koshiha, Finite element formalism for nonlinear slab-guided waves, *IEEE Microwave Theory Tech*, **36**, p.1207, 1988.
- [10] K Hayata and M Koshiha, Full vectorial analysis of nonlinear optical waveguides, *J. Opt. Soc. Am. B*, **5**, p.2494, 1988.
- [11] RD Ettinger, F.A. Fernandez, B.M.A. Rahman and J.B. Davies, Vector finite element solution of saturable nonlinear strip-loaded optical waveguides, *IEEE Photonic Tech. Lett.*, **3**, p.147, 1991.
- [12] BMA Rahman, Y Liu, and KTV Grattan, Finite element modeling of one- and two-dimensional MQW semiconductor optical waveguides, *IEEE Photonic Tech. Lett.*, **5**, p.928, 1993.
- [13] BMA Rahman and M Chowdhury, Finite element characterisation of nonlinear multiple quantum well structures, *Proc. SPIE*, 2212, p.194-199, 1994.
- [14] B Hermansson, *et al*, *Optical Quantum Electronics*, **16**, p.525, 1984
- [15] K Hayata, A Misawa, and M. Koshiha, *J Opt. Soc. Am. B*, **7**, p.1772, 1990.
- [16] PA Buah *et al*. *OSA Nonlinear Guided Wave Optics*, Cambridge, Sept. 1993.
- [17] PA Buah, BMA Rahman and KTV Grattan, Numerical simulation of pulse propagation in nonlinear tapered waveguides, *Proc. SPIE* vol. **2212**, pp66-72, Germany, April 1994.
- [18] PA Buah, M Catuneau, BMA Rahman and KTV Grattan, *CLEO* , Anaheim, May 1994.

HIGHLY EFFICIENT LIGHT-EMITTING DIODES WITH MICROCAVITIES

E. F. Schubert, N. E. J. Hunt, M. Micovic^{a)}, R. J. Malik, D. L. Sivco,
A. Y. Cho, and G. J. Zydzik

AT&T Bell Laboratories
Murray Hill, NJ 07974

ABSTRACT

One-dimensional microcavities are optical resonators with coplanar reflectors separated by a distance on the order of the optical wavelength. Such structures quantize the energy of photons propagating along the optical axis of the cavity and thereby strongly modify the spontaneous emission properties of a photon-emitting medium inside of a microcavity. We report on semiconductor light-emitting diodes (LEDs) with the photon-emitting active region of the LED placed inside a microcavity. We show that these devices have strongly modified emission properties including unprecedented emission efficiencies. The experimental and theoretical slope efficiencies are more than a factor of 5 and 10 times higher than in conventional LEDs, respectively. The new devices will be useful in short-distance optical communication and optical interconnect systems.

INTRODUCTION

Fabry-Perot cavities are optical resonators defined by two coplanar reflectors separated by a macroscopic distance [1]. If this distance is small, namely one half or one single wavelength of operation, i.e., on the order of one μm for visible and near infrared light, the cavities are called optical *microcavities*. The density of optical modes within a microcavity is strongly modified as compared to the mode density in free space surrounding the cavity: The cavity allows for the propagation of optical waves only at the fundamental resonance mode and its harmonics along the optical axis of the Fabry-Perot microcavity. Modes other than the fundamental resonance and its harmonics are not supported by the cavity and such modes are disallowed. The energy of photons confined to the microcavity is thus

a) present address: The Pennsylvania State University, Department of Electrical Engineering, University Park, PA 16802.

quantized, in near perfect analogy to the quantization of electron energy inside a quantum well potential.

Intriguing physics evolves, if an optically active medium, i.e. a photon-emitting medium, is placed between the two reflectors of a coplanar Fabry-Perot microcavity. This novel field of condensed matter research has, during the past few years, made possible a new generation of microresonator devices and the exploration of quantum electrodynamic phenomena [2,3]. Several microcavity geometries have been employed including planar (Fabry-Perot) microcavities [2,3], spherical resonators [4], disk-shaped resonators [2,5], and fully three-dimensional resonators [6]. The optically active materials inside the microcavity structures included optically active rare-earth atoms [7], semiconductors [8-10], and dyes [11,12]. Interaction between active atoms and high-finesse optical and microwave microcavities have led to beautiful demonstrations of cavity quantum electrodynamic effects in recent years including coupled atom-cavity modes, quantum revivals, single-atom masers, and enhanced and inhibited spontaneous emission [2,13].

Microcavity physics is an active field of academic research and the changes in spontaneous emission characteristics in microcavity structures are well documented. It is the purpose of this letter to demonstrate that microcavity physics can be exploited in devices which clearly have superior properties when compared with conventional devices. As an example, we show that a new generation of light-emitting diodes which employs microcavity effects has improved characteristics as compared to conventional LEDs. In particular, we demonstrate unprecedented efficiencies which can be enhanced by a factor of ten. However, the advantageous effects of microcavities go beyond LEDs and may be exploited in any spontaneously emitting or absorbing optoelectronic device including displays, photodetectors, and sensors.

CAVITY ENHANCEMENT

Of particular interest for the technological application of microcavity effects is the enhancement and suppression of radiation. This interest is based on the fact that optical emission rate in microcavities along the cavity axis can be higher under certain experimental conditions which will be defined below. To illustrate this effect we consider the semiconductor microcavity shown in Fig. 1, which consists of two reflectors namely a silver (Ag) mirror and a distributed Bragg reflector (DBR). The reflectivity of the semiconductor/silver interface is 96% for near-infrared light. The 90% reflective DBR consists of 10 pairs of an AlAs/GaAs multilayer structure with each layer being $\lambda/4$ thick, where λ is the resonance wavelength of the cavity. Since the DBR reflectivity is lower than the reflectivity of the silver mirror, photons will escape from the cavity mainly through the DBR. The active region of the cavity contains four $\text{In}_{0.15}\text{Ga}_{0.85}\text{As}$ quantum wells emitting at a wavelength of 930 nm. Two confinement layers are added on both sides of the active region to confine electrons and holes to the active region. The total thickness of the confinement layers plus the active region is chosen to make the fundamental cavity mode resonant with the emission wavelength of the active region.

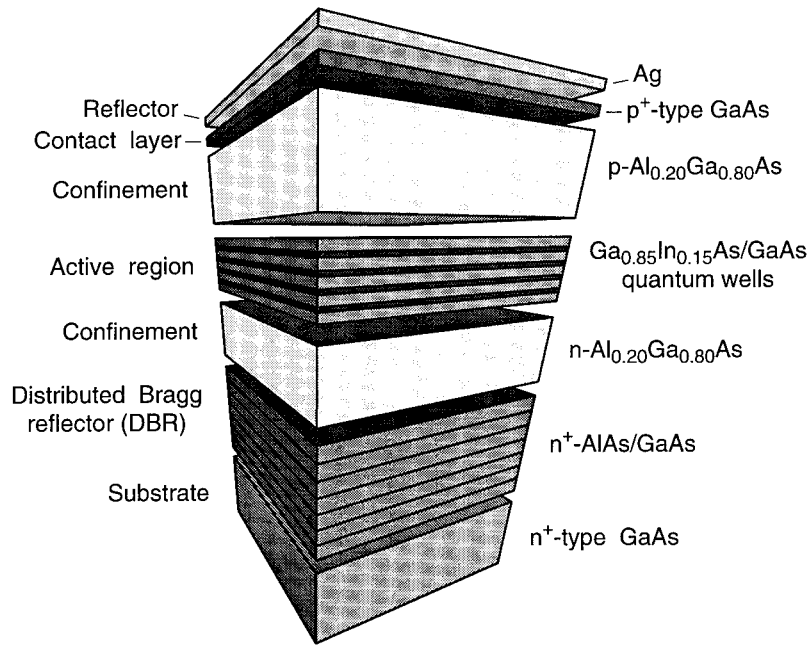


Fig. 1 Layer sequence of a planar semiconductor microcavity defined by a distributed Bragg reflector and a silver mirror. The active region consists of four GaInAs quantum wells.

The enhancement of the emission intensity along the optical axis of the cavity can be calculated in terms of Fermi's Golden Rule. At the resonance wavelength, the emission enhancement factor is given by [14,15]

$$G_e = \frac{\xi}{2} \frac{(1 + \sqrt{R_2})^2 (1 - R_1)}{(1 - \sqrt{R_1 R_2})^2} \frac{\tau_{cav}}{\tau} \quad (1)$$

where R_1 and R_2 are the reflectivities of the mirrors and, since we assume $R_1 < R_2$, most light exits the cavity through the reflector with reflectivity R_1 . The anti-node enhancement factor ξ has a value of 2, if the active region is located exactly at an antinode of the standing optical wave inside the cavity. ξ has a value of unity, if the active region is smeared out over many periods of the optical wave, and finally $\xi = 0$ if the active region is located exactly at an optical node. Calculations of the radiative lifetime τ_{cav} for the

structure revealed that it is changed by less than 10% relative to the spontaneous lifetime τ , i.e. $\tau_{\text{cav}} \cong \tau$ [14,16]. Equation (1) allows us to calculate the on-resonance enhancement and one obtains $G_e = 60$ for the structure shown in Fig. 1.

Rather than the enhancement at the resonance wavelength, the *total* enhancement integrated over all wavelength is relevant for practical devices. Exactly on resonance, the emission is enhanced along the axis of the cavity. However, off resonance, the emission is strongly suppressed. Considering that the natural emission spectrum of the active medium (without cavity) may be much broader than the cavity resonance, it is, *a priori*, not clear if the *integral* emission is enhanced at all. To calculate the integrated enhancement, the spectral width of the cavity resonance and the spectral width of the natural emission spectrum must be determined. The former can be calculated from the uncertainty relation and the photon lifetime in the cavity, τ_{ph} , according to $\Delta E = \hbar/\tau_{\text{ph}}$ or

$$\frac{\Delta\lambda}{\lambda} = \frac{\lambda}{2nL_{\text{cav}}} \left[\frac{1 - \sqrt{R_1 R_2}}{\pi(R_1 R_2)^{1/4}} \right] \quad (2)$$

where L_{cav} is the effective cavity length and n is the refractive index in the cavity. For typical reflectivities of $R_1 = 90\%$ and $R_2 = 96\%$ and an effective cavity length of $2.7(\lambda/n)$, the spectral width is $\Delta\lambda \cong 5$ nm at $\lambda = 900$ nm [14]. The spectral width of the natural emission spectrum of semiconductor is 1.8 kT [17], where k is the Boltzmann constant and $T = 300$ K. The value of 1.8 kT corresponds to $\Delta\lambda_N = 31$ nm at an emission wavelength of 900 nm. Thus a small part of the spectrum is strongly enhanced, whereas the rest of the spectrum is suppressed. The total enhancement/suppression can be calculated by assuming a gaussian natural emission spectrum [14]

$$G_{\text{int}} = G_e \sqrt{\pi \ln 2} (\Delta\lambda/\Delta\lambda_N) \quad (3)$$

For the above values for G_e , $\Delta\lambda$, and $\Delta\lambda_N$, we deduce an integrated enhancement of $G_{\text{int}} \cong 14$. The integrated enhancement can be quite different for different types of materials. Narrow atomic emission spectra can be enhanced by several orders of magnitude [7]. On the other hand, materials having broad emission spectra such as dyes [11,12] or polymers [18,19] may not exhibit any integrated enhancement at all.

LIGHT-EMITTING DIODES

LEDs are the most common optoelectronic semiconductor device. Most of the LEDs are used in displays or in silica and plastic fiber communication systems. Before showing

how microcavities can be integrated with LEDs, we will discuss some general aspects of LEDs.

Einstein [20] showed that photons can be emitted from an atom by either a spontaneous or a stimulated recombination process. LEDs, as opposed to lasers, employ the former process. The spontaneous emission of photons from the active region of an LED is isotropic. The isotropicity of the emission has significant consequences with respect to the efficiency of LEDs. If the active region is in the vicinity of a planar semiconductor surface, light can escape from the semiconductor into the adjacent medium only if the angle of incidence at the interface is smaller than the angle of total reflection. For an air/semiconductor interface with indices of refraction of $n_1 = 1$ and $n_2 = 3.5$, the angle must be smaller than $\alpha = \arcsin(n_1/n_2) \cong 16^\circ$. Only light within the small escape cone defined by this angle can escape from the semiconductor. As a result, planar LEDs have a relatively low quantum efficiency.

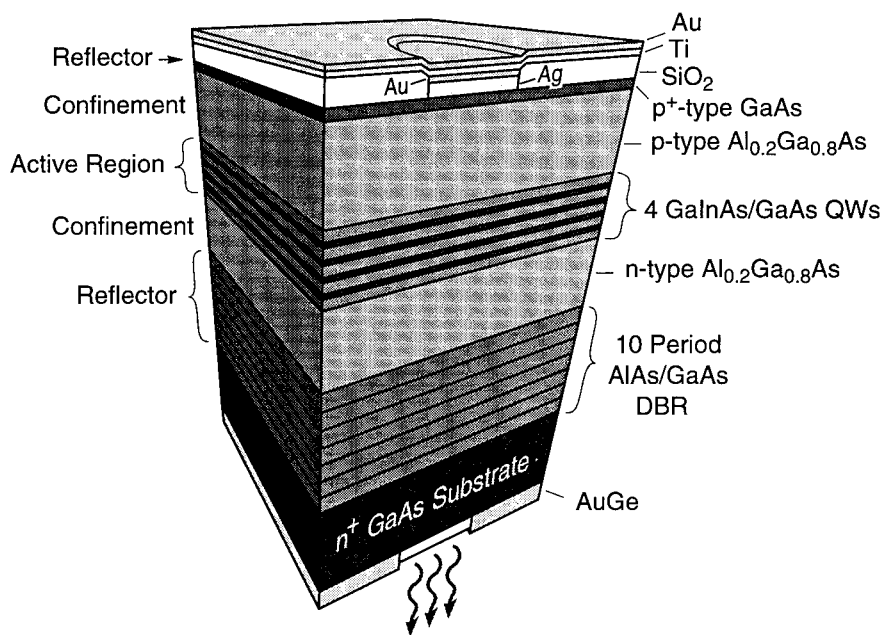


Fig. 2 Layer sequence and structure of the resonant-cavity light-emitting diode. The planar semiconductor microcavity is defined by a distributed Bragg reflector and a silver mirror. The circular silver reflector also serves as ohmic contact. Light emission occurs through the substrate coated with an anti-reflection film.

A significant difference exists between LEDs used for display purposes and for optical fiber communication. The figure of merit for communication LEDs is the photon flux density. A high photon flux density allows one to couple much of the emitted light into an optical fiber. For display LEDs, the figure of merit is the total power emitted into the hemisphere of the observer, i.e., the total number of photons rather than the photon density is relevant. Whereas several structures were proposed and realized to increase the total power (total number of photons) including spherical shapes [21], multiple surfaces [22], reflectors [23], and non-planar surfaces [24], none of these concepts can increase the photon flux density.

An LED structure which provides an enhanced photon flux density is the resonant-cavity light-emitting diode (RCLED). The RCLED is pn junction diode integrated with a microcavity. The fundamental mode of the cavity is in resonance with the light-emitting active region of the diode. The structure of a RCLED is shown in Fig. 2. The four $\text{Ga}_{0.85}\text{In}_{0.15}\text{As}$ quantum wells of the active region emit at 930 nm. At this wavelength, all other materials used in the structure, are transparent including the GaAs substrate. The bottom reflector of the structure is a 10 period AlAs/GaAs distributed Bragg reflector with a reflectivity of 90%. Most light escapes from the cavity through the bottom reflector, since its reflectivity is lower than that of the top Ag reflector. The top silver reflector also serves as a non-alloyed ohmic contact to the heavily doped top p^+ -type GaAs layer. SiO_2 is used to photolithographically define the contact area. The thicknesses of the two confinement layers are chosen in such a way to (i) have the fundamental mode of the cavity at 930 nm, and to (ii) place the active GaInAs region into an optical anti-node of the cavity. Light exits the structure through the substrate. The exit window is coated with cubic zirconium ($\text{ZrO}_2\text{:Y}$) which serves as an anti-reflection coating. Alloyed AuGe surrounding the optical window provides an ohmic contact to the n^+ -type GaAs substrate. The structures discussed here use Si as n-type dopant and C as p-type dopant. Excellent internal quantum efficiencies were demonstrated for C-doped $\text{Al}_x\text{Ga}_{1-x}\text{As}$ GRINSCH lasers [25].

EFFICIENCY OF RCLED

The figure of merit of LEDs used in optical fiber communication systems is the photon flux density emitted from the diode at a given current which, for a given wavelength, will be discussed in terms of $\mu\text{W}/\text{steradian}$. The optical power coupled into a fiber is directly proportional to the photon flux density.

The intensity of the RCLED as a function of the injection current is shown in Fig. 3. For comparison, we also show the calculated intensity of an *ideal isotropic emitter* which is a hypothetical device and is assumed to have a 100% internal quantum efficiency and to be clad by an anti-reflection coating providing $R = 0$ for all wavelengths emitted from the active region. Note that neither the 100% internal quantum efficiency nor such a hypothetical anti-reflection coating can be reduced to practice for fundamental reasons. Therefore, the ideal isotropic emitter represents an upper limit for the intensity attainable

with any conventional LED. In fact, the best conventional LEDs have intensities lower than the ideal isotropic emitter. Also included in Fig. 3 is the state-of-the art ODL50 GaAs LED used for optical fiber communication [26].

Fig. 3 Light intensity versus current for a planar RCLED emitting at 910 nm. Also shown is the theoretical curve of the ideal isotropic emitter which is an upper limit for all conventional LEDs. The shaded area indicates experimental intensities of the best conventional LEDs and of the ODL 50 which is a commercial product.

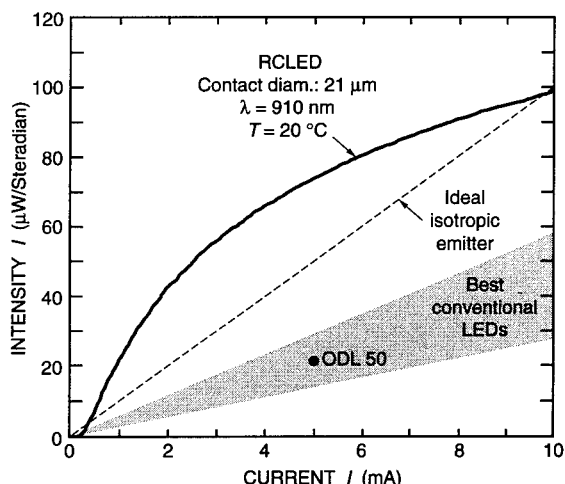


Figure 3 reveals that the RCLED provides unprecedented intensities in terms of both, absolute values as well as slope efficiencies. The slope efficiency is 7.3 times higher than the efficiency of the best conventional LEDs and 3.1 times higher than the calculated efficiency of the ideal isotropic emitter. At a current of 5 mA, the intensity of the RCLED is 3.3 times higher than that of the best conventional LEDs including the ODL50. The unprecedented efficiencies make the RCLED very promising for optical interconnect systems which will be discussed further in a subsequent section.

The RCLED presented here has been designed for an operating current of 5 mA and for usage with optical multimode fibers with a core diameter of 62.5 μm . At higher currents, the RCLED intensity starts to saturate as shown in Fig.3. The saturation is due to band filling. Hunt et al. [24] showed for single-mirror LEDs that the saturation depends on the number of quantum wells in the active region and that the onset of saturation is determined by the design parameters.

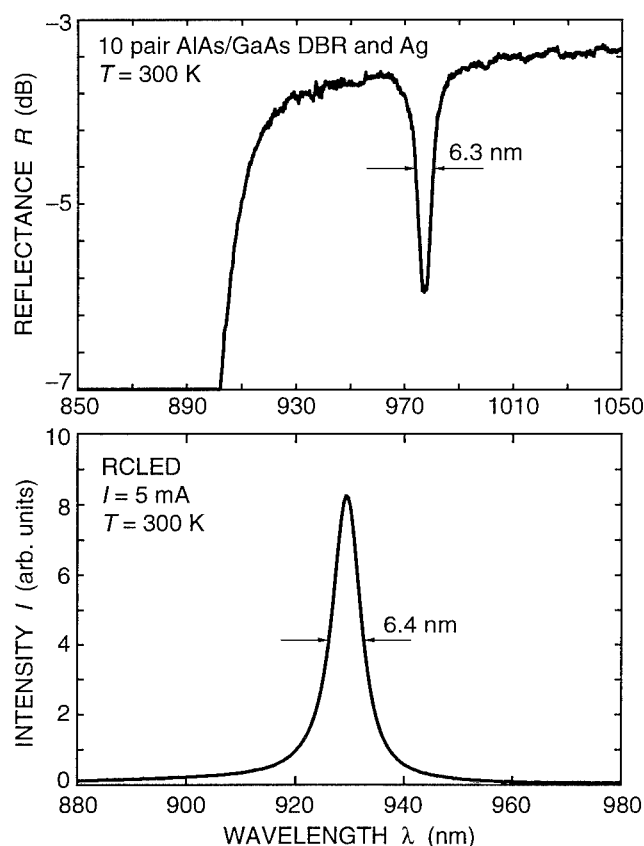


Fig. 4 Reflectivity spectrum (top) from a semiconductor microcavity and emission spectrum (bottom) from a microcavity structure. The similarity of the two spectra shows that optical emission is restricted to the fundamental cavity mode.

SPECTRAL CHARACTERISTICS OF RCLEDs

The reflection and emission properties of the RCLED are shown in Fig. 4. The reflection spectrum of the RCLED exhibits a highly reflective band for wavelengths >900 nm and a dip of the reflectivity at the cavity resonance. The spectral width of the cavity resonance is 6.3 nm. For comparison, the emission spectrum of an electrically pumped device is shown in the lower part of Fig. 4. The emission spectrum has nearly the same shape and width as the cavity resonance width determined by the reflectivity measurement.

In conventional LEDs, the spectral characteristics of the devices reflect the thermal distribution of recombining electrons and holes in the conduction and valence band. The spectral characteristics of light emission from microcavities are as intriguing as they are

complex [27,28]. However, restricting our consideration to the optical axis of the cavity simplifies the cavity physics considerably. If we assume that the cavity resonance is much narrower than the natural emission spectrum of the semiconductor, then the on-resonance luminescence is enhanced whereas the off-resonance luminescence is suppressed. The on-axis emission spectrum should therefore reflect the enhancement, i.e. resonance spectrum of the cavity. The experimental results shown in Fig. 4 confirm this conjecture.

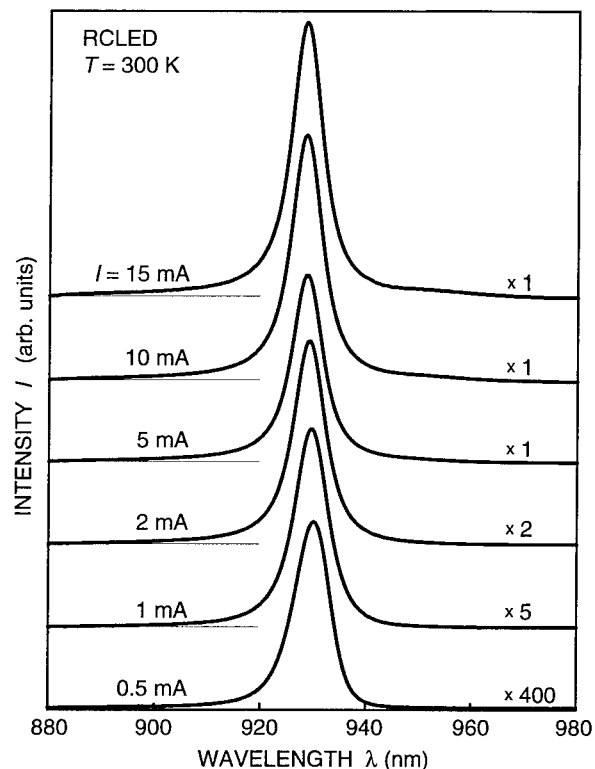


Fig. 5 Emission spectra of a resonant-cavity light-emitting diode at different excitation currents. The spectral shape is independent of the current indicating the absence of stimulated emission or superluminescence.

Microcavities provide enhanced optical feedback through photons oscillating in the cavity. The enhanced photon density results in a higher probability of stimulated emission processes. To test the relevance of stimulated emission processes, we have measured the RCLED spectrum at different excitation intensities and these results are shown in Fig. 5. For injection currents ranging from 0.5 mA to 15 mA, the optical spectra are virtually the same. Spectral narrowing, which is typically observed at the onset of stimulated emission,

is completely absent. The optical spectra thus do not indicate any significant stimulated emission.

A design criterion for the RCLED is $(1 - R_1) \gg \alpha \ell_{\text{active}}$ [15], where α and ℓ_{active} is the absorption coefficient and the thickness of the active region. This condition insures that the exit-mirror loss is much larger than self-absorption in the active region. If the above criterion were not fulfilled, the RCLED would not provide any intensity enhancement. On the other hand, laser oscillation requires that the round-trip gain exceeds the mirror loss. The maximum gain of a population-inverted structure cannot exceed the magnitude of the absorption in the structure, i.e. $|g| \leq |\alpha \ell_{\text{active}}|$ [29]. Thus, the maximum achievable gain is *always* smaller than the mirror loss, irrespective of the pump level, indicating that laser oscillations can not occur in RCLEDs.

OPTICAL INTERCONNECTS

Optical interconnects are a means of transferring information between different components of a system. Optical interconnects will be used in a wide range of systems including cars, airplanes, central office switches and computers. Optical as opposed to electrical interconnects have the potential of lower power consumption, higher transmission rates and distances, and the lack of electro-magnetic interference [30]. A key issue of the transition from electrical to optical interconnects is the electrical power dissipated at the emitter side [31]. The high efficiency and low power consumption achievable with RCLEDs makes them ideally suited for optical interconnect systems. An additional advantage of RCLEDs is their higher spectral purity when compared with conventional LEDs. As a result of the higher spectral purity, chromatic dispersion is reduced for RCLEDs which allows one to transmit over larger distances [14].

The speed of optical interconnect systems is, for most applications ≤ 1000 MHz. Frequently, the bit rate of optical interconnects is determined by the clock frequency of a Si chip. Transmission data rates ≤ 1000 MHz have recently been demonstrated for RCLEDs [32].

LEDs VERSUS LASERS

Optical sources based on spontaneous and stimulated emission, i.e. LEDs and lasers, form the basis of all silica fiber communication. In practice LEDs are preferred over lasers whenever possible and the number of LEDs used in optical fiber transmission greatly exceeds the number of lasers [30].

There are three major reasons for the preferability of LEDs. First, LEDs have much higher reliability which can exceed that of lasers by one order of magnitude [21,33]. Second, the temperature sensitivity, which is known to be governed by the well-known T_0 -law in lasers, is smaller for LEDs [33]. Third, the simpler fabrication process of LEDs

results in lower production cost. However, LEDs cannot be used in high bit rate (>1 Gbit) and long distance (>5 km) communication.

VERTICAL CAVITY LASERS, ZERO-THRESHOLD LASERS, AND OTHER NOVEL DEVICE STRUCTURES

Several intriguing novel device concepts have been proposed or realized during the last five years. These devices include the vertical-cavity surface-emitting lasers (VCSEL) [34], the zero-threshold laser [3,35], the microdisk laser [2,36], photon recycling LEDs [24], and the single mode LED [37]. Most of these devices are high β or unity β devices [2,3] where β is called the spontaneous emission factor which gives the fraction of photons coupled into a single optical mode. In order to achieve this goal, the volume of the device must be reduced to a very small size [2]. The required current densities in such devices will be impractical for any reasonable optical output.

Photon recycling LEDs [24] provide very high external quantum efficiencies but are useful for display rather than optical interconnect applications. Photon recycling prolongs the effective recombination lifetime of free carriers and, as a result, photon recycling LEDs are slow. While this excludes such LEDs for high-speed applications, the slow speed is compatible with display applications.

The VCSEL is considered as a potential candidate for optical interconnect systems. At the first glance, the basic structure of the VCSEL and the RCLED are similar. Note, however, that the VCSEL does not fulfill the RCLED design criterion $(1 - R_1) > \alpha \ell_{\text{active}}$. As a result, the VCSEL has light output intensities in the spontaneous regime which are orders of magnitude lower than that of RCLEDs [32]. In the laser regime, VCSELs can emit high powers at currents of 1-10 mA. Nevertheless, the very high reflectivities required in VCSELs and the tight control of the device parameters still impose a challenge for the manufacturability of VCSELs.

CONCLUSIONS AND PROSPECTS

During recent years, Fabry-Perot microcavities have been employed in condensed matter structures in order to modify the spontaneous emission from an optically active medium inside the microcavity. The emission from active media inside microcavities is spatially anisotropic and dispersive. The changes in spontaneous emission in planar microcavities also include drastic changes of the emission spectrum and moderate changes in the spontaneous lifetime. We have presented evidence that microcavity physics and, in particular, the changes in spontaneous emission properties can be exploited to enhance the performance of optoelectronic devices. We show that light emitting diodes employing microcavities provide unprecedented efficiencies. The experimental slope efficiency of the LED is more than five times higher than that of the best conventional LEDs. Theory predicts that the efficiency can be more than one order of magnitude higher than that of

conventional LEDs. The resonant-cavity LED is ideally suited for the emerging optical interconnect technology, i.e. short-distance communication based on silica fibers. The advantageous properties of microcavity structures may be exploited in other optoelectronic devices including displays, photodetectors, and sensors.

REFERENCES

1. C. Fabry and A. Perot, *Ann. Chim. Phys.* **16**, 115 (1899).
2. Y. Yamamoto and R. E. Slusher *Physics Today*, 66 (June 1993).
3. H. Yokoyama, *Science* **256**, 66 (1992).
4. E. M. Purcell, *Phys. Rev.* **69**, 681 (1946).
5. R. E. Slusher, A. F. J. Levi, U. Mohideen, S. L. McCall, S. J. Pearton, and R. A. Logan, *Appl. Phys. Lett.* **63**, 1310 (1993).
6. S. John, *Physics Today*, 32 (May 1991).
7. E. F. Schubert, A. M. Vredenberg, N. E. J. Hunt, Y.-H. Wong, P. C. Becker, J. M. Poate, D. C. Jacobson, L. C. Feldman, and G. J. Zydzik, *Appl. Phys. Lett.* **61**, 1381 (1992).
8. H. Yokoyama, K. Nishi, T. Anan, H. Yamada, S. D. Brorson, and E. P. Ippen, *Appl. Phys. Lett.* **57**, 2814 (1990).
9. E. Yablonovitch, *Phys. Rev. Lett.* **58**, 2059 (1987).
10. E. F. Schubert, Y.-H. Wang, A. Y. Cho, L.-W. Tu, and G. J. Zydzik, *Appl. Phys. Lett.* **60**, 921 (1992).
11. F. De Martini, G. Innocenti, G. R. Jacobovitz, and P. Mataloni, *Phys. Rev. Lett.* **59**, 2955 (1987).
12. M. Suzuki, H. Yokoyama, S. D. Brorson, and E. P. Ippen, *Appl. Phys. Lett.* **58**, 998 (1991).
13. S. E. Morin, Q. Wu, T. W. Mossberg, *Optics and Photonics News* 8 (August 1992).
14. N. E. J. Hunt, E. F. Schubert, R. F. Kopf, D. L. Sivco, A. Y. Cho, and G. J. Zydzik, *Appl. Phys. Lett.* **63**, 2600 (1993).
15. N. E. J. Hunt and E. F. Schubert, unpublished.
16. X. P. Feng, *Opt. Commun.* **83**, 162 (1991).
17. See, for example, E. F. Schubert, *Doping in III-V Semiconductors* (Cambridge, Cambridge, 1993).
18. J. H. Burroughs, D. D. C. Bradley, A. R. Brown, R. N. Marks, K. D. Mackay, R. H. Friend, P. L. Burn, A. B. Holmes, *Nature*, **347**, 539 (1990).
19. A. Dodabalapour, L. J. Rothberg, T. M. Miller, and E. W. Kwock, *Appl. Phys. Lett.* April, 1994, in press.

20. A. Einstein, Z. Phys. **18**, 121 (1917).
21. For review see R. H. Saul, T. P. Lee, and C. A. Burrus, in *Semiconductors and Semimetals* Vol. 22, Part C p. 193 (1985).
22. Hewlett-Packard, Optoelectronics Components Catalogue, 1994.
23. T. Kato, H. Susawa, M. Hirotsu, T. Saki, Y. Ohashi, E. Shichi, and S. Shibata, J. Cryst. Growth **107**, 832 (1991).
24. I. Schnitzer, E. Yablonovitch, C. Caneau, T. J. Gmitter, and A. Scherer, Appl. Phys. Lett. **63**, 2174 (1993).
25. M. Micovic, P. Evaldsson, M. Geva, G. W. Taylor, T. Vang, and R. J. Malik, Appl. Phys. Lett. **64**, 411 (1994).
26. Optical Data Link 50 or ODL50 is an AT&T product.
27. N. E. J. Hunt, E. F. Schubert, D. L. Sivco, A. Y. Cho, and G. J. Zydzik, Electron. Lett. **28**, 2169 (1992).
28. G. Björk, S. Machida, Y. Yamamoto, and K. Igeta, Phys. Rev. **A44**, 669 (1991).
29. Since the Einstein coefficients $B_{21} = B_{12}$, the gain in a population-inverted structure can not exceed the loss in a non-inverted structure.
30. T. P. Huegerich, Fiberoptic Product News 17 (Nov. 1993).
31. J. Jahns and S. H. Lee (eds) *Optical Computing Hardware* (Academic, Boston, 1994).
32. N. E. J. Hunt, E. F. Schubert, M. Micovic, R. J. Malik, G. J. Zydzik; unpublished.
33. M. Fukuda *Reliability and Degradation of Semiconductor Lasers and LEDs* (Artech, Boston, 1991).
34. J. L. Jewell, J. P. Harbison, A. Scherer, Y. H. Lee, and L. T. Florez, IEEE J. Quant. Electron. **27**, 1332 (1991).
35. T. Kobayashi, T. Segawa, A. Morimoto, and T. Sueta, 43rd fall meeting of the Jpn. Soc. of Appl. Phys. Tokyo, Sept. 1982.
36. S. L. McCall, A. F. J. Levi, R. E. Slusher, S. J. Pearton, and R. A. Logan, Appl. Phys. Lett. **60**, 289 (1992).
37. E. Yablonovitch, personal communication, (1992).

WIDE STOP BAND OPTICAL FILTERS FROM PHOTONIC BAND GAP AIR BRIDGES

J.C. Chen, H.A. Haus, J.N. Winn, S. Fan, and J.D. Joannopoulos

Research Laboratory of Electronics &
Center for Material Science and Engineering
Room 36-315
Massachusetts Institute of Technology
Cambridge, MA 02139

ABSTRACT

Photonic band gap materials can produce optical filters with large stop bands and sharp transmission resonances. The transmission spectrum and radiation characteristics of one such filter are described using a modified finite difference time domain program.

1. INTRODUCTION

A distributed feedback (DFB) grating waveguide acts as a reflection filter in the stopband of the grating. If a quarter-wave shift (QWS) is introduced in the center of the grating, a transmission resonance occurs in the center of the stopband. A QWS-DFB grating waveguide side-coupled to a "signal" waveguide acts as a channel dropping filter that drops the channel with a carrier frequency coincident with the resonance of the grating resonator and passes all other frequencies within the stopband of the grating. Such filters may find application in wavelength division multiplexing systems. In order to cover a set of channels over the bandwidth of erbium amplifiers, gratings are required with a stopband twice that of the erbium gain (approximately 40 nm). Only the large index contrasts found in photonic band gap materials can create such large stopbands. Other potential applications of photonic band gaps include curved waveguides with low losses, laser resonators with low spontaneous emission, and efficient radiation from planar antennae.^[1-4]

Here we present a photonic band gap filter whose stop band is much larger than the gain bandwidth of erbium fiber. In this paper, we will first describe how we model these devices, paying particular attention to our additions to standard finite difference time domain techniques. Next, we discuss how radiation is a limiting factor in photonic band gap gratings. We present the transmission and eigenmode characteristics of this air bridge filter.

2. METHODOLOGY

Standard finite difference time domain programs integrate Maxwell's equations. To improve accuracy, these programs displace the electric field at a half grid point from the magnetic field. Our program calculates only one field component, avoiding the additional complexities and memory requirements associated with staggered grids. For the TM case, the vector wave equation becomes scalar.

$$\frac{\partial^2 E(x, y, t)}{\partial x^2} + \frac{\partial^2 E(x, y, t)}{\partial y^2} - \frac{n(x, y)^2}{c^2} \frac{\partial^2 E(x, y, t)}{\partial t^2} = 0.$$

The equation we solve for 2D TE case is

$$\frac{\partial}{\partial x} \left(\frac{1}{n(x, y)^2} \frac{\partial H(x, y, t)}{\partial x} \right) + \frac{\partial}{\partial y} \left(\frac{1}{n(x, y)^2} \frac{\partial H(x, y, t)}{\partial y} \right) - \frac{1}{c^2} \frac{\partial^2 H(x, y, t)}{\partial t^2} = 0.$$

For second order accuracy, all the derivatives are center differenced. These equations are explicit and so are easy to code. Furthermore, each field quantity at a given time step is independent of fields at the same time step; there are no data dependencies. So, an initial value calculation can run efficiently on parallel^[5] as well as vector machines. The boundary conditions we use are second order absorbing.^[6] We use the finite difference program in two ways, to get either the transmission spectrum or the resonator properties.

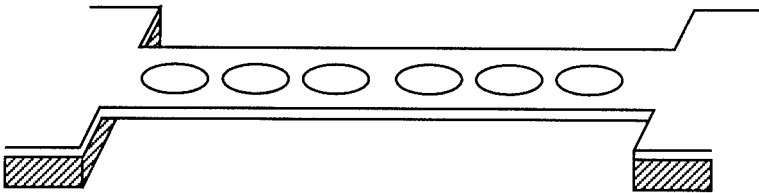


Figure 1. Schematic of air bridge with six circular holes.

By examining the resonator properties, we can extract the quality factor Q caused by the radiation loss and field profile of the highest Q mode. An arbitrary field can be decomposed into many eigenmodes, each of which decays exponentially with a rate ω/Q . A sufficiently long propagation will yield the mode with the largest Q ; the other eigenmodes will be negligibly small.^[7] This calculation can be speeded up if the initial field resembles the high Q eigenmodes.

For the transmission spectrum, we launch a monochromatic sinusoidal wave from one end of the waveguide. The transverse profile of this source is the guide's fundamental mode. The field is explicitly stepped forward in time until steady state is reached. From the field values at two different positions and times, we separate out the forward and backward propagating wave components.

$$E_f \cos(kx - \omega t + \Phi_f) = -\hat{A} + \hat{B} \quad (1)$$

$$E_b \cos(kx + \omega t + \Phi_b) = \hat{A} + \hat{B} \quad (2)$$

where

$$\hat{A} = \frac{E(x, t + \Delta t) - \cos(\omega \Delta t) E(x, t)}{2 \sin(\omega \Delta t)}$$

$$\hat{B} = \frac{E(x + \Delta x, t) - \cos(k \Delta x) E(x, t)}{2 \sin(k \Delta x)}.$$

Choosing Δx and Δt so that the differences — \hat{A} and \hat{B} — are large, enhances accuracy. One can solve for the amplitudes E_f and E_b by evaluating equations 1 and 2 at an additional time step. And by taking the ratios of various field components before and after the filter, we obtain the reflection and transmission coefficients. The radiation power is defined as the incident power minus the power transmitted and the power reflected. This includes the power transferred to higher order transverse modes and to the substrate. For photonic band gap materials, others have calculated transmission and reflection through transfer matrices^[9,10] and transmission and radiation through beam propagation methods.^[11] To the best of our knowledge, this is an original way to measure all three: reflection, radiation and transmission.

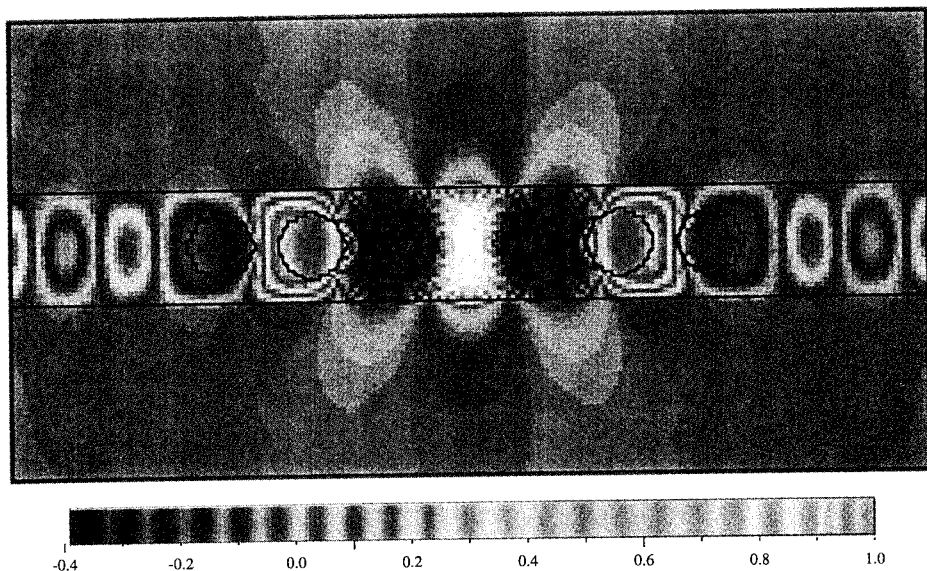


Figure 2. Grayscale contour of TE magnetic field, showing eigenmode with highest Q

3. RESULTS

3.1 Resonator Properties

For the air bridge structure shown in figure 1, we examine a crosssection. The index of refraction is $n = \sqrt{13}$. This air bridge has only six circular air holes. In particular, the period or hole-to-hole spacing is 0.232λ or (for $\lambda = 1.5 \mu\text{m}$) $0.348 \mu\text{m}$. This spacing increases to 0.325λ or $0.487 \mu\text{m}$ for the center two holes. The air holes have a 0.167λ or $0.250 \mu\text{m}$ diameter, while the air bridge is 0.151λ or $0.226 \mu\text{m}$ wide. A longer version of this structure — one with more air holes — can act as a high Q microcavity.^[7,8] Figure 2 shows the magnetic field profile of the highest Q eigenmode. It is TE. The magnetic field has even symmetry, so the electric field would have odd symmetry. Figure 3 shows

the energy decay for an initial excitation. The slope gives the Q . Figure 3 shows a Q of 387. This is a surprisingly large Q for a structure that has only 3 air holes. The total structure is less than 1.5 wavelengths long! This small size allows for a compact integration of many wavelength filters on a small chip.

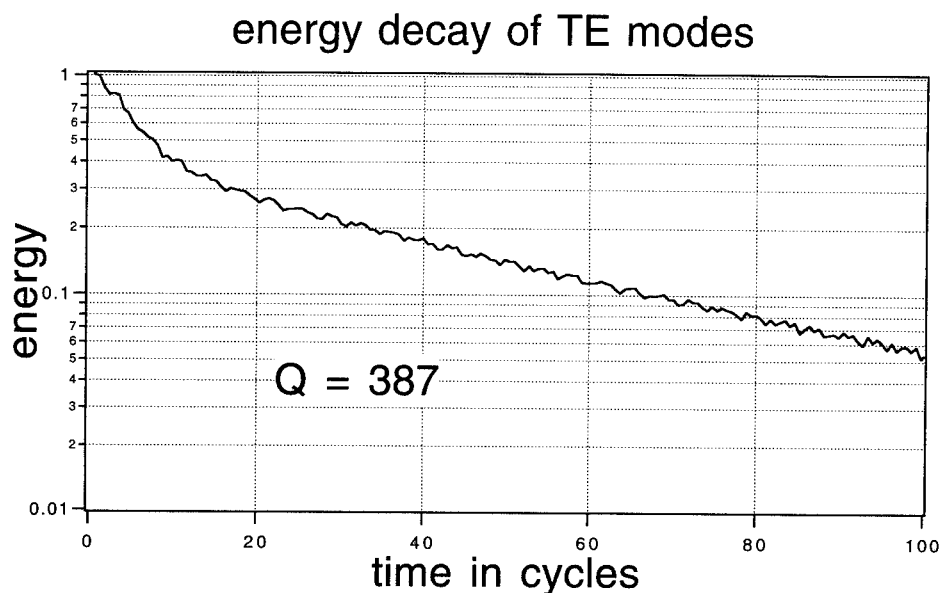


Figure 3. Energy in TE fields plotted versus number of cycles

The fields in figure 2 are strongly localized about the dielectric defect or phase slip. The exponential decay of the field from its maximum can be approximated by a decay constant $\kappa = -\frac{\Delta n}{\langle n \rangle} \frac{2}{\Lambda}$ where Λ is the grating period, Δn is the difference in effective indices of the air hole and dielectric guide, and $\langle n \rangle$ is the average index of the hole and dielectric.^[12] For photonic band gap materials, Δn is large. In some cases, $\Delta n \simeq \langle n \rangle$ so κ is on the order of the free space wave vector. This strong localization of electric field means a large spread of the mode's spatial Fourier spectrum. Radiation occurs when the spectrum extends into the radiation mode spectrum. An analytic approximation for the radiation Q has been formulated.^[13] The Q_{ext} , associated with the coupling of the resonator to the input and output waveguides, is derived in Haus' book.^[12]

$$Q_{ext} = \frac{l}{\lambda} \frac{\pi c}{v_g |\kappa| l} e^{2|\kappa|l} = \frac{l}{\lambda} \frac{\langle n \rangle}{|\kappa| l} e^{2|\kappa|l}.$$

The total Q of a resonator is

$$1/Q_{total} = 1/Q_{ext} + 1/Q_{rad}.$$

For the TM air bridge, the analytic theory makes the following predictions: $Q_{rad} = 500$. $Q_{ext} = 551$. $Q_{total} = 262$. The total Q is comparable to the numerically derived $Q = 387$.

3.2 Transmission Spectra

Higher Q resonators lead to a sharp transmission peak within the stop band. Figure 4 shows the transmission, reflection, and radiation as a function of frequency. Here the

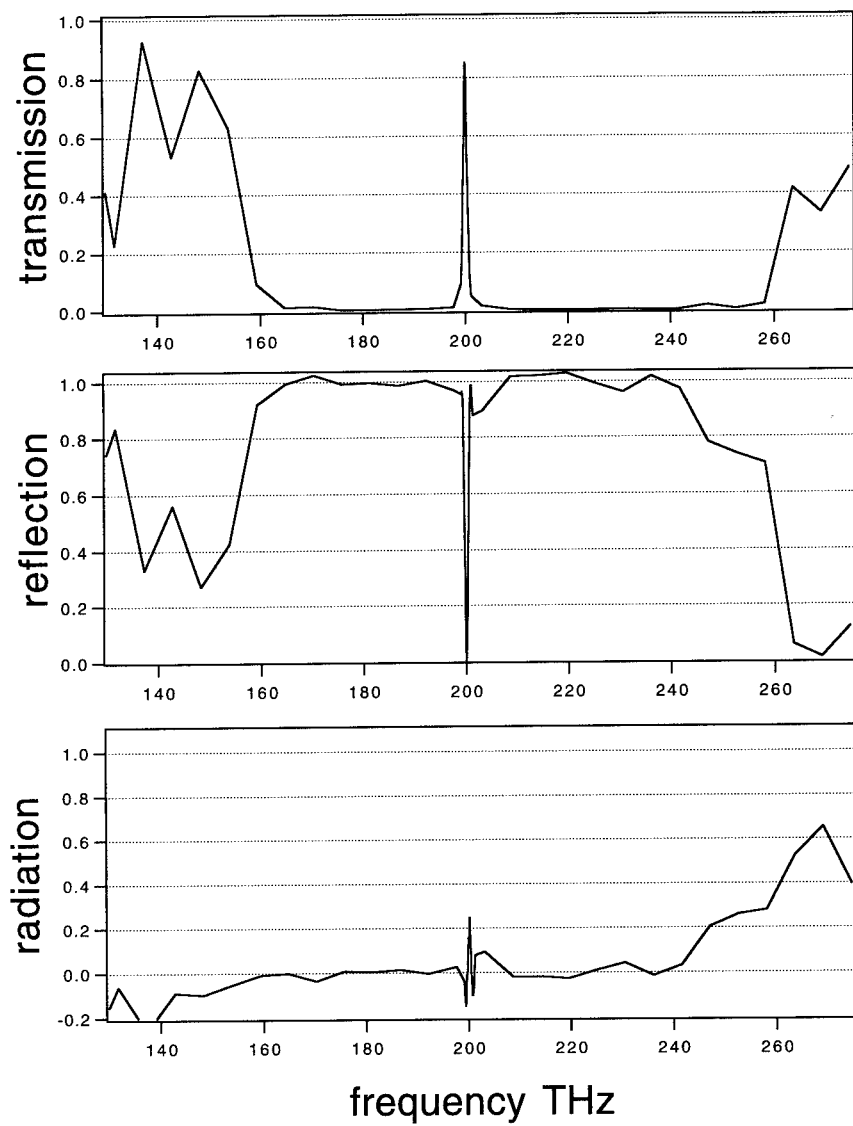


Figure 4. Fraction power transmitted, reflected, and radiated through filter as a function of frequency

transmission coefficient is the fraction of power that remains in the fundamental transverse mode of the waveguide after propagating through the air holes. The transmission resonance occurs at $\lambda = 1.5\mu\text{m}$ or 200 THz. In figure 5, a monochromatic laser source comes in from the left side of the filter. Since the source oscillates at the resonance frequency of the cavity, light is coupled into the resonance mode (figure 2), creating strong field localization about the phase slip or dielectric defect. At this frequency, the transmission is nearly perfect; 85 % is transmitted. The Q from the FWHM of that resonance is 304. The size of the stop band is 100 THz! Reflection and radiation are also plotted. Over much of that range, the reflection is near unity and the radiation near zero. For higher frequencies, the radiation increases since light is transferred to higher order transverse modes. At resonance, the loss due to radiation is surprisingly small despite the sharp decay (large κ).

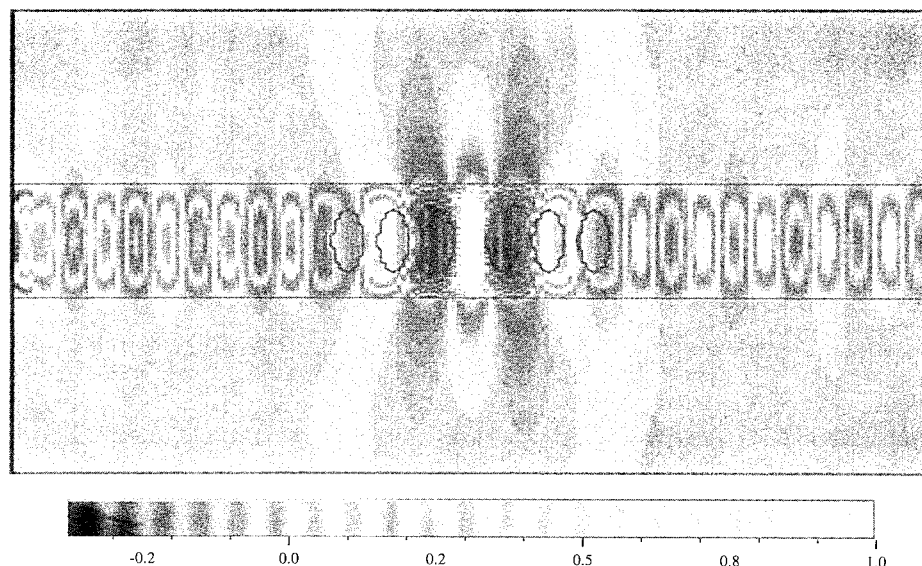


Figure 5. TE Magnetic field propagates down air bridge filter at transmission resonance.

4. CONCLUSION

We have presented a compact, high Q filter. The large index contrasts of this photonic band gap air bridge lead to a 100 THz stop band. A vectorial finite difference time domain program has analyzed this structure yielding both transmission spectrum and radiation decay rates.

ACKNOWLEDGMENTS

These simulations ran on the NSF San Diego Supercomputer Center's Cray C90. Some work was done on the MIT Laboratory of Computer Science's 128 node CM5. This work is support in part by NSF Materials Research Laboratory DMR 90-22933.

REFERENCES

- [1] E. Yablonovitch, "Photonic band-gap structures," *J. Opt. Soc. Am. B*, 10:283 (1993).

- [2] J. W. Haus, "A brief review of theoretical results for photonic band structure," *J. Mod. Optics*, 41:195 (1994).
- [3] R. D. Meade, A. Devenyi, J. D. Joannopoulos, O. L. Alherhand, D. A. Smith, and K. Kash, "Novel applications of photonic band gap materials: Low loss bends and high Q cavities," *J. Appl. Phys.*, 75:4753 (1994).
- [4] P. R. Villeneuve and M. Piché, "Photonic bandgaps in periodic dielectric structures." to be published in *Prog. Quant. Electron.*, 1994.
- [5] J. C. Chen, "A parallel approach for modelling optical waveguides," in *Proceedings of the 1994 M.I.T. Student Workshop on Scalable Computing*, (Cape Cod, MA), July 21-2, 1994. paper 17.
- [6] B. Engquist and A. Majda, "Absorbing boundary conditions for the numerical simulation of waves," *Math. Computat.*, 31:629-51 (1977).
- [7] S. Fan, J. N. Winn, A. Devenyi, J. C. Chen, R. D. Meade, and J. D. Joannopoulos, "Guided and defect modes in periodic dielectric waveguides." submitted to *J. Opt. Soc. Am. B*, 1994.
- [8] S. Fan, P. R. Villeneuve, J. D. Joannopoulos, K. Y. Lim, G. S. Petrich, and L. A. Kolodziejski, "Microcavity air bridge." unpublished.
- [9] J. B. Pendry and A. MacKinnon, "Calculation of photon dispersion relation," *Phys. Rev. Lett.*, 69: 2772 (1992).
- [10] M. Sigalas, C. M. Soukoulis, E. N. Economou, C. T. Chan, and K. M. Ho, "Photonic band gaps and defects in two dimensions: Studies of the transmission coefficient," *Phys. Rev. B.*, 48:121 (1993).
- [11] M. Scalora and M. E. Crenshaw, "A beam propagation method that handles reflections," *Optics Commun.*, 108:191 (1994).
- [12] H. A. Haus, "Distributed feedback structures," in *Waves and Fields in Optoelectronics*, Englewood Cliffs, NJ: Prentice-Hall, Inc., 1984.
- [13] H. A. Haus, "The radiation Q of open photonic-gap bridge resonators." unpublished.

Applications and Characterization of a New Face-Centered-Cubic Photonic Crystal

K. Agi,¹ E.R. Brown,² C.D. Dill,² K.A. McIntosh,² O.B. McMahon,²
K.M. Molvar,² and K.J. Malloy¹

¹Center for High Technology Materials
University of New Mexico
Albuquerque, NM 87131

²Lincoln Laboratory, Massachusetts Institute of Technology
Lexington, MA 02173-9108

ABSTRACT

Recently, a new photonic crystal consisting of a face-centered-cubic (fcc) arrangement of cylindrical air atoms has been developed. In the present work, frequency-domain measurements are performed on this crystal in transmission using a network analyzer. In addition, time-domain measurements in transmission are performed by optoelectronically generating picosecond bursts of free-space electromagnetic radiation by photoconductively switching planar antennas. A direct comparison between the time-domain and frequency-domain measurement is performed. One application of the new fcc crystal involves stacking several sections with different lattice constants in tandem, thereby creating an ultra-wideband (UWB) photonic crystal.

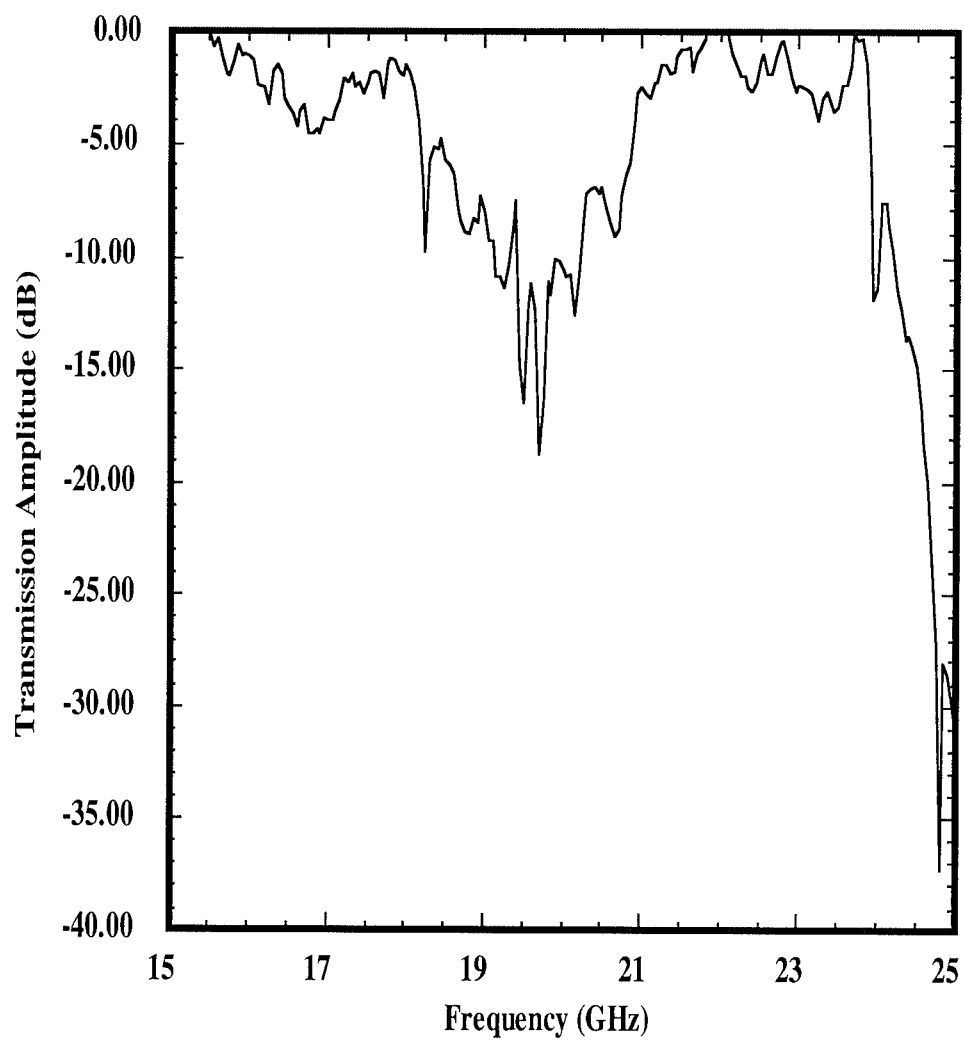


Figure 1. Continuous-wave (CW) frequency-domain measurement using network analyzer. Transmission (S_{21}) measurement of photonic crystal at normal incidence from 15 to 25 GHz.

A three-dimensionally periodic structure that exhibits an electromagnetic stop band in all 4π steradians is called a photonic bandgap (PBG) structure.¹ The original PBG structure, developed by Yablonovitch et al., was a face-centered-cubic (fcc) arrangement of quasi-spherical air atoms in a dielectric host. The fabrication of this crystal consisted of precisely drilling holes in a dielectric block of Stycast-12 (three holes drilled 35° off normal and rotated azimuthally by 120° at each lattice site).² Recently, a simpler method of fabricating an fcc photonic crystal has been developed. Briefly, the fabrication of the new crystal consists of drilling a triangular lattice of vertical holes in lossless dielectric plates (measurements on the dielectric host (Stycast, $\epsilon=10,13$) indicate negligible loss). Three plates are then shifted and stacked one on top of the other to obtain a single period of an fcc lattice along the [111] direction of the cubic unit cell (a detailed description of the fabrication process can be found elsewhere³). The number of lattice periods can subsequently be increased by stacking more plates in the ordered sequence. The simple and robust nature of the new crystal is manifested by the ease of fabrication and mechanical stability associated with drilling cylindrical (vertical) holes.

The characterization of the crystals was done in two ways. First, K-band feedhorns were used to transmit and receive continuous-wave (CW) radiation through the sample. A network analyzer was used to measure the microwave transmission coefficient, S_{21} , from 15 to 25 GHz. The network analyzer was calibrated by first taking a direct measurement (e.g. no crystal) and using it as the baseline. The crystal is then placed in between the antennas and another measurement is taken. This calibration technique de-embeds the system response from the crystal response giving the frequency-domain transfer function of the crystal. The results of the transmission measurement at normal incidence are shown in Fig. 1 with the experimental set up shown in the inset. A shortcoming of this type of measurement is the upper frequency limit of the network analyzer.

In order to study the crystal over wider bandwidths, the second means of characterization was the transmission of short pulses in the time-domain. The experimental set up is shown in Fig. 2. A mode-locked titanium-sapphire laser is used to generate a train of a 250-fs-wide optical pulses at a repetition rate of 76 MHz and a wavelength of 750 nm. The 50 mW (average power) laser output beam is split into two approximately equal power beams. These optical beams are used to switch photoconductive gaps coupled to planar antennas. One beam is chopped at 1 kHz and is focused onto a transmitting antenna, which is dc biased at 40 V. The other is passed through an optical delay line and focused onto an unbiased receive antenna (the electric field of the received signal acts as the bias), which is

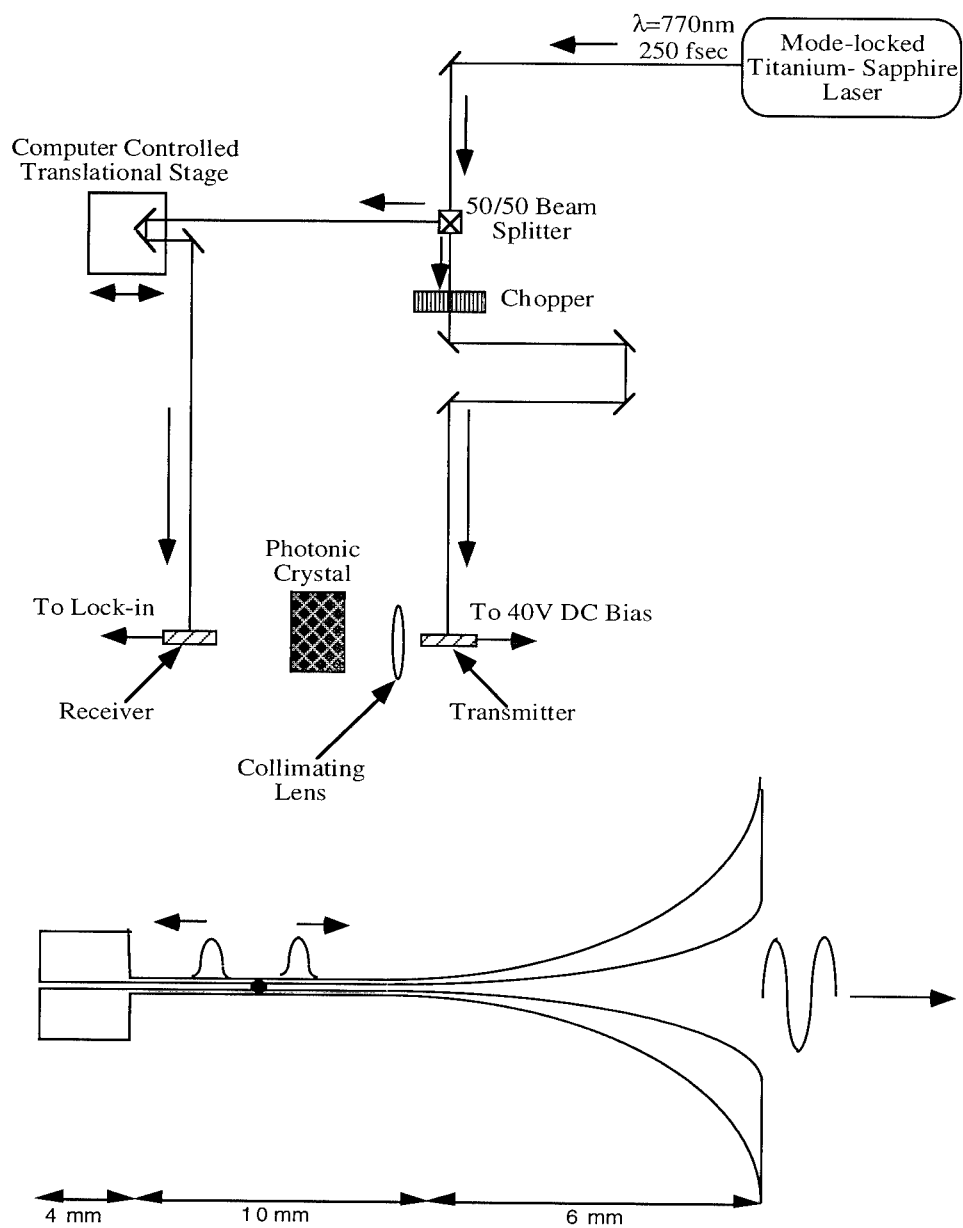


Figure 2(a). Experimental set up for the time-domain measurements. **(b)** Exponentially tapered coupled-strip antennas with a 1 cm coplanar transmission line feed. Two current pulses are generated at the point of switching that determine the frequency resolution of the system

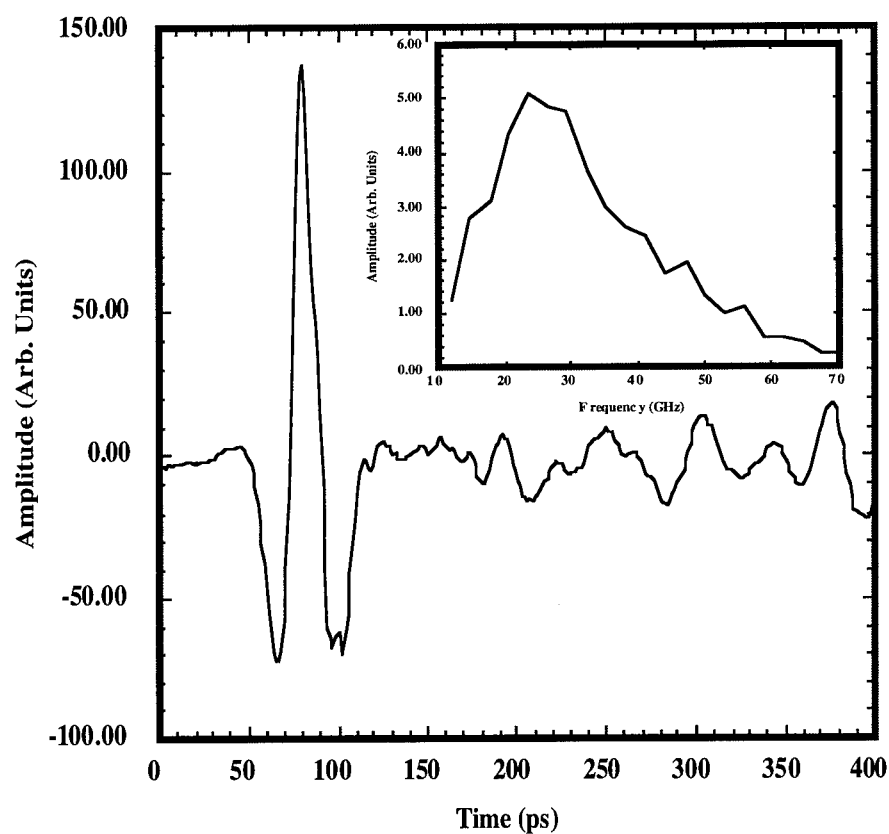


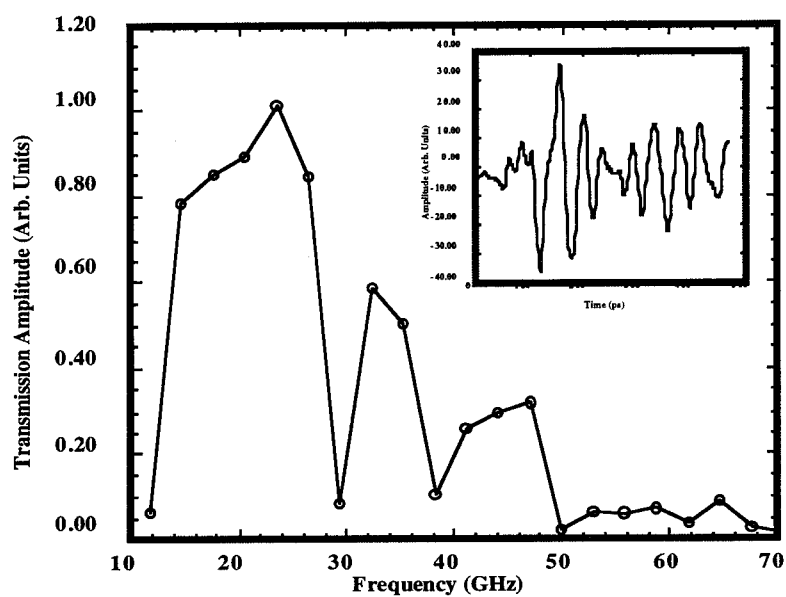
Figure 3. Typical time-domain reference pulse with the Fourier transform shown in the inset. The usable time window is approximately 400 ps which corresponds to a frequency resolution of 2.5 GHz. The pulse has a peak at 24 GHz and has usable frequency components out to 60 GHz.

connected to a lock-in amplifier. As the delay between the optical pulses is increased, the received waveform can be mapped out.⁴

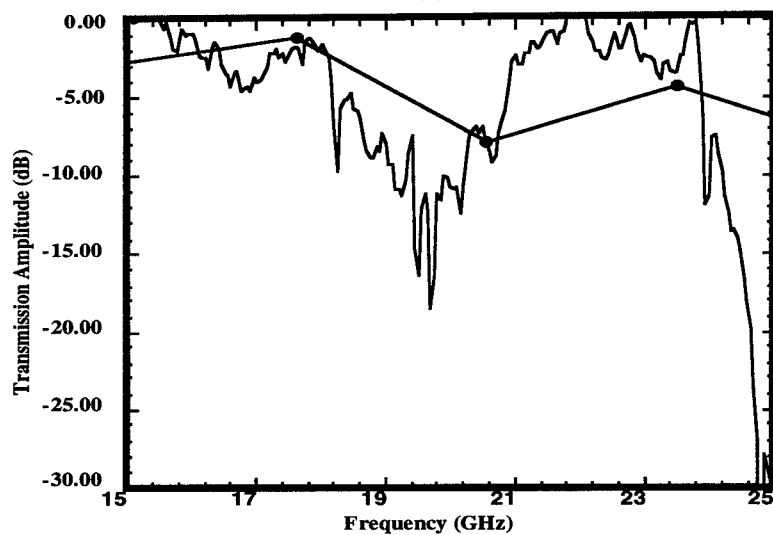
The transmitting and receiving antennas, shown in Fig. 2b, are exponentially tapered coplanar horns similar to those used by other groups in the past.⁴⁻⁶ They are printed on low-temperature-grown GaAs (LTG-GaAs) using standard microfabrication techniques. The LTG-GaAs provides a short carrier lifetime (~ 0.8 ps)⁷ such that the duration of the photoconductively generated current pulse is of the same order as the optical pulse. At the point of switching, two current pulses are generated in the transmitting antenna (see Fig. 2b). The first travels toward the end of the taper and is radiated into free space; the other travels down the coupled strips, reflects from the bonding pads, and is subsequently radiated from the taper. The time delay between radiated pulses dictates the resolution in the frequency domain of the system.

Due to the limited aperture of the antenna, the radiation emanating from the transmitter diverges. To overcome this, a two inch diameter collimating lens is placed in front of the transmitting antenna as shown in Fig. 2. The lens is a standard microwave lens whose loss is negligible in the frequency range of interest. The entire experiment is controlled by a Macintosh running LabVIEW® software. A typical reference pulse (e.g. without the photonic crystal between antennas) is shown in Fig. 3 with its Fourier transform shown in the inset. The power spectrum of the received waveform is centered about 24 GHz and has usable magnitude out to 60 GHz as dictated by the antenna dimensions.⁸ The resolution of the measurement is approximately 2.5 GHz according to the 400 ps time window shown in the time-domain plot in Fig. 3. Although broadband measurements of three-dimensional PBG structures have been recently reported by Özbay et. al.,⁹ their generation method utilized nonlinear transmission line technology as opposed to the photoconductive switching applied here.

The broadband response of the photonic crystal is shown in Fig. 4(a) with the corresponding time-domain plot shown in the inset. The frequency-domain has a dip in the response at approximately 23 GHz. This is the stop band that is seen in the CW frequency-domain response in Fig. 1. Since the resolution of the time-domain system is 2.5 GHz, the stop band isn't as pronounced as in the frequency domain. In addition, higher order stop bands, located between 34 and 47 GHz, appear in the measurement which aren't observed in the frequency domain response because of the 26 GHz limitation of the network analyzer. The nature of these stop bands is currently being investigated. A direct comparison of the time-domain and CW frequency-domain responses is performed. However, in order for a direct comparison, the time-domain system response needs to be deconvolved from the crystal response. The deconvolution technique used is similar to the

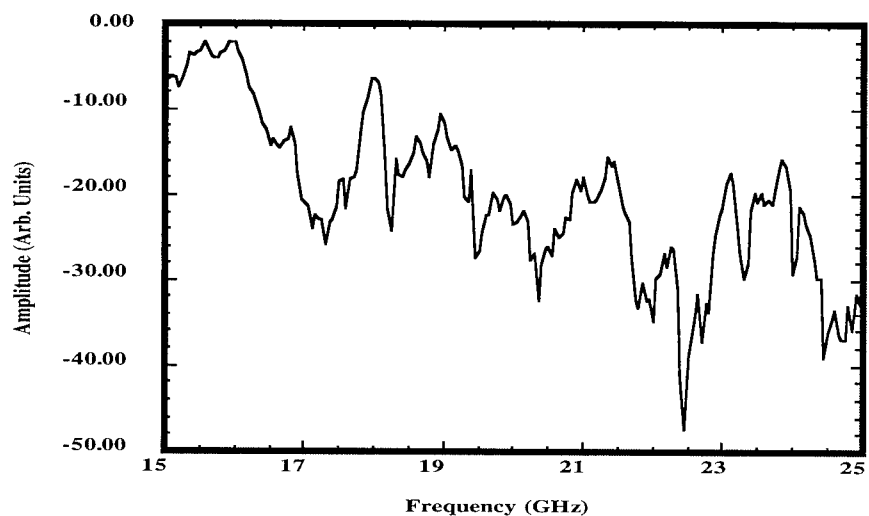


(a)

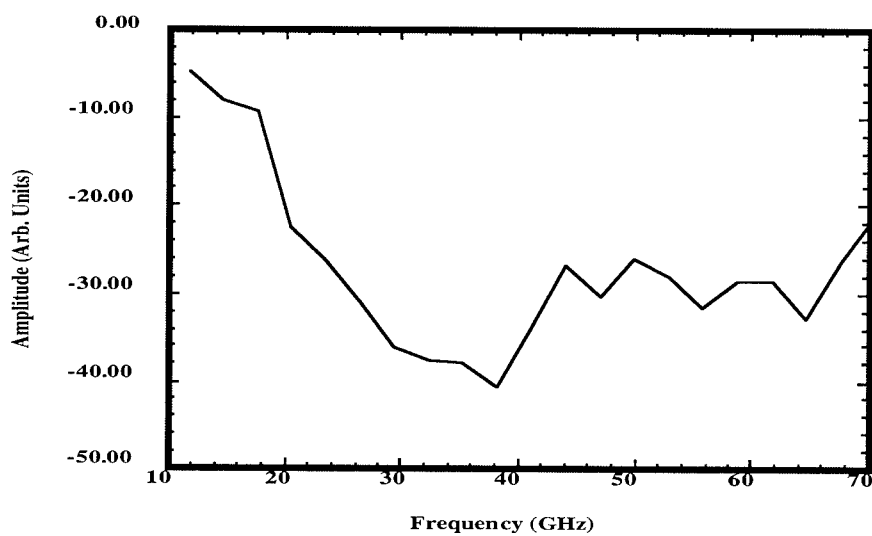


(b)

Figure 4. Transmission measurement of the photonic crystal at normal incidence. (a) Fourier transform of the time-domain data (shown in inset). The dip in frequency at 20 GHz corresponds to the stop band in Fig. 1. In addition the dip at 30 GHz corresponds to a higher order gap. (b) Direct comparison of the time-domain and the frequency-domain data. The points are the time-domain and the solid line is the frequency-domain. Good agreement is obtained within the resolution limit of the time-domain system.



(a)



(b)

Figure 5. Transmission measurement of the ultra-wideband (UWB) photonic crystal at normal incidence. (a) Continuous wave frequency-domain response of UWB crystal. (b). The transfer function obtained from the time-domain response of the UWB crystal. The transformed time-domain measurement gives the broadband response whereas the CW measurement gives the narrowband detailed frequency response.

one used in the past whereby the Fourier transform of the crystal measurement is divided by the Fourier transform of the reference pulse.⁶ This gives the frequency domain transfer function of the crystal and hence a direct comparison can be performed. The results are shown in Fig. 4(b). With the limited resolution of the time-domain measurements, the agreement between the frequency-domain and the time-domain is encouraging. However, in order to get better agreement, the resolution in the time-domain needs to be enhanced. Methods of resolution enhancement are currently being investigated

One application of the new fcc photonic crystal is to stack in tandem multiple, single-period photonic crystals to broaden the stop band, thereby creating an ultra-wideband (UWB) photonic crystal¹⁰. Figure 5(a) shows the CW frequency-domain response of a UWB photonic crystal containing one period each of three different fcc crystals. Figure 5(b) shows the time-domain waveform (shown in the inset) and its Fourier transform for the same UWB photonic crystal containing one period each of three different fcc crystals. While the limited frequency-domain results in Fig. 5(a) shows that the UWB stop band extends from 16 to 25 GHz, the time-domain data of Fig. 5(b) indicate that the stop-band extends well beyond 25 GHz. However, due to the limited resolution, it is unable to definitively resolve the stop bands of the component crystals.

In summary, measuring in the time domain allows a much broader band characterization of the photonic crystal compared to the CW frequency-domain measurement. By photoconductively switching planar antennas, short pulses of electromagnetic radiation were generated, detected, and used to perform time-domain measurements on photonic crystals. However, due to the finite time window, the resolution of the measurements was limited to 2.5 GHz. Therefore, the time-domain measurements are currently complementary to the high-resolution, but limited-bandwidth CW measurements taken with a network analyzer. The agreement between the direct comparison of the time-domain and frequency-domain show encouraging results within the resolution limit of the system. The resolution of the time-domain measurements can be enhanced by improvements in the antenna design (eliminating the back reflection from the contact pad) and by extending the scanned time delay of the system.

® LabVIEW is a registered trademark of National Instruments, Inc.

ACKNOWLEDGMENTS

This work was sponsored by the Department of the Air Force, in part through an AASERT grant from the Air Force Office of Scientific Research.

REFERENCES

1. E. Yablonovitch and T.J. Gmitter, "Photonic Band Structure: The Face-Centered-Cubic Case," *Phys. Rev. Lett.*, vol. 63, no. 18, Oct. 30, 1989.
2. E. Yablonovitch, T.J. Gmitter and K.M. Leung, "Photonic Band Structure: The Face-Centered-Cubic Case Employing Nonspherical Atoms," *Phys. Rev. Lett.*, vol. 67, no. 17, Oct. 21, 1991.
3. E.R. Brown, K. Agi, C.D. Dill, C.D. Parker and K.J. Malloy, "A New Face-Centered-Cubic Crystal for Microwave and Millimeter Wave Applications," to appear in *Opt. Microwave Tech. Lett.*, Dec. 15, 1994.
4. G. Arjavalingam, Y. Pastol, J.-M. Halbout and G.V. Kopcsay, "Broadband Microwave Measurements with Transient Radiation from Optoelectronically Pulsed Antennas," *IEEE Trans. Microwave Theory Tech.*, vol. 38, no. 5, May 1990.
5. A.P. DeFonzo and C.R. Lutz, "Optoelectronic Transmission and Reception of Ultrashort Electrical Pulses," *Appl. Phys. Lett.*, vol. 51, July 1987.
6. L. Carin and K. Agi, "Ultra-Wideband Transient Microwave Scattering Measurements using Optoelectronically Switched Antennas," *IEEE Trans. Microwave Theory Tech.*, vol. 41, no. 2, Feb. 1993.
7. Measured FWHM value using reflectivity (pump/probe) experiment.
8. Y. Pastol, G. Arjavalingam, J.-M. Halbout and G.V. Kopcsay, "Characterization of an Optoelectronically Pulsed Broadband Microwave Antenna," *Electron. Lett.*, vol. 24, no. 21, Oct. 13, 1988.
9. E. Özbay, E. Michel, G. Tuttle, R. Bismas, K.M. Ho, J. Bostak and D.M. Bloom, "Terahertz Spectroscopy of Three-Dimensional Photonic Crystals," *Opt. Lett.*, vol. 19, no. 15, Aug. 1, 1994.
10. K. Agi, E.R. Brown, O.B. McMahon, C. Dill III and K.J. Malloy, "Design of Ultra-Wideband Photonic Crystals for Broadband Antenna Applications," submitted to *Electron. Lett.*

MICROPARTICLE PHOTONICS: FIBER OPTIC EXCITATION OF MDR's

S. Arnold¹, A. Serpengüzel¹, and G. Griffel²

¹ Microparticle Photophysics Laboratory(MP³L), and

² Department of Electrical Engineering, Polytechnic University
6 Metrotech Center, Brooklyn, N.Y. 11201

INTRODUCTION

A great deal of research has established that spherical microparticles produced on Earth and in Space¹ act as extremely high Q ($\sim 10^8$) microresonators.² This property has recently led to the first room temperature spectral hole-burning memory which utilizes an assembly of dielectric polymer microspheres of random size.^{3,4} Aside from this application of solid particles, the number of nonlinear phenomena which have been demonstrated on liquid droplets such as lasing, third harmonic generation, stimulated Brillouin scattering, stimulated Raman scattering, etc.⁵ provide sufficient motivation for extending these studies to solid particles on surfaces. The wave geometry responsible for these high Q states (Morphological Dependent Resonances, MDR's) is of a whispering gallery type, so that the spherical resonator is surrounded by an evanescent tail. Since single mode optical fibers have a nearly Gaussian intensity profile which extends well beyond the core, one might guess that one could excite such a resonance with a particle positioned to the side of such a fiber. In what follows we present the first experiments on the excitation of a microsphere MDR's by a guided wave in an optical fiber.

MODEL AND RESULTS

In order to understand the interaction of a Gaussian beam with a spherical microparticle we must go beyond plane wave (Lorentz-Mie) theory.⁶ In its place we utilize a more comprehensive model allowing us to shift the center of the incident beam to the exterior of the microparticle.⁷ This in turn restricts the partial waves which can be excited to resonant modes having large angular momentum quantum numbers, in accordance with the principle of localization.⁸ The prediction of the model for near 90° TE scattering, from a particle of 15 μm radius, separated from a 4 μm diameter optical fiber is shown in Fig.1(a).

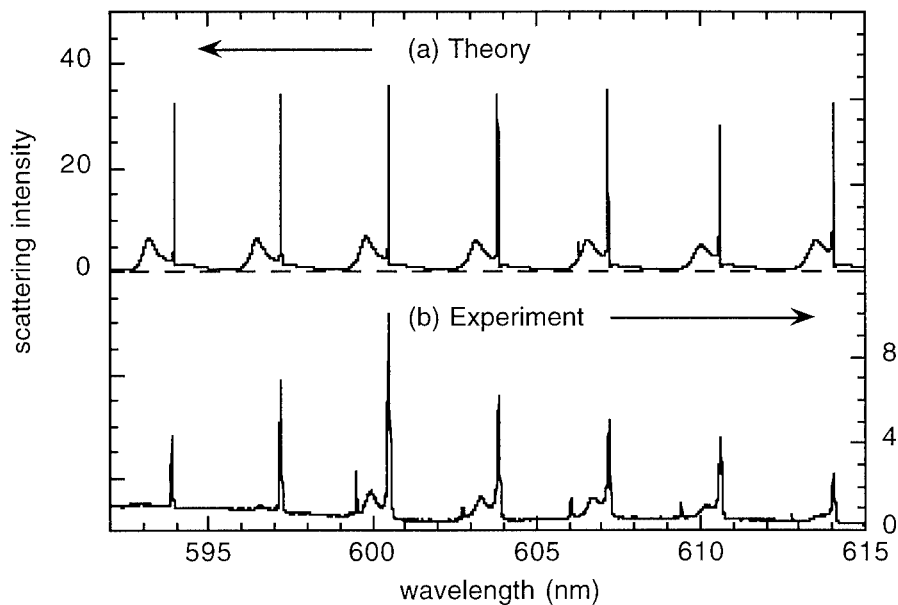


Figure 1. (a) Theoretical and (b) experimental elastic scattering spectra from a microparticle excited by a single-mode optical fiber.

Experiments were carried out on a 15 μm radius particle separated from an optical fiber in keeping with the calculations in Fig.1(a). The experimental results are shown in Fig. 1(b). The experimental set-up is shown in Fig.2 (using detector DT). Comparison between our experiment and the calculations is compelling. Unlike the results of Mie theory for which a number of small angular momentum modes produce significant scattering between MDR's, scattering in these regions in our experiments is insignificant, in agreement with the principle of localization.

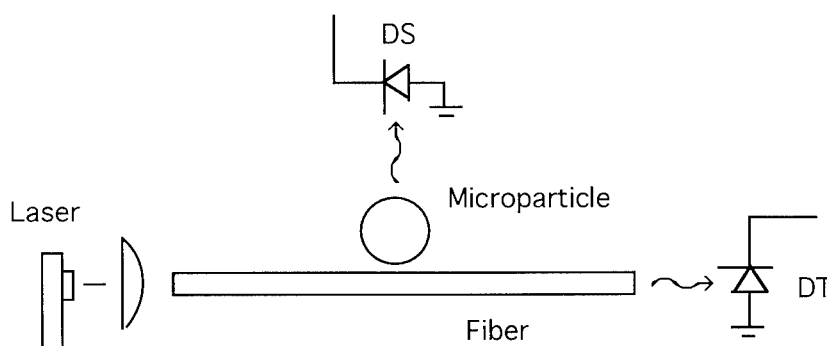


Figure 2. Schematic of the experimental setup.

To avoid suspending a particle in air, particles were also rested on a fiber half-coupler with the cladding shaved so as to space the particle from a single mode fiber by 0.7 μm . In

this configuration one can change the medium surrounding the particle by utilizing various liquid dielectrics (water, oil, etc.). Narrow resonances with linewidths narrower than the dye laser ($< 0.025\text{nm}$) were easily observed using this configuration.⁹

CONCLUSION AND DISCUSSION

We have demonstrated that one can couple energy between a single mode fiber and the high Q Morphological Dependent Resonances of a microsphere. The simplicity of this system has potential for becoming a building block in dispersive microphotonics. The basic physics underlying our approach may be considered a harbinger for coupling semiconductor lasers to spherical μ -resonators. One can even imagine line narrowing semiconductor lasers by using such a scheme.

ACKNOWLEDGMENT

We are grateful for the research support from the AFOSR (Grant#F49620-94-0195).

REFERENCES

1. T.R. Lettieri, A.W. Hartman, G.G. Hembree, and E. Marx, J. Coll. Int. Sci. 13, 1550(1989).
2. A. Ashkin and J.M. Dziedzic, Phys. Rev. Lett. 38 1351(1977).
3. S. Arnold, C.T. Liu, W.B. Whitten and J.M. Ramsey, Opt. Lett. 16, 420(1991).
4. S. Arnold, J. Camunale, W.B. Whitten, J.M. Ramsey, and K.A. Fuller, JOSA B 9, 819(1992).
5. Optical Effects Associated with Small Particles, Eds. P.W. Barber and R.K. Chang, (World Scientific Publishing, 1988).
6. C.F. Bohren and D.R. Huffman, Absorption and Scattering of Light by Small Particles, (Wiley, 1983).
7. see for example, G. Gouesbet and J.A. Lock, JOSA A 11, 1(1994).
8. H.C. van de Hulst, Light Scattering by Small Particles, (Dover, 1981), p.208
9. A. Serpenguzel, S. Arnold and G. Griffel, Opt. Lett. (In Press, 1995).

INDEX

- Acoustooptic, 237, 249
Adiabatic amplification, 416
Air bridges, 477
Anti-guiding, 9

Baseband devices, 250
Beam pattern generators, 333
Beam propagation method (BPM), 156, 187, 195, 221, 382, 424, 435
Beam splitter, 448
Blue-green lasers, 125, 276
Bragg cells, 237, 242
Bragg grating, 321
Broad area lasers, 45
Burstein-Moss effect, 280

Cascading, 371
Cavity enhancement, 464
Cerenkov regime, 381
Channel-dropping filter, 17, 21, 299
Computer aided design, 445
Coupled mode analysis, 84, 188, 382, 424

Delayed self-homodyne, 106
Digital optical links, 287
Directional coupler, 139, 213
Disk resonators, 464
Displacement sensor, 355
Distributed Bragg reflector (DBR), 46, 105, 270
Distributed feedback (DFB), 299, 399, 477
Distributed feedback/Fabry-Perot (DFB/FP), 75
Distributed feedback (DFB) laser, 3, 83, 93, 103, 334
Distributed feedback resonator, 306
Dual-undulation gratings, 342
DuFort-Frankel approximation, 436

Effective index method, 156, 221
Erbium-doped fiber amplifiers, 3
Exciton shift, 292
Excitonic gain, 128

Fabry-Perot cavities, 269, 288, 463
Face-centered-cubic (fcc), 485
Fermi's golden rule, 465
Fermi-Dirac, 128
Fiber half-coupler, 496
Fiber optic gyros (FOG), 6
Field sensor, 35
Field-induced mode beating, 13
Finite element, 213, 455
Finite-difference beam propagation methods, 429, 435
Finite-difference time domain, 423
FM response, 89, 93
Focusing function, 357
Fourier transform, 295
Franz-Keldysh effect, 139, 280
Frequency conversion, 407
Frequency shifters, 249

GaAs, 177, 197, 257

Gain coupled, 93
 Gas sensing, 115
 Gated-sinewave method, 111
 Gaussian beam, 338
 Grating coupling, 333
 Grating-assisted directional coupler, 84, 366
 Group velocity, 238
 Guide/antiguide structure, 197

 Impurity induced disordering (IID), 205
 InGaAs-GaAs, 269, 273
 Integrated photodiodes, 355
 Inverse problem, 321
 Ion implantation, 10
 Ion-exchange, 163, 167, 221

 Kerr media, 391, 415
 KTP, 313

 $\lambda/4$ -shifted device, 299, 403, 477
 Laser amplifier, 451
 Laser array, 49
 Laser-fiber coupling, 67
 Lead-salt, 115
 Light-emitting diodes (LEDs), 463
 Linewidth reduction, 105
 Lithium niobate (LiNbO₃), 4, 5, 9, 17, 35, 215, 231, 315, 375, 407
 Lock-in amplifier, 490
 Logic gates, 177

 Mach Zehnder, 32, 35, 139, 187, 258, 288, 441
 Magneto-optic frequency shifter, 249
 Magneto-optic Bragg cell, 237, 249
 Magnetostatic waves, 237
 Master-oscillator power amplifiers (MOPAs), 45, 46, 105
 MESFET, 257
 Microcavities, 463
 Microparticle photonics, 495
 Microstrip transducers, 238

 Mie theory, 496
 MOCVD, 418
 Modal representations, 363
 Mode beating, 9
 Mode expander laser diode, 68
 Mode transformers, 140
 Molecular beam epitaxy (MBE), 50, 134, 257
 Morphological dependent resonances (MDR), 495
 Multimode waveguides, 143

 N-i-p-i, 258
 Natural emission spectrum, 466
 Nonlinear DFB, 399
 Nonlinear effective index method, 188
 Nonlinear Mach-Zehnder Interferometer, 187
 Nonlinear optical waveguides, 455
 Nonlinear phase shifts, 372, 381
 Nonlinear Schrödinger equation, 391

 Optical frequency mixing, 407
 Optical interconnects, 177, 472
 Optical loop mirror, 25
 Optical transistor, 376
 Optoelectronic integrated circuits (OEICS), 257, 445

 P-i-n, 258
 Packet-switched networks, 25
 Parametric amplification, 407
 Passband devices, 250
 Periodic waveguide, 295, 363
 Periodically segmented waveguides, 313
 Phase modulation, 279
 Photon lifetime, 466
 Photonic band gap, 477
 Photonic crystal, 485
 Photonic switching, 455
 Plasma effect, 280
 Polarization conversion, 19, 321
 Polymer waveguide, 333
 Power splitters, 155
 Proton exchange, 10

Quantum confined Stark effect (QCSE), 258, 269
 Quantum-well lasers, 3, 67, 126, 133, 269
 Radiation leakage, 363
 Reactive ion etching (RIE), 197
 Reflection filter, 300
 Relative intensity noise (RIN), 59, 103
 Relaxation method, 18
 Router components, 297
 Second harmonic generation (SHG), 313, 407
 Self-focusing nonlinearity, 394
 Side mode suppression ratio (SMSR), 93, 103
 Solitons, 377, 455, 459
 Spatial and temporal solitons, 377, 393, 415
 Spherical resonators, 464
 Split filter analysis, 270
 Strain-induced waveguides, 17
 Strained quantum well lasers, 125
 Strained-layer superlattices, 205
 Surface acoustic waves, 250
 Surface polarizability, 281
 Surface-emitting semiconductor lasers, 75
 Switch-arrays, 140
 Tapered layer, 418
 TE-TM conversion, 295, 341
 Terahertz demultiplexer, 25
 Ti-diffusion, 10
 Transmission-line method, 83, 303
 Traveling wave modulators, 231
 Tunable filters, 17
 Ultrashort pulse propagation, 391
 Variable angle spectroscopic ellipsometry
 (VASE), 269
 Vertical cavity surface emitting laser (VCSEL),
 49, 59, 473
 Waveguide grating polarizer, 341
 Waveguide splitters, 143
 Waveguide switches, 140
 Wavelength filters, 167
 Wavelength-flattened couplers, 155
 WDM, 17, 297